I. R. IRAN

ISSN: 1728-144X
e-ISSN: 1735-9244

International Journal of Engineering

Journal Homepage: www.ije.ir

MERC

TRANSACTIONS B: APPLICATIONS

Volume 35, Number 02, February 2022

Materials and Energy Research Center

In the Name of God

INTERNATIONAL JOURNAL OF ENGINEERING
Transactions A: Basics

International **J**ournal of **E**ngineering *Transactions A: Basics* (ISSN 1728-1431) (EISSN 1735-9244)
International **J**ournal of **E**ngineering *Transactions B: Applications* (ISSN 1728-144X) (EISSN 1735-9244)
International **J**ournal of **E**ngineering *Transactions C: Aspects* (ISSN 2423-7167) (EISSN 1735-9244)
Web Sites: www.ije.ir & www.ijeir.info E-mails: ije.editor8@gmail.com, Tel: (+9821) 88771578, Fax: (+9821) 88773352
Materials and Energy Research Center (MERC)

ISSN: 1728-144X, e-ISSN: 1735-9244

International Journal of Engineering, Volume 35, Number 02, February 2022

CONTENTS

Transactions B: Applications

ISSN: 1728-144X, e-ISSN: 1735-9244

International Journal of Engineering, Volume 35, Number 02, February 2022

IJE TRANSACTIONS B: Applications Vol. 35, No. 02, (February 2022) 258- 275

International Journal of Engineering

Journal Homepage: www.ije.ir

Operating Room Scheduling Optimization Based on a Fuzzy Uncertainty Approach and Metaheuristic Algorithms

P. Maghzi[a], M. Mohammadi*[a], S. H. R. Pasandideh[a], B. Naderi[b]

[a] *Department of Industrial Engineering, Faculty of Engineering, Kharazmi University, Tehran, Iran*
[b] *Department of Mechanical, Automotive and Materials, Faculty of Engineering, University of Windsor, Windsor, Canada*

PAPER INFO

Paper history:
Received 03 August 2021
Received in revised form 27 September 2021
Accepted 04 October 2021

Keywords:
Fuzzy Uncertainty Approach
Medical Center Planning
Medical Staff and Equipment Optimization
Metaheuristic Algorithm
Operating Room Planning
Scheduling

ABSTRACT

Today, planning and scheduling problems are the most significant issues in the world and make a great impact on improving organizational productivity and serving systems such as medical and healthcare providers. Since operating room planning is a major problem in healthcare organizations, the optimization of medical staff and equipment plays an essential role. Thus, this study presents a multi-objective mathematical model with a new categorization (preoperative, intraoperative, and postoperative) to minimize operating room scheduling and the risk of using equipment. Time constraints in healthcare systems and medical equipment limited capacity are the most significant considered limitation in the present study. In this regard, since the duration of patient preparation and implementation of treatment processes occur in three states of optimistic, pessimistic, and normal, the introduced parameters are examined relying on a fuzzy uncertainty analysis of the problem. Hence, the model is measured in a real numerical solution sample in a medical center to evaluate and confirm the proposed mathematical model. Then, two meta-heuristic algorithms (NRGA and NSGAII) are implemented on the mathematical model to analyze the proposed model. Finally, the research results indicate that the NSGA-II is more efficient in the operating room scheduling problem.

doi: *10.5829/ije.2022.35.02b.01*

1. INTRODUCTION

Nowadays, changes in people's lifestyles, socio-cultural structures, diseases patterns, people's health requirements along with increasing growth of population, have proved a variety of problems in the provision of health services and facilities. The rapid rise in healthcare costs is considerable and the main problem of medical and healthcare systems in various countries, even the most developed countries in the world is how to control the costs. Accordingly, healthcare organizations are trying to reduce healthcare costs while improving the quality of their services. Considering the healthcare system condition in the current era, it has been undergoing major changes and developments such as rising numbers of patients, aging population, and increasing number of the elderly people [1]. Therefore, the investigation of efficient strategic and operational decisions by healthcare executives is of great significance for costing and risk perspectives in order to minimize the expected costs [2]. Taking into account, the technical limitations of the human resources available in medical centers [3], a large proportion of patients cannot immediately be given treatment [4], and consequently, the longer patients wait for treatment, the less satisfaction will be obtained, and thus, the more lengthy treatment process will move ahead [5]. This is while other medical centers, especially public hospitals face funding crisis, shortage of medical staff, and appropriate equipment [6]. These factors have caused medical centers to improve efficiency performance and reduce healthcare costs [7]. Considering the obtained information, more than 70% of medical referrals are allocated to surgical operations, additionally, more than 15% of wasted time in medical

*Corresponding Author Institutional Email: Mohammadi@khu.ac.ir (M. Mohammadi)

Please cite this article as: P. Maghzi, M. Mohammadi, S. H. R. Pasandideh, B. Naderi, Operating Room Scheduling Optimization Based on a Fuzzy Uncertainty Approach and Metaheuristic Algorithms, ***International Journal of Engineering, Transactions B: Applications*** Vol. 35, No. 02, (2022) 258- 275

centers is related to operating rooms [8]. It verifies the importance of operating room and its proper utilization [9, 10]. The operating room, especially surgical room has a particular sensitivity [11] and is considered as the most vital unit in medical centers [12]. Therefore, the smallest defect or non-compliance with a specific planning and pre-determined standards will cause problems [13]. According to the above-mentioned discussion, operating room can be likened to medical center engine [14]. Operating rooms affect other wards of medical centers, as well as having repercussions on medical staff. So, the increasingly growing demand for surgeries and resource constraints have caused medical centers to efficiently manage their resources, especially expensive resources such as operating rooms and special medical staff. Scheduling surgical operations, including sequencing surgeries, allocating resources, and determining start times, is a complicated task for the medical center manager [15]. The problem of operating room planning and scheduling seeks to propose a solution to reduce costs, increase the efficiency of operating room utilization, and attain other related goals [16]. Moreover, one of the main applications of operations research in health systems management is the improvement of resources allocation mechanism [17]. Therefore, staff scheduling, including nurses and doctors, is regarded as one of the most important and sensitive challenges of medical centers. The importance of medical staff's quality of work has caused scheduling-related problems, preserving the interests of patients and the medical center along with creating staff satisfaction and paying attention to their demands in scheduling that are some of the main points [18]. Some of healthcare operational challenges such as staff scheduling and surgical operation scheduling in operating rooms are highly complicated [19]. The proper scheduling of surgical operations in operating room can reduce idle time, personnel overtime costs, and fixed costs of operating room equipment [20]. Beside these achievements, the proper scheduling will bring patients higher level of healthcare facilities by reducing patient wait time and providing rapid access to emergency medical services for emergency patients [21]. Uncertainties level existing in operating room scheduling, plays an important role in increasing system efficiency and reducing costs. Therefore, it has become difficult to address operating room planning and scheduling [22]. Considering the above-mentioned issues, addressing the uncertainties in operating room scheduling and planning is the most important factor affecting the optimization of the system.

The present study investigates a multi-objective mathematical model by minimizing operating room scheduling based on the MAKESPAN model by considering the problems with earliness/tardiness issues, which occur in the real problem. Evaluating earliness/tardiness in the operation process is critical because the activities before and after the operation are highly significant in operating room scheduling to the extent that the slightest inconsistency between the processes leads to patient death. As a result, this study aims to minimize earliness, which causes inconsistency in recovery room (postoperative units), and tardiness which causes overlap in treatment processes after the operation is done based on the executed plan. In addition, this study, seeks to minimize the risk of performing treatment processes on medical equipment in a two-objective-function model. For instance, if a patient requires a special surgery, the equipment which increases the risk of treatment will be minimized and replaced by a less risky equipment. Accordingly, since the treatment processes can be predicted in three states of optimistic, pessimistic, and normal, in this study triangular fuzzy uncertainty is used to evaluate and estimate the parameters of the mathematical model to integrate the modeling condition with operating room problem in reality. Since the proposed mathematical model is NP-HARD type, two metaheuristic algorithms of NRGA and NSGA-II are evaluated through epsilon-constraint method to confirm and solve the mathematical model in the studies case, and evaluate the validity of the proposed model.

2. LITERATURE REVIEW

Operating room planning is of great importance in medical centers for two reasons. First, the precise scheduling in operating room ensures timely and accurate follow-up treatment, which quickens patients' medical process period. Second, medical administrators always emphasize the optimal use of operating room equipment due to the high cost of such equipment. Thus, operating room planning and scheduling is a strategic concept and key factor to manage medical centers.

In this section different strategies of operating room scheduling and planning such as theoretical foundations and research background, levels of operating room planning and scheduling (strategic level, tactical level, and operational planning level) are discussed.

Today, there is a rapid growth in life expectancy in developed countries, leading to an increase in the population of the elderly [23]. Therefore, it should be noted that the problem of operating room planning and scheduling seeks to propose a solution to reduce costs, improve operating room efficiency, and attain other goals to fulfill health centers' expectations [24]. Operating room planning and scheduling is classified into long-term, mid-term, and short-term solutions at the strategic, tactical, and operational levels [10]. Strategic planning includes long-term decisions, which are usually made on an annual basis [25]. The mid-term decisions are made at tactical level. The two mentioned levels are provided with master surgical scheduling (MSS). At the operational planning level, decisions are made on daily

and weekly basis. In daily scheduling, the sequence of operations in each operation room is determined. There are various criteria for this level of planning including the preferences of surgeons, resource availability, maximum admission capacity, operating room utilization and efficiency, and reducing overtime hours [26]. Operating room planning has begun in 1935. Research studies on this subject have had an upward trend since 1960's that many researchers have joined the healthcare scheduling community [27]. These research studies also continued their incremental trend in the 1970's [28]. Since 2000 onward, the operating room planning has gradually developed and achieved remarkable accomplishments including multi-level operating room planning, presenting different strategies for operating room scheduling, generating more effective solutions based on different methods, which have been added to the operating room planning over recent years. Testi et al. [29] proposed a hierarchical three-phase approach for operating room weekly scheduling. The models aim to maximize the specialists' preferences and profit motives. In another research, overtime issues, ward beds and ICU were also considered. The model was in the definitive state that was solved by a heuristic algorithm [30]. Banditori et al. [31] proposed a model, by which the patients who are on the waiting list of the hospital can be classified in identical surgery groups based on the resources. The objective function in this model is composed of three parts. This model proposed a simulation based-optimization method with real data. Lappas and Gounaris [32] proposed a multi-stage robust optimization method in which uncertainties during scheduling decision making are considered. Jittamai and Kangwansura [33] presented a patient admission scheduling model that improves the operating room efficiency by reducing resource losses. The model considers the existing uncertainties in demand, such as the stay duration, emergency admissions, and non-referral of patients. Al-Refaie et al. [34] developed three optimization models to optimize operating room scheduling during unexpected events and adjust emergency operations to a determined schedule. The first model schedules the emergency patients to the newly established rooms, while the second model aims to allocate emergency patients to unused and empty rooms. The third model specifies emergency patients and emergency units based on the rooms with the freest condition. Abedini et al. [35] presented a model for minimizing block time in preoperative and postoperative care units. In addition, this study deals with an integer model with definitive data for this problem and evaluates the model efficiency under different conditions and variable input of patients by means of simulation. In another study, Abtahi et al. [36] investigated the scheduling problem of prioritized outpatients in a medical center. The objective function of the problem is to minimize the total length of time the patients spend in the medical center. Additionally, a heuristic algorithm was proposed for medium-sized problems. The computational results indicate an increase in the patient satisfaction level, as well as the improvement of the efficiency and productivity of the medical center. Yazdi et al. [15] proposed a mathematical model for the problem of scheduling elective and emergency surgeries. This model considers surgeries as multi-activities projects. They implemented the Break-in-Moments (BIMs) technique in this structure and observed that this method is capable of reducing the waiting time in emergency rooms to be included into the schedule without specifically assigning any operating room to emergencies. Therefore, this method establishes a balance between the efficient use of operating rooms and taking responsibility for emergency surgeries. Khaniyev et al. [37] provided a new mathematical model for calculating the total amount of patient waiting time, operating room idle time, and overtime. The presented model improves the mean of performance gap up to 1.22% and the worst average gap up to 2.77%. Abdeljaouad et al. [38] introduced daily operation planning in hospitals based on a multi-objective mathematical model. The studied problem includes a set of operations, which should be planned in similar operating rooms. Such operations have no specific duration, so that they require adjustment activities before and after operation that are assigned to the surgeons who perform the operation. This study aims to introduce the best sequence of operations in each room to optimize the start time and waiting time for surgeons. Mousavi and Ebrahimnejad [39] presented the problem of operating room scheduling at tactical and operational levels of decision-making by considering the processes before and after the operation. For this purpose, a multi-objective mathematical programming model was proposed for scheduling the specialized operations considering the uncertainty of the operation duration, length of stay, and emergency needs. Finally, a two-step meta-heuristic algorithm was created to solve the large-scale cases. Zhou and Yue [40] introduced a common selection and scheduling problem between random service time and non-display in multi-stage service systems. Thus, the total expected costs for patient waiting time and service providers' idle time were minimized in a few stages, and a two-stage random optimization program and a standard Benders decomposition algorithm were developed. Finally, it was found that the efficiency of the algorithm improved by 6%. Sun et al. [41] modeled the problem of proper appointment scheduling in an emergency hospital system and analyzed the model using simulation algorithm. It was found that block scheduling improved by 11.6%. Due to the multi-objective mathematical model, medical centers could find solutions to accurately reflect their appropriate transactions.

In the final section of literature review, besides taking account of the researches in the field of health

management and medical centers scheduling, the researches of recent years are summarized and reviewed.

Health system management in the world involves different subjects such as supply chain management [42, 43], data management [44, 45, 46], risk management [47], routing and scheduling management [48, 49] and home healthcare management [50, 51, 52].

Therefore, as mentioned above, the present study is designated to the scheduling of medical centers, especially operating rooms. Thus, in this section before evaluating the research gap, the relevant studies in recent years are mentioned. Naderi et al. [52] in their study included a new and exact solution method with the aim of integrating personnel, allocating, routing, planning and scheduling a home care center under uncertain conditions, modelling and problem solving with the aim of creating a weekly program with the presence of a special mathematical structure in the model, as well as developing Banders decomposition algorithm. The results of solving the model and the problem indicate the optimization and efficient results. In another study, they solved the generalized operating room planning and scheduling (GORPS) problem in a hospital in Toronto with the aim of creating a weekly schedule and the primary goal of reducing fixed and overtime costs by modeling and Banders algorithm. Regarding the outbreak of COVID-19, the intended problem was highly optimal [53], and in the next study, they presented the integrated planning and scheduling of the operating room with the development of the Benders solution method for maximizing the total planned surgery time that the efficiency of it was properly validated [54]. Tsai et al. [55] developed a stochastic optimization model for the operating room planning by considering a two-step integer model in uncertain conditions. In addition, they proposed two stochastic algorithms for this problem. In addition, the experimental results indicated that the proposed algorithms are more desirable compared to the present methods. Lin et al. [56] developed an operating room scheduling model for preparing a weekly surgery plan with an open planning strategy aimed at reducing cost. In addition, they developed two heuristic algorithms and finally developed the ant colony algorithm. Furthermore, the results of computational solution indicated that the ant colony method is highly efficient in large-scale problems. Bovim et al. [57] proposed the development of an MSS scheduling model and a simulation-optimization method for evaluating emergency patients with different clinical scenarios. Zhu et al. [58] presented a dynamic operating room planning problem for reducing total costs and developing a mathematical model. In addition, two heuristic algorithms were developed. Ultimately, some computational tests were performed to test the efficiency, stability, and convergence rate of the proposed algorithm. The results of comparison with other main algorithms indicated that their proposed algorithm gives a better performance than the compared algorithms. Park et al. [59] evaluated the efficient operating room scheduling for cost optimization. The scheduling model improved the local treatment processes by 120%, which was a great improvement in defined processes. The proposed model was solved with the branch and bound algorithm. Roshanaei et al. [60] addressed the operating room scheduling problem using a MIP mathematical model that select patients for the treatment process. They developed heuristic approach to solve the proposed NP-HARD problem. Roshanaei et al. [61] formulated a deterministic four-stage model based on the Benders decomposition algorithm in order to solve the operating room scheduling problem. They showed that in the developed four-stage model, Benders algorithm reduced the computational time by 11%.

As discussed in the literature, the research gap observed in these studies is the limitation of capacity in medical staff and equipment, as well as the availability of medical staff in unlimited conditions. Thus, in the present study, the limitation of resources (medical staff and equipment) is considered and a new mathematical model is developed. As mentioned in the introduction, a new fuzzy uncertainty model is evaluated in this study. In addition, an exact solution method (epsilon-constraint) along with two meta-heuristic algorithms of NRGA and NSGA-II are used in order to validate the mathematical model and finally the evaluation of the mathematical model is presented.

3. MATHEMATICAL MODELING

3. 1. Statement of the Problem In this section, the problem and the new mathematical model are proposed. The proposed model is meant to schedule the patient arrival and departure in different wards of the medical center such as operating room, pre-operative and post-operative sections. Therefore, the sequence of providing healthcare services in different stages and the regular queuing system are considered. Besides, in this study, the proposed formulation is established based upon the research by Naderi et al. [62]. In the codified model, the conditions for receiving services from medical personnel are considered in a way that at each stage the patient is visited while receiving required services all at once. In this way, the operating rooms and wards of a medical center are scheduled on a daily basis. Effective scheduling of executive activities is an important subject in the research studies that has been neglected due to the uncertainty of the effective parameters in the mathematical model. So, using fuzzy approach for the mathematical model, the challenge ahead of the scheduling tasks is addressed. In this approach, the patient preparation and the time duration to present services are represented by triangular fuzzy membership functions. Using this new methodology in this study, the

fuzzy uncertainty parameters are definite. Finally, since the introduced mathematical model is of NP-HARD type, two metaheuristic algorithms of NRGA and NSGA-II are evaluated through epsilon-constraint method to confirm, solve, and evaluate the validity of the proposed model.

3. 2. Notation

Indices(Sets & index)	
I	Set of patients
E(i)	Set of common patients
W(i)	Set of special patients
J	Set of stages
K	Set of equipment
P	Set of medical center personnel
i & i′	Patient index
j & j′	Stage index
k & k′	Equipment index
p	Medical center personnel index
Parameters	
ST_{ijk}	Time to prepare patient i at stage j on equipment k
RSK_{ijk}	Risk to service to patient i at stage j on equipment k
SST_{ijk}	The patient i enter time at stage j on equipment k
PT_{ijk}	Time to service to patient i at stage j on equipment k
PPT_{pijk}	Time to providing health service by medical personnel p for patient i at stage j on equipment k
TW_i	The waiting time of patient i from operation time to recovery
Variables	
C_{ijk}	End time of service process to patient i at stage j on equipment k
Y_{ijk}	If medical personnel p provides service on equipment k for patient i at stage j, 1, otherwise it is zero
Q_{pijk}	If medical center p provides service on equipment k for patient i at stage j it is 1, otherwise it is zero
$X_{ii'jk}$	If patient i after patient i′ uses equipment k at stage j it is 1, otherwise it is zero

3. 3. Mathematical Model

$$\text{MIN } C1 = (\sum_i(\text{MAX}\sum_i\sum_k C_{ijk} - SST_{ij})) \quad (1)$$

$$\text{MIN } C2 = \sum_i\sum_j\sum_k Y_{ijk} * RSK_{ijk} \quad (2)$$

$$\sum_{\substack{i\in I\\ i\neq i1}}\sum_{i'\in I} X_{ii'jk} \leq 1 \quad \forall j,k \quad (3)$$

$$\sum_{k\in k_{ij}} y_{ijk} = 1 \quad \forall i,j \quad (4)$$

$$\sum_{k\in k_{ij}} Q_{Pijk} = 1 \quad \forall i,j,p \quad (5)$$

$$C_{ijk} \leq M * y_{ijk} \quad \forall i,j,k \in k_{ij} \quad (6)$$

$$C_{ijk} \leq M * y_{ijk} \quad \forall i,j,k \in k_{ij} \quad (7)$$

$$C_{ijk} \geq \sum_{k'} C_{ij'k'} + ST_{ijk} + SST_{ij} + PT_{ijk} + \sum_p PPT_{pijk} - M(1 - Y_{ijk}) \quad i \in W(i) \quad (8)$$

$$C_{ijk} \geq \sum_{k'} C_{ij'k'} + ST_{ijk} + SST_{ij} + PT_{ijk} + \sum_p PPT_{pijk} - M(1 - Y_{ijk}) \quad i \in E(i), j \neq s_3 \quad (9)$$

$$C_{ijk} \geq Y_{ijk} * (ST_{ijk} + SST_{ij} + PT_{ijk} + \sum_P PPT_{pijk}) \quad \forall i,j,p, \ k \in k_{ij} \quad (10)$$

$$\sum_k C_{ijk} + \sum_k C_{ij'k} \leq TW_i \quad \forall i \in W(i), j = s_2, j' = s_3 \quad (11)$$

$$\sum_k C_{ijk} + \sum_k C_{ij'k} \leq TW_i \quad \forall i \in E(i), j = s_2, j' = s_3 \quad (12)$$

$$X_{ii'jk} + X_{i'ijk} \leq 1 \quad \forall i, i < i', j, k \quad (13)$$

$$2X_{ii'jk} \leq Y_{ijk} + Y_{i'jk} \quad \forall i, i < i', j, k \quad (14)$$

$$Y_{ijk} + Y_{i'jk} \leq X_{ii'jk} + X_{i'ijk} + 1 \quad \forall i, i < i', j, k \quad (15)$$

$$C_{ijk} \geq C_{i'jk} + ST_{ijk} + SST_{ij} + PT_{ijk} - M * X_{i'ijk} - 2M + MY_{ijk} + MY_{i'jk} \quad \forall k,j,i,i', i < i' \quad (16)$$

$$C_{i'jk} \geq C_{ijk} + ST_{i'jk} + SST_{ij} + PT_{i'jk} - M * X_{ii'jk} - 2M + MY_{ijk} + MY_{i'jk} \ \forall k,j,i,i', i < i' \quad (17)$$

$$\text{MAX}\sum_j\sum_k C_{ijk} = t_i \quad t_i \geq \text{MAX}\sum_j\sum_k C_{ijk} - SST_{ij} \quad (18)$$

According to Equation (1), the first objective function of the problem is to minimize patient waiting time in all stages of medical center wards. On the basis of Equation (2), the second objective function is to minimize the risk of using medical equipment. Constraint (3) states that if both patient i and patient i' are in a similar condition, one of the patients enters the stage of receiving treatment process, while the other patient stays in the queue. Constraint (4) states that according to the patient information table defined upon the patient arrival, each patient should pass all the prescribed stages. To put it differently, the patients cannot skip the procedures. Constraint (5) states that in accordance with a pre-considered procedure, as soon as the patient is registered, the patient certainly receives treatment process. Constraint (6) states that there is a relationship between the time of receiving treatment and its binary variable. Constraint (7) states that if the patient receives treatment at each stage, then the corresponding binary variable related to the medical center personnel will get a value. Constraint (8) states that the end of receiving treatment for each patient includes the time of receiving treatment in the previous stages, the time of patient preparation at that stage, the time of receiving treatment using medical equipment, and the time of receiving treatment from personnel in addition to the final condition that the patient

needs services and personnel at that stage. Constraint (9) states that the end time of receiving a service for each common patient includes the time of receiving services in the previous stages (except recovery stage), the time of patient preparation at that stage, the time of receiving services from equipment, and the time of receiving services from personnel, as well as the final condition that the patient needs services and personnel at that stage. Constraint (10) indicates that the time of receiving treatment at different stages includes the patient's preparation time, the time of providing service by medical center personnel, the duration of service, the time of entering into the system in case the given stage and ward are defined in the patient treatment description (this constraint checks if the patient needs to receive treatment at that stage, then the end time of patient process will be the sum of preparation time and receiving treatment). Constraint (11) states that the waiting time to receive recovery services should be less than a fixed value for special patients who have undergone an operation. Constraint (12) states that for common patients who have undergone an operation, the waiting time to receive recovery services should be less than the fixed value. Constraint (13) states that if two patients in a ward ask to receive equipment, only one of the patients receives treatment and the other patient is put in the queue. Constraint (14) states that if a patient is in the queue before another patient, they wait until that specific equipment will be unused. In this way, there is a queue for each medical equipment. Constraint (15) completes constraints (7) and (8). Constraint (16) states that if patient i' receives treatment sooner than patient i and patient i is in the queue before patient i', the time of receiving treatment for patient i is longer than patient i', and constraint (17) is in contradiction to constraint (16). In constraint (18), considering the non-linearity of the model, it is required to transform the variable to make the model linear.

3. FUZZY APPROACH

The defuzzification of regular weighted points was introduced by Opricovic and Tzeng [63] for the first time. In their work, they investigated several methods of defuzzification, and finally, CFCS technique was proposed as the proper method of defuzzification in MCDM techniques. The implementation of this approach which involves a five-step algorithm is as follows:

First step: Normalization of values

The maximum value of the upper bound is subtracted from the lowest value of the lower bound to calculate the lowest to the highest interval.

$$\Phi_{min}^{max} = \max u_{ij}^{t} - \min l_{ij}^{t} \quad (19)$$

where, Φ_{min}^{max} is the upper and lower bound of the fuzzy value, $\max u_{ij}^{t}$ is the greatest value of the upper bound in the triangular fuzzy number, and $\min l_{ij}^{t}$ is the smallest bound value of triangular fuzzy number.

Second step: Each bound is separately subtracted from the range

$$l_{ij}^{n} = \frac{(l_{ij}^{t} - \min l_{ij}^{t})}{\Phi_{min}^{max}} \quad (20)$$

$$m_{ij}^{n} = \frac{(m_{ij}^{t} - \min l_{ij}^{t})}{\Phi_{min}^{max}} \quad (21)$$

$$u_{ij}^{n} = \frac{(u_{ij}^{t} - \min l_{ij}^{t})}{\Phi_{min}^{max}} \quad (22)$$

In the above mentioned equation, l_{ij}^{n} is the correction of the lower bound of the fuzzy number, m_{ij}^{n} is the correction of the middle bound of the fuzzy number, and u_{ij}^{n} is the correction of the upper bound of triangular fuzzy number.

Third step: Calculation of normal values of the upper and lower bound

$$l_{ij}^{s} = \frac{m_{ij}^{n}}{(1 + m_{ij}^{n} - l_{ij}^{n})} \quad (23)$$

$$u_{ij}^{s} = \frac{u_{ij}^{n}}{\left(1 + u_{ij}^{n} - m_{ij}^{n}\right)} \quad (24)$$

At this step, based on the modified bounds in the second step, the normal lower bound and the normal upper bound of the fuzzy numbers are obtained.

Fourth step: Calculation of the total normalized definite values

$$x_{ij} = \frac{\left[l_{ij}^{s} * (1 - l_{ij}^{s}) + u_{ij}^{s} * u_{ij}^{s}\right]}{\left[1 - l_{ij}^{s} + u_{ij}^{s}\right]} \quad (25)$$

At this step, based on the previous step, the final normalized values of each fuzzy number are obtained and in the next step the definite number for triangular fuzzy numbers is obtained.

Fifth step: calculation of the definite values

$$Z_{ij} = \min l_{ij}^{n} + (x_{ij} * \Phi_{min}^{max}) \quad (26)$$

3. 1. Data analysis The performance of the proposed mathematical model is verified corresponding real and random data. The present study addresses a specific scheduling problem in a medical center considering 5 patients and 3 different sections including operating room, surgery preparation section and recovery room (note that all 3 sections are not necessarily used by all 5 patients) wherein 9 types of medical equipment, and 9 members of the medical personnel including nurses, doctors and recovery room personnel are deployed. The main parameters are thus as shown in Table 1.

Therefore, fuzzy values of the patient preparation time (ST), and time of health care provision (PT), are presented in Tables 2 and 4.

TABLE 1. Numerical example data

Parameter	Data Range
SST_{ijk}	Uniform ~ [1,10]
PPT_{pijk}	Uniform ~ [1, 5]
TW_i	Uniform ~ [1, 3]
RSK_{ijk}	Uniform ~ [0, 1]

Considering the fuzzy values and implementation of CFCS method, the definite values obtained from the patients preparation time and time of health care provision are summarized in Tables 3 and 5.

As it can be observed in Figure 1, the operation for all patients is due for completion in 12 hours. Accordingly, the health service procedure of all patients is completed within the certain time. In addition, the deployment of medical staff allocation is presented in Figure 2.

TABLE 2. Fuzzy data of the patients' preparation time

Patient. Section	Equipment																										
	l	m	u	l	m	u	l	m	u	l	m	u	l	m	u	l	m	u	l	m	u	l	m	u	l	m	u
	E1			E2			E3			E4			E5			E6			E7			E8			E9		
i1.s1	2	4	5	2	4	6	1	1	3	2	3	5	1	1	3	2	4	6	2	4	5	2	3	5	1	1	3
i1.s2	3	3	5	2	3	7	2	4	6	2	2	3	2	4	6	2	3	7	3	3	5	2	2	3	2	4	6
i2.s2	2	3	5	3	3	4	2	4	4	1	3	5	2	4	4	3	3	4	2	3	5	1	3	5	2	4	4
i3.s1	4	5	5	1	1	3	2	3	5	2	3	5	2	3	5	1	1	3	4	5	5	2	3	5	2	3	5
i3.s2	2	3	3	2	3	4	3	3	6	2	3	3	3	3	6	2	3	4	2	3	3	2	3	3	3	3	6
i3.s3	1	3	4	1	2	3	1	2	3	3	4	6	1	2	3	1	2	3	1	3	4	3	4	6	1	2	3
i4.s1	1	3	4	2	3	4	2	3	5	3	4	6	2	3	5	2	3	4	1	3	4	3	4	6	2	3	5
i4.s2	2	3	6	3	4	5	5	5	7	3	5	5	5	5	7	3	4	5	2	3	6	3	5	5	5	5	7
i4.s3	3	3	5	2	2	3	2	3	5	2	3	6	2	3	5	2	2	3	3	3	5	2	3	6	2	3	5
i5.s1	2	4	6	3	4	5	3	4	6	2	3	4	3	4	6	3	4	5	2	4	6	2	3	4	3	4	6
i5.s2	3	4	5	2	3	4	2	3	3	2	2	3	2	3	3	2	3	4	3	4	5	2	2	3	2	3	3

TABLE 3. Definite data of the patients' preparation time

Patient. Section	Equipment								
	E1	E2	E3	E4	E5	E6	E7	E8	E9
i1.s1	4	4	1	3	1	4	4	3	1
i1.s2	3	4	4	2	4	4	3	2	4
i2.s2	3	3	4	3	4	3	3	3	4
i3.s1	5	1	3	3	3	1	5	3	3
i3.s2	3	3	4	3	4	3	3	3	4
i3.s3	3	2	2	4	2	2	3	4	2
i4.s1	3	3	3	4	3	3	3	4	3
i4.s2	3	4	5	5	5	4	3	5	5
i4.s3	3	2	3	3	3	2	3	3	3
i5.s1	4	4	4	3	4	4	4	3	4
i5.s2	4	3	3	2	3	3	4	2	3

TABLE 4. Fuzzy data of the time of health care provision

Patient.Section	Equipment																								
	l	m	u	l	m	u	l	m	u	l	m	u	l	m	u	l	m	u	l	m	u	l	m	u	l	m	u
	E1			E2			E3			E4			E5			E6			E7			E8			E9		
i1.s1	2	2	3	2	2	3	3	3	5	3	4	6	2	2	3	3	4	6	3	4	5	2	3	5	2	2	3
i1.s2	2	3	4	2	3	6	3	6	7	4	5	7	2	4	6	3	3	7	3	4	5	2	2	3	2	4	6
i2.s2	5	6	7	2	6	8	4	5	7	4	5	9	2	4	6	3	3	6	2	4	5	2	3	5	2	4	4
i3.s1	3	4	5	3	5	6	4	5	6	3	4	8	2	3	5	2	2	3	4	5	8	2	3	5	2	3	5
i3.s2	3	4	5	3	3	7	3	3	6	3	3	5	3	4	6	2	3	7	2	3	3	2	3	3	3	3	6
i3.s3	2	5	7	3	4	7	2	2	3	3	4	6	2	2	3	2	2	3	2	3	4	3	4	6	1	2	3
i4.s1	3	5	6	3	4	8	3	3	5	3	3	6	2	3	5	2	3	5	2	3	4	3	4	6	2	3	5
i4.s2	1	1	3	2	3	4	3	3	4	3	3	5	5	5	7	3	4	5	2	3	6	3	5	5	5	5	7
i4.s3	3	4	6	2	3	4	2	2	4	2	3	3	2	3	5	2	2	3	3	3	5	2	3	6	2	3	5
i5.s1	4	5	6	3	4	5	2	3	4	2	3	3	3	4	6	3	4	5	2	4	6	2	3	4	3	4	6
i5.s2	4	6	9	2	3	4	3	4	6	2	3	3	2	3	3	2	3	4	3	4	5	2	2	3	2	3	3

TABLE 5. Definite data of the time of health care provision

Patient.Section	Equipment								
	E1	E2	E3	E4	E5	E6	E7	E8	E9
i1.s1	2	2	3	4	2	4	4	3	2
i1.s2	3	3	6	5	4	4	4	2	4
i2.s2	6	6	5	6	4	4	4	3	4
i3.s1	4	5	5	5	3	2	5	3	3
i3.s2	4	4	4	3	4	4	3	3	4
i3.s3	5	4	2	4	2	2	3	4	2
i4.s1	5	5	3	4	3	3	3	4	3
i4.s2	1	3	3	3	5	4	3	5	5
i4.s3	4	3	2	3	3	2	3	3	3
i5.s1	5	4	3	3	4	4	4	3	4
i5.s2	6	3	4	3	3	3	4	2	3

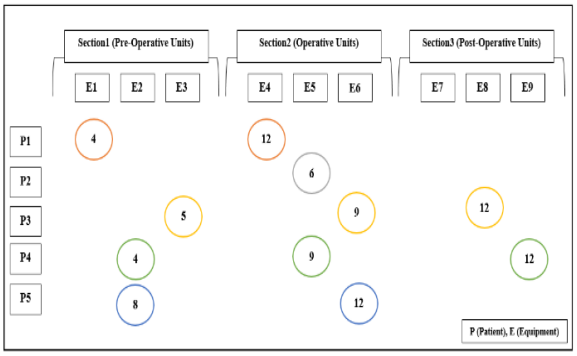

Figure 1. Patient scheduling results

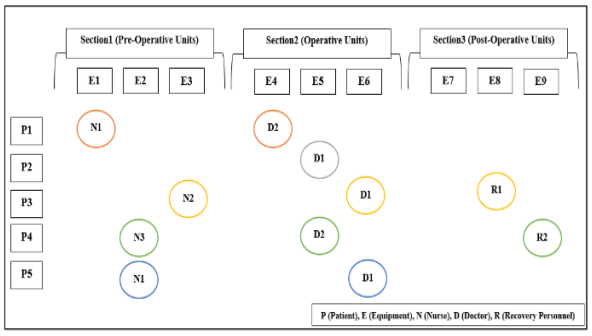

Figure 2. The deployment of medical center personnel allocation

Considering Figure 2, the status of medical staff allocation to the patient's treatment process is obvious.

4. METAHEURISTIC APPROACHES

In this study, a multi-objective mathematical model is presented which is utilized in a NP-HARD operating room scheduling problem based on a fuzzy uncertainty approach. In addition, real problems are generally big in their size and consequently create additional complexity. Regarding the NP-HARD nature of the problem, it would be impossible to solve the problem using exact methods as they are time-consuming and unreliable in order to find an optimal solution. Therefore, two different metaheuristic approaches and the epsilon-constraint method were employed. Moreover, NRGA and NSGA-II are exerted to find the best Pareto solutions for the proposed multi-objective model.

4. 1. The Multi-objective Approach Based on NSGA-II and NRGA Taking into account of NSGA-II and NRGA proposed by Deb et al. [64], Al Jadaan et al. [65] and all above-mentioned studies related to genetic algorithm, it is demonstrated that both algorithms are identical in most of their procedures. They initiate by producing the population. Then, this population is evaluated. In the next steps, two operators are applied to make the selected population even better. The difference between these two algorithms depends on their selection mechanisms as NRGA uses roulette wheel selection while NSGA-II uses binary tournament selection. Figure 3 depicts the pseudo-code of these two algorithms.

4. 1. Parameter Tuning and Computational Results In this section, Taguchi method is employed to increase the efficiency of the proposed meta-heuristic algorithm. This method involves various test experiments along with parameter tuning for each algorithm in order to get the best results regarding the given problem.

4. 1. 1. Parameter Settings In order to prove the applicability of the proposed model, the problem must be solved under various conditions and settings. Hence, here, 12 test problems with various sizes and parameter settings are considered. Different dimensions, parameters and their values to initiate the problem are represented in Table 6.

4. 1. 2. The Obtained Results of Parameter Tuning As mentioned before, Taguchi method is employed to set the algorithms parameters in order to get the optimum results. It also decreases the number of total experiments by eliminating unnecessary ones. In this regard, it uses a cluster of factors, which are based on orthogonal arrays. These factors are categorized into two essential groups namely control and noise factors.

1. Initialize *Population*;
2. Generate random *population*;
3. Evaluate Objectives Values;
4. **For** *each Parent and Child in Population* **do**
5. Assign Rank (level) based on Pareto;
6. Generate sets of *nondominated* solutions;
7. Determine *Crowding* distance
8. Loop (inside) by adding solutions to next generation
9. **End**
10. Determine population front;
11. **For** each determined front
12. Perform Binary tournament selection (NRGA)/Rolette wheel selection (NSGA-II);
13. Generate new population with *mutation* and *crossover*;
14. **End**

Figure 3. Pseudo-code of NRGA and NSGA-II

TABLE 6. Test problems settings

Test problem	i	j	k
1	8	2	2
2	10	4	4
3	20	6	7
4	25	8	8
5	30	10	12
6	41	12	15
7	45	14	18
8	50	16	20
9	55	18	22
10	60	20	30
11	65	22	35
12	70	30	40
13	75	32	45
14	80	34	50
15	85	36	55

The initial step to implement the Taguchi experimental design is to identify the levels for each factor of the algorithm. The next step is to use Minitab software to analyze the experiment with its Taguchi experiment

TABLE 7. Algorithm factors and levels

Algorithms	Factor	Factors levels		
		Level 1	Level 2	Level 3
NSGA-II	A: Pc	0.65	0.75	0.85
	B: Pm	0.04	0.06	0.08
	C: N-pop	90	100	130
	D: Max-iteration	2x	3x	4x
NRGA	A: Pc	0.65	0.75	0.85
	B: Pm	0.04	0.12	0.18
	C: N-pop	50	100	150
	D: Max-iteration	2x	3x	4x

toolbar. In this respect, the L9 design is used for NSGA - II, NRGA, as aforementioned, to identify the best levels for each algorithm. For this purpose, the evaluation of signal-to-noise-ratio is required. Equation (27) represents the selected signal-to-noise-ratio and its evaluation method.

$$\text{Signal/Noise} = -10\log(\sum(Y^2)/n) \quad (27)$$

Here, Y and n are the response time and number of orthogonal arrays respectively. To verify the best levels for each algorithm, the signal-to-noise plot for each algorithm is depicted in Figures 4 and 5.

Considering Figures 4 and 5, the best levels for each algorithm factors are described in Table 8.

4. 1. 3. Metrics for Comparing Algorithms In this section, two different metric indices including Mean Ideal Distance (MID) and CPU time are used to verify the validity of the proposed investigation. The reason for choosing these metric indices is that they measure the different issues of each proposed algorithms. MID considers the convergence rate of each algorithm and CPU time calculates the time to get the optimize solution and answer. In addition, these two metrics are frequently used in the similar studies. So, MID calculates the distance between Pareto solutions and the ideal solution.

The formulation of MID can be described as Equation (28) for two-objective-function model.

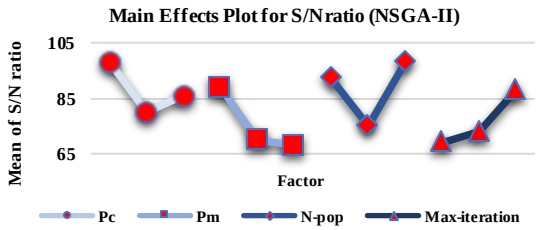

Figure 4. S/N ratio for NSGA-II

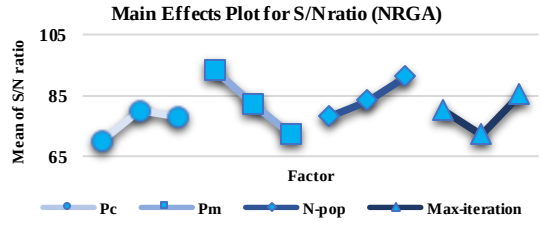

Figure 5. S/N ratio for NRGA

TABLE 8. Tuned parameters of the algorithm

Algorithm	Parameters
NSGA-II	Pc=0.65;Pm=0.04; N-pop=130; Max-iteration=4x
NRGA	Pc=0.75;Pm=0.04; N-pop=150; Max-iteration=4x

$$\text{MID} = \frac{\sum_{i=1}^{n}\sqrt{\left(\frac{f_1^i - f_{1\,best}^i}{f_{1\,total}^{max} - f_{1\,total}^{min}}\right)^2 + \left(\frac{f_2^i - f_{2\,best}^i}{f_{2\,total}^{max} - f_{2\,total}^{min}}\right)^2}}{n} \quad (28)$$

In this equation, n, c1 and c2 are the number of non-dominated answers and the value of i^{th} non-dominated answers, respectively. The ideal, smallest and biggest values between all non-dominated answers are represented by c_{best}^1, c_{best}^2, fj_{total}^{max}, and fj_{total}^{min}, respectively. Smaller values of MID indicate that the algorithm has a better performance. CPU time calculates problem processing time. This value determines how fast an algorithm can get its optimum values that is highly useful in more complex problems in which the running time is very important.

Here, to verify the applicability of the proposed algorithms, the aforementioned metrics are applied to the considered test problems. These 12 test problems are divided into small-sized (1-4), medium-sized (5-8), and large-sized (9-15).

In addition, the Pareto solutions of the considered metaheuristics are depicted in Figure 6.

After designing the test and regulating the parameters, the appropriate parameters in both NSGA II and NRGA have been determined. Now, it is time to implement and compare the algorithms to each other in case of the generated problems. First, an overview of the

TABLE 9. The exact method's results

	Test Problem 1		Test Problem 2		Test Problem 3	
	Obj1	Obj2	Obj1	Obj2	Obj1	Obj2
Epsilon-Constraint	16372	0.05	33346	0.05	125219	90.93
	25105	0.05	24549	0.06	146309	94.16
	25895	0.05	24681	0.06	136259	77.72
	14741	0.05	33960	0.05	154396	90.86
	18880	0.04	26724	0.05	136777	105.56
	24888	0.04	22543	0.08	115376	86.45
	16372	0.05	33346	0.05	125219	90.93
	25105	0.05	24549	0.06	146309	94.16
	25895	0.05	24681	0.06	136259	77.72

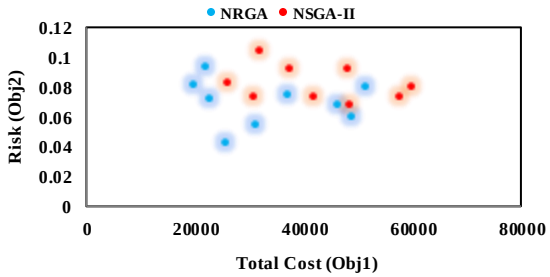

Figure 6. The Pareto solution

problem chromosome and allocation algorithms is displayed in Figures 7, 8 and 9.

As indicated in Figure 7 the problem chromosome has two parts that all numbers of which are filled with random numbers between 0 and 1. Then, they are sorted out and the obtained sequences are used as allocation sequences. It should be noted that this study uses a priority-based coding method.

4. 2. Algorithm Analysis Evaluating the T-Test on the means of the first objective function:

Table 10 indicates the results of the T-Test on the means of the first objective function. In addition, Figures 10 and 11 display a comparative diagram showing the means of the first objective function in each sample test, as well as showing the boxplot for rejecting or accepting the null hypothesis in the T-Test.

t	Section 1								Section 2			
	i			j + k					j		k	
1	0.072	0.132	0.786	0.958	0.799	0.641	0.385	0.650	0.897	0.674	0.115	0.243	0.122
2	0.526	0.268	0.209	0.562	0.123	0.544	0.738	0.726	0.783	0.860	0.168	0.469	0.989
3	0.099	0.332	0.034	0.383	0.339	0.431	0.997	0.350	0.792	0.313	0.852	0.512	0.391
4	0.317	0.877	0.995	0.492	0.892	0.321	0.982	0.195	0.760	0.302	0.678	0.900	0.010
5	0.077	0.771	0.215	0.814	0.055	0.230	0.934	0.830	0.240	0.606	0.543	0.721	0.773

Figure 7. An overview of the problem chromosome

for t = 1 to T

Inputs: I: set of source

J: set of applicant

STijk: Time to prepare patient i at stage j on equipment k

RSKijk: Risk to service to patient i at stage j on equipment k

V(I+J): Encode solution of period t

Outputs: $Xaloc_{ij}$: amount of shipment between nodes

Y_j: binary variable shows the opened applicant

while $\sum_i STijk \geq 0$

Step1: $Xaloc_{ij} = 0 \ \forall i \in I, \forall j \in J$

Step2: select value of first column of sub-segment I for i index

select value of first column of sub-segment J for j index

Step3: $Xaloc_{ij}=min(Ca_i, D_j)$

Update demands and capacities

$STijk = STijk - Xaloc_{ij}$ $RSKijk = RSKijk - Xaloc_{ij}$

Step4: if RSKijk =0 then V(1,I)=0

if STijk =0 then V(1,J)=0

End while

Step5: for j= 1 to J

if $\sum_I Xaloc_{ij} > 0$ *then* $Y_j=1$

End for

End for

Figure 8. Allocation algorithm for the first part of the chromosome

for t = 1 to T

Inputs: I: set of source

J: set of applicant

STijk: Time to prepare patient i at stage j on equipment k

RSKijk: Risk to service to patient i at stage j on equipment k

V(I+J): Encode solution of period t

SSTijk= The patient i enter time at stage j on equipment k

Outputs: $Xaloc_{ij}$: amount of shipment between nodes

INV_{it}: amount of remained goods in storage i at period t

STijk = STijk + SSTijk

while $\sum_j SSTijk \geq 0$ *or* $\sum_i RSKijk \geq 0$

Step1: $Xaloc_{ij} = 0 \ \forall i \in I, \forall j \in J$

Step2: select value of first column of sub-segment I for i index

select value of first column of sub-segment J for j index

Step3: $Xaloc_{ij}=min(Ca_i, D_j)$

Update demands and capacities

$RSKijk = RSKijk - Xaloc_{ij}$ $STijk = STijk - Xaloc_{ij}$

Step4: if $Ca_i=0$ *then V(1,I)=0*

if $D_j=0$ *then V(1,J)=0*

End while

End for

Figure 9. Allocation algorithm for the second part of the chromosome

TABLE 10. T-Test results on the means of the first objective function

Index	Algorithm	
	NSGA-II	NRGA
Sample Test	15	15
Mean	5626072	4497208
S.D	3852039	3821250
Confidence Interval 95%	(4041, 53686)	
T-Test	2.49	
P-Test	0.026	

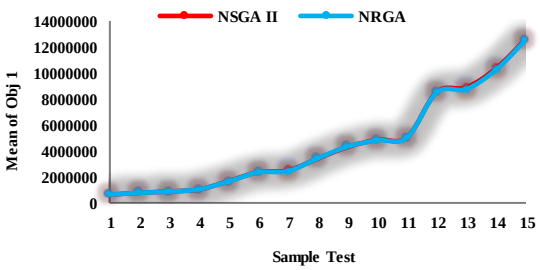

Figure 10. Comparison of the means of the first objective function for sample tests using meta-heuristic algorithms

Based on Table 10 and the p-value, there is a significant difference between the means of the first objective

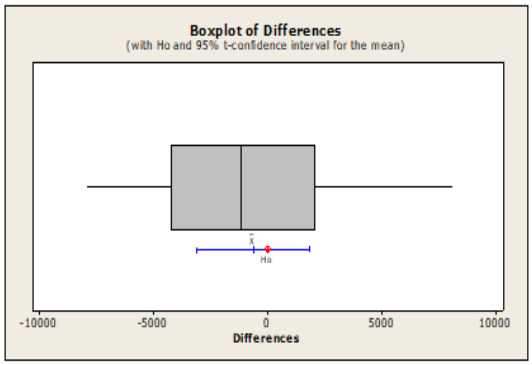

Figure 11. Boxplot for confirming or rejecting the null hypothesis for the means of the first objective function

function obtained from NSGA-II and NRGA. According to the minimization state of the first objective function, it can be concluded that NRGA achieves better results than NSGA-II in this index.

Based on Figure 10, NRGA obtains better results than NSGA-II in regard to the sample test 12-15. As a result, NRGA will be more efficient in obtaining the results of the first objective function in larger scales.

Based on the boxplot in Figure 11, since the null hypothesis is not in the obtained range, there is a significant difference between the means of the first objective function obtained from NSGA-II and NRGA.

Evaluating the T-Test on the means of the second objective function:

Table 11 indicates the results of the T-Test on the means of the second objective function. In addition, Figures 12 and 13 indicate the comparative diagram showing the means of the second objective function in each sample test, as well as the boxplot for rejecting or accepting the null hypothesis in the T-Test.

Regarding the statistics of P-Test at 0.584 obtained from Table 11, it can be concluded that there is no significant difference between the means of the second objective function. Thus, multi-criteria decision making methods such as TOPSIS should be used for comparing the most efficient algorithms.

TABLE 11. T-Test results on the means of the second objective function

Index	Algorithm	
	NSGA-II	NRGA
Sample Test	15	15
Mean	134440	135094
S.D	45240	45418
Confidence Interval 95%	(-3156, 1848)	
T-Test	0.56	
P-Test	0.584	

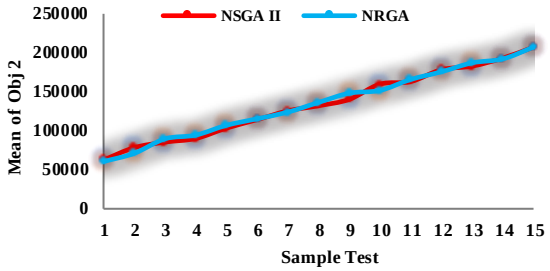

Figure 12. Comparison of the means of the second objective function for sample tests using meta-heuristic algorithms

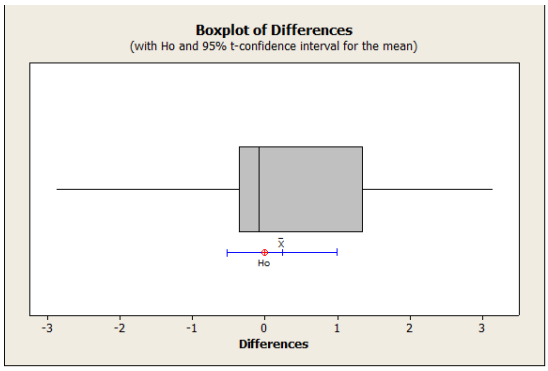

Figure 13. Boxplot for confirming or rejecting the null hypothesis for the means of the second objective function

Figure 12 displays a comparative diagram for the means of the second objective function in different sample tests. It reveals that the results obtained from the sample tests are not different from each other. Thus, it is not easy to comment on the efficiency of algorithms in the second objective function.

Figure 13 completes the results of Table 11 and since the null hypothesis is in a 95% confidence interval, it can be concluded that there is no significant difference between the means of the second objective function obtained by NSGA-II and NRGA.

Evaluating the T-Test on the means of the number of efficient answers:

In this section, statistical comparisons are performed on the comparison indices of meta-heuristic algorithms. Table 12 indicates the results of the T-Test on the means of the number of efficient answers establishing a 95% confidence level.

Since the p-value is more than 0.05 as the base value, it can be concluded that the null hypothesis is accepted. Thus, there is no significant difference between the means of the number of efficient answers obtained from the meta-heuristic algorithms.

Figure 14 compares the means of the number of efficient answers for NSGA-II and NRGA. Based on Figure 14, the number of efficient answers in each sample test is different and no correct answer of the algorithm

TABLE 12. T-Test results on the means of the number of efficient answers

Index	Algorithm	
	NSGA-II	NRGA
Sample Test	15	15
Mean	20.27	1727
S.D	5.04	6.91
Confidence Interval 95%	(-1.48, 7.48)	
T-Test	1.43	
P-Test	0.173	

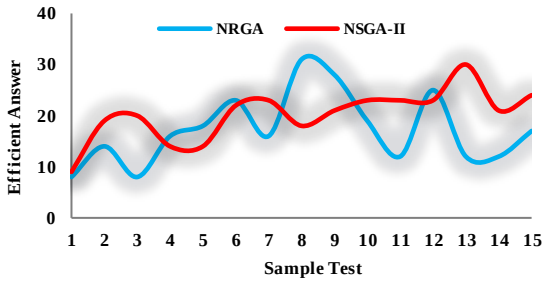

Figure 14. Comparing the means of the number of efficient answers in sample tests using meta-heuristic algorithms

efficiency can be inferred from the obtained results of this index.

Figure 15 demonstrates a boxplot for confirming or rejecting the null hypothesis for the means of the number of efficient answers. It can be concluded that the null hypothesis is accepted due to its location at the confidence interval while hypothesis 1 is rejected.

Evaluating the T-Test on the means of the most extended deviation:

Table 13 represents the statistical comparison of the T-Test on the means of the most extended deviation. Figure 16 shows the comparison of the means of the most extended deviation among all sample tests using NSGA-II and NRGA.

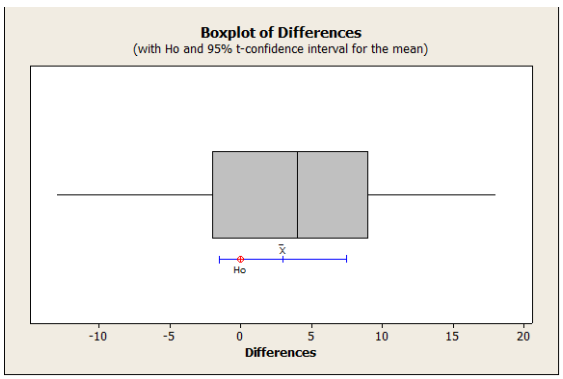

Figure 15. Boxplot for confirming or rejecting the null hypothesis for the means of the number of efficient answers

TABLE 13. T-Test results on the means of the most extended deviation index

Index	Algorithm	
	NSGA-II	NRGA
Sample Test	15	15
Mean	2478417	2260667
S.D	1496766	1661211
Confidence Interval 95%	(-88459, 523960)	
T-Test	1.53	
P-Test	0.149	

Table 13 shows no significant difference in the means of the most extended deviation index obtained from NSGA-II and NRGA. In this test, the p-value is higher than the considered confidence level.

As indicated in Figure 16, NRGA operates more efficiently than NSGA-II in most sample tests. This reveals that the answers obtained from the first and second objective functions using NRGA are more extended than NSGA-II.

Figure 17 shows that the value of the null hypothesis is in a 95% confidence interval for the most extended deviation index.

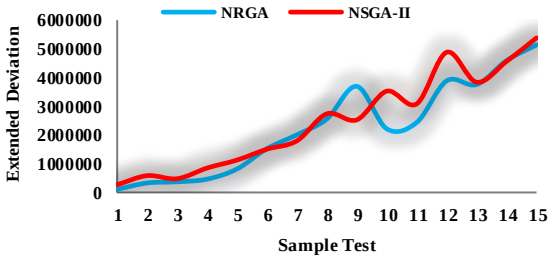

Figure 16. Comparing the means of the most extended deviation index in sample tests using meta-heuristic algorithms

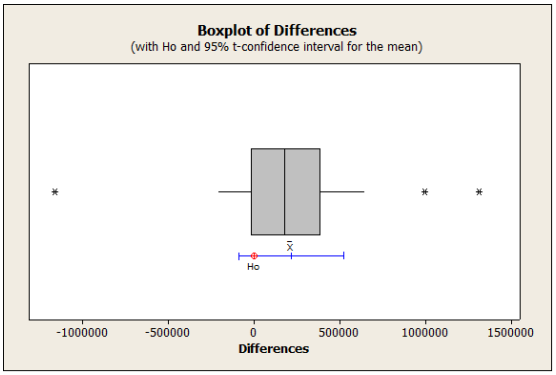

Figure 17. Boxplot for confirming or rejecting the null hypothesis for the means of the most extended deviation index

Evaluating T-Test on the means of Gap index:

Table 14 shows the statistical comparison of the T-Test on the means of gap index. In addition, Figure 18 shows the comparison of the means of gap index in all sample tests employing NSGA-II and NRGA.

The results presented in Table 14 and the obtained p-value (0.205) indicate no significant difference between the means of gap index using NSGA-II and NRGA.

Figure 18 displays the efficiency of NSGA-II compared to NRGA in terms of obtaining the results of gap index. This means that the dispersion of the results of the first and second objective functions in NSGA-II is more systematic than the NRGA.

Furthermore, Figure 19 completes the results of Table 14 and shows the rejection of hypothesis 1 and non-significant difference in comparing the means of gap index.

Evaluating the T-Test on the means of computational time:

Table 15 indicates the results of the T-Test on the means of computational time. In addition, Figures 20 and 21 show the comparative diagram of the means of computational time in each sample test, as well as a boxplot for rejecting or accepting the null hypothesis in the T-Test.

Based on the p-value obtained from the comparisons of T-Test on the means of computational time, it can be acknowledged that there is no significant difference between the means of computational time obtained from NSGA II and NRGA.

TABLE 14. T-Test results on the means of gap index

Index	Algorithm	
	NSGA-II	NRGA
Sample Test	15	15
Mean	0.623	0.557
S.D	0.152	0.148
Confidence Interval 95%	(-0.0405, 0.1725)	
T-Test	1.33	
P-Test	0.205	

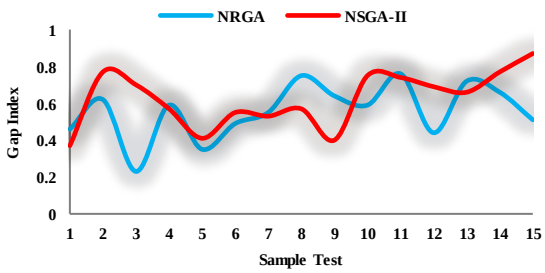

Figure 18. Comparing the means of gap index in sample tests using meta-heuristic algorithms

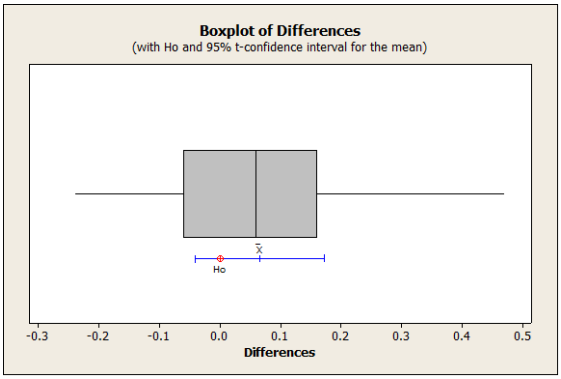

Figure 19. Boxplot for confirming or rejecting the null hypothesis for the means of gap index

TABLE 15. T-Test results on the means of computational time

Index	Algorithm	
	NSGA-II	NRGA
Sample Test	15	15
Mean	844	1041
S.D	730	1220
Confidence Interval 95%	(-483, 88)	
T-Test	1.48	
P-Test	0.160	

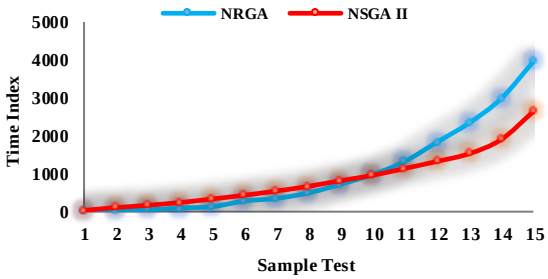

Figure 20. Comparing the means of computational time in sample tests using meta-heuristic algorithms

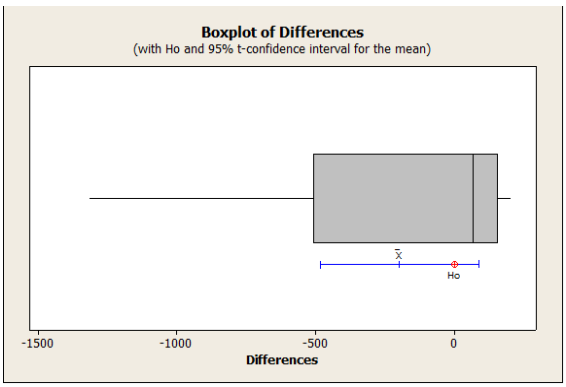

Figure 21. Boxplot for confirming or rejecting the null hypothesis for the means of computational time

Figure 20 more accurately shows that the computational time exponentially increases with the increase of sample size, which is a reason for the NP-hardness of the problem. Nevertheless, it is revealed that NRGA is more efficient than NSGA-II in terms of computational time in medium problems, while the computational time obtained by this algorithm significantly increases with the increase of the problem size.

Finally, Figure 21 shows that the null hypothesis is in a 95% confidence interval that is a reason for the first hypothesis. Thus, it can be concluded that there is no significant difference between the means of computational time obtained from NSGA-II and NRGA.

Therefore, Table 16 shows an overview of the significant differences between the mean of the comparison indices. Based on the previous results and the following table, it can be stated that there is a significant difference only between the means of the first objective function obtained from solving the sample tests using NSGA-II and NRGA.

Selecting the most efficient algorithm using TOPSIS method:

In the previous section, the comparisons were conducted to determine the significant difference between the means of computational index obtained from NSGA-II and NRGA and the results indicate a significant difference only between the means of the first objective function. In this section, the TOPSIS multi-criteria decision making method was used to select the most efficient algorithm. Thus, Table 17 indicates the total means obtained from 15 sample problems.

TABLE 16. Overview of the significant difference between the mean of comparison indices

Index	Significant Difference
The mean of the first objective function	Yes
The mean of the second objective function	No
Number of efficient answers	No
The most extended deviation index	No
Gap index	No
Computational time index	No

TABLE 17. Means of the obtained indices using meta-heuristic algorithms

Index	Algorithm		
	NSGA-II	NRGA	Weight
Obj1	4526072	4497208	0.4
Obj2	45240	45418	0.4
Efficiency Answer	20.27	17.27	0.05
Deviated Extended	2478417	2260667	0.05
Gap	0.623	0.557	0.05
Time	844	1041	0.05

After descaling the results of Table 17, the data were entered into MCDM engine software and the output indicates the efficiency of the NSGA-II with a weight of 0.6945 compared to NRGA with a weight of 0.3055. Consequently, the use of NSGA-II is recommended according to all indices and results.

5. CONCLUSION AND SUGGESTION FOR FUTHER RESEARCH

Numerous studies have been conducted on reducing costs and increasing efficiency of the operating rooms in medical centers. This paper presents a fuzzy model for operating room planning and scheduling as well as concerning the limitations of access to medical staff and patient prioritization. The results reveal the validity of the model by solving a number of problems with regard to different number of patients at small and medium scales with random data. Additionally, in order to solve the problem, defuzzification of values is performed based on the CFCS method. Furthermore, based on the fuzzy mathematical model, two meta-heuristic algorithms of NSGA-II and NRGA are developed. So, after adjusting the parameters based on the Taguchi approach, 15 samples of operating room scheduling problems are designed and the evaluation of two meta-heuristic algorithms are analyzed. The analysis indicates that both meta-heuristic algorithms have a good efficiency compared to the gaps of the obtained solutions. Thus, the hypothetical test is presented for validating the algorithms. In the conducted analysis, no significant difference is observed in other models except between the means of the first objective function in the NSGA-II and NRGA. Ultimately, the algorithms are evaluated using the TOPSIS method indicating that the NSGA-II with a weight of 0.6945 is more effective. Based on the evaluation, it is suggested to implement the mathematical model in medical staff scheduling in order to increase personnel satisfaction. In addition, for further research in this area, the use of recent meta-heuristic algorithms such as red deer and social engineering optimization algorithms is worth being undertaken in a future research project in order to develop and solve problems. Moreover, in this study, Benders' decomposition and Lagrangian relaxation algorithms are deployed.

6. REFERENCES

1. Abedini, A., Ye, H., & Li, W. "Operating room planning under surgery type and priority constraints", ***Procedia Manufacturing***, Vol. 5, (2016), 15-25. DOI: 10.1016/j.promfg.2016.08.005
2. Zarrinpoor, N., Fallahnezhad, M. S., & Pishvaee, M. S. "Design of a reliable facility location model for health service networks", ***International Journal of Engineering, Transactions A: Basics***, Vol. 30, No. 1, (2017), 75-84. DOI: 10.5829/idosi.ije.2017.30.01a.10

3. Leelahavarong, P., Doungthipsirikul, S., Kumluang, S., Poonchai, A., Kittiratchakool, N., Chinnacom, D., Suchonwanich, N., Tantivess, S. "Health technology assessment in Thailand: institutionalization and contribution to healthcare decision making: review of literature", ***International Journal of Technology Assessment in Health Care,*** Vol. 35, No. 6, (2019), 467-473. DOI: 10.1017/S0266462319000321
4. Zhu, S., Fan, W., Yang, S., Pei, J., Pardalos, P. M. "Operating room planning and surgical case scheduling: a review of literature", ***Journal of Combinatorial Optimization,*** Vol. 37, No. 3, (2019), 757-805. DOI: 10.1007/s10878-018-0322-6
5. Samudra, M., Van Riet, C., Demeulemeester, E., Cardoen, B., Vansteenkiste, N., Rademakers, F. E. "Scheduling operating rooms: achievements, challenges and pitfalls", ***Journal of Scheduling,*** Vol. 19, No. 5, (2016), 493-525. DOI: 10.1007/s10951-016-0489-6
6. Molina-Pariente, J. M., Hans, E. W., Framinan, J. M. "A stochastic approach for solving the operating room scheduling problem", ***Flexible Services and Manufacturing Journal,*** Vol. 30, No. 1, (2018), 224-251. DOI: 10.1007/s10696-016-9250-x
7. Hooshmand, F., MirHassani, S., Akhavein, A. "Adapting GA to solve a novel model for operating room scheduling problem with endogenous uncertainty", ***Operations Research for Health Care,*** Vol. 19, (2018), 26-43. DOI: 10.1016/J.ORHC.2018.02.002
8. Hamid, M., Nasiri, M. M., Werner, F., Sheikhahmadi, F., Zhalechian, M. "Operating room scheduling by considering the decision-making styles of surgical team members: a comprehensive approach", ***Computers & Operations Research,*** Vol. 108, (2019), 166-181. DOI: 10.1016/j.cor.2019.04.010
9. Zhang, J., Dridi, M., El Moudni, A. "A two-level optimization model for elective surgery scheduling with downstream capacity constraints", ***European Journal of Operational Research,*** Vol. 276, No. 2, (2019), 602-613. DOI: 10.1016/j.ejor.2019.01.036
10. Roshanaei, V., Booth, K. E., Aleman, D. M., Urbach, D. R., Beck, J. C. "Branch-and-check methods for multi-level operating room planning and scheduling", ***International Journal of Production Economics,*** Vol. 220, (2020), 107433. DOI: 10.1016/j.ijpe.2019.07.006
11. Moosavi, A., Ebrahimnejad, S. "Scheduling of elective patients considering upstream and downstream units and emergency demand using robust optimization", ***Computers & Industrial Engineering,*** Vol. 120, (2018), 216-233. DOI: 10.1016/j.cie.2018.04.047
12. Koppka, L., Wiesche, L., Schacht, M., Werners, B. "Optimal distribution of operating hours over operating rooms using probabilities", ***European Journal of Operational Research,*** Vol. 267, No. 3, (2018), 1156-1171. DOI: 10.1016/j.ejor.2017.12.025
13. Pang, B., Xie, X., Song, Y., Luo, L. "Surgery scheduling under case cancellation and surgery duration uncertainty", ***IEEE Transactions on Automation Science and Engineering,*** Vol. 16, No. 1, (2018), 74-86. DOI: 10.1109/TASE.2018.2834486
14. Belkhamsa, M., Jarboui, B., Masmoudi, M. "Two metaheuristics for solving no-wait operating room surgery scheduling problem under various resource constraints", ***Computers & Industrial Engineering,*** Vol. 126, (2018), 494-506. DOI: 10.1016/j.cie.2018.10.017
15. Yazdi, M., Zandieh, M., Haleh, H. "A Mathematical Model for Scheduling Elective Surgeries for Minimizing the Waiting Times in Emergency Surgeries", ***International Journal of Engineering, Transactions C: Aspects,*** Vol. 33, No. 3, (2020), 448-458. DOI: 10.5829/ije.2020.33.03c.09
16. Díaz-López, D., López-Valencia, N., González-Neira, E., Barrera, D., Suárez, D., Caro-Gutiérrez, M., Sefair, C. "A simulation-optimization approach for the surgery scheduling problem: a case study considering stochastic surgical times", ***International Journal of Industrial Engineering Computations,*** Vol. 9, No. 4, (2018), 409-422. DOI: 10.5267/j.ijiec.2018.1.002
17. Razmi, J., Barati, M., Yousefi, M., Heydari, J. "A stochastic model for operating room planning under uncertainty and equipment capacity constraints", ***Journal of Industrial Engineering International,*** Vol. 11, No. 2, (2015), 269-279. DOI: 10.1007/s40092-015-0100-3
18. Mohammadian, M., Babaei, M., Amin Jarrahi, M., Anjomrouz, E. "Scheduling nurse shifts using goal programming based on nurse preferences: a case study in an emergency department", ***International Journal of Engineering, Transactions A: Basics,*** Vol. 32, No. 7, (2019), 954-963. DOI: 10.5829/IJE.2019.32.07A.08
19. Mateus, C., Marques, I., Captivo, M. E. "Local search heuristics for a surgical case assignment problem", ***Operations Research for Health Care,*** Vol. 17, (2018), 71-81. DOI: 10.1016/j.orhc.2017.04.001
20. Landa, P., Aringhieri, R., Soriano, P., Tànfani, E., Testi, A. "A hybrid optimization algorithm for surgeries scheduling", ***Operations Research for Health Care,*** Vol. 8, (2016), 103-114. DOI: 10.1016/j.orhc.2016.01.001
21. Ansarifar, J., Tavakkoli-Moghaddam, R., Akhavizadegan, F., Hassanzadeh Amin, S. "Multi-objective integrated planning and scheduling model for operating rooms under uncertainty", ***Proceedings of the Institution of Mechanical Engineers, Part H: Journal of Engineering in Medicine,*** Vol. 232, No. 9, (2018), 930-948. DOI: 10.1177/0954411918794721
22. Liu, H., Zhang, T., Luo, S., Xu, D. "Operating room scheduling and surgeon assignment problem under surgery durations uncertainty", ***Technology and Health Care,*** Vol. 26, No. 2, (2018), 297-304. DOI: 10.3233/THC-170825
23. Fathollahi-Fard, A., Hajiaghaei-Keshteli, M., Tavakkoli-Moghaddam, R. "A Lagrangian relaxation-based algorithm to solve a Home Health Care routing problem", ***International Journal of Engineering, Transactions A: Basics,*** Vol. 31, No. 10, (2018), 1734-1740. DOI: 10.5829/ije.2018.31.10a.16
24. Nasiri, M. M., Rahvar, M. "A two-step multi-objective mathematical model for nurse scheduling problem considering nurse preferences and consecutive shifts", ***International Journal of Services and Operations Management,*** Vol. 27, No. 1, (2017), 83-101. DOI: 10.1504/IJSOM.2017.10003965
25. Bouguerra, A., Sauvey, C., Sauer, N. "Mathematical model for maximizing operating rooms utilization", ***IFAC-PapersOnLine,*** Vol. 48, No. 3, (2015), 118-123. DOI: 10.1016/j.ifacol.2015.06.068
26. Nasiri, M. M., Shakouhi, F., Jolai, F. "A fuzzy robust stochastic mathematical programming approach for multi-objective scheduling of the surgical cases", ***OPSearch,*** Vol. 56, No. 3, (2019), 890-910. DOI: 10.1007/s12597-019-00379-y
27. Kamran, M. A., Karimi, B., Dellaert, N. "Uncertainty in advance scheduling problem in operating room planning", ***Computers & Industrial Engineering,*** Vol. 126, (2018), 252-268. DOI: 10.1016/j.cie.2018.09.030
28. Van Riet, C., Demeulemeester, E. "Trade-offs in operating room planning for electives and emergencies: A review", ***Operations Research for Health Care,*** Vol. 7, (2015), 52-69. DOI: 10.1016/j.orhc.2015.05.005
29. Testi, A., Tanfani, E., Torre, G. "A three-phase approach for operating theatre schedules", ***Health Care Management Science,*** Vol. 10, No. 2, (2007), 163-172. DOI: 10.1007/s10729-007-9011-1
30. Tànfani, E., Testi, A. "A pre-assignment heuristic algorithm for the Master Surgical Schedule Problem (MSSP)", ***Annals of Operations Research,*** Vol. 178, No. 1, (2010), 105-119. DOI: 10.1007/s10479-009-0568-6

31. Banditori, C., Cappanera, P., Visintin, F. "A combined optimization–simulation approach to the master surgical scheduling problem", ***IMA Journal of Management Mathematics,*** Vol. 24, No. 2, (2013), 155-187. DOI: 10.1093/imaman/dps033

32. Lappas, N. H., Gounaris, C. E. "Multi- stage adjustable robust optimization for process scheduling under uncertainty", ***AIChE Journal,*** Vol. 62, No. 5, (2016), 1646-1667. DOI: 10.1002/aic.15183

33. Jittamai, P., Kangwansura, T. "A hospital admission planning model for operating room allocation under uncertain demand requirements", ***International Journal of Services and Operations Management,*** Vol. 23, No. 2, (2016), 235-256. DOI: 10.1504/IJSOM.2016.074058

34. Al-Refaie, A., Chen, T., Judeh, M. "Optimal operating room scheduling for normal and unexpected events in a smart hospital", ***Operational Research,*** Vol. 18, No. 3, (2018), 579-602. DOI: 10.1007/s12351-016-0244-y

35. Abedini, A., Li, W., Ye, H. "An optimization model for operating room scheduling to reduce blocking across the perioperative process", ***Procedia Manufacturing,*** Vol. 10, (2017), 60-70. DOI: 10.1016/j.promfg.2017.07.022

36. Abtahi, Z., Sahraeian, R., Rahmani, D. "A Stochastic Model for Prioritized Outpatient Scheduling in a Radiology Center", ***International Journal of Engineering, Transactions A: Basics,*** Vol. 33, No. 4, (2020). DOI: 10.5829/IJE.2020.33.04A.11

37. Khaniyev, T., Kayış, E., Güllü, R. "Next-day operating room scheduling with uncertain surgery durations: Exact analysis and heuristics", ***European Journal of Operational Research,*** Vol. 286, No. 1, (2020), 49-62. DOI: 10.1016/j.ejor.2020.03.002

38. Abdeljaouad, M. A., Bahroun, Z., Saadani, N. E. H., Zouari, B. "A simulated annealing for a daily operating room scheduling problem under constraints of uncertainty and setup", ***INFOR: Information Systems and Operational Research,*** Vol. 58, No. 3, (2020), 456-477. DOI: 10.1080/03155986.2020.1734901

39. Moosavi, A., Ebrahimnejad, S. "Robust operating room planning considering upstream and downstream units: a new two-stage heuristic algorithm", ***Computers & Industrial Engineering,*** Vol. 143, (2020), 106387. DOI: 10.1016/j.cie.2020.106387

40. Zhou, S., Yue, Q. "Sequencing and scheduling appointments for multi-stage service systems with stochastic service durations and no-shows", ***International Journal of Production Research***, (2021), 1-20. DOI: 10.1080/00207543.2020.1862431

41. Sun, Y., Raghavan, U. N., Vaze, V., Hall, C. S., Doyle, P., Richard, S. S., Wald, C. "Stochastic programming for outpatient scheduling with flexible inpatient exam accommodation", ***Health Care Management Science***, (2021), 1-22. DOI: 10.1007/s10729-020-09527-z

42. Tadarok, S., Fakhrzad, M., Jokardarabi, M., Jafari-Nodoushan, A., "A Mathematical Model for a Blood Supply Chain Network with the Robust Fuzzy Possibilistic Programming Approach: A Case Study at Namazi Hospital", ***International Journal of Engineering, Transactions C: Aspects***, Vol. 34, No. 6, (2021), 1493-1502. DOI: 10.5829/IJE.2021.34.06C.13

43. Rabbani, M., Talebi, E., "A comprehensive mathematical model for designing an organ transplant supply chain network under uncertainty", ***International Journal of Engineering, Transactions C: Aspects***, Vol. 32, No. 6, (2019), 835-841. DOI:10.5829/ije.2019.32.06c.06

44. Bora, A., Bezboruah, T., "Evaluating the Reliability of PwCOV: A Loosely Coupled Software as a Service for COVID-19 Data Processing System", ***International Journal of Engineering, Transactions C: Aspects***, Vol. 33, No. 12, (2020), 2496-2502. DOI: 10.5829/IJE.2020.33.12C.09

45. Hamidi, H. & Daraee, A., "Analysis of pre-processing and post-processing methods and using data mining to diagnose heart diseases", ***International Journal of Engineering, Transactions A: Basics,*** Vol. 29, No. 7, (2016), 921-930. DOI: 10.5829/idosi.ije.2016.29.07a.06

46. Khlie, K., Abouabdellah, A., "Identification of the patient requirements using lean six sigma and data mining", ***International Journal of Engineering, Transactions B: Applications,*** Vol. 30, No. 5, (2017), 691-699. DOI: 10.5829/idosi.ije.2017.30.05b.09

47. Zoullouti, B., Amghar, M., Sbiti, N., "Risk analysis of operating room using the fuzzy bayesian network model", ***International Journal of Engineering, Transactions A: Basics,*** Vol. 30, No. 1, (2017), 66-74. DOI: 10.5829/idosi.ije.2017.30.01a.09

48. Mojtahedi, M., Fathollahi-Fard, A., Tavakkoli-Moghaddam, R., & Newton, S. "Sustainable Vehicle Routing Problem for Coordinated Solid Waste Management", ***Journal of Industrial Information Integration,*** Vol. 23, (2021), 100220. DOI: 10.1016/j.jii.2021.100220

49. Fathollahi-Fard, A.M., Woodward, L., Akhrif, O. "Sustainable distributed permutation flow-shop scheduling model based on a triple bottom line concept", ***Journal of Industrial Information Integration,*** (2021), 100233. DOI: 10.1016/j.jii.2021.100233

50. Fathollahi-Fard, A. M., Hajiaghaei-Keshteli, M., Mirjalili, S, "A set of efficient heuristics for a home healthcare problem", ***Neural Computing and Applications,*** Vol. 32, No. 10, (2020), 6185-6205. DOI: 10.1007/s00521-019-04126-8

51. Fathollahi-Fard, A. M., Hajiaghaei-Keshteli, M., Tavakkoli-Moghaddam, R., Smith, N. R., "Bi-level programming for home health care supply chain considering outsourcing", ***Journal of Industrial Information Integration,*** (2021), 100246. DOI: 10.1016/j.jii.2021.100246

52. Naderi, B., Begen, M. A., Zaric, G. S., Rroshanaei, V., "A Novel and Efficient Exact Technique for Integrated Staffing, Assignment, Routing, and Scheduling of Home Care Services Under Uncertainty", ***Assignment, Routing, and Scheduling of Home Care Services Under Uncertainty,*** (2021). DOI: https://dx.doi.org/10.2139/ssrn.3836827

53. Naderi, B., Roshanaei, V., Begen, M. A., Aleman, D. M., & Urbach, D. R., "Increased surgical capacity without additional resources: Generalized operating room planning and scheduling", ***Production and Operations Management,*** (2021) DOI: 10.1111/poms.13397

54. Roshanaei, V., Naderi, B., "Solving integrated operating room planning and scheduling: Logic-based Benders decomposition versus Branch-Price-and-Cut", ***European Journal of Operational Research,*** Vol. 293, No. 1, (2021), 65-78. DOI: 10.1016/j.ejor.2020.12.004

55. Tsai, S. C., Yeh, Y., Kuo, C. Y., "Efficient optimization algorithms for surgical scheduling under uncertainty", ***European Journal of Operational Research,*** Vol. 293, No. 2, (2021), 579-593. DOI: 10.1016/j.ejor.2020.12.048

56. Lin, Y.-K., Li, M.-Y., "Solving Operating Room Scheduling Problem Using Artificial Bee Colony Algorithm", ***Healthcare,*** Vol. 9, No. 2, (2021), 152. DOI: 10.3390/healthcare9020152

57. Bovim, T. R., Christiansen, M., Gullhav, A. N., Range, T. M., & Hellemo, L., "Stochastic master surgery scheduling", ***European Journal of Operational Research,*** Vol. 285, No. 2, (2020), 695-711. DOI: 10.1016/j.ejor.2020.02.001

58. Zhu, S., Fan, W., Liu, T., Yang, S., Pardalos, P. M., "Dynamic three-stage operating room scheduling considering patient waiting time and surgical overtime costs", ***Journal of Combinatorial Optimization,*** Vol. 39, No. 1, (2020), 185-215. DOI: 10.1007/s10878-019-00463-5

59. Park, H.S., Kim, S.H., Bong, M.R., Choi, D.K., Kim, W.J., Ku, S.W., Ro, Y.J. Choi, I.C., "Optimization of the operating room scheduling process for improving efficiency in a tertiary

hospital", ***Journal of Medical Systems,*** Vol. 44, No. 9, (2020), 1-7. DOI: 10.1007/s10916-020-01644-0

60. Roshanaei, V., Luong, C., Aleman, D. M., Urbach, D., "Propagating logic-based Benders' decomposition approaches for distributed operating room scheduling", ***European Journal of Operational Research,*** Vol. 257, No. 2, (2017), 439-455. DOI: 10.1016/j.ejor.2016.08.024
61. Roshanaei, V., Luong, C., Aleman, D. M., Urbach, D. R., "Reformulation, linearization, and decomposition techniques for balanced distributed operating room scheduling", ***Omega,*** Vol. 93, (2020), 102043. DOI: 10.1016/j.omega.2019.03.001
62. Naderi, B., Gohari, S., Yazdani, M., "Hybrid flexible flowshop problems: Models and solution methods", ***Applied Mathematical Modelling,*** Vol. 38, No. 24, (2014), 5767-5780. DOI: 10.1016/j.apm.2014.04.012
63. Opricovic, S., Tzeng, G.-H. "Defuzzification within a multicriteria decision model", ***International Journal of Uncertainty, Fuzziness and Knowledge-Based Systems,*** Vol. 11, No. 05, (2003), 635-652. DOI: 10.1142/S0218488503002387
64. Deb, K., Pratap, A., Agarwal, S., Meyarivan, T. "A fast and elitist multiobjective genetic algorithm: NSGA-II", ***IEEE Transactions on Evolutionary Computation,*** Vol. 6, No. 2, (2002), 182-197. DOI: 10.1109/4235.996017
65. Al Jadaan, O., Rajamani, L., Rao, C.R. "Non-dominated ranked genetic algorithm for solving multi-objective optimization problems: NRGA", ***Journal of Theoretical and Applied Information Technology,*** (2008), 60-67.

Persian Abstract

چکیده

امروزه، مسائل برنامه‌ریزی و زمانبندی مهمترین مسائل در جهان هستند و تاثیر چشمگیری بر بهبود بهره‌وری سازمانی و سرویس دهی به سیستم هایی همچون ارائه دهندگان خدمات درمانی و پزشکی دارند. از آنجا که برنامه‌ریزی اتاق‌های عمل جراحی یک مساله عمده در سازمان های مراقبت از سلامت می باشد، بهینه‌سازی کارکنان مراکز پزشکی و تجهیزات پزشکی نقشی اساسی ایفا می‌کند. از این رو، این مطالعه یک مدل ریاضی چندمنظوره با طبقه‌بندی (پیش از عمل، حین عمل، و پس از عمل) به منظور حداقل سازی زمانبندی اتاق عمل و ریسک استفاده از تجهیزات ارائه می‌کند. محدودیت های زمانی در سیستم های مراقبت از سلامت و ظرفیت محدود تجهیزات پزشکی مهمترین محدودیت لحاظ شده در مطالعه حاضر هستند. همچنین، از آنجا که مدت آماده‌سازی بیمار و پیاده‌سازی فرایندهای درمانی در سه حالت خوشبینانه، بدبینانه و نرمال رخ می‌دهد، پارامترهای معرفی شده با اتکا بر یک تحلیل عدم قطعیت فازی از مساله مورد بررسی قرار گرفته است. از این رو، این مدل در یک نمونه حل عددی واقعی در یک مرکز خدمات درمانی و پزشکی به منظور ارزیابی و تایید مدل ریاضی پیشنهادی مورد سنجش قرار گفته است. و سپس، دو الگوریتم فراابتکاری (NRGA و NSGAII)، برای تحلیل مدل پیشنهادی، بر روی این مدل ریاضی پیاده‌سازی شده است. نهایتا، نتایج این تحقیق نشان می‌دهد که الگوریتم NSGA-II در مساله زمانبندی اتاق عمل کاراتر است.

International Journal of Engineering

Journal Homepage: www.ije.ir

Study on Multi-objects Optimization in EDM with Nickel Coated Electrode using Taguchi-AHP-Topsis

H. Phan Nguyen[a], N. Vu Ngo*[b], C. Tam Nguyen[a]

[a] *Hanoi University of Industry, No. 298, CauDien Street, Bac TuLiem, District, Hanoi, Vietnam*
[b] *Thai Nguyen University of Technology (TNUT), Thai Nguyen, Vietnam*

P A P E R I N F O

Paper history:
Received 31 August 2021
Received in revised form 01 October 2021
Accepted 20 October 2021

Keywords:
Taguchi
Optimization
Topsis
Material Removal Rate
Surface Roughness
EDM

A B S T R A C T

To improve productivity and quality of machining process using EDM, a lot of electrodes such as coated and alloy electrodes has been applied. Study on multi-objects optimization in EDM with coated electrode will increase number of application of this field into practice. In this study, material removal rate (MRR) and surface roughness (SR) in EDM using nickel coated aluminium electrode were optimized simultaneously using Taguchi-AHP-Topsis methods. Technological parameters including Peak Current (I), Gap Voltage (U) and pulse on time (Ton) were investigated. Titanium alloy (Ti-6Al-4V) was selected as workpiece in experimental process. The results show that combination among Taguchi-AHP-Topsis methods is suitable to solve multi-objects optimization in EDM. The optimized technological parameters are I = 30 A, Ton = 500 µs, U = 50 V and optimized quality criterias are MRR = 0.17 mm^3/min and SR = 8.76 µm.

***doi**: 10.5829/ije.2022.35.02b.02*

1. INTRODUCTION

Nowadays, technological parameters in EDM are often selected using the experience of workers or using guide books of equipments in companies and factories. Therefore, efficiency of machine is not high. Study on optimizing technological parameters in EDM using experimental model is a suitable solution to improve the above process [1]. A lot of solutions has been proposed to solve optimized problem in EDM [2, 3]. Not only Taguchi method is used independently but also it is combined with other methods to increase efficiency to solve the optimized problems [4, 5]. Accuracy of the optimized results and multi-objects optimization can be easily solved using Taguchi method and other optimimal methods [6]. A lot of methods which are used to optimize multi-objects and quality criteria presented in EDM field. Researches have been performed to improve productivity, reduce electrode wear and increase machined surface quality. Combination of Taguchi, ANN and RSM is to determine accurate values of MRR and SR in EDM for Ti50Ni40Co10 [7, 8]. Studied results showed that Taguchi - ANN has higher accuracy and less error compare to others. In a research conducted by Rajamanickam et al. [9], four quality criteria in EDM for Ti - 6Al-4V were optimized simultaneously combining RSM with Fuzzy and Topsis methods, and set of optimized parameters were accurately determined. However, comparing with Taguchi method, number of experiment is large and investigated degree of each parameter is small. Taguchi - Triangular Fuzzy - Topsis were combined to optimize simultaneously 5 quality criteria in EDM, and experimental results show that this combination is efficient for multi-objects optimization [10]. MRR is larger and TWR is smaller, this is result which obtains from multi-objects problem in EDM for Silicon Nitride - Titanium Nitride by Taguchi - Topsis và Taguchi - Grey Relationship Grade (GRA). These are suitable solutions for multi-objects problem in this field [11]. Taguchi - GRA were also combined to optimize simultaneously 3 quality criteria including MRR, EWR and OC in EDM for Cp Titanium [12]. Ananyzied results showed that set of optimized parameters which are calculated is different from set of them in ANOVA of

*Corresponding Author Institutional Email: ngocvu@tnut.edu.vn
(N. Vu Ngo)

Please cite this article as: H. Phan Nguyen, N. Vu Ngo, C. Tam Nguyen, Study on Multi-objects Optimization in EDM with Nickel Coated Electrode using Taguchi-AHP-Topsis, ***International Journal of Engineering, Transactions B: Applications,*** Vol. 35, No. 02, (2022) 276-282

S/N of GRA. In another research [13], authors optimized set of technological parameters in multi-objects problem of EDM using Taguchi - Topsis. The results showed that Topsis is a strong method to solve multi-objects problem in EDM and also other technological fields. MRR and SR are quality criteria which was optimized simultaneously in EDM using double solution such as Taguchi - Topsis and Taguchi - GRA [14]. Results were analyzed and compared among these combinations, and it shows that efficiency of Topsis is larger. ANOVA in multi-objects problem was performed in EDM. MRR and TWR are quality criteria. In addition, surface quality also analyzied [15]. Using Taguchi - Topsis methods with ANOVA, machining efficiency in EDM was improved significantly. It is about 10% [16]. Taguchi - Topsis was used to solve multi-objects problem in EDM using nanotube copper electrode [17]. Combination of ANOVA and Taguchi - Topsis was also performed to solve multi-objects problem in µ - EDM drilling for 304 stainless steel. The research showed that efficiency is better. It is about 37%. This is a good solution for manufacturing in fact. Topsis method was used to optimize simultaneously seven quality criteria in EDM for AISI 304 steel [18]. ANOVA was also used to analyze optimized criteria C*, and it showed a parameter which affected significantly to C*. ANOVA technology for S/N of optimized criteria (γ) using Taguchi - GRA determined set of optimized parameters in WEDM [19]. MRR and SR were considered as optimal criteria. Combination among Taguchi - AHP - Topsis was used in multi-objects problem of the non-traditional machining technology [20]. This combination showed that selection for number of weight of quality criteria is simple, error appearing in this method is smaller, and technician is not necessary to have knowledge well to do. AHP - Topsis and AHP - GRA have been introduced and they can be applied in a lot of fields. Quality of surface layer at optimized condition was presented by some researches. White layer on machined surface in WEDM was analynized and investigated deeply using factors such as chemical composition, alloy state, mechanical properties and elastic modulus E [21]. However, it is necessary to study continuously and consider deeply for determining suitability of white layer coresponding to work requiment of molds and dies in fact. There are a lot of optimal algorithms which have studied to solve multi-objetcs optimization in EDM such as GRA, ANN, PSO, Topsis, etc. [22]. However, optimal results from these methods are different at the same experimental condition and it is difficult to select set of optimal parameters and results. Therefore, optimization for increasing machining productivity and surface quality in EDM is necessary to study.

Currently, researchers who are in country or abroad are interested to this field. Number of international publication of optimal field in EDM increases significantly every year. A lot of optimal methods has been used to solve single or multi-objects optimization. Normally, Taguchi method is often applied for single objetcs optimization and Topsis is applied for multi-objects optimization. Therefore, multi-objects optimization in EDM with Nickel coated Al electrode was performed in this study. Taguchi - AHP - Topsis were used. MRR and SR are quality criteria and they were investigated in this work.

2. EXPERIMENTAL SETUP

The experiments have been conducted on the Die-sinking EDM model CM323C of CHMER EDM, Ching Hung machinery & Electric Industrial. Co. LTD. Workpiece material is Titanium alloy (Ti-6Al-4V) with dimension of 25×35×5 mm. Nickel is coated on Al electrode and thickness of coating layer is 50 micro. EDAX report of Nickel coating and it was invident that presence of Nickel material in coating, Figure 1. Based on previous researches, technological parameters including Current (I), Voltage (U) and pulse on time (T_{on}) were selected to investigate, levels of the technological paramters are shown in Table 1. Fixed parameters in this work includes dielectric pressure with 0.5 kg/cm^2, machining time with 10 min, servo sensitivity with 9 and anti-arc sensitivity with 5.

Quality criteria in EDM include MRR and SR. The mass of the workpiece was measured before and after machining using AJ 203 electronic balance (Shinko Denshi Co. LTD - Japan). The surface roughness was measured by a surface tester (Model: SV - 2100,

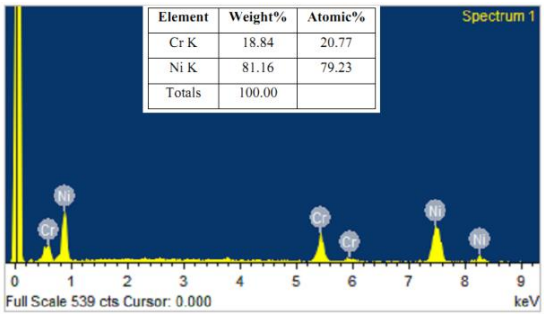

Figure 1. EDX Report of nickel coating tool electrode

TABLE 1. Input process parameters and levels

Parameters	Symbol	Levels				Unit
		1	2	3	4	
Peak Current	I	10	20	30	40	A
Gap Voltage	U	40	45	50	55	V
Pulse-ON Time	T_{on}	100	500	1000	1500	µS

Mitutoyo, Japan) with the cut off length 0.8mm. The results of quality indicators are shown in Figure 2 and Table 2.

3. OPTIMIZED DESIGN METHOD

Taguchi is a popular method used for optimization process in EDM. Comparing with tradition mahining methods, number of experiment is the smallest, and expermental matrix is simple. Therefore, time and cost of experiment process reduce significantly. Number of the input technological parameters and their levers are investigated, as shown in Table 1. This table shows that L16 of Taguchi method is suitable with this study. The expermental matrix is described as Table 2. Howerver, Taguchi method is difficult to solve multi-objetcs problem and it is disadvantage of this method. Currently, combination between Taguchi and other methods such as Topsis, GRA, Deng's, etc. have been introduced and it can improve disadvantage of Taguchi method. Selection of weight of quality criteria in multi-objects problem is the most important, because value of quality weight affects to accuracy of optimal problem. This is complex and it is difficult to determine the suitable weight of quality criteria. A lot of solution has been presented and

Figure 2. Machined Surface after EDM using Nickel Coated Electrode

TABLE 2. Experimental results of L16

Expt. No.	Current (I)	Gap Voltage (U)	Pulse-ON Time (T_{on})	MRR (mm^3/min)	Ra (µm)
1	1	1	1	0.033	6.918
2	1	2	2	0.040	7.267
3	1	3	3	0.026	7.341
4	1	4	4	0.020	7.721
5	2	1	2	0.046	7.941
6	2	2	1	0.066	8.112
7	2	3	4	0.066	8.421
8	2	4	3	0.066	8.731
9	3	1	3	0.079	8.918
10	3	2	4	0.086	9.267
11	3	3	1	0.099	9.341
12	3	4	2	0.113	9.721
13	4	1	4	0.093	9.941
14	4	2	3	0.113	10.11
15	4	3	2	0.139	10.42
16	4	4	1	0.139	10.58

r- number of test in an experiment (repeating times).
y_i- values of experiment.
The higher - the better:
$(S/N)_{HB} = -10\log(MSD_{HB})$

$$MSD_{HB} = \frac{1}{r}\sum_{i=1}^{r}\left(\frac{1}{y_i^2}\right) \quad (2)$$

where, MSD_{HB} - the average square deviation.
AHP is a simple method. This method can determine accurately weight value. Combination amongs Taguchi - AHP- Topsis is a good solution to solve multi-objects problem in technical fields and EDM. Multi-criteria decision using Taguchi - AHP - Topsis is performed as Figure 3.
Analyzing ratio S/N:
The lower - the better:
$(S/N)_{LB} = -10\log(MSD_{LB})$

$$MSD_{LB} = \frac{1}{r}\sum_{i=1}^{r} y_i^2 \quad (1)$$

where,
MSD_{LB} - the average square deviation.

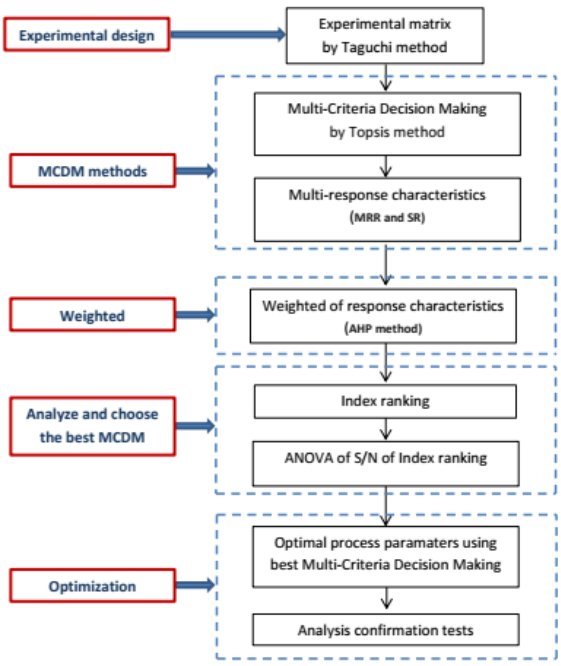

Figure 3. Steps of multi-criteria decision

4. RESULT AND DISCUSSION

4. 1. Determining the Best Experiment

Step 1: Arranging selected criteria in matrix.

$$X=\begin{bmatrix} MRR_1 & SR_1 \\ MRR_2 & SR_2 \\ & \\ MRR_{16} & SR_{16} \end{bmatrix}$$

Step 2: Normalization matrix.

Step 3: Determine values y_{11} and y_{12}. Determine value of weight of criteria using AHP. Based on number of quality criteria and priority degree of each quality criteria, elements of compared matrix is formed, as shown in Table 3. Matrix of compared pair is shown in Table 4. Normalization matrix of concatenated comparisons and calculation of priority weights and value of weight, the quality criteria is shown in Table 5. Weight of criteria is determined as follows: W_{MRR} = 0.333 and W_{SR} = 0.667.

Step 4: Determine the best solution and the worst solution: The higher MRR is the better, The smaller SR is better, so the smallest value is the best and the largest value is the worst. The values are shown in Table 6.

Step 5: Determine values S_i^+ and S_i^-, as shown in Table 7.

Step 6: Determine value C_i^*, as shown in Table 7.

Step 7: Arrange value C* and order is decribled in Table 7. The result shows that C* of the second experiment is the highest. Therefore, it can see that values

TABLE 3. Standartzation data

No.	I (A)	U (V)	T_{on} (µs)	Conversion Vector	
				X_{MRRi1}	X_{SRi2}
1	1	1	1	0.097	0.195
2	1	2	2	0.118	0.205
3	1	3	3	0.077	0.207
4	1	4	4	0.059	0.218
5	2	1	2	0.136	0.224
6	2	2	1	0.194	0.229
7	2	3	4	0.194	0.237
8	2	4	3	0.194	0.246
9	3	1	3	0.233	0.251
10	3	2	4	0.253	0.261
11	3	3	1	0.292	0.263
12	3	4	2	0.333	0.274
13	4	1	4	0.274	0.280
14	4	2	3	0.333	0.285
15	4	3	2	0.410	0.294
16	4	4	1	0.410	0.298

TABLE 4. Matrix of compared pair

Quality Criteria	MRR	SR
MRR	1	0.5
SR	2	1

TABLE 5. Normalization matrix of concatenated comparisons and calculation of priority weights

Quality criteria	MRR	SR	Total	Weight (W)
MRR	0.333	0.333	0.667	0.333
SR	0.667	0.667	1.333	0.667
SUM	1.000	1.000		

TABLE 6. Best and worst solution

	MRR	SR
A+	0.0196	0.1989
A-	0.0196	0.1989

TABLE 7. The conversion values are calculated from step 3 to step 7

No.	y_{i1}	y_{i2}	S_i^+	S_i^-	C_i^*	Ranking
1	0.0324	0.1301	0.0925	0.1080	0.538	10
2	**0.0786**	**0.1366**	**0.0667**	**0.1063**	**0.614**	**1**
3	0.0255	0.1380	0.1034	0.1157	0.528	11
4	0.0196	0.1451	0.1018	0.0894	0.468	14
5	0.0451	0.1493	0.0885	0.0915	0.508	13
6	0.0647	0.1525	0.0845	0.1175	0.582	5
7	0.0647	0.1583	0.0687	0.0903	0.568	7
8	0.0647	0.1641	0.0753	0.0974	0.564	8
9	0.0775	0.1676	0.0666	0.1020	0.605	2
10	0.0844	0.1742	0.0786	0.0817	0.510	12
11	0.0971	0.1756	0.0653	0.0832	0.560	9
12	0.1109	0.1827	0.0628	0.0849	0.575	6
13	0.0912	0.1869	0.0779	0.0669	0.462	15
14	0.1109	0.1901	0.0575	0.0483	0.456	16
15	0.1364	0.1959	0.0670	0.0971	0.591	3
16	0.1364	0.1989	0.0686	0.0965	0.585	4

of SR and MRR are the best at I =10 A, T_{on} = 500 µs and U = 45 V.

4. 2. Analynize Multi-objetcs Optimization using Taguchi–Topsis Figure 4 and Table 8 show set of optimized technology parameters and optimized results of the quality criteria in multi-objects problem in EDM for Niken coated Aluminium electrode using Taguchi-Topsis. The optimized parameters are I = 30 A, T_{on} = 500 µs, U = 50 V. Value of the quality criteria at optimal machining condition can be calculated by Equation (3), and results are shown in Table 8. The highest deviation between calculation and experiment is 13.33%. This shows that the proposed method is suitable.

$$(MRR, SR)_{OPT} = I_3 + T_{on2} + U_3 - 2.T \quad (3)$$

4. 3. Optimal Surface Quality Machined surface quality using EDM affects to work ability of products and cost of next finishing machining. In this study, authors investigated surface quality at optimal conditions, as follows: I =10 A, T_{on} = 500 µs and U = 45 V. The experimental results show that machined surface appears craters under random distribution and thier shape is spherical concave, as shown in Figure 5. There are a lot of particle adhesion appearing on machined surface and their size is different because electrode and workpiece materials are melted and evaporated and cooled rapidly by the dielectric fluid and they adhere to the machined surface, Figure 6. Besides, this created micro-cracks on machined surface and SR increases, Figure 7.

Figure 8 shows that surface layer includes white layer, heat affected zone and background layer. White layer is formed by melting and evaporation of electrode and workpiece materials which were not pushed out by dielectric fluid and they adhere to the machined surface [14]. Therefore, micro-structure and chemical

TABLE 8. Experimental results

Qualify indicator	Optimal paramter	Optimal value		Deviation (%)
		Caculation	Experiment	
MRR (mm^3/min)	I = 30 A, T_{on} = 500 µs, U = 50 V	0.15	0.17	13.33%
SR (µs)		9.81	8.76	10.71%

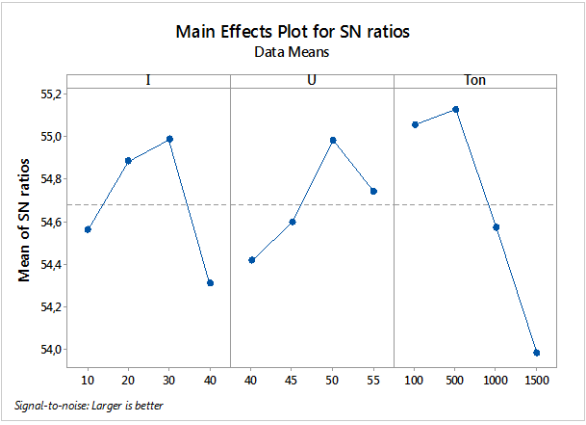

Figure 4. The influence of technological parameters on S/N of C_i

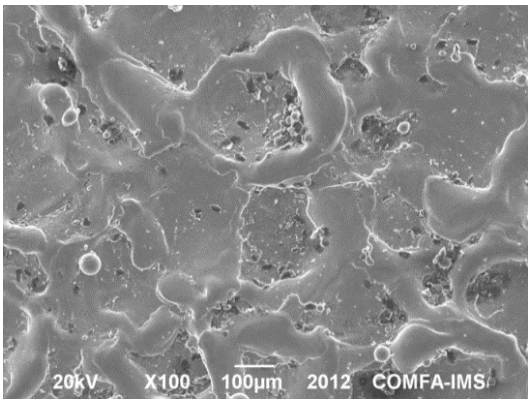

Figure 5. Topography of machined surface

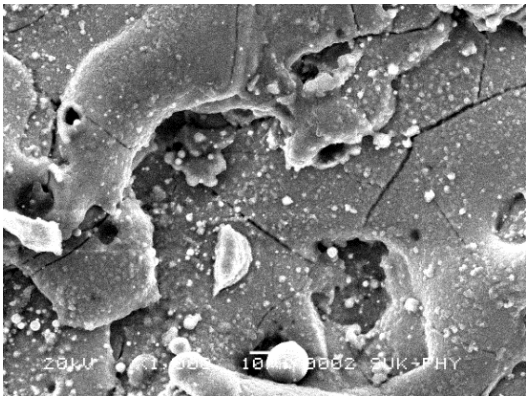

Figure 6. Adhesive particles of machined surface

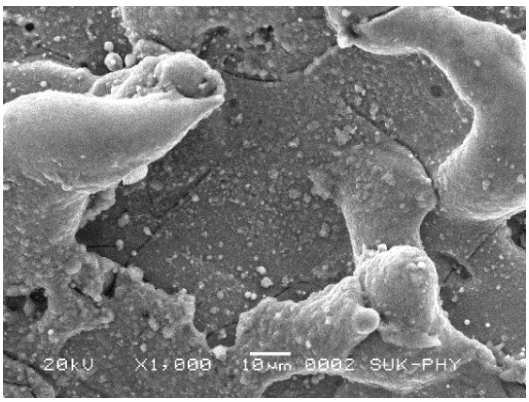

Figure 7. Micro- craks of machined surface

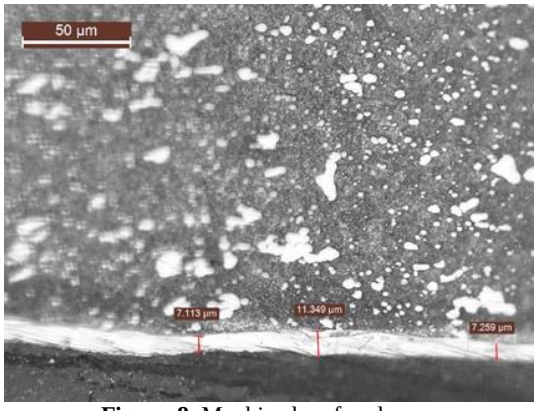

Figure 8. Machined surface layers

composition of the white layer are different from background layer [23]. Middle layer (heat affected zone) is formed by heat energy of sparks impacting metal layer under the white layer, it creates phase transition of metal layer. And hardness of this layer is often harder than background layer [23]. Experimental results show that machined surface layer using EDM is changed comparing background layer, and it is different from machined surface using traditional methods such as milling, lathe or grinding etc.

5. CONCLUSION

This study used Taguchi - AHP - Topsis to solve multi-criteria decision in EDM for Niken coated Aluminium electrode for Ti-6Al-4V. Experimental matrix was designed using Taguchi, therefore, cost of experiment is reduced significantly. AHP was applied to determine the suitable value of weight of quality criteria. Calculation using Topsis method is simple, and number of step is small. Set of technological paremeters is I = 30 A, T_{on} = 500 µs, U = 50 V, and MRR_{OPT} = 0.17 mm^3/min, Ra_{OPT} = 8.76 µm. Surface quality at optimized condition was analyzed, combination among methos is simple and clear. It can say that the proposed method in this study is suitable with this field.

6. ACKNOWLEDGMENTS

The work described in this paper was supported by Thai Nguyen University of Technology (TNUT), Thainguyen, Vietnam.

7. REFERENCES

1. Choudhary, S.K. and Jadoun, R., "Current advanced research development of electric discharge machining (edm): A review", ***International Journal of Research in Advent Technology***, Vol. 2, No. 3, (2014), 273-297.
2. Ribeiro, M., Moreira, M. and Ferreira, J., "Optimization of titanium alloy (6al–4v) machining", ***Journal of Materials Processing Technology***, Vol. 143, (2003), 458-463, doi: 10.1016/S0924-0136(03)00457-6.
3. Phan, N., Dong, P.V., Muthuramalingam, T., Thien, N., Dung, H., Hung, T.Q., Duc, N. and Ly, N., "Experimental investigation of uncoated electrode and pvd alcrni coating on surface roughness in electrical discharge machining of ti-6al-4v", ***International Journal of Engineering, Transactions A: Basics,*** Vol. 34, No. 4, (2021), 928-934, doi: 10.5829/IJE.2021.34.04A.19.
4. Biradar, S., Panchal, D. and Gosavi, V., "Optimization of edm process with coated electrode using gra", ***International Journal of Innovative Science, Engineering & Technology***, Vol. 10, No. 3, (2016), 323-328.
5. Okipnyi, I., Maruschak, P., Zakiev, V. and Mocharskyi, V., "Fracture mechanism analysis of the heat-resistant steel 15kh2mfa (ii) after laser shock-wave processing", ***Journal of Failure Analysis and Prevention***, Vol. 14, No. 5, (2014), 668-674, doi: 10.1007/s11668-014-9869-4.
6. Muttamara, A., "Comparison performances of edm on ti6al4v with two graphite grades", ***International Journal of Chemical Engineering and Applications***, Vol. 6, No. 4, (2015), 250, doi: 10.7763/IJCEA.2015.V6.490.
7. Bhaumik, M. and Maity, K., "Effect of different tool materials during edm performance of titanium grade 6 alloy", ***Engineering Science and Technology, an International Journal***, Vol. 21, No. 3, (2018), 507-516, doi: 10.1016/j.jestch.2018.04.018.
8. Mishra, D.K., Datta, S. and Masanta, M., "Effects of tool electrode on edm performance of ti-6al-4v", ***Silicon***, Vol. 10, No. 5, (2018), 2263-2277, doi: 10.1007/s12633-018-9760-0.
9. S. K. Choudhary and R. Jadoun, "Current advanced research development of electric discharge machining (EDM): A Review," ***International Journal of Research in Advent Technology***, Vol. 2, No. 3, (2014), 273-297.
10. M.V.Ribeiro M.R.V.Moreira J.R.Ferreira, "Optimization of titanium alloy (6Al–4V) machining," ***Journal of Materials Processing Technology***, No. 143-144, (2003), 458-463, doi.org/10.1016/S0924-0136(03)00457-6
11. N. H. Phan, P. V. Dong, T. Mthuramalingam, N. V. Thien, H. T. Dung, T. Q. Hung, N. V. Duc, N. T. Ly, Experimental Investigation of Uncoated Electrode and PVD AlCrNi Coating on Surface Roughness in Electrical Discharge Machining of Ti-6Al-4V, ***International Journal of Engineering, Transactions A: Basics***, Vol. 34, No. 04, (2021) 928-934, DOI: 10.5829/IJE.2021.34.04A.19
12. Panchal D. G. Biradar S. V., "Optimization of EDM Process with Coated Electrode using GRA," ***International Journal of Innovative Science, Engineering & Technology***, Vol. 3, No. 10, (2016), 2348-7968.
13. Okipnyi, I.B., Maruschak, P.O., Zakiev, V.I. et al., Fracture "Mechanism Analysis of the Heat-Resistant Steel 15Kh2MFA(II) After Laser Shock-Wave Processing," ***Journal of Failure Analysis and Prevention*** 14, (2014), 668-674, https://doi.org/10.1007/s11668-014-9869-4.
14. A. Muttamara, "Comparison performances of edm on Ti–6Al–4V with two graphite grades," ***International Journal of Chemical Engineering and Applications***, Vol. 6, No. 4, (2015) 250-258, DOI: 10.7763/IJCEA.2015.V6.490
15. M. Bhaumik and K. Maity, "Effect of different tool materials during EDM performance of Titanium grade 6 alloy," ***Engineering Science and Technology, an International Journal***, Vol. 21, No. 3, (2018), 507-516, doi.org/10.1016/j.jestch.2018.04.018

16. S. Datta, M. Masanta D. K. Mishra, "Effects of tool electrode on EDM performance of Ti-6Al-4V," Silicon, Vol. 10, No. 5, 2263-2277, (2018). doi.org/10.1007/s12633-018-9760-0

17. S. Rajamanickam, O. A. Kumar, G. K. Raj, and P. S. Narayanan J. Prasanna, "MRR and TWR evaluation on electrical discharge machining of Ti-6Al-4V using tungsten: copper composite electrode," in IOP Conference Series: Materials Science and Engineering, Vol. 197 No. 1, 012087. IOP Publishing, 2017.

18. M. A. R. Khan, K. Kadirgama, M. Maleque, and R. A. Bakar M. Rahman, "Parametric optimization in EDM of Ti-6Al-4V using copper tungsten electrode and positive polarity: A statistical approach," ***Mathematical Methods and Techniques in Engineering and Environmental Science***, Vol. 1, 23-29, (2011).

19. Liu, Y., Wang, W., Zhang, W., Ma, F., Yang, D., Sha, Z. and Zhang, S. "Experimental study on electrode wear of diamond-nickel coated electrode in EDM small hole machining", ***Advances in Materials Science and Engineering*** 2019**,** (2019), 1-10, doi.org/10.1155/2019/7181237

20. Maher, A. A. D. Sarhan, H. Marashi, M. M. Barzani & M. Hamdi, "White layer thickness prediction in wire-EDM using CuZn-coated wire electrode – ANFIS modeling", ***The International Journal of Surface Engineering and Coatings***, Vol. 94, No. 4, (2016), 204-210. doi.org/10.1080/00202967.2016.1180847

21. Min Zhang, Dong Ming Guo, Ren Ke Kang Zhu Ji Jin, "Electroforming of Copper/ZrB2 Composites Coatings and Its Performance as Electro-Discharge Machining Electrodes," ***Key Engineering Materials***, Vol. 291-292, (2005), 537-542.

22. Prosun Mandal & Subhas Chandra Mondal, "Surface characteristics of mild steel using EDM with Cu-MWCNT composite electrode," ***Materials and Manufacturing Processes***, Vol. 34, No. 12, (2019), 1326-1332, doi.org/10.1080/10426914.2019.1605179

23. Prosun Mandal & Subhas Chandra Mondal, "Development and application of Cu-SWCNT nanocomposite–coated 6061Al electrode for EDM," ***The International Journal of Advanced Manufacturing Technology***, Vol. 103, (2019), 3067-3076, doi.org/10.1007/s00170-019-03710-5

24. Kumanan S., and Sivakumaran N. Ahilan C., "Application of Grey Based Taguchi Method on Multi Response Optimization of Turning Process," ***Advances in Production Engineering and Management***, Vol. 5 No. 3, (2010), 171-180.

25. C. Tsao, S. Wang, and C. Hsu J. Kao, "Optimization of the EDM parameters on machining Ti–6Al–4V with multiple quality characteristics," ***The International Journal of Advanced Manufacturing Technology***, Vol. 47, No. 1-4, (2010), 395-402, doi.org/10.1007/s00170-009-2208-3

26. S. U. Sapkal, and R. S. Pawade M. S. Mhatre, "Electro discharge machining characteristics of Ti-6Al-4V alloy: A grey relational optimization," ***Procedia Materials Science***, Vol. 5, (2014), 2014-2022, doi.org/10.1016/j.mspro.2014.07.534

27. Tsai Chih-hung and Chen Lieh Chang Ching-liang, "Applying Grey Relational Analysis to the Decathlon Evaluation Method," ***International Journal of the Computer, the Internet and Management***, Vol. 11, No. 3, (2003), 54-62.

28. Nayak B.B., Mahapatra S.S.: Multi-response optimization of WEDM process parameters using the AHP and TOPSIS method. ***International Journal on Theoretical and Applied Research in Mechanical Engineering***, Vol. 3, No. 4, (2013), 2281-2286

29. Gadakh V.S.: Parametric optimization of wire electric discharge machining using TOPSIS method. ***Advances in Production Engineering and Management,*** Vol. 7, No. 3, (2012), 157-164. DOI: 10.14743/apem2012.3.138.

30. Qosim. N., Supriadi. S., Puspitasari. P., Kreshanti. P., "Mechanical Surface Treatments of Ti-6Al-4V Miniplate Implant Manufactured by Electrical Discharge Machining", ***International Journal of Engineering, Transactions A: Basics***, Vol. 31, No. 7, (2018), 1103-1108, DOI: 10.5829/ije.2018.31.07a.14.

31. Mykola Chausov, Pavlo Maruschak, Andriy Pylypenko, Lyudmila Markashova, Enhancing plasticity of high-strength titanium alloys VT 22 under impact-oscillatory loading, ***Part A: Materials Science.*** https://doi.org/10.1080/14786435.2016.1262973.

Persian Abstract

چکیده

برای بهبود بهره وری و کیفیت فرآیند ماشینکاری با استفاده از EDM، تعداد زیادی الکترود مانند الکترودهای روکش دار و آلیاژی استفاده شده است. مطالعه بر روی بهینه سازی چند شیء در EDM با الکترود روکش دار ، کاربرد این زمینه را در عمل افزایش می دهد. در این مطالعه ، میزان حذف مواد (MRR) و زبری سطح (SR) در EDM با استفاده از الکترود آلومینیوم با روکش نیکل به طور همزمان با استفاده از روشهای تاگوچی – AHP - Topsis بهینه شده است. پارامترهای تکنولوژیکی شامل پیک جریان (I)، ولتاژ شکاف (U) و نبض در زمان (تن) مورد بررسی قرار گرفت. آلیاژ تیتانیوم (Ti-6Al-4V) به عنوان قطعه کار در فرایند آزمایشی انتخاب شد. نتایج نشان می دهد که ترکیب روش های تاگوچی – AHP - Topsis برای حل بهینه سازی چند شیء در EDM مناسب است. پارامترهای تکنولوژیکی بهینه I = 30 A ، تن = ۵۰۰ µs، U = 50 V و معیارهای کیفیت بهینه MRR = 0.17 mm3 در دقیقه و SR = 8.76 میکرومتر است.

International Journal of Engineering

Journal Homepage: www.ije.ir

Modified Second Order Generalized Integrator-frequency Locked Loop Grid Synchronization for Single Phase Grid tied System Tuning and Experimentation Assessment

B. Brahmbhatt*[a], H. Chandwani[b]

[a] *Electronics and Communication Department, Government Engineering Collage,Modasa,Gujarat, India*
[b] *Electrical and Electronics Department, The Maharaja Sayajirao University of Baroda,Vadodara,Gujarat,India*

P A P E R I N F O

Paper history:
Received 03 May 2020
Received in revised form19 October 2021
Accepted 27 October 2021

Keywords:
Phase-locked Loop
Frequency Lock Loop
STM32F407VG Microcontroller
DC-Signal Cancellation Block

A B S T R A C T

The phase-locked loop (PLL) is applied in grid-tied systems to synchronise converter operation with grid voltage, affecting converter stability and performance. Synchronous reference frame PLL (SRF-PLL) is a popular grid synchronisation method due to its simplicity and reliability. Normal SRF-PLL cannot suppress DC offset, causing basic frequency and phase oscillations. When a grid is irregular, its bandwidth should be reduced to ensure acceptable disturbance rejection without sacrificing detection speed. To enhance the phase-angle estimation speed and accuracy, the researchers modified structure by adding the pre/in-loop filter in advanced PLLs. The capacity to deliver improved dynamic response and reduced settling time without compromising system stability or the ability to eliminate disturbances is a major issue for PLLs. Among different control methods, SOGI-FLL (second-order generalised integrator-based frequency locked loop) had the best performance. It tracks grid voltage frequency precisely even when there is harmonics, voltage variations, frequency fluctuations, etc. In the event of a dc offset, the calculated frequency incorporates low frequency oscillations. A modified second-order generalised integrator frequency-locked loop (MSOGI-FLL) is presented in this work to address grid voltage anomalies of all types, including dc offset. Using the Waijung Block-set of MATLAB/Simulink, a Modified SOGI-FLL is realized and evaluated by applying abnormal grid voltage situations using a low-cost DSP-based STM32F407VGT microcontroller. The results demonstrate MSOGI-better FLL's performance in harsh circumstances.

***doi**: 10.5829/ije.2022.35.02b.03*

1. INTRODUCTION

Many grid-connected inverters have drawn interest for their economical circuit architecture and advanced control techniques due to the rapid rise in renewable energy [1]. The phase-locked loop (PLL) is an important component in the grid assisted inverter's control strategy since it is primarily utilised to keep the inverter and grid synchronised. A new energy power system's security and stability are directly associated with the performance of the grid-connected inverter [2]. For the converter to work properly, the control algorithm must accurately compute the amplitude, phase-angle, and frequency from the grid voltages. It is difficult when the grid voltage has irregularities(frequency variation, harmonics, voltage fluctuation, dc offset, and/or distortion, switching notches, etc.) [2]. These anomalies can cause measurement and data translation mistakes, making predicting frequency and synchronisation problematic [3]. A phase-locked loop is composed of a phase detector, a filter, and a voltage-regulated oscillator. The PD controls the gain of a voltage-regulated oscillator, whose output signal is frequency and phase synced with the input reference signal. Golestan et al. [3, 4] addressed the categorization of phase lock loop with varying phase detector. Under distorted grid signal

*Corresponding Author Email bhavic0072009@gmail.com (B. Brahmbhatt)

Please cite this article as: B. Brahmbhatt, H. Chandwani, Modified Second Order Generalized Integrator–frequency Locked Loop Grid Synchronization for Single Phase Grid tied System Tuning and Experimentation Assessment, ***International Journal of Engineering, Transactions B: Applications*** Vol. 35, No. 02, (2022) 283-290

circumstances, PD structures based on generalised integrators (GI) function better and are more reliable [4, 5]. Thus, SOGI-PLL is better than other PLL designs [3-5]. It works quickly and accurately in bad grid circumstances. In contrast to SOGI-PLL, where the estimated frequency is utilized as feedback from the SOGI-OSG block, SOGI-FLL use a frequency-locked loop (FLL) to adaptively get the frequency [6]. The adaptive nature prevents PLL and improves performance. Factors including transformer nonlinearity, A/D conversion error, analogue device anomalous temperature, and zero drift all produce DC offset when the power grid failure occurs [7, 8]. There are several ways to reduce the DC offset in SRF-PLL nowadays. Golestan et al. [9] suggested a cascaded second-order generalised integrator-phase lock loop (CSOGI-PLL) to eliminate the DC quantity; however, it comprises se Factors including transformer nonlinearity, A/D conversion error, analogue device anomalous temperature, and zero drift all produce DC offset when the power grid failure occurs. It utilizes several SOGI structures, thus the added computing cost is significant [10]. To speed up DC offset removal, Kulkarni et al. [10] devised a cascade delay signal cancellation PLL technique (CDSC-PLL), while Parag et al. [11] utilised an adaptive filter delay signal cancellation-PLL (APF-DSC-PLL) to increase the speed of DC offset rejection, but the complex structure reduces the dynamic performance of the system. Moreover, a phase-locked loop based on the modified delay signal cancellation-PLL was presented by Li et al. [12] which can enhance dynamic performance by reducing DC offset, but it would induce phase deviation, which necessitates design correction. These notch filter (NF) based on PLL and dq-DSC -PLL, as well as five additional approaches for eliminating the DC offset in the PLL. However, these phase detection approches suffer from a sluggish dynamic performance [13-15]. These approaches have the potential to increase dynamic performance while overcoming the drawbacks of conventional low-pass filters [9-16]. However, selecting and calculating the sliding window width is time-consuming [15, 16]. Thus, a modified SOGI-FLL (MSOGI-FLL) for single-phase systems is suggested to reduce frequency estimation errors caused by DC quantity and other grid irregularities (e.g. harmonics, frequency fluctuation, magnitude variation). Using the third integrator as a DC offset cancellation block, the proposed MSOGI-FLL estimates the DC offset without influencing frequency estimation in the FLL.The better performance of this structure has been demonstrated through modelling and experimental findings. The next sections describe the MSOGI-FLL and its performance under various situations.

2. ORGANIZATION & TRANSFER FUNCTION: SECOND-ORDER GENERALIZED INTEGRATOR (SOGI)-FREQUENCY LOCKED LOOP(FLL)

SRF based PLL uses an additional voltage-controlled oscillator, although SOGI-QSGs serve as filters as well as voltage-controlled oscillators. The SOGI resonator's centre frequency is adjusted to match the input frequency using an auto tune block, as shown in Figure 1. The Frequency-Locked Loop (FLL) block estimates the frequency adaptively by changing the gain (Γ) in SOGI-FLL, thus the PLL block used in SOGI-PLL is omitted. The SOGI-FLL works far better, faster, and more accurately than traditional SRF-PLL-based systems in grid anomalies including harmonics, voltage variations, frequency fluctuations, and phase jump etc. for instance. The transfer functions of band-pass filter (BPF) and low-pass filter (LPF) illustrated in Equations (1) and (2) are derived from the conventional SOGI-QSG in Figure 1. A real positive value of gain k can be tuned to alter the bandpass filter $D_{SOGI-FLL}$and low-pass filter $Q_{SOGI-FLL}(s)$bandwidth (or sharpness). This means that the signals Y(s) and Y'(s) are the BPF and LPF outputs, with a 90° phase difference (as shown in bode diagram, Figure 2), respectively. In reality, the LPF outperforms the BPF when it comes to high-frequency filtering. The output signal ($Y'(s)$) of SOGI-QSG is badly affected by a non-zero dc offset in the measured grid voltage.

$D_{SOGI-FLL}(s)$ and $Q_{SOGI-FLL}(s)$ have the following transfer functions:

$$D_{SOGI-FLL}(s) = \frac{Y(s)}{v_{in}(s)} = \frac{k\ s\ \omega}{s^2 + k\omega s + \omega^2} \quad (1)$$

$$Q_{SOGI-FLL}(s) = Q_v(s) = \frac{Y'(s)}{v_{in}(s)} = \frac{k\,\omega^2}{s^2 + k\omega s + \omega^2} \quad (2)$$

Furthermore, Bode's magnitude responses retain 0 dB at the 50Hz fundamental frequency while attenuating amplitude at the 5th and 7th harmonic frequencies of 250Hz and 350Hz, respectively. It should react as a notch filter with zero gain and 180° phase leap at centre frequency to produce auto-tunable SOGI-QSG (see Figure 3).

The transfer function of voltage error signal $\mathbf{E_{SOGI-FLL}}$ can be described as:

$$E_{SOGI-FLL}(s) = E_v(s) = \frac{\varepsilon_{v(s)}}{v_{in(s)}} = \frac{s^2 + \omega^2}{s^2 + k\omega s + \omega^2} \quad (3)$$

In the SOGI-FLL, a frequency error signal (ε_f) is generated from the product of $\boldsymbol{E_{SOGI-FLL}(s)}$ & $\boldsymbol{Q_{SOGI-FLL}(s)}$. As illustrated in Figures 1 and 3, the frequency locking loop may be built utilising the

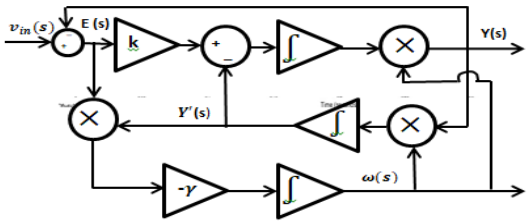

Figure 1. The fundamental architecture SOGI –FLL

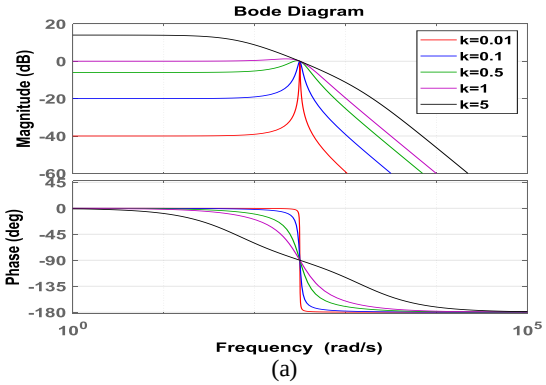

(a)

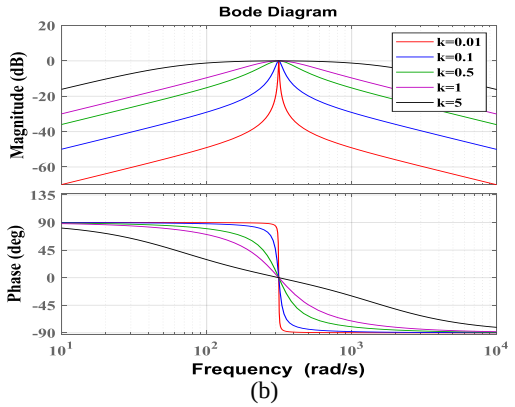

(b)

Figure 2. Bode Graph of (a) $\boldsymbol{D_{SOGI-FLL}(s)}$, and (b) $\boldsymbol{Q_{SOGI-FLL}(s)}$ with various value of k

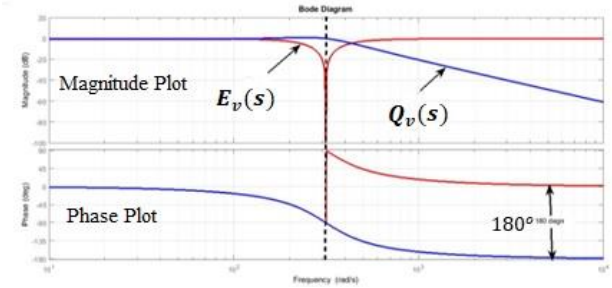

Figure 3. Bode Graph of the $\boldsymbol{E_{SOGI-FLL}(s)}$ & $\boldsymbol{Q_{SOGI-FLL}(s)}$ in an SOGI- QSG

frequency error signal (ε_f) and a negative controller gain($-\gamma$)of frequency loop. The SOGI resonance frequency(ω') is changed until it equals the input frequency (ω) using the frequency loop controller gain ($-\gamma$). A feed-forward variable, ω_c, is included in the FLL to accelerate initial synchronisation. By incorporating feedback, a value of γ should be normalised and defined as follows:

$$\gamma = \frac{k\omega}{V^2} \quad \Gamma \tag{4}$$

With a feed-forward of $2\pi * 50.$, the dynamic response of frequency estimationin SOGI-FLL is studied. As observed the dynamic response of frequency estimation in Figures 4(a), 4(b), 4(c) and 4(d) using progressive values of k and constant values of γ, and vice versa. Table 1 contains the evaluation of parameter k and γ for SOGI-FLL, as shown in Figure 4 (a)-(d). Transient responsiveness and bandwidth of SOGI-FLL are affected by the para-meter k. The choice of gain k compromises between good signal filtering and transient response of system dynamic responsiveness (Figure 4). The choice of value γ compromises frequency estimate precision and SOGI-FLL dynamics. Reduction in a bandwidth increases rise time (t_{rise} = 0.35/ BW), but improves other metrics.

3. STRUCTURE & TRANSFER FUNCTIONS : MSOGI-FLL

Figure 5 depicts the SOGI-FLL's fundamental structure.

When the third integrator estimates the DC offset, it subtracts it from the signal to improve the system's DC offset rejection capabilities. In addition, Figure 5 shows the suggested MSOGI-FLL structure, which incorporates a DC signal cancellation (DSC) block and a SOGI-FLL structure. In general, a DC-offset can be introduced into the grid signal by the signal conditioning or measuring equipment, as well as other factors like half-wave rectification. Because of this, the pre-filtering stage includes a DC signal cancellation (DSC) block that provides excellent DC-offset rejection and SOGI-FLL rejects the low-order harmonic.

A new version of the band-pass SOGI-FLL (Figure 5) filter [17-19] designated as MSOGI-FLL can be proposed by including the DSC operator. A grid signal polluted with a DC-offset, MSOGI transfer functions is represented as follows for comprehension purposes:

$$D_{MSOGI-FLL}(s) = \frac{Y(s)}{v_{in}(s)} = \frac{k\omega' s^2}{s^3 + k\omega' s^2 + k'\omega' s^2 + \omega'^2 s + k'\omega'^3} \tag{5}$$

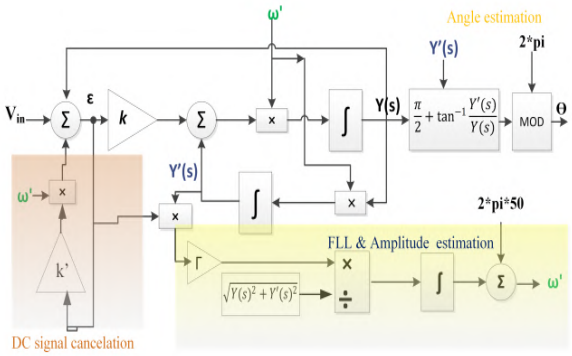

Figure 5. Fundamental architecture of a MSOGI-Frequency lock loop

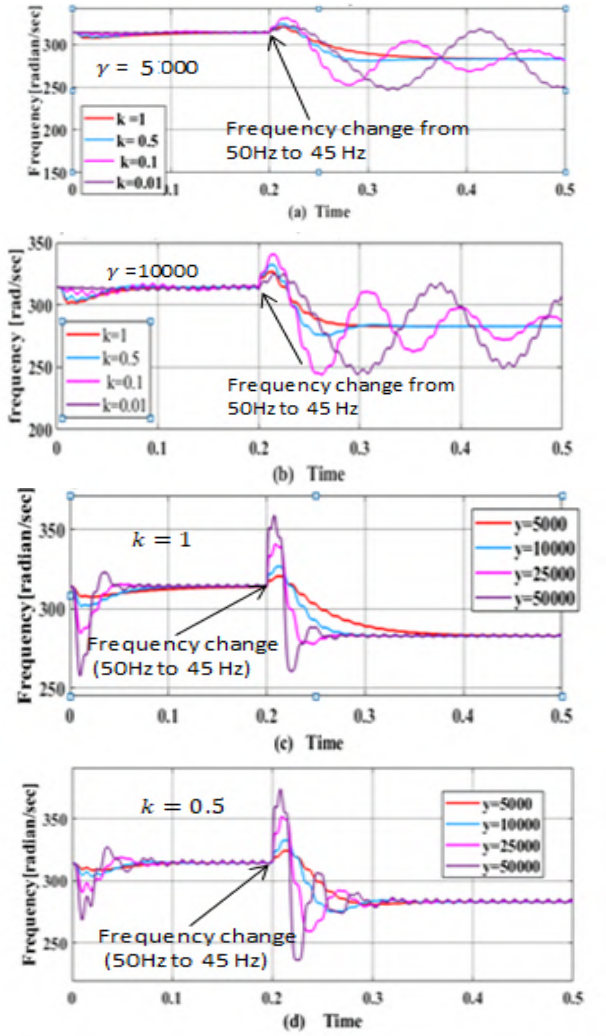

Figure 4. Step response for Frequency Estimation: various values for kand Constant Values (a) γ=5000,(b) γ=10000, (c) &(d)various value of γ and constant value k=1, and k=0.5, respectively

TABLE 1. Evaluation of parameter for SOGI-FLL

Parameter	Variation in parameter	Dynamic response	Steady-state response	Filter response	Settlement time
k	Increase ↑	Worthy	Worthy	Worthy	Reducing
	Decrease↓	Poor	Poor	Poor	Increasing
γ	Increase ↑	Poor	Average	No change	Reducing
	Decrease↓	Worthy	Good	No change	Increasing

$$Q_{MSOGI-FLL}(s) = \frac{Y\prime(s)}{v_{in}(s)} = \frac{k\omega\prime s}{s^3+k\omega' s^2+k'\omega' s^2+\omega'^2 s+k\prime\omega'^3} \quad (6)$$

$$E_{MSOGI-FLL}(s) = \frac{V_{dc}(s)}{v_{in}(s)} = \frac{k'\omega' s^2+k\prime\omega'^3}{s^3+k\omega' s^2+k'\omega' s^2+\omega'^2 s+k\prime\omega'^3} \quad (7)$$

Using Routh hurtiz criteria, the gain k is given as:

$$k = \frac{9.2}{\omega' t_s}\,;\, t_s = 4.6 * \tau\,;and\ \tau = \frac{1}{\zeta\omega_n} \quad (8)$$

In order to filter out low and high-frequency components in the input signals, gain k must be properly tuned. These graphs (see Figures 2 and 3) show that unlike $D_{SOGI-FLL}(s)$, $Q_{SOGI-FLL}(s)$ attenuates low frequency components, leaving the dc offset.The quantities k and k' are chosen from the roots of the denominator of transfer functions/characteristic equation of MSOGI-FLL($D_{MSOGI-FLL}(s), and\, Q_{MSOGI-FLL}(s)$) with equal real parts (Figure 6) (all three poles have equal natural frequency of oscillation). On the other hand, ω_{n1} =ω_{n2} =2*pi*50 rad/s (same as for tuning SOGI-FLL) is used to compute the gain k and k' respectively. The bode graphs in Figure 6 demonstrates the impact of both gain adjustments as well as performance assessment of SOGI-FLL and MSOGI-FLL using magnitude plots of transfer functions from equations [1-3] and [5-7]. Figures 6 (a) and 6(b) show magnitude bode graphs of $D_{MSOGI-FLL}(s)$ and $Q_{MSOGI-FLL}(s)$ (Equations 5 and 6), below 0dB for low frequency components, indicating attenuation of low frequency and DC components. It is clear that a positive gain $Q_{SOGI-FLL}(s)$,which does not reduce the DC signal. Due to presence of third generalised integrator, the magnitude of the transfer function $E_{MSOGI-FLL}(s)$ is close to 0dB. Moreover, $Q_{MSOGI-FLL}(s)$ has negative gain at frequencies over 50Hz, which reduces higher order harmonics. But it's considerably lower than50Hz. With the third integrator component (and higher order frequencies) are greatly attenuated, leaving only the low order frequencies to pass, as seen below. It aids in estimating and eliminating the DC offset from grid voltage.

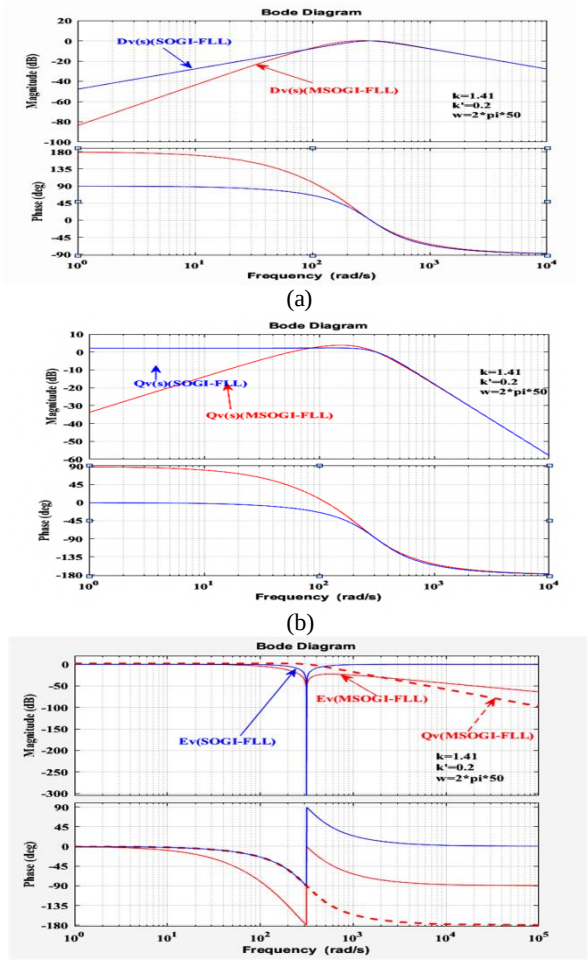

Figure 6. Bode Graph of the transfer function MSOGI-FLL and SOGI-FLL

4. EXPERIMENTAL RESULTS

MATLAB/ Simulink is used to design and implement the MSOGI-FLL on a downscaled STM32F407VGT6 microcontroller. The discrete MSOGI-FLL model (see Figure 7) is translated to c code before being compiled and dumped into the microcontroller. Microcontroller STM32F407VGT6 has two digital analogue converters (12bit-DAC) and supports waijung environment in SIMULINK/MATLAB (i.e. model-based programming).

It is low cost and 32-bit. Simulated results back up the experimental findings, demonstrating the efficacy of MSOGI-FLL when used in model-based programming There are a few useful parameters for MSOGI-FLL: k = 0,5, k'=0,2,=-5000, sapling time ts = 300 usecond, and f g = 50 Hz for grid voltage frequency. The ADC conversion unit and other digital/discrete units introduce DC-offset, causing inaccuracy in phase estimation of SOGI-FLL.While this was going on, a slew of researchers presented new and better as well ascomplexSOGI-FLL structures of filters. Using the third integrator in MSOGI-FLL to estimate the dc offset allows for better DC offset rejection by subtracting the estimate from the signal. In the experimental setup, MSOGI-FLL is validated by testing each instance separately in the following ways:

Assessment case 1: Experimentation is performed with 0.65p.u. voltage sag on the grid voltage.

Assessment case 2: Examination are performed on grid frequency by imposing a 5% step change (i.e. frequency leap from 50Hz to 45Hz) and a phase angle shift from 0° to 45° on grid frequency and phase.

Assessment 3:grid voltage that has been subjected to harmonic distortion is used.

Figure 8 presents the experimental findings obtained to evaluate the MSOGI-FLL settling time on a grid voltage influenced by a 0.65 p.u voltage sag at Figure 8 depicts the SOGI-FLL v_α / v_{in} settle down near to the fourth cycle, or 45 m-second, when utility voltage is influenced by a voltage drop in grid voltage. A frequency step change from 50Hz to 45Hz and a phase angle shift from 50^0 to 45^0 are applied to the grid voltage during experimental test 2, as illustrated in Figure 9. Only at t =400m-second, as shown in Figure 8, is the phase angle shifted from 50^0 to 45^0. Preliminary results show that the MSOGI-FLL frequency and phase-angle readings are stable, withjust a little frequency shift occurring before the third cycle is reached. This test uses a microcontroller's ADC pin to control the frequency of a sine wave generated inside MATLAB/Simulink (see Figure 7), rather than an AC grid simulator. For experimental test-3, the dynamic response of SOGI-FLL is tested by applying harmonic voltages of 3rd, 5th, and 7th order with amplitudes of 0.35p.u., 0.1p.u., and 0.08p.u. in relation to the fundamental grid voltage (as shown in Figure 10).

As illustrated in Figure 10, MSOGI-QSG is experimentally shown to be a band-pass filter for the Figure 10 shows that the SOGI-FLL is immune to distorted grid voltage. Figure 9 demonstrates that the measured phase-angle is devoid of harmonic distortion and the 100Hz phase-angle frequency component.

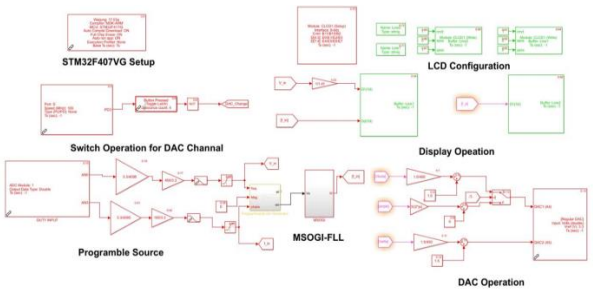

Figure 7. Model based programmingin STM32F407VG using waijung blockset of MATLAB/Simulink

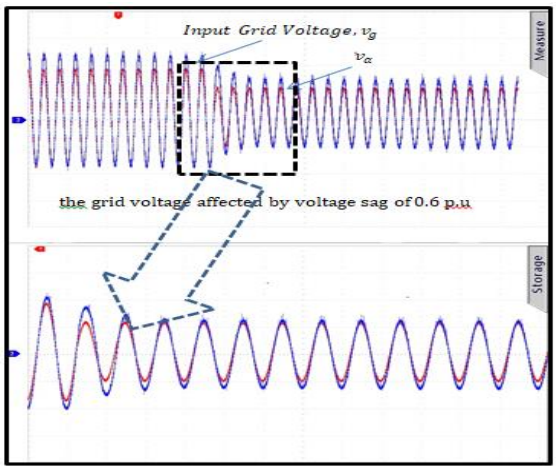

Figure 8. Experimental results of Test case:1. (Time Scale:20m-second/div; 0.5V/div)

MSOGI-FLL output signals, i.e. v_α/v_{in} and v_β/v_{in}, which are likewise devoid of harmonic distortion. Despite various irregularities affecting the grid voltage, the MSOGI-FLL continues to operate the same way. There is a single-phase voltage source converted, 10mH line inductor, auto-transformer and ARM cortex M4 microprocessor built as an experimental prototype for testing. The control algorithm was created in MATLAB/Simulink using the waijung blockset and then loaded onto a low-cost STM32F407VG ARM Cortex M4 microcontroller for general-purpose digital signal processing. Experimental results (see Figure 12) are carried out at 110V RMS grid voltage on experimental set-up (see Figure 11) at the point of common coupling. The sampling time of model base program is choosen 300micro-second. The control of single-phase grid tied inveter is developed using well-known synchronous reference frame current control techqnique.

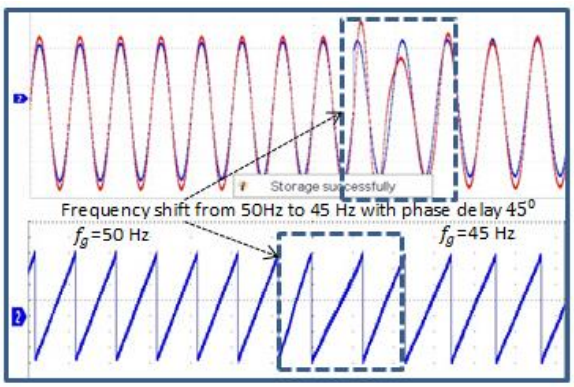

(a)

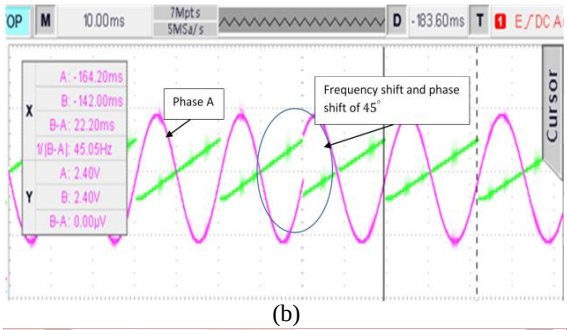

(b)

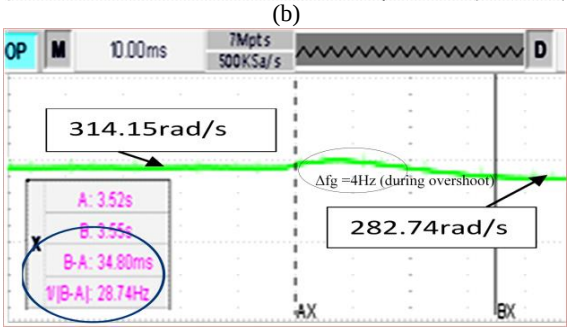

(c)

Figure 9. Experimental results of Test case:2. .(For (a)Time Scale:20m-second/div; 0.5V/div; (b) Time Scale:10m-second/div; 1V/div)

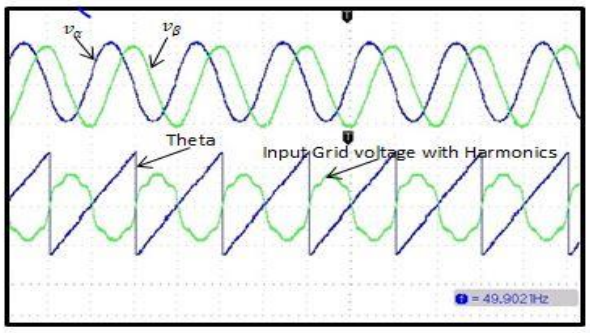

Figure 10. Experimental results of Test case:3.(Time Scale:10m-second/div; 1V/div)

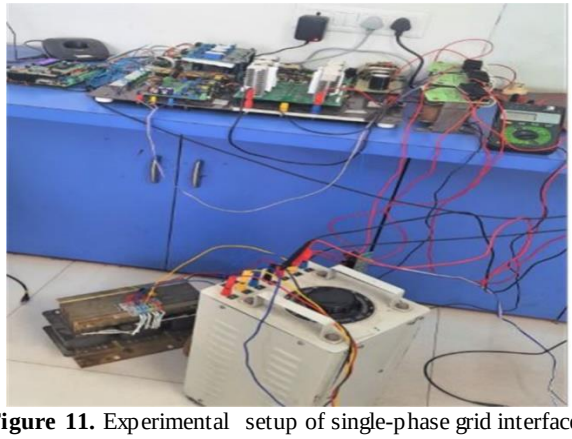

Figure 11. Experimental setup of single-phase grid interfaced voltage source converter

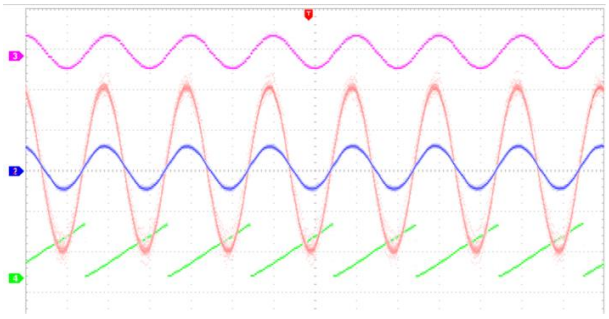

Figure 12. Experimental result of single-phase grid interfaced voltage source converter(Time scale:10ms//div) : (a)i_g(Pink and blue; Scale 4A/div), (b) i_g(Orage; Scale: 75V/div), and (c) theta (green)

5.DISCUSSION

Table 2 summarises the experimental findings for the single- phase grid voltage test scenarios.

It's possible to estimate the peak errors in the fundamental grid's parameters(e.g. amplitude, phase and frequency information), and tr stands for the settling time performance. The presented technique takes around 2.4 times as long to compute the grid's parameters as the current standard.

With the SOGI-OSG and DC signal cancellation block, MSOGI-FLL can achieve better immunity to DC-offset and harmonic noise. Both the SOGI–FLL and the SRF-PLL have frequency information that is impacted by the phase angle change. However, in the instance of the suggested method, the predicted frequency has a maximum overshoot of 4 Hz. With a net settling time of 34 ms, the suggested single-phase system has proven to have strong harmonics elimination and DC-offset rejection capabilities. There is therefore significant potential for the suggested system to identify harmonic and fundamental grid voltage characteristics selectively.

TABLE 2. Highlights of Comparative Performance Assessment

Cases	Peak Errors	SRF-PLL	SOGI-FLL	MSOGI-FLL
Voltage Drops	ΔA_g	-	-	-
	Δf_g	-	-	-
	$\Delta \theta_g$	-	-	-
	t_r	≈ 80	≈ 55	≈ 45
Freq.Step change	ΔA_g	≈ 2	-	-
	Δf_g(during oveshoot)	≈ 9	≈ 5	≈ 4
	$\Delta \theta_g$	≈ 5^0	≈ 1.5^0	≈ 1.5^0
	t_r	≈ 80	≈ 40	≈ 34
DC-Offset Elimination		NO	NO	YES
Harmonics Attenuation		NO	YES	YES
Steady-state Accuracy		Average	Good	Good
Control parameters		2	2	3
PI Tunning Required		YES	NO	NO

6. CONCLUSIONS

A good rejection of DC-offset, harmonics, and the frequency and phase-angle extraction may be achieved using MSOGI-FLL technique. Except for the existence of DC offset, SOGI-FLL can properly estimate the grid signal's frequency. Due to a DC offset in grid voltage, the predicted frequency has a 100Hz low frequency component. When harmonics are present, the distortion on this 100Hz ripple is amplified. The DG based inverter's synchronisation and control may be compromised as a result of this frequency estimate inaccuracy. Control parameter selection of SOGI-FLL is an art that balances the dynamic responsiveness, filtering capabilities, and required precision in detecting frequency and phase angle for single-phase grid-tied inverters under less than ideal grid circumstances.There is no ripple in the predicted synchronised frequency when using the Two essential blocks constitute the MSOGI-FLL structure: a basic SOGI-QSG architecture block modified with DC offset cancellation block, and a FLL for adaptively computing grid frequency.The dc offset cancellation block (i.e.third integrator) in MSOGI-FLL reduces the DC offset compared to the normal SOGI-FLL structure.Thus, the suggested technique is capable of rejecting DC offset and therefore correctly tracking the basic grid-voltage component frequency under all grid irregularities, in addition to the advantages of standard SOGI-FLL. In addition, the suggested systemis resistant to volatage sag/swell in the grid voltage and frequency fluctuations. Experiments results have shown that the proposed MSOGI-FLL seems to be more precise and has a superior transient stability than the conventional SOGI-FLL.

7.REFERENCES

1. Chishti, F., Murshid, S. and Singh, B.J.I.T.o.I.A., "Development of wind and solar based ac microgrid with power quality improvement for local nonlinear load using mlms" ***IEEE Transactions on Industrial Electronics***, Vol. 55, No. 6, (2019), 7134-7145. doi: 10.1109/TIA.2019.2923575
2. Kouro, S., Leon, J.I., Vinnikov, D. and Franquelo, L.G.J.I.I.E.M., "Grid-connected photovoltaic systems: An overview of recent research and emerging pv converter technology", ***IEEE Industrial Electronics Magazine,*** Vol. 9, No. 1, (2015), 47-61. doi: 10.1109/MIE.2014.2376976

3. Golestan, S., Guerrero, J.M. and Vasquez, J.C.J.I.T.o.P.E., "Single-phase plls: A review of recent advances" ***IEEE Transactions on Power Electronics,*** Vol. 32, No. 12, (2017), 9013-9030. doi: 10.1109/TPEL.2017.2653861
4. Golestan, S., Guerrero, J.M. and Vasquez, J.C.J.I.T.o.P.E., "Three-phase plls: A review of recent advances",***IEEE Transactions on Power Electronics***, Vol. 32, No. 3, (2016), 1894-1907. doi: 10.1109/TPEL.2016.2565642
5. Brahmbhatt, B. and Chandwani, H., "Single phase transformerless photovoltaic inverter with reactive power control", IEEE 1st International Conference on Power Electronics, Intelligent Control and Energy Systems (ICPEICES) in 2016 IEEE. (2016), 1-5.
6. He, X., Geng, H. and Yang, G.J.I.T.o.I.E., "A generalized design framework of notch filter based frequency-locked loop for three-phase grid voltage", ***MLMS IEEE Transactions on Industrial Electronics*** Vol. 65, No. 9, (2017), 7048-7072, doi: 10.1109/tie.2017.2784413
7. Santos Filho, R.M., Seixas, P.F., Cortizo, P.C., Torres, L.A. and Souza, A.F.J.I.T.o.i.e., "Comparison of three single-phase pll algorithms for ups applications", ***IEEE Transactions on Industrial Electronics*** Vol. 55, No. 8, (2008), 2923-2932. doi: 10.11/۰۹TIE.2008.924205
8. Thacker, T., Boroyevich, D., Burgos, R. and Wang, F.J.I.T.o.I.E., "Phase-locked loop noise reduction via phase detector implementation for single-phase systems", ***IEEE Transactions on Industrial Electronics,*** Vol. 58, No. 6, (2010), 2482-2490 .doi: 10.1109/TIE.2010.2069070
9. Golestan, S., Guerrero, J.M. and Gharehpetian, G.B.J.I.T.o.P.E., "Five approaches to deal with problem of dc offset in phase-locked loop algorithms: Design considerations and performance evaluations", ***IEEE Transactions on Power Electronics,*** Vol. 31, No. 1, (2015), 648-661.doi: 10.1109/TPEL.2015.2408113
10. Kulkarni, A. and John, V.J.E.P.S.R., "Design of a fast response time single-phase pll with dc offset rejection capability", ***Electrical Power System Research***, Vol. 145, (2017), 35-43. doi: 10.1016/j.epsr.2016.12.023
11. Kanjiya, P., Khadkikar, V. and El Moursi, M.S.J.I.T.o.I.E., "Adaptive low-pass filter based dc offset removal technique for three-phase plls", ***IEEE Transactions on Industrial Electronics,*** Vol. 65, No. 11, (2018), 9025-9029. doi: 10.1109/tie.2018.2814015
12. Li, Y., Wang, D., Ning, Y. and Hui, N.J.E.L., "Dc-offset elimination method for grid synchronisation", ***Electronics Letter*** Vol. 53, No. 5, (2017), 335-337. doi: 10.1049/el.2016.4570
13. Wu, F., Li, X.J.I.J.o.E. and Electronics, S.T.i.P., "Multiple dsc filter-based three-phase epll for nonideal grid synchronization", ***IEEE Journal Emerging Selected Topics Power Electronics***, Vol. 5, No. 3, (2017), 1396-1403. doi: 10.1109/JESTPE.2017.2701498
14. Li, Y., Wang, D., Han, W., Tan, S. and Guo, X.J.I.A., "Performance improvement of quasi-type-1 pll by using a complex notch filter", ***IEEE Access,*** Vol. 4, (2016), 6272-6282. doi: 10.1109/ACCESS.2016.2614008
15. Hui, N., Feng, Y. and Han, X.J.E.R., The International Conference on Power Engineering (ICPE 2020), Guangzhou, China,Energy Reports Science Direct" Dc offset elimination method of phase-locked loop based on novel generalized integrator", Vol. 7, (2021), 30-35. doi: 10.1016/j.egyr.2021.02.030
16. Hui, N., Feng, Y. and Han, X.J.I.A., "Design of a high performance phase-locked loop with dc offset rejection capability under adverse grid condition", ***IEEE Access, 2020*** Vol. 8, (2020), 6827-6838. doi: 10.1109/ACCESS.2020.2963993
17. Mirhosseini Moghadam, M., Tavakoli, A. and Alizadeh, B.J.I.J.o.E., "Stability analysis of ac/dc microgrids in island mode", ***International Journal of Engineering, Transactions A: Basics,*** Vol. 34, No. 7, (2021), 1750-1765. doi: 10.5829/ije.2021.34.07a.20
18. Ardeshir, G. and Gholami, M.J.I.J.o.E., "Dual phase detector based delay locked loop for high speed applications", ***International Journal of Engineering, Transactions A: Basics*** Vol. 27, No. 4, (2014), 517-522. doi: 10.5829/idosi.ije.2014.27.04a.02
19. Rahimi Mirazizi, H. and Agha Shafiyi, M.J.I.J.o.E., "Evaluating technical requirements to achieve maximum power point in photovoltaic powered z-source inverter", ***International Journal of Engineering, Transactions C: Aspects,*** Vol. 31, No. 6, (2018), 921-931. doi: 10.5829/ije.2018.31.06c.09

Persian Abstract

چکیده

حلقه قفل فاز (PLL) در سیستم های متصل به شبکه برای همگام سازی عملکرد مبدل با ولتاژ شبکه اعمال می شود که بر پایداری و عملکرد مبدل تأثیر می گذارد. قاب مرجع سنکرون (SRF-PLL) PLL یک روش همگام سازی شبکه محبوب به دلیل سادگی و قابلیت اطمینان آن است. SRF-PLL معمولی نمی تواند آفست DC را سرکوب کند، که باعث نوسانات فرکانس و فاز اساسی می شود. وقتی یک شبکه نامنظم است، پهنای باند آن باید کاهش یابد تا از رد اختلال قابل قبول بدون کاهش سرعت تشخیص اطمینان حاصل شود. برای افزایش سرعت و دقت تخمین زاویه فاز، محققان ساختار را با افزودن فیلتر pre/in-loop در PLL های پیشرفته اصلاح کردند. ظرفیت ارائه پاسخ دینامیکی بهبود یافته و کاهش زمان ته نشینی بدون به خطر انداختن پایداری سیستم یا توانایی حذف اختلالات است. یک مشکل عمده برای PLL ها. در بین روش‌های کنترل مختلف، SOGI-FLL) حلقه قفل فرکانس مبتنی بر انتگرال‌گر تعمیم‌یافته مرتبه دوم) بهترین عملکرد را داشت. فرکانس ولتاژ شبکه را دقیقاً حتی زمانی که هارمونیک ها، تغییرات ولتاژ، نوسانات فرکانس و غیره وجود دارد، ردیابی می کند. در صورت افست DC، فرکانس محاسبه شده دارای نوسانات فرکانس پایین است. یک حلقه قفل فرکانس انتگرال‌گر تعمیم‌یافته مرتبه دوم (MSOGI-FLL)در این کار برای رسیدگی به ناهنجاری‌های ولتاژ شبکه از همه نوع، از جمله افست DC ارائه شده است. با استفاده از مجموعه بلاک Waijung از MATLAB/Simulink، یک SOGI-FLL اصلاح شده با اعمال موقعیت های ولتاژ شبکه غیرعادی با استفاده از یک میکروکنترلر STM32F407VGT مبتنی بر DSP کم هزینه تحقق و ارزیابی می شود. نتایج نشان‌دهنده عملکرد بهتر MSOGI FLL در شرایط سخت است.

International Journal of Engineering

Journal Homepage: www.ije.ir

Root System Traits and Mechanical Properties of Three Shrub Species: Implications for the Structural Stability of the Ecological Slope

Y. Li,[a] M. Zhou,[b] H. Zuo*[a], Q. Wang[c], Y. Xing[c], G. Yan[c]

[a] *School of Civil Engineering, Northeast Forestry University, Harbin, China*
[b] *Heilongjiang Institute of Construction Technology, Harbin, China*
[c] *School of Life Sciences, Qufu Normal University, Qufu, China*

PAPER INFO

Paper history:
Received 07 September 2021
Received in revised form 17 October 2021
Accepted 23 October 2021

Keywords:
Root System Traits
Root Mechanical Properties
Three Shrubs Species
Ecological Slope Structure Stability

ABSTRACT

The purpose of this paper is to find the shrub species more suitable to enhance the structural stability of the ecological slope in the study area. Through the investigation, we found three common shrubs, there are Amorpha fruticosa Linn. (AFL), Syringa oblata Lindl. (SOL) and Forsythio mandshurica Uyeki. (FMU). In this study, the root system traits and mechanical properties were characterized and described using reliable experimental approaches. The results shown that the root withdrawal force was proportional to diameter (from 0.6-6 mm). The mean specific root length, individual length, surface area, and mean diameter of fine roots in different slopes were higher for AFL and SOL than for FMU, especially for high root orders. Although previous studies have focused on the relevant content, the reinforcement ability of different shrubs is rarely quantitatively compared under the same road conditions. Moreover, the morphology traits of the fine root were considered in this study. These results suggested that the root system traits and mechanical properties of AFL would enable more effective consolidated slopes structure than SOL and FMU, revealing that planting AFL might be a better way for enhancing ecological slope structure stability.

doi: *10.5829/ije.2022.35.02b.04*

1. INTRODUCTION

Expressway landslides caused by rainfall are a major engineering problem worldwide [1]. So far, it has affected extensive areas in different parts of the world for a longtime [2]. Factors leading to slope damage include natural rainfall, soil erosion, and soil characteristics [3]. They are usually caused by reduced soil suction and shear strength after rainfall on slope terrain [4]. Normally, the compacted soil layers during the construction stage and service life is unsaturated [5]. After natural rainfall, the soil becomes saturated. Weak soil composed of saturated clay is prone to fail and causes stability problems [6]. The continuous occurrence of soil erosion will not only reduce the soil quality, but also cause a series of problems such as the deterioration of the water environment [7].

Planting plants on the ecological slope to improve the shear strength and hydrological response of the soil is an effective measure to slow down the landslide of the ecological slope [8]. The positive effect of planting plant on road ecological slope structure stability and erosion resistance is mainly related to the mechanical strengthening effect of plant roots and the soil hydrological effect [9]. Previous studies have found that plant mechanical reinforcement can directly enhance the shear strength of the soil in a variety of ways [10]. Plant fine roots (<1mm) can form a membrane structure, increase the apparent cohesion of the soil, and is conducive to ecological slope structure stability [11]. Through some field hydrologic effect studies, we have some understanding of the hydrological effect of roots on ecological slope structure stability [12-13].

*Corresponding Author Institutional Email: hongliangzuo1972@163.com (H. Zuo)

Please cite this article as: Y. Li, M. Zhou, H. Zuo, Q. Wang, Y. Xing, G. Yan, Root System Traits and Mechanical Properties of Three Shrub Species: Implications for the Structural Stability of the Ecological Slope, ***International Journal of Engineering, Transactions B: Applications*** Vol. 35, No. 02, (2022) 291-299

In this study, after field investigation, three typical types of shrubs in the northeast range were selected. The three shrub species are Amorpha fruticosa Linn. (AFL); Syringa oblata Lindl. (SOL); Forsythio mandshurica Uyeki. (FMU). In the process of selection, we choose the shrubs with the same life type, age, living environment to ensure better comparison. Due to differences in different species traits, we assumed the mechanical reinforcement of root traits, such as scour resistance and hydrological effects, in different response directions to different shrubs. The research results are expected to provide data support for the selection and cultivation of shrubs on ecological shrubs slope roads in northeast China to determine the plant species needed for the stability of ecological slope in specific places, and produce positive ecological and economic benefits to the construction of roads in cold regions.

2. MATERIALS AND METHODS

2. 1. Study Sites Expressway Heha Expressway starts in Harbin and ends in Hegang City, the traffic mileage is 303 km. The Heha Expressway natural zoning is II_2 (heavy-freeze zone of mountain-front plain in the central of northeast china). The site test was conducted on the slope of the Heha Expressway form Suihua to Tieli, which is in the northeastern China. The study area has longer winter, shorter summer, cold winter and warm summer. It is typical of a temperate continental monsoon climate. In the study area, the shrub species planted in the ecological slopes of the Expressway mainly include AFL, SOL and FMU. The map of the study area is presented in Figure 1.

2. 2. Experimental Design and Sampling The selection and setting of the experimental research area were completed in July 2020. Due to different shrub planting areas along the test region, six 20m × 20m plots are randomly established between each two plots and a buffer zone greater than 10 m wide between each one. Three of these were on the slopes of 30° and three are on the slopes of 60°. A total of eighteen plots were established.

In each site, three plants of each study shrub species were randomly selected, and then root samples of 0-20 cm soil depth within the 1 m range for each study shrub main stem were excavated and manually collected in July 2020. Then, we mixed all root samples taken from the same plot. The sub-sample was treated for root morphological traits experiments. Using stainless steel spirals of 5cm in diameter, six cores were randomly collected from each site at a depth of 0-20cm. Combine all soil samples of each lot and then remove visible foreign material (e. g., roots, stone, etc.) by hand. This one was used to measured basic soil properties. Based on the experimental data and statistical analyses, the final conclusion can be reached. The flowchart of the methodology is presented in the Figure 2.

2. 2. 1. Soil Properties The sub-sample was retrieved from the sample to the laboratory and the soil sub-samples were weighed in the laboratory. Natural soil density (g/cm^3) was measured by wet soil weight and core volume. The sample was then placed in the drying box and the temperature adjusted to 75 ℃ to dry the sample. When the drying was complete, the samples already dried were weighed and the dry density (g/cm^3) of the soil was measured.

We used a pH meter (Sartorius PB-10, Gottingen, Germany) to measure the pH, and used the oil bath-$K_2Cr_2O_7$ titration method to measure the soil organic

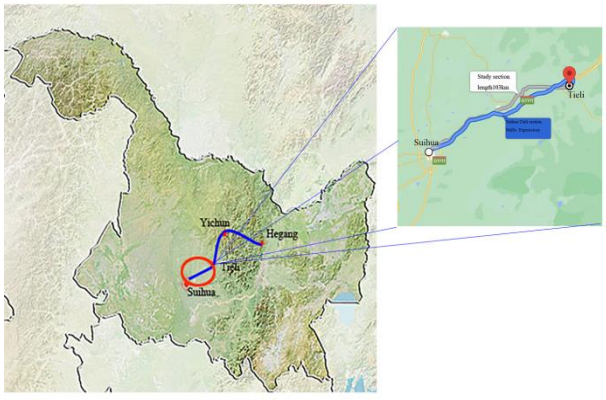

Figure 1. The map of the study area, which is in the Heha Expressway form Suihua to Tieli

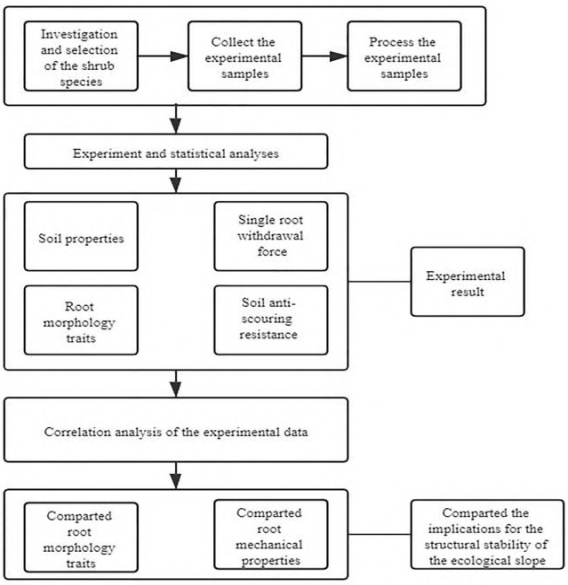

Figure 2. The flowchart of the methodology

matter. We used the shear-testing device (Nanjing Soil Machine DZJ-1, Nanjing, China) to measure the mechanical properties of the disturbed soil, and used the shear-testing device (Nanjing Soil Machine DZJ-1) to measure the elasticity modulus (EM) [14]. We placed undisturbed soil samples in a shear-testing device. A series of shear tests were conducted with three replications for each species under each normal load, and then the value of Elasticity Modulus (EM) was recorded. Soil cohesion (Sc) was calculated from the intercept of the failure envelope with the point of zero shear strength, and the friction angle was determined from the angle between the failure envelope and the normal stress axis (horizontal).

2. 2. 2. Root Withdrawal Force Tests The test was measured by a hand-held tension meter. At the beginning of the survey, the portion of wild plant growth was manually removed and the plant roots were excavated to the soil at a depth of 0.4m. After the root system was exposed, the main root was all removed with a saw bar. The root was pulled in a parallel and opposite direction to the root growth. After the root system was removed, record the maximum tension, the exposed root diameter and the root diameter at the fracture [15]. Methods were as follows: The root length between the branch nodes was measured by the natural growth length of the root system, with the longest root length along the direction of the root growth growing from the main root stem [16]. The roots growing from each branch node were divided into primary, secondary and below secondary side roots according to the number of branch nodes.

2. 2. 3. Root Morphological Traits In the laboratory, the residual soil particles from the roots were carefully cleaned with tweezers in deionized water. Identified the different root orders, a different roots were separated one by one [17]. The sample root was scanned using a scanner which was the Expression scanner (Expression 11000XL, Epson, NSW , Australia) with a scan resolution of 600 dpi. Measured the root number, mean diameter, single and total root length, single root surface area and root volume using root analysis software (WinRHIZO TronMF 2012, Regent Instrument Inc., Quebec, Canada). The root samples were dried at 75°C oven and the weight was recorded. Then, the specific root length (SRL) and branch ratio were calculated. The specific root length was defined as the total root length divided by the corresponding dry mass. The branch ratio (%) is calculated as the number of root roots divided by the number of root roots above it.

2. 2. 4. Soil Anti-scouring Resistance Index The device of experiment in this study was modified based on the original soil wash tank (Figure 3). Not to damage the original soil structures, made a sampler for the 20 cm × 18 cm × 10 cm, the ram-resistant tank was set to two slopes of 30° and 60° . According to the natural rainfall situation of the study area, our experimental design was divided into two kinds, which were large rainfall (2 L/min) and small rainfall (0.5 L/min), with the experimental scouring time length of 10 min [18]. Cut off the ground part of the plant before washing, cut the pot, divided the two layers of the plant soil, marked, and followed Lu lixia's methods for specific operations. We did 3 repeats for each sample. This paper used the water quantity Q required to wash away 1 g of soil with a certain water flow rate to indicate the soil anti-scouring resistance.

3. STATISTICAL ANALYSES

The normal distribution and variances homogeneity of all the data were tested by the Kolmogorov-Smirnov test and Levene's test, respectively. The difference of soil properties, root architectural and morphological traits among different shrub species were determined with one-way analysis of variance (ANOVA) with Tukey Kramer HSD. The interaction effects of species and diameter or slopes on different parameters were evaluated using a multi-factor analysis of variance. All data analysis was performed using the SPSS software version22.0 (SPSS, IBM, USA). All figures were conducted using SigmaPlot 12.5 (Systat Software Inc., San Jose, CA, USA).

4. RESULTS

4. 1. Soil Properties Based on the results obtained, the soil moisture and density did not significantly differ among different species and slopes (Table 1). Meanwhile, the difference in soil density and soil moisture of the three shrubs remained insignificant after considering the slope (30° and 60°) (Table 1). EM

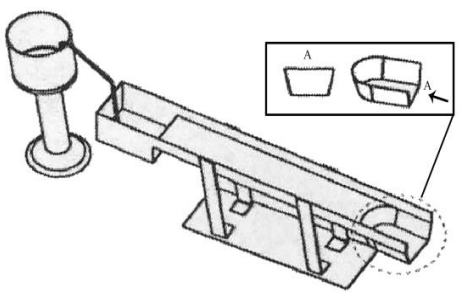

Figure 3. The experiment device based on the original soil wash tank

and Sc were relatively highest for AFL, followed by SOL and lowest for FMU at the same slope (Table 2). EM and Sc were generally higher at 30° slopes than at 60° slopes among all species (Table 2).

TABLE 1. The main physical traits of study site soils in different soil slopes at soil depth 0-20cm (n=3, Mean±SE).

	Slope	Soil Moisture (%)	Natural soil density (g/cm^3)
AFL	30°	17.01±0.73aA	1.58±0.03aA
	60°	16.55±0.16aA	1.59±0.01aA
SOL	30°	16.12±0.21aA	1.56±0.02aA
	60°	15.53±0.41aA	1.57±0.01aA
FMU	30°	16.07±0.19aA	1.55±0.02aA
	60°	15.37±0.25aA	1.53±0.02aA

	Slope	Dry density of soil (g/cm^3)	Sand (%)	Clay (%)
AFL	30°	1.34±0.01aA	40.12±1.36aA	21.07±2.01aA
	60°	1.36±0.01aA	41.12±1.71aA	22.53±1.33aA
SOL	30°	1.33±0.02aA	38.37±1.92aA	19.25±1.92aA
	60°	1.35±0.01aA	41.01±1.65aA	20.69±2.33aA
FMU	30°	1.33±0.01aA	37.93±1.77aA	19.04±2.36aA
	60°	1.34±0.01aA	38.04±2.08aA	19.65±1.09aA

Note: Each value is the Mean (SE) of three replications. Different lowercase letters represent statistical significances in different soil slopes for the same plant types; different capital letters represent statistical significances in same soil slopes for the different plant types. AFL, Amorpha fruticosa Linn; SOL, Syringa oblata Lindl; FMU, Forsythio mandshurica Uyeki.

TABLE 2. Mechanical properties and chemical characteristics of study site soils in different soil slopes. Elasticity modulus (EM); Soil cohesion (Sc), (n=3, Mean±SE).

	Slope	Organic matter (%)	pH
AFL	30°	1.77±0.18aA	5.98±0.39aA
	60°	1.49±0.21bA	6.01±0.25aA
SOL	30°	1.74±0.31aA	5.87±0.21aA
	60°	1.47±0.21bA	5.93±0.25aA
FMU	30°	1.73±0.12aA	5.89±0.22aA
	60°	1.45±0.16bA	5.95±0.19aA
	Slope	**EM(kPa)**	**Sc(kPa)**
AFL	30°	7.69±0.21aA	42.12±2.38aA
	60°	7.24±0.22bA	35.79±2.08bA
SOL	30°	7.45±0.11aB	40.59±1.78aB
	60°	7.05±0.21bB	33.57±1.45bB
FMU	30°	7.35±0.12aB	40.17±1.87aB
	60°	6.99±0.19bB	33.27±1.79bB

Note: Different lowercase letters represent statistical significances in different soil slopes for the same plant types; different capital letters represent statistical significances in same soil slopes for the different plant types.

4. 2. Single Root Withdrawal Force With the root diameter increased, the root withdrawal force of AFL, SOL and FMU increased at both of 30° and 60° slopes (Figure 4). The maximum pull force appeared in AFL and the maximum value reaches 517.9N. Minimal appeared in samples of smaller root diameters of different plants, and in samples of smaller root lengths (Figure 4). At the slope of 60°, with the same root diameter, the AFL had the highest root withdrawal force, the second FMU and the lowest SOL. On the other hand, at the slope of 30°, with the same root diameter, the FMU had the highest root withdrawal force, the second AFL and the lowest SOL (Figure 4). At 30° slope, the AFL root withdrawal force was the highest, except at 2-3mm diameter; At 60° slope, the AFL root withdrawal force was the highest at all of diameter, the FMU was significantly above SOL, except at less than 2mm diameter (Figure 5). The main factors affecting the root withdrawal force were the root diameter, root length, branching nodes, and plant species (Table 3).

4. 3. Root Morphology Traits The specific root length was significantly higher in AFL than that in

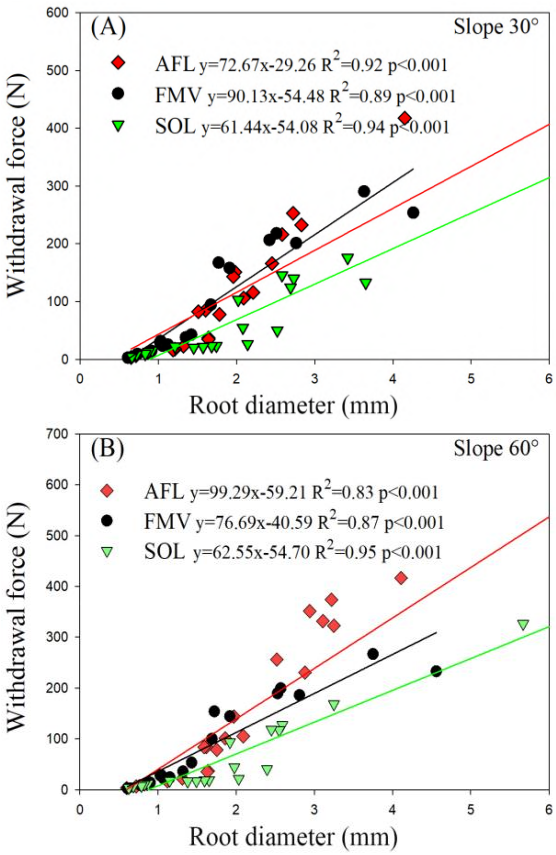

Figure 4. Relationship between root withdrawal forces of three shrub species at different slopes with root diameter (from 0.6 to 6 mm)

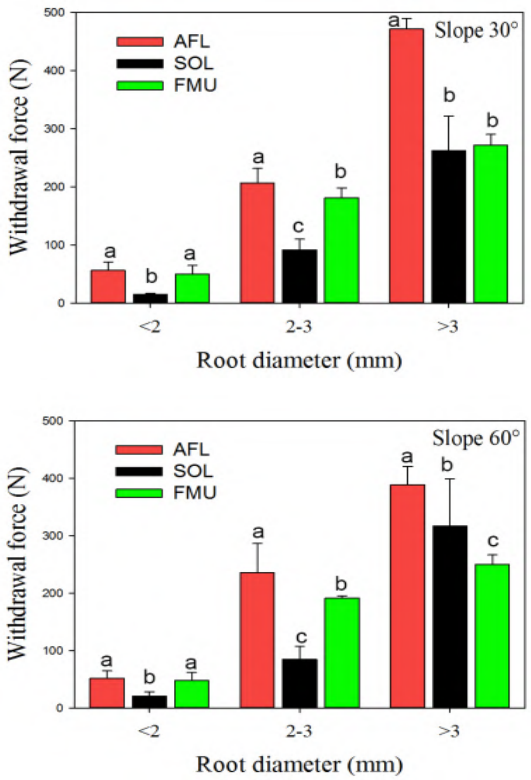

Figure 5. Withdrawal force of the fine roots in different diameter levels among different plant types (Mean±SE). Different lowercase letters represent statistical significances among different plant types. AFL, Amorpha fruticosa Linn; SOL, Syringa oblata Lindl; FMU, Forsythio mandshurica Uyeki

TABLE 3. Correlation between root diameter, maximum root length, total root length number of branch nodes and withdrawal force

Species	Slope	Diameter	MRL	TRL	NBN
AFL	30°	0.96***	0.92***	0.97***	0.97***
	60°	0.91***	0.86***	0.93***	0.95***
FMV	30°	0.94***	0.88***	0.86***	0.89***
	60°	0.93***	0.92***	0.89***	0.97***
SOL	30°	0.97***	0.70***	0.81***	0.86***
	60°	0.98***	0.83***	0.84***	0.95***

Note: MRL, Maximum root length (cm); TRL, Total root length (cm); NBN, Number of branch nodes; ***, $p<0.001$.

SOL and FMU in the second to fourth root orders at 30° slope (Figure 6A), and the specific root length was significantly higher in AFL than that in SOL and FMU in all root orders at 60° slope (Figure 6B). The individual root length, which was significantly higher in AFL than that in SOL and FMU in the fifth root orders at 30° slope (Figure 6C). The individual root length was significantly higher in AFL than that in SOL and FMU in the third to fifth root orders at 60° slope (Figure 6D). The individual root length was significantly higher in SOL than that in AFL and FMU in the fourth root orders at 30° slope (Figure 6C). The individual surface area, which was significantly higher in AFL than that in SOL and FMU in the third to fifth root orders at both of 30° and 60° slopes (Figure 6EF). The mean diameter, which was significantly higher in AFL than that in SOL and FMU in the all-root orders at all slopes (Figure 6GH). Furthermore, plant types, root order, slope, and their interaction had a significantly effect on all root anatomical, architectural and morphological traits at all slopes (Table 4).

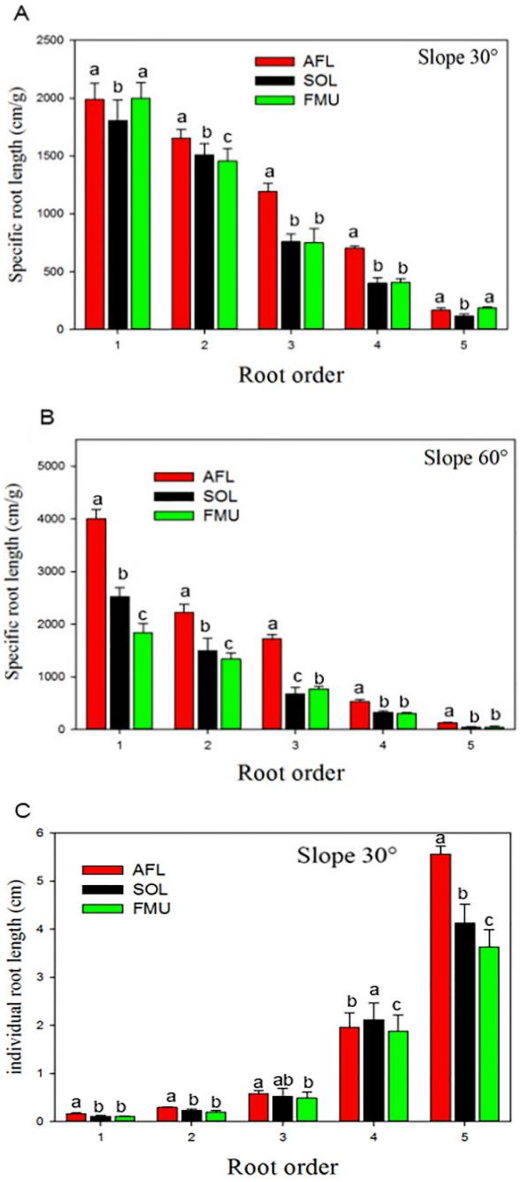

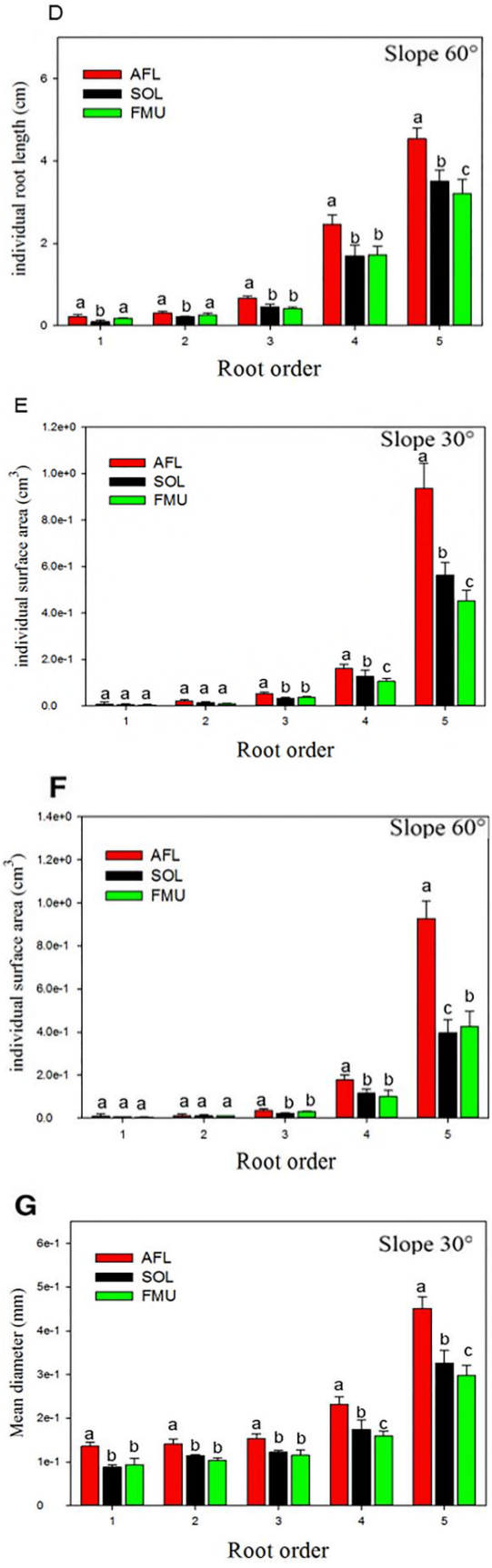

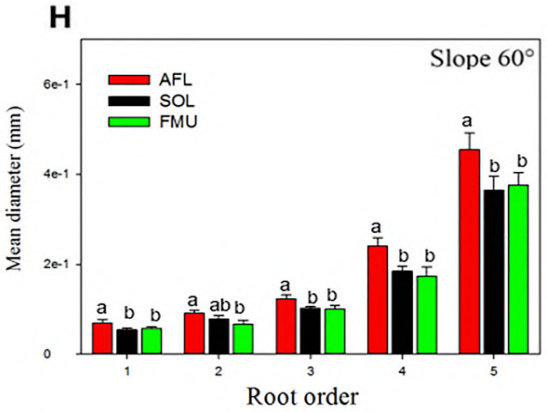

Figure 6. Specific root length, individual root length, individual root surface area, and mean diameter of fine roots at different slope among five roots orders of three plant types (Mean±SE). Different lowercase letters represent statistical significances among different plant types. AFL, Amorpha fruticosa Linn; SOL, Syringa oblata Lindl; FMU, Forsythio mandshurica Uyeki

TABLE 4. A general linear regression model (GLM) was used to examine the effect of plant type, root order, and their interaction on specific root length, individual length and surface area, and mean diameter, and the significances (p-value) were presented on the graphs. Results of general linear regression model (GLM) on the influence of root order (1-5), slope (30° slope and 60° slope) and species (AFL, Amorpha fruticosa Linn; SOL, Syringa oblata Lindl; FMU, Forsythio mandshurica Uyeki.) including all the interaction terms on four root morphology

	df	P value			
		SRL	IRL	IRS	MRD
Species	2	<0.001	<0.001	<0.001	<0.001
Order	4	<0.001	<0.001	<0.001	<0.001
Slope	1	<0.001	<0.001	<0.001	<0.001
Species*Order	8	<0.001	<0.001	<0.001	<0.001
Species*Slope	3	<0.001	<0.001	<0.001	<0.001
Order*Slope	4	<0.001	<0.001	<0.001	<0.001
Species*Order *Slope	8	<0.001	<0.001	<0.001	<0.001

Note: Shown are degrees of freedom (df) and the P value of the respective variables and the model itself. SRL represents the specific root length; IRL represents the individual root length; IRS represents the individual root surface area; MRD represents the mean root diameter.

4. 4. Soil Anti-scouring Resistance The impulse resistance index under heavy rain scouring is significantly lower than that under light rain scouring. Under the light rain, AFL has stronger soil anti-scouring resistance than SOL and FMU at both of slopes 30° and 60° (Figure 7). Under the heavy rain, AFL has stronger

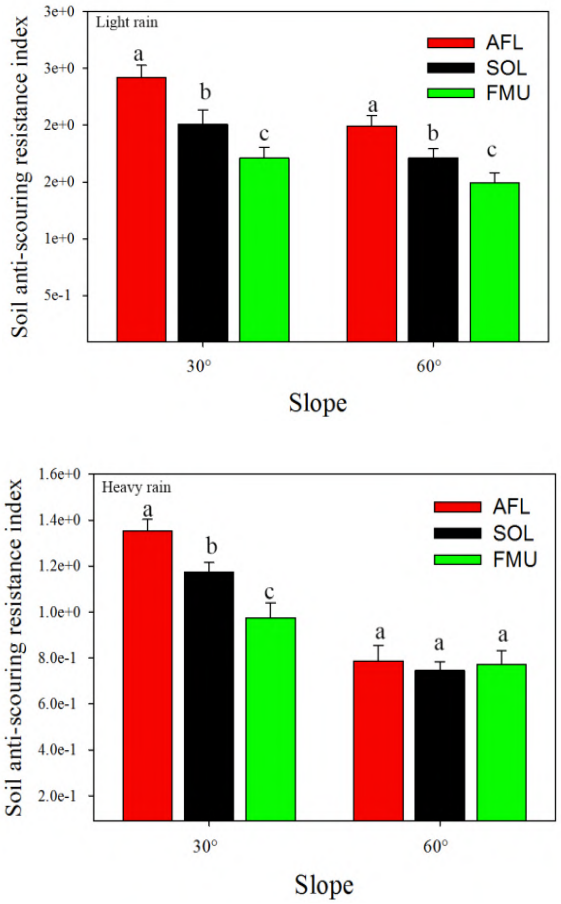

Figure 7. Soil anti-scouring resistance index in different rain intensity among different plant types (Mean±SE). Different lowercase letters represent statistical significances among different plant types. AFL, Amorpha fruticosa Linn; SOL, Syringa oblata Lindl; FMU, Forsythio mandshurica Uyeki

soil anti-scouring resistance than SOL and FMU at the slope of 30° (Figure 7). However, under the heavy rain, the soil anti-scouring resistance of AFL was almost equal to SOL and FMU at the slope of 60° (Figure 7).

5. DISCUSSION

The ability of root reinforcement provided by different shrubs can represent the role of ecological slope in improving the stability of road slope structure [19]. Under the same geological, geomorphological, and hydrological conditions, if a shrub has a better ability to enhance the stability of the slope structure, the smaller the probability of the slope structure being destroyed [20]. In this study, by comparing the root strengthening traits of AFL, SOL and FMU, under the same vertical conditions, the shrubs that are more suitable for enhancing the structure stability of the target slope can be obtained. In the context of carbon neutrality, we use the method of planting plants to improve the shallow slope structural stability, which can achieve the goal of enhancing the structural stability of road slope, but also improving the win-win ecological benefits [21].

5. 1. Comparted Root Morphology Traits

In previous studies, many studies have focused on the length of the root. Usually, associate the length of the plant root with the biomass of the plant root, yielding a specific parameter: specific root length (SRL), one of the most studied features in the root system [22]. Higher SRL, may be associated with a faster relative growth rate (RGR) and metabolic activity [23]. High SRL is more beneficial to slopes against sliding and erosion [22]. Therefore, according to previous studies found that the higher the proportion of fine roots (i. e. higher SRL), the higher the ability to prevent ecological slope landslides and erosion is an ideal feature of plant roots [24]. This conclusion is consistent with our results measuring the root morphology traits of all shrub species with different slopes. The study of the root system of the subject found that the SRL of the 3 shrubs showed great differences at both slopes of 30° and 60°. The SRL of AFL is highest at both slopes of 30° and 60°. These results show that AFL can not only meet the structure stability of gentle slope, but also adapt to the challenging environment on steep slope.

5. 2. Comparted Root Withdrawal Force

The withdrawal force of root system is an important index of soil slope consolidation and is related to soil withdrawal strength [25]. The shrub root system mainly uses reinforcement and anchor to prevent and control shallow landslide [23]. The wool beard root mainly plays the reinforcement role, and the coarse root with large root diameter mainly plays the anchorage role [26]. Previous studies have found that the withdrawal force was the root system buried in the soil against the withdrawal force, which reflected the combination of the root soil [287]. Also in previous studies have found that the main factors affecting the withdrawal force were the root diameter, root length, branching node and plant species, and the extraction force was proportional to the root diameter, root length and branching node [28]. This conclusion was consistent with our results measuring the root withdrawal force of all shrub species with different slopes. Under the same conditions, the root withdrawal force of the subject (AFL, SOL, FMU) is significantly differed; the root withdrawal force is stronger AFL than SOL and FMU. These results show that AFL can enhance the stability of the slope structure better than SOL and FMU.

5. 3. Comparted Root Anti-scouring Properties

Few previous studies involved the connection between

root structures and ecological slope anti-scouring traits [29]. Therefore, we should comprehensively consider the mechanical properties and hydrologic process of the root system, and their interaction, so as to study the ecological slope structure stability more scientifically [30]. Studies have shown, as the rainfall increases, the value of the soil anti-scouring resistance gradually decreased. Rainfall intensity is inversely proportional to the soil anti-scouring resistance [31]. The results of previous studies have shown that with the increase of the slope the anti-scouring traits decrease [32]. Our results are in good agreement with the above research results. That is, the enhancement effect of the same tree species on the soil impulse resistance decreases with the increasing slope [33]. These changes fully illustrate the important role of the root system in improving the soil impulse resistance [34]. The study found that the anti-scouring traits of the 3 shrubs showed great differences at the slope of 30°. The soil anti-scouring resistance of AFL is highest at both slopes of 30° and 60°, especially in light rain. These results show that the soil anti-scouring resistance of AFL was better than SOL and FMU. AFL was more conducive to improving the slope structural stability.

6. CONCLUSIONS

In this study, we selected three shrubs with similar living types and cross-compare under the two slopes to reveal the effect of different plants on ecological slope structural stability in the respect of root system traits and mechanical properties. The following conclusions are observed from the study.

a. The SRL of AFL is highest at all slopes. These results show that AFL is more conducive to enhance the structure stability in gentle slope and steep slope.

b. The root withdrawal force is stronger AFL than SOL and FMU at all slopes. These results show that AFL can enhance the stability of the slope structure better than SOL and FMU.

c. In light rain, the soil anti-scouring resistance of AFL is highest at all slopes. These results show that AFL is more conducive to improve the slope structural stability.

In conclusion, AFL has more ideal traits than SOL and FMU in improving ecological slope stability. Therefore, AFL may be a shrub species more suitable for ecological slope structural reinforcement than SOL and FMU in our study area. This research will have a positive application significance for expressway construction and ecological environment improvement of the study region.

7. REFERENCES

1. Sidle, R.C., Bogaard, T.A., "Dynamic earth system and ecological controls of rainfall-induced landslides", ***Earth-Science Reviews***, 159, (2016), 275-291. DOI: 10.1016/j.earscirev.2016.05.013
2. Kavianpour, M., Seyedabadi, M., Moazami, S., Yamini, O.A., "Copula Based Spatial Analysis of Drought Return Period in Southwest of Iran", ***Periodica Polytechnica Civil Engineering***, (2020), 16301. DOI:10.3311/PPci.16301
3. Alsharifi, Z., Shakir Mahmood, M., Akhtarpour, A., "Numerical Evaluation of Slope Stability for Construction and Seismic Loads: Case Study", ***International Journal of Engineering, Transactions A: Basics*** Vol. 34, No. 7, (2021) 1602-1610. DOI: 10.5829/ije.2021.34.07a.05
4. Iverson, R.M., "Landslide triggering by rain infiltration", ***Water Resources Research***, 36, (2000), 1897-1910. DOI: 10.1029/2000wr900090
5. Sharanya, A. G., Heeralal, M., Thyagaraj, T., "Soil Shrinkage Characterization of Low Plasticty Soil using Digital Image Analysis Process", ***International Journal of Engineering, Transactions A: Basics***, Vol. 34, No. 10, (2021) 2206-2212. DOI: 10.5829/ije.2021.34.10a.02
6. Mir, B. A., Reddy, S. H., "Mechanical Behaviour of Nano-material (Al2O3) Stabilized Soft Soil", ***International Journal of Engineering, Transactions C: Aspects*** Vol. 34, No. 03, (2021) 636-643. DOI: 10.5829/ije.2021.34.03c.07
7. Gonzalez-Ollauri, A., Mickovski, S. B., "Plant-soil reinforcement response under different soil hydrological regimes", ***Geoderma***, 285, (2016), 141-150. DOI: 10.1016/j.geoderma.2016.10.002
8. Gonzalez-Ollauri, A., Mickovski, S. B., "Hydrological effect of vegetation against rainfall-induced landslides", ***Journal of Hydrology***, 549, (2017), 374-387. DOI: 10.1016/j.jhydrol.2017.04.014
9. Giadrossich, F., Cohen, D., Schwarz, M., Ganga, A., Marrosu, R., Pirastru, M., Capra, G. F., "Large roots dominate the contribution of trees to slope stability", ***Earth Surface Processes and Landforms***, 44, (2019), 1602-1609. DOI: 10.1002/esp.4597
10. Perez, J., Salazar, R.C., Stokes, A., "An open access database of plant species useful for controlling soil erosion and substrate mass movement", ***Ecological Engineering***, 99, (2017), 530-534. DOI: 10.1016/j.ecoleng.2016.11.035
11. Boldrin, D., Leung, A.K., Bengough, A.G., "Root biomechanical properties during establishment of woody perennials", ***Ecological Engineering***, 109, (2017), 196-206. DOI: 10.1016/j.ecoleng.2017.05.002
12. Rahardjo, H., A. Satyanaga, E., Leong, V., Santoso, Y. N., "Performance of an instrumented slope covered with shrubs and deep-rooted grass", ***Soils and Foundations***, 54, No. 3, (2014), 417-425. DOI: 10.1016/j.sandf.2014.04.010
13. Kim, J.H., Fourcaud, T., Jourdan, C., Maeght, J.L., Mao, Z., Metayer, J., Meylan, L., Pierret, A., Rapidel, B., Roupsard, O., de Rouw, A., Sanchez, M.V., Wang, Y., Stokes, A., "Vegetation as a driver of temporal variations in slope stability: The impact of hydrological processes", ***Geophysical Research Letters***, 44, (2017), 4897-4907. DOI: 10.1002/2017GL073174
14. Wang, X., Hong, M., Huang, Z., Zhao, Y., Ou, Y., Jia, H., Li, J., "Biomechanical properties of plant root systems and their ability to stabilize", ***Soil & Tillage Research***, 189, (2019), 148-157. DOI: 10.1016/j.still.2019.02.003
15. Ghestem, M., Cao, K., Ma, W., Rowe, N., Leclerc, R., Gadenne, C., Stokes, A., "A framework for identifying plant species to Be used as 'Ecological Engineers' for fixing soil on unstable slopes", ***PLoS One***, 9, No. 8, (2014a), e95876. DOI: 10.1371/journal.pone.0095876
16. Giadrossich, F., Schwarz, M., Cohen, D., Cislaghi, C., Vergani, C., Hubble, T., Phillips, C., Stokes, A., "Methods to measure the

mechanical behaviour of tree roots: a review", ***Ecological Engineering***, 109(B), (2017), 256-271. DOI: 10.1016/j.ecoleng.2017.08.032

17. Lan, H., Wang, D., He, S., Fan, Y., Chen, W., Zhao, P., Qi, Y., "Experimental study on the effects of tree planting on slope stability", ***Landslides***, 17, (2020), 1021-1035. DOI: 10.1007/s10346-020-01348-z
18. Liu, H.W., Feng, S., Ng, C.W.W., "Analytical analysis of hydraulic effect of vegetation on shallow slope stability with different root architectures", ***Computers and Geotechnics***, 80, (2016), 115-120. DOI: 10.1016/j.compgeo.2016.06.006
19. Balzano, B., Tarantino, A., Ridley, A., "Preliminary analysis on the impacts of the rhizosphere on occurrence of rainfall-induced shallow landslides", ***Landslides***, 16, (2019), 1885-1901. DOI: 10.1007/s10346-019-01197-5
20. Cohen, D., Schwarz, M., "Tree-root control of shallow landslides", ***Earth Surface Dynamics***, 5, (2017), 451-477. DOI: 10.5194/esurf-5-451-2017
21. Lee, J., Chu, M., Lin, Y., Kung, K., Lin, W., Lee, M., "Root Traits and Biomechanical Properties of Three Tropical Pioneer Tree Species for Forest Restoration in Landslide Areas", ***Forests***, 11, (2020), 179-189. DOI: 10.3390/f11020179
22. Stokes, A., Atger, C., Bengough, A. G., Fourcaud, T., Sidle, R.C., "Desirable plant root traits for protecting natural and engineered slopes against landslides", ***Plant and Soil***, 324, (2009), 1-30. DOI: 10.1007/s11104-009-0159-y
23. Clarke, M., Williams, M., Stokes, T., "Soil creep: problems raised by a 23-year study in Australia", ***Earth Surface Processes and Land Forms,*** 24, No. 2, (1999), 151-175. DOI: 10.1002/(sici)1096-9837(199902)24:2<151::aid-esp964>3.0.co;2-g
24. Genet, M., Stokes, A., Salin, F., Mickovski, S.B., Fourcaud, T., Dumail, J.F., Van Beek, R., "The influence of cellulose content on tensile strength in tree roots", ***Plant and Soil***, 278, No. 1, (2005), 1-9. DOI: 10.1007/978-1-4020-5593-5_1
25. Mao, Z., Wang, Y., McCormack, M.L., Rowe, N., Deng, X., Yang, X., Xia, S., Nespoulous, J., Sidle, R.C., Guo, D., Stokes, A., "Mechanical traits of fine roots as a function of topology and anatomy", ***Annals of Botany***, 122, (2018), 1103-1116. DOI: 10.1093/aob/mcy076
26. Ghestem M., Sidle R. C., Stokes A., "The Influence of Plant Root Systems on Subsurface Flow: Implications for Slope Stability", ***BioScience***, 61, (2011), 869-879. DOI: 10.1525/bio.2011.61.11.6
27. Genet, M., Stokes, A., Salin, F., Mickovski, S.B., Fourcaud, T., Dumail, J.F., Van Beek, R., "The influence of cellulose content on tensile strength in tree roots", ***Plant and Soil***, 278 (1-2), (2005), 1-9. DOI: 10.1007/978-1-4020-5593-5_1
28. Bischetti, G., Chiaradia., Simonato, T., Speziali, B., Vitali, B., Vullo,P., Zocco, A., "Root strength and root area ratio of forest species in Lombardy(Northern Italy)", In Eco-and ground bio-engineering: The use of vegetation to improve slope stability, Springer, Dordrecht, (2007). DOI: 10.1007/978-1-4020-5593-5_4
29. Mao, Z., Saint-André, L., Genet, M., Mine, F.X., Jourdan, C., Rey, H., Courbaud, B., Stokes, A., "Engineering ecological protection against landslides in diverse mountain forests: choosing cohesion models", ***Ecological Engineering***, 45, (2012), 55-69. DOI: 10.1016/j.ecoleng.2011.03.026
30. Giadrossich, F., Schwarz, M., Cohen, D., Cislaghi, C., Vergani, C., Hubble, T., Phillips, C., Stokes, A., "Methods to measure the mechanical behaviour of tree roots: a review", ***Ecological Engineering,*** 109(B), (2017), 256-271. DOI: 10.1016/j.ecoleng.2017.08.032
31. Zhou, Z. C., Shangguan, Z. P., "Soil anti-scouribility enhanced by plant roots", ***Journal of Integrative Plant Biology***, 47(6), (2005), 676-682. DOI: 10.1111/j.1744-7909.2005.00067.x
32. Reubens, B., Poesen, J., Danjon, F., Geudens, G., Muys, B., "The role of fine and coarse roots in shallow slope stability and soil erosion control with a focus on root system architecture: a review", ***Trees***, 21, (2007), 385-402. DOI: 10.1007/s00468-007-0132-4
33. Guns, M., Vanacker, V., "Forest cover change trajectories and their impact on landslide occurrence in the tropical Andes", ***Environmental Earth Sciences***, 70, No. 7, (2013), 2941-2952. DOI: 10.1007/s12665-013-2352-9
34. Kim, J.H., Fourcaud, T., Jourdan, C., Maeght, J.L., Mao, Z., Metayer, J., Meylan, L., Pierret, A., Rapidel, B., Roupsard, O., de Rouw, A., Sanchez, M.V., Wang, Y., Stokes, A., "Vegetation as a driver of temporal variations in slope stability: The impact of hydrological processes", ***Geophysical Research Letters***, 44, (2017),4897-4907. DOI: 10.1002/2017gl073174

Persian Abstract

چکیده

هدف این مقاله یافتن گونه‌های درختچه‌ای مناسب تر برای افزایش پایداری ساختاری شیب اکولوژیکی در منطقه مورد مطالعه است. از طریق بررسی، ما سه درختچه معمولی یافتیم، Amorpha fruticosa Linn. (AFL)، سیرینگا اوبلاتا لیندل. (SOL) و Forsythio mandshurica Uyeki. (FMU). در این مطالعه، ویژگی‌های سیستم ریشه و خواص مکانیکی با استفاده از روش های تجربی قابل اعتماد توصیف و توصیف شد. نتایج نشان داد که نیروی خروج ریشه متناسب با قطر (از ۰/٦ تا ٦ میلی متر) است. میانگین طول ریشه ویژه، طول فردی، سطح و قطر متوسط ریشه های ریز در شیب های مختلف برای AFL و SOL بیشتر از FMU بود، به خصوص برای ردیف های ریشه بالا. اگرچه مطالعات قبلی بر محتوای مربوطه متمرکز شده‌اند، توانایی تقویت درختچه‌های مختلف به ندرت تحت شرایط جاده‌ای یکسان از نظر کمی مقایسه می‌شود. همچنین صفات مورفولوژیکی ریشه ریز در این مطالعه مورد توجه قرار گرفت. این نتایج نشان داد که ویژگی‌های سیستم ریشه و خواص مکانیکی AFL ساختار شیب‌های تلفیقی مؤثرتری را نسبت به SOL و FMU ممکن می‌سازد، و نشان می‌دهد که کاشت AFL ممکن است راه بهتری برای افزایش پایداری ساختار شیب‌های اکولوژیکی باشد.

International Journal of Engineering

Journal Homepage: www.ije.ir

Characterization of Ceramic Membrane based on Calcium Carbonate from Onyx Stone and Its Application for Coconut Sap Treatment

H. Aripin*[a], E. Priatna[a], D. Dedi[b], I. N. Sudiana[c], S. Sabchevski[d]

[a] *Department of Electrical Engineering, Faculty of Engineering, Siliwangi University, Tasikmalaya, West Java, Indonesia*
[b] *Research Centre for Electronics and Telecommunication, Indonesian Institute of Sciences, Bandung, Indonesia*
[c] *Department of Physics, Faculty of Mathematics and Natural Sciences, Haluoleo University, Kendari Indonesia*
[d] *Laboratory of Plasma Physics and Engineering, Institute of Electronics of the Bulgarian Academy of Sciences, Sofia, Bulgaria*

PAPER INFO

Paper history:
Received 16 September 2021
Received in revised form 28 October 2021
Accepted 29 October 2021

Keywords:
Ceramic Membrane
Calcium Carbonate
Onyx Stone
Zeolite
Silica Xerogel
Coconut Sap
Sap Permeate Flux

ABSTRACT

In this study, the calcium carbonate from onyx stone used as a pore-forming agent in the ceramic membrane of kaolin, zeolite, and silica xerogel composites were investigated. Four different membrane samples were prepared with varying onyx stone content from 5 wt.% to 30 wt.% into composite and then the prepared samples were sintered at 1200°C. The structural properties of the prepared sample was investigated in detail using X-ray diffraction (XRD), Fourier transform infrared (FTIR) spectroscopy, Scanning Electron Microscopy (SEM), and N_2 adsorption-desorption isotherms. The removal performance of the membrane was successfully tested during coconut sap treatment. It has been found that the prepared samples have a porous structure made up of interconnected pores and their volume fraction depends on onyx stone content. The sample with the onyx stone content of 30 wt.% provides the largest volume fraction of homogeneously interconnected pores and its presence demontrates the largest value for sap permeate flux and the flux rate in the initial phase. The pores formed in this produced membrane provide favorable conditions for the removal of the non-sugar impurities in the coconut sap.

doi: *10.5829/ije.2022.35.02b.05*

1. INTRODUCTION

The coconut sap is the raw material derived from the coconut tree for production of sugar. In addition to sucrose, it also contains about 50% of non-sugar impurities such as soluble and insoluble organic and inorganic materials, amino acid, etc., which come from coconut plant cultivation place and raw sap production process [1]. Because the sap is converted into coconut sugar through a heating process, then during heating the sap undergoes chemical and physical changes such as caramelization of sugar. As a result, the impurities deteriorate the product quality of the produced sugar and dietary nutritional as the dark brown color, hard texture, reducing protein contents, and degradation of amino acid. Therefore, they must be removed before the thermal treatment of sap. Such consideration inspires us to look for a way out to remove the non-sugar impurities from the coconut sap. As one of the most promising technologies, the ceramic membranes have been selected as an alternative approach for the treatment of coconut sap.

Many studies on membrane separation technology (MST) have been carried out for sugar processing. The MST utilization has been reported for use in an ultrafiltration membrane (UF) and it inflicts positive changes in the quality of sugar (e.g. increased purity, reduced turbidity, natural color, higher Brix value (°Bx), and protein content) [2]. When the UF is replaced by a reverse osmosis (RO) membrane for clarification of sugarcane juice an increase in the Brix value of the syrup concentrate has been observed as well [2]. The fact that both UF and RO polymer membranes are not

*Corresponding Author Institutional Email: aripin@unsil.ac.id (H. Aripin)

Please cite this article as: H. Aripin, E. Priatna, D. Dedi, I. N. Sudiana, S. Sabchevski, Characterization of Ceramic Membrane based on Calcium Carbonate from Onyx Stone and Its Application for Coconut Sap Treatment, ***International Journal of Engineering, Transactions B: Applications***, Vol. 35, No. 02, (2022) 300-306

resistant to organic solvents is a serious drawback. To overcome this, ceramic membranes have been developed. Microfiltration (MF) membrane formed as ceramic pipes have been prepared from TiO_2/α-Al_2O_3 and used to purify sugar cane juice [3]. MF membrane pores with a diameter of 0.6 µm is effective in reducing turbidity and improving the color of sugarcane juice by about 92% and 16%, respectively. Furthermore, two tubular membranes of TiO_2/α-Al_2O_3 composites (pore sizes of 0.1 µm and 0.3 µm) have been investigated for their use in clarifying the sugarcane juice [4]. The purification process has produced a good result with the degree of turbidity and color removal as much as 99.4% and 44.8%, respectively. When the pore diameter of the UF membrane is reduced to 0.5 µm [5], the turbidity and color of sugarcane juice reduce to 89.96% and 10.42%, respectively. The results of these studies have shown that the membranes of TiO_2 and Al_2O_3 composites have several advantages such as good resistance to thermal and organic solvents, and a longer lifetime compared with the polymer membranes. However, the raw materials prepared are expensive and their economic feasibility is less useful. Another drawback is that the formation of such ceramics requires very high temperatures of about 1600°C [6]. Several attempts have been made to reduce production costs and to lower the firing temperature of the ceramic membrane. For example, adding clay to Al_2O_3 has allowed a significant reduction in pore size of multichannel ceramic membrane [7]. It was reported that the pore size of clay and Al_2O_3 composite ceramic sintered at 1100°C were about 1 µm. In another study, the ceramic membrane prepared from corn cob ash at 1100°C has demonstrated a flexural strength value of 31 MPa and a pore size value of 0.13 µm [8]. These studies have revealed that the properties of ceramic membranes depend strongly on porosity. Therefore, by controlling porosity, it is possible to obtain an appropriate performance of the membrane.

Recently, SiO_2 (silica xerogel) ceramic has been prepared using a sago waste ash [9] and geothermal sludge [10] as a starting powder. Amorphous silica xerogels have micro-to nanopore sizes and they have poor mechanical properties (e.g. fragility) which do not allow to form a single mechanical unit in water. Furthermore, in the reports on zeolite ceramic membranes, the pore size formed in the range of 0.1 µm to 0.4 µm, the membrane has a great potential to remove impurities from coconut sap [11] and waste water [12]. However the membranes are limited in their mechanical strengths, so it causes a rapid membrane breakage when the applied pressure is in the range of 1 to 5 bars in the operation. One way to produce a ceramic membrane of the xerogel silica and zeolite composite with high mechanical strength and porosity is to add a pore-forming and plasticity agents in the composite.

Calcium carbonte ($CaCO_3$) can be added as a pore-forming agent and kaolin as a plasticity agent in the composition of the xerogel silica and zeolite composite for porous ceramic membranes. $CaCO_3$ decomposes into calcium oxide (CaO) and carbon dioxide (CO_2) at a temperature of above 650°C. The empty spaces formed by the release of CO_2 gas bubbles during the sintering impart a porous texture to the membrane [13]. Because the commercially available $CaCO_3$ is expensive, it is replaced by $CaCO_3$ from onyx stone. It is reported that the main phase of the onyx stone composed of $CaCO_3$ in the form of the calcite mineral [14]. The purpose of this work is to produce low-cost ceramic membrane made from silica xerogel and abundant inexpensive inorganic materials like zeolite, kaolin, and onyx stone. In this paper, we discuss the influence of different onyx stone content on the structural properties of the membranes and evaluate their performance for coconut sap treatment.

2. MATERIAL AND METHODS

2. 1. Materials and Membrane Sample Preparation The raw materials for the prepared membranes are silica xerogel, zeolite, onyx stone and kaolin. The silica xerogel was prepared from sago waste ash by extract method. The extraction steps have been described in detail in previous studies [9]. The other raw materials were prepared from natural materials in Karangnunggal, Tasikmalaya, Indonesia. After cleaning and drying, they were ground using milling machine to pass through a 100 µm sieve.

Table 1 presents the compositional formulations for the prepared membrane samples. For example, the M1 sample was prepared using the composition on a dry basis of 60 wt.% silica xerogel, 30 wt.% zeolite, 5 wt.% onyx stone, and 5 wt.% kaolin. Then, it was mixed with 4 mL polyvinyl alcohol (2 wt.%) solution and then stirred at 50°C for two hours. The mixture has been heated at 50°C until all solvent was evaporated. The resultant mixture is inserted into a circular disk-type mold with a size of 55 mm in diameter and 5 mm in thickness. The molded sample was dried in an oven at 100°C for 24 hours. The M2, M3, and M4 samples were prepared following the same steps

.

2. 2. Sintering The Prepared Membrane Sample The prepared membrane samples were sintered at a heating rate of 5°C/min up to the temperature of 1200°C in the air using an electric furnance. The constant temperature at 1200°C for 2 hours is treated on the sample during sintering. The cooling was performed by natural convection after turning off the electric furnace and leaving the samples inside. The samples of M1, M2,M3, and M4 sintered at 1200°C are labeled by CM1, CM2, CM3, and CM4, respectively.

TABLE 1. The compositional formulations for the prepared membrane sample

Sample	Mass percentages (wt.%)			
	Silica xerogel	Zeolite	Onyx stone	Kaolin
M1	60	30	5	5
M2	60	20	15	5
M3	60	15	20	5
M4	60	5	30	5

2. 3. Characterization In this study, the contents of various oxides for the raw material was determined by the XRF measurements using an instrument of the Philips PW2400 wavelength-dispersive spectrometer. During measurement, the instrument operates at a voltage of 24 kV, a current of 100 mA, and collimator mask of 27 mm, and it uses the Rh-X ray tube as an excitation source. Furthermore, the crystalline phases of the sample were identified by a Smartlab X-ray diffractometer with having Cu Kα radiation at 0.15418 nm. The operating voltage and the current used were 40 kV and 30 mA, respectively. The sample functional groups of were tested by a Varian 800 Fourier FTIR spectrometer. The data recorded is in the wavelength range from 400 to 4000 cm^{-1} and the spectral resolution is 4 cm^{-1}. The KBr pellet technique was used for reflecting the FTIR spectra at room temperature. The fracture surfaces of the samples were imaged by SEM at a magnification of 5000 times and an operating voltage of 5 kV. The pore properties of sample were tested by a nitrogen adsorption-desorption method (Quantachrome, Nova-1000).

2. 4. Permeation Experiments The detailed experimental procedures for coconut sap permeation are described elsewhere [11]. The concentration of coconut sap used for the experiment was 0.86 g/L. The permeation parameters were calculated using the equation for permeate flux [15].

3. RESULTS AND DISCUSSIONS

Table 2 presents the contents of various oxides for silica xerogel, zeolite, onyx stone, and kaolin. The SiO_2 is the main oxide constituent for silica xerogel, zeolite and kaolin, whereas the CaO is for onyx stone. The ZrO_2, Al_2O_3, Fe_2O_3, K_2O, and CaO contribute to significant amount of oxide content for zeolite. The presence of loss on ignition (LOI) in all raw material is related to additional components of volatile, organic mater and hydroxides.

Figure 1a presents the XRD patterns of the un-sintered membrane sample and those sintered at 1200°C. It reveals that the crystalline phases detected for the un-sintered sample (M1) consists of kaolin at $2\theta = 20.9^{o}$ and 24.9^{o} [16-18], quartz, zeolite at $2\theta = 27.2^{o}$ [19], and calcite ($CaCO_3$) at $2\theta = 30^{o}$. In the sample sintered at 1200°C (CM1), a zeolite crystal is formed followed by cristobalite, mullite ($3Al_2O_32SiO_2$), and then by the crystallization of gehlenite ($Ca_2Al_2SiO_7$). and anorthite ($Ca_2Al_2Si_2O_8$). It can be observed that the calcite phase disappears in the sintered sample and it is replaced by an gehlenite and anorthite phases. It was thought that gehlenite phase is as a reaction result between the metakaoline and calcium. Anorthite is formed from silica, aluminum oxide and gehlenite. Such interpretation agrees with the observed results of the XRD pattern for samples prepared from a mixture of metakaoline and calcium oxide based stone [20]. As the content of onyx stone increases, the intensity peak of anorthite increase, whereas that of crystalline cristobalite and mullite decreases. It indicates that the anorthite is an unstable intermediate phase.

Figure 1b presents the FTIR spectra of the sample sintered at 1200°C. The absorption band of peak 1 at about 464 cm^{-1} is associated to tetrahedral Si–O bending vibrations, which is characteristic of the starting metakaoline [17]. The intensity decreases as the onyx stone content increases. In the case of higher onyx stone content, most of the metakaoline particles can react with calcite. The absorption band of peak 2 and 4 at about 538 cm^{-1} and 775 cm^{-1} is related to anorthite characteristics (Si-O-Al bond) [21]. The peaks at 626 cm^{-1} (3) that is ascribed to crystalline cristobalite [18]. The peak 5 near 800 cm^{-1} and the strong absorption band of the peak 6 at 1100 cm^{-1} are related to the Si–O–Si bonds for the symmetric and anti-symmetric stretching vibrations, respectively [22]. The absorption band of peaks 7 located at about 3420 cm^{-1} is assigned to the H–O–H bonds. The bands is the characteristic for the adsorbed water molecules. Respectively, the peaks 8, 9, and 10 that appear at 3600, 3680, 3800 cm^{-1} correspond to the kaolinite [18].

TABLE 2. Contents of various oxides for the raw material

Oxide constituent	Silica xerogel (wt.%)	Zeolite (wt.%)	Onyx stone (wt.%)	Kaolin (wt.%)
SiO_2	98.81	59.30	0.20	42.20
TiO_2	0.01	0.70	ND	1.10
ZrO_2	ND	5.02	1.80	0.46
MgO	ND	0.12	1.09	ND
Al_2O_3	0.41	5.02	0.08	24.80
Na_2O	0.12	ND	ND	30.10
Fe_2O_3	0.11	8.47	14.7	1.11
K_2O	0.34	12.30	0.12	ND
CaO	0.14	7.81	82.0	ND
LOI	0.04	1.27	0.01	0.23

Figure 2 presents the SEM images of the CM samples at different content of the onyx stone. For CM1, the microstructure is characterized by rough surface texture with small and inhomogeneous pores. Their pores are not evenly distributed. In the CM2 sample, in some locations, a few larger isolated pores and open pores are present. Furthermore, the opened and interconnected array of pores are characteristic for the sample CM3. The texture of the CM4 sample is similar to that of the CM3 sample, although the CM3 presents a much denser structure with more uniform pores. As a whole, the analysis of the SEM images indicates that the addition of onyx stone with content larger than 20% results in homogeneous interconnected and organized pores with a highly porous structure. The pores are produced due to the escapement of the gases [13] and ceramic expansion by the formation of crystalline anorthite and gehlenitesintering [23]. From this SEM observation, it can be said that the samples with an onyx stone content of 10 wt.% (CM1) and 20 wt.% (CM2) shows isolated pores and poor porosity if compared with other samples. This is due to the limited connections of the small pores in the MC1 and MC2 samples. In all other (MC3 and MC4) the addition of onyx stone changes the appearance of the ceramic surface which becomes more porous.

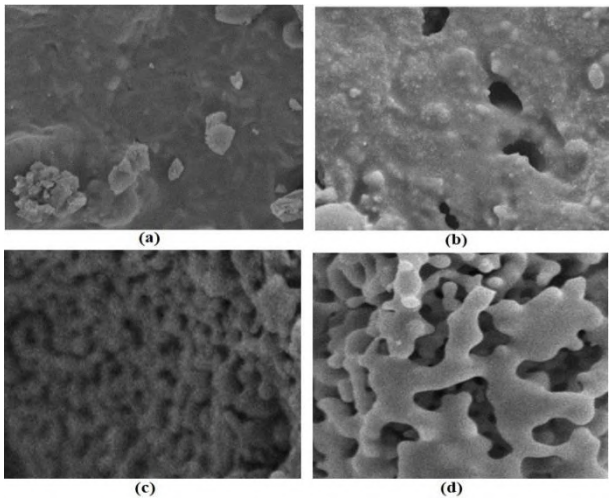

Figure 2. SEM images of (a) CM1, (b) CM2, (c) CM3, and (d) CM4

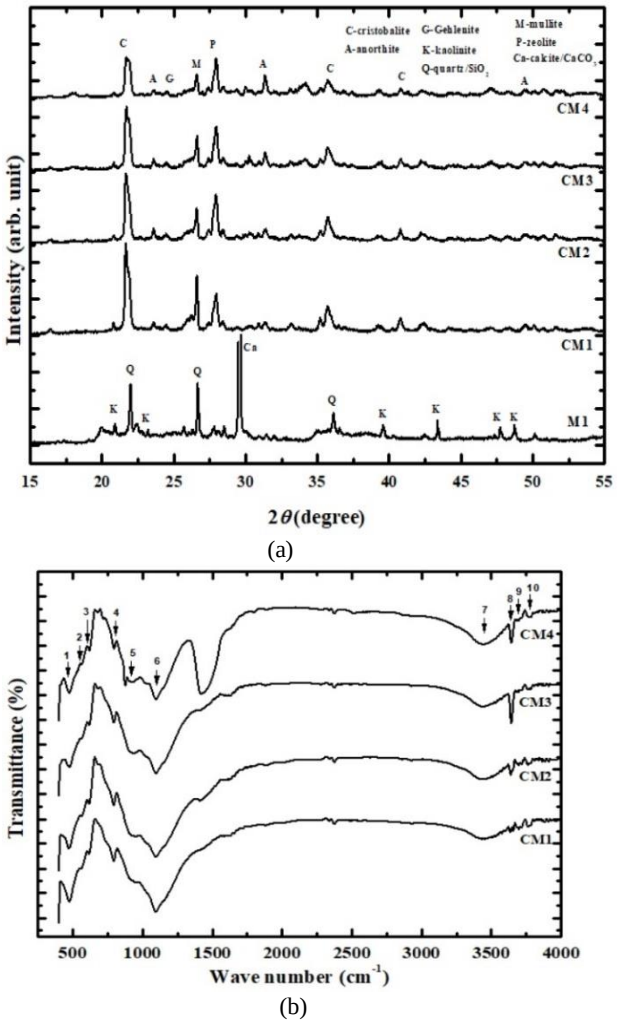

Figure 1. XRD patterns and (b) FTIR spectra of the un-sintered membrane (M1) and membranes sintered at 1200°C (CM)

Figures 3a and 3b show the N_2 gas adsorption-desorption isotherms at 77 K and pore size distributions of CM sample sintered at 1200°C, respectively. According to the recognized classification of International Union of Pure and Applied Chemistry (IUPAC), the shape of N_2 gas adsorption-desorption isotherm and hysteresis loop of the sintered membrane samples are type IV and type H3, respectively [24], which is characteristic of a slit-type mesoporous structure. In the isotherm, the adsorption increases slowly as the relative pressure increases up to about P/Po= 0.9 and after that rapid adsorption can be observed in the samples. As shown in Figure 3a, the N_2 uptake increases as the onyx stone content increases in the sample, which may be associated with a higher mesopore ratio. It can be understood that at 1200°C, the higher content of onyx stone in the sample results in more vacant spaces created by the release of CO_2 gas bubbles. This is in line with the interpretation of the results for the CaO/SiO_2 composite, where the porosity tends to increase with increasing the ratio up to 38%[25]. According to pore size distribution in Figure 3b, one could clearly see that the log differential intrusion increases with increasing the onyx stone content. This increase is attributed to an increase in the volume fraction of the interconnected pores [26], which inevitably results in an increased total porosity in the ceramic membrane. Thus, the CM4 sample has the largest fraction of interconnected pores.

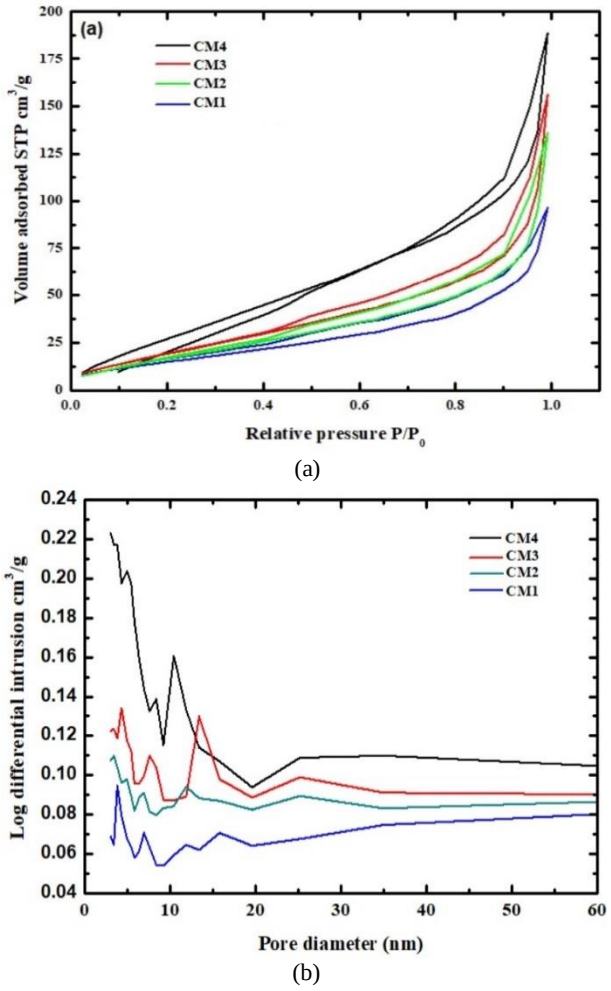

Figure 3. (a) Typical N_2 adsorption-desorption isotherms, and (b) pore size distributions of the sintered membrane sample

Figure 4 presents the change of the sap permeate flux with respect to time for ceramic membranes with a different onyx stone content. The sap permeate flux values increased with an increasing onyx stone content. The initial permeate fluxes gradually increase from 0.44 to 0.68 mL/min.cm^2 for the onyx stone content in the interval from 5 wt.% (CM1) to 30 wt.% (CM4), respectively. As can be seen in Figures 4 and 3b, obviously, there is a clear correlation between the flux and the log differential intrusion. Therefore, this flux increase is due to an increase in the volume fraction of the interconnected pores. CM3 and CM4 samples have greater fluxes than CM1 and CM2. In this case, CM3 and CM4 have a greater volume fraction of interconnected pores than CM1 and CM2, so that its presence accelerates the process of separating impurities from coconut sap through the pores. Its largest flux value is higher than that obtained for ceramic membrane prepared from the sintered zeolite [11]. Furthermore, the values of the sap permeate flux also decrease gradually with time, and initially, their value decreases at different

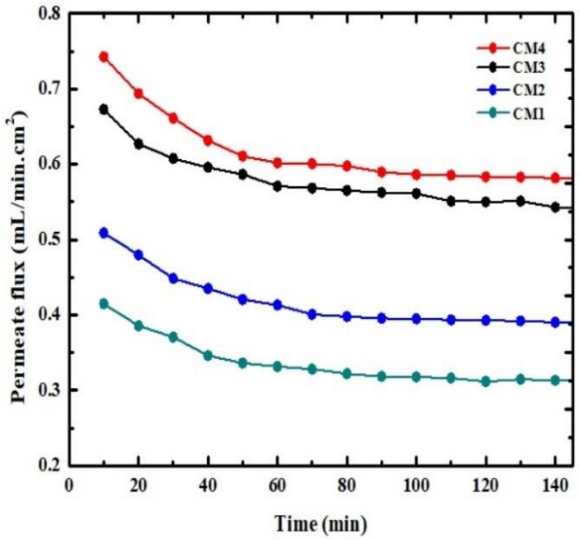

Figure 4. Change of the sap permeate flux with time for ceramic membranes with a different onyx stone content

rates until the same time of about 80 min and finally reach a constant value. The decrease in flux value is due to a reduction in the volume fraction of interconnected pores. In the case, the pores are blocked by a deposited layer of impurities from non-sugar ingredients during operation [27]. As time increases, more and more impurities fill the volume of the interconnected pores. This behavior was also found in the studies on water purification [28] using ceramic membranes. Furthermore, in the initial phase, the flux rate increases as the onyx stone content increases. It is attributed to the presence of the larger volume fraction of large mesopores (pore size greater than 20 nm). The volume fraction of large pores gradually increases with increasing onyx content. Thus, smaller impurity particles tend to be rejected by the membrane having smaller pores and are more likely to enter larger pores and create more polarized impurity layers. This is consistent with the previous findings reported by Novoa et al. [29], where the formation of a deposited layer occurs in larger pores.

4. CONCLUSION

A porous ceramic membrane for the treatment of coconut sap has been successfully produced from a sintered composition made of kaolin, zeolite, onyx stone, and silica xerogel. In it, the onyx stone is used as a pore-forming agent. The prepared ceramic membrane have a porous structure made up of interconnected pores with a relatively high volume fraction of pores that depends on onyx stone content. The pores were developed due to release of CO_2 and ceramic expansion by the formation of crystalline anorthite and gehlenite. The membran sample with an onyx stone content of 30

wt.% has demonstrated the largest value of the sap permeate flux and the flux rate in the initial phase. As a whole, the experimental results demonstrate that the calcium carbonate from onyx stone is an appropriate pore-forming agent for ceramic membrane. The obtained data can be used for an envisaged further optimization of the properties of this promising material.

5. ACKNOWLEDGMENTS

This research was funded by Minister of Education, Cultural, Research and Technology, Republic of Indonesia through the Project of Higher Education Applied Research in 2018 (Contract Number: 091/SP2H/LT/DRPM/2018).

6. REFERENCES

1. Pandiselvam, R., Manikantan, M., Binu, S.M., Ramesh, S., Beegum, S., Gopal, M., Hebbar, K., Mathew, A., Kothakota, A. and Kaavya, R., "Reaction kinetics of physico-chemical attributes in coconut inflorescence sap during fermentation", ***Journal of Food Science and Technology***, Vol. 58, No., (2021), 1-9. DOI: 10.1007/s13197-021-05088-3.
2. Jegatheesan, V., Shu, L., Phong, D.D., Navaratna, D. and Neilly, A., "Clarification and concentration of sugar cane juice through ultra, nano and reverse osmosis membranes", ***Membrane Water Treatment***, Vol. 3, No. 2, (2012), 99-111. DOI: 10.12989/mwt.2012.3.2.099.
3. Moreno, R.M.C., de Oliveira, R.C. and de Barros, S.T.D., "Comparison between microfiltration and addition of coagulating agents in the clarification of sugar cane juice", ***Acta Scientiarum. Technology***, Vol. 34, No. 4, (2012), 413-419. DOI: 10.4025/actascitechnol.v34i4.8890.
4. dos Santos Gaschi, P., dos Santos Gaschi, P., Barros, S.T.D. and Pereira, N.C., "Pretreatment with ceramic membrane microfiltration in the clarification process of sugarcane juice by ultrafiltration", ***Acta Scientiarum. Technology***, Vol. 36, No. 2, (2014), 303-306. DOI: 10.4025/actascitechnol.v36i2.17322.
5. Li, W., Ling, G., Lei, F., Li, N., Peng, W., Li, K., Lu, H., Hang, F. and Zhang, Y., "Ceramic membrane fouling and cleaning during ultrafiltration of limed sugarcane juice", ***Separation and Purification Technology***, Vol. 190, No., (2018), 9-24. DOI: 10.1016/j.seppur.2017.08.046.
6. Landek, D., Ćurković, L., Gabelica, I., Kerolli Mustafa, M. and Žmak, I., "Optimization of sintering process of alumina ceramics using response surface methodology", ***Sustainability***, Vol. 13, No. 12, (2021), 6739. DOI: 10.3390/su13126739.
7. Souza, M.Y.M.d., Lira, H.d.L., Santana, L.N.d.L. and Rodríguez, M.A., "Preparation and application in crude oil-water separation of clay-based membranes", ***Materials Research***, Vol. 24, No., (2021). DOI: 10.1590/1980-5373-MR-2020-0508.
8. Kamarudin, N., Harun, Z., Othman, M.D., Hubadillah, S., Jamaluddin, M. and Yusof, K., "Preliminary characterization of corn cob ash as an alternative material for ceramic hollow fiber membrane (chfm/cca)", ***International Journal of Engineering, Transactions B: Applications***, Vol. 31, No. 8, (2018), 1389-1397. DOI: 10.5829/ije.2018.31.08b.30.
9. Aripin, H., Mitsudo, S., Sudiana, I.N., Tani, S., Sako, K., Fujii, Y., Saito, T., Idehara, T. and Sabchevski, S., "Rapid sintering of silica xerogel ceramic derived from sago waste ash using sub-millimeter wave heating with a 300 ghz cw gyrotron", ***Journal of Infrared, Millimeter, and Terahertz Waves***, Vol. 32, No. 6, (2011), 867-876. DOI: 10.1007/s10762-011-9797-2.
10. Widiyandari, H., Pardoyo, P., Sartika, J., Putra, O., Purwanto, A. and Ernawati, L., "Synthesis of mesoporous silica xerogel from geothermal sludge using sulfuric acid as gelation agent", ***International Journal of Engineering, Transactions A: Basics***, Vol. 34, No. 7, (2021), 1569-1575. DOI: 10.5829/ije.2021.34.07a.02.
11. Aripin, H., Busaeri, N., Gufroni, A.I. and Sabchevski, S., "Activated natural zeolite membrane for separating dissolved impurities in coconut sap", in Materials Science Forum, Vol. 1000, No. Issue, (2020), 293-302. DOI: 10.4028/www.scientific.net/MSF.1000.293.
12. Othman, M.D., Adam, M., Hubadillah, S.K., Puteh, M.H., Harun, Z. and Ismail, A., "Evaluating the sintering temperature control towards the adsorptivity of ammonia onto the natural zeolite based hollow fibre ceramic membrane", ***International Journal of Engineering, Transactions B: Applications***, Vol. 31, No. 8, (2018), 1398-1405. DOI: 10.5829/ije.2018.31.08b.31.
13. Gilstrap, W.D., Meanwell, J.L., Paris, E.H., López Bravo, R. and Day, P.M., "Post-depositional alteration of calcium carbonate phases in archaeological ceramics: Depletion and redistribution effects", ***Minerals***, Vol. 11, No. 7, (2021), 749. DOI: https://doi.org/10.3390/min11070749.
14. Quiroga-González, E. and Morales-Merino, E., "Mexican onyx waste as active material and active material's precursor for conversion anodes of lithium ion batteries", ***Frontiers in Energy Research***, Vol. 9, No., (2021), 41. DOI: 10.3389/fenrg.2021.593574.
15. Bagheripour, E., Moghadassi, A. and Hosseini, S.M., "Incorporated poly acrylic acid-co-fe3o4 nanoparticles mixed matrix polyethersulfone based nanofiltration membrane in desalination process", ***International Journal of Engineering, Transactions C: Aspects***, Vol. 30, No. 6, (2017), 821-829. DOI: 10.5829/ije.2017.30.06c.01.
16. Sverguzova, S., Miroshnichenko, N., Shaikhiev, I., Sapronova, Z., Fomina, E., Shakurova, N. and Promakhov, V., "Application of sorbent waste material for porous ceramics production", ***International Journal of Engineering, Transactions C: Aspects***, Vol. 34, No. 3, (2021), 621-628. DOI: 10.5829/ije.2021.34.03c.05.
17. Yang, X., Yang, W. and Hu, J., "Preparation of low-dielectric-constant kaolin clay ceramics by chemical cleaning method", ***Frontiers in Materials***, Vol. 8, No., (2021), 198. DOI: 10.3389/fmats.2021.692759.
18. Valášková, M., Blahůšková, V. and Vlček, J., "Effects of kaolin additives in fly ash on sintering and properties of mullite ceramics", ***Minerals***, Vol. 11, No. 8, (2021), 887. DOI: 10.3390/min11080887.
19. Shi, J.Z., Zhu, X.L., Li, L. and Chen, X.M., "Zeolite ceramics with ordered microporous structure and high crystallinity prepared by cold sintering process", ***Journal of the American Ceramic Society***, Vol. 104, No. 11, (2021), 5521-5528. DOI: 10.1111/jace.17964.
20. Simão, L., Caldato, R., Innocentini, M. and Montedo, O., "Permeability of porous ceramic based on calcium carbonate as pore generating agent", ***Ceramics International***, Vol. 41, No. 3, (2015), 4782-4788. DOI: 10.1016/j.ceramint.2014.12.031.
21. Harabi, A., Zaiou, S., Guechi, A., Foughali, L., Harabi, E., Karboua, N.-E., Zouai, S., Mezahi, F.-Z. and Guerfa, F., "Mechanical properties of anorthite based ceramics prepared

from kaolin dd2 and calcite", ***Cerâmica***, Vol. 63, No., (2017), 311-317. DOI: 10.1590/0366-69132017633672020.

22. Popescu, C.-M. and Broda, M., "Interactions between different organosilicons and archaeological waterlogged wood evaluated by infrared spectroscopy", ***Forests***, Vol. 12, No. 3, (2021), 268. DOI: https:10.3390/f12030268.
23. Simão, L., Montedo, O.R.K., Caldato, R., Innocentini, M.D.d.M., da Silva Paula, M.M., Angioletto, E., Dal-Bó, A.G. and da Silva, L., "Porous ceramic structures obtained from calcium carbonate as pore generating agent", in Materials Science Forum, Vol. 775, No. Issue, (2014), 755-760. DOI: 10.4028/www.scientific.net/MSF.775-776.755.
24. Yang, W., Li, C., Tian, S., Liu, L. and Liao, Q., "Influence of synthesis variables of a sol-gel process on the properties of mesoporous alumina and their fluoride adsorption", ***Materials Chemistry and Physics***, Vol. 242, No., (2020), 122499. DOI: 10.1016/j.matchemphys.2019.122499.
25. Yang, Z., Lin, Q., Lu, S., He, Y., Liao, G. and Ke, Y., "Effect of cao/sio2 ratio on the preparation and crystallization of glass-ceramics from copper slag", ***Ceramics International***, Vol. 40, No. 5, (2014), 7297-7305. DOI: 10.1016/j.ceramint.2013.12.071.
26. Es-saddik, M., Laasri, S., Taha, M., Laghzizil, A., Guidara, A., Chaari, K., Bouaziz, J., Hajjaji, A. and Nunzi, J., "Effect of the surface chemistry on the stability and mechanical properties of the zirconia-hydroxyapatite bioceramic", ***Surfaces and Interfaces***, Vol. 23, No., (2021), 100980. DOI: 10.1016/j.surfin.2021.100980.
27. Yang, M., Zhao, C., Zhang, S., Li, P. and Hou, D., "Preparation of graphene oxide modified poly (m-phenylene isophthalamide) nanofiltration membrane with improved water flux and antifouling property", ***Applied Surface Science***, Vol. 394, No., (2017), 149-159. DOI: 10.1016/j.apsusc.2016.10.069.
28. Arumugham, T., Kaleekkal, N.J., Gopal, S., Nambikkattu, J., Rambabu, K., Aboulella, A.M., Wickramasinghe, S.R. and Banat, F., "Recent developments in porous ceramic membranes for wastewater treatment and desalination: A review", ***Journal of Environmental Management***, Vol. 293, No., (2021), 112925. DOI: 10.1016/j.jenvman.2021.112925.
29. Novoa, A.F., Vrouwenvelder, J.S. and Fortunato, L., "Membrane fouling in algal separation processes: A review of influencing factors and mechanisms", ***Frontiers in Chemical Engineering***, Vol. 3, No., (2021), 21. DOI: 10.3389/fceng.2021.687422.

Persian Abstract

چکیده

در این مطالعه، کربنات کلسیم از سنگ اونیکس به عنوان عامل منفذ ساز در غشای سرامیکی کامپوزیت های کائولن، زئولیت و سیلیس زیروژل مورد بررسی قرار گرفت. چهار نمونه غشایی مختلف با محتوای سنگ اونیکس متفاوت از ۵ درصد وزنی تا ۳۰ درصد وزنی به کامپوزیت تهیه و سپس نمونه‌های آماده شده در دمای ۱۲۰۰ درجه سانتیگراد ت حرارت دیدند. خواص ساختاری نمونه تهیه شده با استفاده از پراش پرتو ایکس (XRD)، طیف‌سنجی فروسرخ تبدیل فوریه (FTIR)، میکروسکوپ الکترونی روبشی (SEM)و ایزوترم‌های جذب-واجذبی N2 مورد بررسی قرار گرفت. عملکرد حذف غشا با موفقیت در طول تسویه پساب شیره نارگیل آزمایش شد. مشخص شده است که نمونه های تهیه شده دارای ساختار متخلخلی هستند که از منافذ به هم پیوسته تشکیل شده است و کسر حجمی آنها به محتوای سنگ اونیکس بستگی دارد. نمونه با محتوای سنگ اونیکس ۳۰ درصد وزنی، بزرگترین کسر حجمی از منافذ همگن به هم پیوسته را فراهم می کند و حضور آن بیشترین مقدار را برای شار نفوذ شیره و نرخ شار در فاز اولیه نشان می دهد. منافذ تشکیل شده در این غشای ساخته شده شرایط مطلوبی را برای حذف ناخالصی های غیر قندی موجود در شیره نارگیل فراهم می کند.

IJE TRANSACTIONS B: Applications Vol. 35, No. 02, (February 2022) 307-318

International Journal of Engineering

Journal Homepage: www.ije.ir

Numerical Study of Water-air Ejector using Mixture and Two-phase Models

M. R. Assari*[a], H. Basirat Tabrizi[b], A. Jafar Gholi Beik[a], K. Shamesri[a]

[a] *Department of Mechanical Engineering, Jundi-Shapur University of Technology, Dezful, Iran*
[b] *Department of Mechanical Engineering, Amirkabir University of Technology, Tehran, Iran*

P A P E R I N F O

Paper history:
Received 22 July, 2021
Received in revised form 14 October 2021
Accepted 16 October 2021

Keywords:
Liquid-gas Ejector
Two-phase Flow
Mixture Method
Eulerian-Eulerian Method
Numerical Simulation

A B S T R A C T

In this research, steady-state Mixture and Eulerian-Eulerian method for liquid-gas parallel flow ejector were examined. The simulation demonstrated that the Mixture model simulation represents better and efficient. The Eulerian-Eulerian model needed longer computational time and had a complexity to achieve the optimal convergence. However, both methods' performances were shown slightly similar. The models indicated a difference of about 6% in the flow rate ratio, their pressure diagrams nearly coincide, and their velocity parameter varies by 7% by comparing to the existing experimental data. Additionally, the Mixture model results appropriately conformed much better to the experimental data. So, the Mixture model was chosen for futher parametric study. Simulation results indicated that the flow rate ratio decreases by increasing the throat's cross-sectional area, and the flow rate ratio increases by increasing the nozzle's cross-sectional area. In this regard, e.g., the flow rate ratio of ejector by increasing pressure from 70 to 80 kPa, the air inlet increases up to 94%, and by increasing ejector outlet pressure, the flow rate ratio reduces such that no suction can be observed at 160 kPa. Consequently, at 150 kPa pressure ratio, the flow rate ratio was reduced by almost 100%.

***doi**: 10.5829/ije.2022.35.02b.06*

NOMENCLATURE

Model coefficients	c	-	Stress	τ	$\frac{N}{m^3}$
Generation of turbulence	G	-	Turbulent Schmidt number	σ	-
Turbulence kinetic energy	k	$\frac{m^2}{s^2}$	Turbulent Prandtl number	σ	-
Pressure	P	Pa	Model coefficients	σ_k ,σ_ε	-
Source	S	$\frac{kg}{s.m^3}$	Kinetic energy dissipation	ε	$\frac{m^2}{s^3}$
Strain rate	S_{IJ}	$\frac{1}{s}$	dynamic viscosity	μ	Pa.s
Velocity	u	$\frac{m}{s}$	Kinetic viscosity	v	Pa.s
Fluctuating velocity	$\acute{u}$	$\frac{m}{s}$	**Subscript Symbols**		
Position	x	m	Vector / Types	i , j , k	
Contribution of the fluctuating dilatation	Y	-	Turbulence	t	
Volumetric fraction	α	-	Effective	eff	
Density	ρ	$\frac{kg}{m^3}$	Phase	q	

*Corresponding Author Institutional Email: Assari@jsu.ac.ir (M. R. Assari)

Please cite this article as: M. R. Assari, H. Basirat Tabrizi, A. Jafar Gholi Beik, K. Shamesri, Numerical Study of Water-air Ejector using Mixture and Two-phase Models, ***International Journal of Engineering, Transactions B: Applications*** Vol. 35, No. 02, (2022) 307-318

1. INTRODUCTION

Nowadays, there are a wide range of engineering research area, which can not be assessed, only by means of experiments. Computational Fluid Dynamic (CFD) is a suitable tool to investigate many engineering problems, e.g. aerodynamic [1], cavitation [2], hydraulic [3, 4], energy systems [5, 6], heat transfer [7, 8], multiphase flow [9-11]. Today, two-phase ejectors are highly efficient and widely applied in various industries. Ejectors are categorized into two types of constant-pressure and constant-area depending on the nozzle exit position (NXP) of the ejector. If the nozzle exit is located in the constant-pressure mixing chamber, the ejector is pressure-constant. On the other hand, if the nozzle exit is placed in the constant-area, the ejector is of constant-area type. The ejector with constant pressure was initially proposed by Keenan et al. [12]. Although the constant-area ejector can create a higher suction mass flow rate, the constant-pressure ejector is considered more appropriate since it provides a greater backpressure range. The liquid-gas ejector includes a nozzle, a suction chamber, a throat, and a diffuser. The shock in ejectors occurs in the constant-area throat. Through this, the flow velocity instantly decreases; afterward, a higher mixing rate is achieved as the two-phase flow passes the diffuser [13]. The mixing flow behavior in two-phase ejectors is highly complex; thus, it cannot be simply described through theoretical and experimental methods [14-16].

CFD is a proper approach, as a research tool, for investigating a liquid-gas ejector's performance [17]. The ejector nozzle is critically significant due to the creation of a partial vacuum in the ejector. In a study by Zhu [18], a nozzle type with a circular geometry was proposed at the primary nozzle throat section. In cases that the ejector geometry is constant, changing the ejector operating conditions will also have a significant impact on its performance. Moreover, according to Zhu and Li [19], mixing chamber considerably affects the ejector performance. The convergence angle was reported 6° and -8°, as wll as values of 1.45° and -2.4° were achieved, 28° was acquired in Chong and Liu [20], and approximately 6° reported by Kouhikamali and Sharifi [21]. The mentioned differences in obtaining convergence angles correspond to some other aspects: type of ejector, working fluid, and operation.

Wang and Li [22] examined the primary nozzle geometry impression on the ejector performance by simulating computational fluid dynamics. The process was carried out by considering various geometries, including the mixing chamber's convergence angle and the divergent diffuser, the length of the diffuser's divergent section, the throat length, and the wall surface roughness. Among these geometric parameters, it has been noted that the throat and divergent sections of the nozzle have a significant impression on the flow rate ratio. The ejector performance was sorted into three modes: critical mode, subcritical mode, and back-flow. In the sub-critical mode, a constant and appropriate flow rate ratio was observed. The back pressure increases to a certain amount, critical back pressure will not make an impression, and the flow rate ratio initiates reduction by increasing back pressure.

According to the above literature review, this research has been initially attempted to investigate the impression of ejector modeling using computational fluid dynamics and suggested two multiphase flow modeling, which is Mixture and Eulerian-Eulerian approches. After examining and comparing with existed similar studies, the Mixture model was chosen as an efficient two-phase flow model. Subsequently, the effects of throat cross-section, nozzle exit, inlet, outlet, and secondary pressures in the liquid ejector are investigated and discussed.

2. MODELING

The corresponding liquid-gas ejector includes two inlets and one outlet. One of the inlets is water with a density and viscosity of 998.2 $(\frac{kg}{m^3})$ and 0.001003 $(\frac{kg}{m.s})$, respectively. The other inlet is gas (air) with a density and viscosity of 1.225 $(\frac{kg}{m^3})$ and 1.7894×10^{-5} $(\frac{kg}{m.s})$, respectively. The outlet is a Mixture of air and water, and the utilized ejector is symmetrical about the x-axis. The liquid-gas test model's geometrical dimensions are shown in Figure 1, and the ejector's length is 1 meter. In this study, the two-dimensional axial symmetry is utilized to model and analyze the ejector's flow.

Two Mixture and Eulerian-Eulerian-Eulerian multiphase flow models are considered for identical operating conditions in the simulation process of the liquid-gas parallel flow ejector. The simulation is performed under steady-state conditions, and the flow is assumed incompressible, turbulent, and two-dimensional axially symmetric. The Realizable K-ε model is applied for the turbulence model (see Figure 2).

In the Appendix, Table A, the governing equations are displayed. Moreover, independency of the computational grid is a crucially significant step in the simulations. In the present study as shown in Figure 3,

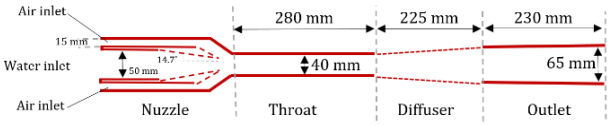

Figure 1. Exact geometry and dimensions of the ejector

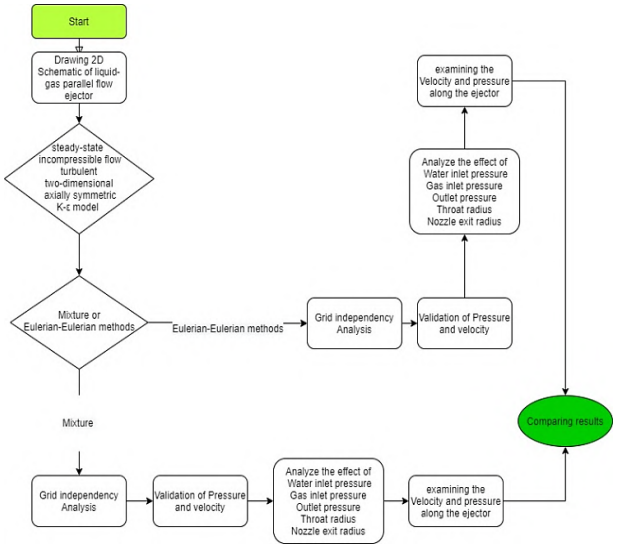

Figure 2. Flowchart of modelling

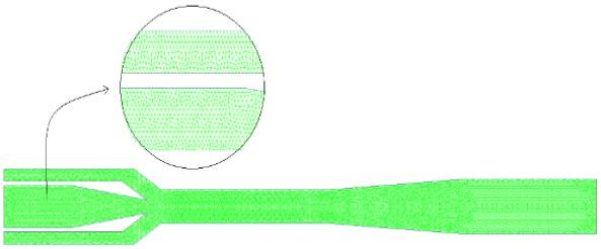

Figure 3. Ejector's grid

three mesh numbers of 12517, 15066, and 20150 were compared in both Mixture and Eulerian-Eulerian methods.

In both methods, no considerable changes were observed in the results. Therefore, the 20150-mesh number was considered for higher accuracy and better convergence.

The simulation results were obtained through a computer with the configurations of 2.50 GHz CPU and 8 GB of RAM. The solution time using the Eulerian-Eulerian method is about 4 hours, and it is reduced to about 3 and a half hours using the Mixture method. Examining grid independency in the simulation process is highly significant. The ejector's pressure and velocity for both methods were examined and validated as shown in Figure 4 and Table 1.

The solution is also reiterated to achieve convergence. The convergence criterion is where the gas flow rate from the secondary inlet becomes constant, and the remainder of each equation completely reaches below 10e-4.

The longer duration of the Eulerian-Eulerian solution is due to its higher complexity and the higher number of solved equations in comparison to the

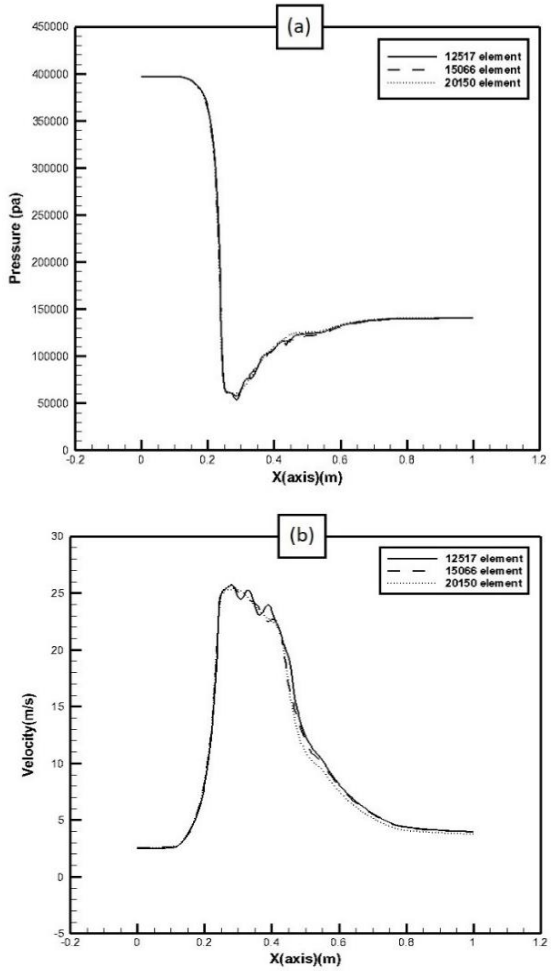

Figure 4. Mesh independency for Mixture Model, (a) pressure, (b) velocity

TABLE 1. Mesh analysis

Mesh size	Profile	Max. mesh error 12517 relative to mesh 15066	Max. mesh error 15066 relative to mesh 20150
Mixture Model	Pressure	2%	0.5%
	Velocity	4%	1.5%
Eulerian-Eulerian Model	Pressure	2%	1%
	Velocity	3.5%	1%

Mixture method. Consequently, the Eulerian-Eulerian method requires greater duration than the Mixture method to obtain the optimal convergence.

In the Mixture method, a second-order discretization method has been applied for momentum and turbulence kinetic energy, and the first-order discretization method has been exploited for volume fraction. Nevertheless, to acquire a solution of optimal convergence through the

Eulerian-Eulerian method, the first-degree discretization method was initially applied for momentum, turbulence kinetic energy, and volume fraction. After reaching relative stability in the solution, the method was changed to a second-order discretization method for momentum and turbulence kinetic energy. However, the first-order discretization method was still utilized for volume fraction. Additionally, the Flow courant number reduced to 20, and the under-relaxation factor for volume fraction was reduced to 0.5. Furthermore, the couple method was used for pressure and velocity coupling. The longer duration of the Eulerian-Eulerian solution is due to its higher complexity and the higher number of solved equations in comparison to the Mixture method. Consequently, the Eulerian-Eulerian method requires greater duration than the Mixture method to obtain the optimal convergence. In the Mixture method, a second-order discretization method has been applied for momentum and turbulence kinetic energy, and the first-order discretization method has been exploited for volume fraction. Nevertheless, to acquire a solution of optimal convergence through the Eulerian-Eulerian method, the first-degree discretization method was initially applied for momentum, turbulence kinetic energy, and volume fraction. After reaching relative stability in the solution, the method was changed to a second-order discretization method for momentum and turbulence kinetic energy. However, the first-order discretization method was still utilized for volume fraction. Additionally, the Flow courant number reduced to 20, and the under-relaxation factor for volume fraction was reduced to 0.5. Furthermore, the couple method was used for pressure and velocity coupling.

In Table 2, the geometric parameters and utilized boundary conditions have been presented, which are a total of 22 cases. In each related part of the examined parameter, the corresponding simulation number in the script is mentioned. The inlet pressure of the ejector for water and gas (air) and outlet are shown in table, and the wall boundary conditions have been considered for the ejector wall.

TABLE 2. Geometric parameters and conditions

Simulation conditions	Water inlet pressure (kPa)	Gas (air) inlet pressure (kPa)	Outlet pressure (kPa)	Throat radius (mm)	Nozzle exit radius (mm)
1-4	390 400 410 420	60	140	20	8
5-8	400	50 60 70 80	140	20	8
9-12	400	60	130 140 150 160	20	8
13-17	400	60	160	19 19.5 20 20.5 21	8
18-22	400	60	160	20	7 7.5 8 8.5 9

3. VALIDATION

Simulation results were compared with the obtained experimental data and numerical results of similar studies to evaluate the accuracy of this numerical study. It must be noted that the suction flow rate is regarded as one of the most significant parameters in determining the liquid ejector's performance. Therefore, obtained numerical results are presented along with the experimental data of Bhutada and Pangarkar [23], Cai's [24] and the results of Wang's numerical research [25]. Figure 5 shows comparison of Eulerian-Eulerian Method which indicates a good agreement and similar trend. Further, the suction flow ratio and the pressure ratio comparison with reported data in literature [24, 25] are illustrated in Table 3.

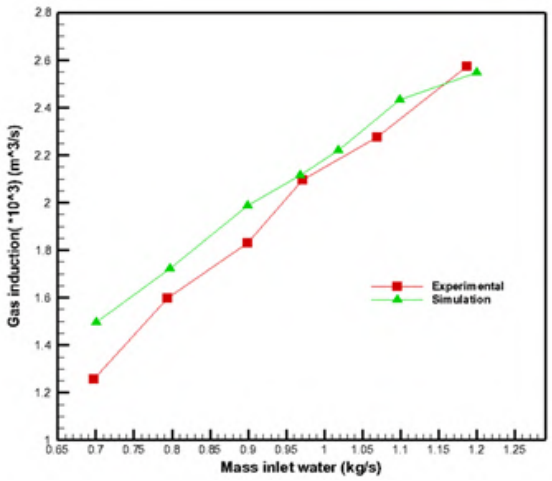

Figure 5. Comparison of Eulerian-Eulerian Method with Bhutada and Pangarkar [23]

TABLE 3. Validation

Flow rate ratio	Pressure ratio of simulation	Pressure ratio, Exp. [24]	Exp. error %	Pressure ratio [25]	Simulation [25] %
0.0245	0.287	0.272	5.5	0.286	0.6
0.173	0.275	0.261	5.3	0.281	1.8
0.371	0.270	0.247	8.5	0.276	2
0.494	0.269	0.238	11.5	0.271	0.7
0.687	0.267	0.224	16.1	0.267	0

As can be observed, the maximum error is 16.1% for the flow rate ratio. The pressure ratio decreases by increasing the flow rate ratio. In Equations (1) and (2), the flow rate ratio and the ejector pressure ratio are represented, respectively:

$$\text{Flow rate ratio} = \frac{Q_{gas}}{Q_{water}} \quad (1)$$

$$\text{Pressure ratio} = \frac{p_{outlet} - p_{gas(air)inlet}}{p_{waterinlet} - p_{gas(air)inlet}} \quad (2)$$

The solution methods of two-phase flow in problem modeling are shown in Figure 6. It can be observed in these figures, the velocity and pressure along the ejector using the Mixture and Eulerian-Eulerian models, as well as the flow rate ratio. According to Figure 6 the most considerable difference is identified in the velocity, and the pressure, which both models nearly similar. The difference reaches about 7% in the velocity profile. Moreover, if they are compared based on a similar output, the flow rate ratio in the Eulerian-Eulerian, and Mixture models will be 1.3217 and 1.2394, respectively, under identical operating conditions. In this regard, the Eulerian-Eulerian model has increased by about 6.23% compared to the Mixture model. Further, as can be seen in the velocity and pressure diagrams, the highest difference has occurred during the velocity reduction and the pressure increase, around 300 mm.

Moreover, Figure 7 shows the velocity contour for the Mixture and Eulerian-Eulerian models. The pressure of water inlet, gas (air) inlet, and outlet are taken 400, 60, and 140 kPa, respectively, as stated in Table 2. As can be observed in both the velocity diagram and the ejector velocity contour, the Mixture model's velocity is lower than the Eulerian-Eulerian model in the constant-area section of the ejector's end. On the other hand, the Eulerian-Eulerian model velocity is lower in the throat section. Due to the proximity of the Mixture model obtained results and time-saving purposes, the Mixture model has been used for other parameters examination.

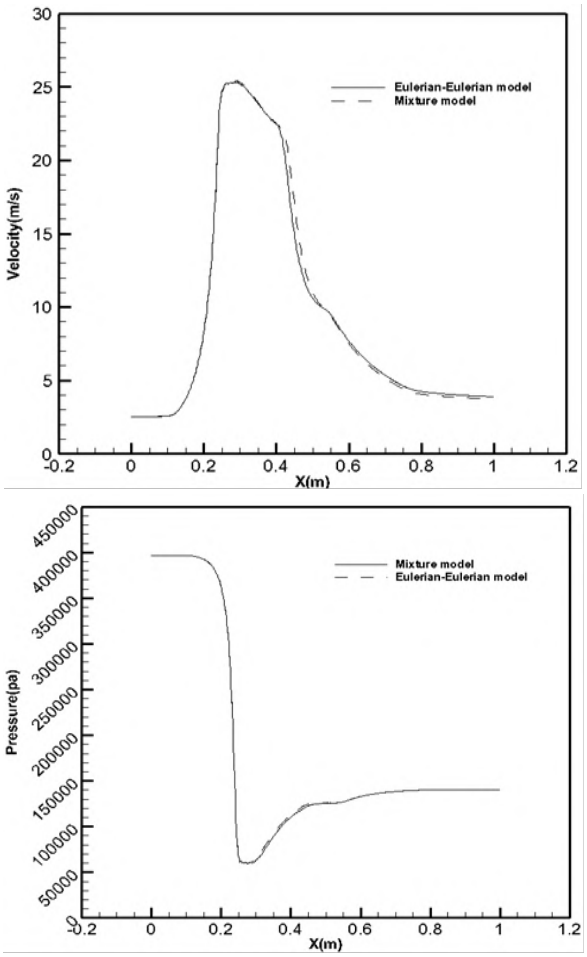

Figure 6. Comparison of a) velocity and b) pressure in Mixture and Eulerian-Eulerian methods

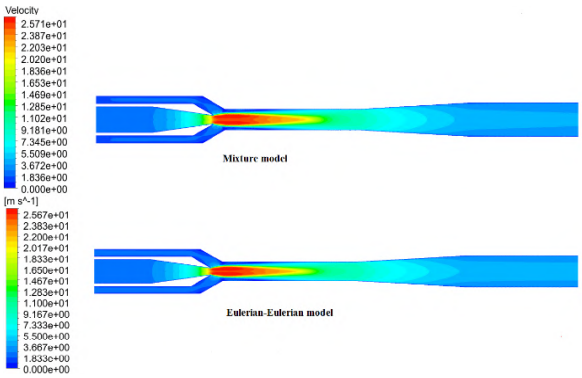

Figure 7. Pressure along the ejector for different the solution method

4. RESULTS AND DISCUSSION

As stated in Figure 8, the water velocity increases after its entry and passing through the nozzle. This velocity increase reduces the pressure at the nozzle exit that

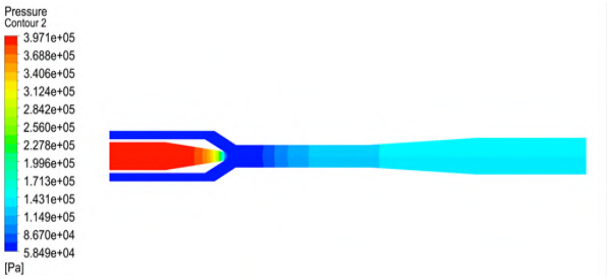

Figure 8. Pressure along the ejector for different the solution method

creates a partial vacuum, which is detectable in Figure 7 for the pressure contour. This pressure reduction causes the secondary fluid (air) suction. After the mixing process in the mixing chamber, the air passes through the constant-area section with a slight velocity decrease; afterward, its velocity decreases. Moreover, in the diffuser, the velocity decreases, and the pressure slightlyi ncreases.

Inlet air pressure parameter influentially contributes to the ejector performance. In Figure 9, the inlet air pressure effect on the water phase distribution along the symmetry axis has been displayed. As the inlet air pressure increases, the air momentum amount and its penetration power through the primary water fluid will increase. Additionally, it will affect the water and air phase distribution along the axis. The water volume fraction will decrease by increasing air inlet pressure along the axis. Moreover, the water primary layer's dispersion rate increases while its continuity decreases. The air presence within the water layer will gradually increase along the axis as the axial distance increases. As shown in Figure 9, increasing air inlet pressure from 50 to 60 to 70 and 80 kPa, the volume fraction of water at the center of the ejector's output decreases by 14.6%, 21.03%, and 15.22%, respectively. The flow enters the ejector's entry in the form of two flows and subsequently, the two flows are combined with a part of the airflow at the end of the water primary nozzle exit, which causes the air suction. Afterward, they are passing as a single fluid. The fluid velocity increases by increasing the inlet air pressure; this will change the mixing percentage of two fluids of the flow. Thus, the water volume fraction decreases, and the air volume fraction increases by increasing the inlet air pressure along the axis.

In Figure 10, the distribution of water velocity at different inlet pressures is demonstrated. As pressure increases, the primary fluid velocity increases; thus, higher momentum of primary fluid can be observed at the output. Through the air inlet pressure increase from 50 to 60, 60 to 70, and 70 to 80 kPa, the outlet velocity will increase by 22.24%, 27.8%, and 14.23%, respectively.

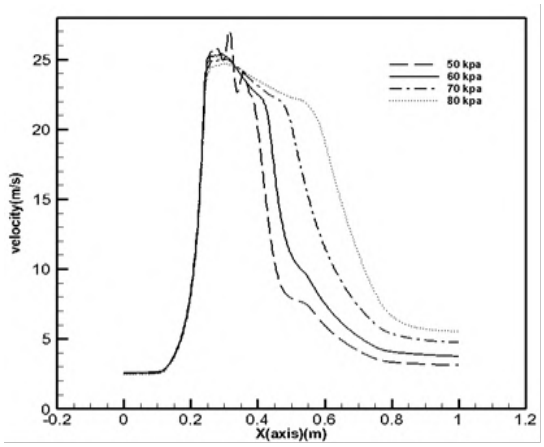

Figure 9. Air inlet pressure effect on the axial velocity along with the ejector

Table 4 illustrates through increasing suction secondary fluid pressure from 50 to 60, 60 to 70, and 70 to 80 kPa, the ejector flow rate ratio increases by 42.83%, 9.38%, and 94.9% respectively. Additionally, by the secondary fluid pressure increase from 50 to 60, 60 to 70, and 70 to 80 kPa, the minimum created pressure for suction increases by 30.11%, 13.99%, and 14.22%, respectively.

Again from Table 2, simulations of 9 to 12, consider the output pressure impact on the ejectors inside flow. Figure 10 depicts the ejector outlet pressure effect on the water and air phase distribution. The air momentum amount decreases through the ejector outlet pressure increase. Thus, its penetration power into the primary fluid of water also decreases. This reduction affects the air and water phase distribution along the axis. The water phase amount will increase by increasing pressure along the axis. Moreover, the dispersion of the water primary layer will decrease, and its continuity increases.

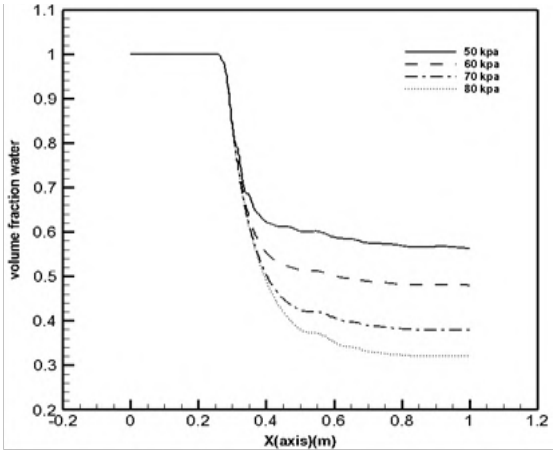

Figure 10. Inlet air pressure effect on the water phase distribution along with the ejector

TABLE 4. Flow rate ratios in different parameters

Parameter	Value	Flow rate ratio
Water inlet pressure (kPa)	390	1.0761
	400	1.2394
	410	1.4831
	420	1.6809
Air inlet pressure (kPa)	50	0.8677
	60	1.2394
	70	1.3557
	80	2.6423
Ejector Outlet pressure (kPa)	130	2.1472
	140	1.2394
	150	0.6646
	155	0
Throat radius (mm)	19	1.6952
	19.5	1.5534
	20	1.2394
	2.5	1.2434
	21	0.9067
Nozzle exit radius (mm)	7	0.7835
	7.5	0
	8	1.2394
	8.5	1.7424
	9	1.9473

The presence of the air phase inside the water layer will gradually decrease as axial distance increases.

As can be noticed, the phases' turbulence has increased at the pressure of 150 kPa, at the ejector's end. This pressure has reached zero after a further increase of the outlet pressure of air suction. After this pressure increase, there would be a back-flow. In other words, instead of suction, the water exits, and it has been observed that there is only the water phase at a pressure of 160 kPa on the symmetry axis. According to Figure 10, through the ejector outlet pressure increase from 130 to 140kPa, from 140 to 150kPa, and from 150 to 160 kPa, the water volume fraction in the ejector output has increased by 32.65%, 18.63%, and 75.31%, respectively. As the ejector's outlet pressure increases, the fluid velocity decreases along the ejector. This causes the mixing percentage of the two fluids of the flow to reduce. Therefore, the water volume fraction increases, and the air volume fraction decreases by increasing the ejector's outlet pressure.

In Figure 11, the water velocity distribution has shown at different outlet pressures. As the pressure increases, the primary fluid velocity decreases. Thus, it has a lower momentum at the output. As the ejector output pressure increases from 130 to 140kPa, 140 to 150kPa, and from 150 to 160 kPa, the velocity at the ejector output is decreased by 26.36%, 23.87%, and 52.79%, respectively. If the discharge pressure increases and exceeds the breaking point's pressure, a back-flow will be generated. In other words, the fluid exits the ejector instead of entering through the secondary inlet.

It can also be seen in Table 4, that by increasing the ejector outlet pressure, the air inlet amount decreases, and the primary fluid energy will be more dissipated for making the secondary fluid entry. Moreover, the air and water fluids will move with lower velocity. As the ejector outlet pressure increases from 130 to 140kPa, 140 to 150kPa, and from 150 to 160 kPa, the flow rate ratio is decreased by 42.27%, 46.37%, and 100%, respectively, and the symmetry axis pressure increases through outlet pressure increase. In Figure 12, the water inlet pressure effect on the air and water phases' distribution has demonstrated (in Table 2-Simulations 1 to 4). Furthermore, the axial velocity in the air-water ejector increases as the water inlet pressure increases. Increasing the inlet pressure causes more pressure drop at the primary nozzle's end.

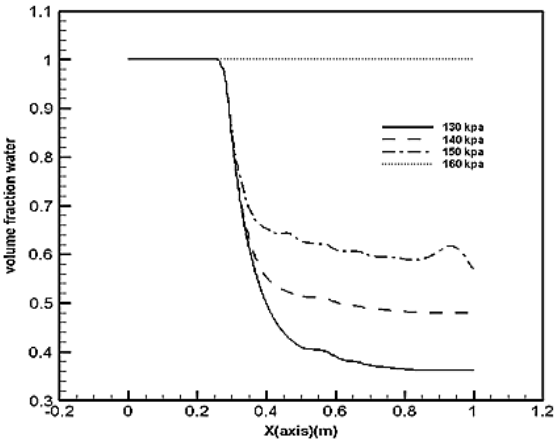

Figure 11. Ejector outlet pressure effect on water phase distribution along the axis

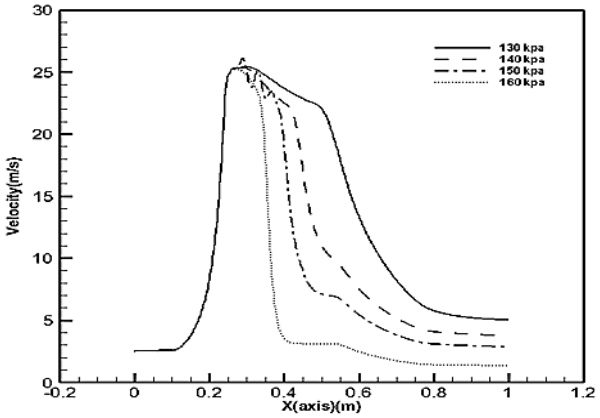

Figure 12. Outlet pressure effect on the axial velocity along the ejector axis

Additionally, the nozzle fundamentally increases the velocity and decreases the pressure. Therefore, it produces a greater vacuum; consequently, the ejector sucks a greater amount of fluid. By water inlet pressure increase, the water phase amount represents a decreasing trend, while the air phase amount indicates an increasing trend.

According to Figure 13, water inlet pressure is increased from 390 to 400kPa, 400 to 410kPa, and from 410 to 420 kPa, causing the water volume fraction at the ejector's end to decrease by 7.28%, 8.76%, and 6.72%, respectively. The fluid velocity increases by increasing the water inlet pressure. This point increases the mixing percentage of the two fluids of the flow. For this reason, the water volume fraction decreases, and the air volume fraction increases by increasing the water inlet pressure.

Now water inlet pressure increases from 390 to 400kPa, 400 to 410kPa, and from 410 to 420 kPa, causing the flow rate to be increased by 15.17%, 19.66%, and 13.33%, respectively. If the water inlet pressure increases, the axial velocity will also increase. In Figure 14, the inlet pressure impact on the velocity distribution has displayed. As can be noted in this figure, the axial velocity in the ejector will increase by increasing the water inlet pressure. This pressure increase has a more significant impact on the velocity after passing through the nozzle. Moreover, it increases the output velocity of the ejector. Additionally, through a more significant velocity increase, the created vacuum will increase that will cause the air suction to enhance. Water inlet pressure increase from 390 to 400, 400 to 410, and from 410 to 420 kPa, causing the velocity at the ejector output to be increased by 9.38%, 12.8%, and 6.33%, respectively.

Figure 15 presents the throat radius impact on the air and water phases in the symmetry axis. As shown in this figure, the flow ratio decreases by increasing the ejector throat radius. As previously mentioned, the secondary

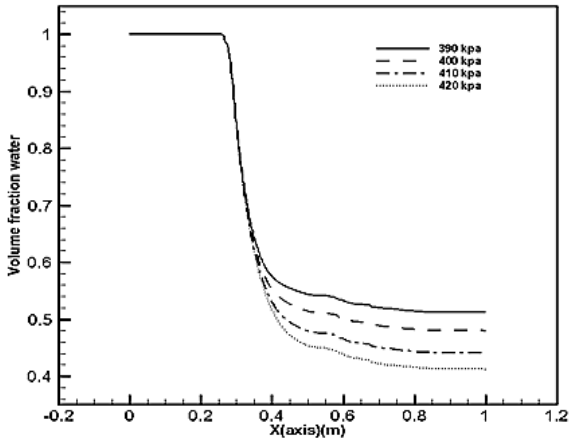

Figure 13. Ejector water inlet pressure impact on water phase distribution along the axis

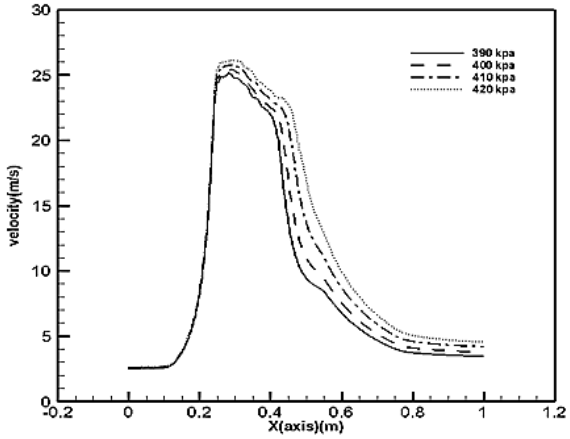

Figure 14. Water inlet pressure effect on the velocity along with the ejector

fluid water is drawn into the ejector due to the working fluid's vacuum and velocity. Moreover, as the throat cross-sectional area increases, a lower amount of fluid is sucked due to pressure increase. The ejector throat radius increases from 19 to 19.5mm and from 19.5 to 20mm, causing the ejector suction to decrease by 8.36% and 20.21%, respectively. However, by increasing the radius from 20 to 20.5 mm, the flow rate ratio increased by 0.3%. Nevertheless, in the case of radius increase from 20.5 to 21 mm, the flow rate ratio decreased by 27.07%. Therefore, the throat radius increase will lead to a volume fraction increase of the water phase in the ejector and result in the air volume fraction decrease. The reason for this point is the pressure increase since by increasing the pressure at the primary nozzle exit, the amount of air suction amount decreased. As we can be seen, a critical state is created at 21 mm, causing inconsistency and oscillation in the air and water phases. According to Figure 16, the ejector throat radius increases results in the velocity reduction in the ejector axis. This velocity decrease contributes to the air suction reduction. The inside behavior of the ejector can be appropriately observed in the contours of Figure 16. It can be noted, the momentum penetration impression on the front layers decreases by increasing the radius. Moreover, the radius increase causes the partial vacuum at the primary nozzle exit to be reduced, while that area's pressure increases.

In Figure 17, the fluid flow vector has been illustrated. As can be noted, increasing the throat radius at the outlet section will cause vortices. Created vortices will generate a resistance barrier, which is one of the reasons for the suction reduction. Considering that the air density is significantly lower than water density, the air momentum has entirely overcome these vortices. Now considering Table 2 simulations of 18 to 22, the water volume fraction in the ejector's central axis is shown in Figure 18.

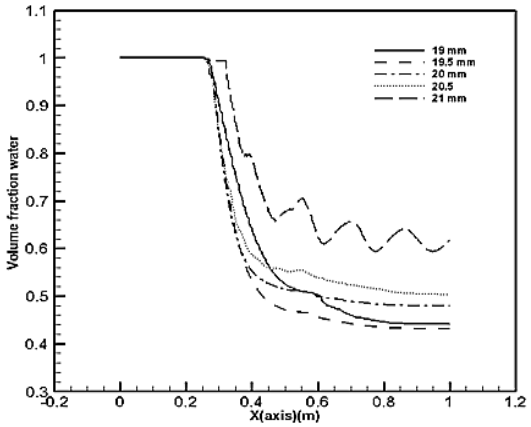

Figure 15. Throat radius on the water volume fraction

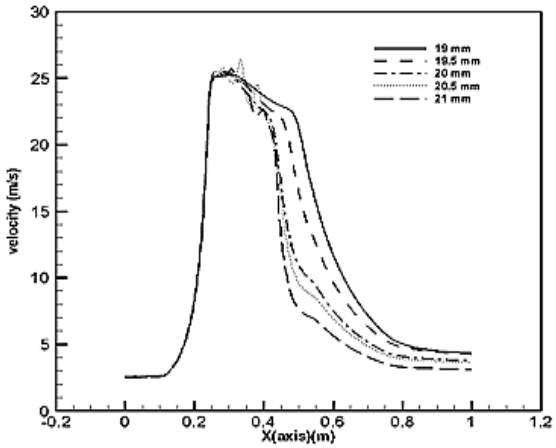

Figure 16. Throat radius impact on the velocity in the ejector

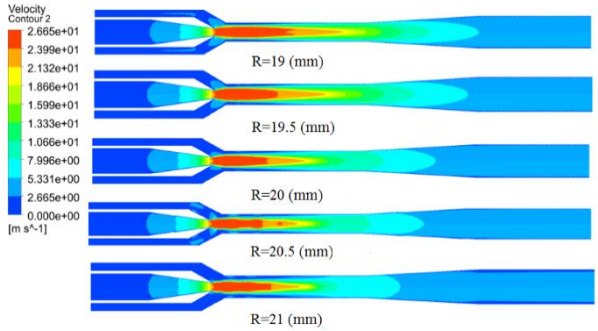

Figure 17. Velocity contour in various throat radius

As shown in Figure 19, increasing the radius of the ejector nozzle exit from 7 to 7.5 mm, from 7.5 to 8 mm, from 8 to 8.5 mm, and from 8.5 to 9 mm, respectively, leads to the reduction of the flow rate ratio by 100% (reaches zero), afterward, increases from zero to 1.23; subsequently increasing by 40%, and 20.49%. Moreover, as the distance increases, the volume fraction of water decreases, and the air volume fraction increases.

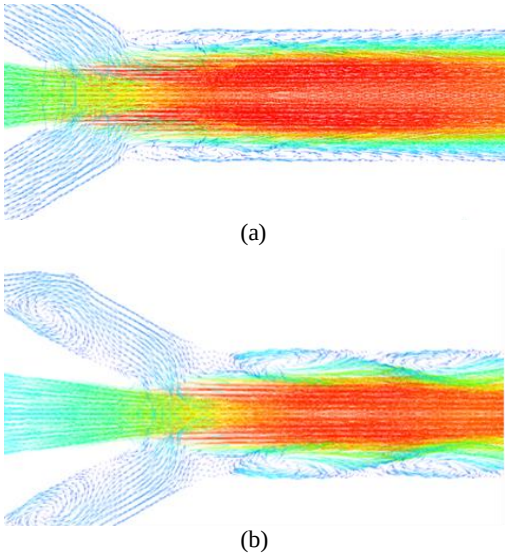

(a)

(b)

Figure 18. Fluid behavior within the ejector at throat radius of a) 19.5 (mm) b) 20.5 (mm)

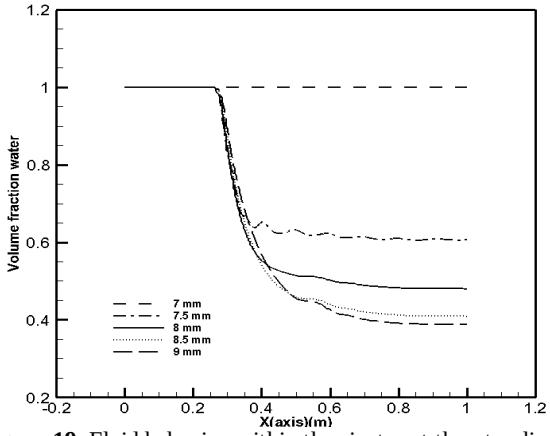

Figure 19. Fluid behavior within the ejector at throat radius of 20.5 (mm)

Figure 20 represents the velocity contour of the cases mentioned above. The radius increase will result in the velocity, and the suction rate increases.

It can be seen from Figure 21 that the velocity increases along with the ejector too. Furthermore, increasing the radius from 7 to 7.5, from 7.5 to 8, from 8 to 8.5, and from 8.5 to 9 mm, leads to enhancement of the velocity at the outlet by 155.29%, 46.51%, 30.53%, and 18.7%, respectively. Additionally, the velocity at the inlet is increased by 14.98%, 15.21%, 15.09%, and 11.46%, respectively. Moreover, by increasing the nozzle radius, the partial vacuum increases, and the air suction amount will increase, as well. Therefore, as discussed in this study, increasing air and water inlet pressure, the flow rate ratio increases. Moreover, by increasing ejector outlet pressure, the flow rate ratio decreases.

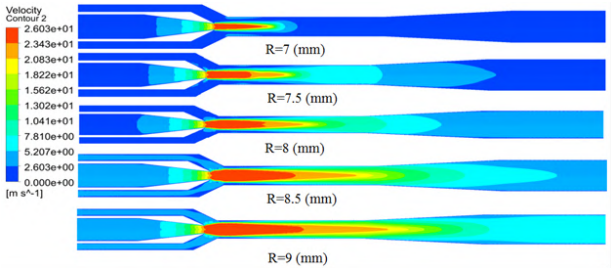

Figure 20. Velocity contour in various throat radius

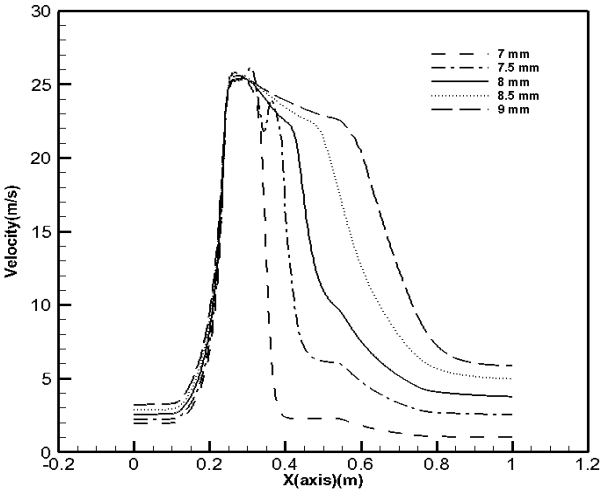

Figure 21. Impact of various ejector nozzle radius on velocity

Further, as the nozzle outlet radius and the ejector throat radius increase, the flow rate ratio increases and decreases, respectively.

5. CONCLUSION

A mixture model and Euleraian-Euleraian two-phase simulation were performed for gas-liquid jet study. Mixture method indicated better, friendlier, and an efficient rather than Eulerian-Eulerian method by comparing to experimental and numerical reported research. Therefore, mixture model was used for parametric study. Results demonstrated that the flow rate ratio increases by increasing the air and water inlet pressure, and by increasing the outlet pressure, the ejector flow rate ratio decreases. In this liquid ejector, unlike the steam ejector, the ejector's flow rate has decreased by increasing the throat's cross-sectional area. The optimal throat radius is considered 20 mm in this study, since it led to the highest flow rate ratio. Additionally, the flow rate increased by increasing the nozzle exit area's radius. The flow rate ratio was increased by 94% by increasing the air inlet pressure from 70 to 80 kPa. Moreover, by increasing the outlet pressure of the liquid ejector, the flow rate decreased. No suction was observed at 160kPa pressure; more specifically, the flow rate was reduced by almost 100% at a pressure of 150 kPa.

6. APPENDIX

TABLE A. Governing equations of this study

Definition	Equations of the Mixture model [25]
Continuity	$\frac{\partial \rho}{\partial t}+\frac{\partial \rho u_i}{\partial x_i}=0$
Momentum	$\frac{\partial \rho u_i}{\partial t}+\frac{\partial \rho u_i u_j}{\partial x_j}=-\frac{\partial p}{\partial x_i}+\frac{\partial \tau_{ij}}{\partial x_j}$
Stress	$\tau_{ij}=\mu_{eff}\left(\frac{\partial u_i}{\partial x_j}+\frac{\partial u_j}{\partial x_i}\right)-\frac{2}{3}\mu_{eff}\frac{\partial u_k}{\partial x_j}$
Density	$\rho=\sum_{k=1}^{k}\alpha_k\rho_k$
Phases	$\sum_{k=1}^{k}\alpha_k\rho_k=1$
Reynolds stress	$-\rho\overline{u_i'u_j'}=\mu_t\left(\frac{\partial u_i}{\partial x_j}+\frac{\partial u_j}{\partial x_i}\right)-\frac{2}{3}\left(\rho k+\mu_t\frac{\delta u_i}{\delta x_i}\right)\delta$
Realizable k–ε model k equation	$\frac{\partial \rho k}{\partial t}+\frac{\partial \rho k u_j}{\partial x_j}=\frac{\partial\left(\left(\mu+\frac{\mu_t}{\sigma_k}\right)\frac{\partial k}{\partial x_j}\right)}{\partial x_j}+G_K+G_b+\rho\varepsilon-Y_M+S_K$

Realizable k–ε model ε equation	$\frac{\partial \rho \varepsilon}{\partial t}+\frac{\partial \rho \varepsilon u_j}{\partial x_j}=\frac{\partial\left(\left(\mu+\frac{\mu_t}{\sigma_k}\right)\frac{\partial k}{\partial x_j}\right)}{\partial x_j}+\rho C_1 S_\varepsilon-\frac{\rho C_2 \varepsilon^2}{K+\sqrt{\nu\varepsilon}}+\frac{C_{1\varepsilon}\varepsilon}{KC_{3\varepsilon}G_b}+S_\varepsilon$
Coefficient	$C_1=Max\left(0.43,\frac{\mu}{n+5}\right)$ $\quad n=\frac{sk}{\varepsilon}$ $\quad S=\sqrt{2S_{ij}S_{ij}}$
Equations of Eulerian-Eulerian model [23]	
Continuity	$\frac{\partial(\alpha_k\rho)}{\partial t}+\nabla.(\alpha_k\rho u_k)=0$
Momentum	$\frac{\partial(\alpha_k\rho u_k)}{\partial t}+\nabla.(\alpha_k\rho u_k u_k)=-\alpha_k\nabla p+\nabla.\tau_k$
Reynolds stress	$-\rho\overline{u_i'u_j'}=\mu_t\left(\frac{\partial u_i}{\partial x_j}+\frac{\partial u_j}{\partial x_i}\right)-\frac{2}{3}\left(\rho k+\mu_t\frac{\delta u_i}{\delta x_i}\right)\delta$
Realizable k–ε model, k equation	$\frac{\partial \rho k}{\partial t}+\frac{\partial \rho k u_j}{\partial x_j}=\frac{\partial\left(\left(\mu+\frac{\mu_t}{\sigma_k}\right)\frac{\partial k}{\partial x_j}\right)}{\partial x_j}+G_K+G_b+\rho\varepsilon-Y_M+S_K$
Realizable k–ε model, ε equation	$\frac{\partial \rho \varepsilon}{\partial t}+\frac{\partial \rho \varepsilon u_j}{\partial x_j}=\frac{\partial\left(\left(\mu+\frac{\mu_t}{\sigma_k}\right)\frac{\partial k}{\partial x_j}\right)}{\partial x_j}+\rho C_1 S_\varepsilon-\frac{\rho C_2 \varepsilon^2}{K+\sqrt{\nu\varepsilon}}+\frac{C_{1\varepsilon}\varepsilon}{KC_{3\varepsilon}G_b}+S_\varepsilon$
Density relation	$\rho=\sum_{k=1}^{k}\alpha_k\rho_k$
Phases	$\sum_{k=1}^{k}\alpha_k\rho_k=1$

7. REFERENCES

1. Bagheri-Esfe, H. and Dehghan Manshadi, M., "A low cost numerical simulation of a supersonic wind-tunnel design", ***International Journal of Engineering, Transactions A: BAsics***, Vol. 31, No. 1, (2018), 128-135. doi: 10.5829/ije.2018.31.01a.18
2. Aminoroayaie Yamini, O., Mousavi, S.H., Kavianpour, M. and Safari Ghaleh, R., "Hydrodynamic performance and cavitation analysis in bottom outlets of dam using cfd modelling", ***Advances in Civil Engineering***, Vol. 2021, (2021). Article ID 5529792, doi.org/10.1155/2021/5529792
3. Mousavimehr, S., Yamini, O.A. and Kavianpour, M., "Performance assessment of shockwaves of chute spillways in large dams", ***Shock and Vibration***, Vol. 2021, (2021). Article ID 6634086, doi.org/10.1155/2021/6634086
4. Movahedi, A., Kavianpour, M. and Aminoroayaie Yamini, O., "Experimental and numerical analysis of the scour profile downstream of flip bucket with change in bed material size", ***ISH Journal of Hydraulic Engineering***, Vol. 25, No. 2, (2019), 188-202. doi.org/10.1080/09715010.2017.1398111
5. Khatamnejad, H., Khalilarya, S., Jafarmadar, S., Mirsalim, M. and Dahodwala, M., "Toward an improvement of natural gas-diesel dual fuel engine operation at part load condition by detail cfd simulation", ***International Journal of Engineering, Transactions A: BAsics***, Vol. 31, No. 7, (2018), 1082-1087. doi: 10.5829/ije.2018.31.07a.11
6. Shiravi, A.H., Firoozzadeh, M. and Lotfi, M., "Experimental study on the effects of air blowing and irradiance intensity on the performance of photovoltaic modules, using central composite design", ***Energy***, Vol. 238, Part A, (2022), 121633. doi.org/10.1016/j.energy.2021.121633
7. Azizi, K. and Keshavarz Moraveji, M., "Computational fluid dynamic-two fluid model study of gas-solid heat transfer in a riser with various inclination angles", ***International Journal of Engineering, Transactions A: BAsics***, Vol. 30, No. 4, (2017), 464-472. doi: 10.5829/idosi.ije.2017.30.04a.02
8. Shiravi, A.H., Shafiee, M., Firoozzadeh, M., Bostani, H. and Bozorgmehrian, M., "Experimental study on convective heat transfer and entropy generation of carbon black nanofluid turbulent flow in a helical coiled heat exchanger", ***Thermal Analysis and Calorimetry***, Vol. 145, No. 2, (2021), 597-607. doi.org/10.1007/s10973-020-09729-1
9. Hasanpour, B., Irandoost, M., Hassani, M. and Kouhikamali, R., "Numerical investigation of saturated upward flow boiling of water in a vertical tube using vof model: Effect of different boundary conditions", ***Heat and Mass Transfer***, Vol. 54, No. 7, (2018), 1925-1936. doi.org/10.1007/s00231-018-2289-3
10. Khan, R., "Numerical investigation of the influence of sand particle concentration on long radius elbow erosion for liquid-solid flow", ***International Journal of Engineering, Transactions A: BAsics***, Vol. 32, No. 10, (2019), 1485-1490. doi: 10.5829/ije.2019.32.10a.18
11. Torfeh, S. and Kouhikamali, R., "Numerical study of different gas–solid flow regimes effects on hydrodynamics and heat

transfer performance of a fluidized bed reactor", ***Heat Transfer—Asian Research***, Vol. 49, No. 1, (2020), 213-235. doi.org/10.1002/htj.21607

12. Keenan, J.H., Neumann, E.P. and Lustwerk, F., "Investigation of ejector design by analysis and experiment", ***Journal of Applied Mechanics***, (1950) 299-309.
13. D. Sharma, P., A., Ranade, V, "Effect of turbulent dispersion on hydrodynamic characteristics in a liquid jet ejector," ***Energy***, Vol. 164, (2018) 10-20. doi.org/10.1016/j.energy.2018.08.171
14. K. Pianthong, S., W., Behnia, M., Sriveerakul, T., Aphornratana, Senthil Kumar, R., Kumaraswamy, S., Mani, A, "Investigation and improvement of ejector refrigeration system using computational fluid dynamics technique ", ***Energ Conversion and Management,*** Vol. 48, No. 9 (2007), 2556-2564. doi.org/10.1016/j.enconman.2007.03.021
15. P. Cramers, B., A, "Influence of the ejector configuration, scale and the gas density on the mass transfer characteristics of gas–liquid ejectors", ***Chemical Engineering Journal,*** Vol. 82, No. 1-3 (2001): 131-141. doi.org/10.1016/S1385-8947(00)00363-6
16. R. Senthil Kumar, K., S., Mani, A, "Experimental investigations on a two-phase jet pump used in desalination systems", ***Desalination***, Vol. 204, No. 1-3, (2007), 437-447. doi.org/10.1016/j.desal.2006.03.546
17. Jafarmadar, S., "The effects of pressure difference in nozzle's two phase flow on the quality of exhaust mixture", ***International Journal of Engineering, Transactions B: Applications***, Vol. 26, No. 5, (2013), 553-562. doi: 10.5829/idosi.ije.2013.26.05b.12
18. Zhu, P.J.Y., "Bypass ejector with an annular cavity in the nozzle wall to increase the entrainment: Experimental and numerical validation", ***Energy***, Vol. 68, (2014), 174-181. doi.org/10.1016/j.energy.2014.02.046
19. W.C. Y. Zhu, C.W., Y. Li, "Numerical investigation of geometry parameters for design of high performance ejectors", ***Applied Thermal Engineering***, Vol. 29, No. 5-6, (2009): 898-905. doi.org/10.1016/j.applthermaleng.2008.04.025
20. J.Y. D. Chong, G.W., J. Liu, "Structural optimization and experimental investigation of supersonic ejectors for boosting low pressure natural gas", ***Applied Thermal Engineering***, Vol. 29, No. 14-15, (2009), 2799-2807. doi.org/10.1016/j.applthermaleng.2009.01.014
21. Kouhikamali.R., N. Sharifi, "Experience of modification of thermo-compressors in multiple effects desalination plants in assaluyeh in iran", ***Applied Thermal Engineering***, Vol. 40, (2012), 174-180. doi.org/10.1016/j.applthermaleng.2012.02.002
22. J.Y. L. Wang, C.W., X. Li, "Numerical study on optimization of ejector primary nozzle geometries", ***International Journal of Refrigeration***, Vol. 76, (2017), 219-229. doi.org/10.1016/j.ijrefrig.2017.02.010
23. Bhutada, S.R., Pangarkar, V.G., "Gas induction and hold-up characteristics of liquid jet loop reactors", ***Chemical Engineering Communications***, Vol. 61, No. 1-6, (1987), 239-258. doi.org/10.1080/00986448708912041
24. Wang, X., Chen, Y., Li, M., Xu, Y., Wang, B. and Dang, X., "Numerical investigation of the cavitation performance of annular jet pumps with different profiles of suction chamber and throat inlet", ***Engineering Applications of Computational Fluid Mechanics***, Vol. 14, No. 1, (2020), 1416-1428. doi.org/10.1080/19942060.2020.1824875
25. H.L. Xiaodong Wang, J.D., Jiaqi Wu, Ji-yuan Tu, "Numerical study on mixing flow behavior in gas–liquid ejector", ***Experimental and Computational Multiphase Flow***, Vol. 3, (2021), 108-112. doi.org/10.1007/s42757-020-0069-z

Persian Abstract

چکیده

در این تحقیق ، مخلوط حالت پایدار و روش Eulerian-Eulerian برای خارج کننده جریان موازی گاز مایع –گاز مورد بررسی قرار گرفت. شبیه سازی نشان داد که شبیه سازی مدل مخلوط نشان دهنده بهتر و کارآمدتر است. مدل Eulerian-Eulerian به زمان محاسباتی طولانی تری نیاز داشت و برای دستیابی به همگرایی مطلوب دارای پیچیدگی بود. با این حال ، عملکرد هر دو روش کمی مشابه نشان داده شد. مدل ها اختلاف حدود ٦ درصد را در نسبت جریان نشان دادند ، نمودارهای فشار آنها تقریباً منطبق است و پارامتر سرعت آنها در مقایسه با داده های تجربی موجود ۷ درصد متغیر است. علاوه بر این ، نتایج مدل مخلوط بسیار بهتر با داده های تجربی مطابقت دارد. بنابراین ، مدل مخلوط برای مطالعه پارامتری بعدی انتخاب شد. نتایج شبیه سازی نشان داد که نسبت دبی با افزایش سطح مقطع گلو کاهش می یابد و نسبت جریان با افزایش سطح مقطع نازل افزایش می یابد. در این رابطه ، به عنوان مثال ، نسبت دبی خروجی با افزایش فشار از ۷۰ به ۸۰ کیلو پاسکال ، ورودی هوا تا ۹٤ درصد افزایش می یابد ، و با افزایش فشار خروجی خروجی ، نسبت جریان کاهش می یابد به طوری که هیچ مکشی در آن مشاهده نمی شود. ١٦٠ کیلو پاسکال در نتیجه ، در نسبت فشار ١٥٠ کیلو پاسکال ، نسبت جریان تقریباً ١٠٠ کاهش یافت.

IJE TRANSACTIONS B: Applications Vol. 35, No. 02, (February 2022) 319-326

International Journal of Engineering
Journal Homepage: www.ije.ir

The Ensemble of Unsupervised Incremental Learning Algorithm for Time Series Data

D. Beulah*[a], P. Vamsi Krishna Raj[b]

[a] *Aditya Engineering College, Surampalem, AP, India*
[b] *CIIS, Swarnandhra College of Engineering. & Tech. (Autonomous), Narsapur, AP, India*

PAPER INFO

Paper history:
Received 14 May 2020
Received in revised form 19 October 2021
Accepted 06 November 2021

Keywords:
Data mining
Data Stream Mining
Unsupervised Learning
Incremental Learning

ABSTRACT

Data mining is one of the key concepts to discover hidden knowledge from available data. Along with the data mining, data analytics is a field to analyze and process data in a scientific and cognitive angle. It is more helpful to convert knowledge to actionable knowledge for accurate decision making. Data Stream Mining is another challenging area than normal Data Mining due to its dynamics. Dynamics of data in a stream includes changes in data frequency, volume and nature. This paper focuses on the behavior of data mining of machines in process/manufacturing industries. In general, such data is continuous numerical and time series data captured by various industrial sensors. By nature, equipment or machinery behaviour can change over time. It requires calibration/replacement before failure of machinery. By analyzing data, one can find the behavior or state change. To identify that, dynamic models are required to be built using data mining and data stream mining. Thus, we are following a semi-novel approach for building such models using "*Ensemble of Unsupervised Incremental Learning*" method. Results show how the existing methods are different from the proposed method. This method can be applied for any other domain like image/audio/video or text mining.

doi: *10.5829/ije.2022.35.02b.07*

NOMENCLATURE

D	Dataset	$\|C_i\|$	Density of i^{th} Cluster
$\|D\|$	Number of samples in the dataset (Dataset size)	Q_i	Quality of i^{th} Cluster
X_i	i^{th} Sample of Dataset D	Q	Quality of Cluster method
X_{ij}	j^{th} dimension of i^{th} Sample	SC	Representation for Sub Cluster
C	Cluster Set	F	Field Set
C_i	i^{th} Cluster	F_i	i^{th} Field
C_{ih}	Head or Center of i^{th} Cluster	$\|F\|$	Number of Fields in Dataset
$\|C\|$	Total Clusters		

1. INTRODUCTION

In general, data mining is a collection of methods for knowledge discovery on static data. Data stream mining is a little bit advanced operating on live or stream data. So, existing data mining methods need to be altered to support stream and concept drifts in data streams. Finally, data analytics is used to analyze large historical data and data on highway (live data) with various advanced mathematical, statistical and logical methods. Apart from that, incremental learning is an approach in data stream mining in which incoming data is continuously fed to the model. But the current model with pre-defined parameters or constraints may or may not give accurate results if incoming data behavior is changed. To cater to those requirements for a long time, existing models must be rebuilt or extended. Applications of such models/learning include predictive maintenance, anomaly detection, and pattern recognition.

This paper focuses and describes what are the challenges/limitations of some of the traditional methods and try to integrate them in a systematic way by considering their strengths and try to overcome the weaknesses. This integration improves the robustness of

*Corresponding Author Institutional Email: *beulah@aditya.ac.in*
(D. Beulah)

Please cite this article as: D. Beulah, P. Vamsi Krishna Raj, The Ensemble of Unsupervised Incremental Learning Algorithm for Time Series Data, ***International Journal of Engineering, Transactions B: Applications***, Vol. 35, No. 02, (2022) 319-326

the learning model to increase the reliability and accuracy with considerable positive results in performance metrics.

Paper Organization: Rest of the paper contains the following sections. "*Related work*" section describes some of the work that was done. "*Proposed work*" section describes the definitions, notations, algorithms and their description in detail. Finally, the "*Results"* section describes results comparison with some of the existing methods and performance gains of proposed methods.

2. RELATED WORK

A number of papers are published on incremental learning. According to literature [1-3], it is a process of adopting new behavior on arrival of an incoming data stream. It becomes important to improve the accuracy of the model prediction in interactive environments with the help of human feedback in a timely fashion as described Rico-Juan and Inesta [4]. Specifically, data stream processing must be done in a single pass and cannot mine repeatedly according to Morales and Samoa [5]. Apart from these methods some of the investigators [6-8] paid attention and publicized on unsupervised learning for data stream using cluster methods. Because this paper also depends on clustering, it is worth mentioning some of the existing works with respect to this topic. One of such work is STREAM [6]. It will cluster given data stream in two phases. In the first phase, this algorithm divides incoming stream into various sets/batches of samples and apply an efficient clustering algorithm named as LOCAL SEARCH. After this phase whatever the number of cluster points created, are sent to the next phase. In the second phase, all these cluster points can be re-clustered and generate a global set of clusters. But it is an NP-hard (non-deterministic polynomial-time hardness) problem. Space requirement is proportional to the time. Some other cases include both online and offline scenarios to support live and historical data mining. Even our paper also belongs to this category. It is also having two stages/phases. Offline phase to create an initial set of clusters and online phases are treated as incremental learning. This was proposed by Aggarwal et al. [9].

Other sets of algorithms focus on sliding windows. It was based on the principle that new or recent data samples are more important than the samples arrived long back. Sliding window can be viewed as a set of N recent samples in the data stream. And each set can be viewed as a block. This sliding window method is further divided into fixed length and variable length windows. Each block summary or statistics can be maintained by calculating boundaries or sketches to that block. The sketch can be calculated based on the algorithm described by Greenwald and Khanna [10]. Further, some of the applications are described by Arasu and Manku [11]. An agglomerative hierarchical clustering with random swap was proposed by Hautamaki [12] in Euclidian space. Other approach proposed by Lian and Lei [13] essentially stated that all types of time series data applications need an efficient and effective similarity search over stream data.

2. 1. Challenges of Incremental Learning for Data Stream

Parameter tuning and adaption: Parameters are the most affecting elements in any algorithm. They need to change based on the type of data, domain, signature etc. It is difficult to tune the parameter even for a single model to give accurate results with static or historical data. In that case, it will be far more difficult to tune the parameters in models built for data streams.

Dynamic Normalization: Normalization is a transformation process of raw data from different scales to the same scale. It is very simple in historical data processing but very challenging in data stream processing.

Concept drift detection and handling: Data stream is a collection of samples coming sequentially and changes its frequency and behaviour over time. In that condition, if the model was built based on some set of samples, the prediction coming out of that model may not be accurate when the incoming set of recent samples does not fit in current scale or range. At that time model must be intelligent enough to detect that change and update itself and must be able to give accurate or decent results. But, this is not that easy.

Boundary Samples/ Points analysis: This is a special case in clustering and applicable for some type of clustering methods. It leads to misinterpretation of samples if boundary points are selected as cluster heads. In turn, it leads to wrong tagging or labelling. There should be a proper method to detect boundary points and not to make them as cluster heads, but in those methods this situation may probably occur.

Space and Time Complexity Management: Most of the big data management and data stream applications are memory and time intensive. It is difficult to achieve a balance between space and time complexity. If we try to achieve performance in terms of space, then time must be compromised and/or vice versa. Efficient data structures are required to balance this situation.

3. PROPOSED APPROACH

By considering some of the above challenges, we are proposing certain functionality to handle dynamic normalization, concept drift handling, boundary point interpretation with good space and time complexity management.

3. 1. Definitions

Dataset: It is a collection of samples and fields. Each sample in the data set must have different values for each dimension.

Time series: If each sample in a dataset is associated with a timestamp then it will be treated as Timeseries dataset. Moreover, each value of each dimension in each sample is not random value. It must relate to a concept or context.

Unsupervised Machine Learning: If the samples in the given dataset are not assigned to any predefined labels or classes then processing or learning of such dataset is called unsupervised machine learning.

Cluster: It is a collection or group of samples exhibiting with at most similar behavior.

Crisp/Hard Clustering: Every point/sample in the dataset belongs to only one cluster.

Fuzzy/Soft Clustering: Every point/sample in the dataset can belong to more than one cluster with membership value or weight.

Incremental/Dynamic Learning: In static learning, once model building is over, it cannot be updated or learned. This type is suitable only for historical data mining. To process or mine the data stream, a trained model must be retrained or learn from new samples on a continuous basis.

Signature: It is a collection of independent variables with a single dependent variable. Dependent variable means it is the variable most affected with any small change in any one of the related independent variables. Signature, in other words is the logical representation of an equipment or section in the industry.

3. 2. Dataset

Nature of Dataset we are considering for selection of ensemble algorithm is time series with numerical values and bad data as well. This is a real-time data set retrieved from an Oil and Gas company and belongs to some oil wells. Details of the wells and company are hidden due to a privacy agreement.

3. 3. Proposed Ensemble of Algorithms

The proposed algorithm must run in two phases, offline and online with hierarchical clustering. But we choose the parent level cluster algorithm as different from the child level algorithm by understanding the nature of the data. Parent algorithm is used to divide or partition the given input data into meaningful groups in such a way each group or some set of groups belongs to one state and another set of groups belongs to another state. State here refers to various operating conditions or zones such as off, on, start-up, steady, transient and stale. Off means, the value of certain sensor is equal to 0 or less than minimum "on" range. On means greater than or equal to some value. Start-up range means state between on and steady state or general operating condition. Steady state means variance must be maintained between +/- certain percent. Stale means variance of last n-samples equals 0. Transient means irregular variance among last n samples. State calculation requires domain knowledge and thus out of the scope for this paper. We are using some variables to specify thresholds for state ranges. Parent algorithm uses incremental learning.

Child/Sub Level algorithm is any traditional algorithm such as K-Means. We are also using the K-means for sub level clustering.

One can get the question in their mind, why to choose 2 different algorithms in parent and child levels. In our case, if we choose K-means as a parent or only algorithm for both levels it leads to inaccurate results due to the value of K, because K-means must cluster all the available samples into K-clusters at any cost, whether their behavior really belongs to that cluster or not. It leads to mislabelling or misinterpretation. But we adopted and extended the idea, leader-follower algorithm in parent level clustering which was proposed by Parthasarathy et al. [14] Davies and Bouldin [15] fits the need of the paper.

Apart from the Clustering algorithm, normalization in pre-processing step also refined to adaptive normalization to get more accurate results for test and live streaming data. We are assuming that data with text values are treated as bad data and cannot be part of clustering. We are calculating the running statistics for the last n samples to find the ‘stale' state. Values or samples belong to stale are also not suitable for prediction.

Off-line phase creates multiple signatures and each signature has multiple clusters. Each signature specifies a partial representation of an equipment or machinery in the selected domain. As already told, the proposed model can fit into any domain with a little bit of parameter tuning. On the other hand, online phase utilizes the signatures created in the offline phase and makes the model robust with incremental learning method. Figure 1 shows the proposed system and steps involved in the process flow chart.

Without any doubt above mentioned model is not new in any data mining application but the approach is fresh at Pre-processing, Signature Building and Online Processing stages.

Each Stage is described in detail in the following paragraphs.

System Input: Models must be built on historical data or data at rest. The data source can be anyone like files, databases or historians. As mentioned previously, here data is numerical time series data extracted from various industrial sensors. The proposed model is part of Industrial IoT and analytics.

Pre-processing: This is a filtering and transformation stage to ignore the text and missing values. Handling the missing values itself is a separate concept and not part of this paper. Next step is converting or transforming given data of multiple scales to a single scale. We are using min-max normalization. It requires a single pass of entire

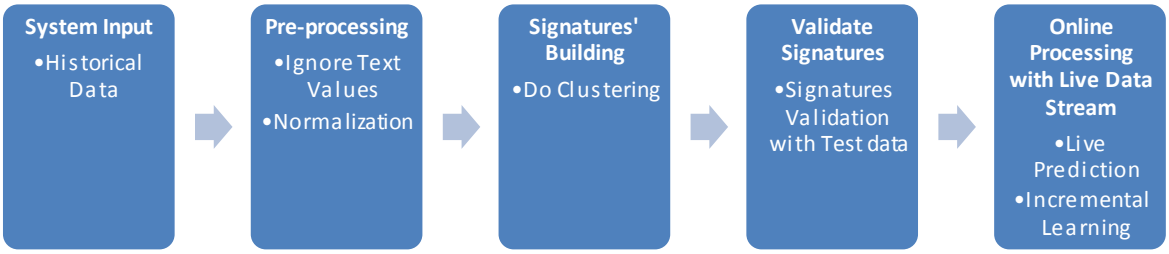

Figure 1. Proposed System Process Flow

dataset to find min and max values of each dimension. But, here the issue arises whenever new min-max comes into the picture with arriving sample.

Finally, we are also calculating the statistics of each dimension to check the quality of input data. If input data for any dimension is having text%>30 and if that dimension is part of any signature, then it is not possible to build the model for that signature.

Signature Building: This is the actual area of our research interest. The proposed unsupervised incremental learning is as follows.

Algorithm:

Procedure *mainProc*

Input: Signature File
Dataset File
Distance threshold (th),
Maximum number of results of recent iterations to match for k-means (noi)
The minimum density of any cluster to give prediction (minden)

Output: Cluster Set (C)

Steps:

1. Build in memory dataset D
2. Calculate each field statistics such as min, max, mean, var, sd, text% at the time of dataset building itself
3. Do min-max normalization on D
4. Build Signature Set (S) from Signature File and sub divide the given dataset D into multiple datasets based on a number of signatures.
5. For Each Signature S_i in S
    a. Call BuildClusters (D,th,noi,minden)
    b. Output Clusters and Save Signature Output with predictions

Description:

Above mainProc is entry point and control point of all other procedures that contain algorithm implementation steps. Step 1 is used to read the data from the input file and create a logical in-memory dataset for next processing. If the size of the dataset is large and if it cannot fit in memory, there are two solutions. First one is to increase the heap size. Second one is to divide the actual file again into multiple files. Next apply algorithm to cluster individually and merge results to achieve global result. The second option is not part of the paper and it is an extension of current work and left as future work. Thus, we are assuming that the input file size can fit in current memory by increasing the default heap size. Step 2 is used to calculate Field/Column/Dimension wise statistics to understand the quality of the data. If data is not having quality, then there is no point to proceed further. Step 3 is used to find the normalization based on min and max values of each dimension. One strong point here is min and max are not min and max of the entire dataset; they are min and max of each dimension separately. Step 4 is used to build the logic in memory signature list from given signature file. As told in the definition each signature has a name, dependent and some set of independent variables. Thus, each signature must have a separate set of data samples i.e. given data set D is divided into multiple data sets based on a number of signatures. Finally, step 5 is used to invoke a clustering algorithm in procedure '*BuildClusters()*' for each signature.

Procedure *BuildClusters* (D,th,noi,minden)

Steps

1. Initialize Cluster Set C
2. For each X_i in X
   do
3. If X_i is the first sample
   then
    a. Create new Cluster newclu and Append newclu to C
    b. Make X_i as cluster head to newclu and add to the cluster
4. Else
    a. Initialize min-dist-clu=null, cnt=0, min-dst=0
    b. For each C_j in C
       do
        i. Calculate ed=EuclDist(X_i,C_j)
        ii. If ed<=th and cnt=0
            Then

1. minclu=C_j
2. mindist=ed;
3. Increment cnt by 1

iii. else if ed<=th and ed<mindist then
1. mindist=ed;
2. minclu=C_j

iv. End if

c. End for-2

5. If minclu =null
Then
a. Create new Cluster newclu and Append newclu to C
b. Make X_i as cluster head to newclu and add to the cluster
6. Else
a. Add X_i to Cluster minclu
b. Update member list(minclu)
7. End if
8. End for-1
9. For each C_i in C
do
a. If $|C_i|$>=minden
b. Then
i. MakeSubCluster(C_i)
c. End if
10. End for
11. For each C_i in C
do
a. If SC(C_i) is not empty
b. Then
i. For each SC_j in SC(C_i)
1. Append SC_j to C
ii. End for
c. End if
12. End for
13. Return C;
14. End *BuildClusters*

Description

Above procedure is the heart of the entire process. As discussed previously no single algorithm outperforms and each will have some limitations. Hence, we introduced two separate algorithms in parent and child level of hierarchical clustering. Parent algorithm strength is, it can well separate samples into multiple groups based on their actual nature. Moreover, it is very much extent suitable for incremental learning. When coming to Child level K-means is used. It becomes very robust when optimal 'K' is found. By combining the strength of two algorithms we designed and implemented the solution. To find the optimal K again we followed the same parent algorithm. But it only restricted to find the maximum number of clusters to be generated. The clusters formed in this stage cannot be used or merged to original cluster list. Only clusters generated from K-Means are appended to the final cluster list.

Coming to the steps, outer for loop is used to find the cluster of each sample X_i in dataset D. If the current sample is the first sample then, itself forms a new cluster and marks itself as cluster head to that new cluster. Then add the new cluster to already initiated cluster set C.

From the second sample onwards, each sample X_i must find nearest clusters among available clusters. Step 4 is used to find that minimum distance cluster "*minclu*". Unlike K-means, the nearest cluster must obey two rules here. The first distance from current sample X_i to current cluster head C_{jh} must be less than or equal to given distance threshold (th). Now the minimum distance of all such clusters will give final minimum cluster (minclu). Here there is no rule like K-means that current sample must fit in any one of the clusters. If it is unable to find the cluster of its nature, it will form a new cluster and marks itself as head to that cluster. Otherwise, it will add to the existing cluster and update the cluster statistics. Steps 5 and 6 describe one more point here, that is, final clusters created from these clustering algorithms are micro-clusters means it maintain only cluster head and cluster statistics to find the quality of the cluster. Another thing is values of a dependent variable must not be included in the distance calculation. It is only used to calculate prediction. Prediction of an incoming sample is mean of values included in the current cluster of respective dependent variable so far. There is a provision also to give the prediction based on density. If the density of the given cluster exceeds a certain number, then only that cluster is eligible to give a prediction. But here we didn't place such restriction. So, from second member onwards prediction is given by each cluster.

According to the above discussion, clusters will be created dynamically based on the distance threshold. Here distance threshold is a tuneable parameter and specifies the radius of the cluster. Thus, this clustering is suitable for incremental learning and type is crisp or hard clustering scheme. Finally, there is no need to create sub clusters for all clusters. The cluster those met minimum density threshold i.e. density of the cluster greater than given '*minden'* parameter, sub clusters are built as described in step 9.

Step 10 is used to merge existing clusters with sub-clusters to generate the final set of clusters to end the model building. At this point, it is possible to calculate cluster quality and cluster scheme quality on whole. This quality measure is used to specify intra and inter cluster similarity. For that purpose, we used Davies-Bouldin Index measure. According to the value of this measure, this index value is inversely proportional to the quality. i.e., increase in the index means a decrease in quality. But < 0.2 also not treated as good quality because it will specify at most one cluster for one or 2 samples. Then it's of no use. In that case, do the above procedure by changing the distance threshold parameter. Auto tuning of this parameter is also possible but it is out of scope for this paper.

Procedure *MakeSubClusters(C)*

Steps

1. Apply Same BuildClusters() logic on Members(C), only to find optimal K
2. Now Call Traditional K-mean on members(C)
3. Return Sub Clusters set SC
4. End *MakeSubClusters*

Description:

The above procedure is used to do sub-clustering. As discussed, the parent cluster algorithm is very intelligent enough to separate given dataset into meaningful state groups. But the limitation is, if boundary point is elected as cluster head then the result will be inaccurate for high-density clusters. Because, once the cluster head is selected, it cannot be changed. We can overcome this limitation through K-means, but difficult in this is getting optimal K. This can be achieved by applying parent algorithm one more time and find that K. Now high-density clusters can be further divided into subclusters and parent clusters of these clusters are of no use after forming sub clusters. Thus, the final cluster set contains sub-clusters and non-dense parent clusters.

Validate Signatures:

This stage is used to validate the signatures based on testing data. But clusters must not be updated because intra cluster statistics will be updated. This is only to understand and evaluate generated signatures and respective clusters' performance.

Online Processing with Live Data Stream:

Finally, this stage is used to read real-time data from live data sources and predict the values based on existing signatures. The advantage of this approach is, this also performs incremental learning. If new sample fits the existing cluster, then its statistics will be updated otherwise form a new cluster and update the cluster set C in the respective signature. Thus, concept drift can be efficiently handled without modifying existing logic. Even though the domain or data type is changed logic will be the same. Normalization part is also dynamically modified. Figure 2 illustrates the data distribution of each dimension. Table 1 summarized the comparative results.

4. RESULTS AND DISCUSSION

Dataset description:
Training Instances: 47200
Testing instance: 65000
Attributes: 4
RTOR (Rotor Torque)
MCUR (Motor Current)
MSP (Moto Speed)
MTOR (Motor Torque)
Where n = number of samples
m = part of n (because, no need to apply sub-clustering for all the samples)

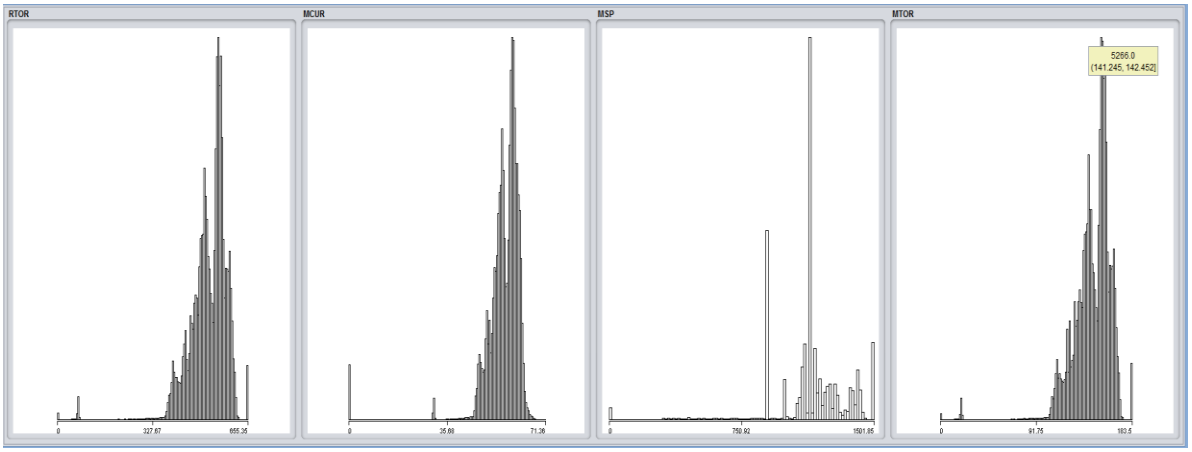

Figure 2. Data Distribution of Each Dimension

TABLE 1. Results Comparison

Measure	Traditional K-Means	Simple Incremental Learning	Hierarchical Incremental Ensemble
No of Cluster	10	12	46
Outlier Clusters	N/A	4	15
Cluster Quality	6.4497	4.1742	2.0723
Time Complexity	$O(n^2)$	O (n log n)	O (n log n) $+O(m^2)$

Even though time complexity of Proposed approach (Hierarchical Incremental Ensemble) is a little bit high when compared to other two methods, quality is good. Both 2nd and 3rd columns are part of the proposed approach; we merged that approach with the ensemble approach to get more accurate results. Outlier clusters are decided based on the density of the cluster. i.e., if the cluster is having a density less than given threshold it is treated as outlier cluster. It is not shown in the algorithm in the procedure because these clusters' density might be increased in the online process when new samples might fit into these clusters. Thus, these clusters not ignored as well.

Figure 3 depicts a scatter plot of clusters with two dimensions' distributions. This distribution will be changed for the other two dimensions. But the important thing here is X-axis must represent independent and Y-axis must represent dependent variables.

Apart from the above discussions some of the points we did not highlight due to space problem are such as dataset file format, signature list file format, output file format, cluster-wise field statistics and cluster statistics, visual representation of parent and child clusters, cluster tagging that is useful for anomaly detection and other cluster measures used in K-means like sum of squared errors. We can provide those details based on readers' interest.

Applications

The proposed Clustering Algorithm can be effectively applied in the following areas:

- Data Pre-processing
- Operating Modes Identification in Industrial IoT Sensor Data
- Outlier Detection
- Anomaly Detection
- Pattern Recognition

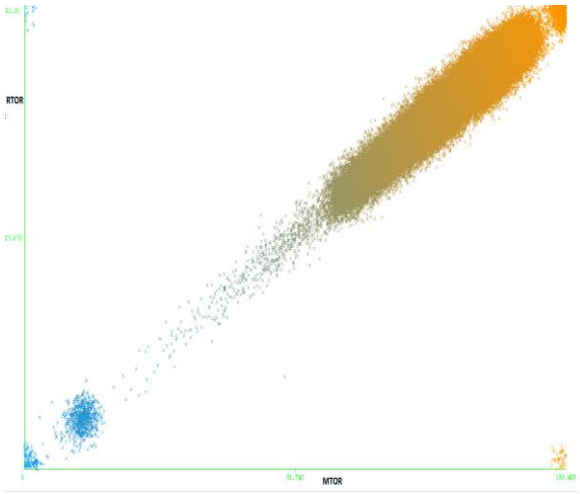

Figure 3. Cluster distributions by considering 2 dimensions

- Document Categorization
- Effective Concept Drift Handling in Data Stream Processing
- Image Processing
- Video Processing

5. CONCLUSION AND FUTURE WORK

This paper mainly focused on ensemble-based incremental learning to achieve more accurate results by using clustering methods for Industrial IoT data. Addressed some of the challenges in data streaming such as concept drift handling, dynamic normalization, incremental learning with hierarchical clustering and border point handling.

As we mentioned in earlier sections, parameter tuning can be automated, make the algorithm more robust by converting into the distributed algorithm. Anomaly detection using cluster pattern recognition is also treated as future work.

6. REFERENCES

1. Silver, D.L., Yang, Q. and Li, L., "Lifelong machine learning systems: Beyond learning algorithms", in 2013 AAAI spring symposium series. (2013).
2. Silver, D.L., "Machine lifelong learning: Challenges and benefits for artificial general intelligence", in International conference on artificial general intelligence, Springer. (2011), 370-375.
3. Luo, Y., Yin, L., Bai, W. and Mao, K.J.E., "An appraisal of incremental learning methods", Vol. 22, No. 11, (2020), 1190, doi: 10.3390/e22111190.
4. Rico-Juan, J.R. and Iñesta, J.M.J.N., "Adaptive training set reduction for nearest neighbor classification", Vol. 138, (2014), 316-324, doi: 10.1016/j.neucom.2014.01.033.
5. Morales, G.D.F. and Bifet, A.J.J.M.L.R., "Samoa: Scalable advanced massive online analysis", Vol. 16, No. 1, (2015), 149-153, doi.
6. O'callaghan, L., Mishra, N., Meyerson, A., Guha, S. and Motwani, R., "Streaming-data algorithms for high-quality clustering", in Proceedings 18th International Conference on Data Engineering, IEEE. (2002), 685-694.
7. Wankhade, K.K., Jondhale, K.C. and Dongre, S.S.J.A.S.C., "A clustering and ensemble based classifier for data stream classification", Vol. 102, (2021), 107076, doi: 10.1016/j.asoc.2020.107076.
8. Dubey, A.K., Gupta, R. and Mishra, S., "Data stream clustering for big data sets: A comparative analysis", in IOP Conference Series: Materials Science and Engineering, IOP Publishing. Vol. 1099, No. 1, (2021), 012030.
9. Aggarwal, C.C., Philip, S.Y., Han, J. and Wang, J., "A framework for clustering evolving data streams", in Proceedings 2003 VLDB conference, Elsevier. (2003), 81-92.
10. Greenwald, M. and Khanna, S.J.A.S.R., "Space-efficient online computation of quantile summaries", Vol. 30, No. 2, (2001), 58-66, doi: 10.1145/1055558.1055598.
11. Arasu, A. and Manku, G.S., "Approximate counts and quantiles over sliding windows", in Proceedings of the twenty-third ACM

SIGMOD-SIGACT-SIGART symposium on Principles of database systems. (2004), 286-296.

12. Hautamaki, V., Nykanen, P. and Franti, P., "Time-series clustering by approximate prototypes", in 2008 19th International conference on pattern recognition, IEEE. (2008), 1-4.
13. Lian, X., Chen, L.J.I.T.o.K. and Engineering, D., "Efficient similarity search over future stream time series", Vol. 20, No. 1, (2007), 40-54, doi: 10.1109/TKDE.2007.190666.
14. Parthasarathy, D., Shah, D. and Zaman, T.J.a.p.a., "Leaders, followers, and community detection", (2010), arXiv preprint arXiv:1011.0774.
15. Davies, D.L., Bouldin, D.W.J.I.t.o.p.a. and intelligence, m., "A cluster separation measure", No. 2, (1979), 224-227, doi: 10.1109/T PAMI.1979.4766909.

Persian Abstract

چکیده

داده کاوی یکی از مفاهیم کلیدی برای کشف دانش پنهان از داده های موجود است. در کنار داده کاوی، تجزیه و تحلیل داده ها زمینه ای برای تجزیه و تحلیل و پردازش داده ها در یک زاویه علمی و شناختی است. تبدیل دانش به دانش عملی برای تصمیم گیری دقیق مفیدتر است. داده کاوی زنده به دلیل پویایی آن، یکی دیگر از حوزه های چالش برانگیز نسبت به داده کاوی معمولی است. دینامیک داده ها در یک جریان شامل تغییرات در فرکانس، حجم و ماهیت داده است. این مقاله بر رفتار داده کاوی ماشین‌ها در صنایع فرآیندی/تولیدی تمرکز دارد. به طور کلی، چنین داده‌هایی، داده‌های عددی و سری زمانی پیوسته هستند که توسط حسگرهای صنعتی مختلف گرفته می‌شوند. طبیعتاً، رفتار تجهیزات یا ماشین آلات می تواند در طول زمان تغییر کند. قبل از خرابی ماشین آلات نیاز به کالیبراسیون / تعویض دارد. با تجزیه و تحلیل داده ها، می توان رفتار یا تغییر حالت را پیدا کرد. برای شناسایی آن، مدل های پویا باید با استفاده از داده کاوی و جریان کاوی ساخته شوند. بنابراین، ما یک رویکرد نیمه جدید را برای ساخت چنین مدل‌هایی با استفاده از روش «مجموعه یادگیری افزایشی بدون نظارت» دنبال می‌کنیم. نتایج نشان می‌دهد که چگونه روش های موجود با روش پیشنهادی متفاوت است. این روش برای هر حوزه دیگری مانند تصویر/صوت /ویدئو یا متن کاوی. قابل استفاده است.

IJE TRANSACTIONS B: Applications Vol. 35, No. 02, (February 2022) 327-336

International Journal of Engineering

Journal Homepage: www.ije.ir

An Experimental Investigation on Durability Properties of Reactive Powder Concrete

A. A. Dhundasi*[a], R. B. Khadiranaikar[a], A. A. Momin[b], K. Motagi[a]

[a] *Department of Civil Engineering, Basaveshwar Engineering College, Bagalkot, Affiliated to VTU, Belagavi, Karnataka, India*
[b] *Department of Civil Engineering, BLDEA's Vachana Pitamaha Dr. P.G Halakatti College of Engineering and Technology Vijayapur, Affiliated to VTU, Belagavi, Karnataka, India*

PAPER INFO

Paper history:
Received 05 September 2021
Received in revised form 03 November 2021
Accepted 09 November 2021

Keywords:
Acid Immersion Test
Durability
Rapid Chloride Penetration Test
Reactive Powder Concrete
Salt Crystallization Test

ABSTRACT

The durability of concrete subjected to an aggressive environment is a major issue faced by constructional engineers. Many researchers have tried to evaluate the durability characteristics of concrete against aggressive fluids. Amongst the fluids, compounds of sulphuric acid and chloride ions caused massive deterioration in concrete. Reactive powder concrete (RPC) is a type of ultra-high-strength cement composite. In the present study, an effort is made to assess durability properties of RPC. The RPC with compressive strengths 110, 120 and 130 MPa have been produced. Acid immersion test, salt crystallization test and chloride ion penetration tests have been carried out to assess the degradation of concrete. Samples were exposed to sulphuric acid solutions over a period of 60 days with concentrations varying from 0.5-2%. The salt crystallization tests were carried out by immersing samples in 14% Na_2SO_4 solutions. Visual observations and deterioration in terms of mass and compressive strength reductions are recorded. The RPC showed high resistance towards the crystallization of salts. A significant amount of weight loss and strength loss was observed for the samples exposed to high concentrations of sulphuric acid. A negligible amount of chloride ion penetration was observed.

doi: *10.5829/ije.2022.35.02b.08*

1. INTRODUCTION

1. 1. General The mechanical and durability properties are the two main aspects that govern the performance of any concrete throughout its service life. The concrete is classified into 3 categories based on compressive strengths i.e., normal strength, high strength and ultra-high-strength concretes. Reactive powder concrete is a type of ultra-high-performance concrete with strengths varying from 100MPa to 800MPa. It is used in the construction of chemical industries, nuclear waste storage units, marine structures, sewage treatment units, drain canals, highways, piers and pathways of bridges.

The durability of concrete may be defined as the ability of a material to retain its physical, chemical and visual performance characteristics in the intended environment, within a reasonable tolerance for an economic life expectancy. Early age deterioration is observed in concrete subjected to an aggressive environment. The deterioration is caused by chemical attacks and acid rain precipitating in the form of dissolved acids. The degree of decay depends mainly upon the physical and chemical characteristics of concrete.

1. 2. Durability Studies on Concrete The concrete used in the construction of chemical industries and sewer lines is subjected to the acidic environment. A massive deterioration of concrete is observed due to the action of compounds of various acids such as sulphuric acid, nitric acid, hydrochloric acid etc. An investigation was carried out to study the durability properties of concrete [1]. The concrete was exposed to 0.1%, 1% and 5% concentrations of sulphuric acid. The factors for strength and weight reduction were provided depending on the depth of sulphuric acid penetration. Due to the high alkalinity of portland cement and chemical reactions

*Corresponding Author Email: abbasdhundasi@gmail.com (A. A. Dhundasi)

Please cite this article as: A. A. Dhundasi, R. B. Khadiranaikar, A. A. Momin, K. Motagi, An Experimental Investigation on Durability Properties of Reactive Powder Concrete, ***International Journal of Engineering, Transactions B: Applications***, Vol. 35, No. 02, (2022) 327-336

of such acids, corrosion is induced in the concrete, which leads to the deterioration of structure [2]. The effect of sulphuric acid attack on normal strength concrete (NSC) was studied by immersing cylindrical specimens in 1% sulphuric acid solutions. The degree of deterioration was expressed in terms of changes in weight and thickness of specimen. The measurement was obtained for 10, 20, 30 and 70 days immersion periods. The results indicated that the volumetric expansion in specimens was in the range of 5-10%. The weight loss was observed to be 15-20%. Silica fume and fly ash were added as supplementary cementitious materials in reinforced cement concrete (RCC) [3]. It was observed that, the addition of supplementary cementitious material as a replacement for aggregates and cement content reduced the carbonation depth. Significant resistance towards chloride ion content was also observed. The degradation due to chemically and microbiologically induced corrosion was studied on high sulphate resistant portland cement concrete and polymer modified concrete [4]. Addition of polymers increased expansion in concrete along with increased loss of material. Acid resistance of self-compacting concrete (SCC) was compared with conventional concrete for 1% of sulphuric and hydrochloric acid solutions [5]. The SCC has high resistance to sulphuric acid attack than compared to conventional concrete. A laboratory investigation on portland cement systems exposed to aggressive environments was carried out to predict the durability characteristics [6]. The results indicated that the type of cement and water-binder (w/b) ratio have significant effect on the extent of degradation. It was suggested to lower the w/b ratio to increase durability.

High volume fly ash concrete (HVFC) was produced by replacing cement with 10-70% of ACTM class C - fly ash [7]. The loss in weight, compressive strength and split tensile strength were obtained for 5% H_2SO_4 solutions over the period of 90 days. A higher rate of deterioration was observed for steam cured samples than compared to normal cured samples. The durability properties of geopolymer concrete (GPC) with compressive strengths 53MPa and 62MPa were studied to understand the effect of sulphuric acid attack [8]. The mass reduction was observed to be 40% after 4th week. The compressive strength loss was in the range of 32-37%. An air entrained metakaolin concrete with a lower w/b ratio and autoclave curing showed better durability properties towards sulphate attack [9]. The anaerobic bacteria present in sewer pipes produce hydrogen sulphide (H_2S) under low pH values. In the presence of oxygen and moisture, this dissolved H_2S is then oxidized to form sulphuric acid, which leads to corrosion in concrete [10]. ASTM class - F fly ash 20% by weight and silica fume 8% by weight of cement were added to produce ternary blended concrete [11]. M20, M30 and M40 grade concretes were produced and durability studies were carried out for 5% H_2SO_4 and 5% HCL solutions. A maximum of 30-40% mass loss was observed with the strength values reducing up to 60-70%. The performance of GPC under 10% H_2SO_4 and 10% $MgSO_4$ solutions was evaluated [12]. The results for 15-45 days exposure period, indicated that heat cured GPC samples show better durability characteristics than conventional concrete. Change in color from dark grey to lime grey with deposits of whitish compounds of burite on concrete exposed to seawater was observed [13]. The solutions of inorganic and organic chemicals were used to evaluate flexural behaviour of polyester polymer concrete [14]. After two months of exposure, an average loss of 35% in flexural strength was observed for inorganic acids. The durability of concrete was improved by addition of glass fibres. The fibres reduced the shrinkage cracks by 40% and hence permeability of chloride ions was observed to decrease [15]. An environmentally friendly green concrete (GC) was produced by replacing cement with 20% alccofine [16]. The pore structure was improved due to addition of alccofine which in turn decreased the water absorption. Investigations were carried out to evaluate durability performance of SCC [17 -19]. Different compositions of SCC were produced by incorporating fly ash, alccofine, nanoparticles of aluminum oxide, super absorbent polymers and glass fibres. The results showed that partial replacement of pozzolanic material increased the durability properties to a greater extent along with an improvement in mechanical properties.

1. 3. Reactive Powder Concrete Reactive powder concrete (RPC) is a type of ultra-high strength concrete, with a strength greater than 80MPa. It was first developed in France [20]. The optimum granular mixture was achieved by addition of superfine silica fume as a pozzolanic material and by eliminating coarse aggregates. Steel fibre, 1.5-3% by volume, were added to enhance the ductility. The application of heat and pressure during curing resulted in producing RPC with strengths 200-800MPa. The durability studies for RPC with strengths 200MPa was studied by performing various tests [21]. The durability properties were assigned by measuring porosity, water absorption, chloride ion penetration, carbonation and corrosion of reinforcement. The influence of coarse aggregates on mechanical properties of RPC was studied by replacing fine sand with natural, well graded coarse aggregates of maximum size 8mm [22]. The results indicated the compressive strength did not change due to partial replacement of fine quartz sand with coarse aggregates. When the fine quartz sand was fully replaced with the coarse aggregates, the homogeneity and effective bond strength between cement matrix and aggregates was reduced. As a result, the compressive strength and flexural strength was observed to decrease. The effect of water, steam and autoclave curing on production of RPC

with various proportions of steel fibre content was investigated [23]. The results concluded that ultra-high strength concrete (200-300MPa) can be produced with commonly available materials and traditional curing methods. The durability properties of steel fibre reinforced RPC with strength 180MPa were studied by performing the acid tests, accelerated corrosion tests and rapid chloride penetration tests [24]. The mass was reduced by 20% and strength was reduced by 60% for 60days exposure period. The mechanical properties, stress-strain under uniaxial compression and flexural loads, along with frost resisting durability properties were investigated for RPC used for construction of highway bridge [25]. An extensive investigation on the production of RPC was carried to study the effect of mixing method, mixing duration and speed, dosage of polypropylene fibres, and effect of different curing regimes [26-30]. The effect of the dosage of superplasticizer and quartz powder on mechanical properties was studied [31]. An optimum of 15% of quartz powder with cement content 900 kg/m^3 and 1000kg/m^3 resulted in RPC with strengths 160MPa and 170MPa, respectively. A study was carried out to understand the effect of different curing temperatures on properties of RPC. An optimum temperature of 90ºC was obtained and RPC with compressive strength 111.43MPa was produced [32].

1. 4. Research Significance In recent years, the applications of reactive powder concrete are increasing in the construction of bridges, harbours, seashore structures, nuclear powerplants, etc. These structures are subjected to severe environmental changes which affect the durability properties of materials used for construction. Many investigations have been carried out to study the durability properties by considering the effect of various acids. A vast amount of literature is available for normal strength, high strength, self-compacting, geopolymer, green concrete etc. However, there are limited researches on durability studies of RPC. The present research focuses on producing an ultra-high strength reactive powder concrete with compressive strength 110MPa, 120MPa and 130MPa. The durability studies are carried out by performing acid tests for various concentrations of sulphuric acid, salt crystallization tests and rapid chloride ion penetration tests. The results obtained will help the constructional engineers to predict and assess the degree of deterioration based on visual and physical inspection.

2. EXPERIMENTAL PROGRAM

Three grades of reactive powder concrete mixtures are produced with locally available materials. The constituents for mix proportions are 53grade ordinary portland cement (OPC), river sand, quartz powder (QP) and water. Silica fume (SF) is added as a pozzolanic material. To get a workable mix, superplasticizer (SP) Glanium-8233 is used. The mix proportions have compressive strengths in the range of 110MPa (M1), 120MPa (M2) and 130MPa (M3). The details of mix proportions have been provided in Table 1. The durability aspects are studied by conducting various laboratory tests. The tests conducted are:

- Acid immersion tests
- Salt crystallization tests and
- Rapid Chloride Penetration Test (RCPT).

2. 1. Acid Immersion Test For immersion of RPC samples, special acid resistant trays of size 750mm×650mm×50mm were used. The arrangement of specimens is shown in Figure 1. Separate specimens are used for the different observation periods which varies from 3, 7, 28 and 60 days. For each concentration of sulphuric acid, there were four trays which includes three grades of concrete. After every observation period, the samples were removed from the respective solutions and thoroughly washed with pure water, oven-dried at 60°C and then cooled for taking further observations to measure the degradation. Due to the decay of samples and change in environmental conditions, the concentration of the solution may vary; therefore, care is to be taken to maintain the pH value constant throughout the period of exposure with the pH meter.

After removal, weight loss due to the acid effect was evaluated, hence the extent or rate of deterioration is

TABLE 1. Design Mix Proportions for RPC with cement content 900 kg/m^3

Mix	Sand	W/B	SF		QP	SP	
	Kg/m^3	ratio	Kg/m^3	%	Kg/m^3	Kg/m^3	%
M1	954.68	0.21	45	5	90	13.5	1.5
M2	910.26	0.20	90	10	90	18	2.0
M3	875.87	0.19	135	15	90	22.5	2.5

Figure 1. Specimens immersed in H_2SO_4 solution

known. The compressive strength after decay was obtained and compared with initial strength. The percentage of reduction in strength is calculated. The percentage of losses in strength and weight were calculated from equations 1 and 2.

Reduction in compressive strength (%) =

$$\frac{f'_{c\text{-}28} - f'_{c\text{-}AD}}{f'_{c\text{-}28}} \times 100 \quad (1)$$

where, $f'_{c\text{-}28}$, $f'_{c\text{-}AD}$ are compressive strengths at 28 days and after decay respectively. Percentage mass loss is calculated as follows:

$$\frac{\text{Initial Mass } M_1 - \text{Mass after decay } M_2}{\text{Initial Mass } M_1} \times 100 \quad (2)$$

2. 2. Salt Crystallization Test The test was conducted on untreated reactive powder concrete specimens. The samples were cleaned and oven dried, which were then immersed in 14 % Na_2SO_4 solution for 18 hours at room temperature as shown in Figure 2. After the required immersion period, samples were removed and allowed to drain for half an hour. Later they were dried in oven for 4 hours at a temperature of 105 ± 5° C and then cooled for one hour at room temperature. That forms one cycle of 24 hours and the same was repeated for the required number of cycles.

For the evaluation of the progressive change in the physical and durability characteristics a sample of three specimens were taken out at every five cycles. All such specimens withdrawn were thoroughly washed to remove the salt deposited and then cooled and weighed. Weight losses and compressive strength values were calculated.

2. 3. Rapid Chloride Penetration Test The specimens of required thickness were obtained by slicing cylinders of size 100 mm diameter and 200 mm length. A water-cooled diamond saw cutter was used to cut the samples. The diameter of each specimen is 100mm with a thickness of 50mm. These samples were subjected to 60V DC voltage across their thickness. It was applied between two cells containing sodium chloride (3% NaCl) and sodium hydroxide (0.3M NaOH) solutions. Tests were carried out for a duration of 6 hours. To avoid any leakage of solution from the cell, the surface was cut at a right angle to the length of cylinder and was perfectly plane. The laboratory setup is shown in Figure 3. RCPT setup consists of mainly three functional units; which are specimen conditioning unit, sample holding cell and measuring unit. The microprocessor based electronic unit provides a constant 60 ± 0.1 V DC voltage across the two circular surfaces of the test specimen. The measurement of total electrical charge in terms of Coulombs is also done by the same unit. It also displays the set time, test time duration and remaining time for completion of the test. The total charges passed through the specimen are obtained after 360minutes.

3. RESULTS AND DISCUSSION

3. 1. Acid Test Results The 28 days cured samples of RPC were immersed in dilute sulphuric acid solutions of different concentrations, thereby creating the actual media which happens in the environment. The concentration of solution is varied in the range of 0.5, 1, 1.5 and 2%. The samples were removed at various periods of exposure and tested. The compressive strength, weight loss and strength variation with exposure intervals of 3, 7, 28 and 60 days, were obtained

3. 1. 1. Visual Observations For visual observations, the shape of specimens is taken into account. It was observed that samples immersed in different concentrations exhibit different types of decay. After 3 days of exposure period, there was no change in shape, also the samples exhibit a significant resistance to any scaling and spalling of concrete (Figure 4).

At 7 days of exposure, a negligible amount of surface erosion in the form of white deposits is seen to occur at 0.5 and 1% solutions. It is shown in Figure 5. At 1.5 and 2% concentration discolouration of specimens takes place from grey to white. For samples immersed in 1.0, 1.5 and 2% solutions we can see scaling or peeling of concrete where top surface layer of samples get eroded which goes on increasing with the increase in concentration. Some specimens show reddish-brown colour on the top surface with damage to edges. The

Figure 2. Specimens immersed in Na_2SO_4 solution

Figure 3. Rapid Chloride ion Penetration Test

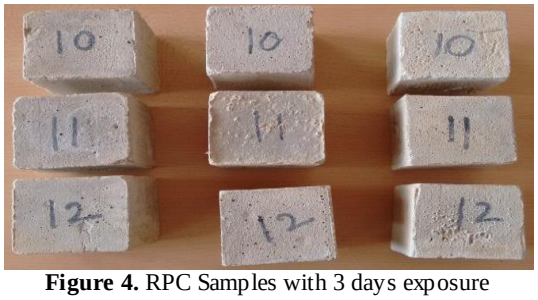

Figure 4. RPC Samples with 3 days exposure

Figure 5. RPC Samples with 7 days exposure

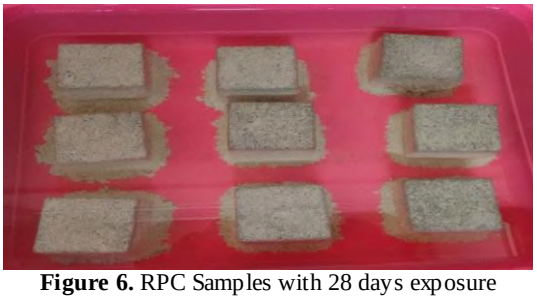

Figure 6. RPC Samples with 28 days exposure

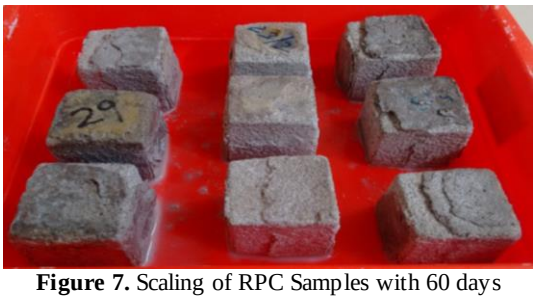

Figure 7. Scaling of RPC Samples with 60 days

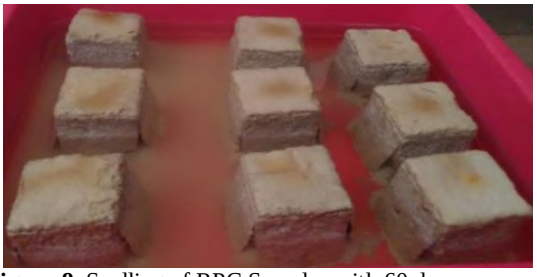

Figure 8. Spalling of RPC Samples with 60 days exposure

scaling indirectly leads to change in shape, thereby reducing strength carrying capacity.

The samples for normals strength concrete (NSC) immersed in 1% H_2SO_4 solution over the period of 28 days show disintegration and peeling of the surface layer [5]. The appearance of white pulpy mass over external surface was seen. For SCC samples, expansion and peeling is observed. After 28 days of exposure period, the RPC specimens get degraded severely than 7 days. The samples exposed to 0.5% solutions show scaling of concrete from all four sides with peeling of edges. The samples also exhibit discolouration from grey to light greenish but no spalling of concrete is observed. The spalling of concrete is seen in 1.0, 1.5 and 2% solutions in 28 days and specimens are eroded from all four sides by forming white deposits surrounding the cubes as shown in Figure 6.

Samples placed in for 60 shows that even at 0.5% solution of acid there is a considerable scaling of concrete which is absent in 7 and 28-days immersed specimens. From the clean observations, we can judge that scaling in the samples of M1 is predominant when compared to M2 and M3, shown in Figure 7.

In the remaining solutions, samples have lost a significant amount of material from surface, edges and original shape is completely disrupted. Spalling is predominant with discolouration of reddish-brown on the top surface. It is shown in Figure 8.

3. 1. 2. Physical Observation For 1% H_2SO_4 solution and 28 days exposure period the weight loss observed for NSC is 11% [1], SCC is 5% [5], HVFC is 5% [7] and GPC is 3% [13]. It is observed that the rate of weight loss decreases with an increase in grade of reactive powder concrete. The maximum weight loss at 28 days was observed to be less than 1% for all the grades of RPC considered. But a progressive increment is obtained in weight loss with an increase in exposure time and concentration of solutions. The samples for M1 show significant weight loss compared to M2 and M3. The maximum amount of weight loss obtained are, M1-13.98%, M2- 10.09% and M3-8.38%, respectively, at 60 days exposure and 2% solutions. The weight loss obtained, for considered exposure time and different percentages of solution, are shown in Figures 9, 10 and 11 for M1, M2 and M3, respectively.

3. 1. 3. Compressive Strength From the experiments conducted with different conditions, it is observed that samples lose their visual and physical properties for longer duration of exposure and higher concentrations of solutions, which in turn reduce the compressive strengths of RPC. For 1% H_2SO_4 solution and 28 days exposure period the strength loss observed

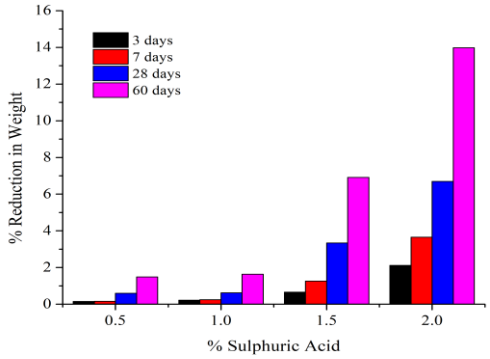

Figure 9. Variation of reduced weight for M1

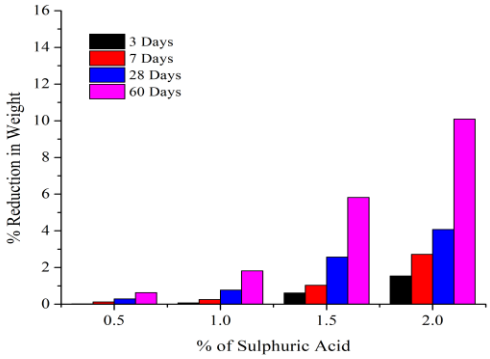

Figure 10. Variation of reduced weight for M2

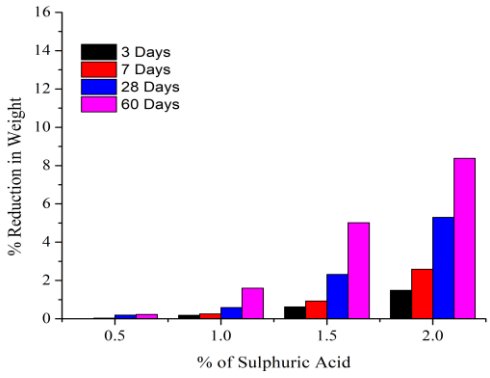

Figure 11. Variation of reduced weight for M3

for NSC is 70% [1], SCC is 62% [5], HVFC is 58.5% [7] and GPC is 40% [13]. All the specimens of RPC show that there is a significant reduction in compressive strength. For samples immersed for 3days show small amount of strength reduction i.e. in the range of 9-14%, whereas 7 days and 28 days samples show a considerable amount of strength reduction. It is in the range of 25-35%. This shows that RPC has better resistance to sulphuric acid attack compared to other types of concrete. The maximum amount of strength loss is observed at 60 days samples in the range of 45-70%. The reduction of compressive strengths are shown in Figures 12-14.

3. 2. Salt Crystallization Test (SCT)

3. 2. 1. Visual Observations Sodium sulphate crystallization is initiated for samples kept in Na_2SO_4 solution for 5days cycle. It shows a progressive

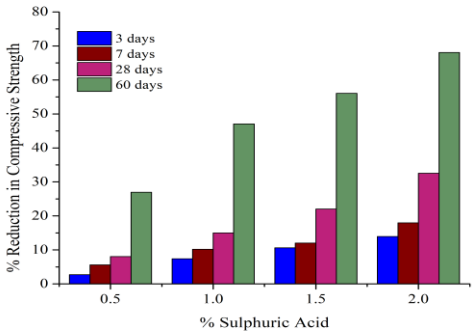

Figure 12. Variation of Compressive strength for M1

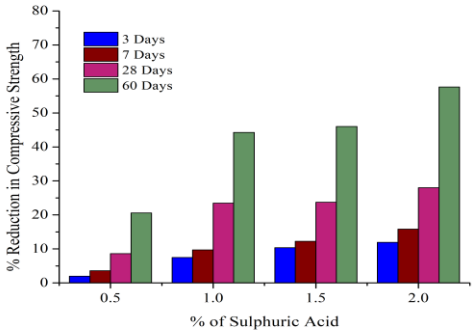

Figure 13. Variation of Compressive strength for M2

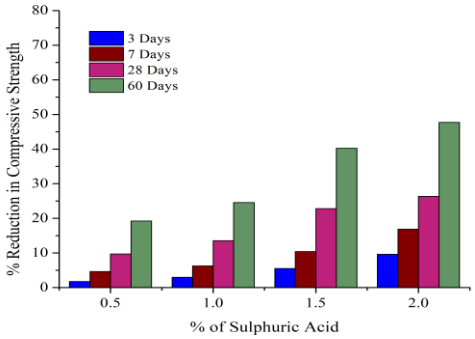

Figure 14. Variation of Compressive strength for M3

development till 20 days cycle, as shown in Figures 15-18. There is not much change in shape or structure of specimens. However, at 20 -30 days cycles a clear salt layer of greenish white color is formed on all edges and surfaces of the specimens. These are shown in Figures 19 and 20. Surface erosion and change in shapes have been observed. The effective surface area is reduced. Cracks are initiated at edges of surface and continue to propagate throughout the body of the samples. From 35 days samples, it is observed that the samples have grown a significant amount of salt crystalline layer. Due to the cracks initiated in early cycles. the samples show a significant amount of scaling over the surface. The edges are distorted and discoloration of samples was observed. The effects are shown in Figure 21.

3. 2. 2. Physical Observations The results of durability tests show that the rate of decay is not uniform. It is slow up to 20 cycles and increases rapidly after 20 cycles. At five days of durability cycles, the initial reduction in weight is 0.06-0.08%, where very slight appearance of salt crystalline layer is observed. At 15 days cycle weight loss observed is 0.16-0.19% which is 60% greater than five days cycle. Similarly, the percentage of weight loss at 20 days cycle obtained is 0.25-0.30%, which is almost 75 % greater than five-day cycle. From Figure 22, it is clear that the samples exhibit similar behaviour of weight reduction till 25days cycle and after that, the curve shows a steep increase. The maximum weight reduction for M1, M2 and M3 are 1.52%, 1.29% and 1.11%, respectively. The reduction in weight decreases as the grade of concrete is increased.

3. 2. 3. Compressive Strength At the initial stages of cycles, the reduction in compressive strength shows a linear behavior as shown in Figure 23. At 15 days cycle, a clear salt layer appeares with increased intensity of salt at all sides of the sample with a 10% decrease in strength for all the grades of concrete. The strength reduction is up to 13-16 MPa at 20 days samples. The decrease in magnitudes of water absorption and weight takes place progressively. At the end of 35 cycles the strengths are reduced up to 28-34 MPa, which is nearly one fourth of the original strength with huge amount of formation of crystalline salt layer as shown in Figure 21. The variation of strength with durability cycle is shown in Table 2.

Figure 15. 5 days cycle specimens

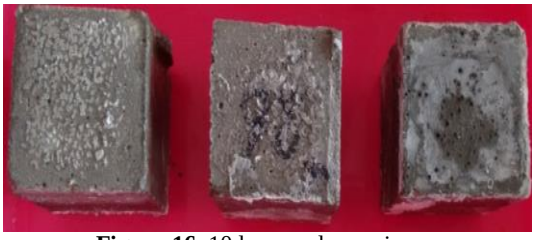

Figure 16. 10days cycle specimens

Figure 17. 15 days cycle specimens

Figure 18. 20 days cycle specimens

Figure 19. 25 days cycle specimens

Figure 20. 30 days cycle specimens

Figure 21. 35 days cycle specimens

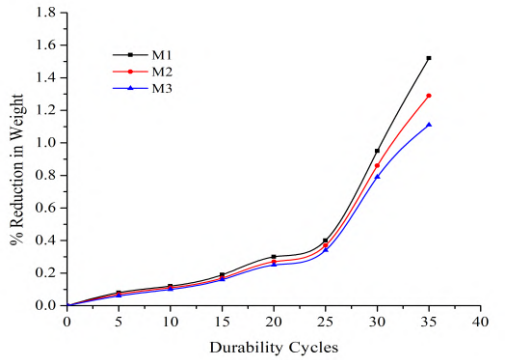

Figure 22. Reduction in Weigh from SCT

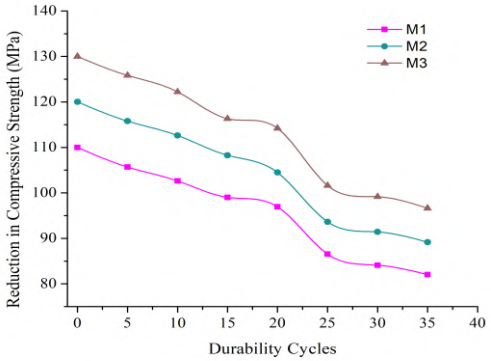

Figure 23. Variation of Compressive strength from SCT

TABLE 2. Variation of Weight loss and Compressive strength with durability cycles

Cycles	Weight reduction (%)			Compressive strength (MPa)		
	M1	M2	M3	M1	M2	M3
0	0.00	0.00	0	110.00	120.00	130.00
5	0.08	0.07	0.06	105.69	115.79	125.83
10	0.12	0.11	0.10	102.63	112.62	122.21
15	0.19	0.17	0.16	99.03	108.27	116.32
20	0.30	0.27	0.25	96.94	104.49	114.2
25	0.40	0.37	0.34	86.56	93.64	101.62
30	0.95	0.86	0.79	84.11	91.42	99.17
35	1.52	1.29	1.11	82.03	89.15	96.62

3. 3. Rapid Chloride Ion Penetration Test (RCPT)

For this experiment, 3 samples were cast for each grade of concrete. The M1 is cast with a 0.21, M2 with 2.0 and M3 with 0.19 water cement ratio, respectively. This test is carried out to know the effect of water-cement ratio on chloride permeation. The average passed charges (in coulombs) through all the mixes is noted and presented in Table 3.

TABLE 3. RCPT test results for 3 grades of RPC

Samples	W/C ratio	Charges passed	Average passed charges	Chloride ion permeability
M1 (110MPa)	0.21	141 147 143	144	Very Low
M2 (120MPa)	2.0	115 109 111	112	Very Low
M3 (130MPa)	0.19	83 79 85	82	Negligible

From the results, it is clear that the RPC samples with higher water-cement ratios show higher charges passed when compared low water-cement ratio. The RPC with grade 130 MPa (M3) exhibits negligible chloride ion penetration showing homogeneous and dense microstructure. RPC with grades 120MPa (M2) and 110MPa (M1) shows very low chloride ion penetration.

4. CONCLUSIONS

Based on the experimental investigation on RPC specimens for durability studies, the following conclusions are drawn.

The durability aspects have been assigned by carrying out visual observations and reduction in weight and compressive strengths of RPC samples.

1. The acid immersion tests with different concentrations of H_2SO_4 and Na_2SO_4 solutions have resulted in the determination of decay caused by acid attacks and crystallization of salts.
2. The lower concentration of sulphuric acid (0.5%,1.0 %) have less effect on the durability of RPC. Whereas higher concentration (1.5%, 2%) leads to discoloration, erosion, scaling, appreciable degradation in weight and significant reduction in strength of concrete.
3. At Higher concentration of acid, the RPC specimens show that the compressive strengths are reduced up to 75% of their original strengths.
4. RPC samples exhibit resistance towards salt crystallization up to 20 days cycles. However, at 35 days cycles, disruption of surfaces and edges is observed leading to a huge amount of weight loss and reduction in compressive strengths up to 30MPa.
5. The RCPT indicated negligible to very low charges passing through all the samples. It signifies the high resistance of RPC towards the effects of chloride ion penetration.

7. REFERENCES

1. Raju, P. S. N., and P. Dayaratnam. "Durability of Concrete Exposed to Dilute Sulphuric Acid." ***Building and Environment***, vol. 19, No. 2, (1984), 75-79, doi:10.1016/0360-1323(84)90032-5.
2. Attiogbe, Emmanuel K., and Sami H. Rizkalla. "Response of Concrete to Sulfuric Acid Attack." ***ACI Materials Journal***, Vol. 85, No. 6, (1988), 481-488, doi:10.14359/2210.
3. Papadakis, Vagelis G. "Effect of Supplementary Cementing Materials on Concrete Resistance against Carbonation and Chloride Ingress." ***Cement and Concrete Research***, Vol. 30, No. 2, (2000), 291-299, doi:10.1016/S0008-8846(99)00249-5.
4. Monteny, J., Belie N. De, Vinckeb E., Verstraeteb W., Taerwe L., "Chemical and Microbiological Tests to Simulate Sulfuric Acid Corrosion of Polymer-Modified Concrete." ***Cement and Concrete Research***, Vol. 31, No. 9, (2001), 1359-1365, doi:10.1016/S0008-8846(01)00565-8.
5. Al-Tamimi, A. K., and M. Sonebi. "Assessment of Self-Compacting Concrete Immersed in Acidic Solutions." ***Journal of Materials in Civil Engineering***, Vol. 15, No. 4, (2003), 354-357, doi:10.1061/(asce)0899-1561(2003)15:4(354).
6. Maltais, Y., Samson E., Marchand J., "Predicting the Durability of Portland Cement Systems in Aggressive Environments - Laboratory Validation." ***Cement and Concrete Research***, Vol. 34, No. 9, (2004), 1579-1589, doi: 10.1016/j.cemconres.2004.03.029.
7. Aydin, Serdar, Yazici Halit, Yigiter Huseyin, Baradan Bulent "Sulfuric Acid Resistance of High-Volume Fly Ash Concrete." ***Building and Environment***, Vol. 42, No. 2, (2007), 717-721, doi: 10.1016/j.buildenv.2005.10.024.
8. Song X. J., Marosszeky M., Brungs M., Munn R., "Durability of fly ash based Geopolymer concrete against sulphuric acid attack", International Conference on Durability of Building Materials and Components, LYON [France], (2005),17-24.
9. Al-Akhras., Nabil M. "Durability of Metakaolin Concrete to Sulfate Attack." ***Cement and Concrete Research***, Vol. 36, No. 9, (2006), 1727-1734, doi: 10.1016/j.cemconres.2006.03.026.
10. Okabe Satoshi, Odagiri Mitsunori, Ito Tsukasa, and Satoh Hisashi, "Succession of Sulfur-Oxidizing Bacteria in the Microbial Communityon Corroding Concrete in Sewer Systems", ***Applied and Environmental Microbiology***, Vol. 73, No. 3, (2007), 971-980, doi:10.1128/AEM.02054-06
11. Murthi, P., and V. Sivakumar. "Studies on Acid Resistance of Ternary Blended Concrete." ***Asian Journal of Civil Engineering (Building and Housing)***, Vol. 9, No. 5, (2008), 473-486.
12. Sanni, S. H., and R. B. Khadiranaikar. "Performance of Geopolymer Concrete under Severe Environmental Conditions." ***International Journal of Civil and Structural Engineering***, Vol. 3, No. 2, (2012), 396-407, doi:10.6088/ijcser.201203013037.
13. Islam, S., Islam M., Mondal Chandra B., "Deterioration of Concrete in Ambient Marine Environment." ***International Journal of Engineering***, ***Transactions B: Applications***, Vol. 25, No. 4, (2012), 289-301, doi: 10.5829/idosi.ije.2012.25.04b.05.
14. Hashemi, M. J., and M. Jamshidi. "Flexural Behavior of Polyester Polymer Concrete Subjected to Different Chemicals." ***International Journal of Engineering***, Vol. 28, No. 7, (2015), 978-983, doi: 10.5829/idosi.ije.2015.28.07a.03.
15. Rath, B., Deo S., Ramtekkar G. "Durable Glass Fiber Reinforced Concrete with Supplementary Cementitious Materials." ***International Journal of Engineering***, ***Transactions A: Basics***, Vol. 30, No. 7, (2017), 964-971, doi:10.5829/ije.2017.30.07a.05.
16. Reddy, P. Narasimha, and J. Ahmed Naqash. "Effect of Alccofine on Mechanical and Durability Index Properties of Green Concrete", ***International Journal of Engineering***, ***Transactions C: Aspects***, Vol. 32 No. 6, (2019), 813-819. doi: 10.5829/ije.2019.32.06c.03
17. Kavyateja B. V., Jawahar J. G., Sashidhar C., "Durability Performance of Self Compacting Concrete Incorporating Alccofine and Fly Ash", ***International Journal of Engineering***, ***Transactions B: Applications*** Vol. 33, No. 8, (2020), 1522-1528, doi: 10.5829/ije.2020.33.08b.10
18. Delaram F., Mohammadi Y., Adlparvar M. R., "Evaluation of Combined Use of Waste Paper Sludge Ash and Nanomaterials on Mechanical Properties and Durability of High Strength Concretes", ***International Journal of Engineering***, ***Transactions A: Basics*** Vol. 34, No. 7, (2021), 1653-1666, doi: 10.5829/ije.2021.34.07a.10
19. Moghaddam H. Heidarzad, Lotfollahi-Yaghin M. A., Maleki A., "Durability and Mechanical Properties of Self-compacting Concretes with Combined Use of Aluminium Oxide Nanoparticles and Glass Fiber", ***International Journal of Engineering***, ***Transactions A: Basics*** Vol. 34, No. 1, (2021), 26-38, doi: 10.5829/ije.2021.34.01a.04
20. Richard, Pierre, and Marcel Cheyrezy. "Composition of Reactive Powder Concretes." ***Cement and Concrete Research***, Vol. 25, No. 7, (1995), 1501-1511, doi:10.1016/0008-8846(95)00144-2.
21. Roux, N., Andrade,z and M. A. Sanjuan "Experimental Study Of Durability of Reactive Powder Concretes", ***Journal of Materials in Civil Engineering***, Vol. 8, No. 3, (1996), 1-6. https://doi.org/10.1061/(ASCE)0899-1561(1996)8:1(1)
22. Collepardi S., Coppola L., Troli R., M. Collepardi, "Mechanical properties of modified reactive powder concrete", Spec. Publ. 173 (1997), 1-22.
23. Zdeb, T., and J. Śliwiński. "The Influence of Selected Material and Technological Factors on Mechanical Properties and Microstructure of Reactive Powder Concrete (RPC)." ***Archives of Civil Engineering***, Vol. 57, No. 2, (2011), 227-246, doi:10.2478/v.10169-011-0017-1.
24. Muranal Santosh M and Khadiranaikar R B, "Study on The Durability Characteristics of Reactive Powder Concrete", ***International Journal of Structural and Civil Engineering Research (IJSCER)***, Vol. 3, No. 2, (2014), 45-56.
25. Song, Junwei, and Shuhua Liu. "Properties of Reactive Powder Concrete and Its Application in Highway Bridge." ***Advances in Materials Science and Engineering***, Vol. 2016, (2016), doi:10.1155/2016/5460241.
26. Hiremath, Parameshwar N., and Subhash C. Yaragal. "Influence of Mixing Method, Speed and Duration on the Fresh and Hardened Properties of Reactive Powder Concrete." ***Construction and Building Materials***, Vol. 141, (2017), 271-288, doi: 10.1016/j.conbuildmat.2017.03.009.
27. Hiremath, Parameshwar, and Subhash C. Yaragal. "Investigation on Mechanical Properties of Reactive Powder Concrete under Different Curing Regimes." ***Materials Today: Proceedings***, Vol. 4, No. 9, (2017), 9758-9762, doi: 10.1016/j.matpr.2017.06.262.
28. Hiremath, Parameshwar N., and Subhash C. Yaragal., "Effect of different curing regimes and durations on early strength development of reactive powder concrete", ***Construction and Building Materials***, vol 154, (2017), 72-87,
29. Abdulrahman, Mazin, et al. "Effect of Different Curing Conditions on the Mechanical Properties of Reactive Powder Concrete." MATEC Web of Conferences, Vol. 162, (2018), doi:10.1051/matecconf/201816202014.
30. Hiremath, Parameshwar N., and Subhash C. Yaragal. "Performance Evaluation of Reactive Powder Concrete with Polypropylene Fibers at Elevated Temperatures." ***Construction and Building Materials***, Vol. 169, (2018), 499-512, doi: 10.1016/j.conbuildmat.2018.03.020.

31. Dhundasi, Abbas Ali, and Khadiranaikar R. B., "Effect of Curing Conditions on Mechanical Properties of Reactive Powder Concrete with Different Dosage of Quartz Powder", ***Sustainable Construction and Building Materials***, Springer Singapore, (2019), 359-368, doi: 10.1007/978-981-13-3317-0_33.

32. Saloma, Hanafiah, Agistin Veriza, "Mechanical Properties Analysis of Reactive Powder Concrete with Curing Temperature Variation." IOP Conference Series: Materials Science and Engineering, Vol. 620, No. 1, (2019), doi:10.1088/1757-899X/620/1/012045.

Persian Abstract

چکیده

دوام بتن در معرض یک محیط تهاجمی یکی از مسائل مهمی است که مهندسان ساختمان با آن مواجه هستند. بسیاری از محققین سعی در ارزیابی ویژگی های دوام بتن در برابر سیالات مهاجم داشته اند. در بین سیالات، ترکیبات اسید سولفوریک و یون های کلرید باعث تخریب شدید بتن می شود. بتن پودری راکتیو (RPC) نوعی کامپوزیت سیمانی با مقاومت فوق العاده بالا است. در مطالعه حاضر، تلاشی برای ارزیابی خواص دوام RPC انجام شده است. RPC با مقاومت فشاری ۱۱۰ مگاپاسکال، ۱۲۰ مگا پاسکال و ۱۳۰ مگا پاسکال تولید شده است. آزمایش غوطه وری در اسید، آزمایش کریستالیزاسیون نمک و آزمایش های نفوذ یون کلرید برای ارزیابی تخریب بتن انجام شده است. نمونه ها در یک دوره ۶۰ روزه در معرض محلول های اسید سولفوریک با غلظت های متفاوت از ۰,۵٪ تا ۲٪ قرار گرفتند. آزمایش کریستالیزاسیون نمک با غوطه ور کردن نمونه ها در محلول های Na_2SO_4 14 درصد انجام شد. مشاهدات بصری و کاهش وزن و کاهش مقاومت فشاری ثبت شده است. RPC مقاومت بالایی در برابر تبلور نمک ها نشان داد. مقدار قابل توجهی کاهش وزن و کاهش قدرت برای نمونه های در معرض غلظت های بالای اسید سولفوریک مشاهده شد. مقدار ناچیزی از نفوذ یون کلرید مشاهده شد.

International Journal of Engineering

Journal Homepage: www.ije.ir

Performance of Prefabricated Foam Concrete as Infilled Wall Under Cyclic Lateral Loading

M. Mansyur*, M. W. Tjaronge, R. Irmawaty, A. Arwin Amiruddin

Civil Engineering Department, Hasanuddin University, Makassar, South Sulawesi, Indonesia

P A P E R I N F O

Paper history:
Received 25 July 2021
Received in revised form 11 November 2021
Accepted 17 November 2021

Keywords:
Cyclic Lateral Loading
Infill Wall
Performance Levels
Prefabricated Foam Concrete

A B S T R A C T

Every year earthquakes occur in various regions in Indonesia because Indonesia is located near earthquake faults. The cyclic lateral loading test in the laboratory has been widely used to simulate lateral loads caused by earthquake events. This research is an experimental study on the behavior of prefabricated foam concrete as an infill wall against lateral cyclic loads. Prefabricated foam concrete was used in this study to make it an alternative to brick and autoclaved lightweight concrete (ALC) blocks that have been widely used as infill walls. This study analyzes the relationship between performance levels, lateral loads and drifts ratio on RC infilled prefabricated foam concrete. Lateral cyclic loading with displacement control method was applied to evaluate the structural behavior where the test refers to ASTM E2126-02a. This study adopts FEMA 273, which regulates the performance levels to be achieved by the structure of a building. The results showed that at performance levels Operational Level (OL), Immediate Occupancy (IO) and Life Safety (LS), the RC frame infilled with prefabricated foam concrete blocks had a drift ratio of 0.2%, 1.2% and 2.4%, respectively. Damage to the RC frame infilled with prefabricated foam concrete blocks was similar to the masonry infilled RC frame.

doi: *10.5829/ije.2022.35.02b.09*

NOMENCLATURE

ALC	Autoclaved Lighweight Concrete	LS	Life Safety
RC	Reinforce Concrete	CP	Collapse Prevention
FEMA	Federal Emergency Management Agency	MPa	Mega Pascal
ASTM	American Standard Testing and Material	LVDT	Linear Variable Displacement Transducer
OL	Operational Level	Δm	Ultimate Displacement
IO	Immediate Occupancy	N	Newton

1. INTRODUCTION

In Indonesia, non-engineered buildings can generally be found in two forms. The first form is a traditional building built based on local customs and wisdom passed down from generation to generation. The second non-engineered building is a masonry building found in the form of one to two-story residential houses or three or four-story buildings used for residential and commercial purposes. RC frame infilled with masonry is widely used as main element to build the residential house. However, it is widely known that sometimes the RC frame of a residential house is built using inappropriate design standards and insufficient work specification details. Concerning the material for exterior walls and interior walls of residential houses, until now the most commonly used material is burnt clay brick, some use bataco (block made from a mixture of coarse sand and cement). In recent years autoclaved concrete (ALC) blocks have been widely used as walls [1, 2].

In recent decades many researchers and construction experts have focused on the efficient cross-section of structural elements such as beams, columns and foundations. In this regard, the manufacture of walls

*Corresponding Author Email: mansyurusn14@gmail.com (M. Mansyur)

Please cite this article as: M. Mansyur, M. W. Tjaronge, R. Irmawaty, A. Arwin Amiruddin, Performance of Prefabricated Foam Concrete as Infilled Wall Under Cyclic Lateral Loading, ***International Journal of Engineering, Transactions B: Applications***, Vol. 35, No. 02, (2022) 337-343

based on lightweight materials is carried out to reduce the dead load carried by structural elements in the form of beams, columns, and foundations.

Foamed concrete is a type of lightweight concrete that in fresh condition takes the form of slurry principally made of cement paste or mortar with about 20% of its volume as foam bubbles. Hardened foamed concrete has a density (weight per unit volume) and compressive strength of about 400-1800 kg/m^3 and 1-20 MPa, respectively [3–6].

Foamed concrete is a concrete made by portland composite cement and natural sand mixture provided that it cannot exceed the volume weight maximum of concrete 1850 kg/m^3 [7]. Lightweight concrete can be further divided into three groups based on the level of density and strength of the concrete produced and based on the type of lightweight aggregate used [8–10].

a. Insulating concrete : Lightweight concrete with a weight (density) between 300 - 800 kg/m^3 and compressive strength ranges from 0.69 to 6.89 MPa, which is usually used as heat-resisting concrete (heat insulation) is also called Low Density Concrete.
b. Moderate strength concrete : Lightweight concrete with a weight between 800 - 1440 kg /m^3, which is usually used as lightweight structural concrete or as fill concrete.
c. Structural concrete : Lightweight concrete with a weight (density) between 1440 - 1850 kg/m^3 which can be used as structural concrete if it is mechanical (compressive strength) can meet the requirements at the age of 28 days having compressive strength ranges from > 17.24 MPa.

Hardened lightweight foamed concrete provides favorable solutions to decrease the self-weight of building, where as the inner voids with less than 5 mm in size and interconnected to form networks make it suitable for use as thermal insulation, sound absorbance, and fire-resistant hence can be appropriately implemented as infill walls. RC frames filled with prefabricated lightweight foamed concrete blocks as non-structural infill wall have developed and become part of the construction of multi-story buildings and residential houses in many countries worldwide.

The use of foam concrete material in high-rise building structures and residential houses is part of sustainable innovation based on environmentally friendly materials. The use of foam concrete material as infilled wall can be reduced the borne load by structural elements so as to reduced the dimensions of beams, columns and foundations which have implications for reduced the use of concrete materials. Fuel consumption can be reduced by the used of prefabricated element structures with those made of foam concrete.

In pursuit of recent development of foam concrete technology and application, Eco Material and Concrete Laboratory, Civil Engineering Department, Hasanuddin University collaborated with a local real estate development company to develop prefabricated foam concrete blocks for the exterior walls and inner walls of residential houses. The main innovation of this development activity lies in the use of fly ash-based blended cement produced by a national company used as a cementitious material where together with local river sand and foam agent and water are mixed to make prefabricated foam concrete blocks. With the widespread availability of prefabricated foam concrete blocks on the market, people have additional wall materials other than the commonly known ones.

Most of Indonesia's areas are prone to earthquakes [11]. Post-earthquake study showed that many buildings were heavily damaged, including non-engineered buildings mostly dominated by residential houses [12]. Most recent earthquake events (Palu earthquake, 2018 and Majene-Mamuju earthquake, 2021) proved the seismic vulnerability of non-engineered buildings with RC frame infilled with masonry.

In harsh earthquake events, the ground motion shaking induces large lateral deformation and caused seismic damage to buildings, including residential houses. Currently, masonry as a wall was considered a non-structural element that does not carry the load and is still neglected in calculating the structure of a building. A number of post-earthquake technical reports indicate that masonry as a wall was mostly damaged. It is well known that the reversed cyclic loads behave seismic loads that arise during the earthquake event, hence, the artificial reversed cyclic load generated from lateral loading device was used to evaluate RC frame with masonry infill and without masonry infill specimens in the laboratory [13].

The primary purpose of the structural design of the building is to ensure safe life, maintenance function, and property safeguarding in the event of a disaster, including earthquake event during the service life. In Indonesia, concerning building damage caused by earthquakes, efforts to emphasize the necessity for building performance-based design have increased in recent years. As mentioned in many available technical investigation reports [14], the RC frame infilled with masonry is essential in building performance, including residential houses. Accordingly, this study aimed to examine the use of prefabricated foam concrete blocks on the performance of RC frame. Specifically, the damage that increases with an increase in amplitude of the applied lateral load is classified according to FEMA's reference level of performance. In the future, the performance level of RC infilled with prefabricated foam concrete resulted from this research can be used as a reference for performance based design of RC frame infilled with prefabricated foam concrete.

2. BUILDING PERFORMANCE LEVELS

The level of damage caused by an earthquake will be different for each building according to the capabilities of each constituent material or structural element of the building. FEMA 273 has set up the performance level for a building [15].

Table 1 summarized the damage control and building performance levels based on FEMA 273, whereas concrete structural performance levels and damage is reported in Table 2. This study adopted FEMA 273 to determine building performance levels. The performance level of interest can be described as Immediate Occupancy (IO), Damage Limitation (DL), Life Safety (LS) and Near Collapse (NC). Figure 1 shows the location of IO, DL and LS in the graph of the relationship between lateral load and deflection.

3. RESEARCH MATERIALS AND METHOD

3. 1. Materials Table 1 stated the properties of the RC frame. This study tested experimentally one infilled RC frame. In this research, concrete with compressive strength of f'c 22.60 MPa was used to produce the bottom beam, and 31.87 MPa concrete for the columns and the top beam of the RC frames. Coarse aggregates with a maximum diameter of 10 mm were used to make concrete for the columns and the bottom beam of RC frames because of their thinner shape.

A plain bar with a diameter of 8 mm was installed every 125 mm in the bottom beam as transverse reinforcement. A plain bar with a diameter of 10 was used as longitudinal reinforcement. In both columns, plain bar with a diameter of 8 mm was used which is installed every 125 mm to function as a transverse reinforcement.

TABLE 1. Damage control and building performance levels [15]

Target building performance levels	Overal Damage	General	Non-structural components
OL (Operational Level)	Very light	No permanent drift. Structure substantially retains original strength and stiffness. Minor cracking of facades, partitions, and ceilings as well as structural elements. All systems essential to normal operation are functional.	Negligible damage occurs. Power and other utilities are available, possibly from standby sources.
IO (Immediate Occupancy)	Light	No permanent drift. Structure substantially retains original strength and stiffness. Minor cracking of facades, partitions and cellings as well as structural elemements. Elevators can be restarted. Fire protection operable.	Equipment and contents are generally secure, but many not operate due to mechanical failure or lack of utilities.
LS (Life Safety)	Moderate	Some residual strength and stiffness left in all stories. Gravity-load-bearing elements function. No out-of-plane failure of walls or tipping of parapets. Some permanent drift. Damage to partitions. Building may be beyond economical repair.	Falling hazards mitigated but many architectural, mechanical, and electrical systems are damaged.
CP (Collapse Prevention)	Severe	Little residual stiffness and strength, but load-bearing columns and walls function. Large permanent drifts. Some exits blocked. Infills and unbraced parapets failed or at incipient failure. Building is near collapse.	Extensive damage.

TABLE 2. Structural (concrete frame) performance levels and damage [15]

Structural performance levels	Primary	Secondary	Drift
IO (Immediate Occupancy)	Minor hairline cracking. Limited yielding possible at a few locations. No crushing (strains below 0.003).	Minor spalling in a few places in ductile columns and beams. Flexural cracking in beams and columns. Shear cracking in joints <1/16" width.	1% transient; negligible permanent
LS (Life Safety)	Extensive damage to beams. Spalling or cover and shear cracking (<1/8" width) for ductile columns. Minor spalling in non-ductile columns, joint cracks <1/8" wide.	Extensive cracking and hinge formation in ductile elements. Limited cracking and/or splice failure in some nonductile columns. Severe damage in short columns.	2% transient; 1% permanent
CP (Collapse Prevention)	Extensive cracking and hinge formation in ductile elements. Limited cracking and/or splice failure in some non-ductile columns. Severe damage in short columns.	Extensive spalling in columns (limited shortening) and beams. Severe joint damage. Some reinforcing buckled.	4% transient or permanent

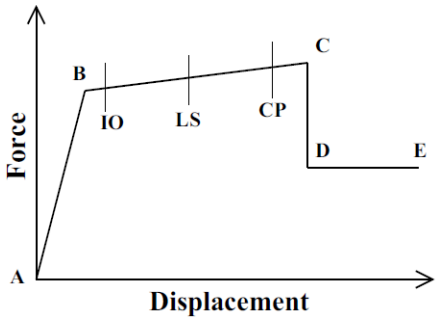

Figure 1. Performance levels IO, LS dan CP

In the upper beam, plain reinforcement with a diameter of 8 mm was installed every 125 mm used as transverse reinforcement. A deformed bar with a diameter of 13 mm was used as longitudinal reinforcement in the beams as well as in the columns of RC frames. A plain bar with a diameter of 8 mm has yield stress and peak stress of 377.87 MPa and 420.96 MPa, respectively. Deformed bars with a diameter of 13 mm have yield stress and peak stress of 473.74 MPa and 643.15 MPa, respectively.

Plain bars with a diameter of 10 mm used as stirrups in the beams and columns have yield stress and peak stress of 469.76 MPa and 598.88 MPa, respectively. Deformed bars with a diameter of 13 mm used as longitudinal reinforcement in beams and columns have yield and peak stress of 473.74 MPa and 643.15 MPa, respectively.

The dimension and reinforcement of the concrete frame infilled with prefabricated foam concrete are shown in Figure 2.

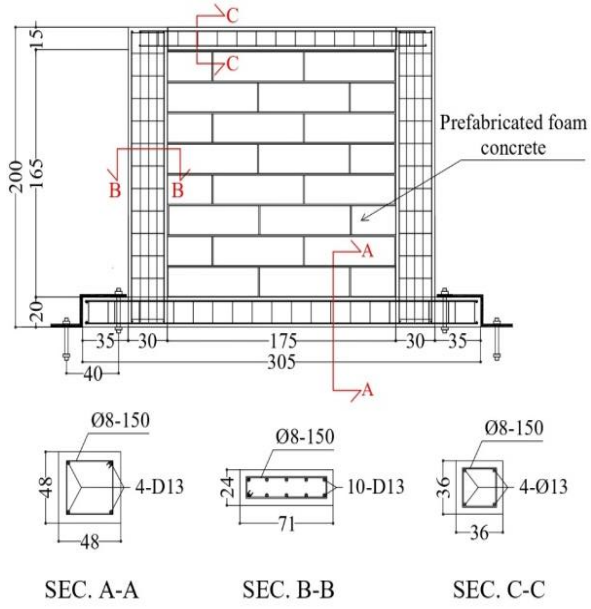

Figure 2. Prefabricated foam concrete infilled RC frame

3. 2. Prefabricated Foam Concrete The compressive strength test was carried out on cylindrical specimens with a diameter of 10 x 20 cm (height), showing that foam concrete had a compressive strength of 7.38 MPa and modulus of elasticity of 12,768 MPa, respectively. The result of the tensile splitting strength test on the cylindrical specimen with a diameter of 100 x 200 mm (height) showed that foam concrete has a tensile strength of 0.75 MPa. The size of prefabricated foam concrete was 40 mm (thickness) x 700 mm (length) and height of 400 mm.

3. 3. Mortar The mortar used to bind prefabricated foam concrete had a compressive strength of 3.32 MPa. The thickness of the mortar was 25 mm.

3. 4. Test Setup, Instrumentation and Procedure This study operated a displacement-controlled lateral loading procedure. A hydraulic actuator equipped with a load cell was used to impose cyclic lateral in-plane load at the middle of the top beam. A linear variable displacement transducer (LVDT) was installed in the center of the upper beam to measure the displacement caused by the lateral loading. An electronic data acquisition system was used to monitor and record the load and LVDT reading.

Figure 3 shows the set up of RC frame infilled with prefabricated plain-foamed concrete blocks specimen. According to the standard test for cyclic lateral load testing ASTM E2126-02a tests, the test consists of three-test methods, namely testing with method A (Sequential-Phased Displacement), testing with method B (ISO 16670 Protocol), and testing with method C (CUREE Basic Loading Protocol). This study used a cyclic lateral loading test of method B where the amplitudes' order is shown in Table 3.

The first displacement pattern consisted of fully reversed five single cycles at 1.25, 2.5, 5, 7.5, and 10% of maximum displacement at maximum load. The second displacement pattern consisted of phase, each containing three cycles of equal inverse amplitude, at 20, 40, 60, 80, 100, and 120% displacement of the maximum displacement Δm.

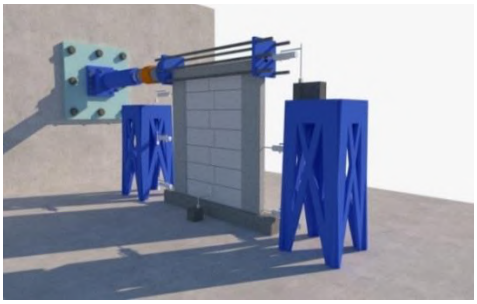

Figure 3. Setting up of RC frame infilled with prefabricated plain foamed concrete blocks specimen

TABLE 3. Test method B—Amplitudes of the reversed cycles

Pattern	Step	Minimum number of cyde	Amplitude, % Δ_m	Horizontal displacement (cm)	Drift ratio (%)
1	1	1	1.25	0.00	0.025
	2	1	2.50	0.10	0.05
	3	1	5.00	0.20	0.10
	4	1	7.50	0.30	0.15
	5	1	10.00	0.40	0.20
2	6	3	20.00	0.80	0.40
	7	3	40.00	1.60	0.80
	8	3	60.00	2.40	1.20
	9	3	80.00	3.20	1.60
	10	3	100.00	4.00	2.00
	11	3	Additional increments of 20 (until specimen failure)	4.80	2.40

4. RESULTS AND DISCUSSION

4. 1. Load and Displacement Relationship The relationship between load and displacement on the specimen is shown in Figure 4. It can be seen that until the end of the tested, the strength of the specimen had a strength of 44.88 kN under push lateral loading and 52.30 kN under pull lateral loading. Displacement readings under push loading and pull loading were 50 mm and 52.9 mm, respectively.

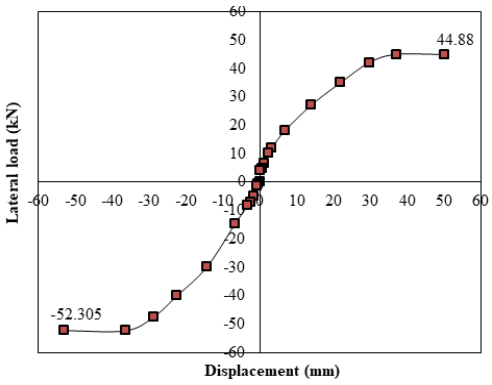

Figure 4. Load and displacement relationship

With an increased in cyclic loading, there is a gradual change in behavior of the prefabricated foam concrete infill wall a linear gradient which turned into a non-linear gradient which showed an inelastic behavior when it reached the post yield zone, so this change caused a change in the lateral stiffness of the specimen.

4. 2. Performance Levels and Drift Ratio Table 4 shows the performance level of RC infilled with prefabricated foam concrete, which had a relationship between %Δm, drift ratio, and lateral load, which was the test result in this research. It can be seen that structural (concrete frame) performance levels and damage Immediate Occupancy (IO) and Life Safety (LS) occurred at a drift ratio of 1.2 and 2.4%, respectively. Meanwhile, based on FEMA 273 IO and LS occurred at 1.0 and 2.0%. Thus, the IO and LS levels of the RC frame infilled with prefabricated foam concrete blocks are 20% greater than the performance levels of FEMA 273.

TABLE 4. The performance level of RC infilled with prefabricated foam concrete [10]

Structural (concrete frame) performance levels and damage	Lateral load (N)		Δm (%)	Drift Ratio	Description
	Push (+)	Pull (-)			
Operational level (OL)	8,100	7,900	10.00	≈ 0.2%	RC and infills (prefabricated foam concrete blocks) were considered undamaged
Intermediate Occupancy (IO)	22,230	15,540	60.00	≈ 1.2%	Some of RC parts and infills (prefabricated foam concrete blocks) were slightly damaged but can be easily and economically repaired
Life Safety (LS)	52,310	41,220	120.00	≈ 2.4%	A significant number of infills (prefabricated foam concrete blocks) were severely damaged and repairability questionable, lives are not threadened

4. 3. Performance Level and Damage Pattern Figure 5 shows the damage levels of RC frame infilled with prefabricated foam concrete blocks in performance level OL (drift ratio 0.2%). Cracks that occurred in prefabricated foam concrete blocks have spread to the joints between blocks where the lateral load at that time was 8,100 N with %Δm of 10.00%, respectively.

Figure 6 depicts the damage levels of RC frame infilled with prefabricated foam concrete blocks in performance level IO (drift ratio 1.2%). Damage patterns in the form of increasing new cracks and previous cracks that were getting longer and wider occurred in prefabricated foam concrete blocks and joints between blocks. New cracks appeared in the joints between beams and columns. Previous cracks in beams and columns spread and grew in width. This damage pattern occurred at lateral loads, and %Δm were 22,230 N and 60.00%, respectively.

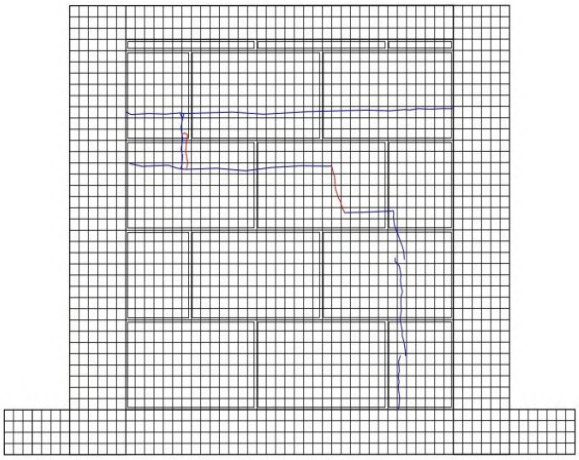

Figure 5. Damage pattern at OL (drift ratio 0.2%) performance level

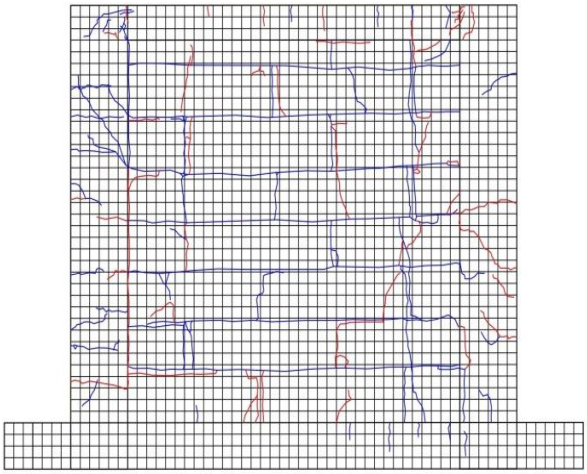

Figure 6. Damage pattern at IO (drift ratio 1.2%) performance level

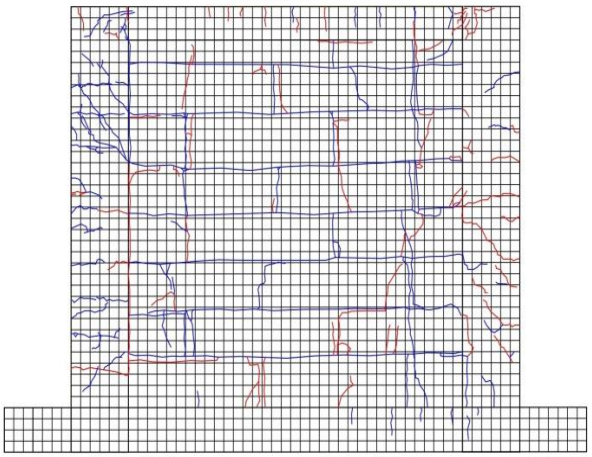

Figure 7. Damage pattern at IO (drift ratio 2.4%) performance level

Figure 7 shows the damage levels of RC frame infilled with prefabricated foam concrete blocks in LS (drift ratio 2.4%). The damage pattern was in the form of cracks in prefabricated foam concrete blocks, between blocks, on the sides of beams and columns, connections between beams and columns, on beams and columns that were increasingly spreading and growing. Spalling of cover concrete in several places in columns and beams occurred, which formed severe damage. This damage occurred at lateral and %Δm loads of 52.310 N and 120.00%, respectively.

Based on Figures 5, 6, and 7, it can be concluded that the damage pattern that occurred in prefabricated foam concrete as infilled walls are in the form of cracks that form corner crushing, diagonal compression, sliding shear, and diagonal cracking. The damage pattern was similar to the damage pattern of the masonry infilled RC frame were the infill made of clay bricks. In contrast, the damage pattern that occurred in the beam and column was shear cracks.

Prefabricated foam concrete panels can be used as an alternative material for infilled wall of reinforced concrete frame structures to replace bricks, hebel, bricks, etc. In most buildings, the wall was not part of the structural element, but served as a stiffener and insulated or separator between building spaces. However, the results of this study indicate that prefabricated foam concrete panels which were used as infill materials have a good structural response in received seismic loads or earthquake loads.

5. CONCLUSION

1. At performance levels OL, IO and LS, the RC frame infilled with prefabricated foam concrete blocks had a drift ratio of 0.2, 1.2, and 2.4%, respectively.

2. Damage to the RC frame infilled with prefabricated foam concrete blocks was similar to the masonry infilled RC frame.

6. ACKNOWLEDGMENT

This work was supported by the Indonesian Lecturer's Excellence Scholarship Program (BPPDN). The RC frame infilled with prefabricated foamed concrete blocks specimens was prepared and conditioned at the Eco Material and Concrete and Structural Earthquake Engineering Laboratory at the Civil Engineering Department of Hasanuddin University, Indonesia. The authors would like to express their sincere thanks to Dr. Muhammad Akbar Caronge, Dr. Miswar Tumpu and Muhammad Hamdar Yusri, ST, for this research through their assistance with providing helps during this study.

7. REFERENCES

1. Watanabe, S., Shima, N., and Fujita, K., "Research on Non-Engineered Housing Construction Based on a Field Investigation in Jakarta," ***Journal of Asian Architecture and Building Engineering***, Vol. 12, No. 1, (2013), 33–40. Doi: 10.3130/jaabe.12.33.
2. Tumengkol, H. A., Irmawaty R., Parung H, and Amiruddin A., "Precast Concrete Column Beam Connection Using Dowels Due to Cyclic Load," ***International Journal of Engineering, Transaction A: Basics***, Vol. 35, No. 1, (2022), 81–91. Doi: 10.5829/ije.2022.35.01A.09.
3. Amran, Y. H. M., Farzadnia, N., and Abang Ali, A. A., "Properties and applications of foamed concrete; a review," ***Construction and Building Materials***, Vol. 101, (2015), 990–1005. Doi: 10.1016/j.conbuildmat.2015.10.112.
4. Lesovik. V, Voronov. V, Glagolev. E, Fediuk. R, Alaskhanov. A, Amran. YHM, Murali. G, and Baranov. A., "Improving the behaviors of foam concrete through the use of composite binder," ***Journal of Building Engineering***, Vol. 31, (2020), 101414. Doi: 10.1016/j.jobe.2020.101414.
5. Sunarno, Y., Tjaronge, M. W., and Irmawaty, R., "Preliminary study on early compressive strength of foam concrete using Ordinary Portland Cement (OPC) and Portland Composite Cement (PCC)," ***IOP Conference Series: Earth and Environmental Science***, Vol. 419, No. 1, (2020), 012033. Doi: 10.1088/1755-1315/419/1/012033.
6. Syahrul, Tjaronge. MW, Djamaluddin. R, and Amiruddin. AA., "Flexural Behavior of Normal and Lightweight Concrete Composite Beams," ***Civil Engineering Journal***, Vol. 7, No. 3, (2021), 549–559. Doi: 10.28991/cej-2021-03091673.
7. Standard National of Indonesia. Standard Test Spesification for Lightweight Aggregates for Structural Concrete. SNI 03-3449-2002.
8. Bindiganavile, V. and Hoseini, M., "Foamed concrete," in *Developments in the Formulation and Reinforcement of Concrete*, (2019), 365–390. , Doi: 10.1016/B978-0-08-102616-8.00016-2.
9. Narayanan, N. and Ramamurthy, K., "Structure and properties of aerated concrete: a review," ***Cement and Concrete Composites***, Vol. 22, No. 5, (2000), 321–329. Doi: 10.1016/S0958-9465(00)00016-0.
10. Hajimohammadi, A., Ngo, T., and Mendis, P., "Enhancing the strength of pre-made foams for foam concrete applications," ***Cement and Concrete Composites***, Vol. 87, (2018), 164–171. Doi: 10.1016/j.cemconcomp.2017.12.014.
11. Hamzah, L., Puspito, N. T., and Imamura, F., "Tsunami Catalog and Zones in Indonesia.," ***Journal of Natural Disaster Science***, Vol. 22, No. 1, (2000), 25–43. Doi: 10.2328/jnds.22.25.
12. Siqi, L., Tianlai, Y., and Junfeng, J., "Investigation and Analysis of Empirical Field Seismic Damage to Bottom Frame Seismic Wall Masonry Structure," ***International Journal of Engineering, Transaction B: Applications***, Vol. 32, No. 8, (2019), 1082–1089. Doi: 10.5829/ije.2019.32.08b.04.
13. Luca. FD, Woods. GED, Galasso. C, and Ayala. DD, "RC infilled building performance against the evidence of the 2016 EEFIT Central Italy post-earthquake reconnaissance mission: empirical fragilities and comparison with the FAST method," ***Bulletin of Earthquake Engineering***, Vol. 16, No. 7, (2018), 2943–2969. Doi: 10.1007/s10518-017-0289-1.
14. Shing, P. B. and Mehrabi, A. B., "Behaviour and analysis of masonry-infilled frames," ***Progress in Structural Engineering and Materials***, Vol. 4, No. 3, (2002), 320–331. Doi: 10.1002/pse.122.
15. Building Seismic Safety Council. NEHRP Guidelines for the Seismic Rehabilitation of Buildings, FEMA-273, Federal Emergency Management Agency, Washington, D.C. (1997).

Persian Abstract

چکیده

هر ساله زمین‌لرزه‌هایی در مناطق مختلف اندونزی رخ می‌دهد زیرا اندونزی در نزدیکی گسل‌های زلزله قرار دارد. آزمایش بارگذاری جانبی چرخه‌ای در آزمایشگاه به طور گسترده‌ای برای شبیه‌سازی بارهای جانبی ناشی از حوادث زلزله استفاده شده است. این تحقیق یک مطالعه تجربی بر روی رفتار فوم بتن پیش ساخته به عنوان دیوار پرکننده در برابر بارهای سیکلی جانبی است. در این مطالعه از فوم بتن پیش ساخته استفاده شد تا آن را به عنوان جایگزینی برای بلوک‌های آجری و بتن سبک اتوکلاو شده (ALC) که به طور گسترده به عنوان دیوارهای پرکننده استفاده می‌شود، تبدیل کند. این مطالعه رابطه بین سطوح عملکرد، بارهای جانبی و نسبت رانش را بر روی بتن فوم پیش ساخته پر شده با RC تجزیه و تحلیل می‌کند. بارگذاری چرخه‌ای جانبی با روش کنترل جابجایی برای ارزیابی رفتار ساختاری در جایی که آزمون به ASTM E2126-02a اشاره دارد، اعمال شد. این مطالعه FEMA 273 را اتخاذ می‌کند که سطوح عملکردی را که باید توسط ساختار یک ساختمان به دست می‌آید تنظیم می‌کند. نتایج نشان داد که در سطوح عملکرد، سطح عملیاتی (OL)، اشغال فوری (IO) و ایمنی زندگی (LS)، قاب RC پر شده با بلوک‌های فوم بتنی پیش ساخته به ترتیب دارای نسبت رانش ۰/۲ ٪، ۱/۲ ٪ و ۲/٤ ٪ بود. آسیب به قاب RC پر شده با بلوک‌های بتنی فوم پیش ساخته مشابه قاب RC پر شده با بنایی بود.

IJE TRANSACTIONS B: Applications Vol. 35, No. 02, (February 2022) 344-350

International Journal of Engineering

Journal Homepage: www.ije.ir

Design of Soil Remediation Techniques from Column Leaching Test Results

J. Sumalatha[a], C. L. Mahesh Kumar*[b], S. Prashant[a], K. G. Shwetha[b]

[a] *Department of Civil Engineering, M S Ramaiah Institute of Technology, Bangalore, India*
[b] *Department of Civil Engineering, Nitte Meenakshi Institute of Technology, Yelahanka, Bengaluru, Karnataka, India*

P A P E R I N F O

Paper history:
Received 11 October 2021
Received in revised form 14 November 2021
Accepted 17 November 2021

Keywords:
Column Leaching Test
Dispersion Coefficient
Elution Curve
Immobilization
Retardation Factor
Soil Washing

A B S T R A C T

The soil remediation at a contaminated site requires knowledge of contaminant transport parameters and processes. This paper presents the determination of transport parameters from column leaching tests in context with two soil remediation techniques i.e., soil washing and immobilization. To evaluate the soil washing technique, the column leaching tests on the polluted soil were conducted with diluted acid solutions of hydrochloric acid, ethylene diamine tetraacetic acid and ferric chloride to evaluate the leaching efficiencies of the selected leaching solutions. It was observed that the efficiency of diluted ferric chloride solution was higher as it removed the higher percentage of metals from the soil. From these test results, the contaminant transport parameters i.e., retardation factor and dispersion coefficient were determined which are useful to calculate the volume of leaching solution that will be required for soil washing at a site. As part of immobilization study on this soil, the soil was mixed with the selected amendments (lime, sodium hydroxide and cement) to increase the pH of the soil to 10 and the retardation factors were estimated through batch leaching test results. The retardation factors of different metals obtained with lime addition were found higher than the other amendments. To analyze the long-term stability of the amended mixtures, the leaching tests were conducted on amended soil samples and the immobilization efficiencies were estimated. It was found that the immobilization efficiencies were higher with lime addition and also concluded that the immobilization effiencies are directly related to retardation factors.

doi: *10.5829/ije.2022.35.02b.10*

1. INTRODUCTION

The pollution of soil may take place due to various reasons such as unregulated disposal of wastes, mining and industrial activities, modern agricultural practices, construction activities etc. [1–3]. The heavy metal pollution of soil may create health problems for living beings as they can enter into the living beings through several ways [4]. The pollution of groundwater due to migration of heavy metals from the contaminated soil is a serious problem as the ground water will be used for various purposes including spa treatments (medicinal thermal water) [5]. For the developing or residential areas a soil remediation is very much required and before planning the remediation, it is important to conduct a survey similar to work conducted by Ezirim and Okpoechi [6].

The various soil remediation techniques in practice are immobilization, chemical treatment, electrokinetic processes, biochemical processes, soil washing, incineration techniques and thermal desorption technique [7–9]. The two important and widely used soil remediation techniques are soil washing and immobilization. Diluted acids such as hydrochloric acid (HCl) and ethylenediamine tetra acetic acid (EDTA) can be used for soil washing treatment [10–14]. The soil washing technique is effective for granular soils as the textutre of the soil is more permeable. For less permeable soils such as clay, the soil washing is not very effective as the washing technique requires sufficient void spaces to wash out the pollutants from the soil. In such cases, immobilization is an alternate remediation technique where the migration of pollutants is restricted by converting the metals in soil to their stable hydroxide

*Corresponding Author Institutional Email: maheshkumar.cl@nmit.ac.in (C. L. Mahesh Kumar)

Please cite this article as: J. Sumalatha, C. L. Mahesh Kumar, S. Prashant, K. G. Shwetha, Design of Soil Remediation Techniques from Column Leaching Test Results, ***International Journal of Engineering, Transactions B: Applications,*** Vol. 35, No. 02, (2022) 344-350

form. The soil washing require treatment of wastewater after washing the contaminants from the soil and the extracted metals need to be disposed safely [15, 16].

The immobilization technique avoids excavation of the contaminated soil, treatment of wastewater, disposal of the contaminated fluid and provides relatively cost-effective solution to treat the contaminated soil [17]. The metal hydroxides formed after immobilization will not migrate because of their low soluble form and reduces the probability of contamination of nearby water bodies [18]. Various organic and inorganic additives can be used to restrict the mobility of contaminants in the soil using immobilization technique [19–25]. The additives such as clay, calcium hydroxide, cement, zeolites, hydroxyapatite, phosphates, organic compost, microbes, activated carbon, fly ash and lime are widely used materials to immobilize the metals in soil and sludge [26–33]. Long-term stability of the amended soils also depends on the solubility of metals in their converted form [34–36]. The selection of materials or chemicals required for these soil remediation techniques depends on the transport parameters of the contaminants in the soil to be treated. In the present study, it is proposed to demonstrate the determination of contaminant transport parameters through batch tests and column leching tests results. The one-dimensional advection-dispersion transport equation describes the rates of migration which is given in Equation (1) [37].

$$R\frac{\partial C}{\partial t} = D\frac{\partial^2 C}{\partial Z^2} - v_s\frac{\partial C}{\partial Z} \quad (1)$$

where,
R = retardation factor = 1+ρK/n
ρ = dry density (g/cm^3)
K = distribution coefficient (c m^3/g)
n = porosity
D = dispersion coefficient (cm^2/s)
v_s = seepage velocity (cm/s)

As part of the investigation, a contaminated soil was studied to know the suitability of the soil washing and immobilization techniques. The column leaching tests were carried out with 0.1 normal chemical solutions of HCl, EDTA, and Ferric Chloride ($FeCl_3$) on the contaminated soil and found that $FeCl_3$ is effective in the removal of metals. The transport rates were anticipated via preparing the elution curves using trial values substituted in theoretical equation and matching them with elution curves of experimental values. The transport rates of contaminants during column leaching tests were modeled using the MATLAB programming for the analytical solution which is based on the Shackelford and Glade's [38] leaching mass ratio (LMR) approach. Since the column leaching tests represent the leaching process in the field during soil washing, the transport rates obtained by this method are useful in the field to estimate the volume of flushing solution needed to wash out the various contaminants. The immobilization studies were also conducted by mixing the soil with additives such as lime, sodium hydroxide and cement which increases the pH of soil and immobilize the metals in it. The amended samples were tested for their leachability to evaluate the efficiencies of additives and found that the leaching of metals from lime amended sample were less. The batch tests were performed on amended soil samples to estimate the retardation factors and found that the retardation factor of lime amended sample was higher. The values of retardation factors were compared with the efficiencies of amendments obtained from leaching tests and found that the retardation factors are useful to identify the best additive.

2. MATERIALS AND METHODS

The research methodology of the current research work is illustrated in the flow chart (Figure 1).

2. 1. Characteristics of Contaminated Soil The soil samples were collected from a dumping yard located at the outskirts of Bangalore, India. The composition of the soil was estimated to be of 34% sand, 12% silt and 54% clay. The soil is classified as low plasticity clay (CL) as per Indian Standard classification system. The plasticity and compaction characteristics of the contaminated soil are as given in Table 1. The quantities of metal ions presented in the contaminated soil were estimated by following the methods specified in USEPA [39] and the estimated quantities are given in Table 2. The maximum permissible limits of heavy metals in soil specified by World Health Organization (WHO) [40] are also presented in Table 2.

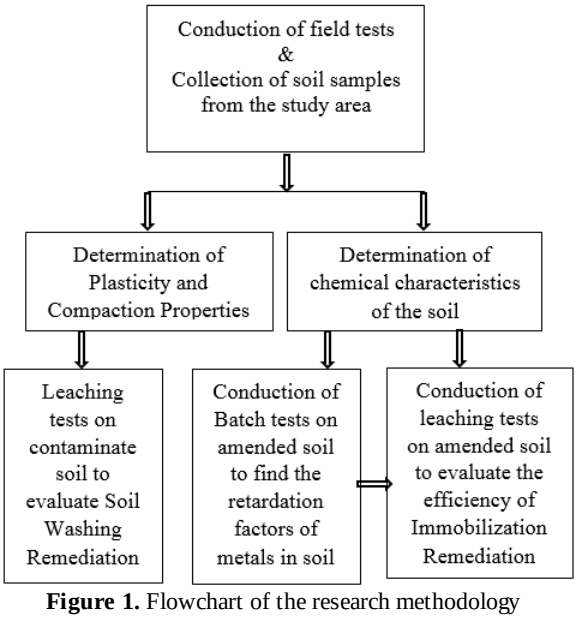

Figure 1. Flowchart of the research methodology

TABLE 1. Plasticity and compaction characteristics of contaminated soil

Specific gravity (G)	Maximum dry density (g/cc)	Optimum water content (%)	Liquid limit (%)	Plastic limit (%)	Shrinkage limit (%)	Plasticity index (Ip) (%)
2.69	1.62	24.6	56.2	24.8	13.6	31.4

TABLE 2. Heavy metals in contaminated soil

Metals in soil	Cu	Zn	Fe	Cr	Cd	Ni	Pb
Quantity of metals in soil (mg/kg)	112.8	148.6	198.7	18.9	1.2	44.6	4.8
Permissible limits of heavy metals in soil (mg/kg)	36	50	-	100	0.8	35	85

2. 2. Column Leaching Tests on Contaminated Soil The in-situ soil washing program was simulated by performing the column leaching tests with various leaching solutions. The diluted acid solution was permitted to flow through the soil column and the effluent concentrations were measured periodically. The effluent volume (V) and the mass of contaminant leached (Δm) were found periodically. For each time interval, the leached pore volumes of flow (T^1= V/Vv) were calculated. The LMR which is the ratio of leached mass of contaminant (Δm) from the soil to initial mass of contaminant (M_0) was computed periodically and the Cumulative LMR (LMR_m) was calculated with respect to time. These values were plotted with respect to their respective leached pore volumes (T^1). The plots, thus prepared are called experimental elution curves which are important to analyze the efficiency of leaching solution.

2. 3. Estimation of Transport Parameters from Column Leaching Tests The analytical solution developed by Shackelford and Glade [38] is as given below (Equation (2)).

$$\text{LMRm} = \frac{\sum \Delta m}{M_0} = \frac{T^I}{R} - \frac{1}{2}\left\{\left(\frac{T^I}{R} - 1\right) erfc\left(\frac{R - T^I}{2\sqrt{\frac{T^I R}{P_L}}}\right) + \left(\frac{T^I}{R} + 1\right)\exp(P_L) erfc\left(\frac{R - T^I}{2\sqrt{\frac{T^I R}{P_L}}}\right)\right. \quad (2)$$

LMR_m = cumulative leaching mass ratio = $\sum (\Delta m / M_0)$
P_L=column Peclet number = $v_s L/D$;

To plot the theoretical elution curves, experimental values of T^1 and P_L along with trial values of transport parameters (D and R) were taken as input in the MATLAB program which was generated out of the above equation (Equation (2)). The theoretical elution curve was then coordinated with the experimental one to estimate the transport parameters.

2. 4. Batch Tests on Amended Soil Samples The Batch tests were conducted to find the distribution coefficients (K) as per ASTM specifications [41]. The distribution coefficient was then calculated from Equation (3):

$$K = \frac{(C_o - C_t)V}{M.C_t} \quad (3)$$

where,
C_o and C_t respectively are initial and final concentrations of the pollutants. M and V are mass of soil taken (g) and the volume of solution used (ml) respectively. The value of K will be zero for non-reactive solutes reducing R=1.

2. 5. Amended Soil Samples and Leaching Tests The contaminated soil sample of about 110 grams was taken in a container and the additive / amendment was added to the soil in such a way that the pH value of the mixture achieved the desired value. The samples were prepared with 3 inorganic additives, i.e., lime, cement and NaOH. Since the immobilization efficiencies increases with increasing pH value [27–31] and the effiencies were observed to be higher corresponding to a pH value of 10, each selected additive was added to adjust the pH of the mixture to maintain a pH value of 10. To evaluate the long-term stability of the soil mixtures, leaching tests were conducted by passing water through the soil placed in the containers and the effluent was collected in a container. The concentrations of heavy metals in effluents were found by Atomic Absorption Spectroscopy (AAS) to know the amounts of various contaminants leached out after solidification and to assess the capabilities of these solidifying agents. From the effluent concentrations estimated, the cumulative percentage leached and the immobilization efficiency were estimated for each metal ion (Table 3).

3. RESULTS AND DISCUSSION

3. 1. Column Leaching Tests and Analytical Method The removal efficiencies of leaching solutions studied with respect to each metal ion (copper, zinc, iron, nickel, cadmium, lead and chromium) in the sludge were

analyzed. From the column leaching tests it was observed that with diluted HCl, EDTA and $FeCl_3$, the removal efficiencies of metals were around 30-50%, 50-70% and 70-80%, respectively. The removal efficiencies of $FeCl_3$ were observed high among the three solutions. The effiencies were in the sequence of $FeCl_3$ > EDTA > HCl which is similar to data reported in literature [42, 43]. The removal efficiencies were observed slightly lower than the reported data [43, 44]. This may be due to the presence of more clay fraction in the soil studied. Out of the metals studied, the removal efficiencies were in the following order which are similar to the studies conducted by Sumalatha et al. [45]. It can be observed that the removal efficiency of cadmium is the highest and that of chromium is the lowest.

Cd> Pb> Zn> Cu> Fe> Ni> Cr

The elution curves obtained by washing the soil with diluted acids are shown in Figures 2 to 4. The transport parameters were found with 0.1M $FeCl_3$ since the higher efficiencies were achieved with this solution. The elution curves (theoretical) plotted for copper and zinc are shown in Figures 5 and 6 along with their experimental values. Similar plots were prepared for other metals and their transport parameters are reported in Table 3. The parameters thus estimated can be substituted in the MATLAB program along with the field parameters to estimate the leached pore volumes of flow required in the field and thus the volume of leaching solution needed at the site to implement the in-situ soil washing program.

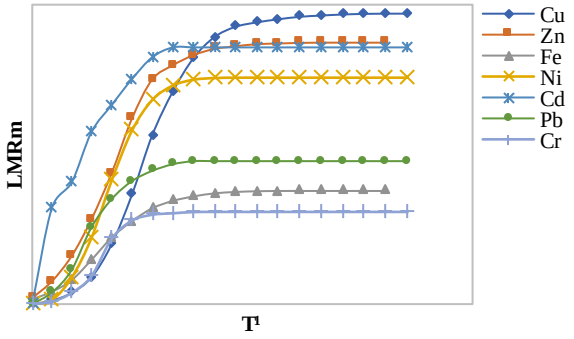

Figure 2. Elution curves (experimental) with diluted HCl

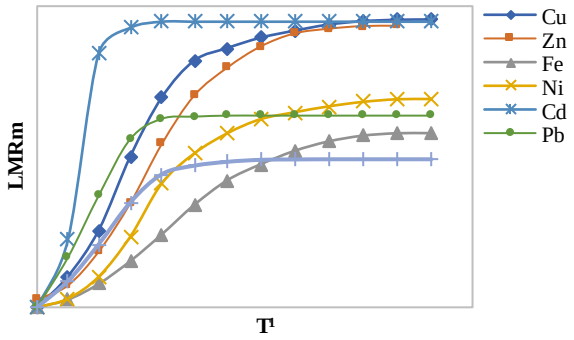

Figure 3. Elution curves (experimental) with diluted EDTA

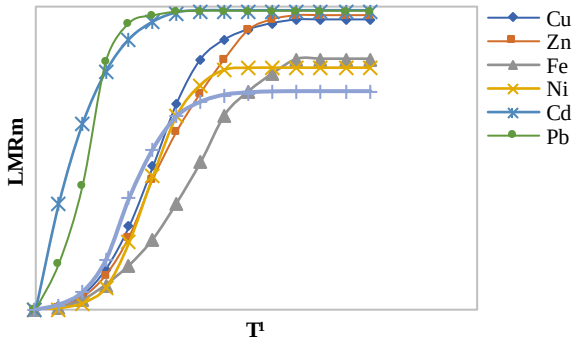

Figure 4. Elution curves (experimental) with diluted $FeCl_3$

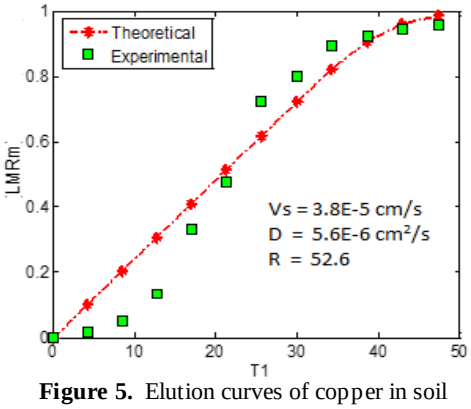

Figure 5. Elution curves of copper in soil

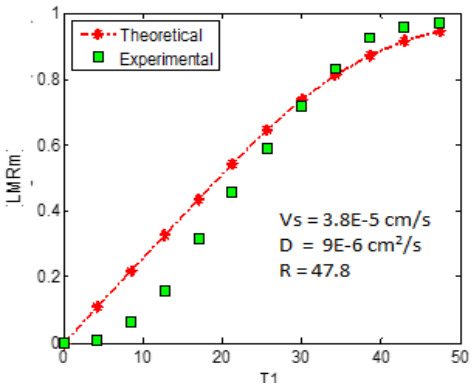

Figure 6. Elution curves of zinc in soil

TABLE 3. Transport rates of pollutants in soil

Pollutant	Dispersion coefficient (D) (cm^2/s)	Retardation Factor (R)
Copper (Cu)	5.6×10^{-6}	52.6
Zinc (Zn)	9.0×10^{-6}	47.8
Iron (Fe)	1.9×10^{-7}	67.7
Chromium (Cr)	1.1×10^{-6}	59.2
Cadmium (Cd)	7.0×10^{-5}	22.6
Nickel (Ni)	2.8×10^{-6}	62.8
Lead (Pb)	3.7×10^{-5}	28.4

3. 2. Batch Tests and Leaching Tests on Amended Soil Samples The retardation factors estimated from the batch tests on amended soil samples with respect to the additives used are given in Table 4. The immobilization efficiencies of the additives estimated through the results of leaching tests are summarized in Table 5. From these tables, it can be observed that the immobilization efficiencies of the additives are directly proportional to the retardation factors obtained from the batch tests. Hence it can be concluded that the retardation factors play an important role in selecting the suitable amendment for immobilization remediation. The immobilization efficiencies of metals with lime addition were higher than the other two additives. These results were similar to the data reported by Salihoglu [46]. The leachability of metals from the amended mixtures of this study were in the following order.

Cadmium> Lead> Iron> Nickel> Zinc> Copper> Chromium

The standard sequences of solubility of metal hydroxides with pH value are in the following order [47].

$Cd(OH)_2$> $Pb(OH)_2$> $Zn(OH)_2$> $Cr(OH)_3$> $Fe(OH)_2$> $Ni(OH)_2$> $Cu(OH)_2$

The leachability orders of metals from this study were observed to be similar to these sequences with small variations. These variations may be due to the solid matrix created by cementing agents and cation exchange with soil.

TABLE 4. Results of batch tests on amended soil

Amendment	Retardation factors						
	Copper	Zinc	Iron	Nickel	Cadmium	Lead	Chromium
Lime	58.3	56.2	76.2	68.2	29.8	32.1	69.9
NaOH	54.8	52.4	69.6	63.8	23.9	29.8	61.2
Cement	55.7	55.8	71.3	64.4	25.6	30.9	64.7

TABLE 5. Results of leaching tests on amended soil

Amendment	% leached and % efficiency	Metals in soil						
		Copper	Zinc	Iron	Nickel	Cadmium	Lead	Chromium
Lime	% Leached	22.6	24.5	36.8	31.2	44.1	43.4	17.5
	% Efficiency	77.4	75.5	63.2	68.8	55.9	56.6	82.5
NaOH	% Leached	39.8	38.6	41.9	43.7	51.5	49.8	29.6
	% Efficiency	60.2	61.4	58.1	56.3	48.5	50.2	70.4
Cement	% Leached	31.6	32.5	39.8	38.1	47.5	44.2	20.1
	% Efficiency	68.4	67.5	60.2	61.9	52.5	55.8	79.9

4. CONCLUSIONS

The determination of transport parameters has been described through batch tests and column leaching tests. The usefulness of the transport parameters, thus determined is demonstrated in the design of soil remediation techniques such as soil washing and immobilization. The column leaching tests carried out with diluted acid solutions on a contaminated dump site soil were evaluated to assess the suitability of the chemical solutions for soil washing remediation. The contaminant transport parameters of the pollutants were estimated through elution curves and the importance of these parameters in selecting the type and quantity of leaching solution for soil washing was discussed. The immobilization efficiencies of three additives were studied corresponding to a pH value of 10. The retardation factors and long-term efficiencies of the amended soil samples were estimated through batch tests and leaching tests respectively. The results of these tests showed that the retardation factors are directly related to the immobilization efficiencies. Hence it was concluded that the retardation factors are useful to select suitable amendment for soil remediation using immobilization technique.

5. REFERENCES

1. Gebreyesus, S. T. "Heavy Metals in Contaminated Soil: Sources & Washing through Chemical Extractants." ***American Academic Scientific Research Journal for Engineering, Technology, and Sciences***, Vol. 10, No. 1, (2014), 54–60. Retrieved from https://www.asrjetsjournal.org/index.php/American_Scientific_Journal/article/view/730

2. Morais, S., e Costa, F. G., and Lourdes Pereir, M. de. "Heavy Metals and Human Health." In Environmental Health - Emerging Issues and Practice. InTech. https://doi.org/10.5772/29869
3. Shayler, H., McBride, M., and Harrison, E. Sources and impacts of contaminants in soils. Cornell Waste Management Institute.
4. Lin, C.-F., Lo, S.-S., Lin, H.-Y., and Lee, Y. "Stabilization of cadmium contaminated soils using synthesized zeolite." ***Journal of Hazardous Materials***, Vol. 60, No. 3, (1998), 217–226. https://doi.org/10.1016/S0304-3894(98)00092-2
5. Langer, P. "Groundwater Mining in Contemporary Urban Development for European Spa Towns." ***Journal of Human, Earth, and Future***, Vol. 1, No. 1, (2020), 1–9. https://doi.org/10.28991/HEF-2020-01-01-01
6. Ezirim, O. N., and Okpoechi, C. U. "Community-driven Development Strategy for Sustainable Infrastructure." ***Journal of Human, Earth, and Future***, Vol. 1, No. 2, (2020), 48–59. https://doi.org/10.28991/HEF-2020-01-02-01
7. Bolan, N., Kunhikrishnan, A., Thangarajan, R., Kumpiene, J., Park, J., Makino, T., Kirkham, M. B., and Scheckel, K. "Remediation of heavy metal(loid)s contaminated soils – To mobilize or to immobilize?" ***Journal of Hazardous Materials***, Vol. 266, (2014), 141–166. https://doi.org/10.1016/j.jhazmat.2013.12.018
8. Hamby, D. M. "Site remediation techniques supporting environmental restoration activities—a review." ***Science of the Total Environment***, Vol. 191, No. 3, (1996), 203–224. https://doi.org/10.1016/S0048-9697(96)05264-3
9. Mulligan, C. N., Yong, R. N., and Gibbs, B. F. "Remediation technologies for metal-contaminated soils and groundwater: an evaluation." ***Engineering Geology***, Vol. 60, No. 1–4, (2001), 193–207. https://doi.org/10.1016/S0013-7952(00)00101-0
10. Huang, K., Shen, Y., Wang, X., Song, X., Yuan, W., Xie, J., Wang, S., Bai, J., and Wang, J. "Choline-based deep eutectic solvent combined with EDTA-2Na as novel soil washing agent for lead removal in contaminated soil." ***Chemosphere***, Vol. 279, (2021), 130568. https://doi.org/10.1016/j.chemosphere.2021.130568
11. Ahn, Y., Pandi, K., Cho, D.-W., and Choi, J. "Feasibility of soil washing agents to remove fluoride and risk assessment of fluoride-contaminated soils." ***Journal of Soils and Sediments***, Vol. 21, No. 8, (2021), 2770–2777. https://doi.org/10.1007/s11368-020-02808-8
12. Xiao, R., Ali, A., Wang, P., Li, R., Tian, X., and Zhang, Z. "Comparison of the feasibility of different washing solutions for combined soil washing and phytoremediation for the detoxification of cadmium (Cd) and zinc (Zn) in contaminated soil." ***Chemosphere***, Vol. 230, (2019), 510–518. https://doi.org/10.1016/j.chemosphere.2019.05.121
13. Kaurin, A., Gluhar, S., Tilikj, N., and Lestan, D. "Soil washing with biodegradable chelating agents and EDTA: Effect on soil properties and plant growth." ***Chemosphere***, Vol. 260, (2020), 127673. https://doi.org/10.1016/j.chemosphere.2020.127673
14. Mohamadi, S., Saeedi, M., and Mollahosseini, A. "Desorption Kinetics of Heavy Metals (Lead, Zinc, and Nickel) Coexisted with Phenanthrene from a Natural High Buffering Soil." ***International Journal of Engineering, Transaction C: Aspects***, Vol. 32, No. 12, (2019), 1716–1725. https://doi.org/10.5829/ije.2019.32.12c.04
15. Chair, K., Bedoui, A., Bensalah, N., Sáez, C., Fernández-Morales, F. J., Cotillas, S., Cañizares, P., and Rodrigo, M. A. "Treatment of Soil-Washing Effluents Polluted with Herbicide Oxyfluorfen by Combined Biosorption–Electrolysis." ***Industrial & Engineering Chemistry Research***, Vol. 56, No. 8, (2017), 1903–1910. https://doi.org/10.1021/acs.iecr.6b04977
16. Satyro, S., Race, M., Marotta, R., Dezotti, M., Guida, M., and Clarizia, L. "Photocatalytic processes assisted by artificial solar light for soil washing effluent treatment." ***Environmental Science and Pollution Research***, Vol. 24, No. 7, (2017), 6353–6360. https://doi.org/10.1007/s11356-016-6431-9
17. Wuana, R. A., and Okieimen, F. E. "Heavy Metals in Contaminated Soils: A Review of Sources, Chemistry, Risks and Best Available Strategies for Remediation." ***ISRN Ecology***, Vol. 2011, (2011), 1–20. https://doi.org/10.5402/2011/402647
18. Basta, N. T., and McGowen, S. L. "Evaluation of chemical immobilization treatments for reducing heavy metal transport in a smelter-contaminated soil." ***Environmental Pollution***, Vol. 127, No. 1, (2004), 73–82. https://doi.org/10.1016/S0269-7491(03)00250-1
19. Abbott, D. E., Essington, M. E., Mullen, M. D., and Ammons, J. T. "Fly Ash and Lime-Stabilized Biosolid Mixtures in Mine Spoil Reclamation: Simulated Weathering." ***Journal of Environmental Quality***, Vol. 30, No. 2, (2001), 608–616. https://doi.org/10.2134/jeq2001.302608x
20. Cao, X., Ma, L. Q., and Shiralipour, A. "Effects of compost and phosphate amendments on arsenic mobility in soils and arsenic uptake by the hyperaccumulator, Pteris vittata L." ***Environmental Pollution***, Vol. 126, No. 2, (2003), 157–167. https://doi.org/10.1016/S0269-7491(03)00208-2
21. Clemente, R., Walker, D. J., Roig, A., and Bernal, M. P. "Heavy metal bioavailability in a soil affected by mineral sulphides contamination following the mine spillage at Aznalcóllar (Spain)." ***Biodegradation***, Vol. 14, No. 3, (2003), 199–205. https://doi.org/10.1023/A:1024288505979
22. Friesl, W., Lombi, E., Horak, O., and Wenzel, W. W. "Immobilization of heavy metals in soils using inorganic amendments in a greenhouse study." ***Journal of Plant Nutrition and Soil Science***, Vol. 166, No. 2, (2003), 191–196. https://doi.org/10.1002/jpln.200390028
23. Walker, D. J., Clemente, R., and Bernal, M. P. "Contrasting effects of manure and compost on soil pH, heavy metal availability and growth of Chenopodium album L. in a soil contaminated by pyritic mine waste." ***Chemosphere***, Vol. 57, No. 3, (2004), 215–224. https://doi.org/10.1016/j.chemosphere.2004.05.020
24. Brunori, C., Cremisini, C., Massanisso, P., Pinto, V., and Torricelli, L. "Reuse of a treated red mud bauxite waste: studies on environmental compatibility." ***Journal of Hazardous Materials***, Vol. 117, No. 1, (2005), 55–63. https://doi.org/10.1016/j.jhazmat.2004.09.010
25. Guo, G., Zhou, Q., and Ma, L. Q. "Availability and Assessment of Fixing Additives for The in Situ Remediation of Heavy Metal Contaminated Soils: A Review." ***Environmental Monitoring and Assessment***, Vol. 116, No. 1–3, (2006), 513–528. https://doi.org/10.1007/s10661-006-7668-4
26. Kong, X., Ge, R., Liu, T., Xu, S., Hao, P., Zhao, X., Li, Z., Lei, X., and Duan, H. "Super-stable mineralization of cadmium by calcium-aluminum layered double hydroxide and its large-scale application in agriculture soil remediation." ***Chemical Engineering Journal***, Vol. 407, (2021), 127178. https://doi.org/10.1016/j.cej.2020.127178
27. Finžgar, N., Kos, B., and Leštan, D. " Bioavailability and mobility of Pb after soil treatment with different remediation methods." ***Plant, Soil and Environment***, Vol. 52, No. 1, (2011), 25–34. https://doi.org/10.17221/3342-PSE
28. Chuon Yi, O., and Chui Peng Cheong, A. Solidification of Industrial Waste Sludge with Incineration Fly Ash and Ordinary Portland Cement. Undergraduate Research Opportunities Program (UROP, 2002), Nanyang Technological University.
29. Kogbara, R. B. "A review of the mechanical and leaching performance of stabilized/solidified contaminated soils." ***Environmental Reviews***, Vol. 22, No. 1, (2014), 66–86. https://doi.org/10.1139/er-2013-0004

30. Martin, T. A., and Ruby, M. V. "Review ofin situ remediation technologies for lead, zinc, and cadmium in soil." ***Remediation Journal***, Vol. 14, No. 3, (2004), 35–53. https://doi.org/10.1002/rem.20011

31. Heidari, S., Basiri, H., Nourmoradi, H., Kamareei, B., and Omidi, Y. "Hexadecyl Trimethyl Ammonium Bromide-Modified Montmorillonite as a Low-Cost Sorbent for the Removal of Methyl Red from Liquid-Medium." ***International Journal of Engineering, Transaction A: Basics***, Vol. 29, No. 1, (2016), 60–67. https://doi.org/10.5829/idosi.ije.2016.29.01a.09

32. Ajemba, R. "Adsorption of Malachite Green from Aqueous Solution using Activated Ntezi Clay: Optimization, Isotherm and Kinetic Studies." ***International Journal of Engineering, Transaction C: Aspects***, Vol. 27, No. 6, (2014), 839–854. https://doi.org/10.5829/idosi.ije.2014.27.06c.03

33. Wen, D., Fu, R., and Li, Q. "Removal of inorganic contaminants in soil by electrokinetic remediation technologies: A review." ***Journal of Hazardous Materials***, Vol. 401, (2021), 123345. https://doi.org/10.1016/j.jhazmat.2020.123345

34. McGowen, S. L., Basta, N. T., and Brown, G. O. "Use of Diammonium Phosphate to Reduce Heavy Metal Solubility and Transport in Smelter-Contaminated Soil." ***Journal of Environmental Quality***, Vol. 30, No. 2, (2001), 493–500. https://doi.org/10.2134/jeq2001.302493x

35. Valipour, M., Shahbazi, K., and Khanmirzaei, A. "Chemical Immobilization of Lead, Cadmium, Copper, and Nickel in Contaminated Soils by Phosphate Amendments." ***CLEAN - Soil, Air, Water***, Vol. 44, No. 5, (2016), 572–578. https://doi.org/10.1002/clen.201300827

36. Zeng, G., Wan, J., Huang, D., Hu, L., Huang, C., Cheng, M., Xue, W., Gong, X., Wang, R., and Jiang, D. "Precipitation, adsorption and rhizosphere effect: The mechanisms for Phosphate-induced Pb immobilization in soils—A review." ***Journal of Hazardous Materials***, Vol. 339, (2017), 354–367. https://doi.org/10.1016/j.jhazmat.2017.05.038

37. Sharma, H., and Lewis, S. Waste containment systems, waste stabilization, and landfills: design and evaluation. John Wiley & Sons.

38. Shackelford, C. D., and Glade, M. J. "Analytical Mass Leaching Model for Contaminated Soil and Soil Stabilized Waste." ***Ground Water***, Vol. 35, No. 2, (1997), 233–242. https://doi.org/10.1111/j.1745-6584.1997.tb00080.x

39. US Environmental Protection Agency (USEPA), Method 3050B. EPA 660 13-75-009, Acid Digestion of Sediments, Sludges and Soils, Washington, D.C., 1996.

40. World Health Organization. Permissible limits of heavy metals in soil and plants (Geneva: World Health Organization). Geneva, Switzerland, 1996.

41. ASTM, Standard test method for 24-h batch type measurement of contaminant sorption by soils and sediments, (D 4646-87), Annual book of ASTM Standards, American Society for Testing and Materials, Philadelphia, 04.04: 44-47, 1993.

42. Gitipour, S., Ahmadi, S., Madadian, E., and Ardestani, M. "Soil washing of chromium- and cadmium-contaminated sludge using acids and ethylenediaminetetra acetic acid chelating agent." ***Environmental Technology***, Vol. 37, No. 1, (2016), 145–151. https://doi.org/10.1080/09593330.2011.597784

43. Bilgin M, and Tulun S. "Heavy metals (Cu, Cd and Zn) contaminated soil removal by EDTA and FeCl3." ***Global NEST Journal***, Vol. 18, No. 1, (2016), 98–107.

44. Shi, J., Pang, J., Liu, Q., Luo, Y., Ye, J., Xu, Q., Long, B., Ye, B., and Yuan, X. "Simultaneous removal of multiple heavy metals from soil by washing with citric acid and ferric chloride." ***RSC Advances***, Vol. 10, No. 13, (2020), 7432–7442. https://doi.org/10.1039/C9RA09999A

45. Sumalatha, J., Naveen, B. P., and Malik, R. K. "Toxic Metals Removal from Industrial Sludge by Using Different Leaching Solutions." ***Journal of The Institution of Engineers (India): Series A***, Vol. 100, No. 2, (2019), 337–345. https://doi.org/10.1007/s40030-019-00361-3

46. Salihoglu, G. "Immobilization of antimony waste slag by applying geopolymerization and stabilization/solidification technologies." ***Journal of the Air & Waste Management Association***, Vol. 64, No. 11, (2014), 1288–1298. https://doi.org/10.1080/10962247.2014.943352

47. Snoeyink, V. L., and Jenkins, D. Water chemistry. Wiley. Retrieved from https://www.wiley.com/en-us/Water+Chemistry-p-9780471051961

Persian Abstract

چکیده

اصلاح خاک در یک سایت آلوده نیاز به آگاهی از پارامترها و فرآیندهای انتقال آلاینده دارد. این مقاله تعیین پارامترهای حمل و نقل از آزمایش‌های آبشویی ستون را در زمینه با دو تکنیک اصلاح خاک یعنی شستشوی خاک و بی‌حرکتی ارائه می‌کند. برای ارزیابی تکنیک شستشوی خاک، آزمایش‌های آبشویی ستونی بر روی خاک آلوده با محلول‌های اسید رقیق شده اسید هیدروکلریک، اتیلن دی آمین ترا استیک اسید و کلرید آهن برای ارزیابی کارایی آبشویی محلول‌های شستشوی انتخابی انجام شد. نتایج بدست آمده نشان می‌دهد که بازده محلول کلرید آهن رقیق شده بیشتر بود، زیرا درصد بیشتری از فلزات را از خاک حذف می گردد. از این نتایج آزمایش، پارامترهای انتقال آلاینده یعنی ضریب تاخیر و ضریب پراکندگی تعیین شد که برای محاسبه حجم محلول شستشو که برای شستشوی خاک در یک سایت مورد نیاز، مفید است. به عنوان بخشی از مطالعه تثبیت بر روی این خاک، خاک با اصلاحات انتخابی (آهک، هیدروکسید سدیم و سیمان) مخلوط شد تا pH خاک به ۱۰ افزایش یابد و عوامل تاخیری از طریق نتایج آزمایش آبشویی ناپیوسته برآورد شد. فاکتورهای تاخیری فلزات مختلف به‌دست‌آمده با افزودن آهک بالاتر از سایر اصلاح‌ها بود. برای تجزیه و تحلیل پایداری طولانی‌مدت مخلوط‌های اصلاح‌شده، آزمایش‌های آبشویی روی نمونه‌های خاک اصلاح شده انجام شد و راندمان تثبیت تخمین زده شد. مشخص شد که راندمان تثبیت با افزودن آهک بیشتر بوده و همچنین نتیجه گرفته شد که راندمان تثبیت مستقیماً با عوامل عقب ماندگی مرتبط است.

International Journal of Engineering

Journal Homepage: www.ije.ir

Optimization of Biodiesel Production from Sunflower Oil Transesterification using Ca-K/Al_2O_3 Nanocatalysts

P. Andami[a], A. A. Zinatizadeh*[a,b], M. Feyzi[c], H. Zangeneh[d], S. Azizi[e,f], L. Norouzi[c], M. Maaza[e,f]

[a] *Department of Applied Chemistry, Faculty of Chemistry, Razi University, Kermanshah, Iran*
[b] *Department of Environmental Sciences, School of Agriculture and Environmental Sciences, University of South Africa, Florida, South Africa*
[c] *Department of Physical Chemistry, Faculty of Chemistry, Razi University, Kermanshah, Iran*
[d] *Department of Chemical Engineering, Isfahan University of Technology, Isfahan, Iran*
[e] *UNESCO-UNISA Africa Chair in Nanosciences and Nanotechnology, College of Graduate Studies, University of South Africa, Muckleneuk Ridge, Pretoria, South Africa*
[f] *Nanosciences African Network (NANOAFNET), iThemba LABS-National Research Foundation, 1 Old Faure Road, Somerset West, Somerset West, Western Cape, South Africa*

PAPER INFO

Paper history:
Received 19 March 2021
Received in revised form 04 November 2021
Accepted 10 November 2021

Keywords:
Biodiesel
Ca-K/Al_2O_3
Response Surface Methodology
Sunflower Oil
Transesterification

ABSTRACT

In this study, an attempt was made to optimize the conditions for the transesterification of sunflower oil with methanol, catalyzed by Ca-K/Al_2O_3 nanocatalysts, using response surface methodology. The examined variables were reaction temperature (55, 65 and 75 °C), reaction time (1, 2, 3, 4 and 5 h), catalyst weight base oil (3, 6, 9 and 12 wt%), Ca content (20, 30, 50, 60 and 80 wt%), K content (5, 10, 15 and 20), methanol:sunflower oil molar ratio (3:1, 6:1, 9:1 and 12:1), calcination temperature (600, 700 and 800 °C) and calcination time (1, 2, 3 and 4 h). Catalyst characterization was done by X-ray diffraction (XRD), scanning electron microscopy (SEM), Fourier transform-infrared spectroscopy (FT-IR) and temperature programmed desorption (TPD). The maximum fatty acid methyl esters (FAME) conversion efficiency (biodiesel production efficiency) was 98.3%, at a calcination temperature of 800 °C for 3 h, a methanol-to-oil ratio of 9:1, a reaction temperature of 75 °C, a reaction time of 3 h and a catalyst-to-oil mass ratio of 9%.

doi: *10.5829/ije.2022.35.02b.11*

1. INTRODUCTION

The increasing demand for energy, the rising price of crude oil, global warming resulting from the emission of greenhouse gases, environmental pollution and the rapidly decreasing supply of fossil fuels are the key factors motivating the search for alternative energy sources. Some of the most significant alternative sources of energy that have the ability to replace fossil fuels are hydropower, solar and wind energy, and biofuels. Today, 86% of the energy consumed worldwide, as well as nearly 100% of energy demanded in the transportation sector, is produced using non-renewable fossil fuels despite the various alternative fuels that are being explored to replace existing fossil diesel [1].

Biodiesel is a fuel comprised of mono-alkyl esters of fatty acids derived from animal fats or vegetable oils. It reveals diesel quality and is identified as a clean and renewable fuel [2]. In recent years, many researchers have paid a lot of attention to biodiesel development due to the rate of fossil fuel depletion and because of the resemblance of biodiesel to diesel based on petroleum [3, 4]. Biodiesel can also be used in diesel engines without any engine modifications. Biodiesel is produced through triglyceride transesterification using alcohol in the presence of a catalyst or through deoxygenative ecofining of triglycerides in a non-alcohol situation [5].

Biodiesel can be produced using a wide variety of feedstocks. These feedstocks can be broken up into two categories, unrefined oils and waste oils [6]. Unrefined

*Corresponding Author Institutional Email: zinatizadeh@razi.ac.ir (A. A. Zinatizadeh)

Please cite this article as: P. Andami, A. A. Zinatizadeh, M. Feyzi, H. Zangeneh, S. Azizi, L. Norouzi, M. Maaza, Optimization of Biodiesel Production from Sunflower Oil Transesterification using Ca-K/Al_2O_3 Nanocatalysts, ***International Journal of Engineering, Transactions B: Applications*** Vol. 35, No. 02, (2022) 351-359

oils are further divided into edible and non-edible oil sources [7]. Edible oil feedstocks include soybean, sunflower, peanut, rapeseed (canola), and coconut oils. Nonedible feedstocks are less widely talked about than edible oils. Non-edible oil sources include jatropha, pongamia, argemone, and castor oils. The advantages of using unrefined oil include low levels of impurities and known lipid composition. The main disadvantage of virgin oils is the high cost [8].

Waste oil often comes from the same sources originally. It has just been used, for example in cooking, before being converted into biodiesel. Waste oils can also come from other sources such as animal fat from slaughterhouses [9]. Waste oils are a good feedstock for personal biodiesel production, people making biodiesel in small batches in their garage, because the waste oil can be obtained very cheaply or even for free from restaurants needing to dispose of used frying oil. However, due to the fact that oil has already been used, there are higher amount of animal fats and other contaminants in the oil [6].

There are four primary ways to produce biodiesel, namely, direct use and mixing of raw oils, microemulsions, thermal cracking and transesterification. The most commonly used method of biodiesel production is transesterification (also identified as alcoholysis) in the presence of a catalyst. The process of substituting the alkoxy group of an ester compound with another alcohol is called transesterification [10].

Fatty acid chains are long hydrocarbon chains, and include R1, R2 and R3 [11]. Transesterification involves a series of successive, reversible reactions [12, 13]. The triglyceride is transformed stepwise into diglyceride, monoglyceride and, finally, glycerol by reacting with preliminary alcohol, as illustrated in following reactions [11]:

$$\text{Triglyceride} + \text{ROH} \leftrightarrow \text{Diglyceride} + \text{RCOOR}_1$$

$$\text{Diglyceride} + \text{ROH} \leftrightarrow \text{Monoglyceride} + \text{RCOOR}_2$$

$$\text{Monoglyceride} + \text{ROH} \leftrightarrow \text{Glycerine} + \text{RCOOR}_3$$

Methanol and ethanol are two types of alcohol (R-OH) that are commonly applied in transesterification, but methanol is the most popular considering its low cost, low reaction temperatures, fast reaction times and high quality methyl ester products [14, 15]. The transesterification of unrefined oils and waste oils to biodiesel with methanol can be accomplished by applying both homogeneous (acid or base) and heterogeneous (acid, base and enzymatic) catalysts [16].

Base catalyst transesterification is extensively applied commercially due to its very rapid reaction rate in contrast to other catalysts. A base-catalyzed process is very permeable to water and free fatty acids (FFA) in lipid sources because of the formation of soap. It causes catalyst utilization in which soap production hinders the separation of glycerol from methyl esters and helps emulsion formation through the water wash. The base-catalyzed transesterification is 4000 times faster than acid-catalyzed transterification and requires a low triglyceride-to-alcohol ratio [17].

Heterogeneous catalysts, compared to homogeneous catalysts, are environmentally benign and can be operated in consecutive processes. In addition, they can be reapplied and reproduced. Thus, heterogeneous catalysts are now being examined widely for biodiesel synthesis [18, 19]. It should be noted that solid bases are more active than metal compounds and need milder reaction situations than acids [20, 21].

Experimental design is a strategy for collecting empirical knowledge that relies on experimental data analysis and not theoretical models. The objective of experimental design is to attain efficiency (to obtain more information from fewer experiments) and focus (to gather only the information you really require) [22, 23]. Central composite design is the most common design of response surface methodology (RSM); it is efficient and flexible, providing sufficient data on the effects of variables and overall experimental error with a minimum number of experiments [24, 25].

In this study, the effects of eight independent numerical factors, namely, calcination temperature, calcination time, temperature of transesterification, time of transesterification, weight ratio of methanol to oil, weight ratio of catalyst to oil and weight ratio of potassium and calcium were examined. Characterization of catalysts was conducted by X-ray diffraction (XRD), scanning electron microscopy (SEM), Fourier transform-infrared spectroscopy (FT-IR) and temperature programmed desorption (TPD).

2. MATERIALS AND METHODS

2. 1. Materials KNO_3, Al_2O_3 Na_2CO_3, ethanol (98%) and Ca $(NO_3)_2.4H_2O$ were supplied by Merck (Darmstadt, Germany). Materials for refining sunflower oil were prepared from a local grocery store. The triglyceride and fatty acid values in the sunflower oil were specified by gas chromatography. The fatty acid values were as follows: palmitic acid 7.68%, stearic acid 3.1%, oleic acid 19.95% and linoleic acid 65.95%. The acid value, the water content, the viscosity and the density of the oil were specified according to the current European Union Quality Standard (EN-14214). These values are summarized in Table 1.

TABLE 1. Sunflower oil properties

Property	Value
Acid value (%)	0.1
Water content (%)	0.1
Viscosity at 40°C (cSt)	29.6
Density at 40°C (g/cm^3)	0.924

2. 2. Preparation of the Ca-K/Al_2O_3 Nanocatalyst Based on coprecipitating $Ca(NO_3)_2.4H_2O$ and KNO_3, a Ca/K oxide catalyst was prepared and Na_2CO_3 was applied as a precipitant. A sequence of catalysts with various Ca/K molar ratios was prepared by dissolving defined values of $Ca(NO_3)_2.4H_2O$ and KNO_3 in deionized water and by adding an aqueous Na_2CO_3 solution under vigirous stirring at room temperature until the pH became fixed [26, 27].

The catalyst preparation was performed in a three-neck round-bottom flask (250 mL) equipped with a reflux condenser, a temperature indicator and a mechanical stirrer. Al_2O_3 was added into the three-neck round-bottom flask as a supporter. The impregnation of Ca $(NO_3)_2.4H_2O$ with KNO_3 at a temperature of 65°C for 3 h under continuous stirring was performed. On completion of the impregnation process, the slurry was dried in an oven at 80°C for 12 h to eliminate water. Thereafter, the catalyst was calcined in a tubular muffle furnace at a temperature of 800°C for 3 h.

2. 3. Catalyst Characterization The prepared catalysts were characterized using several methods, such as XRD, FT-IR, TPD and SEM. Calcined samples and the XRD patterns of all the precursors were registered on a Philips X' Pert (40 kV, 30 mA) X-ray diffract meter, applying a Cu Kα radiation source (λ=1.542 Å) and a nickel filter in the 2θ range of 20–80°. SEM analysis was applied to specify morphology, aggregate particles, grain boundaries and defects. The surface morphologies were observed and estimated by a Philips XL30 microscope at a rising voltage of 10 kV. The fourier transform infrared (FT-IR) spectra of the samples in the form of KBr pellets were recorded using a Bruker FT-IR in the area of 400–4000 cm^{-1}. Temperature programmed desorption (TPD) in the presence of H_2 gas was performed from 200 to 1100 K for measuring of H_2 consumption with a linear heating rate of 10°C/min in 5% H_2 per 95% Ar [27].

2. 4. Sunflower Oil Transesterification The transesterification of 15 g waste sunflower oil was performed using a 250 mL round-bottomed flask equipped with a magnetic stirring system (reaction system) and a condenser. First, the reaction system was heated to reach the desired temperature while the oil reached the desired temperature; then, the catalyst and the methanol were added with continuous stirring (500 rpm). The catalytic solid was separated from the reaction combination by applying an external magnetic field on fulfilment of the reaction. The products obtained were evaporated to eliminate additional methanol and then fixed in a separating funnel. The upper phase was composed of fatty acid methyl esters (biodiesel) and the lower phase consisted of glycerol as a byproduct.

Minitab.16 software based on RSM was used in this study. For each system, 13 experiments were designed based on two variables. The experimental range and the levels of the independent variables are indicated in Table 2. Weight ratio of methanol to oil (A, w/w %) ranged from 3:1 to 18:1 at 5 levels (3:1, 6:1, 9:1, 12:1 and 18:1); weight ratio of catalyst to oil (B, w/w %) ranged from 3 to 12% at 4 levels (3, 6, 9 and 12); weight ratio of calcium (C, wt. %) ranged from 20 to 80% at 5 levels (20, 30, 50, 60 and 80%); weight ratio of potassium (D, wt. %) ranged from 5 to 20% at 4 levels (5, 10, 15 and 20 %); calcination temperature (E, °C) ranged from 600 to 800 °C at 3 levels (600, 700 and 800 °C); calcination time (F, h) ranged from 1 to 4 h at 4 levels (1, 2, 3 and 4 h); time of transesterification (G, h) ranged from 1 to 5 h at 5 levels (1, 2, 3, 4 and 5 h); temperature of transesterification (H, °C) ranged from 55 to 75 °C at 3 levels (55, 65 and 75 °C).

Based on the values of the variables that were studied and the responses obtained after the transesterification process, the viscosity was evaluated and the yield of biodiesel was calculated. The applied data for the software were uncoded and the real data were considered. Equation (1) was obtained for each system. A group of coefficients was presented for each series and the most effective coefficient was considered in the response. In this research, the experiments had two variables; this equation included two X values. The number of X was increased by increasing the number of variables, as follows:

$$Y = ß0 + ß1\,X1 + ß2\,X2 + ß11\,X12 + ß22\,X22 + ß12\,X1 \quad (1)$$

The impact on the yield increased along with an increase in the value of coefficients. The impact on the response was raised by raising the value of the F parameter and reducing the P parameter.

3. RESULTS AND DISCUSSION

3. 1. Catalyst Characterization Figure 1 indicates FT-IR spectra of the Ca-K/Al_2O_3 nanocatalyst. The stronger broadening band at 3400 cm^{-1} can be attributed to the hydrogen bond between the different hydroxyl groups in the product. The intense expansive band at 1630 and 1078 cm^{-1} is related to Al-O vibration [17]. The bands at 3644 and 1420 cm^{-1} correspond to K_2O/CaO [18]. The intense characteristics of IR spectral lines for

TABLE 2. Experimental range and levels of the independent variables

Variables	A	B	C	D	E	F	G	H
Levels	5	4	5	4	3	4	5	3
Min	3:1	3%	20	5	600	1	1	55
Max	18:1	12%	80	20	800	4	5	75

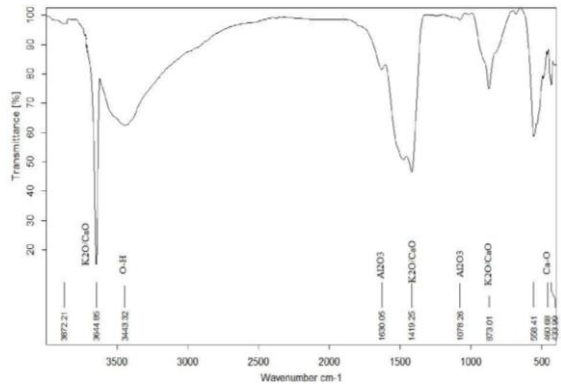

Figure 1. FT-IR spectra of Ca-K/Al_2O_3 nanocatalyst

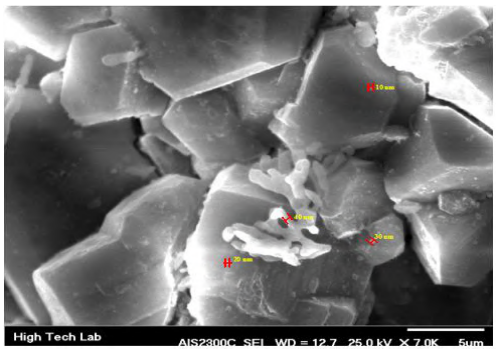

Figure 3. SEM of Ca-K/Al_2O_3 nanocatalyst

CaO occur in the far-infrared range (~480 cm^{-1} and 433 cm^{-1}) and one weak band is placed in the range of 500 cm^{-1} to 560 cm^{-1} [19].

X-ray diffraction was confirmed for the Ca-K/Al_2O_3 catalyst, as shown in Figure 2. The results obtained indicated the recognized phases for this sample. The recognized phases for the calcined Ca-K/Al_2O_3 catalyst were Al_2O_3 ((hexagonal), K_2O (cubic) and CaO (cubic). The particle size of catalyst could be calculated 33.64 nm by Scherer equation [20]. As shown in Figure 3, the surface morphology of the Ca-K/Al_2O_3 nanocatalyst was investigated with SEM image. As can be seen in Figure 3, the Ca/K oxide catalyst is successfully deposited on Al_2O_3 surface.

Characterization of the basic property of catalyst Ca-K/Al_2O_3 nanocatalyst was investigated as displayed in Figure 4. Usually, two desorption peaks were observed in the TPD profile, as shown in Figure 4; these are in the low and high temperatures of desorption. The strength of basic sites was deduced from the work by Pasupulety et al. [21], where it was suggested that desorption temperature between 330-620 ˚C indicates basic sites of weak and medium strength, and desorption temperature range of 770-980 ˚C indicates strong basic sites. The peak at 850 ˚C is desorption of CO_2 which was adsorbed on the basic sites [21].

The total amount of CO_2 desorbed for a Ca-K/Al_2O_3 nanocatalyst is equal to 1.42×10^{21} (atom g^{-1}). The high basic sites of the catalyst bring about high-yield biodiesel. Regarding the relationship between transesterification and the surface basicity of a La_2O_3/ZrO_2 catalyst, Sun et al. argue [22] that a correlation between basic properties occurs when the catalytic reaction is activated, so that a higher biodiesel yield is attained with stronger basicity.

3. 2. Effect of Molar Ratio of Methanol and Mass Ratio of Catalyst to Oil Table 3 indicates the experimental results at various mole ratios of methanol and mass ratios of catalyst to oil. This reaction stoichiometry needs 3 mol methanol per mol triglyceride to produce 3 mol biodiesel and 1 mol glycerol. The biodiesel is increased in an additionalamount of methanol to shift the balance toward the right-hand side [28]. To completely understand the factors that affect the catalytic performance of the optimal Ca-K/Al_2O_3 catalyst, many experiments were performed at various methanol:oil ratios, ranging from 3:1 to 18:1, under the reaction situations (T=75°C, stirring rate of 500 rpm and reaction time of 3 h). The table indicates that the biodiesel yield percent considerably increased in methanol oil ratio =9:1. Thus, it can be said that increasing the methanol value postponed the reaction and exacerbated the solvent recovery. However, recovering solvent with a high ratio

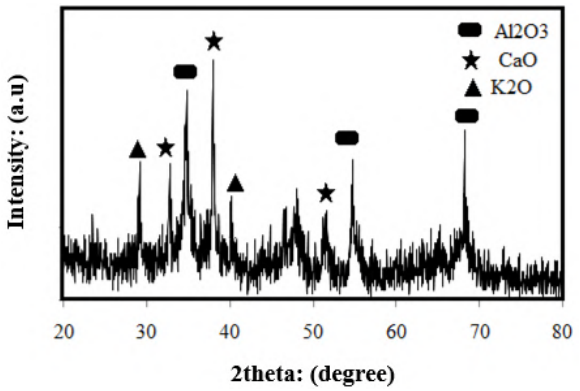

Figure 2. X-ray diffraction of Ca-K/Al_2O_3 nanocatalyst

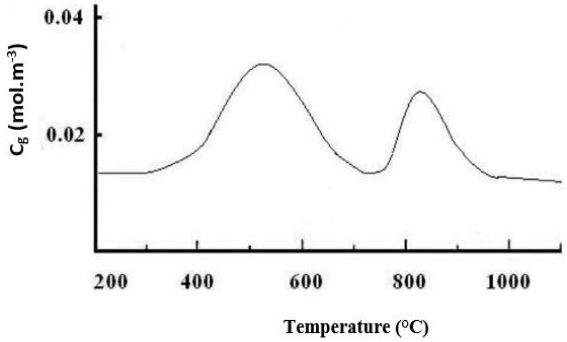

Figure 4. TPD of Ca-K/Al_2O_3 nanocatalyst

TABLE 3. The effect of methanol:oil ratio and catalyst:oil ratio on biodiesel yield

Methanol to oil (w/w %)	Catalyst to oil (w/w %)	Viscosity (cp)	Yield (%)
3	6	10.53	33.70
12	6	3.18	99.29
12	6	3.18	99.29
12	3	5.04	75.48
12	12	3.73	91.59
12	6	3.18	99.29
9	6	4.39	83.15
18	6	3.18	99.23
3	3	11.62	28.68
18	3	3.29	97.70
3	12	10.53	33.70
12	6	3.18	99.29
9	9	3.14	99.89

of methanol to oil was very difficult, and emulsification could take place in washing products. A catalyst possessing powerful basic locations and a big surface area should indicate high activity. In this research, the mass ratio of Ca-K/Al_2O_3 to sunflower oil differed within a range of 3–12%. According to the results obtained, as set out in Table 3, the biodiesel yield percent significantly increased in catalyst oil ratio =9:1.

A model presented by DoE software was fitted with the actual data presented in Equation (2) to describe the effect of the variables examined.

$$\text{Yield} = 49.1140 + 14.5286A + 9.1274B - 0.4111A^2 - 0.3837B^2 - 0.1844AB \quad (2)$$

The ANOVA results on the effect of the variables are summarized in Table 4, where A is the methanol-to-oil ratio and B is the weight fraction of the catalyst (%). The impact on the biodiesel yield was more considerable when the value of coefficients was increased [23]. The impact on the response was raised by raising the value of the F parameter and reducing the P parameter. As can be seen, the remarkable parameters of reaction were included (most to least significant) [24]: methanol-to-oil ratio (14.52) > weight fraction of the catalyst (9.12) > second-order effect of methanol-to-oil ratio (− 0.41) > second-order effect of the weight fraction of the catalyst (− 0.38) > interaction between methanol-to-oil ratio and weight fraction of the catalyst (- 0.18). The F value and the P value were applied to measure the significance of the coefficients (see Table 4). The negative effects of quadratic terms on biodiesel yield in the polynomial expression were shown by their negative coefficients. This result can be related to the experimental range of independent variables selected in this research. The F value and the P value indicated the significance of the coefficients (see Table 4).

The correlation coefficient square for each response was calculated as the coefficient of determination (R^2). The R^2 coefficient presents the proportion of the total response variation forecasted by the model, representing the ratio of squares due to regression (SSR) to total sum of squares (SST). The coefficient of determination R^2 can be examined by the accuracy and variability of the model. It is always between 0 and 1, and when the R^2 value is closer to 1, the model is stronger and predicts the response better [25, 29]. An R^2 value of 0.9 relatively ensures a desirable adjustment of the model to the experimental data.

3. 3. Effect of Reaction Temperature and Reaction Time The experimental findings at various reaction temperatures and times are indicated in Table 5. Reaction temperature can affect the reaction rate as well as biodiesel yield. In this research, the reaction temperature differed within a range of 55–75°C. At low temperatures, the rate of reaction was slow and the biodiesel yield was only 31.59% at 55°C after 60 min.

The biodiesel yield increased with a rise in reaction temperature to approximately 99.7% at 75°C. A shorter reaction time is a preliminary benefit of a higher temperature; however, if the reaction temperature were to be above the boiling point of methanol (64.7°C), the methanol would vaporize and form many bubbles, which would prevent the reaction on the three-phase interface. In the setup applied in this research, a system with a high-performance condenser was applied to prevent high temperature inhibition. Thus, the optimized reaction temperature for sunflower oil transesterification to biodiesel is about 75°C.

Overall, the lipid transformation rate increased as the reaction time increased. At the reaction start, the speed was very low due to the need to combine and distribute alcohol into the oil. After this step for vegetable oil, 80% of the transesterification reaction could be completed in a short period and almost completed in another hour. However, the lipid conversion rate remained relatively

TABLE 4. ANOVA results on the effect of methanol:oil ratio and catalyst:oil ratio

Term	Coefficient (ß)	F value	P value
Constant	-49.114	-	-
A	14.5286	15.30	0.006
B	9.1274	1.87	0.214
A^2	-0.4111	7.53	0.029
B^2	-0.3837	0.68	0.436
AB	-0.1844	0..44	0.529

TABLE 5. The effect of reaction temperature and reaction time on biodiesel yield

Reaction time (h)	Reaction temperature (°C)	Viscosity (cp)	Yield (%)
3	65	6.58	60.22
3	65	6.58	60.22
3	65	6.58	60.22
3	65	6.58	60.22
3	75	3.07	99.70
1	75	9.43	39.59
1	65	10.31	34.80
1	55	10.96	31.59
5	55	8.55	45.05
5	65	3.51	94.60
3	55	9.87	37.12
3	65	6.58	60.22
5	75	3.29	97.70

stable with a further rise in reaction time [17]. In addition, more reaction time resulted in a reduction in product yield because the reversible transesterification lead to ester loss and more fatty acids for soap formation.

Many tests were carried out to investigate the function of the optimum Ca-K/Al_2O_3 catalyst at different reaction times within the range of 1–5 h, at the optimized reaction situations (methanol:oil=9:1, catalyst:oil=9:1, T=75ºC and stirring rate of 500 rpm). The biodiesel yield percent slightly increased with an increase in reaction time. Thus, a reaction time of 3 h for biodiesel production seemed optimal. Owing to increased contact time between reactants, enhancing the reaction time enhances the biodiesel yield, whereas enhancing the reaction time further has no remarkable impact on the biodiesel yield since the balance situation is almost completed [30].

A model presented by DoE software was fitted with the actual data presented in Equation (3) to describe the effect of the variables examined.

$$\text{Yield} = 77.1881 - 12.9134G - 2.5822H - 2.0756G^2 + 0.0248H^2 + 0.5452HG \quad (3)$$

The ANOVA results regarding biodiesel yield are summarized in Table 6, where G is reaction time and H is reaction temperature. Reaction time and interaction between reaction time and reaction temperature were chosen as the effective terms with higher coefficient values than other variables. The F value and the P value specified the significance of the coefficients (see Table 6). The square of the correlation coefficient for every response was measured as the coefficient of determination (R^2). A value of 0.84 for R^2 indicates that some other variables might have interacted on the response, but those variables were not considered in this study.

3. 4. Effect of Weight Fraction of Calcium and Potassium The weight fraction of calcium and potassium can affect the biodiesel product yield, which indicates the relationship of the weight fraction of calcium and potassium with the rate of lipid conversion. With reference to Table 7, when the concentration of potassium was 15% and the concentration of calcium was 20%, the highest lipid conversion rate (97.41%) was obtained. The lipid conversion rate (37.12%) decreased sharply when the concentration of potassium was 20% and the concentration of calcium was 60% and it continued to decrease as the weight fraction of calcium and potassium increased. Increasing the weight fraction of calcium and potassium leads to the production of more soap, which consumes the catalyst and decreases the catalytic efficiency [31].

TABLE 6. ANOVA results on the effect of reaction temperature and reaction time

Source	Coefficient (ß)	F value	P value
Constant	77.1881	-	-
G	-12.9134	0.23	0.644
H	-2.5822	0.06	0.814
G^2	-2.0756	0.91	0.372
H^2	0.0248	0.09	0.769
HG	0.5452	2.46	0.161

TABLE 7. The effects of calcium and potassium weight fraction on biodiesel yield

Ca (%)	K (%)	Viscosity (cp)	Yield (%)
50	10	3.96	88.43
50	5	3.93	88.92
50	15	7.99	48.94
60	20	9.87	37.12
50	10	3.96	88.43
20	15	3.30	97.41
80	5	4.03	87.61
80	20	5.43	71.27
50	10	3.96	88.43
60	15	3.75	91.33
20	5	3.92	89.00
50	10	3.96	88.43
50	10	3.96	88.43

A model presented by DoE software was fitted with the actual data presented in Equation (4) to describe the effect of the variables examined.

$$\text{Yield} = 199.847 + 0.386D - 3.848C - 0.245D^2 + 0.028C^2 + 0.052DC \quad (4)$$

The ANOVA results regarding biodiesel yield are summarized in Table 8, where C is the weight fraction of calcium and D is the weight fraction of potassium. The weight fraction of calcium (%) was selected as the effective term with the highest coefficient value and F value. A value of 0.79 for R^2 indicates that some other variables might have interacted on the response, but those variables were not considered in this study.

3. 5. Effect of Calcination Time and Calcination Temperature The Ca-K/Al_2O_3 nanocatalyst for producing biodiesel was prepared. Thereafter, the impact of different weight percents of Ca to K/Al_2O_3 and various operational conditions on the catalytic function of Ca-K/Al_2O_3 were examined. The experimental findings at various calcination times and temperatures are indicated in Table 9. The best operational conditions were methanol:oil=9:1 and a catalyst-to-oil mass ratio of 9% at 75˚C with mechanical stirring at 500 rpm for 3 h. The optimum catalyst revealed high catalytic performance for producing biodiesel, and the biodiesel yield reached 97%. The physical features, such as viscosity and refractive index, decreased when the biodiesel yield increased; they are suggested as reliable physical properties for calculating biodiesel yield and decreasing the cost of analysis.

A model presented by DoE software was fitted with the actual data presented in Equation (5) to describe the effect of the variables examined.

$$\text{Yield} = -333.362 + 1.210E + 14.554F - 0.001E^2 - 8.421F^2 + 0.059EF \quad (5)$$

The ANOVA results regarding biodiesel yield are presented in Table 10, where E is calcination temperature and F is calcination time. Table 10 presents statistical characteristics of the chosen significant model terms to indicate the biodiesel yield as a function of the variables examined (that is, calcination time and calcination temperature).

TABLE 8. ANOVA results on the effect of calcium and potassium weight fraction

Source	Coefficient (ß)	F value	P value
Constant	199.847	-	-
D	0.386	0.00	0.952
C	-3.848	5.42	0.059
D^2	-0.245	2.01	0.206
C^2	0.028	6.31	0.046
DC	0.052	1.02	0.352

TABLE 9. The effect of calcination time and calcination temperature on biodiesel yield

Temperature (℃)	Time (h)	Viscosity (cp)	Yield (%)
700	3	4.73	78.99
700	3	4.73	78.99
700	3	4.73	78.99
600	3	4.25	84.74
700	3	4.73	78.99
800	1	16.99	13.01
800	4	5.20	73.77
700	3	4.73	78.99
600	4	3.77	90.95
800	3	3.15	98.3
600	1	4.78	77.52
700	4	3.52	94.41
700	2	2.86	98.01

TABLE 10. ANOVA results on the effect of calcination time and calcination temperature

Source	Coefficient (ß)	F value	P value
Constant	-333.362	-	-
E	1.210	0.53	0.489
F	14.554	0.02	0.898
E^2	-0.001	0.96	0.361
F^2	-8.421	1.34	0.285
EF	0.059	0.31	0.597

Based on the analysis, second-order calcination time and calcination temperature are significant terms with higher F values and lower P values than other model terms. The determination coefficient (R^2) was computed to be 0.71, which indicates that some other variables might have interacted on the response, but those variables were not considered in this study.

4. CONCLUSIONS

The Ca-K/Al_2O_3 heterogeneous nanocatalyst was made ready and used in the transesterification of sunflower oil with methanol or the methanolysis of sunflower oil. The effects of effective parameters on transesterification were investigated. The optimum conditions for the catalytic reaction using the Ca-K/Al_2O_3 catalyst were determined

to be 20 wt% Ca and 15 wt% K, a calcination temperature of 800°C for 3 h, a methanol-to-oil ratio of 9:1, a reaction temperature of 75°C, a reaction time of 3 h and a catalyst-to-oil mass ratio of 9%. The optimum catalyst indicated high catalytic function for producing biodiesel, and the biodiesel yield reached 98.3%. The physical features, such as viscosity and refractive index, decreased when biodiesel yield increased; they are suggested as reliable physical properties for calculating biodiesel yield and decreasing the cost of analysis.

5. ACKNOWLEDGEMENT

The authors would like to express their deepest gratitude to Kermanshah's Water and Wastewater Company for the financial support provided for this research. The authors also wish to express their gratitude for the support provided by the Iran Nanotechnology Initiative Council. The authors further express their appreciation for the Razi University (Iran) patronage.

6. REFERENCES

1. Ghoreyshi, A. A., Hassani, M., and Najafpour, G. "A Two-step Catalytic Production of Biodiesel from Waste Cooking Oil." ***International Journal of Engineering, Transaction C: Aspects***, Vol. 26, No. 6, (2013), 563–570. https://doi.org/10.5829/idosi.ije.2013.26.06c.01
2. N., M. K., W., A. B., Toemen, S., and Ali, R. "Biodiesel Production via Transesterification of Low Grade Cooking Oil over Heterostructure Nano Particles of Ni/Mg/Al2O3 Catalyst." ***International Journal of Engineering, Transaction B: Applications***, Vol. 31, No. 8, (2018), 1318–1325. https://doi.org/10.5829/ije.2018.31.08b.21
3. Zullaikah, S., Lai, C.-C., Vali, S. R., and Ju, Y.-H. "A two-step acid-catalyzed process for the production of biodiesel from rice bran oil." ***Bioresource Technology***, Vol. 96, No. 17, (2005), 1889–1896. https://doi.org/10.1016/j.biortech.2005.01.028
4. Knothe, G., and Steidley, K. R. "A comparison of used cooking oils: A very heterogeneous feedstock for biodiesel." ***Bioresource Technology***, Vol. 100, No. 23, (2009), 5796–5801. https://doi.org/10.1016/j.biortech.2008.11.064
5. Mohamad, M., Ngadi, N., Wong, S., Yahya, N. Y., Inuwa, I. M., and Lani, N. S. "Synthesis and Characterization of CaO-TiO2 for Transesterification of Vegetable Palm Oil." ***International Journal of Engineering, Transaction B: Applications***, Vol. 31, No. 8, (2018), 1326–1333. https://doi.org/10.5829/ije.2018.31.08b.22
6. Khalili, M., and Zamani, F. "Development of Clay Foam Ceramic as a Support for Fungi Immobilization for Biodiesel Production." ***International Journal of Engineering, Transaction B: Applications***, Vol. 27, No. 11, (2014), 1691–1696. https://doi.org/10.5829/idosi.ije.2014.27.11b.06
7. Barnard, T. M., Leadbeater, N. E., Boucher, M. B., Stencel, L. M., and Wilhite, B. A. "Continuous-Flow Preparation of Biodiesel Using Microwave Heating." ***Energy & Fuels***, Vol. 21, No. 3, (2007), 1777–1781. https://doi.org/10.1021/ef0606207
8. Willson, R. M., Wiesman, Z., and Brenner, A. "Analyzing alternative bio-waste feedstocks for potential biodiesel production using time domain (TD)-NMR." ***Waste Management***, Vol. 30, No. 10, (2010), 1881–1888. https://doi.org/10.1016/j.wasman.2010.03.008
9. Canakci, M., and Sanli, H. "Biodiesel production from various feedstocks and their effects on the fuel properties." ***Journal of Industrial Microbiology & Biotechnology***, Vol. 35, No. 5, (2008), 431–441. https://doi.org/10.1007/s10295-008-0337-6
10. Vyas, A. P., Verma, J. L., and Subrahmanyam, N. "A review on FAME production processes." ***Fuel***, Vol. 89, No. 1, (2010), 1–9. https://doi.org/10.1016/j.fuel.2009.08.014
11. Ozcanli, M., Gungor, C., and Aydin, K. "Biodiesel Fuel Specifications: A Review." ***Energy Sources, Part A: Recovery, Utilization, and Environmental Effects***, Vol. 35, No. 7, (2013), 635–647. https://doi.org/10.1080/15567036.2010.503229
12. Moser, B. R. "Biodiesel production, properties, and feedstocks." ***In Vitro Cellular & Developmental Biology - Plant***, Vol. 45, No. 3, (2009), 229–266. https://doi.org/10.1007/s11627-009-9204-z
13. Freedman, B., and Bagby, M. O. "Predicting cetane numbers of n-alcohols and methyl esters from their physical properties." ***Journal of the American Oil Chemists' Society***, Vol. 67, No. 9, (1990), 565–571. https://doi.org/10.1007/BF02540768
14. Helwani, Z., Othman, M. R., Aziz, N., Fernando, W. J. N., and Kim, J. "Technologies for production of biodiesel focusing on green catalytic techniques: A review." ***Fuel Processing Technology***, Vol. 90, No. 12, (2009), 1502–1514. https://doi.org/10.1016/j.fuproc.2009.07.016
15. Suppes, G. "Transesterification of soybean oil with zeolite and metal catalysts." ***Applied Catalysis A: General***, Vol. 257, No. 2, (2004), 213–223. https://doi.org/10.1016/j.apcata.2003.07.010
16. Di Serio, M., Ledda, M., Cozzolino, M., Minutillo, G., Tesser, R., and Santacesaria, E. "Transesterification of Soybean Oil to Biodiesel by Using Heterogeneous Basic Catalysts." ***Industrial & Engineering Chemistry Research***, Vol. 45, No. 9, (2006), 3009–3014. https://doi.org/10.1021/ie051402o
17. Montgomery, D.C., Peck, E.A., and Vining, G.G., Introduction to Linear Regression Analysis. John Wiley & Sons, New York, NY, 2001.
18. John, P.W.M., John, P.W., Statistical design and analysis of experiments. 1st edition, Wiley-CH, Weinheim, 1971.
19. Shi, S., Valle-Rodríguez, J. O., Siewers, V., and Nielsen, J. "Prospects for microbial biodiesel production." ***Biotechnology Journal***, Vol. 6, No. 3, (2011), 277–285. https://doi.org/10.1002/biot.201000117
20. Uggetti, E., Llorens, E., Pedescoll, A., Ferrer, I., Castellnou, R., and García, J. "Sludge dewatering and stabilization in drying reed beds: Characterization of three full-scale systems in Catalonia, Spain." ***Bioresource Technology***, Vol. 100, No. 17, (2009), 3882–3890. https://doi.org/10.1016/j.biortech.2009.03.047
21. Pasupulety, N., Gunda, K., Liu, Y., Rempel, G. L., and Ng, F. T. T. "Production of biodiesel from soybean oil on CaO/Al2O3 solid base catalysts." ***Applied Catalysis A: General***, Vol. 452, (2013), 189–202. https://doi.org/10.1016/j.apcata.2012.10.006
22. Sun, H., Ding, Y., Duan, J., Zhang, Q., Wang, Z., Lou, H., and Zheng, X. "Transesterification of sunflower oil to biodiesel on ZrO2 supported La2O3 catalyst." ***Bioresource Technology***, Vol. 101, No. 3, (2010), 953–958. https://doi.org/10.1016/j.biortech.2009.08.089
23. Zangeneh, H., Zinatizadeh, A. A., Rahimi, Z., Zinadini, S., Sadeghi, M., and Abdulgader, M. "Evaluation of dynamic behavior of hydrophilic and photocatalytic self-cleaning PES nanofiltration membrane post treating biologically treated palm oil mill effluent (POME)." ***Chemical Engineering and Processing - Process Intensification***, Vol. 169, , (2021), 108635. https://doi.org/10.1016/j.cep.2021.108635
24. Mousavi, S. A., Zangeneh, H., Almasi, A., Nayeri, D., Monkaresi,

M., Mahmoudi, A., and Darvishi, P. "Decolourization of aqueous methylene blue solutions by corn stalk: modeling and optimization." ***Desalination and Water Treatment***, Vol. 197, (2020), 335–344. https://doi.org/10.5004/dwt.2020.25952

25. Rafiee, E., Noori, E., Zinatizadeh, A., and Zanganeh, H. "([n-C4H9)4 N]3PMo2W9(Sn4+.xH2O)O39/TiO2): a new visible photocatalyst for photodegradation of DR16 characterization and optimization process by RSM." ***Journal of the Iranian Chemical Society***, Vol. 18, No. 7, (2021), 1761–1772. https://doi.org/10.1007/s13738-020-02149-w
26. Thangaraj, B., Solomon, P. R., Muniyandi, B., Ranganathan, S., and Lin, L. "Catalysis in biodiesel production—a review." ***Clean Energy***, Vol. 3, No. 1, (2019), 2–23. https://doi.org/10.1093/ce/zky020
27. Mohammadi, F., Rahimi, M., Parvareh, A., and Feyzi, M. "Biodiesel production from soybean oil using ionic liquid as a catalyst in a microreactor." ***Iranian Journal of Chemical Engineering (IJChE)***, Vol. 15, No. 1, (2018), 102–114. Retrieved from http://www.ijche.com/article_63151.html
28. Lefton, R., Weiss, D., Center for American Progress, 2010, accessed on 12 January 2015. Retrieved from https://www.americanprogress.org
29. Zangeneh, H., Rahimi, Z., Zinatizadeh, A. A., Razavizadeh, S. H., and Zinadini, S. "l-Histidine doped-TiO2-CdS nanocomposite blended UF membranes with photocatalytic and self-cleaning properties for remediation of effluent from a local waste stabilization pond (WSP) under visible light." ***Process Safety and Environmental Protection***, Vol. 136, (2020), 92–104. https://doi.org/10.1016/j.psep.2020.01.022
30. Federer, W. T. "Some Recent Results in Experiment Design with a Bibliography-II: Bibliography A-K on JSTOR." ***International Statistical Review***, Vol. 49, No. 1, (1981), 95–109. Retrieved from https://www.jstor.org/stable/1403040
31. Marchetti, J. M., Miguel, V. U., and Errazu, A. F. "Possible methods for biodiesel production." ***Renewable and Sustainable Energy Reviews***, Vol. 11, No. 6, (2007), 1300–1311. https://doi.org/10.1016/j.rser.2005.08.006

Persian Abstract

چکیده

در این مطالعه، شرایط ترانس استریفیکاسیون روغن آفتابگردان با متانول توسط نانوکاتالیست $Ca\text{-}K/Al_2O_3$ با استفاده از روش پاسخ سطح بهینه‌سازی شد. متغیرهای مورد آزمایش شامل دمای واکنش (۵۵، ٦۵ و ۷۵ درجه سانتی‌گراد)، زمان واکنش (۱، ۲، ۳، ٤ و ۵ ساعت)، نسبت وزنی کاتالیست به روغن (۳، ٤، ۹ و ۱۲ درصد)، محتوای کلسیم (۲۰، ۳۰، ۵۰، ٦۰ و ۸۰ درصد وزنی)، محتوای پتاسیم (۵، ۱۰، ۱۵ و ۲۰)، نسبت مولی متانول به روغن آفتابگردان (۳:۱، ٦:۱، ۹:۱ و ۱۲:۱)، دمای کلسیناسیون (٦۰۰، ۷۰۰ و ۸۰۰ درجه سانتی‌گراد) و زمان کلسیناسیون (۱، ۲، ۳ و ٤ ساعت) بود. مشخصات کاتالیست با استفاده از نتایج XRD، SEM، FTIR، و TPD مورد آنالیز قرار گرفت. حداکثر راندمان تبدیل استرهای متیل اسید چرب (راندمان تولید بیودیزل) ۹۳ درصد بود که در دمای کلسیناسیون ۸۰۰ درجه سانتی‌گراد برای مدت ۳ ساعت، نسبت متانول به روغن معادل ۹:۱، دمای واکنش ۷۵ درجه سانتی‌گراد، زمان واکنش ۳ ساعت و نسبت جرمی کاتالیست به روغن ۹٪ بدست آمد.

IJE TRANSACTIONS B: Applications Vol. 35, No. 02, (February 2022) 360-371

International Journal of Engineering

Journal Homepage: www.ije.ir

A Neutrosophic Fuzzy Programming Method to Solve a Multi-depot Vehicle Routing Model under Uncertainty during the COVID-19 Pandemic

H. Nozari[a], R. Tavakkoli-Moghaddam*[a], J. Gharemani-Nahr[b]

[a] *School of Industrial Engineering, College of Engineering, University of Tehran, Tehran, Iran*
[b] *Faculty Member of Academic Center for Education, Culture and Research, Tabriz, Iran*

PAPER INFO

Paper history:
Received 15 September 2021
Received in revised form 20 October 2021
Accepted 23 October 2021

Keywords:
COVID-19 Pandemic
Multi-depot Vehicle Routing
Neutrosophic Fuzzy Programming
Robust Fuzzy Method

ABSTRACT

The worldwide prevalence of coronavirus disease (COVID-19) and the severe problems in the distribution of medical equipment have led to the modeling of multi-depot vehicle routing under uncertainty in the COVID-19 pandemic. The primary purpose of the proposed model is to locate warehouses and production centers and route vehicles for the distribution of medical goods to hospitals. A robust fuzzy method controls uncertain parameters, such as demand, transmission, and distribution costs. The effect of uncertainty using a neutrosophic fuzzy programming method shows that by increasing demand, the volume of medical goods exchanges and the number of vehicles used to distribute goods increase. This leads to an increase in the total cost of the problem and the amount of greenhouse gas (GHG) emissions. The results also show that using more vehicles reduces staff fatigue to distribute medical products and reduces the prevalence of the COVID-19 pandemic. In the most important sensitivity analysis of the problem on the capacity of the vehicle, it was determined that by increasing the capacity of the vehicle, fewer vehicles are used, and as a result, the cost and amount of greenhouse gas emissions are reduced. On the other hand, this has led to a decrease in the prevalence of the COVID-19 virus.

doi: *10.5829/ije.2022.35.02b.12*

1. INTRODUCTION

Logistics is a recognized science as a value-added activity for companies and their products and services by coordinating activities, such as materials management and management, optimizing resource use, minimizing costs, and maximizing service levels. In traditional systems, traffic flows are provided from one category of the supply chain to another. More flexible systems allow for relocation at one level, divide inventory between wholesalers and thus inventory, and manage costs without changing the level of service [1]. Logistics systems are emerging as an essential tool for competition and efficiency for companies to maintain sustainable business and achieve global scale [2]. Their primary purpose is to coordinate activities (e.g., transportation, order processing, warehousing, inventory management, and maintenance) designated as inventory management. Along with the level of services, the total logistical cost of these activities has become one of the most important economic indicators for the efficiency of a supply chain [3]. In 2014, logistics costs accounted for 11.2% of Brazilian companies' revenues. Vehicle routing and inventory management are essential for logistics systems that directly impact design costs [4].

Dantzig and Ramser [5] first proposed the problem of vehicle routing in 1959. This is a combination of the two issues of the traveling salesman (unlimited consideration of vehicle capacity) and the packing of boxes (zero consideration of freight costs on the ridges), trying to optimally design a set of routes for the transport fleet in such a way that a certain number of customers to be served and has different side restrictions [6]. The variety of this problem is so great that it is challenging and time-consuming to classify them and express the various states in which it occurs. Since its inception in the 1960s, many

*Corresponding Author Email: tavakoli@ut.ac.ir (R. Tavakkoli-Moghaddam).

Please cite this article as: H. Nozari, R. Tavakkoli-Moghaddam, J. Gharemani-Nahr, A Neutrosophic Fuzzy Programming Method to Solve a Multi-depot Vehicle Routing Model under Uncertainty during the COVID-19 Pandemic, ***International Journal of Engineering, Transactions B: Applications*** Vol. 35, No. 02, (2022) 360-371

extensions have been derived based on their different applications in the real world as there are now versions, such as heterogeneous type [7], simultaneous receipt and delivery [8], open type [9], and others [10].

One of the factors is the application of this issue in the real world that has made the issue of vehicle routing as one of the most important issues of combinatorial optimization and has attracted the attention of many researchers. For example, suppose that a factory can reduce the length of time, on when it takes to deliver goods to its customers or the number of its vehicles and thus its cost [10, 11]. Therefore, by reducing the length of the delivery or receipt of goods, the company can provide better services to its customers by reducing the cost of goods and increasing delivery speed [12]. As a result, the company will increase its competitiveness against other similar companies, expand its product market, and ultimately make more profit [13]. In general, inventory and transportation are two important factors in the cost component [14]. This shows why companies and academic researchers are working so hard to find efficient and economical hybrid management systems for transportation and inventory. According to Anderson et al. [4], no commercial systems are available to support decisions about inventory management and vehicle routing issues simultaneously. In this regard, a recurring theme in recent research is the inventory-routing problem (IRP), which results from a combination of vehicle routing and inventory management.

The use of IRP models allows the simultaneous determination of the optimal level of inventory, delivery routes, and vehicle schedules based on the minimum cost criterion. Guemri et al. [15] considered minimizing distribution and inventory costs as the goals of the IRP. They also mentioned some components, including the vehicle and the storage capacity of the facility. According to Coelho et al. [16], scientific research on the IRP is relatively new than optimization issues, such as vehicle routing problems (VRP). They also noted that although several studies have reviewed the literature on inventory management and routing issues, relatively few have examined the integration of these two issues. Inventory systems are hierarchical, with traffic flowing from one floor of the supply chain to another, from manufacturers to wholesalers, and then from wholesalers to retailers. More flexible systems allow for lateral transportation on one level (i.e., between wholesalers or retailers). In this case, members of the same category can share their inventory, which allows them to reduce the inventory level while ensuring some of the required level services. When transport is included, the problem is defined as IRP with transportation (IRPT) [17].

The importance of a multi-depot VRP has led to the inventory discussion leading to the design of a new model under uncertainty under the COVID-19 pandemic. Today, due to the presence of COVID-19, the transportation of products, especially medical equipment, is of the greater importance, and researchers are seeking to provide models to reduce vehicle traffic to reduce congestion and the spread of COVID-19. Considering the stability aspects of the model in the COVID-19 pandemic conditions has led to the design of a multi-depot vehicle routing model consisting of production centers, warehouses, and hospitals. The most important decisions taken in this issue include locating warehouses and production centers, optimal routing of medical equipment transportation to hospitals, determining the optimal amount of inventory in warehouses. Since the demand for medical goods in the pandemic conditions of COVID-19 is very variable, the robust fuzzy method is used to control the demand parameters, transmission, and distribution costs.

The remaining structure of this paper is as follows. Section 2 reviews the research literature and determines the research gap. In Section 3, a model of the VRP is presented several times, and the fuzzy parameters of the problem are controlled using the robust fuzzy method. Section 4 describes the neutrosophic fuzzy programming method as a tri-objective model solution. In section 5, a numerical example and its sensitivity are analyzed. Finally, in section 6, the conclusions of the model and solution method are presented.

2. LITERATURE REVIEW

The importance of vehicle routing has extensively been studied in recent decades with various developments and solutions. One of the areas considered recently in the routing issue is the green VRP, whose objective is to route vehicles considering the effects of the environment and fuel consumption [18]. Sustainable vehicle routing issues are divided into three general routing branches: optimized fuel consumption, environmental pollution, and logistics. In the routing field with optimization of fuel consumption, a model minimization of energy consumption in the VRP was presented. The objective function presented in this model was the product of the distance traveled in the vehicle's total weight, including the weights of the vehicle and cargo [19]. In addition to the distance traveled and the total weight, the vehicle speed was studied to calculate the fuel consumption in the time-dependent VRP and solved using the refrigeration simulation algorithm. Of course, a mathematical model for the problem was not presented [20].

Xiao et al. [21] considered a capacity routing problem in the distribution of goods minimizing fuel consumption and used a refrigeration simulation algorithm. The problem of cross-docking two-tier vehicle routing in a three-tier supply chain includes suppliers, cross-dock, and retailers. Two levels (i.e., suppliers and cross-docks)

of network routing are considered and solved by the genetic algorithm (GA) and local search method [22]. The open VRP uses cross storage while comparing the results of CPLEX and refrigeration simulation algorithm [23]. Lalla-Ruiz et al. [24] proposed a new mathematical model for the multi-depot VRP by adding further limitations to previous papers. The computational results obtained from the sample problems showed the high efficiency of the mathematical model. Du et al. [25] developed a fuzzy linear programming model to minimize the risk of expected transportation when preparing hazardous materials and transporting products from different warehouses to customers. To solve the problem, four meta-innovative algorithms (i.e., GA, particle swarm optimization, refrigeration simulation, and ant colony optimization) were used, and comparisons were made between the proposed algorithms by providing numerical examples.

Alinaghian and Shokouhi [26] presented a mathematical model to solve the reservoir routing problem. The objective function of this model was to minimize the number of vehicles and then minimize the distance between the total routes traveled. Each vehicle's cargo space has several sections; each tank is assigned to one type of product. They used a hybrid algorithm to solve the model and compared the obtained results with the results of the exact method, which concluded that the hybrid algorithm presented by them has high efficiency in problem-solving. Brandao [27] designed an open VRP with a time window in mind and used an iterative local search algorithm to solve it. This algorithm was used for larger size data and was implemented on a total of 418 sample problems. The results showed the high efficiency of this algorithm in solving larger-sized problems. Polyakovskiy et al. [28] examined and modeled the product layout problem in two-dimensional space. For this purpose, they presented a mixed-integer linear programming (MILP) model and solved the model in small sizes by CPLEX software. They also used innovative algorithms to solve problems in larger sizes. Ghahramani et al. [29] implemented a new fuzzy method in a closed-loop supply chain (CLSC) network, including locating potential facilities and optimally allocating product flows. They used the whale optimization algorithm to solve their model and showed that the efficiency of the proposed algorithm is higher than the existing algorithms. Li et al. [30] determined the optimal location of warehouses and vehicle routing. They used the firewall algorithm to solve the problem. Sadati et al. [31] presented a skeleton game to determine the optimal location of warehouses and vehicle routing to reduce costs. In the first and second levels, the decision-maker as the leader chooses the facility's optimal location and determines the vehicles' optimal route, respectively. Mojtahedi et al. [32]. Developing a sustainable vehicle routing problem considering different fleet sizes for coordinated solid waste management.

Zhang et al. [33] considered a multi-depot green VRP and proposed an ant colony algorithm to solve the problem. In their study, a significant limitation is the vehicle capacity added to the model to make it more meaningful and closer to the real world. Dell Amico et al. [34] solved their model by the branch-and-price algorithm and examined their problem under various problems. Mirzaei and Seifi [35] considered the IRP for perishable goods and proposed a combined algorithm of tabu search of simulated annealing to solve large-sized problems. Soysal et al. [36] proposed an IRP model for perishable products based on environmental impacts and uncertainty demand. This model was confirmed through a case study of a fresh tomato supply chain. Nunes Bezerra et al. [37] proposed a location-inventory model for a CLSC and considered an integer nonlinear programming model under some constraints. Guimarães et al. [38] minimized the loss of the IRP using a GA. Chen et al. [39] modeled a VRP to distribute food among residents under COVID-19 conditions. They used the PEABCTS algorithm to solve the problem. Xu et al. [40] proposed a mixed-integer linear programming model to optimize the routing problem of the benzene emergency distribution vehicle by considering the time window. They used a particle swarm optimization algorithm to solve the problem. Ghiyasvand et al. [41] modeled and solved the home health care routing and scheduling problem with public and private transportation modes. The objective minimizes the total travel distance and overtime costs. They used three algorithms (i.e., IWO, GOA, and SA) to solve their problem.

Saffarian et al. [2] developed a hybrid genetic-simulated annealing-auction algorithm for a fully fuzzy multi-period multi-depot vehicle routing problem. The obtained results showed that the algorithm provides satisfactory results in terms of different performance criteria. Salamati [42] considered an Integrated Neutrosophic SWARA and VIKOR method for ranking risks of green supply chain. Fallah and Nozari [43] used neutrosophic mathematical programming for optimization of multi-objective sustainable biomass supply chain network design. By examining the rate of uncertainty, it was observed that with increasing this rate, the total costs of supply chain network design, greenhouse gas emissions, and product transfer times have increased. In contrast, the potential employment rate of individuals has decreased. Islam et al [44] introduced a novel particle swarm optimization-based grey model to predict warehouse performance. Beiki et al [45] developed a multi-objective model as a multi-vehicle relief logistic problem considering satisfaction levels by concerning the environmental conditions paying attention to uncertainty. To solve the problem, an

exact solver by using the epsilon-constraint method is conducted to validate the model. Fallahtafti et al [46] proposed a two-echelon location routing framework for cash-in-transit. To mitigate the risk of robbery in cash transportation, a dynamic risk index is considered. The case study is researched in more depth to obtain managerial insights. The results show that depending on the risk or cost efficiency of the solutions on a Pareto frontier, the risk of traversing longer routes or transporting more significant amounts of cash can be determined in locating new bank vaults.

By examining the literature, some researchers have modeled the multi-depot VRP, each of which has unique characteristics. Therefore, considering the comprehensiveness of the model, the main features of the present paper can be summarized as follows:

- Considering the sustainability in the multi-depot VRP in COVID-19 pandemic conditions.
- Using the neutrosophic fuzzy programming method to solve the problem.
- Using the robust fuzzy method to control demand, transfer, and operating costs.

3. PROBLEM DEFINITION AND MODELING

According to Figure 1, this paper presents a multi-depot vehicle routing model for distributing essential medical supplies to hospitals under the COVID-19 pandemic. Accordingly, the main goal is to make integrated strategic and tactical decisions for the location of warehouses and the routing of the vehicle for the distribution of medical goods. According to this figure, as the last level of the supply chain, several hospitals have different demands for essential medical goods in different periods. Each warehouse has a level of inventory capacity that, after receiving the demand of hospitals, distributes medical goods to hospitals based on its inventory. Each hospital has a time window to receive essential medical supplies. This is due to the reduced traffic for the outbreak of the COVID-19 virus. In case of a shortage of inventory, the warehouses send their order for production to the production centers.

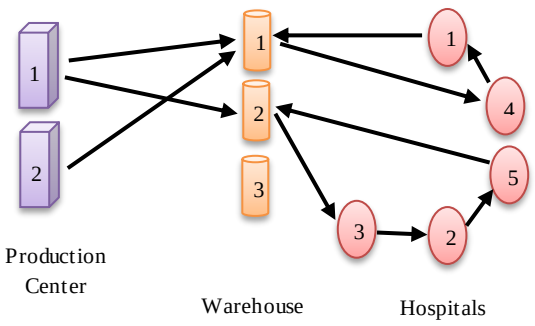

Figure 1. Multi-depot vehicle routing network

In this paper, in addition to the objective function of reducing the costs of location, routing and inventory of goods, the economic and social aspects are also addressed (i.e., minimizing greenhouse gas emissions and reducing the maximum working hours of drivers). Therefore, the timely delivery of medical goods according to a difficult time window leads to social distance, and the prevalence of the COVID-19 virus is reduced due to reduced driver density. Considering the mentioned aspects in problem modeling will lead to the closeness of the model to the real world, given that the multi-depot vehicle routing model is considered in sustainable conditions. Therefore, in one of the objective functions, the environmental aspect is discussed. Hence, minimizing greenhouse gas emissions as an environmental aspect has been proposed as an objective function in the problem. According to the definition of the above problem, the multi-depot VRP can be modeled according to the following assumptions:

- It is a multi-period and multi-product model.
- The number and location of hospitals are fixed and known in advance.
- All the capacity of production centers and warehouses is known and specified.
- A difficult time window is set for the distribution of essential medical supplies.
- Medical goods are transported from a production center to hospitals to minimize pollution with identical vehicles.
- Demand parameters, transmission costs, and distribution costs are considered indefinitely, and fuzzy triangular numbers are considered.

In the following, according to the problem assumptions, the symbols used in problem modeling are described. These symbols include model sets, parameters, and decision variables.

3. 1. Sets

K	Set of production centers
L	Set of warehouses
C	Set of hospitals
P	Set of medical goods
T	Period set
V	Set of vehicles

3. 2. Parameters

H_k	Cost of establishing warehouse k
U_l	Cost of establishing distribution center l
F_v	Fixed cost of using vehicle v
$\tilde{T}_{k,l,v}$	The cost of transportation between production center k and warehouse l by vehicle v
$\tilde{T}_{l,c,v}$	The cost of transportation between warehouse l and hospital c by vehicle v $l, c \in L \cup C$

$Co2_{k,l,v}$ The amount of greenhouse gas emissions in the movement of vehicle v between production center k and warehouse l

$Co2_{l,c,v}$ The amount of greenhouse gas (GHG) emissions in the movement of vehicle v between warehouse l and hospital c $(l,c \in L \cup C)$

$Ti_{l,c,v}$ Transportation time between warehouse l and hospital c by vehicle v $(l,c \in L \cup C)$

$H_{l,p}$ The cost of maintaining each unit of medical goods p in warehouse l

$\tilde{C}_{l,p}$ Cost of distribution per unit of medical goods p by warehouse l

$\widetilde{Dem}_{c,p,t}$ Hospital c demand for medical goods p in period t

$CapK_{k,p}$ Maximum capacity of the production center k of the production of medical goods p

$CapL_{l,p}$ Maximum capacity of warehouse l of storage and distribution of medical goods p

Cap_v Maximum capacity of vehicle v

$[AH_c, BH_c]$ Hard time window for delivery of medical goods to hospital c

3. 3. Decision Variables

$X_{k,l,p,t}$ Amount of medical goods p transferred between production center k and warehouse l in period t

$V'_{l,p,t}$ The total amount of medical goods p transferred from warehouse l in period t

$Q_{l,p,t}$ Inventory level of medical goods p in stock l in period t

Z_k 1 if production center k is established; 0, otherwise

Z_l 1 if warehouse l is established; 0, otherwise

Z_v 1 if vehicle v is used; 0, otherwise

$Y_{l,c,t}$ 1 if hospital c is allocated to warehouse l in period t; 0, otherwise

$Z_{l,c,v,t}$ 1 if hospital c is visited by vehicle v in period t after warehouse l; 0, otherwise $(l,c \in L \cup C)$

$U_{c,v,t}$ Auxiliary variable for sub-tour remove constraint

$R_{k,l,v,t}$ 1 if the route between production center k and warehouse l is visited by vehicle v in period t; 0, otherwise

$Tc_{l,c,v,t}$ Time of arrival of vehicle v to hospital c and out of warehouse l in period t

$Tw_{l,v,t}$ Maximum working hours of the driver of vehicle v who leaves warehouse l in period t

3. 4. Multi-depot VRP Model Given the expression of the sets, parameters, and decision variables expressed, the multi-depot VRP under the COVID-19 pandemic as a mixed-linear programming model is as follows:

$$\text{Min } \omega 1 = \sum_{k=1}^{K} H_k Z_k + \sum_{l=1}^{L} U_l Z_L + \sum_{v=1}^{V} F_v Z_v + \sum_{l=1}^{L\cup C}\sum_{c=1}^{L\cup C}\sum_{v=1}^{V}\sum_{t=1}^{T} \tilde{T}_{l,c,v} Z_{l,c,v,t} + \sum_{k=1}^{K}\sum_{l=1}^{L}\sum_{v=1}^{V}\sum_{t=1}^{T} \tilde{T}_{k,l,v} R_{k,l,v,t} + \sum_{l=1}^{L}\sum_{p=1}^{P}\sum_{t=1}^{T} H_{l,p} Q_{l,p,t} + \sum_{l=1}^{L}\sum_{p=1}^{P}\sum_{t=1}^{T} \tilde{C}_{l,p} V'_{l,p,t} \quad (1)$$

$$\text{Min } \omega 2 = \sum_{l=1}^{L\cup C}\sum_{c=1}^{L\cup C}\sum_{v=1}^{V}\sum_{t=1}^{T} Co2_{l,c,v} Z_{l,c,v,t} + \sum_{k=1}^{K}\sum_{l=1}^{L}\sum_{v=1}^{V}\sum_{t=1}^{T} Co2_{k,l,v} R_{k,l,v,t} \quad (2)$$

$$\text{Min } \omega 3 = max\{TW_{l,v,t}, \quad \forall l \in L, v \in V, t \in T\} \quad (3)$$

s. t.

$$\sum_{c=1}^{C}\sum_{l=1}^{C\cup L}\sum_{p=1}^{P} \widetilde{Dem}_{c,p,t} Z_{l,c,v,t} \le Cap_v Z_v, \quad \forall v,t \quad (4)$$

$$V'_{l,p,t} = \sum_{c=1}^{C}\sum_{v=1}^{V} \widetilde{Dem}_{c,p,t} Z_{l,c,v,t}, \quad \forall l,p,t \quad (5)$$

$$\sum_{v=1}^{V}\sum_{l=1}^{C\cup L} Z_{l,c,v,t} = 1, \quad \forall c,t \quad (6)$$

$$Q_{l,p,t} = \sum_{k=1}^{K} X_{k,l,p,t} + Q_{l,p,t-1} - V'_{l,p,t}, \quad \forall l,p,t \quad (7)$$

$$U_{m,v,t} - U_{c,v,t} + |C| Z_{m,c,v,t} \le |C| - 1, \quad \forall m,c \in C, v, t \quad (8)$$

$$\sum_{c=1}^{C\cup L} Z_{l,c,v,t} = \sum_{c=1}^{C\cup L} Z_{c,l,v,t}, \quad \forall v,t,l \in C \cup L \quad (9)$$

$$\sum_{l=1}^{L}\sum_{c=1}^{C} Z_{l,c,v,t} \le 1, \quad \forall v,t \quad (10)$$

$$-Y_{l,c,t} + \sum_{u=1}^{C\cup L}\left(Z_{l,u,v,t} + Z_{u,c,v,t}\right) \le 1, \quad \forall l,c,v,t \quad (11)$$

$$\sum_{l=1}^{L} X_{k,l,p,t} \le CapK_{k,p} Z_k, \quad \forall k,p,t \quad (12)$$

$$V'_{l,p,t} + Q_{l,p,t} \le CapL_{l,p} Z_l, \quad \forall l,p,t \quad (13)$$

$$\sum_{p=1}^{P} X_{k,l,p,t} \le \sum_{p=1}^{P} Cap_v R_{k,l,v,t}, \quad \forall k,l,t \quad (14)$$

$$Tc_{l,c,v,t} \ge Ti_{l,c,v} - M.\left(1 - Z_{l,c,v,t}\right), \quad \forall l,c,v,t \quad (15)$$

$$Tc_{l,m,v,t} \ge Tc_{l,c,v,t} + Ti_{c,m,v} - M.\left(2 - Z_{c,m,v,t} - Y_{l,c,t}\right), \quad \forall l,c,m,v,t \quad (16)$$

$$Tc_{l,c,v,t} \le BH_c.Z_{l,c,v,t}, \quad \forall l,c,v,t \quad (17)$$

$$Tc_{l,c,v,t} \ge AH_c.Z_{l,c,v,t}, \quad \forall l,c,v,t \quad (18)$$

$$Tw_{l,v,t} \ge Tc_{l,c,v,t} + Ti_{c,l,v} Z_{c,l,v,t}, \quad \forall l,c,v,t \quad (19)$$

$$\sum_{k=1}^{K} R_{k,l,v,t} \le \sum_{c=1}^{C} Z_{l,c,v,t}, \quad \forall l,v,t \quad (20)$$

$$X_{k,l,p,t}, V'_{l,p,t}, Q_{l,p,t}, U_{c,v,t}, Tc_{l,c,v,t}, Tw_{l,v,t} \geq 0 \quad (21)$$

$$Z_k, Z_l, Z_v, Y_{l,c,t}, Z_{l,c,v,t}, R_{k,l,v,t} \in \{0,1\} \quad (22)$$

Equation (1) represents the first objective function value of the considered problem and minimize the total costs of location, routing, and inventory. Equation (2) minimizes GHG emissions between supply chain network levels. Equation (3) minimizes the maximum working hours of drivers in each time period. This relationship acts as an equilibrium relationship in the distribution of working hours between the drivers of each vehicle. Equation (4) shows the maximum transport capacity of the product available by the vehicle. Equation (5) shows the total flow of products (demand) in stock for transport to hospitals. Equation (6) ensures that each warehouse can only be allocated to one hospital. Equation (7) calculates the amount of inventory at the end of the period in the selected warehouse. Equation (8) is a constraint on sub-net removal. Equation (9) ensures that the vehicle can enter and leave each hospital only once.

Equations (10) and (11) ensure that the starting and ending points of the vehicle routing in the delivery of medical supplies to hospitals are the selected warehouse. Equations (12) and (13) show, respectively, the location of production and warehousing centers and ensure that their capacity for the production/distribution and storage of medical goods cannot be used until such centers are selected. Equation (14) shows the vehicle used to transport medical goods between production centers and warehouses. Equation (15) shows the time of arrival of the vehicle to the first hospital. Equation (16) shows the vehicle's arrival time to other hospitals based on the loading and unloading time and the traffic between nodes. Equations (17) and (18) ensure that the vehicle's arrival time to each hospital must be within a strict time frame. Equation (19) calculates the maximum working hours of the vehicle driver. Equation (20) shows the planned transport and ensures that the vehicle, upon entering the warehouse, is also responsible for distributing medical supplies to the hospitals. Equations (21) and (22) show the type of decision variables.

3. 5. Controlling the Uncertain Parameters with a Robust Fuzzy Method Because of the dynamic and volatile nature of some important parameters (including transportation, operating, and demand costs) that are beyond planning, as well as the unavailability and even unavailability of historical data required at the design stage, these parameters are mainly based on expert opinions and experiences are estimated; Therefore, the above ambiguous parameters are formulated as indeterminate data in the form of triangular fuzzy numbers [47]. It is worth noting that it is difficult or sometimes impossible to assess the cost of transportation, operations, and definite demand for long-term decisions. Even if one can estimate a distribution function for these parameters, they may not behave similarly to previous data. Therefore, these parameters, which change in a long-term planning horizon, are considered as uncertain data. With this in mind, the robust fuzzy method is used to control the uncertain parameters of the considered problem.

$$\begin{aligned}&\text{Min } \omega 1 = E[\omega 1] + \xi\left(E[\omega 1] - \omega 1_{(\min)}\right) + \eta \\ &\sum_{c=1}^{C}\sum_{p=1}^{P}\sum_{t=1}^{T}\sum_{l=1}^{L\cup C}\left(\begin{matrix} Dem^3_{c,p,t} - Dem^2_{c,p,t} - \\ \alpha\left(Dem^3_{c,p,t} - Dem^2_{c,p,t}\right)\end{matrix}\right) Z_{l,c,v,t}\end{aligned} \quad (24)$$

$$\begin{aligned}&E[\omega 1] = \sum_{k=1}^{K} H_k Z_k + \sum_{l=1}^{L} U_l Z_L + \sum_{v=1}^{V} F_v Z_v + \\ &\sum_{l=1}^{L\cup C}\sum_{c=1}^{L\cup C}\sum_{v=1}^{V}\sum_{t=1}^{T}\left(\frac{T^1_{l,c,v}+2T^2_{l,c,v}+T^3_{l,c,v}}{4}\right) Z_{l,c,v,t} + \\ &\sum_{k=1}^{K}\sum_{l=1}^{L}\sum_{v=1}^{V}\sum_{t=1}^{T}\left(\frac{T^1_{k,l,v}+2T^2_{k,l,v}+T^3_{k,l,v}}{4}\right) R_{k,l,v,t} + \\ &\sum_{l=1}^{L}\sum_{p=1}^{P}\sum_{t=1}^{T} H_{l,p}\, Q_{l,p,t} + \\ &\sum_{l=1}^{L}\sum_{p=1}^{P}\sum_{t=1}^{T}\left(\frac{C^1_{l,p}+2C^2_{l,p}+C^3_{l,p}}{4}\right) V'_{l,p,t}\end{aligned} \quad (25)$$

$$\begin{aligned}&\omega 1_{(\min)} = \sum_{k=1}^{K} H_k Z_k + \sum_{l=1}^{L} U_l Z_L + \sum_{v=1}^{V} F_v Z_v + \\ &\sum_{l=1}^{L\cup C}\sum_{c=1}^{L\cup C}\sum_{v=1}^{V}\sum_{t=1}^{T} T^1_{l,c,v} Z_{l,c,v,t} + \\ &\sum_{k=1}^{K}\sum_{l=1}^{L}\sum_{v=1}^{V}\sum_{t=1}^{T} T^1_{k,l,v} R_{k,l,v,t} + \\ &\sum_{l=1}^{L}\sum_{p=1}^{P}\sum_{t=1}^{T} H_{l,p}\, Q_{l,p,t} + \\ &\sum_{l=1}^{L}\sum_{p=1}^{P}\sum_{t=1}^{T} C^1_{l,p}\, V'_{l,p,t}\end{aligned} \quad (26)$$

$$\begin{aligned}&\sum_{c=1}^{C}\sum_{l=1}^{C\cup L}\sum_{p=1}^{P}\left(\alpha Dem^3_{c,p,t} + (1 - \right. \\ &\left.\alpha)\, Dem^2_{c,p,t}\right) Z_{l,c,v,t} \leq Cap_v Z_v, \quad \forall v, t\end{aligned} \quad (27)$$

$$\begin{aligned}&V'_{l,p,t} = \\ &\sum_{c=1}^{C}\sum_{v=1}^{V}\left(\begin{matrix}\alpha Dem^3_{c,p,t} + \\ (1-\alpha)\, Dem^2_{c,p,t}\end{matrix}\right) Z_{l,c,v,t}, \quad \forall l, p, t\end{aligned} \quad (28)$$

Equations (2), (3), (6) – (23) (29)

In Equation (24), the first term refers to the expected value of the first objective function using the mean values of the uncertain parameters of the model. The second term refers to the cost of the penalty for deviating from the expected value of the first objective function (optimality stability). The third term also shows the total cost of the demand deviation penalty (uncertain parameter). Therefore, parameter ξ is the weight coefficient of the objective function, and η is the penalty for not estimating the demand. The parameter α, as the rate of uncertainty, indicates the value of the levels of fuzzy numbers, which must be a number between 0.1 and 0.9.

4. NEUTROSOPHIC FUZZY PROGRAMMING METHOD

Since the model is considered a multi-objective problem, the neutrosophic fuzzy method is thus proposed to solve

the problem in this paper. Multi-objective decision models are the most common type of mathematical model that have conflicting goals. In such cases, the aim is to achieve the optimal value of all conflicting objective functions simultaneously. In such problems, the decision-maker expresses the importance of his/her preferences by providing an optimal weight $\beta \in [0,1]$ to each objective function. With a high value of β weight in an objective function value, the decision-maker's preference in that function is higher. Zimmermann [48] maximized decision-making preferences in simultaneously achieving objective function values by introducing a multi-objective fuzzy programming method. Developing a multi-objective fuzzy programming method called intuitive fuzzy programming could solve various mathematical problems in the following years. In these programming methods, flexibility in element membership functions was also possible.

This method has been studied in various real-life issues and problems extensively. In recent years, it has been observed that living conditions may have neutral thoughts about an element in the set. Neutral or uncertain ideas about the elements fall between a degree of falsehood and truth. Thus, by developing the intuitive fuzzy programming method, Smarandache [49] examined the neutrosophic fuzzy programming method, which has three sets of memberships: truth (i.e., degree of belonging), uncertainty (i.e., degree of belonging to some extent), and falsehood (i.e., degree of non-belonging). According to the neutrosophic fuzzy programming method developed in this paper, the sustainable biomass supply chain network model with four conflicting objective functions is solved. Hence, each objective function has three terms: truth membership, non-determination, and falsehood. Therefore, the neutrosophic fuzzy programming method is important in optimizing multi-objective problems by considering neutral thoughts.

Consider a multi-objective model, where D represents a set of fuzzy decisions, G is a set of fuzzy objective functions, and C represents fuzzy constraints. Therefore, the set of fuzzy decisions is represented as $D = G \cap C$. The set of fuzzy neutrosophic decisions (D_n) along with the set of neutrosophic fuzzy target functions (G_o) and the set of neutrosophic fuzzy constraints (C_m) are expressed as follows:

$$D_n = (\cap_{o=1}^{O} G_o)(\cap_{m=1}^{M} C_m) = \\ \left(w, P_D(w), Q_D(w), R_D(w)\right) \tag{30}$$

s. t.

$$P_D(w) = \begin{Bmatrix} min\ PG_o(w), & \forall o \in O \\ s.t. & \\ PC_m(w), & \forall m \in M \end{Bmatrix}$$

$$Q_D(w) = \begin{Bmatrix} max\ QG_o(w), & \forall o \in O \\ s.t. & \\ QC_m(w), & \forall m \in M \end{Bmatrix}$$

$$R_D(w) = \begin{Bmatrix} max\ RG_o(w), & \forall o \in O \\ s.t. & \\ RC_m(w), & \forall m \in M \end{Bmatrix}$$

where $P_D(w)$ is a truth membership function, $R_D(w)$ is a non-deterministic membership function, and $R_D(w)$ is a false membership function under neutrosophic fuzzy decisions D_n. Each of the above membership functions has a top and bottom boundary, which is obtained as the following relation for all membership functions:

$$U_o = max\left(Z_o(X)\right) \\ L_o = min\left(Z_o(X)\right) \tag{31}$$

Therefore, the upper and lower bounds of the neutrosophic fuzzy membership function can be calculated for truth, non-determination, and falsehood, respectively, as follows.

$$U_o^P = U_o, \quad L_o^P = L_o \\ U_o^Q = L_o^P + a_o, \quad L_o^Q = L_o \\ U_o^R = U_o^P, \quad L_o^R = L_o^P + b_o \tag{32}$$

In the above relation a_o and b_o is a predefined value between 0 and 1. Given the above, the linear membership function for a neutrosophic fuzzy framework is as follows.

$$D_n = (\cap_{o=1}^{O} G_o)(\cap_{m=1}^{M} C_m) = \\ \left(w, P_D(w), Q_D(w), R_D(w)\right) \tag{33}$$

$s.t.$:

$$P_o\left(Z_o(X)\right) = \begin{Bmatrix} 1 & if \quad Z_o(X) < L_o^P \\ \frac{U_o^P - Z_o(X)}{U_o^P - L_o^P} & if \quad L_o^P \le Z_o(X) \le U_o^P \\ 0 & if \quad Z_o(X) > U_o^P \end{Bmatrix}$$

$$Q_o\left(Z_o(X)\right) = \begin{Bmatrix} 1 & if \quad Z_o(X) < L_o^Q \\ \frac{U_o^Q - Z_o(X)}{U_o^Q - L_o^Q} & if \quad L_o^Q \le Z_o(X) \le U_o^Q \\ 0 & if \quad Z_o(X) > U_o^Q \end{Bmatrix}$$

$$R_o\left(Z_o(X)\right) = \begin{Bmatrix} 1 & if \quad Z_o(X) > U_o^R \\ \frac{Z_o(X) - L_o^R}{U_o^R - L_o^R} & if \quad L_o^R \le Z_o(X) \le U_o^R \\ 0 & if \quad Z_o(X) < L_o^R \end{Bmatrix}$$

Therefore, the controlled model of the multi-depot VRP under COVID-19 pandemic conditions by a neutrosophic fuzzy programming method based on the above equations is as follows:

$$\begin{aligned}
&\max \textstyle\sum_{o=1}(\mu_o + \vartheta_o - \delta_o)\\
&\text{s.t.}\\
&P_o\big(Z_o(X)\big) \geq \mu_o, \quad \forall o\\
&Q_o\big(Z_o(X)\big) \geq \vartheta_o, \quad \forall o\\
&R_o\big(Z_o(X)\big) \leq \delta_o, \quad \forall o\\
&\mu_o \geq \vartheta_o, \quad \forall o\\
&\mu_o \geq \delta_o, \quad \forall o\\
&0 \leq \delta_o + \mu_o + \vartheta_o \leq 3, \quad \forall o\\
&\delta_o, \mu_o, \vartheta_o \in (0,1)\\
&Equations\ (24-29)
\end{aligned} \tag{34}$$

5. PROBLEM ANALYSIS

5. 1. Solving the Small-sized Problem In this section, considering the three objective functions of the mathematical model, a numerical example is designed to analyze and solve the small-sized problem by a neutrosophic fuzzy programming method. This test problem consists of 3 production centers, 3 warehouses, 4 hospitals, 2 types of medical goods, 5 types of vehicles, 2 periods, and random data based on uniform distribution function as described in Table 1. Using random data based on the uniform distribution function is the lack of access to real-world data.

Table 2 shows the membership functions for the neutrosophic fuzzy method for truth, non-determination, and falsehood, respectively. Using Equation (34), the efficient solution obtained using the membership functions obtained is also shown in this table.

According to the obtained efficient solution, it is observed that the total cost, the amount of GHG emission, and the maximum working hours of drivers are 45305, 252, and 46, respectively. Therefore, Figure 2 shows the output variables of the problem based on the solution obtained from the neutrosophic fuzzy programming method. Based on the results of this figure, it can be stated that when the three objective functions are optimized simultaneously, the number of warehouses constructed and the type and routing of vehicles will change. Therefore, it can be seen that two warehouses are used to distribute medical goods to hospitals. On the other hand, it can be said that the vehicle is routed with minimal driver density, and this leads to a possible reduction in the prevalence of the COVID-19 virus.

TABLE 1. Values of the problem parameters based on the uniform distribution function

Parameter	Approximate interval	Parameter	Approximate interval
H_k, U_l	$\sim U[10000,12000]$	$CapK_{k,p}$	$\sim U[25,60]$
F_v	$\sim U[1000,2000]$	$CapL_{l,p}$	$\sim U[25,60]$
$Co2_{k,l,v}$	$\sim U[30,40]$	Cap_v	$\sim U[150,160]$
$Ti_{l,c,v}$	$\sim U[10,30]$	AH_c	$\sim U[5,10]$
$H_{l,p}$	$\sim U[3,5]$	BH_c	$\sim U[150,300]$
Parameter	**Optimistic**	**Possible**	**Pessimistic**
$Dem_{c,p,t}$	$\sim U[20,25]$	$\sim U[25,30]$	$\sim U[30,35]$
$T_{k,l,v}, T_{l,c,v}$	$\sim U[10,15]$	$\sim U[15,20]$	$\sim U[20,25]$
$C_{l,p}$	$\sim U[1,2]$	$\sim U[2,3]$	$\sim U[3,4]$

TABLE 2. Membership functions obtained from the neutrosophic fuzzy method

	$\omega 1$	$\omega 2$	$\omega 3$
Upper bound	75148	281	48
Lower bound	34703	234	36
U_o^P	75148	281	48
U_o^Q	75182	293	50
U_o^R	75148	281	48
L_o^P	34703	234	36
L_o^Q	34703	234	36
L_o^R	34810	240	38
Solution	45305	252	46

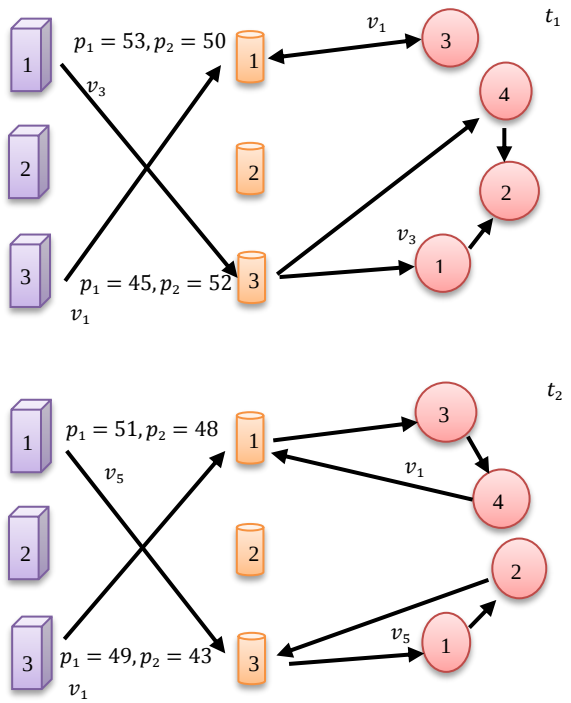

Figure 2. Routing of a multi-warehouse vehicle based on the neutrosophic fuzzy method

5. 2. Sensitivity Analysis In this section, the effect of the behavior of output variables due to changes in the main parameters of the model is investigated. Therefore, first, the effect of the behavior of the values of the objective functions in exchange for changes in the uncertainty rate is investigated. Considering the efficient solution of the problem with the neutrosophic fuzzy method at an uncertainty rate of 0.5, Table 3 shows the values of the objective functions of the problem at different rates of uncertainty.

According to the results of Table 3, it can be stated that by increasing the uncertainty rate, due to the increase in production and distribution volume and limited capacity of vehicles, more equipment should be used to distribute and transfer medical goods from the production center to the warehouse. Accordingly, the costs of the entire network increase. While increasing the number of vehicles and the proper distribution of goods between vehicles, the drivers' maximum working hours decrease, and the amount of GHG emissions increases. Also, by examining the effect of the uncertainty rate, it can be concluded that by increasing the uncertainty rate, due to an increase in the number of vehicles and the number of people involved in the distribution of medical goods, the probability of increasing the prevalence of COVID-19 increases. Figure 4 shows the trend of changes in the objective function values of the problem in exchange for changes in the rate of uncertainty.

In the following and another analysis, changes in the objective function values in exchange for changes in the time window of delivery of medical goods to the hospital are examined. Since the intended time window is of the hard type, vehicles must meet the hospital's request within the stipulated time and have no right to exceed that time. Table 4 shows the changes in the objective function values of the problem in exchange for changes in the upper bound of the time window. According to the results of this table, it is observed that by reducing the upper limit of the time window, due to the limited delivery time

TABLE 3. Trend of changing the objective function values of the problem in exchange for changes in the uncertainty rate

α	$\omega 1$	$\omega 2$	$\omega 3$
0.1	42523	229	52
0.2	43125	236	50
0.3	44268	240	50
0.4	44923	248	48
0.5	45305	252	46
0.6	45823	258	46
0.7	45936	263	45
0.8	46290	271	42
0.9	46730	283	42

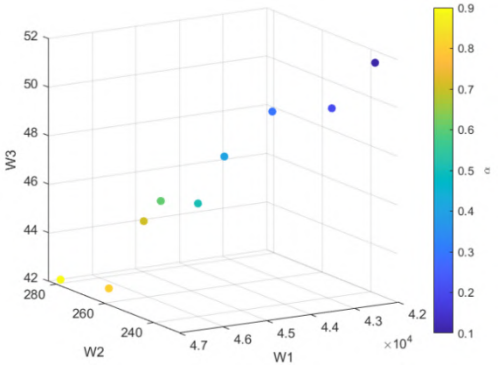

Figure 4. Trend of changing the objective function values of the problem in exchange for changes in the amount of the uncertainty rate

of hospital demand, vehicles have to travel shorter routes. Therefore, the need to use more vehicles is evident. Therefore, by reducing the upper limit of the time window, the total costs and the amount of greenhouse gas emissions increase, and the maximum working hours of drivers decrease.

Figure 5 shows the changes in the objective function values of the considered problem in exchange for changes in the upper bound of the time window. Based

TABLE 4. Process of changing the objective function values of the problem in exchange for changes in demand

BH_c	$\omega 1$	$\omega 2$	$\omega 3$
-30%	47110	263	42
-20%	46250	260	42
-10%	45930	258	44
0	45305	252	46
+10%	44830	243	47
+20%	44730	240	49
+30%	43250	237	50

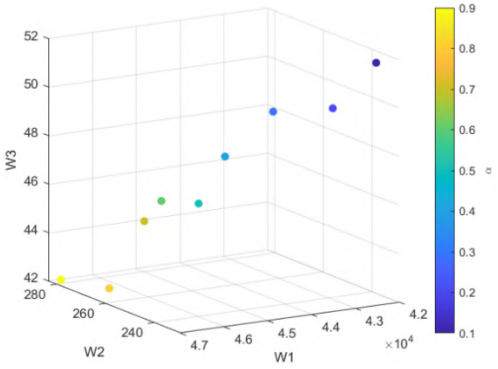

Figure 5. Process of changing the first and second objective function values in exchange for changes in the upper limit of the time window

on the results of this figure, it can be stated that with the shortening of the time window, the timing of the distribution of medical goods to the hospital has become more complex. As a result, more vehicles should be used to distribute medical goods. This is a waste of more drivers. As a result, the prevalence of the COVID-19 virus is likely to increase.

Table 5 shows the changes in the values of the objective functions in exchange for changes in vehicle capacity.

In the most important sensitivity analysis of the problem on the capacity of the vehicle, it was determined that by increasing the capacity of the vehicle, fewer vehicles are used, and as a result, the cost and amount of greenhouse gas emissions are reduced. On the other hand, this has led to a decrease in the prevalence of the COVID-19 virus. Figure 6 shows the changes in the objective function values of the considered problem in exchange for changes in the vehicle capacity.

TABLE 5. Process of changing the objective function values of the problem in exchange for changes in vehicle capacity

Cap_v	$\omega 1$	$\omega 2$	$\omega 3$
-30%	46123	269	43
-20%	45973	262	44
-10%	45845	257	46
0	45305	252	46
+10%	45126	249	47
+20%	44975	245	47
+30%	44235	240	49

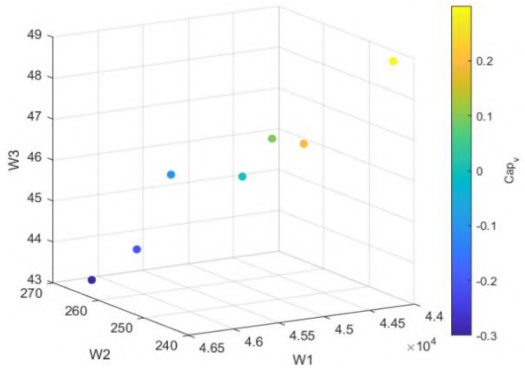

Figure 6. Trend of changing the objective function values of the problem in exchange for changes in the vehicle capacity

6. CONCLUSION

Due to the importance of vehicle routing and inventory management in this research, a multi-warehouse vehicle routing model under the COVID-19 pandemic conditions has been presented. The importance of locating warehouses and distribution centers in logistics systems was not less than vehicle routing and covered most system costs. In the model presented in this paper, three levels (i.e., production centers, warehouses, and hospitals as the first, second, and final levels, respectively) were considered. Therefore, the location of facilities in production centers, warehouses, and routing-inventory was at the level between warehouses and the customer. The prevalence of the COVID-19 virus and the need for careful planning for the transfer of hospital equipment led to the design of an uncertain model of vehicle navigation in this paper. They then controlled the model using a robust fuzzy method.

To optimize the multi-objective model (i.e., minimizing the total cost, minimizing the amount of GHG emissions, and minimizing the maximum working hours of drivers) led to the use of the neutrophilic fuzzy programming method. The model implementation results showed that reducing the number of vehicles decreased the amount of GHG emissions and the prevalence of the COVID-19 virus. In contrast, the drivers' working hours increased and were unbalanced. Also, by examining the amount of the uncertainty rate, it was observed that by increasing this parameter due to the increase in production, distribution volume, and limited capacity of vehicles, more equipment should be used for distribution and transfer of medical goods from the production center to the warehouse. Accordingly, the costs of the entire network increased. While increasing the number of vehicles and the proper distribution of the volume of goods between vehicles, the maximum working hours of drivers decreased, and the amount of GHG emissions increased. In the most important sensitivity analysis of the problem on the capacity of the vehicle, it was determined that by increasing the capacity of the vehicle, fewer vehicles are used. As a result, the cost and amount of greenhouse gas emissions are reduced. On the other hand, this has led to a decrease in the prevalence of the COVID-19 virus. At the end, according to the analysis, the greatest impact on the spread of the COVID-19 virus is related to the uncertainty rate. Therefore, with the increase of uncertainty rate, due to the increase in demand and increase in vehicle traffic, the probability of spreading the COVID-19 virus increases. According to the presented mathematical model in this paper, it is suggested that this model be solved using meta-heuristic algorithms and implemented in a real-case study to develop and apply it. It is also recommended that, due to the market's competitive nature, competition between two similar supply chain networks be considered.

7. REFERENCES

1. Peres, I. T., Repolho, H. M., Martinelli, R., and Monteiro, N. J.

"Optimization in inventory-routing problem with planned transshipment: A case study in the retail industry." ***International Journal of Production Economics***, Vol. 193, (2017), 748–756. https://doi.org/10.1016/j.ijpe.2017.09.002

2. Saffarian, M., Niksirat, M., and Kazemi, S. M. "A Hybrid Genetic-Simulated Annealing-Auction Algorithm for a Fully Fuzzy Multi-Period Multi-Depot Vehicle Routing Problem." ***International Journal of Supply and Operations Management***, Vol. 8, No. 2, (2021), 96–113. https://doi.org/10.22034/IJSOM.2021.2.1
3. Ghahremani-Nahr, J., Nozari, H., and Bathaee, M. "Robust Box Approach for Blood Supply Chain Network Design under Uncertainty: Hybrid Moth-Flame Optimization and Genetic Algorithm." ***International Journal of Innovation in Engineering***, Vol. 1, No. 2, (2021), 40–62. https://doi.org/10.52547/ijie.1.2.40
4. Andersson, H., Hoff, A., Christiansen, M., Hasle, G., and Løkketangen, A. "Industrial aspects and literature survey: Combined inventory management and routing." ***Computers & Operations Research***, Vol. 37, No. 9, (2010), 1515–1536. https://doi.org/10.1016/j.cor.2009.11.009
5. Dantzig, G. B., and Ramser, J. H. "The Truck Dispatching Problem." ***Management Science***, Vol. 6, No. 1, (1959), 80–91. https://doi.org/10.1287/mnsc.6.1.80
6. Gupta, P., Govindan, K., Mehlawat, M. K., and Khaitan, A. "Multiobjective capacitated green vehicle routing problem with fuzzy time-distances and demands split into bags." ***International Journal of Production Research***, (2021), 1–17. https://doi.org/10.1080/00207543.2021.1888392
7. Ghahremani Nahr, J., Kian, R., and Rezazadeh, H. "A Modified Priority-Based Encoding for Design of a Closed-Loop Supply Chain Network Using a Discrete League Championship Algorithm." ***Mathematical Problems in Engineering***, Vol. 2018, (2018), 1–16. https://doi.org/10.1155/2018/8163927
8. Ghahremani Nahr, J. "Improvement the efficiency and efficiency of the closed loop supply chain: Whale optimization algorithm and novel priority-based encoding approach." ***Journal of Decisions and Operations Research***, Vol. 4, No. 4, (2020), 299–315. https://doi.org/10.22105/DMOR.2020.206930.1132
9. Yousefikhoshbakht, M., and Khorram, E. "Solving the vehicle routing problem by a hybrid meta-heuristic algorithm." ***Journal of Industrial Engineering International***, Vol. 8, No. 1, (2012), 11. https://doi.org/10.1186/2251-712X-8-11
10. Ghahremani Nahr, J., Bathaee, M., Mazloumzadeh, A., and Nozari, H. "Cell Production System Design: A Literature Review." ***International Journal of Innovation in Management, Economics and Social Sciences***, Vol. 1, No. 1, (2021), 16–44. https://doi.org/10.52547/ijimes.1.1.16
11. Moosavi, J., Naeni, L. M., Fathollahi-Fard, A. M., and Fiore, U. "Blockchain in supply chain management: a review, bibliometric, and network analysis." ***Environmental Science and Pollution Research***, (2021), 1–15. https://doi.org/10.1007/s11356-021-13094-3
12. Pasha, J., Dulebenets, M. A., Fathollahi-Fard, A. M., Tian, G., Lau, Y., Singh, P., and Liang, B. "An integrated optimization method for tactical-level planning in liner shipping with heterogeneous ship fleet and environmental considerations." ***Advanced Engineering Informatics***, Vol. 48, (2021), 101299. https://doi.org/10.1016/j.aei.2021.101299
13. Fathollahi-Fard, A. M., Woodward, L., and Akhrif, O. "Sustainable distributed permutation flow-shop scheduling model based on a triple bottom line concept." ***Journal of Industrial Information Integration***, Vol. 24, (2021), 100233. https://doi.org/10.1016/j.jii.2021.100233
14. Hosseinzadeh Lotfi, F., Najafi, S. E., and Nozari, H. Data Envelopment Analysis and Effective Performance Assessment. IGI Global, 2017. https://doi.org/10.4018/978-1-5225-0596-9
15. Guemri, O., Bekrar, A., Beldjilali, B., and Trentesaux, D. "GRASP-based heuristic algorithm for the multi-product multi-vehicle inventory routing problem." ***4OR***, Vol. 14, No. 4, (2016), 377–404. https://doi.org/10.1007/s10288-016-0315-1
16. Coelho, L. C., and Laporte, G. "The exact solution of several classes of inventory-routing problems." ***Computers & Operations Research***, Vol. 40, No. 2, (2013), 558–565. https://doi.org/10.1016/j.cor.2012.08.012
17. Kumar, R., Dey, A., Broumi, S., and Smarandache, F. "A Study of Neutrosophic Shortest Path Problem." In Neutrosophic graph theory and algorithms (pp. 148–179). IGI Global, 2020. https://doi.org/10.4018/978-1-7998-1313-2.ch006
18. Diao, X., Fan, H., Ren, X., and Liu, C. "Multi-depot open vehicle routing problem with fuzzy time windows." ***Journal of Intelligent & Fuzzy Systems***, Vol. 40, No. 1, (2021), 427–438. https://doi.org/10.3233/JIFS-191968
19. Kara, I., Kara, B. Y., and Kadri Yetis, M. "Energy minimizing vehicle routing problem." In Lecture Notes in Computer Science (including subseries Lecture Notes in Artificial Intelligence and Lecture Notes in Bioinformatics) (Vol. 4616 LNCS, pp. 62–71). Springer Verlag, 2007. https://doi.org/10.1007/978-3-540-73556-4_9
20. Kuo, Y. "Using simulated annealing to minimize fuel consumption for the time-dependent vehicle routing problem." ***Computers & Industrial Engineering***, Vol. 59, No. 1, (2010), 157–165. https://doi.org/10.1016/j.cie.2010.03.012
21. Xiao, Y., Zhao, Q., Kaku, I., and Xu, Y. "Development of a fuel consumption optimization model for the capacitated vehicle routing problem." ***Computers & Operations Research***, Vol. 39, No. 7, (2012), 1419–1431. https://doi.org/10.1016/j.cor.2011.08.013
22. Ahmadizar, F., Zeynivand, M., and Arkat, J. "Two-level vehicle routing with cross-docking in a three-echelon supply chain: A genetic algorithm approach." ***Applied Mathematical Modelling***, Vol. 39, No. 22, (2015), 7065–7081. https://doi.org/10.1016/j.apm.2015.03.005
23. Yu, V. F., Jewpanya, P., and Redi, A. A. N. P. "Open vehicle routing problem with cross-docking." ***Computers & Industrial Engineering***, Vol. 94, (2016), 6–17. https://doi.org/10.1016/j.cie.2016.01.018
24. Lalla-Ruiz, E., Expósito-Izquierdo, C., Taheripour, S., and Voß, S. "An improved formulation for the multi-depot open vehicle routing problem." ***OR Spectrum***, Vol. 38, No. 1, (2016), 175–187. https://doi.org/10.1007/s00291-015-0408-9
25. Du, J., Li, X., Yu, L., Dan, R., and Zhou, J. "Multi-depot vehicle routing problem for hazardous materials transportation: A fuzzy bilevel programming." ***Information Sciences***, Vol. 399, (2017), 201–218. https://doi.org/10.1016/j.ins.2017.02.011
26. Alinaghian, M., and Shokouhi, N. "Multi-depot multi-compartment vehicle routing problem, solved by a hybrid adaptive large neighborhood search." ***Omega***, Vol. 76, (2018), 85–99. https://doi.org/10.1016/j.omega.2017.05.002
27. Brandão, J. "Iterated local search algorithm with ejection chains for the open vehicle routing problem with time windows." ***Computers & Industrial Engineering***, Vol. 120, (2018), 146–159. https://doi.org/10.1016/j.cie.2018.04.032
28. Polyakovskiy, S., and M'Hallah, R. "A hybrid feasibility constraints-guided search to the two-dimensional bin packing problem with due dates." ***European Journal of Operational Research***, Vol. 266, No. 3, (2018), 819–839. https://doi.org/10.1016/j.ejor.2017.10.046
29. Ghahremani-Nahr, J., Kian, R., and Sabet, E. "A robust fuzzy mathematical programming model for the closed-loop supply chain network design and a whale optimization solution

algorithm." ***Expert Systems with Applications***, Vol. 116, (2019), 454–471. https://doi.org/10.1016/j.eswa.2018.09.027

30. Li, J., Li, T., Yu, Y., Zhang, Z., Pardalos, P. M., Zhang, Y., and Ma, Y. "Discrete firefly algorithm with compound neighborhoods for asymmetric multi-depot vehicle routing problem in the maintenance of farm machinery." ***Applied Soft Computing***, Vol. 81, (2019), 105460. https://doi.org/10.1016/j.asoc.2019.04.030
31. Sadati, M. E. H., Aksen, D., and Aras, N. "The r -interdiction selective multi-depot vehicle routing problem." ***International Transactions in Operational Research***, Vol. 27, No. 2, (2020), 835–866. https://doi.org/10.1111/itor.12669
32. Mojtahedi, M., Fathollahi-Fard, A. M., Tavakkoli-Moghaddam, R., and Newton, S. "Sustainable vehicle routing problem for coordinated solid waste management." ***Journal of Industrial Information Integration***, Vol. 23, (2021), 100220. https://doi.org/10.1016/j.jii.2021.100220
33. Zhang, S., Zhang, W., Gajpal, Y., and Appadoo, S. S. "Ant Colony Algorithm for Routing Alternate Fuel Vehicles in Multi-depot Vehicle Routing Problem." In Decision Science in Action (pp. 251–260). Springer, Singapore, 2019. https://doi.org/10.1007/978-981-13-0860-4_19
34. Dell'Amico, M., Furini, F., and Iori, M. "A branch-and-price algorithm for the temporal bin packing problem." ***Computers & Operations Research***, Vol. 114, (2020), 104825. https://doi.org/10.1016/j.cor.2019.104825
35. Mirzaei, S., and Seifi, A. "Considering lost sale in inventory routing problems for perishable goods." ***Computers & Industrial Engineering***, Vol. 87, (2015), 213–227. https://doi.org/10.1016/j.cie.2015.05.010
36. Soysal, M., Bloemhof-Ruwaard, J. M., Haijema, R., and van der Vorst, J. G. A. J. "Modeling an Inventory Routing Problem for perishable products with environmental considerations and demand uncertainty." ***International Journal of Production Economics***, Vol. 164, (2015), 118–133. https://doi.org/10.1016/j.ijpe.2015.03.008
37. Nunes Bezerra, S., Souza, M. J. F., de Souza, S. R., and Nazário Coelho, V. "A VNS-Based Algorithm with Adaptive Local Search for Solving the Multi-Depot Vehicle Routing Problem." In International Conference on Variable Neighborhood Search (pp. 167–181). Springer, Cham, 2018. https://doi.org/10.1007/978-3-030-15843-9_14
38. A. Guimarães, T., C. Coelho, L., M. Schenekemberg, C., and T. Scarpin, C. "The two-echelon multi-depot inventory-routing problem." ***Computers & Operations Research***, Vol. 101, (2019), 220–233. https://doi.org/10.1016/j.cor.2018.07.024
39. Chen, D., Pan, S., Chen, Q., and Liu, J. "Vehicle routing problem of contactless joint distribution service during COVID-19 pandemic." ***Transportation Research Interdisciplinary Perspectives***, Vol. 8, (2020), 100233. https://doi.org/10.1016/j.trip.2020.100233
40. Xu, G., and Lyu, Q. "Vehicle Routing Problem for Collaborative Multidepot Petrol Replenishment under Emergency Conditions." ***Journal of Advanced Transportation***, Vol. 2021, (2021), 1–20. https://doi.org/10.1155/2021/5531500
41. Ghiasvand Ghiasi, F., Yazdani, M., Vahdani, B., and Kazemi, A. "Multi-depot home health care routing and scheduling problem with multimodal transportation: Mathematical model and solution methods." ***Scientia Iranica***, (2021). https://doi.org/10.24200/sci.2021.57338.5183
42. Salamai, A. A. "An Integrated Neutrosophic SWARA and VIKOR Method for Ranking Risks of Green Supply Chain." ***Neutrosophic Sets & Systems***, Vol. 41, (2021), 113–126.
43. Fallah, M., and Nozari, H. "Neutrosophic Mathematical Programming for Optimization of Multi-Objective Sustainable Biomass Supply Chain Network Design." ***Computer Modeling in Engineering & Sciences***, Vol. 129, No. 2, (2021), 927–951. https://doi.org/10.32604/cmes.2021.017511
44. Islam, M. R., Ali, S. M., Fathollahi-Fard, A. M., and Kabir, G. "A novel particle swarm optimization-based grey model for the prediction of warehouse performance." ***Journal of Computational Design and Engineering***, Vol. 8, No. 2, (2021), 705–727. https://doi.org/10.1093/jcde/qwab009
45. Beiki, H., Seyedhosseini, S. M., Ghezavati, V. R., and Seyedaliakbar, S. M. "Multi-objective Optimization of Multi-vehicle Relief Logistics Considering Satisfaction Levels under Uncertainty." ***International Journal of Engineering, Transaction B: Applications***, Vol. 33, No. 5, (2020), 814–824. https://doi.org/10.5829/IJE.2020.33.05B.13
46. Fallahtafti, A., Ardjmand, E., Young, W. A., and Weckman, G. R. "A multi-objective two-echelon location-routing problem for cash logistics: A metaheuristic approach." ***Applied Soft Computing***, Vol. 111, (2021), 107685. https://doi.org/10.1016/j.asoc.2021.107685
47. Fathollahi-Fard, A. M., Hajiaghaei-Keshteli, M., Tavakkoli-Moghaddam, R., and Smith, N. R. "Bi-level programming for home health care supply chain considering outsourcing." ***Journal of Industrial Information Integration***, (2021), 100246. https://doi.org/10.1016/j.jii.2021.100246
48. Zimmermann, H.-J. "Fuzzy programming and linear programming with several objective functions." ***Fuzzy Sets and Systems***, Vol. 1, No. 1, (1978), 45–55. https://doi.org/10.1016/0165-0114(78)90031-3
49. Smarandache, F. "A Unifying Field in Logics: Neutrosophic Logic." In Philosophy . American Research Press, 1999.

Persian Abstract

چکیده

شیوع ویروس COVID-19 در سراسر جهان و ایجاد مشکلات جدی در توزیع تجهیزات پزشکی، منجر به آن شده است تا در این مقاله به مدل‌سازی مسئله مسیریابی وسیله نقلیه چند انباره تحت عدم قطعیت در شرایط پاندمی COVID-19 پرداخته شود. هدف اصلی مدل ارائه‌شده مکان‌یابی انبارها و مراکز تولید و مسیریابی وسایل نقلیه جهت توزیع کالاهای پزشکی به بیمارستان‌ها می‌باشد. برای کنترل پارامترهای غیرقطعی مسئله نظیر تقاضا، هزینه‌های انتقال و توزیع از روش استوار فازی استفاده شده است. نتایج تاثیر عدم قطعیت با به کارگیری روش برنامه‌ریزی فازی نوتروسوفیک نشان می‌دهد، با افزایش مقدار تقاضا، حجم تبادلات کالاهای پزشکی افزایش یافته و تعداد وسایل نقلیه مورد استفاده جهت توزیع کالاها نیز افزایش یافته است. این امر منجربه افزایش هزینه‌های کل مسئله و میزان انتشار گازهای گلخانه‌ای شده است. همچنین بررسی نتایج نشان می‌دهد استفاده از وسایل نقلیه بیشتر منجربه کاهش خستگی کارکنان به جهت توزیع کالاهای پزشکی و کاهش شیوع ویروس COVID-19 می‌شود. در مهمترین تجزیه و تحلیل حساسیت مشکل بر روی ظرفیت وسیله نقلیه، مشخص شد که با افزایش ظرفیت خودرو، از وسایل نقلیه کمتری استفاده می‌شود و در نتیجه هزینه و میزان انتشار گازهای گلخانه‌ای کاهش می‌یابد. از سوی دیگر، این امر منجر به کاهش شیوع ویروس COVID-19 شده است.

International Journal of Engineering

Journal Homepage: www.ije.ir

Election Prediction Based on Sentiment Analysis using Twitter Data

A. Yavari[a], H. Hassanpour*[a], B. Rahimpour Cami[b], M. Mahdavi[c]

[a] Faculty of Computer Engineering and IT, Shahrood University of Technology, Shahrood, Iran
[b] Faculty of Computer and IT Engineering, Mazandaran University of Science and Technology, Babol, Iran
[c] Sydney International School of Technology and Commerce, Sydney, Australia

PAPER INFO

Paper history:
Received 10 October 2021
Received in revised form 22 November 2021
Accepted 23 November 2021

Keywords:
Predicting Elections
Virtual Social Network
Twitter Data Analysis
Aging Estimation Method

ABSTRACT

Election prediction has always been of interest to many people. In the last decade, an increasing influence of social networks and the possibility of sharing opinions and ideas has rendered election prediction based on social network data analysis. This paper, drawing on Twitter data and sentiment analysis, uses the proportion of positive messages rate to negative messages rate as an effective indicator for predicting elections. Then, using the aging estimation method, it predicts the values of this indicator in future time windows. The experiments conducted on Twitter data related to the 2020 United States presidential election in a four-month time window indicate that the indicator values and eventually the election results can be predicted with high accuracy.

doi: *10.5829/ije.2022.35.02b.13*

1. INTRODUCTION

With the advent of virtual social networks, communication between people and sharing of opinions and significant social events are easier than ever. Hence, social networks are currently considered an important source of public opinions. Election, as an important social event, attracts a great deal of attention in societies as well as in social media. The prediction of elections is particularly important from such perspectives as planning future political and economic programs, investigating its impacts on economic development and preventing some social crises. Traditionally, people made predictions by conducting surveys through phone calls or distributing questionnaires. Several models for making survey-based predictions were provided in literature [1]. Such surveys, apart from their considerable cost, lack of sufficient accuracy because they usually do not target the right population, and some respondents do not approach them appropriately. Salunke et al. [2] cited several survey-based predictions which did not turn out to be true. But, social media, which are easily accessible, constitute a valuable source of survey data [3]. Twitter, as the biggest source of news [4], with over 250 million active users per month, provides a user friendly environment for expressing opinions and sharing viewpoints in the form of short messages. Making predictions based on Twitter data analysis has attracted considerable attention in recent years. The prediction of stock prices [5], sports competition results [6], spread of diseases [7], and election results [4] are instances of such predictions.

Using Twitter data analysis, this paper introduces a new method for predicting the 2020 United States (US) presidential election result based on sentiments analysis. In the proposed method, the proportion of positive messages rate to negative messages rate at a specific time interval is defined as an effective indicator for predicting elections. Next, the election result is predicted by predicting the indicator values at future time intervals. The next indicator values are predicted by calculating the exponential average or by the aging estimation method. The aging estimation method is a dynamic method of estimating the process execution time. In some process scheduling methods using the operating system such as the Shortest Process First, the process execution times should be estimated to choose the shortest one possible [8].

*Corresponding Author Institutional Email: h.hassanpour@shahroodut.ac.ir (H. Hassanpour)

Please cite this article as: A. Yavari, H. Hassanpour, B. Rahimpour Cami, M. Mahdavi "Election Prediction Based on Sentiment Analysis using Twitter Data", ***International Journal of Engineering, Transactions B: Applications*** Vol. 35, No. 02, (2022) 372-379

Although sentiment analysis has previously been used for predicting election results, the innovation and features of the proposed method include the simplicity of its implementation using only the rate of sending tweets, the introduction of a new and effective indicator in predicting election, the possibility of making predictions at favorite time intervals prior to the election, and considering the impact of electoral events such as debates and speeches on the outcome of prediction using a coefficient.

The remaining sections of this paper have been organized as follows. In section 2, related studies on the prediction of elections are reviewed. In section 3, the proposed method is explained, and in section 4, the experiments, results and evaluation of the proposed method are discussed.

2. RELATED STUDIES

For the first time in use of social media for election prediction, the 2009 German election results were predicted through Twitter data analysis [9]. The authors made predictions on the basis of the number of tweets related to each political party. As it will be shown in this paper, comparing the number of tweets sent by the supporters of one party with those sent by the supporters of another party cannot be a suitable criterion for predicting election results, because the supporters of a particular candidate are likely to be more active in social networks.

Consideration of the sentiments in people's tweets contributes to the accuracy of election predictions [10]. Burnap et al. [11] proposed a model for predicting the results of the 2015 British election based on sentiment analysis. On the basis of the sentiment analysis method [12], they assigned a score between -5 and +5 to each tweet as indexes of strongly negative to strongly positive sentiments, and made predictions about the number of seats to be held by the members of each party in the Parliament based on the total sentiment scores of that party. Nugroho [13] predicted the US election results on the basis of lexicon-based sentiment analysis. First, based on the geographical information of each tweet, they identified the state from which the tweet had been sent. Next, they counted the positive and negative sentimental tweets for both parties in each state and announced the party with more tweets as the winner in that state. Finally, they predicted the eventual winner based on the total counts in all the states. Of course, the data that they collected from Twitter was limited to the last week remaining to the election.

Xia et al. [14] collected a dataset of 260000 tweets related to the 2020 US presidential election and classified them into positive, negative, and neutral sentimental tweets using a multilayer neural network. Examining the number of positive and negative tweets, they predicted that the election results would be very close. In addition, they showed that analysing sentiments using social media data is a low-cost and accurate method to gain general feedback on candidates and predict election results.

A multi-factor method for prediction the 2020 US presidential election was introduced by Sabuncu et al. [15]. They used various factors such as number of positive and negative tweets, number of people, number of likes, and retweets simultaneously on a dataset of 11 million tweets. Other studies reported in literature [16-18] have predicted elections based on sentiment analysis.

Liu et al. [19] proposed a combined model for predicting elections. They combined the sentiment analysis method with the traditional models of political sciences and predicted election results locally in Georgia. The *traditional models of political sciences* is meant to refer to such issues as the rate of economic development or decrease in the rate of unemployment which take place in the current government or are proposed as election promises by candidates.

3. THE PROPOSED METHOD

The prediction of elections only based on the number of tweets sent by the supporters of one party, irrespective of other factors especially the hidden sentiments in tweets, will not be accurate [10]. Therefore, other criteria, especially the hidden sentiments in each tweet, have been taken into consideration in different studies. The positive sentiments in the tweets associated with a particular party are considered an advantage for that party, while the tweets containing negative sentiments are considered a weakness. The methods which extract sentiments from a tweet are often based on a dictionary. In such dictionaries, each word is experientially assigned a score relative to its sentimental load. Then, the sentimental score of a sentence or tweet is calculated based on the words which comprise it. Hence, each sentence can contain positive, negative or neutral sentiments. This paper excludes the tweets with neutral sentiments.

The index or indicator which has been used in the proposed method as the determining factor in predicting elections is the proportion of positive tweets rate to negative tweets rate in a fixed time window i:

$$A_i = \frac{(Positive\ Tweets\ Rate)_i}{(Negetive\ Tweets\ Rate)_i + 1} = \frac{(Positive\ Tweets\ Count)_i}{(NegetiveTweets\ Count)_i + 1} \quad (1)$$

The prediction indicator (A_i) in Equation (1) is obtained from the proportion of positive tweets rate to negative tweets rate in the time window i. As the rate of sending tweets is calculated in a fixed time window, this equation is equal to the proportion of positive tweets number to negative tweets number. As the number of

negative tweets in a time window might be equal to zero, number 1 has been put in the denominator. The comparison of the values of this indicator for the candidates in each time window indicates their chances of success. Therefore, the length of the time window is decided based on how long before the election we are going to make a prediction. In other words, to predict the result of an election d days earlier, the length of the time window will be equal to d. In the proposed method, to predict the indicator value in the next time window, the aging estimation method is used. The aging estimation method functions on the basis of an exponential averaging of previous observations:

$$A_{i+1} = \alpha O_i + (1-\alpha)A_i \quad (2)$$

In Equation (2), the indicator prediction value A_{i+1} is for the next time window $(i+1)$. O_i is the real, observed value of the indicator in the current time window and A_i is its predicted value at stage i. α is a parameter between zero and one which predicts the relative weight of the prediction history and the weight of the recent observation value. The closer the value of α to one, the greater the effect of recent observations on the calculation of exponential average; and the closer its value to zero, the greater the effect of previous observations on the calculation of average (Equation (3)).

$$A_{i+1} = \alpha O_i + (1-\alpha)\alpha O_{i-1} + \cdots + (1-\alpha)^{i+1} A_0 \quad (3)$$

As α and (1 –α) are both smaller than one, the next sentences in Equation (3) will gradually become smaller. The value of α as a function of its position in Equation (3) is shown in Figure 1. For α = 0.8, the weight is almost totally assigned to the four recent observations. In other words, the four recently observed values of the indicator will have the greatest effect on the prediction of its next value, while for α = 0.5, averaging is distributed on almost the last eight observations.

The advantage of using a close-to-one value for α is that the quick changes in observations are reflected in the average value faster and the accuracy of prediction increases considerably. Therefore, in the months remaining to election, especially the month leading to the election, when election debates and candidates' final propaganda increase, closer-to-one α values will be more effective in making predictions.

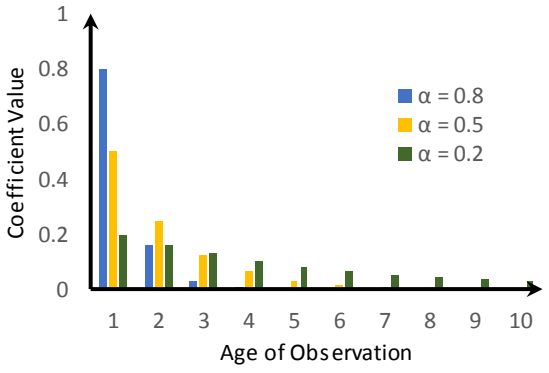

Figure 1. The Effect of Alpha Coefficient on Recent Observation Values

4. RESULTS AND EVALUATION

In this section, two Twitter datasets related to the 2020 US presidential election are evaluated in order to examine the ability of the proposed method to predict the election results. First, the accuracy of the proposed method is checked by performing various experiments on a dataset and then its output is compared with three other methods in the field of election prediction.

4. 1. Accuracy of The Proposed Method The first dataset has been extracted from literature [20]. It includes about 24 million tweets related to the 2020 US presidential election collected within the time interval between July 1st and November 12th. Each tweet has been assigned to one of democratic and republican parties based on the keywords used such as "The Democrats", "Joe Biden", "real Donald trump", or "Keep America Great".

Of course, as some tweets contain keywords associated with both parties, they are labeled *both*, but they are not used in the proposed method. Using the sentiment analysis method VADER (Valence Aware Dictionary and sEntiment Reasoner) [21], each tweet is assigned a score within the [–1 +1] interval. The values +1 and –1 indicate strongly positive sentiments and strongly negative sentiments, respectively. VADER is a tool for analyzing sentiments based on rules and a dictionary. In fact, it calculates the strength of hidden sentiments in a tweet by combining the syntactic rules of a language with a set of terminologies which have gradually been assigned their sentimental weight.

Figure 2 displays the changes in the number of tweets sent by both parties in a one-day time window. Considering the final 2020 US presidential election result, this figure shows that the number of tweets sent by the supporters of a particular party cannot be a reliable index for predicting elections.

Figure 3 shows the number of tweets sent with positive sentimental loads for the two parties in a one-day interval. If the number of positive tweets is normalized, the obtained result will be interesting in terms of its concordance with the eventual result of the election in which the Democratic Party was the eventual winner (Figure 4).

Figure 5 displays the proportion of positive tweets number to negative tweets number for both parties in a one-day time window. In comparison to Figure 4, there

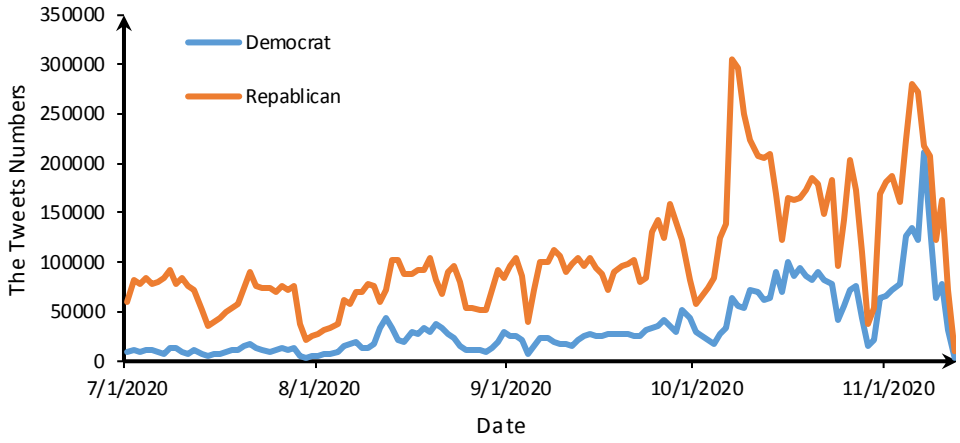

Figure 2. Number of tweets associated with Democratic and Republican parties in a one-day interval

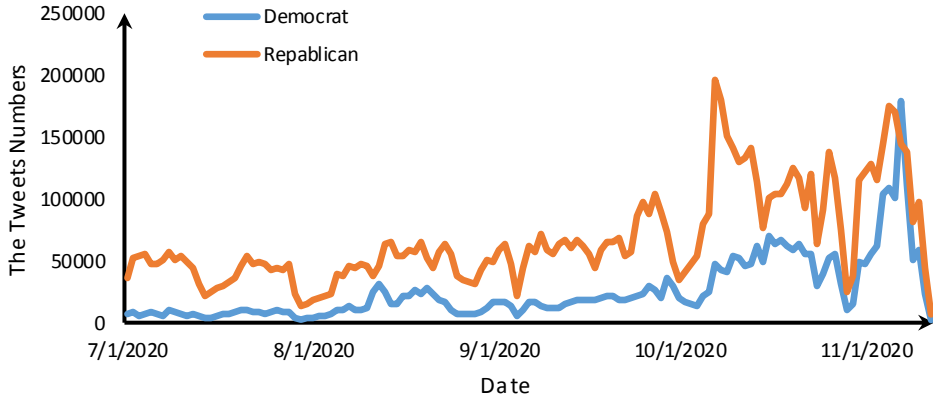

Figure 3. Number of positive tweets for Democrats and Republicans on a daily basis

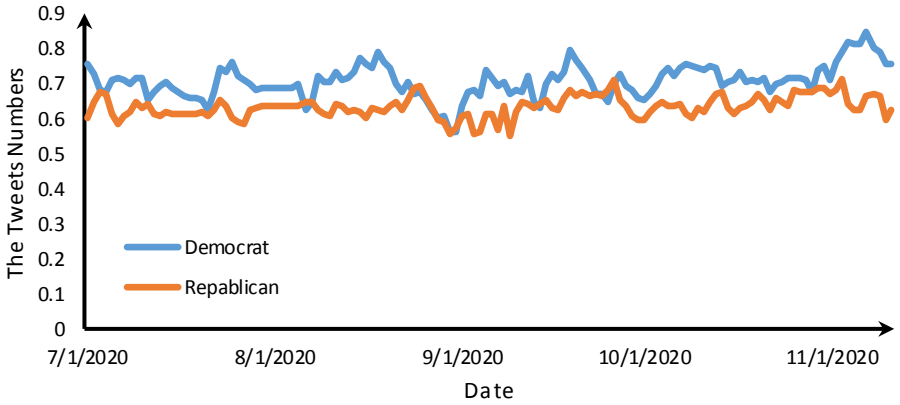

Figure 4. Number of normalized positive tweets for Democrats and Republicans on a daily basis

is a bigger difference between the graphs for the two parties and there are more noticeable peaks and valleys. Each peak and valley in this figure can be associated with a real event. For example, peak 1 occurred after Kamala Harris was nominated as Vice President by Joe Biden. Trump's support for the followers of the right-wing extremism as a controversial and incorrect act led to peak 2. Peak 3 stands for the announcement of Joe Biden's victory by the Associated Press after the election.

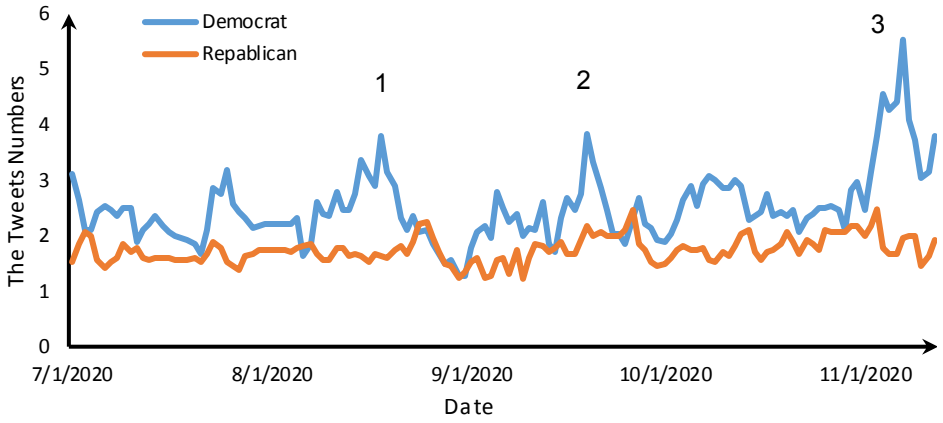

Figure 5. Proportion of positive tweets number to negative tweets number for both parties on a daily basis

In another experiment, the prediction accuracy of the indicator value at different time intervals and the effects of different α values have been studied. Table 1 shows the prediction value of the indicator based on the aging method at different time intervals and the criterion for measuring accuracy. The prediction accuracy of the indicator value for each party is obtained based on Equation (4).

$$Accuracy = 1 - mean\left[\frac{abs(A-O)}{O}\right] \quad (4)$$

In Equation (4), A stands for predicted values and O stands for observed values. The obtained accuracy average is presented in Table 1.

Based on Table 1, for the larger α values in each time window, the prediction accuracy of the indicator value is higher, and vice versa. For instance, as shown in Table1, 14 days remaining to the election, the fact that the Democrats had a larger indicator value than the Republicans was predicted with an average accuracy of 97 percent. In other words, two weeks prior to the election, it was predicted that in the 14 days to come the proportion of positive tweets number to negative tweets number would be higher for the Democrats than for the Republicans, which was considered as strong evidence of the democrats' victory in the election. The third row in Table 1 shows how increasingly assigning values to α affects the indicator. To show this effect, between four months to one week remaining to the election, we have changed α value from 0.2 to 0.9. The accuracy of prediction is higher than when α is defined small and constant.

Figure 6 shows the increasing prediction accuracy of the indicator compared to the days remaining to the election. Hence, the closer it gets to the election, the more accurately the indicator vale is predicted.

Finally in another experiment, the indicator value was calculated only by analyzing the data related to the month leading to the election. The results are displayed in Table 2.

It can be understood from Table 2 that to make accurate predictions based on the data related to the

TABLE 1. The prediction of the indicator at different time intervals in four months

Time window length (day)	□	Democrat indicator	Republican indicator	Accuracy Average
14	0.8	2.47	1.94	0.97
	0.2	2.60	1.85	0.91
7	0.8	2.67	2.06	0.97
	0.2	2.56	1.98	0.93
7	Gradual increase	2.70	1.98	0.96
1	0.8	3.64	2.4	0.98
	0.2	3.29	2.15	0.96

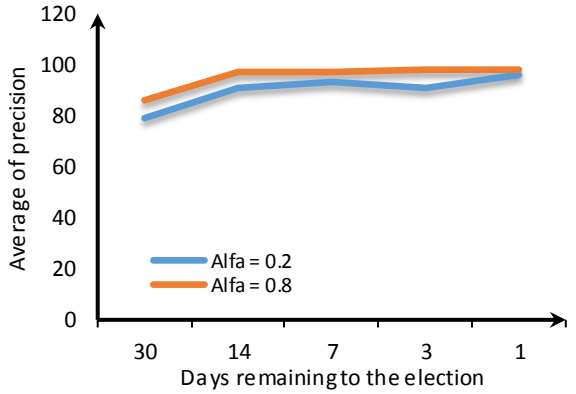

Figure 6. The prediction accuracy of the indicator value on the days remaining to the election

TABLE 2. The prediction of the indicator in different time windows on the month leading to the election.

Time window length (day)	α	Democrat indicator	Republican indicator	Accuracy Average
14	0.8	2.52	1.89	0.94
	0.2	2.59	1.76	0.89
7	0.8	2.67	2.05	0.97
	0.2	2.43	1.80	0.93
1	0.8	3.64	2.40	0.98
	0.2	2.90	2.14	0.91

month leading to the election when election events increase, assigning a larger value to α will be more effective.

According to the experiments conducted and Tables 1 and 2 in which the predicted indicator value for the Democrats was greater than that for the Republicans, Joe Biden's victory in the 2020 US presidential election was predictable.

4. 2. Comparison With Other Methods In this section, the proposed method is compared with the three methods of election prediction. For this experiment, in addition to the dataset reported by Sabuncu [20] described in the previous section, the dataset by Sabuncu et al. [15] has also been used. This dataset includes approximately 11 million tweets related to the 2020 US presidential election, collected from September 1, 2020 to November 2, 2020. The statistical summary of this dataset is given in Table 3.

In the first method, introduced by Singh et al. [22], each party's sentimental score is calculated based on Equation (5). Whichever party gets the higher score is expected to win the election.

$$SS(A) = \frac{pos(A) - pos(A)}{T(A)+T(B)} \quad (5)$$

In Equation (5), *SS(A)* is sentimental score of party *A*, *pos(A)* and *pos(B)* are the total number of positive and negative tweets for party A respectively, and *T(A)* and *T(B)* are the total number of tweets related to parties *A* and B.

In the second method [4], the popularity of each party is calculated based on Equation (6). Whichever party is more popular is expected to win the election.

$$P(A) = \left[\frac{pos(A)}{pos(A)+neg(A)}\right]\left[\frac{T(A)}{T(A)+T(B)}\right] \quad (6)$$

P(A) in Equation (6) is the popularity of party *A*.

The third method is introduced by Wicaksono [23]. In this method, the success rate of each party in the elections is calculated based on Equation (7).

$$SR(A) = \frac{pos(A)+neg(B)}{T(A)+T(B)} \quad (7)$$

SR(A) is the success rate of party *A*.

Table 4 shows the output of the proposed method with three other methods based on the first dataset, for different time periods before the election. As can be seen in Table 4, the proposed method, unlike the other three methods, has been able to accurately predict the outcome in all pre-election time periods. Table 5 shows the output of the proposed method with the other three methods based on the second dataset in the day before the election.

According to Tables 4 and 5, the proposed method in both datasets has succeeded in correctly predicting the elections, while the first and second methods have only succeeded in the second dataset.

5. CONCLUSION AND FURTHER RESEARCH

In this study, a new approach based on sentiment analysis on Twitter data is introduced to predict election

TABLE 3. The statistical summary of the second dataset

	Total Tweet	Positive	Negative	Neutral
Democrats	3851293	1663373	1639495	548424
Republicans	7109941	2831179	3791732	487031
Total	10961234	4494552	5431227	1035455

TABLE 4. Comparison of the proposed method with three other methods based on the first dataset

	Party name	The number of days till the election			
		30	14	7	1
First method [22]	Dem	0.076	0.084	0.091	0.094
	Rep	**0.207**	**0.206**	**0.203**	**0.206**
Second method [4]	Dem	0.135	0.144	0.156	0.161
	Rep	**0.506**	**0.503**	**0.490**	**0.489**
Third method [23]	Dem	0.434	0.438	0.443	0.443
	Rep	**0.565**	**0.561**	**0.556**	**0.556**
Proposed method	Dem	**2.07**	**2.47**	**2.67**	**3.64**
	Rep	1.74	1.94	2.06	2.4

TABLE 5. Comparison of the proposed method with three other methods based on the second dataset

Party name	First method [22]	Second method [4]	Third method [23]	Proposed method
Democrats	**0.002**	0.177	**0.498**	**1.014**
Republicans	- 0.08	**0.277**	0.408	0.747

results. The proposed method was evaluated on twitter data related to the 2020 US presidential election as a case study. In this method, The proportion of positive tweets number to negative tweets number in a time window with fixed length was proposed as an indicator and, using the aging estimation method, the value of this indicator in the next time window was predicted for each party with a high degree of accuracy. Since the indicator value was greater for the Democrats than for the Republicans, the victory of the former was predictable using the proposed method. In the continuous of this study, fuzzy logic can be used for the sentimental score of tweets. In other words, in the proposed method, tweets with a sentimental score +0.1 and +1 are both labled as positive tweets, while applying fuzzy logic can be useful. Furthermore, as the eventual US presidential election result is determined based on Electoral votes and the number of Electoral votes for both parties is determined based on the votes cast in each state, predicting the number of Electoral votes based on analyzing Twitter data locally in each state can yield more accurate and reliable results. Also, this method can be used in other domains such as the prediction of stock prices, although, due to the complexity of the data in this domain, probably several different indicators should be used.

6. REFERENCES

1. Lewis-Beck, M. S., "Election forecasting: Principles and practice", ***The British Journal of Politics and International Relations***, Vol. 7, No. 2, (2005), 145-164. DOI: 10.1111/j.1467-856X.2005.00178.x.
2. Salunkhe, P., Deshmukh, S., "Twitter based election prediction and analysis", ***International Research Journal of Engineering and Technology***, Vol. 4, No. 10, (2017), 539-544.
3. Pak, A., Paroubek, P., "Twitter as a corpus for sentiment analysis and opinion mining", ***Language Resources and Evaluation***, Vol. 10, (2010), 1320-1326.
4. Wang, L., Gan, J. Q., "Prediction of the 2017 French election based on Twitter data analysis", In 9th Computer Science and Electronic Engineering, (2017), 89-93. DOI: 10.1109/CEEC.2018.8674188.
5. Kolasani, S. V., Assaf, R., "Predicting Stock Movement Using Sentiment Analysis of Twitter Feed with Neural Networks", ***Journal of Data Analysis and Information Processing***, Vol. 8, No. 4, (2020), 309-319. DOI: 10.4236/jdaip.2020.84018.
6. Patel, R., Passi, K, "Sentiment Analysis on Twitter Data of World Cup Soccer Tournament Using Machine Learning", ***Internet of Things***, Vol. 1, No. 2, (2020). 218-239. DOI: 10.3390/iot1020014.
7. Fu, X., Jiang, X., Qi, Y., Xu, M., Song, Y., Zhang, J., Wu, X., "An event-centric prediction system for COVID-19," IEEE International Conference on Knowledge Graph, (2020), 195-202. DOI: 10.1109/ICBK50248.2020.00037
8. Silberschatz, A., Galvin, P. B., Gagne, G, "Operating System Concepts (9 Ed.)." Wiley Publishing. 187. (2012). ISBN 978-0470128725.
9. Tumasjan, A., Sprenger, T., Sandner, P., Welpe, I., "Predicting elections with twitter: What 140 characters reveal about political sentiment", In Proceedings of the International AAAI Conference on Web and Social Media, Vol. 4, No. 1, (2010).
10. Ceron, A., Curini, L., Iacus, S. M., "Using sentiment analysis to monitor electoral campaigns: Method matters—evidence from the United States and Italy", ***Social Science Computer Review***, Vol. 33, No. 1, (2015), 3-20, DOI: 10.1177/0894439314521983.
11. Burnap, P., Gibson, R., Sloan, L., Southern, R., Williams, M., "140 characters to victory?: Using Twitter to predict the UK 2015 General Election", ***Electoral Studies***, Vol. 41, (2016), 230-233. DOI: 10.1016/j.electstud.2015.11.017.
12. Thelwall, M., Buckley, K., Paltoglou, G., Cai, D., Kappas, A., "Sentiment strength detection in short informal text", ***Journal of the American Society for Information Science and Technology***, Vol. 61, No. 12, (2010), 2544-2558. DOI: 10.1002/asi.21416.
13. Nugroho, D. K., "US presidential election 2020 prediction based on Twitter data using lexicon-based sentiment analysis" 11th International Conference on Cloud Computing, Data Science & Engineering (Confluence), (2021), 136-141. DOI: 10.1109/Confluence51648.2021.9377201.
14. Xia, E., Yue, H., Liu, H. "Tweet Sentiment Analysis of the 2020 US Presidential Election", In Companion Proceedings of the Web Conference 2021, (2021), 367-371. DOI: 10.1145/3442442.3452322.
15. Sabuncu, I., Balci, M. A., Akguller, O., "Prediction of USA November 2020 Election Results Using Multifactor Twitter Data Analysis Method", *arXiv:2010.15938*, (2020).
16. Baccianella, S., Esuli, A., Sebastiani, F., "Sentiwordnet 3.0: an enhanced lexical resource for sentiment analysis and opinion mining", ***In Language Resources and Evaluation***, Vol. 10, (2010), 2200-2204.
17. Ibrahim, M., Abdillah, O., Wicaksono, A. F., Adriani, M., "Buzzer detection and sentiment analysis for predicting presidential election results in a twitter nation", IEEE International Conference on Data Mining Workshop, (2015), 1348-1353. DOI: 10.1109/ICDMW.2015.113.
18. Sharma, P., Moh, T. S., "Prediction of Indian election using sentiment analysis on Hindi Twitter." IEEE International Conference on Big Data, (2016), 1966-1971. DOI: 10.1109/BigData.2016.7840818.
19. Liu, R., Yao, X., Guo, C., Wei, X., "Can We Forecast Presidential Election Using Twitter Data? An Integrative Modelling Approach", ***Annals of GIS***, Vol. 27, No. 1, (2021), 43-56, DOI: 10.1080/19475683.2020.1829704.
20. Sabuncu, I., "USA Nov.2020 Election 20 Mil. Tweets (with Sentiment and Party Name Labels) Dataset", IEEE Dataport, (2020). DOI: 10.21227/25te-j338.
21. Hutto, C.J. Gilbert, E.E., "VADER: A Parsimonious Rule-based Model for Sentiment Analysis of Social Media Text." 8th International Conference on Weblogs and Social Media, (2014).
22. Singh, P., Dwivedi, Y. K., Kahlon, K. S., Pathania, A., Sawhney, R. S., "Can twitter analytics predict election outcome? An insight from 2017 Punjab assembly elections." ***Government Information Quarterly***, Vol. 37, No. 2, (2020), DOI: 10.1016/j.giq.2019.101444.
23. Wicaksono, A. J., "A proposed method for predicting US presidential election by analyzing sentiment in social media." 2nd International. Conference on Science in Information Technology, (2016), 276-280. DOI: 10.1109/ICSITech.2016.7852647.

Persian Abstract

چکیده

پیش‌بینی نتیجه انتخابات همواره مورد توجه بوده است. در دهه اخیر با افزایش ضریب نفوذ شبکه‌های اجتماعی مجازی و امکان اشتراک‌گذاری نظرات و عقاید افراد، پیش‌بینی نتایج انتخابات به کمک تحلیل داده‌ها در شبکه‌های اجتماعی بسیار مورد توجه پژوهشگران قرار گرفته است. در این مقاله، با استفاده از داده‌های توییتر و تحلیل احساسات، نسبت نرخ ارسال پیامهای احساسی مثبت به نرخ ارسال پیامهای احساسی منفی به عنوان یک اندیکاتور موثر جهت پیش‌بینی نتیجه انتخابات استفاده شده است. سپس با استفاده از روش تخمین سالمندی، مقادیر این اندیکاتور در پنجره‌های زمانی آینده پیش‌بینی می‌شود. نتایج آزمایشات بر روی داده‌های توییتر مرتبط با انتخابات ریاست جمهوری آمریکا در سال ۲۰۲۰ در یک بازه زمانی چهار ماه نشان می‌دهد که می‌توان با دقت بسیارخوبی مقدار اندیکاتور و نهایتا نتیجه انتخابات را پیش‌بینی نمود.

IJE TRANSACTIONS B: Applications Vol. 35, No. 02, (February 2022) 380-386

International Journal of Engineering

Journal Homepage: www.ije.ir

Numerical Analysis of Backscatter Radiography for Prediction of Pipelines Situation: Their Bursting and Casing Failure Consideration from inside

V. Jamshidi, R. Davarnejad*

Department of Chemical Engineering, Faculty of Engineering, Arak University, Arak, Iran

P A P E R I N F O

Paper history:
Received 08 November 2021
Received in revised form 20 November 2021
Accepted 28 November 2021

Keywords:
Pipeline Bursting
Casing Failure
Backscatter Radiography
Simulation
In-situe

A B S T R A C T

Backscatter radiography as a technique can successfully be applied for predicting the pipeline bursting and casing failure. A valid numerical technique will allow predicting these issues without needing to access the outside of the pipelines. Furthermore, this technique has the ability to estimate the shape and depth of damages. It is normally preferred to apply non-destructive testing (NDT) methods which can monitor the status of a pipeline from the internal surface of it without needing to access both sides of it depending on various locations of pipe such as underground or submarine. In the current study, backscatter radiography as an applicable and NDT method to detect locations with potential for pipeline bursting or casing failure was carefully investigated using the Monte Carlo simulation tool. The data obtained by the simulation process showed that backscatter radiography could detect deformations, corroded areas, depositions, creation of load on the casing, lacking proper cementation, excessive pressure inside the pipelines, and other factors which may increase the risk of pipelines bursting or casing failure (in-situ and online) with an acceptable accuracy.

***doi**: 10.5829/ije.2022.35.02b.14*

1. INTRODUCTION

Casings are steel alloys pipes that are inserted into a drilled borehole for prevention from wall collapse, control of formation pressures, and separation of low-pressure and high-pressure zones. After the installation of the casing in the borehole, a special mixture of concrete is injected behind it [1, 2]. Several factors such as corrosion, creation of load on the casing due to lacking proper cementation, reservoir subsidence, and casing material may lead to casing collapse [2-4]. The maximum resistance to in-situ horizontal stresses in casing can be generated by applying special alloys and the implementation of efficient concrete operations [5]. The other event which threatens the integrity of oil and gas transmission is pipelines bursting. High internal pressure and temperature can damage steel alloy pipes with different wall thicknesses and create deformations in radial directions [6, 7]. Excessive pressure inside the pipeline and some other factors such as aging, corrosion, deposition, and deformation can also increase the risk of bursting in the pipelines [8, 9].

In petroleum industries, in the case of damage to deeply buried casings, it is problematic, costly, or, in some cases, impossible to repair. Therefore, continuous monitoring of casing and pipelines is a necessary factor for safe operation and avoiding adverse consequences [3]. Casings and pipelines can be inspected by various methods such as acoustic technology, magnetic tools, eddy currents, thermal imaging, multi-arms caliper pigs, or determining fluid pressure at different points. There is information in the literature about the strengths and weaknesses of inspection methods and comparison between them [10-12].

Compton scattering, and inspection methods based upon it, have good potential for use in the field of monitoring pipelines. Backscatter radiography is a technique that previously has been proposed by Jamshidi et al. [13] for detecting corrosion and deposition inside pipelines without the need to access

*Corresponding Author's Email: *R-Davarnejad@araku.ac.ir* (R. Davarnejad)

Please cite this article as: V. Jamshidi, R. Davarnejad, Numerical Analysis of Backscatter Radiography for Prediction of Pipelines Situation: Their Bursting and Casing Failure Consideration from Inside, ***International Journal of Engineering, Transactions B: Applications*** Vol. 35, No. 02, (2022) 380-386

the back of them. In the current study, the possibility of applying this method in a tool or equipment for detecting locations with the potential of pipeline bursting or casing failure was investigated by a simulation tool.

2. METHODOLOGY

In conventional radiography configuration, the source of radiation is fixed on one side of a material, and a detector or film is installed on the other side [14]. The backscatter radiography is encouraged for some objects which both sides of them are not accessible such as buried pipelines underground. For inspection of a pipeline by backscatter radiography, radiation source and detectors are located inside it. Then, its internal will be irradiated and monitored [15, 16]. While transmitting oil and gas by pipelines, the internal fluid pressure can damage and deform the pipe body. Chemical reactions such as corrosion can reduce pipe resistance against the internal pressure, as well [7]. Bursting in the corroded areas in a pipeline is more probable than the other ones. Corrosion detection inside pipes by backscatter radiography technique was already investigated [11]. Deformation as a bulge on the outside surface of the pipe is a result of excessive pressure on the internal surface. For the simulation process, changes in the internal pressure are equivalent to changes in the density of the fluid flowing in the pipelines [17].

Casing failure may be caused by corrosion, change in internal fluid density, or change in internal or external pressure on the casing [18]. In some cases, when the pipe is almost empty, the external load may collapse the casing. The other factor that should be considered is the existence of small empty spaces as voids between the concrete and the casing. These voids may be filled by a high-pressure fluid [4, 17]. Most of the time, the overpressure on the concrete and consequently on the casing may lead to collapse. Some relationships between the density of concrete and its compressive strength based on the experiments have been developed [19, 20]. However, the concrete density increases with increasing the pressure but, there would be a high potential for collapse after achieving the maximum compressive strength of concrete [18]. To apply backscatter radiography technique for detecting areas with potential of bursting or collapse in pipelines, the assembly of source and detectors that is justified in the middle of the casing or pipeline, monitors 360 degrees of the pipe at the same time, and moves along it. The installed detectors count the number of backscattered photons or neutrons using a ring-shaped source with a mono-energetic sharp pencil beam. Change in the number of photons shows abnormalities along the pipeline.

The speed of inspection by this method will depend on several factors. Source strength or exposure rate of sources is the most crucial parameter. Considering photon or neutron energies, the efficiency of the detectors and electronics used in the setup can also have an essential role in the inspection speed.

In this research, simulation of backscatter radiography for monitoring factors that increase the possibility of casing collapse or pipeline bursting was performed by the Monte Carlo simulation tool. Figure 1 shows the simulated geometry used in the MCNP code, which is internationally recognized for analyzing the transport of neutrons and photons [21]. Although, backscattered photons or neutrons are counted in all detector cells considered in the design section (as shown in Figure 1) but, the results obtained by the cell that produces sharpest peaks during the inspection are presented in the results and discussion section.

The speed of inspection by backscatter radiography in the experiment depends on several factors. The most important parameter is the source strength or exposure rate of photon sources. The efficiency of the detectors and electronics used in the setup can have an essential role in the inspection speed, as well.

3. RESULTS AND DISCUSSION

The energy of photon and neutron sources, irradiation angle, beam type, and atomic densities of materials required for the simulation were obtained from the literature, considering the ALARA principle [4, 13, 22-28].

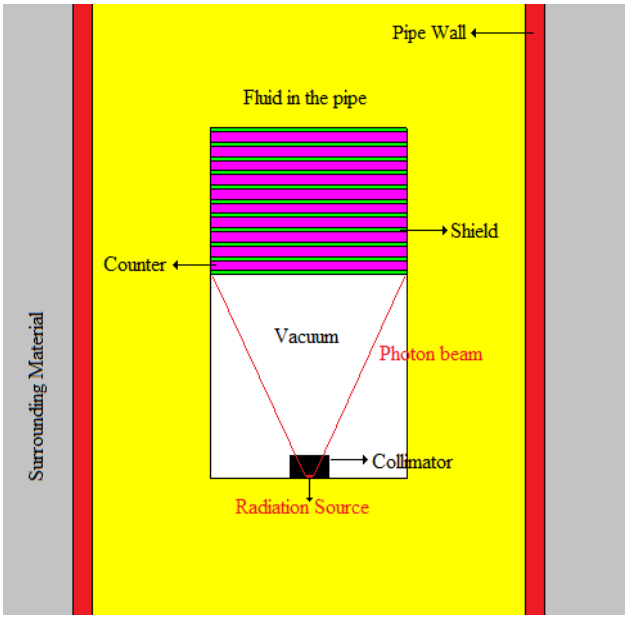

Figure 1. The geometry used in the simulation

Figure 2 shows two types of deformations that were simulated in this study for pipeline bursting. The peak of these deformations was less than 20% of the inside diameter of the pipe. The thickness of the pipeline and casing in all of the simulations was at 1 cm. To prevent photons from entering other areas and affecting the counts, shields (made of lead) were used.

Figures 3 and 4 show photon logs (based on Figure 2) by 75, 200, and 660 keV photon sources. The results clearly showed that high-energy photons could produce logs with sharper peaks in comparison with low-energy ones. These deformations can start the bursting in transmission pipelines.

Figure 5 shows the backscatter radiography data by 660 keV photons when a pipe is surrounded by various materials such as concrete, water, air, and soil. Since in this energy range, few photons may pass through the thickness of the pipe wall and reach behind it, the backscatter photons will then be returned to the pipe. Figure 6 shows detecting deformations when the pipe is filled with oil, gas, or brine.

According to this figure, log peaks are more distinctive when gas (with low density) flows inside the pipe. Figure 7 shows backscatter radiography data for deformations with different sizes. In this simulation, the

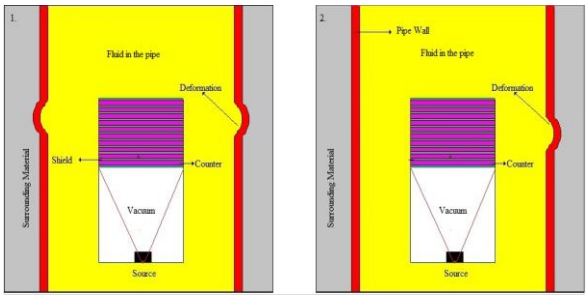

Figure 2. Two types of deformations investigated in pipeline bursting

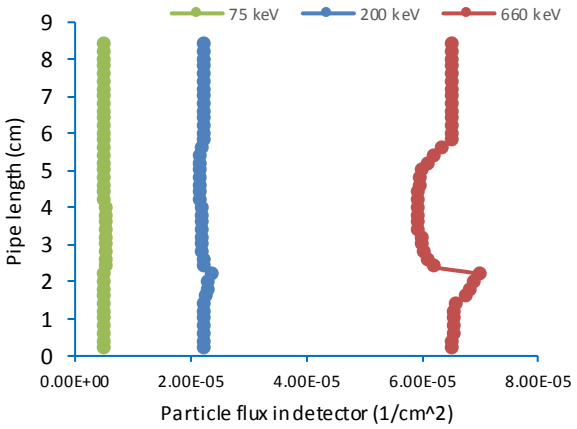

Figure 3. Photon log by various photon energies for detection of deformation shown in Figure 2 (left)

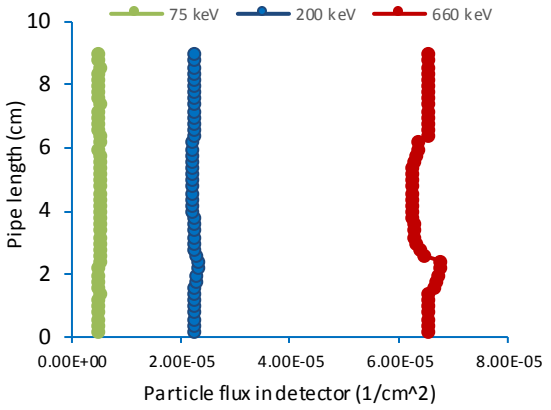

Figure 4. Photon log by various photon energies for detection of deformation shown in Figure 2 (right)

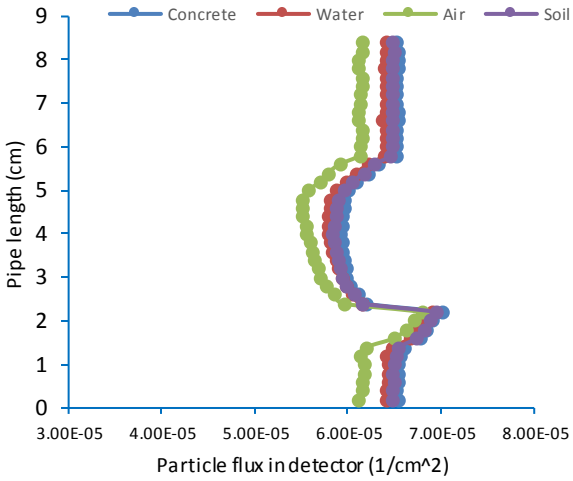

Figure 5. Photon log for detection of deformation in a pipe considering different surrounding materials (photon energy=660 keV)

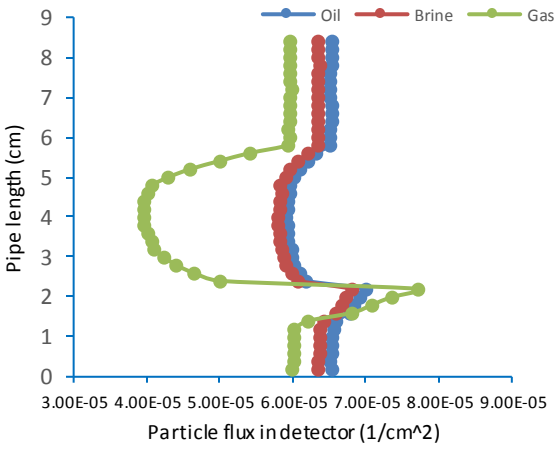

Figure 6. Photon log for detection of deformation in a pipe considering different fluids in the pipe (photon energy=660 keV)

depth of deformation was assumed to be around 5, 10, and 15% of internal pipe diameter. The results showed that this method could detect small deformations (even 5%). Figures 8 and 9 show backscatter photon radiography data by 660 keV photons and 4.2 MeV, respectively neutrons (neutron source of Am-Be with an average energy of 4.2 MeV) inside a pipe when the crude oil is under compression. The oil density can vary from 0.75 to 0.95 g/cm^3 with pressure change. The results show that the neutron log is more distinctive for detecting fluid density change in a pipeline compared with the photon log. Considering deformation shown in Figure 2. (left) is more frequent than Figure 2 (right), the results in Figures 5 to 9 are based on the deformation shown in this figure.

Several phenomena that may lead to casing collapse were also considered in the simulation process. Figure 10 shows two different geometries used for the detection of deformations in the casing. In these geometries, the size of deformation at the peak was less than 20% of the inside diameter of the casing.

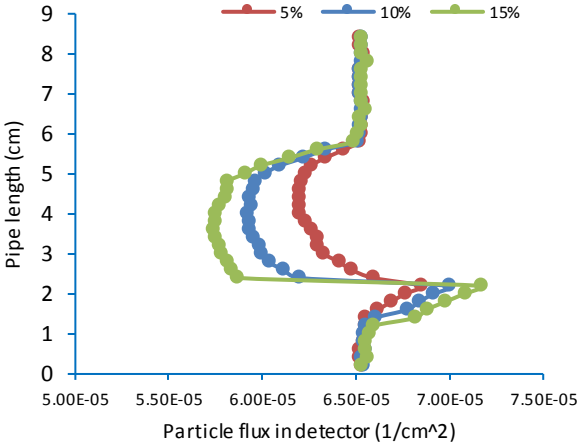

Figure 7. Photon log for detection of deformations in a pipe in terms of percentage of internal diameter by 660 keV photons

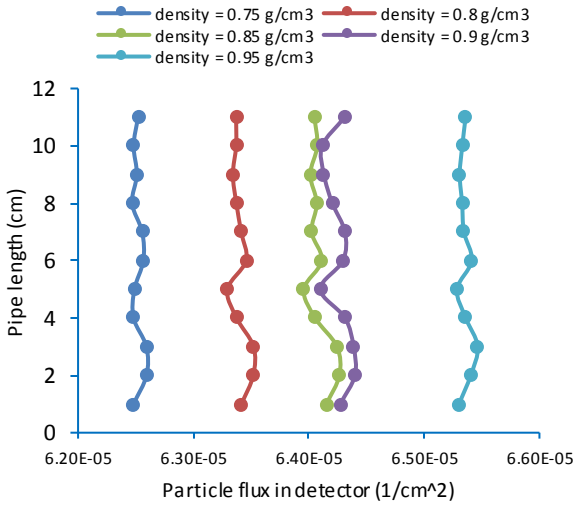

Figure 8. Photon log for different densities of crude oil in the pipeline (photon energy=660 keV)

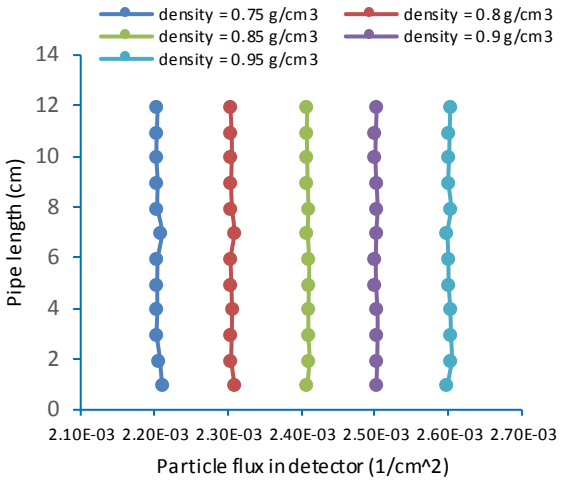

Figure 9. Neutron log for different densities of crude oil in the pipeline (neutron energy=4.2 MeV)

Figures 11 and 12 show deformation detection by 75, 200, and 660 keV photon sources. According to these figures, sharper peaks in the obtained logs are observed by applying photon sources with higher energies compared with the other sources.

Figure 13 shows results of radiography by 660 keV photons when the crude oil inside the casing was diluted in comparison with the standard conditions. As shown in this figure, there might be no fluid in a part of the casing in some cases. Empty casing or decreasing the fluid density inside the casing provides enough potential for collapse. Changes in the density of the fluid in the casing could accurately be monitored by backscatter photon radiography.

Figure 14 shows the results of backscatter radiography for monitoring spaces between the casing and concrete where filled by gas, brine, or oil. This simulation was repeated by applying an average 4.2 MeV neutron source, as well.

Results of counting produced photons during neutron-gamma interactions were presented in Figure

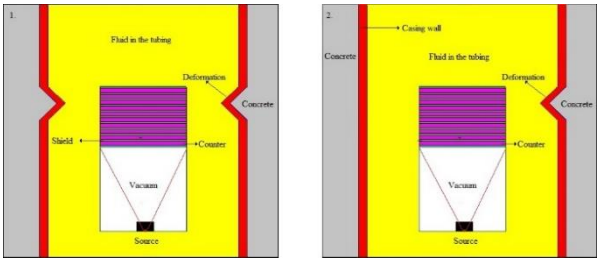

Figure 10. Two types of deformations investigated in casing collapse

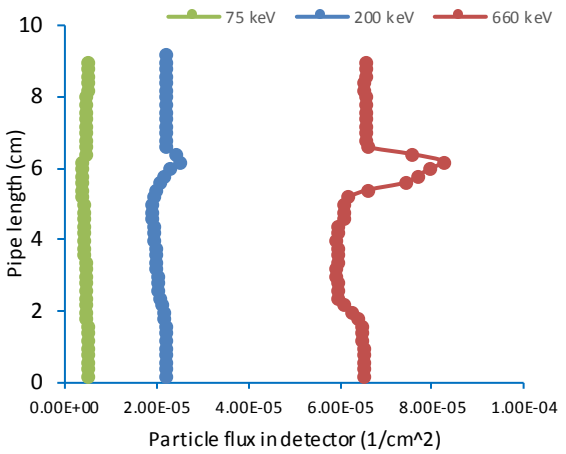

Figure 11. Photon log by various photon energies for detection of deformation shown in Figure 10.1

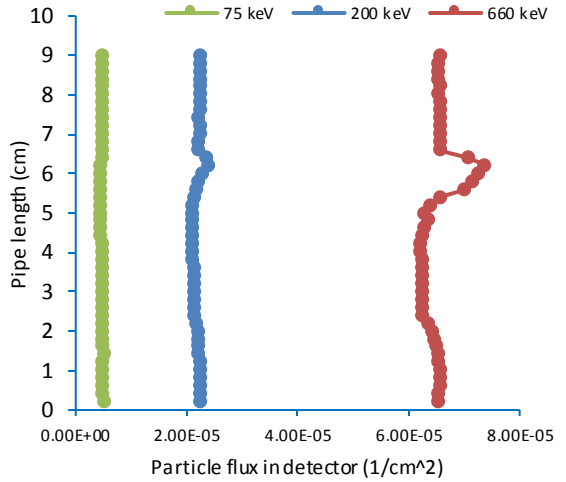

Figure 12. Photon log by various photon energies for detection of deformation shown in Figure 10 (right)

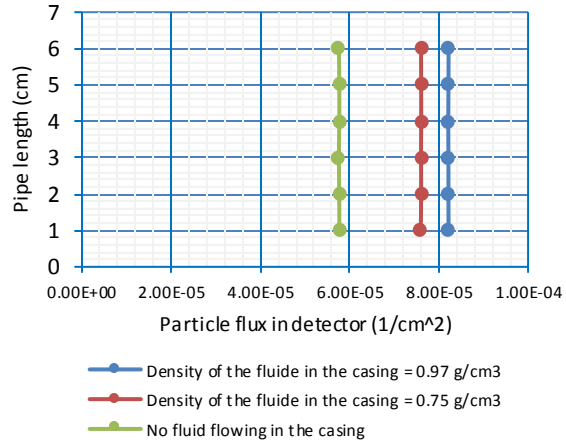

Figure 13. Photon log for different densities of fluid flowing in the casing (photon energy=660 keV)

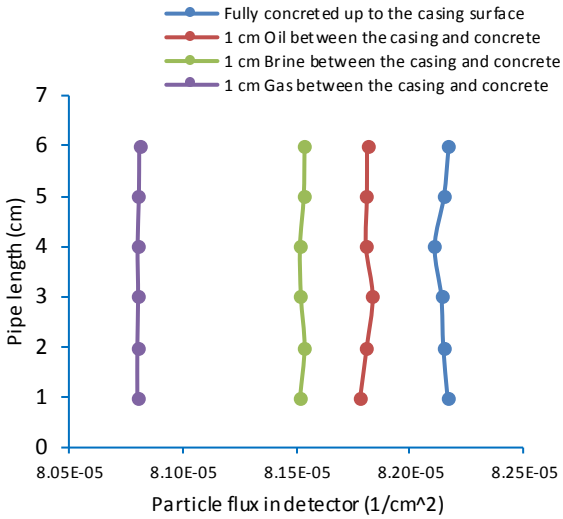

Figure 14. Photon log for detection of space between the casing and concrete filled by oil, gas, and brine (photon energy=660 keV)

15. As shown in this figure, there is a good distinction between the state fully concreted and the state with the presence of voids where filled by oil or gas. Figure 16 shows the radiography data with a neutron source and counting produced photons.

Results in Figures 13 to 16 are based on the deformation shown in Figure 10. The primary purpose of the simulation was to realize the pressure increment on the outer surface of the casing. The mentioned parameter was detected via its consequence in the density of concrete. A change in the density of concrete could be identified by applying a neutron source.

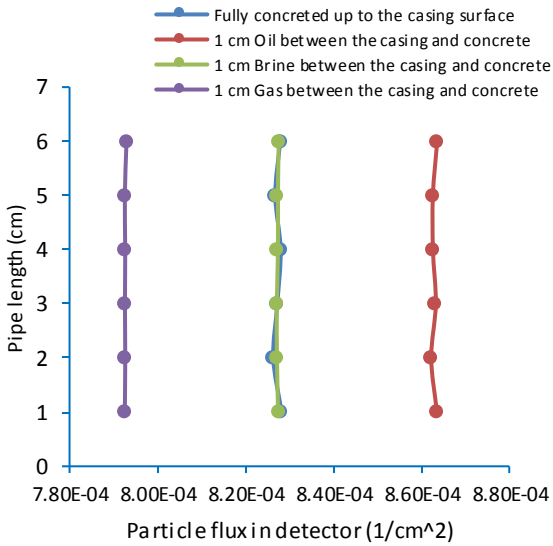

Figure 15. Photon log for detection of space between the casing and concrete filled by oil, gas, and brine by applying neutron source (source average energy=4.2 MeV)

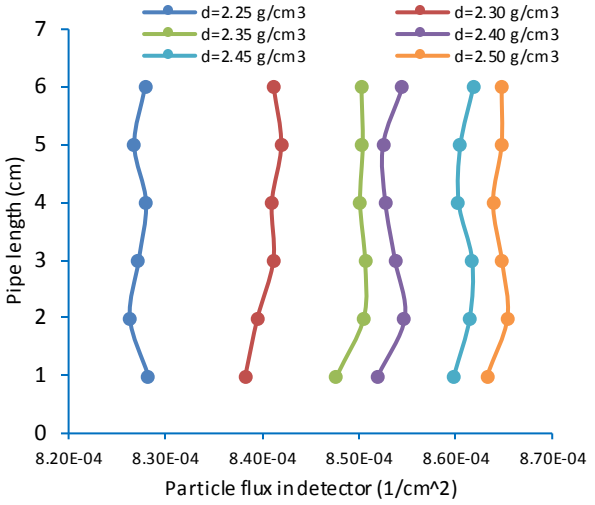

Figure 16. Photon log obtained by neutron source considering various concrete densities behind the casing (source of Am-Be, average energy = 4.2 MeV)

Neutrons could pass through the steel body of the casing and enter the concrete material. In the concrete, photons with different energies might be produced and scattered in the medium due to interacting neutron-gamma. A number of these photons might backscatter to the detectors placed in the middle of the casing. The pressure on the outside surface of the casing can be obtained by counting the photons and comparison with typical situations. In fact, the concrete density will change with changes in photons count. This may be a potential for casing collapse. Based on the results obtained by the simulations, creating an initial prototype for more extensive research and applying it to identify and correct issues in the design can be recommended as a future direction.

4. CONCLUSIONS

Casing failures and pipeline bursting are significant problems in upstream oil industries, and every year, a lot of resources are spent on repairing, rehabilitating, and re-drilling due to the consequences of this phenomenon. In this research, Monte Carlo method was fully applied to investigate probable pipeline bursting and casing failure. The backscatter radiography technique in the early detection of destructive factors was successfully used. The results showed that backscatter radiography by the source of photon or neutron as a fast, in-situ, and non-destructive testing method could monitor inside pipeline or casing and detect abnormalities which may cause bursting or collapse. This method, along with the other inspection techniques, can be applied for the pipeline inspection.

5. REFERENCES

1. Rabia, H.," Oil well drilling engineering: principles and practice", London: Graham & Trotman, (1985).
2. Chilingar, G.V., Serebrykov, V.A., Robertson, J., "Origin and Prediction of Abnormal Formation Pressures", Elsevier Science, First Edition, (2002), 373.
3. Zhi, Z., Jianping, H., Minghua, H., Jun, H., Genda, C., "Casing pipe damage detection with optical fiber sensors: A case study in oil well constructions", ***Advances in Civil Engineering***, (2010), 1-9. DOI: 10.1117/12.848727
4. Ghodusi, F., Jalilfar, H., Jafari, S. "Analysis of the casing collapse in terms of geomechanical parameters and solid mechanics", ***Journal of Chemical and Petroleum Engineering***, 53, No. 2, (2019), 211-225. DOI: 10.22059/jchpe.2019.274240.1267
5. Abdideh, M., HedayatiKhah, S., "Analytical and numerical study of casing collapse in Iranian Oil field", ***Geotechnical and Geological Engineering*** 36, (2018), 1723-1734. https://doi.org/10.1007/s10706-017-0428-0
6. Taylor, N., Clubb, G., Atkin, I.M., 2015. The effect of bending and axial compression on pipeline burst capacity. ***Society of Petroleum Engineers***. https://doi.org/10.2118/175464-MS
7. Pleşcan, C., Tanciu, M.D., Zasz, M., "The Effect of Internal Pressure on Radial Strain of Steel Pipe Subjected to Monotonic and Cyclic Loading", ***Materials*** 12, No. 18, (2019), 1-12. DOI: 10.3390/ma12182849
8. Wypych, G., "Handbook of Plasticizers", Third Edition, Chem. Tec Publishing. (2017), DOI: 10.1515/ijnaoe-2015-0031
9. Lee, G.H., Pouraria, H., Seo, J.K.W., Paik, J.K., "Burst strength behavior of an aging subsea gas pipeline elbow in different external and internal corrosion-damaged positions", ***International Journal of Naval Architecture and Ocean Engineering*** 7, No. 3, (2015), 435-451.
10. Rahmani, F., Azimi, S., Bayat, E., Dost Mohammadi, V., "Comparison of the time behavior in the separation of light and heavy materials in X-ray backscattered method as a diagnostic tool in inspection", ***Nuclear Instruments and Methods in Physics Research Section A: Accelerators, Spectrometers, Detectors and Associated Equipment*** 812, (2016), 86-91. DOI: 10.1016/j.nima.2015.12.052
11. Jamshidi.V., Davarnejad, R., "Simulation of corrosion detection inside wellbore by X-ray backscatter radiography", ***Applied Radiation and Isotopes*** 145, (2019), 116-119. https://doi.org/10.1016/j.apradiso.2018.12.026
12. Jamshidi, V., Davarnejad, R. "Simulation of deposition detection inside wellbore by photon backscatter radiography", ***International Journal of Engineering Transactions C: Aspects***, Vol. 33, (2020), 2450-2454. DOI: 10.5829/IJE.2020.33.12C.03
13. Jamshidi, V., Davarnejad, R. "Photon backscatter radiography application for the simulation of corrosion detection inside a pipeline: A novel proposal for 360o corrosion consideration in the pipelines", ***Applied Radiation and Isotopes*** 176, (2021), 109844. https://doi.org/10.1016/j.apradiso.2021.109844
14. Knoll, G.F., 2010. Radiation detection and measurement, Wiley, New York, US.
15. Kelley, J., Cui, S., Baciak, J., "Measurement of the modulation transfer function for a backscatter radiography system used in nondestructive examination", ***Radiation Physics and Chemistry*** 155, (2019), 202-208. DOI: 10.1016/j.radphyschem.2018.10.004
16. Shuang, C., Jyothier, K.N., Saniiv, S., Bence, B., James, E.B., "Low-cost current mode data acquisition board for X-ray backscatter imaging systems", ***Nuclear Instruments and Methods in Physics Research Section A: Accelerators,***

Spectrometers, Detectors and Associated Equipment 954, (2020), 162210. DOI: 10.1016/j.nima.2019.05.051

17. Kaldal, G., Jonsson, M., Pálsson, H., Karlsdottir, S., "Collapse analysis of the casing in high temperature geothermal wells", Thirty-Eighth Workshop on Geothermal Reservoir Engineering, Stanford University, Stanford, California, (2013).
18. Asadi, A., Parhizgar, N., Momeni, E., "Prediction of collapse in a casing and tubing: with case study of Iran", ***Australian Journal of Basic and Applied Sciences*** 5, No. 11, (2011), 831-840.
19. Karlsdottir, S.N., Thorbjornsson, I.O., "High Temperature Geothermal Wells Center of Excellence in Iceland - Phase I: Corrosion testing of steel in high temperature geothermal wells in Iceland", Technical Report for RANNIS (The Icelandic Centre for Research), Reykjavik. (2009).
20. Shohanna, I., 2015. Relation between density and compressive strength of hardened concrete, ***Concrete Research Letters*** 6, No. 4, 182-189.
21. Briesmeister, F.J., "MCNP-A General Monte Carlo, N-Particle Transport Code", Version 4C, Los Alamos National Laboratory, (2000).
22. McKinney, G.W., "MCNP6 Cosmic & Terrestrial Background Particle Fluxes – Release 3". Los Alamos National Laboratory, United States. (2013).
23. NRC's Regulations, "Title 10, Code of Federal Regulations", Standards for protection against radiation, Section 20.1003. (2016).
24. Shedlock, D., Hammerschmidt, A., "X-ray backscatter device for wellbore casing and pipeline inspection", US patent: 8138471 B1, 20 March, (2012).
25. StanojevPeriera, M.A., Pugliesi, R., Pugliesi, F., 2008. Neutron induced alpha radiography, ***Radiation Measurements***, 43(7): 1226-1230.
26. Williams, R.G., Gesh, C.J., Pagh, R.T., "Compendium of Material Composition Data for Radiation Transport Modeling", Pacific Northwest National Laboratory. (2006).
27. Speight, J.G. "Handbook of petroleum analysis", John Wiley & Sons, US. (2001).
28. Prenga, Dode., "General Features of the q-XY Opinion Model", ***Journal of Human, Earth, and Future*** 1, No. 2, (2020), 87-96. Doi: 10.28991/HEF-2020-01-02-05

Persian Abstract

چکیده

در صنایع نفت و گاز، رادیوگرافی پس پراکنده به عنوان یک تکنیک موفق می تواند در تشخیص تغییر حالت و فروشکست خطوط لوله جداری به کار گرفته شود. یک تکنیک عددی معتبر اجازه پیشگویی درخصوص این موضوعات بدون نیاز به دسترسی به پشت خطوط لوله را میسر می سازد. علاوه بر این، این تکنیک قابلیت تخمین شکل و عمق آسیب ها را نیز دارد. بسته به موقعیت مکانی این خطوط که ممکن است در زیر زمین یا دریا باشند، معمولا ترجیح داده می شود از روش های آزمون غیر مخرب (NDT) که می توانند وضعیت خطوط را از داخل آنها و بدون نیاز به دسترسی به پشت آنها پایش کنند استفاده شود. در این مطالعه، رادیوگرافی پس پراکنده به عنوان یک روش کاربردی و غیرمخرب برای شناسایی نقاط با قابلیت تغییر حالت تورمی و یا فروشکست به کمک ابزار شبیه سازی مونت کارلو به کار گرفته شده است. نتایج حاصل از شبیه سازی ها نشان می دهد این روش می تواند به خوبی تغییر حالات، نواحی خورده شده، رسوبات، فشارات وارده بر جدار، سیمان کاری نامناسب، فشار بیش از حد داخلی و یا سایر عواملی که ممکن است ریسک احتمال وقوع این دو پدیده را افزایش دهند (به صورت درجا و زنده) و با دقت قابل قبولی آشکار سازد.

International Journal of Engineering

Journal Homepage: www.ije.ir

Generating Electrical Power using Movement of Various Vehicles in New Lighting Base

M. M. Peiravi*, D. Domiri Ganji

Department of Mechanical Engineering, Babol Noushirvani University of Technology, Babol, Iran

P A P E R I N F O

Paper history:
Received 28 September 2021
Received in revised form 18 November 2021
Accepted 20 November 2021

Keywords:
Automatic Guidance System
Generating Electricity Power
Helical Savonius
New Lighting Base
Various Vehicles Movement

A B S T R A C T

This work represent a proposed design to supply street lighting power using moving vehicles with an automatic system to guide the fluid flow. In the present design, wind turbines are integrated on the body of the lighting base, which can reduce the construction cost compared to previous designs and use the fluid flow of all vehicles movement with different dimensions to increase system efficiency. Also, present investigation, has been used an automatic system to direct the fluid flow to the wind turbines to increase the efficiency in supplying electricity, which was not installed in the previous designs. Other features of this system include the production of electricity in inappropriate weather and storm conditions, unlike previous designs that had to stop the wind turbine in these conditions to decrease damage. Finally, illuminating the streets and alleys, the stored energy can be used for other purposes, such as charging car batteries and lighting resort stations. Then, comparison between the best design of the third model based on lighting and second model with four vertical wind turbines (VWT) and solar panel (SP), the power generation has increased by 35.55 %. Finally, using an automatic guidance systems (AGS) of fluid flow in the third model based on lighting, the power generation was enhamced by 64.86 %.

doi: *10.5829/ije.2022.35.02b.15*

1. INTRODUCTION

The lighting base in the present design is independent of AC electricity and by using the automatic guidance system of air flow due to the movement of various vehicles, it can produce more electricity for the consumption of street lighting. One of the basic methods of lighting in the current plan in the streets and highways to supply and store electricity is completely independent of municipal electricity. In addition to illuminate the streets and alleys, the stored energy can be used for other purposes, such as charging car batteries and lighting resorts and recreation area. So, recently works in this area represented as follow:

Chinforoush and Latif-Shabgahi [1] investigated a new method for detecting heterogeneities in wind data set to predict wind speed based on the well-known Hidden Markov Model. Kashyzadeh et al. [2] presented the line of action of wind or aero-dynamical force applied to the vehicle model to pass through the vehicle mass center. The vibrations of the half-vehicle model have been found via the Runge-Kutta method. Peiravi et al [3, 4], Peiravi and Alinejad [5] numerically investigated arrangement fins in the systems with stable conditions of fluid flow velocity. Also, Marchione [6] numerically investigated the stress distribution in the adhesive layer under buckling condition. The study presented develops with the analysis of a single-lap joint with a combination of steel adherents and three different structural adhesives with different thickness and Young's modulus. Martynyuk et al. [7] surveyed the photovoltaic system that operated in different conditions such as changing solar irradiance and environmental temperature. In addition, Ganji et al. [8], Alinejad and Peiravi [9] numerically surveyed fluid flow phenomena in different condition of systems. Asadollahzadeh et al. [10] studied

*Corresponding Author Email: Mohsenpeiravi@gmail.com (M. M. Peiravi)

Please cite this article as: M. M. Peiravi, D. Domiri Ganji, Generating Electricity Power using Movement of Various Vehicles in New Lighting Base, ***International Journal of Engineering, Transactions B: Applications***, Vol. 35, No. 2, (2021) 387-396

the ionic liquid application development to extract europium ions in single and binary systems. A green procedure for europium extraction from aqueous chloride solution was investigated using phosphonium ionic liquid Cyphos. An extensive work conducted by Peiravi and Alinejad [11], Pasha et al. [12] on numerically simulated fluid flow in a channel and between two equal plates. Jond et al. [13] solved the control problem of a vehicle convoy modeled with linear dynamics. They considered the control problem of a vehicle convoy modeled with linear dynamics. The convoy formation requirement is presented in terms of a quadratic performance index. Zhang et al. [14] proposed a novel method for system failure reasoning based on Bayesian networks to solve emergency airflow control system reliability problems. A system fault tree model was established to identify the logical relationship between the units, which was then transformed into a Bayesian network fault analysis model to determine network node states and the conditional probability table, as well as to carry out diagnostic reasoning on the system node branches. Umana et al. [15] focused on biomass production from palm oil. This work stated on the utilization of biomass products derived from oil palm and oleochemical derivatives extracted. Kerich [16] surveyed on safe drinking water source for the residents and defined a suitable system for potable water treatment from pesticides polluted surface water source. Ha [17] proposed a simple but effective trailing edge flap system. This preliminary concept used a more practical and stable actuation system which consists of a motor-driven worm gear drive and flexible torsion bar. Sawant et al. [18] represented a review of state-of-the-art review works on wind-energy-related issues that classification into several main topics in the field of energy research.

The present work illustrated the lighting base, which is independent of electricity of city power source and includes wind turbines that are installed at regular intervals on the lighting base. Fluid flow is independent of the movement of all types of vehicles in different directions using an automatic flow guidance system for turbines. As a result, with the energy supply unit, the electricity stored for lighting of streets and other uses. This device consists of 6 main parts: wind turbine unit, control unit, energy supply unit, solar panel unit, lighting unit and body.

2. GEOMETRY OF THE INVENTION

This work represented three models of new lighting base that work with the movement of various vehicles for AC electricity power equipped with an automatic guidance system of fluid flow. According to Figure 1, this paper described all models with details that third model is our new patent.

Helical savonius wind turbine used in all models to lighting base has maximum performance for producing AC electricity power. Figures 2 and 3, illustrated schematics of helical savonius wind turbine with presentation view.

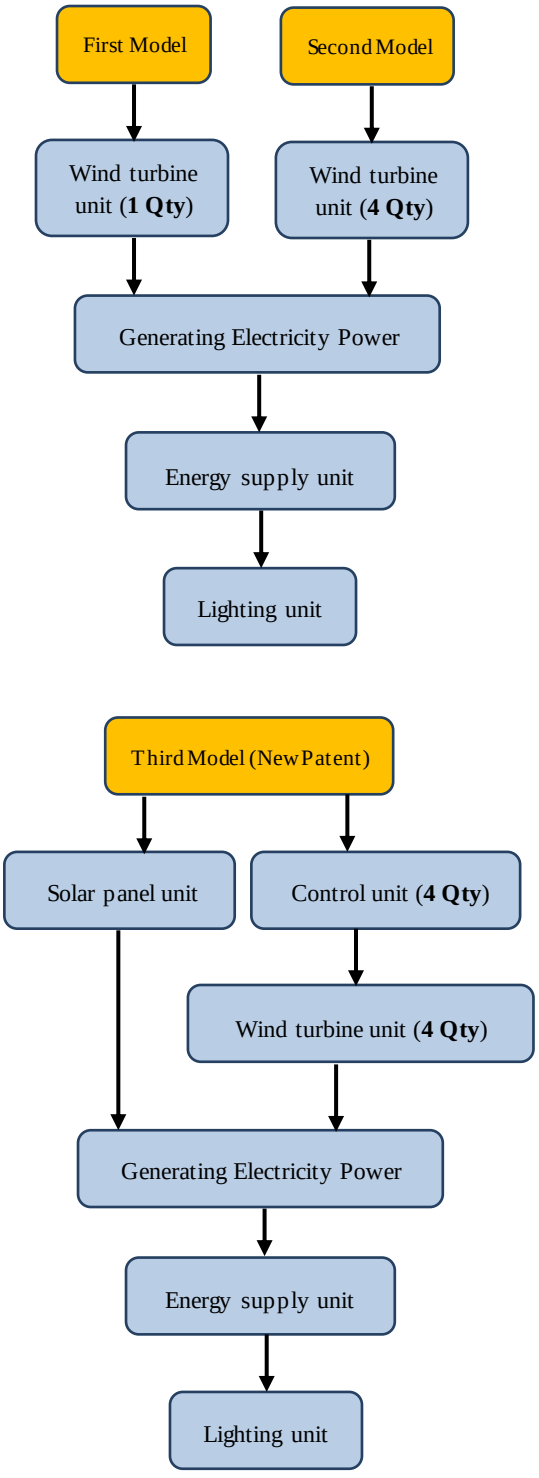

Figure 1. Flowchart of research methodology

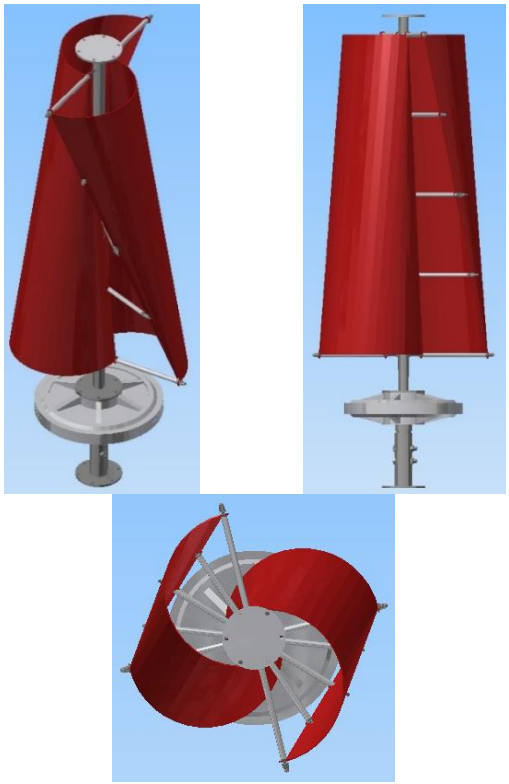

Figure 2. 3D Schematics of helical savonius wind turbine

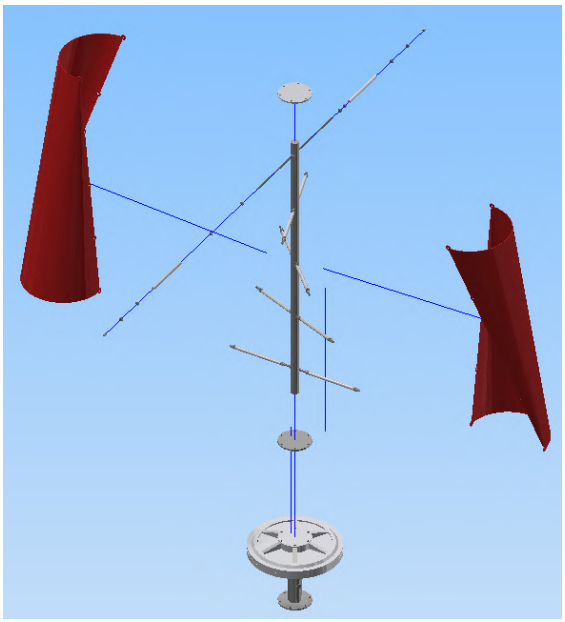

Figure 3. Presentation view of helical savonius wind turbine

The physical characteristics of the savonius blades wind turbine are summarized in Table 1.

2. 1. First Model Lighting base for producing electricity power required to power supply unit. This unit depends on wind turbine unit. So, according to Figure 4, power supply unit and wind turbine unit designed at the top and down of the box in first model, respectively. Figure 5 illustrated installation of these units with details. Also, first model has a fixed guidance systemof air flow as shown in Figure 4.

First model has three units that power supply unit and wind turbine unit represented in Figures 4 and 5. Lighting unit is the third unit with two LED lamps that is illustrated with details in Figure 6.

Table 2 and Figiure 7, represents power generation in the first model based on lighting with changing in use of solar panel (SP), and fixed guidance systems (FGS) of fluid flow as shown below

TABLE 1. Physical properties of savonius wind turbine

Material	Aluminum 6061
Density (g/cm^3)	2.7
Mass (kg)	2.25562
Area (mm^2)	841671
Volume (mm^3)	835416
Yield Strength (MPa)	275
Ultimate Tensile Strength (MPa)	310
Young's Modulus (GPa)	68.9
Poisson's Ratio (ul)	0.33
Shear Modulus (GPa)	25.9023
Power Generation (W)	500

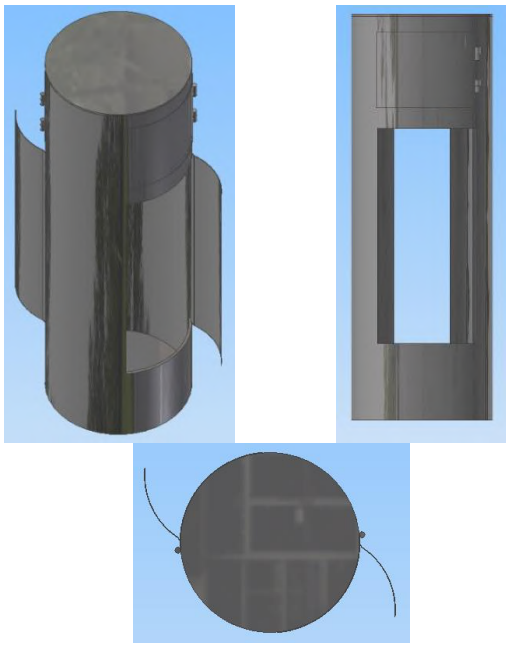

Figure 4. Power supply unit and wind turbine units in first model

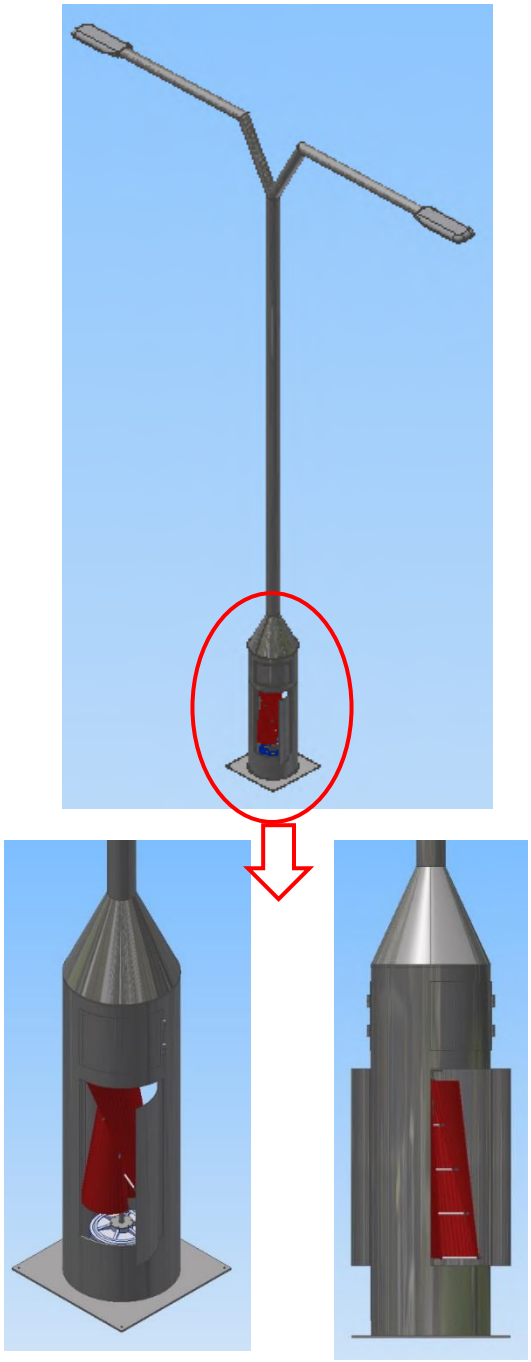

Figure 5. First model of lighting base

2. 2. Second Model The novelty in the second model was based on using four wind turbine units without guidance system of air flow according to Figure 9. So, air flow of the movement of different vehicles and free air flow applied on wind turbines. Three dimensional of second model illustrated in Figure 10. Power supply unit and lighting unit designed in down and top of lighting base that represented in Figures 8 and 11.

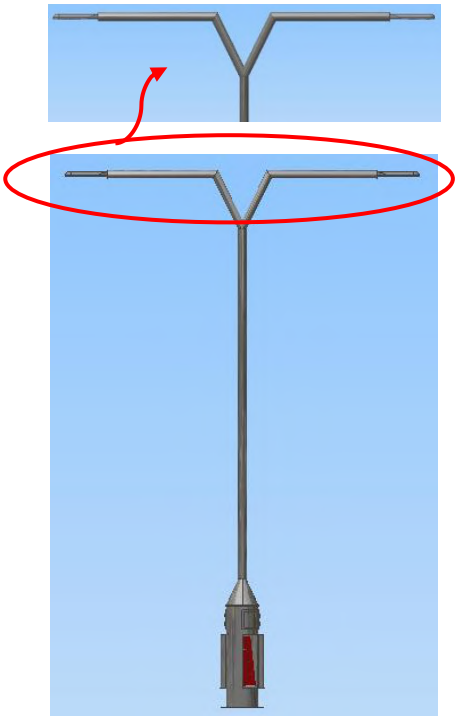

Figure 6. Lighting unit in first model

TABLE 2. Analysis of power generation in the first model base on lighting

Models	Power generation, W
First Model without FGS and SP (A)	400
First Model with FGS and without SP (B)	600
First Model without FGS and with SP (C)	650
First Model with FGS and SP (D)	850

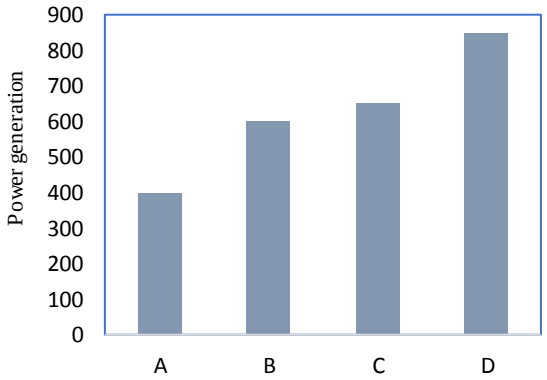

Figure 7. Comparison of power generation in the first model based on lighting

According to Table 3 and Figure 10, power generation in second model based on lighting with modification on quantity of vertical wind turbines

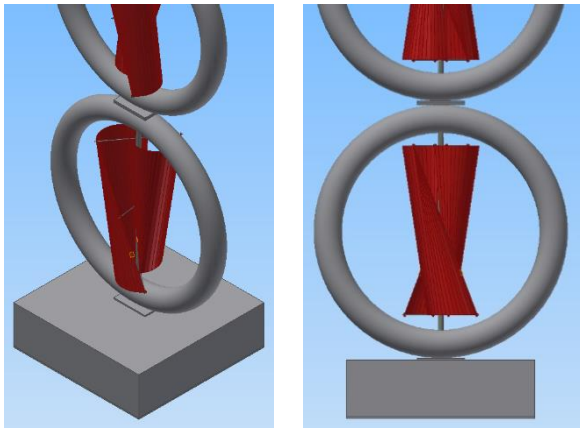

Figure 8. Power supply unit in second model

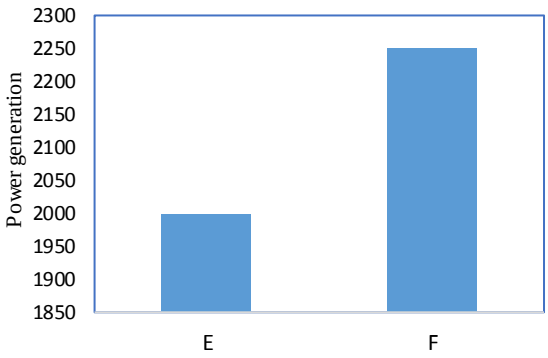

Figure 10. Comparison of power generation in second model based on lighting

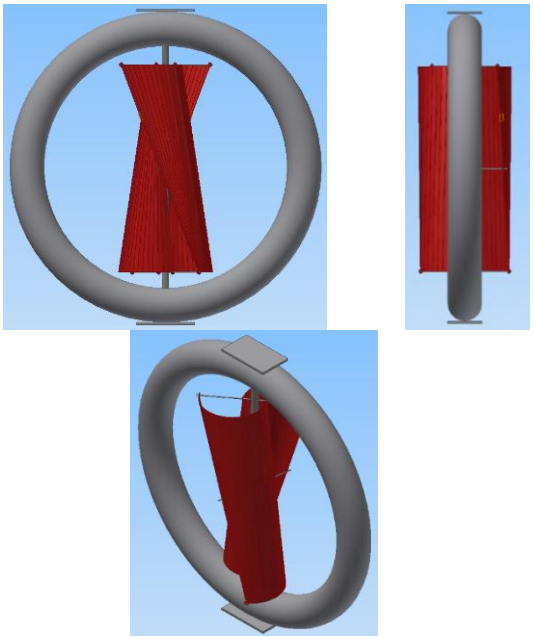

Figure 9. Wind turbine unit in second model

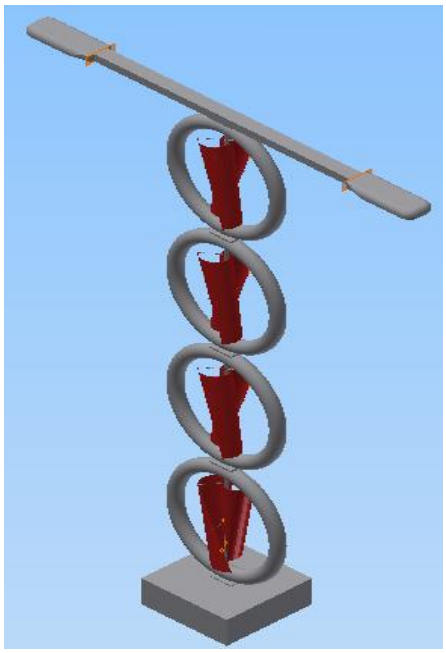

Figure 11. Second model of lighting base

(VWT) and presented with solar panel (SP). This model does not have the fixed guidance systems (FGS) and automatic guidance systems (AGS) of fluid flow.

2. 3. Third Model In this design, wind turbines are used at regular and independent intervals using an automatic system for directing the fluid flow due to the movement of various vehicles in different dimensions to provide street lighting. According to Figure 13, the height of the lighting base is about 7 *m* and its diameter is about 80 *cm*. The present lighting base, is completely independent of the city electricity and consists of 4 basic parts that is described as follows:

TABLE 3. Analysis of power generation in second model based on lighting

Models	Power generation
Second Model with four VWT and without SP (E)	2000 w
Second Model with four VWT and with SP (F)	2250 w

2. 3. 1. Wind Turbine Unit The lighting base in the present design uses four wind turbines to take advantage of the fluid flow of the movement of various vehicles as shown in Figure 14. According to Figure 15, the wind turbines embedded in the lighting base are completely independent of each other for more performance. So each turbine is installed at different heights to take advantage of the fluid flow using the movement of various vehicles.

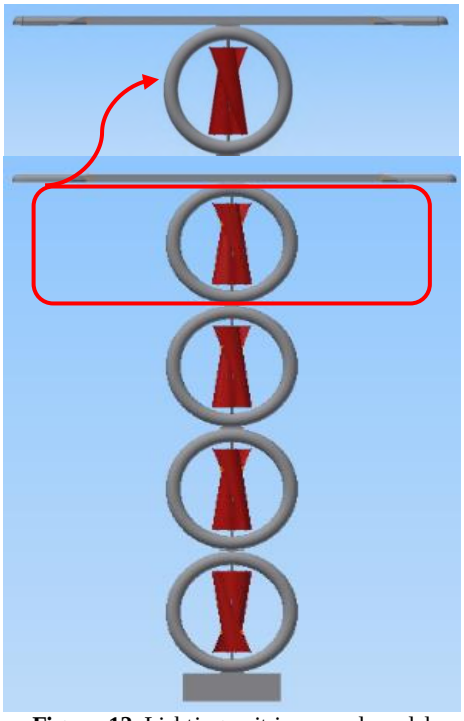

Figure 12. Lighting unit in second model

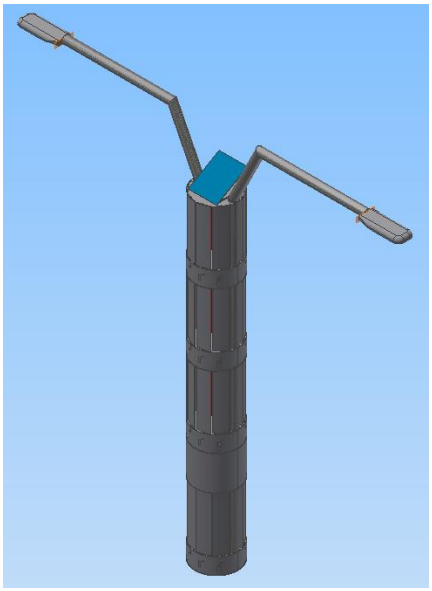

Figure 13. Third model of lighting base

In this section, according to Figure 16, semilunar plates have been used to direct the fluid flow with larger volume to the wind turbine. In each of these turbines, eight semilunar plates have been used, and the rotational motion of each of these plates will be performed in the control unit. Also, in each unit of wind turbine, four rectangular plates are installed next to the body of the lighting base in pairs and with a specific angle, so, its application will be explained in control unit.

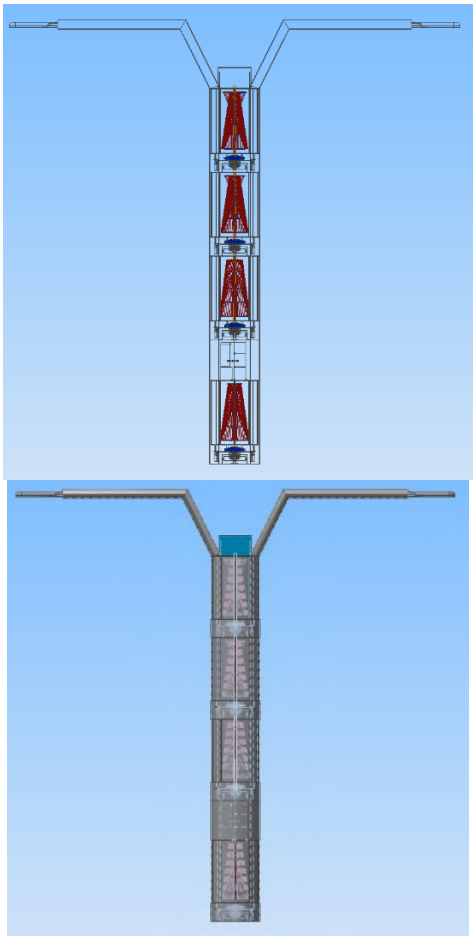

Figure 14. Inside view of third model

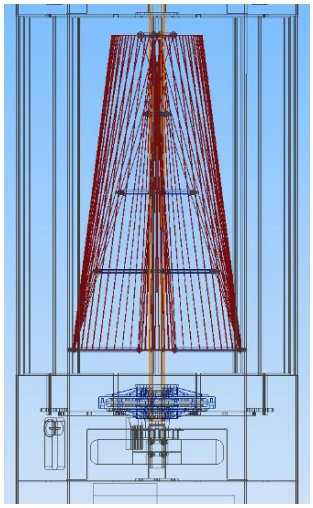

Figure 15. Wind turbine unit in third model

2. 3. 2. Control Unit Due to the fact that in urban areas the velocity of air flow due to the movement of cars is slow, so the use of wind turbines will be challenged in practice. On the other hand, in some areas, due to stormy

Figure 16. Automatic guidance system of fluid flow in third model

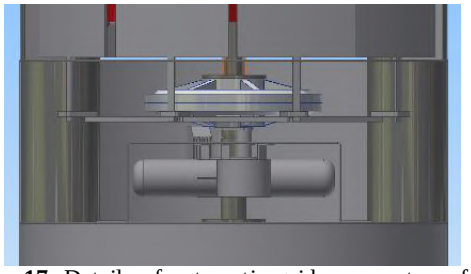

Figure 17. Details of automatic guidance system of fluid flow

weather, the intensity of the air flow may be so more that it causes the blades to rotate too much and the wind turbine to fail. To solve these problems, the current lighting base uses an automatic guidance system for airflow, according to Figure 17. The operation of this system, which some parts is in the control unit and another parts in the wind turbine unit, is described as follows.

First, according to Figure 18, using the anemometers that are installed on the door, the direction and velocity of air flow that is caused by the movement of various vehicles and natural wind is measured. The stored information from the anemometer is transferred to the analog input of the PLC device. The PLC device is installed on the door. According to the program code

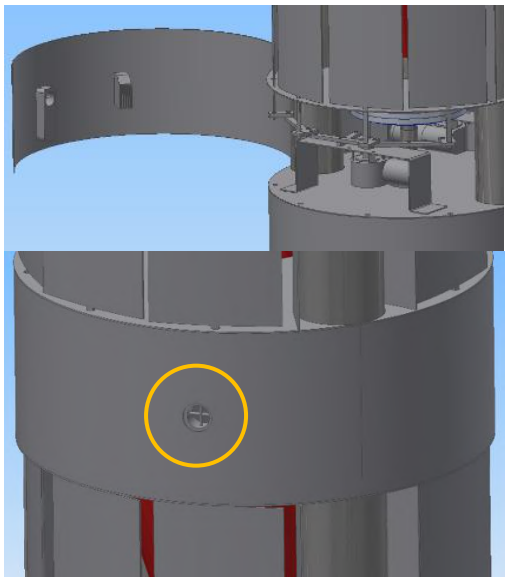

Figure 18. Anemometer and plc on the door

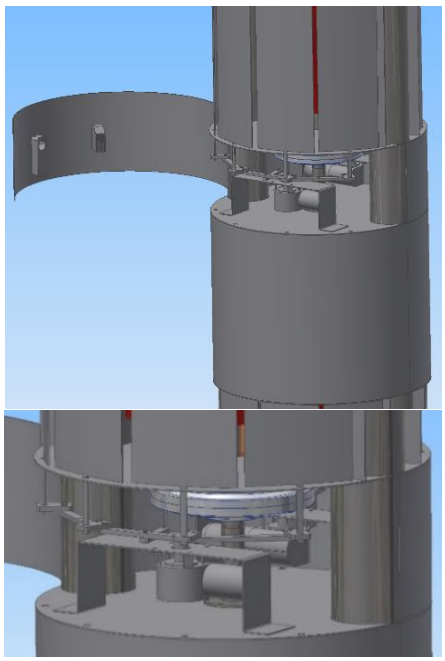

written in this device, in accordance with the speed and direction of the air fluid caused by the movement of the vehicle and the natural air flow, the desired commands and instructions are transmitted to the engine installed in the control unit. Each of semilunar plates, according to the velocity and direction of the air flow, is located in a direction that transmits the maximum air flow rate to the wind turbine so that the wind turbine has the maximum efficiency in order to supply electricity. Also, in cases where the intensity of the air flow is so more (such as storm air), according to the program code that defined in the PLC device, order to the semilunar plates to close in a circular direction and be closed. So, prevent the air flow from entering the wind turbine completely. These components help to completely close the semilunar plates in unfavorable weather conditions and the air flow is sufficient to rotate the turbine blades. Moreover, in this unsuitable condition, the turbine can provide the desired fluid flow and efficiency without decreasing. As a result, in unfavorable weather conditions, not only the additional costs decreased, also, electricity can be generated for the intended use.

2. 3. 3. Power Supply Unit In this unit, an inverter is used to convert the DC current of the photovoltaic cell to the AC current. Also, 4 batteries are used to store energy and one charge controller is used to control the charge of the batteries. according to Figure 19, for controlling, maintenance and repair of electrical equipment, this compartment includes two separate doors. One door has direct access to the inverter and the second door access to other electrical equipment in the enclosure. The number of batteries used varies according to the amount of electricity stored in them for use in the lighting base and other uses. The position of the electrical equipment housing will change according to the installation position of the lighting base and can be moved to the ground with the nearest wind turbine.

2. 3. 4. Solar Panel and Lighting Unit This part of the lighting base is intended to complete the design and achieve maximum energy from renewable sources. According to Figure 20, the desired solar panel with dimensions of 530 × 670 mm^2 is installed on top of the last wind turbine. The location and direction of the solar panel is considered appropriate to the position of the sun's radiations at the desired angle and direction.

In the present design, two sets of LED lighting with low energy consumption and high exposure have been used. The choice of power consumption for each of these lamps is determined by the height of the lighting base and its position.

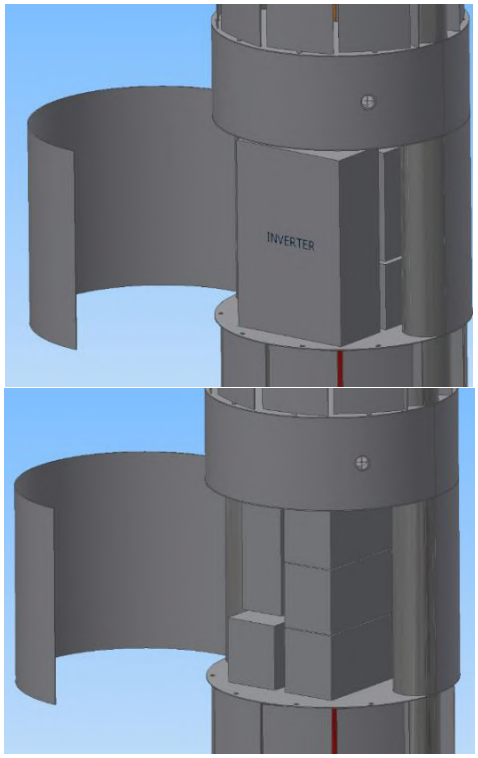

Figure 19. Power supply unit in the third model

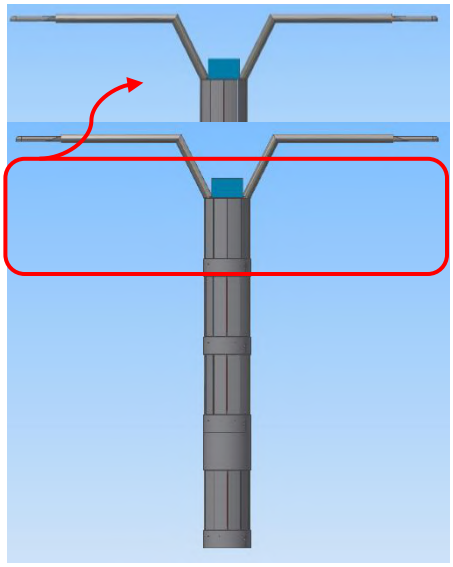

Figure 20. Lighting unit in the first model

Table 4 and Figure 21, represent power generation of the third model based on lighting base with modification on quantity of vertical wind turbines (VWT), solar panel (SP) and automatic guidance systems (AGS) of fluid flow as illustrated below:

Figure 22, illustrates power generation for ten cases of the third model based on lighting. According to this

TABLE 4. Analysis of power generation in all models of lighting base

Models	Power generation
Third Model without AGS and SP (G)	1600 W
Third Model without AGS and with SP (H)	1850 W
Third Model with AGS and without SP (I)	2800 W
Third Model with AGS and SP (K)	3050 W

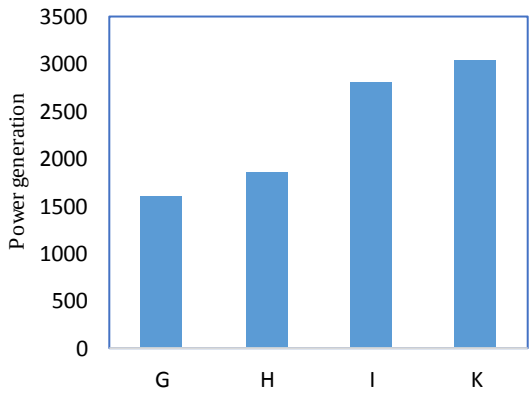

Figure 21. Comparison of power generation in the third model based on lighting

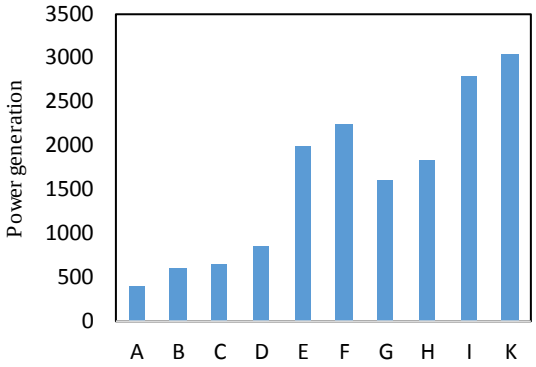

Figure 22. Comparison of power generation between all models based on lighting

figure, the third model based on lighting with automatic guidance systems (AGS) of fluid flow and solar panel (SP) has maximum power generation of 3050 W. Also, comparison between the third and second models with four vertical wind turbines (VWT) and solar panel (SP), power generation has increased by 35.55%.

3. CONCLUSION

study represented the basic methods of lighting in the streets and highways to supply and store electricity completely independent of municipal electricity. The stored energy used for charging the batteries of electric cars and lighting the resort stations. The heights of lighting base and wind turbine unit are 7m and 1 m, respectively. Also, the height of control unit and energy supply unit is 0.3 and 0.65 m, respectively. So, critical results summarized as follows:

- Unlike previous lighting base, in the current design, the wind turbine is integrated on the body of the lighting base. This integration of the design reduces the cost of body construction and power supply, as well as increases the beauty of the lighting base.
- In the present design, several independent wind turbines are installed on the body, which can be used to the fluid flow of all vehicles movement with different dimensions to increase the efficiency of the power generation system.
- In the present design, an automatic system for directing the fluid flow to the wind turbines has been used to increase the efficiency in supplying electricity, which was not installed in the previous designs of this system.
- In the previous designs, in unfavorable weather and storm conditions due to high rotation of the blades, the wind turbine had to be controlled to cause less damage to it, but in the present system, in addition to not damaging the wind turbine, also the turbine can continue to operate and generate electricity.
- Comparison between the third model based on lighting with automatic guidance systems (AGS) of fluid flow and solar panel (SP) and the second model with four vertical wind turbines (VWT) and solar panel (SP), power generation has increased by 35.55 %.
- Using of the automatic guidance systems (AGS) of fluid flow in the third model based on lighting, the power generation has increased by 64.86 %.

4. REFERENCES

1. Chinforoush, N., and Latif Shabgahi, Gh., "A Novel Method for Forecasting Surface Wind Speed using Wind-direction based on Hierarchical Markov Model." ***International Journal of Engineering, Transactions B: Applications,*** Vol. 34, No. 2, 414-426, (2021). DOI: 10.5829/IJE.2021.34.02B.13
2. Reza Kashyzadeh, K., Mousavi Bafrouyi, S. M., and Khorsandijou, S. M., "Effects of Road Roughness, Aerodynamics, and Weather Conditions on Automotive Wheel Force." ***International Journal of Engineering, Transactions B: Applications***, Vol. 34, No. 2, 536-546, (2021). DOI: 10.5829/IJE.2021.34.02B.27
3. Peiravi, M. M., Alinejad, J., Ganji, D. D., and Maddah, S, "3D optimization of baffle arrangement in a multi-phase nanofluid natural convection based on numerical simulation." ***International Journal of Numerical Methods for Heat & Fluid Flow,*** Vol. 30, No. 5, 2583-2605, (2020). DOI: 10.1108/HFF-01-2019-0012
4. Peiravi, M. M., Alinejad, J., Ganji, D. D., and Maddah, S., "Numerical study of fins arrangement and nanofluids effects on three-dimensional natural convection in the cubical enclosure." ***Challenges in Nano and Micro Scale Science and Technology,*** Vol. 7, No. 2, 97-112, (2019). DOI: 10.22111/TPNMS.2019.4845
5. Peiravi, M. M., and Alinejad, J., "Nano particles distribution characteristics in multi-phase heat transfer between 3D cubical enclosures mounted obstacles." ***Alexandria Engineering Journal,*** Vol. 60, No. 6, 5025-5038, (2021). DOI: 10.1016/j.aej.2021.04.013
6. Marchione, F., "Analytical Stress Analysis in Single-lap Adhesive Joints under Buckling." ***International Journal of Engineering, Transactions B: Applications,*** Vol. 34, No. 2, (2021), 313-318. DOI: 10.5829/IJE.2021.34.02B.02.
7. Martynyuk, V. V., Voynarenko, M. P., Boiko, J. M., and Svistunov, O., "Simulation of Photovoltaic System as a Tool of a State's Energy Security." ***International Journal of Engineering, Transactions B: Applications,*** Vol. 34, No. 2, 487-492, (2021). DOI: 10.5829/IJE.2021.34.02B.21
8. Ganji, D. D., Peiravi, M. M., and Abbasi, M., " Evaluation of the heat transfer rate increases in retention pools nuclear waste." ***International Journal of Nano Dimension,*** Vol. 6, No. 4, 385-398, (2015). DOI: 10.7508IJND.2015.04.007
9. Alinejad, J., and Peiravi, M. M., " Numerical analysis of secondary droplets characteristics due to drop impacting on 3D cylinders considering dynamic contact angle." ***Meccanica,*** Vol. 55, 1975–2002, (2020). DOI: 10.1007/s11012-020-01240-z
10. Asadollahzadeh, M., Torkaman, R., and Torab-Mostaedi, M., "Optimization of Green Technique Develop for Europium (III) Extraction by using Phosphonium Ionic Liquid and Central Composite Design Approach." ***International Journal of***

Engineering, Transactions B: Applications, Vol. 34, No. 2, 508-516, (2021). DOI: 10.5829/IJE.2021.34.02B.24

11. Peiravi, M. M., and Alinejad, J., " Hybrid conduction, convection and radiation heat transfer simulation in a channel with rectangular cylinder." ***Journal of Thermal Analysis and Calorimetry,*** Vol. 140, 2733–2747, (2020). DOI: 10.1007/s10973-019-09010-0
12. Pasha, P., Nabi, H., Peiravi, M. M., Pourfallah, M., and Ganji, D. D., "The application of analytical methods in the investigation effects of Magnetic parameter and Brownian motion on the fluid flow between two equal plates." ***International Journal of Engineering, Transactions A: Basics,*** Vol. 34, No. 10, 2341-2350, (2021). DOI: 10.5829/IJE.2021.34.10A.15
13. Jond., H. B., Platoša, J., and Sadreddini, Z., "Autonomous Vehicle Convoy Formation Control with Size/Shape Switching for Automated Highways." ***International Journal of Engineering, Transactions B: Applications,*** Vol. 33, No. 11, 2174-2180, (2021). DOI: 10.5829/IJE.2020.33.11B.07
14. Zhang., J., Ai, Z., Guo, L., and Cui, X., "Reliability Evaluation of a Disaster Airflow Emergency Control System Based on Bayesian Networks." ***International Journal of Engineering, Transactions B: Applications,*** Vol. 33, No. 11, 2416-2424, (2019). DOI: 10.5829/IJE.2020.33.11B.32
15. Umana, U. S., Ebong, M. S., and Godwin, E. O., "Biomass Production from Oil Palm and Its Value Chain." ***Journal of Human, Earth, and Future,*** Vol. 1, No. 1, (2020). DOI: 10.28991/HEF-2020-01-01-04
16. Kerich, E. C., " Households Drinking Water Sources and Treatment Methods Options in a Regional Irrigation Scheme." ***Journal of Human, Earth, and Future,*** Vol. 1, No. 1, (2020). DOI: 10.28991/HEF-2020-01-01-02
17. Ha, K., " Innovative Blade Trailing Edge Flap Design Concept using Flexible Torsion Bar and Worm Drive." ***HighTech and Innovation Journal,*** Vol. 1, No. 3, (2020). DOI: 10.28991/HIJ-2020-01-03-01
18. Sawant, M., Thakare, S., Prabhakara Rao, A., Feijóo-Lorenzo, A. E., and Bokde, N. D., " A Review on State-of-the-Art Reviews in Wind-Turbine- and Wind-Farm-Related Topics." ***Energies,*** Vol. 14, No. 8, (2021). DOI: 10.3390/en14082041

Persian Abstract

چکیده

در این اختراع، طرح پیشنهادی جهت تامین نیروی برق روشنایی خیابان ها با کمک حرکت انواع وسایل نقلیه به همراه سیستم خودکار جهت هدایت جریان سیال هوا ارایه گردیده است. در طرح حاضر برخلاف طرح های پیشین، توربین های بادی بر روی بدنه پایه روشنایی به طور یکپارچه نصب شده اند که می توان هزینه ساخت را نسبت به طرح های پیشین کاهش داد و از حرکت جریان سیال هوای تمام خوردوها با ابعاد مختلف جهت بالابردن بازدهی سیستم استفاده کرد. همچنین در طرح حاضر از سیستم خودکار جهت هدایت جریان سیال هوا به توربین های بادی برای افزایش بهره وری در تامین انرژی الکتریسیته استفاده شده است که در طرح های قبلی این سیستم تعبیه نشده بود. از قابلیت های دیگر این سیستم می توان به تولید انرژی الکتریسیته در شرایط نامناسب جوی و طوفانی اشاره کرد برخلاف طرح های پیشین که می بایست توربین بادی را در این شرایط نامناسب متوقف می کردند تا آسیب کمتری به آن وارد شود.

International Journal of Engineering

Journal Homepage: www.ije.ir

Effect of using Waste Rubber as Partial Replacement of Coarse Aggregate on Torsional Strength of Square Reinforced Concrete Beam

A. A. H. Beiram*, H. M. K. Al-Mutairee

Civil Engineering Department, College of Engineering, Babylon University, Iraq

P A P E R I N F O

Paper history:
Received 18 October 2021
Received in revised form 20 November 2021
Accepted 25 November 2021

Keywords:
Rubberized Concrete
Chip Rubber
Pure Torsion
Angle of Twist
Replacement Aggregate

A B S T R A C T

The aim of this study is to test the rubberized concrete beams subjected to pure torsional moments. The study focused on the effect of the partial replacement of coarse aggregates with waste rubber chips of different proportions 10%, 20%, and 30% in volume on the beams ultimate torque, and rotation, as well as the ductility index, stiffness, cracking torque, and failure modes. Six specimens of concrete beams as the same size (225×225mm) have been tested. The same steel reinforcement has been applied to four specimens and two without reinforcement. According to experimental findings for reinforced specimens, the ultimate torque for the control beam (without replacement) is higher than beams with replacement rubber but the angle of twist of beams with replacement rubber rose more than the control beam. the ultimate torque decreases compared with the control beam by 4.49%, 10.08%, 13.98%, while the twist angle increases at ultimate torque by 11.16%, 26.79%, 39.69% when the percentage replacement of rubber is 10%, 20%, 30% respectively. When coarse aggregate was replaced with 30% rubber, the ductility index of specimens increased by 39.83%, and ultimate cracking stiffness was lowered by 38.42% as compared with the control beam.

***doi**: 10.5829/ije.2022.35.02b.16*

1. INTRODUCTION

Cement and aggregates are the most important ingredients of concrete, which is one of the most commonly and consistently used as a construction material in the world. Due to the high demand for concrete as a building material in society, substitute materials derived from recycled or waste materials are needed to conserve natural aggregates [1].

Since the car industry is rising, it is becoming increasingly difficult to get rid of waste tires as shown in Figure 1. Every year, a huge amount of waste tire rubber accumulates, and the easiest way to decompose it is to burn it; anyway, burning rubber causes a lot of smoke and emissions. Another way to get rid of waste rubber is to dump it; anyway, the supply and capacity of landfills is decreasing [1]. As a result, the best scrap tire management technique is recycling, which contributes to scrap tire use while minimizing environmental damage and enhancing natural resource conservation. Low unit weight, high abrasion resistance, toughness, stress and vibration absorption, and ductility can all be increased by partially replacing coarse particles in concrete with recycled discarded tires [2].

Torsion may be a major issue in concrete structural members including eccentrically loaded beams, horizontally bent beams, spandrel beams, and helical stairways, among others. Torsional loadings are divided into two types: equilibrium torsion, in which the torsional moment is necessary for the structure's equilibrium, and compatibility torsion, in which the torsional moment is induced by the compatibility of deformations between members meeting at a joint as shown in Figure 2 [3].

*Corresponding Author Institutional Email: ammar@atu.edu.iq (A. A. H. Beiram)

Please cite this article as: A. A. H. Beiram, H. M. K. Al-Mutairee, Effect of using Waste Rubber as Partial Replacement of Coarse Aggregate on Torsional Strength of Square Reinforced Concrete Beam, ***International Journal of Engineering, Transactions B: Applications***, Vol. 35, No. 2, (2021) 397-405

Figure 1. Industrial landfill for processing of waste tires [4]

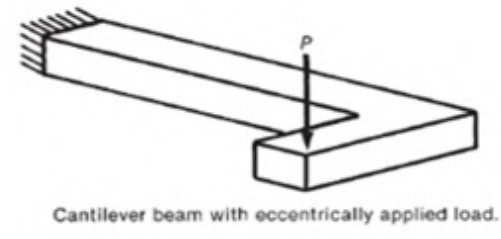

(a) Equilibrium torsion

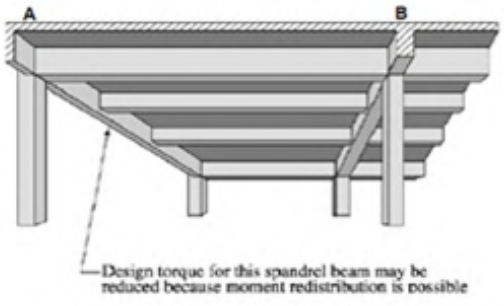

(b) Compatibility torsion

Figure 2. Illustrates example of torsion [3]

Aiello and Leuzzi [5] replaced coarse aggregates with chip tire rubber by volume of coarse aggregate, chip rubber accounted for 25%, 50%, and 75%. They discovered that as the chip tire content grew, the workability also did. Additionally, as the rubber percentage increased, the unit weight, compressive strength, and flexural strength decreased.

Gunasekaran et al. [6] studied eight beams, four of which are made of coconut shell concrete and four of which are made of normal concrete subjected to pure torsion, the results proved that the concrete specimens made from coconut shells are more ductile than conventional concrete specimens. Also, Both normal and coconut shell concrete with corresponding reinforcement ratios have almost identical crack widths at initial cracking torque.

Mohaisen et al. [7] investigated the effect of pure torsion on reinforced concrete continuous beams with variable load eccentricity. They discovered that when load eccentricity rose from 30cm to 60cm, the angle of twist enhanced by 45.76% and the final failure loads reduced by 49.65%.

Siddiqui [8] investigated rubber fragments as a partial substitution for gravel in concrete. The varying percentages of partial replacement of rubber was from 0 to 15% of normal aggregates. From the experimental test results rubberized concrete leads to decrease in slump, workability, unit weight and compressive strength compared to normal concrete.

Kadhim and Al-Mutairee [9] studied chip and crumb rubbers as a partial volumetric replacement for aggregate (gravel and sand) in four separate amounts (5, 10, 15 and 20 %). When 20 % aggregates (gravel and sand) were replaced with crump and chip tier rubber, mechanical properties (compressive, flexural, and splitting tensile strength) were reduced, but impacts resistance has increased by 426 % and 396 %, respectively.

Sahib and Al-Mutairee [10] investigated rubberized concrete's behavior in flat plate punching shear. By punching, the 10-sample experimental model is supposed to fail. The model form column (square and rectangular) and the chips rubber ratios were (0, 5, 10, 15 and 20%), which used instead of coarse aggregate. The experimental findings show that replacing coarse aggregate with chips rubber from zero to 20% decreases the punching shear capability by 13.54% and 18.52% in two case studies (square and rectangular) column, while increased ductility by 20.38% and 15.60%, respectively, and substantially improved the energy absorbing index by 41.41% and 28.75%, respectively.

Kadhim and Al-Mutairee [11] studied 14 continuous deep beams had two-span made of normal concrete with steel reinforcement served as an indication and rubberized reinforced concrete. Rubber ratios can be used to partially replace gravel and sand, as well as shear span/depth ratios of 1.33 and 1.66, are the key parameters. Rubbers (Chip and crumb) were used in four different quantities by volume to substitute coarse and fine aggregate, respectively (5, 10, 15 and 20%). While still producing structural concrete, the proposed mix will substitute 20% of the aggregate (gravel or sand). The data indicated that substituting tier rubber for natural coarse or fine aggregates by 20% decreased the ultimate load upon twin span deep beams by 32.06 and 32.65 percent, respectively, and increased the maximum deflection by 83.07 and 106.28 percent. When crumb rubber is used as a 20% replacement, the ductility of rubberized beams increases to 36.95%.

Other researchers looked at the impact of partially replacing aggregate with rubber or other material on concrete characteristics [12-14].

The majority of current research has focused on the structural behavior of beams normal concrete or with strengthened material under the effect of combined loads or pure torsion, but research on reinforced concrete beams under pure torsion with partial replacement of corse aggregate with rubber is too limited or otherwise unavailable. To the best of the authors' knowledge, this is the first experiment to compare the structural performance of rubberized concrete beams to normal concrete beams under pure torsion. The major goal of this study is to determine the differences in behavior between a conventional concrete beam and a rubberized concrete beam under pure torsion, as well as the effect of the volumetric ratio of replacement rubber and steel reinforcement on structural behavior. As a result of the laboratory results, it was determined that the traditional method of beam design for pure torsion needs to be modified to include the rubber effect resulting from partial replacement of coarse aggregate, that their torsional strength was also lower than the normal concrete beam, and their angle of twist was greater than the normal concrete beam.

2. EXPERIMENTAL WORK

2. 1. Specimens Preparation Six specimens were tested as part of the experimental program with dimensions 225 mm width, 225 mm height and 2200 mm total length and effective span 1800 mm. The variable of this study is the replacing the waste rubber chips partially to the coarse aggregate in concrete with different volumetric percentage as 10, 20 and 30%. Four beams have the same torsional steel reinforcement as shown in Figure 3 and other two beams without steel reinforcement (plain concrete). The beams' cross section, main reinforcement, and transverse reinforcement are all chosen to meet the specifications of ACI Code 318-19 [15]. All beams tested under pure torsion to find the effect of rubber replacement on the beams ultimate torque, angle of twist, ductility index, stiffness, cracking torque, and failure modes. The details and properties of all beams as illustrated in Table 1.

2. 2. Properties of Material The form of cement used in this study was ordinary Portland cement; cement is needed to stratify the specification (Iraq Specification No. 5) limitations [16]. As fine aggregates, natural sand with a maximum size of (4.75) mm was used, which complies with Iraqi requirements (Iraq Specification No.45), Zone (2) [17]. The coarse aggregate in this experiment is rounded gravel with a maximum size of 14 mm. The coarse aggregate grading is verified to the IQS No.45 [17]. The rubber samples for the study were collected by cutting scrap tire rubber and passing it through a 14 mm sieve**.** The specified size was that grading is similar to that of coarse aggregates. Glenium 54 (G54), a high-range water-reducing admixture, is used to change the workability of concrete mixtures. It is

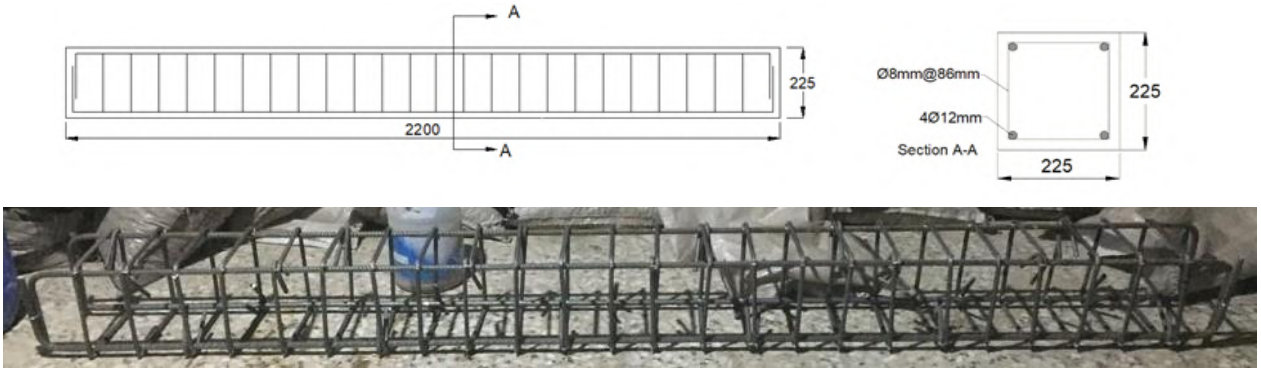

Figure 3. Geometry and details of reinforcement of specimens

TABLE 1. Summary of all specimens

Symbol	Beam Details	% Rubber by vol.
S0	Beam of normal concrete with steel reinforcement	0
S10		10
S20	Beams with steel reinforcement & partial replacement of coarse aggregate by recycle rubber	20
S30		30
S0P	Beam of normal concrete without steel reinforcement (plain concrete)	0
S30P	Beam without steel reinforcement (plain concrete) & partial replacement of coarse aggregate by recycle rubber	30

manufactured by the corporation (BASF) and meets the specifications of (ASTM C494/C494 M) [18]. The primary longitudinal reinforcement was made of 12 mm diameter deformed steel reinforcement, while the transverse reinforcement was made of 8 mm diameter deformed steel reinforcement. The yielding and ultimate strength are summarized in Table 2. according to ASTM A615 [19].

2. 2. Mix Design and Casting Many trial mixes were designed to achieve cylinder strength of reference concrete mixture equal to 35MPa at 28 days. Water/cement ratio was 0.36. The amount of cement and water in the mix remains constant with the following values (440, 158.4 kg/m^3), respectively. Fine aggregate content is constant and equal to 710 Kg/m^3. The superplasticizer percentage is constant with value 0.45% from cement content. Table 3 shows the composition of the mixture.

The first step was to choose the materials, which were prepared and weighed according to the mix's volume requirements. All of the specimens utilized in this study were cast in plywood moulds with a specific dimension of (225×225×2200 mm) as shown in Figure 4. Before putting the steel reinforcement inside the formworks, the inner faces of the plywood formworks were oiled to ensure the ease of the demoulding and using 20 mm concrete spacers as a concrete cover from all sides. Electric concrete mixer used to mix concrete and cast the concrete into the formwork then a vibrator was used to help the trapped air to escape. After 24 hours the plywood mould removed and curing the specimen.

According to ASTM C78-02 [20], the flexural tensile strength of prisms with dimensions of (100×100×400) mm was calculated. Tensile strength is also tested using the ASTM C496/C496M-04 method for concrete cylinders with a diameter of 100 mm and a length of 200 mm [21]. The concrete modulus of elasticity was tested using cylindrical specimens with a dimension of (100×200) mm, according to the method (ASTM C469-14) [22]. The hardened properties were evaluated by

TABLE 2. Steel reinforcement test results

ϕ (mm)	Fy (MPa)	Fu (MPa)
8	543.3	665.1
12	570.8	718.1

TABLE 3. Details of the mixture

Specimens	Gravel (Kg/m^3)	rubber (Kg/m^3)
S0	1050	0
S10	945	31.82
S20	840	63.64
S30	735	95.45
S0P	1050	0
S30P	735	95.45

(a) Prepair mold (b) Casting & vibrator (c) finishing (d) curing

Figure 4. Prepair mold and casting Specimens

compressive strength, splitting tensile strength, flexural tensile strength, and modulus of elasticity test as mentioned in Table 4.

2. 3. Test Setup and Procedure Every one of the specimens were tested using a basic span (L) of 1800 mm between supports and were painted white to aid in crack detection. The load must be transmitted from the testing hydraulic machine's core to external sites reflecting load eccentricity, such as the torsion arm, according to the experimental requirements. The unique clamping loading frame used in this study is shown on both ends of the beam as demonstrated in Figure 5. The centre of support must correspond with the centre of the torsion arm, the torsion moment arm (500mm) from the middle of the beam, so as to achieve pure torsion. The twist angle of the bottom fibre at the near corner of the beam end was determined using a dial gage with 0.01 mm divisions and a 30 mm capacity at the end of the beam span. After being measured under pure torque, the beams were loaded at a constant concentration of 0.1 KN/s. At each loading interval, the twist angle readings were registered, as well as the load of the first crack was recorded, to monitor the types of cracking and load failure as shown Figure 6.

TABLE 4. Hardened properties of mixes

Specimens	(fc') for cylinder (MPa)	Splitting Tensile Strength (ft) (MPa)	Modulus of Rupture (fr) (MPa)	Modulus of Elasticity (GPa)
S0	34.97	3.65	4.67	27.68
S10	28.67	3.18	3.95	21.228
S20	23.46	2.83	3.20	16.582
S30	18.31	2.36	2.58	13.705
S0P	34.97	3.65	4.67	27.68
S30P	18.31	2.36	2.58	13.705

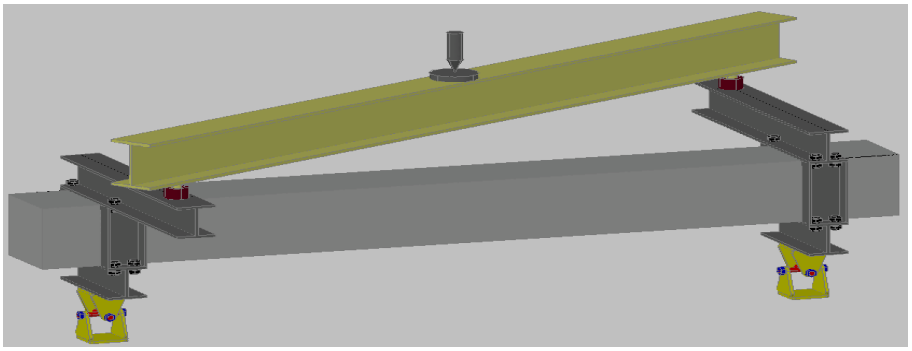

Figure 5. Set-up a mutual of pure torsion in a schematic test diagram

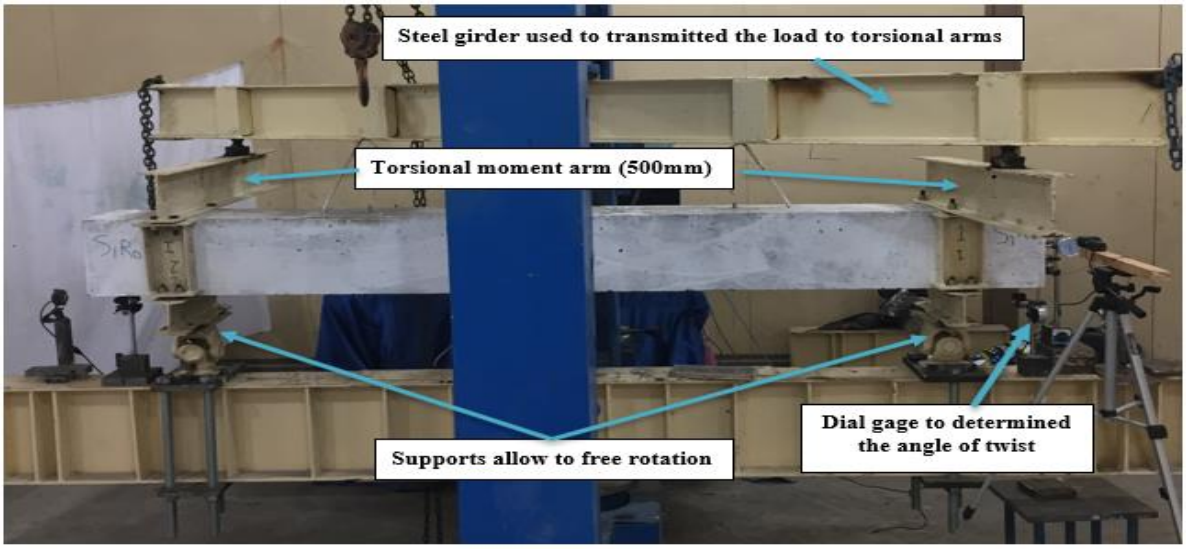

Figure 6. The universal measuring machine is used to test specimens

3. DISCUSSION OF THE FINDINGS

3. 1. Failure Modes of Specimens Tables 5 and 6 show the experimental test results for beams S0, S10, S20, and S30. It can be noticed that, prior to breaking, both cases of beams displayed a linear torque versus twist relationship, indicating that both normal and rubberized concrete beams were elastic. The curves become non-linear after cracking. The first cracks emerged on one of the beam's two wider faces and quickly travelled along with the entire depth of the face, before spreading to the shorter face and failing. As stated in ACI 318-19 [15], concrete behaves as a nonlinear discontinuous medium after cracking, generating a truss action in which reinforcement serves as a tensile link and concrete acts as a compression diagonal. The spiral cracks developed at about 45 degrees and propagated across the test zone as the applied torque increased. When replacing gravel with rubber, the spread of cracks increases along the beam, and the width of the cracks decreases as the percentage of rubber increases. During the first cracking period, the torque decreased as the percentage of rubber increased from 10 to 30%, about 4.82 to 10.18%, whereas the angle of twist increased with values equal to 7.96, 15.83, and 24.02% compared to the control beam S0. At the ultimate stage, the torque decreased by about 4.49, 10.08, and 13.98% when the percentage of chip rubber was increased from 10 to 30%, whereas the twisting increased by about 11.16, 26.79, and 39.69% compared with the control beam S0 as shown in Figure 7. The cracks formed on all other faces formed a helical pattern around the beam scattered along the beam shown in Figure 8.

The reason for the reduction in torque and increased angle of twist is that the difference in particle softness between scrap tire rubber and aggregates is the cause of this reduction. Rubber and cement paste has poor adherence (The interfacial transition area between the rubber particles and the cement paste has low strength).

Increased rubber substitution for gravel particles in concrete lowers the elastic modulus and, as a result, the elastic modulus for concrete, which is mainly correlated here to the proportion of rubber provided, due to the lower rubber module of elasticity, therefore the rubber cement combination becomes more flexible.

The failure torque of plain concrete beam (S30P) decreased about 8.84% with respect to beam (S0P) but the angle of twist increased about 25.43% as shown in Table 7. The cracking torque for plain concrete is roughly equal to the ultimate torque because the beam would fail in a brittle manner once the maximum shear stress equals the concrete tensile cracking strength. The effect of reinforcement can be noted by comparing the results of specimen S0 with S0P and specimen S30 with S30P for normal and rubberized concrete respectively. The failure torque of beam (S0P) reduced about 33.41% compared with failure torque for beam (S0) and that the angle of twist decreased about 73.52%. Also, the failure torque of beam (S30P) reduced about 29.43% compared with failure torque for beam (S30) and that the angle of twist decreased about 76.22% as shown Figure 9. The failure shape of beams is depicted in Figure 10.

3. 2. Ductility of Beams A structure's ductility is defined as its ability to withstand load after deformation beyond the initial yield deformation. The rotation ductility factor (μ) required formula Θmax/ ΘY to determine the ductility of the tested specimens, where

TABLE 5. Results of testing RC beams at cracking torque

Sample	Torque (kN.m)	*Decreeing in Torque%	Twist $\times 10^{-3}$ (rad/m)	**Increasing in Twist %
S0	9.33	-----	12.82	-----
S10	8.88	4.82	13.84	7.96
S20	8.60	7.82	14.85	15.83
S30	8.38	10.18	15.90	24.02

* Compare the torque with control beam(S0).

** Compare the twist with control beam (S0).

TABLE 6. Results of testing RC beams at ultimate torque

Sample	Torque (kN.m)	*Decreeing in Torque%	Twist $\times 10^{-3}$ (rad/m)	**Increasing in Twist %
S0	13.59	-----	52.26	-----
S10	12.98	4.49	58.09	11.16
S20	12.22	10.08	66.26	26.79
S30	11.69	13.98	73.00	39.69

* Compare the torque with control beam(S0).

** Compare the twist with control beam (S0).

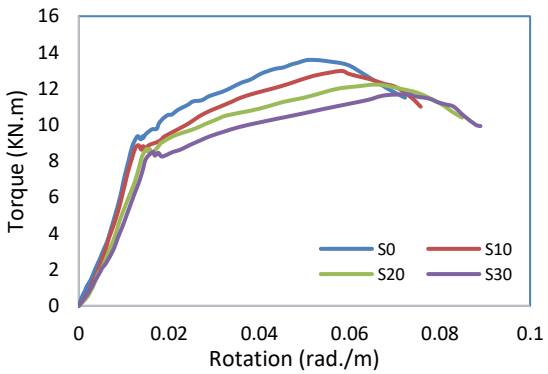

Figure 7. Variation of torsional moment with angle twist for rubberized concrete

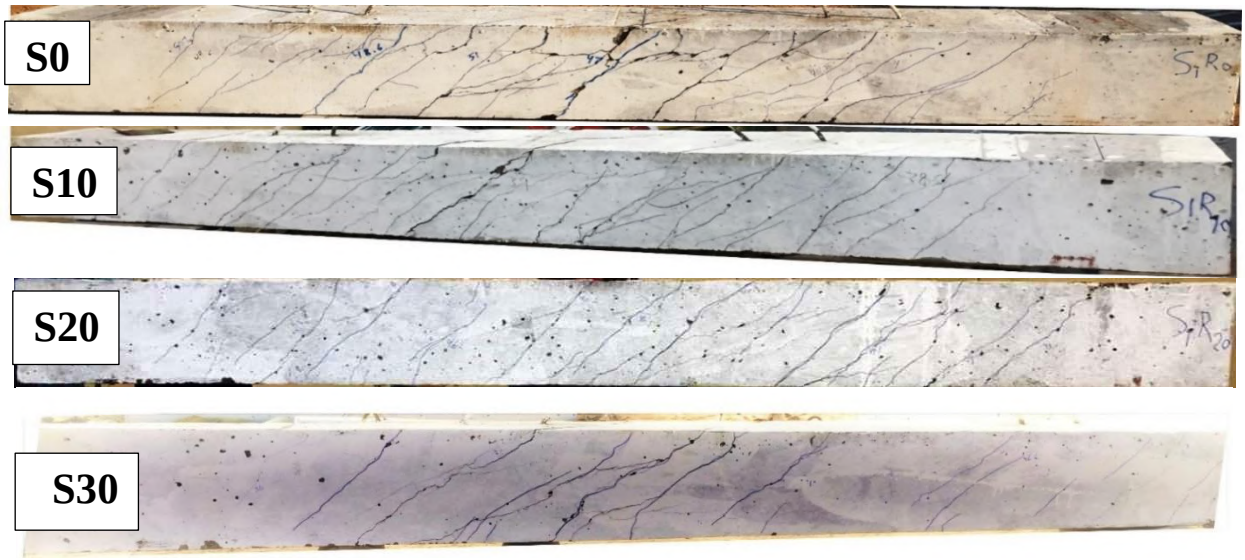

Figure 8. R.C. beam crack patterns : (a) S0 , (b) S10, (c) S20, (d) S30

TABLE 7. Experimental test results of plain concrete beams

Sample	Torque (kN.m)	Decreeing in Torque%	Twist, θ (Rad/m) $\times 10^{-3}$	Increasing in Twist %
S0P	9.05	-----	13.84	-----
S30P	8.25	8.84	17.36	25.43

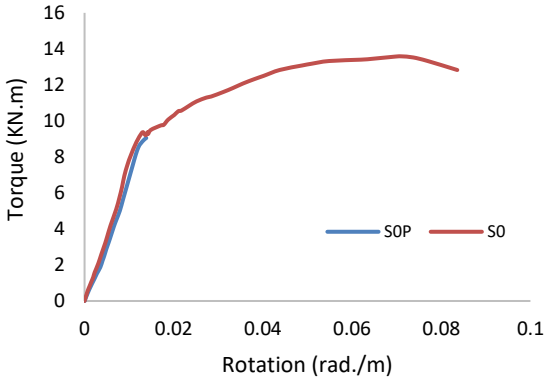

(a) Normal concrete

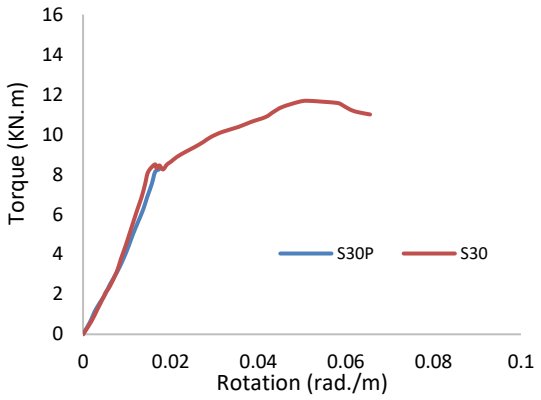

(b) Replacement 30%

Figure 9. Variation of torsional moment with angle twist of plain concrete with reinforced concrete (a, b)

Θmax is the maximum rotational just at the plastic hinge and ΘY is the rotational in the plastic hinge region at yield as shown Figure 11 [23-24]. The twist–rotation curve was used to tabulate the results of the ductility index of beams in Table 8.

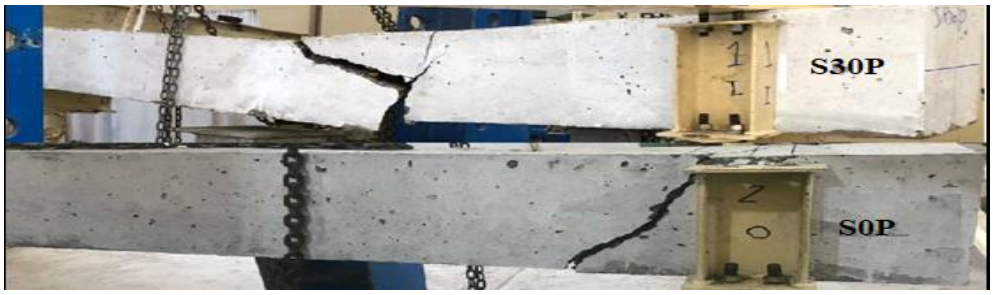

Figure 10. Failure shape of plain concrete beams

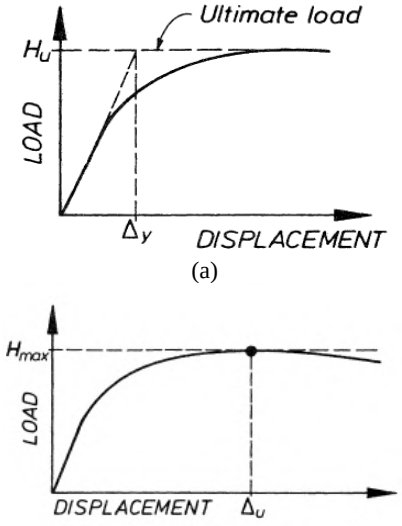

Figure 11. Definitions of ductility, (a) Θ_Y: Based on Equivalent Elasto-Plastic Yield,(b) Θ_{max}: Based on peak torque [23]

TABLE 8. Ductility index of test beams

Sample	Θ_{max} (rad./m)	Θ_Y (rad./m)	μ
S0	0.0523	0.0210	2.49
S10	0.0581	0.0190	2.83
S20	0.0663	0.0195	3.11
S30	0.07300	0.0185	3.35

The ductility of rubberized concrete increased by about 13.65, 24.90 and 34.54% when the ratio of replacing coarse aggregate with chip rubber increased from 10% to 30% compared with control beam S0.

3. 3. Stiffness of Beams The rigidity of an object and the range to which it resists deformation in response to an applied force are the basic concepts of stiffness. As shown in Figure 12, the stiffness of all specimens was determined as the ratio of ultimate torque to angle of twist from the experimental findings [6]. Cracking stiffness is a proposed method for determining the stiffness of concrete structures (K). Table 9 shows the results of cracking stiffness testing.

Replacement chips rubber with 10%, 20%, and 30% reduced the torsional stiffness of the specimens by 14.07%, 29.13%, and 38.42%, respectively.

From the results above, the control beam (S0) has the better ultimate torque but low rotation, whereas the beam S30 has reduced torque by about 13.98% and increased rotation by about 39.69%. It also increased ductility by about 34.54% compared with beam S0. Therefore, the beam S30 is considered the best beam for a structure that needs more flexibility, such as structures exposed to earthquakes, explosions, and shocks.

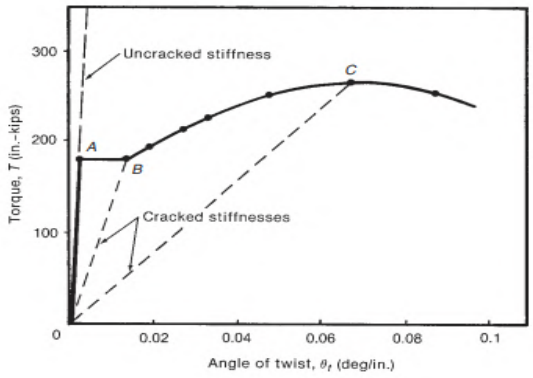

Figure 12. Calculation cracking stiffness [3]

TABLE 9. Cracking stiffness of test beams

Sample	Tu (kN.m)	Θu (rad./m)	Kθ (kN.m)
S0	13.59	0.05226	260.05
S10	12.98	0.05809	223.45
S20	12.22	0.06626	184.42
S30	11.69	0.07300	160.14

4. CONCLUSION

From the experimental program, specimens under pure torsion, the results where:

1- The decrement in ultimate torque is 4.49, 10.08, 13.98% and the increment in twist angle is 11.16, 26.79, 39.69% compared with references beam (S0) when replacement of rubber of 10, 20, 30%, respectively.
2- The torque decrement at first crack was 4.82, 7.82 and 10.18%, when increase in rubber percentage of 10%, 20%, and 30%, respectively, compared with references beam (S0).
3- As rubber was replaced at 0% and 30%, the ultimate torque for non-reinforcement beams decreased by 33.41 and 29.43%, respectively, as compared to reinforced beams.
4- By comparing reinforced and non-reinforced beams, the ultimate twist of the non-reinforced beam decreased by 76.22% for replacement of rubber 30%.
5- The increment in twist angle is 25.43% with the percent replacement of rubber 30% for non-reinforcement beam as compared to control beam (S0P).
6- The ductility index of specimens increased by 13.65, 24.90and 35.54% when coarse aggregate was replaced with 10, 20 and 30% rubber respectively.

7- Increases in rubber replacement ratio from 0 to 30% reduced cracking stiffness by 14.07, 29.13 and 38.42 %, respectively.

4. REFERENCES

1. H. A. Darshan, U. G. Puru V, U. G. Manjunatha R, U. G. Naveen Kumar N V, and U. G. Naveen B M, "An Experimental Study on Rubberized Concrete," ***International Journal of Innovative Research in Science, Engineering and Technology***, Vol. 6, No. 7, (2017), 12543-12550, doi: 10.15680/IJIRSET.2017.0607012.
2. S. M. DUMNE, "An Experimental Study on Performance of Recycled Tyre Rubber-Filled Concrete," ***International Journal of Engineering Research & Technology***, Vol. 2, No. 12, (2013), 766-772, doi: IJERTV2IS120377.
3. James K. White and J. G. Macgregor, *REINFORCED CONCRETE Mechanics and Design*, 6th Editio .(2012).
4. S. A. Alfayez, A. R. Suleiman, and M. L. Nehdi, "Recycling tire rubber in asphalt pavements: State of the art," ***Sustainability (Switzerland)***, Vol. 12, No. 21, (2020), 1-15, doi: 10.3390/su12219076.
5. M. A. Aiello and F. Leuzzi, "Waste tyre rubberized concrete: Properties at fresh and hardened state," ***Waste Management***, Vol. 30, No. 8-9, (2010), 1696-1704, doi: 10.1016/j.wasman.2010.02.005.
6. K. Gunasekaran, R. Ramasubramani, R. Annadurai, and S. Prakash Chandar, "Study on reinforced lightweight coconut shell concrete beam behavior under torsion," ***Materials and Design***, Vol. 57, (2014), 374-382, doi: 10.1016/j.matdes.2013.12.058.
7. S. K. Mohaisen, A. A. Abdulhameed, and M. M. Kharnoob, "Behavior of Reinforced Concrete Continuous Beams under Pure Torsion," ***Journal of Engineering,*** Vol. 22, No. 12, (2016), 1-15,
8. M. M. A. Siddiqui, "Study of Rubber Aggregates in Concrete an Experimental Investigation," ***International Journal of Latest Research in Engineering and Technology***, Vol. 02, No. 12, (2016), 36-57, [Online]. Available: http://www.iaeme.com/MasterAdmin/UploadFolder/STUDY OF RUBBER AGGREGATES.pdf.
9. A. Abdulameer and H. M. K. Al-mutairee, "An Experimental Study on Behavior of Sustainable Rubberized Concrete Mixes," ***Civil Engineering Journal***, Vol. 6, No. 7, (2020), 1273-1285, doi: http://dx.doi.org/10.28991/cej-2020-03091547.
10. F. N. Sahib and H. M. K. Al-mutairee, "Punching strength behavior of reinforced concrete slabs with chips waste tire rubber," ***Periodicals of Engineering and Natural Sciences***, Vol. 8, No. 4, (2020), 2389-2404, doi: DOI: http://dx.doi.org/10.21533/pen.v8i4.1735.
11. A. Abdulameer Kadhim and H. Mohammed Kadhim, "Experimental Investigation of Rubberized Reinforced Concrete Continuous Deep Beams," ***Journal of King Saud University - Engineering Sciences***, Vol. 33, No. 4, (2021), 1-11, doi: 10.1016/j.jksues.2021.03.001.
12. A. A. Kadhim and H. M. Kadhim, "Loading Capacity Prediction of Rubberized Reinforced Concrete Continuous Deep Beams," IOP Conference Series: Materials Science and Engineering, Vol. 1090, No. 1, (2021), 012031, doi: 10.1088/1757-899x/1090/1/012031.
13. H. M. K. Al-Mutairee and O. M. Makki, "Rubberized concrete mix - discussions for literature review," Journal of Physics: Conference Series, Vol. 1895, No. 1, (2021), 012011, doi: 10.1088/1742-6596/1895/1/012011.
14. K. Gunasekaran and S. Choudhury, "Experimental Study on Single Bay Reinforced Coconut Shell Concrete Portal Frame under Lateral and Cyclic Load," ***International Journal of Engineering, Transactions B: Applications***, Vol. 34, No. 08, (2021), 1905-1912, doi: 10.5829/ije.2021.34.08b.12.
15. ACI 318-19, "Building Code Requirements for Structural Concrete and Commentary," American Concrete Institute. p. 628, (2019), doi: 10.14359/51716937.
16. The second modify, Iraqi Specification No.5 -1984, "Portland cement." (2010).
17. Second modify, Iraq Specification No.45/1984, "Natural Sources for Gravel that is used in concrete and construction." Baghdad, (2010).
18. ASTM C494/C494M, "Standard Specification for Chemical Admixtures for Concrete," (2017), doi: 10.1520/C0494_C0494M-17.
19. ASTM A615 / A615M-16, "Standard Specification for Deformed and Plain Carbon-Steel Bars for Concrete Reinforcement." ASTM International, West Conshohocken, PA, (2016), doi: 10.1520/A0615_A0615M-16.
20. A. C78/C78M-18, "Standard Test Method for Flexural Strength of Concrete (Using Simple Beam with Third-Point Loading) 1," ASTM International, Vol. C78-18, No. C, (2018), 1-4, doi: DOI: 10.1520/C0078_C0078M-18. 2.
21. ASTM C496/Ca96M-11, "Standard Test Method for Splitting Tensile Strength of Cylindrical Concrete Specimens," ASTM International, (2011), 1-5, doi: 10.1520/C0496_C0496M-11.
22. ASTM C469/469M-14, "Standard Test Method for Static Modulus of Elasticity and Poisson's Ratio of Concrete," ASTM International, 2-6, (2014), doi: 10.1520/C0469-C0469M-14.
23. R. Park, "Structural Assemblages from Laboratory Testing," Bulletin of the New Zealand National Society for Earthquake Engineering, vol. 22, No. 3, (1989), 155-166.
24. M. S. Mohsin, N. A. Alwash, and M. M. Kadhum, "Comparative Study on Structural Behavior of Reinforced Concrete Straight Beam and Beams with out Plane Parts," ***International Journal Engineering, Transactions A: Basics***, Vol. 34, No. 10, (2021), 2280-2293, doi: 10.5829/ije.2021.34.10a.09.

Persian Abstract

چکیده

هدف از این مطالعه آزمایش تیرهای بتنی لاستیکی شده در معرض گشتاورهای پیچشی خالص است. این مطالعه بر روی تأثیر جایگزینی جزئی سنگدانه‌های درشت با تراشه‌های لاستیکی ضایعاتی با نسبت‌های مختلف ۱۰٪، ۲۰٪ و ۳۰٪ در حجم بر گشتاور و چرخش نهایی تیرها و همچنین شاخص شکل‌پذیری، سفتی، ترک‌خوردگی متمرکز بود. حالت های گشتاور و خرابی شش نمونه از تیرهای بتنی به همان اندازه (۲۲۵×۲۲۵ میلی متر) آزمایش شده است. همان آرماتور فولادی روی چهار نمونه و دو نمونه بدون آرماتور اعمال شده است. بر اساس یافته‌های تجربی برای نمونه‌های تقویت‌شده، گشتاور نهایی برای تیر کنترل (بدون تعویض) بیشتر از تیرهای با لاستیک جایگزین است اما زاویه پیچش تیرها با لاستیک جایگزین بیشتر از تیر کنترل افزایش یافته است. گشتاور نهایی در مقایسه با پرتو کنترل ٤،٤٩٪، ١٠،٠٨٪، ١٣،٩٨٪ کاهش می یابد، در حالی که زاویه پیچ در گشتاور نهایی ١١،١٦٪، ٢٦،٧٩٪، ٣٩،٦٩٪ زمانی که درصد جایگزینی لاستیک ١٠٪، ٢٠٪، ٣٠٪ است افزایش می یابد. به ترتیب. هنگامی که سنگدانه درشت با لاستیک ٣٠٪ جایگزین شد، شاخص شکل پذیری نمونه ها ٣٩،٨٣٪ افزایش یافت و سفتی نهایی ترک ٣٨،٤٢٪ در مقایسه با تیر کنترل کاهش یافت.

IJE TRANSACTIONS B: Applications Vol. 35, No. 02, (February 2022) 406-416

International Journal of Engineering

Journal Homepage: www.ije.ir

Numerical Study of Shunting Effect in Three-steel Sheets Resistance Spot Welding

K. Reza Kashyzadeh*[a], G. H. Farrahi[b,c], M. Minaei[c], R. Masajedi[d], M. Gholamnia[d], M. Shademani[d]

[a] *Department of Transport, Academy of Engineering, Peoples' Friendship University of Russia (RUDN University), 6 Miklukho-Maklaya Street, Moscow, Russian Federation*
[b] *School of Mechanical Engineering, Sharif University of Technology, Tehran, Iran*
[c] *Materials Life Estimation and Improvement Laboratory, Sharif University of Technology, Tehran, Iran*
[d] *IKCO, Karaj Highway, Tehran, Iran*

PAPER INFO

Paper history:
Received 29 September 2021
Received in revised form 14 November 2021
Accepted 02 December 2021

Keywords:
Resistance Spot Weld
Three-sheet Spot Welded Joint
Shunting
Electrical Current Density
Electrode Displacement

ABSTRACT

The main purpose of the present research is to investigate the shunting phenomenon in a three-sheet RSW joint using finite element simulation. To this end, a three-sheet resistance spot welding joint was simulated as an electrical-thermal-mechanical coupling problem. To validate the presented simulation, the finite element results were compared with the experimental results, including nugget size and geometric shape in the resistance spot welding joint. Afterwards, the multi-spot welds of three-sheet low carbon steels with the same thicknesses were analyzed considering the sequential distance of 45 mm. Various techniques, including new spot-weld diameter measurement, electrical current density, electrical contact conductivity, and electrode displacement, were used to study shunting effects in the process of consecutive spot welds. The results obtained from different methods have greatly matched each other. Also, finite element results indicated that the assumption of neglecting the sheet deformation effect for low intervals between consecutive spot welds is acceptable. However, it is necessary to consider sheet deformation for distance intervals more than 45 mm.

doi: *10.5829/ije.2022.35.02b.17*

1. INTRODUCTION

Weight reduction of the mechanical structures is one of the most important concerns of transportation industries including land, air, and rail transportation whose most elementary one is fuel consumption reduction. Therefore, the use of the Resistance Spot Welding (RSW) method in comparison with other connection methods has received more attention in the industry. For example, we can mention the widespread use of this welding method for connecting thin metal sheets in the automotive industry. In this regard, approximately 3000 to 5000 resistance spot welding joints are required to produce a passenger car [1-3]. In general, resistance spot welding is used to connect two metal sheets. However, it is necessary to use this process in some positions to connect three sheets in the construction of the car body.

One of the effective factors on the quality of successive spot weld and resulting in weld strength is the electric current escape phenomenon, namely shunting. This phenomenon means the electric current pass through the previously created spot weld while creating a new one. The obvious effects of this phenomenon usually include generated heat reduction in the welding process and diameter reduction of the new spot weld. However, based on different standards with application of automotive engineering, the strength of spot-welded joint is directly related to the weld core diameter. In addition, impair diameter (IM) is one of the most important defects of RSW in the classification of strength defects due to the small diameter of the weld core. Accordingly, if the value of the weld core diameter is less than the value specified in the standard, this is IM defect, which is led to reduce the strength of the spot-welded joint. Therefore, the joint strength can be increased by preventing the shunting phenomenon. A schematic of the shunting phenomenon at a connection with more than one spot

*Corresponding Author's Email: reza-kashi-zade-ka@rudn.ru (K. Reza Kashyzadeh)

Please cite this article as: K. Reza Kashyzadeh, G. H. Farrahi, M. Minaei, R. Masajedi, M. Gholamnia, M. Shademani, Numerical Study of Shunting Effect in Three-steel Sheets Resistance Spot Welding, ***International Journal of Engineering, Transactions B: Applications***, Vol. 35, No. 2, (2021) 406-416

weld and diameter reduction of the welding core is shown in Figure 1 [4].

A few studies have been conducted to investigate shunting effects in the spot-welded joint as simulations, theoretical, and analytical models. Jafari Vardanjani et al. [4] have reviewed research about hunting phenomenon and its effect on RSW joint. Various parameters are effective on the intensity of shunting phenomenon, including number of previous spot welds, nugget size of previous spot welds, distance between spot welds, and so on which decrease the welding core diameter (new spot weld) and consequently decrease strength of the RSW joint. In addition, the parts of the sheet that are in contact with each other will be the electric current passage area where the presence of the oxide layer and the reduction of the electrode pressure have a significant effect on the intensity reduction of shunting phenomenon. Xing et al. [5] have studied the shunting effects in the resistance spot welding joint of medium carbon steel sheets based on the electrode displacement signals technique. In this research, the effect of the welding distance parameter was studied on the shunting phenomenon and its effect on welding core diameter in the new spot weld. Moreover, the minimum gap between multi-spot welds was reported about 20 mm. The most important achievement of the present work revealed that electrode displacement curves can be used as a proper tool to monitor the health status and quality control of RSW joint. In this regard, the electric current was set based on the electrode displacement curve at the previous spot-welded characteristics, like shunting effect, to create new spot weld. Figure 1 shows a schematic of the shunting phenomenon at a connection with more than one spot and diameter reduction of the welding core [4].

An analytical model has been presented for the shunting effect in the RSW joint of AA2219 aluminum alloy sheets with a thickness of 1 mm considering two consecutive spot welds [6]. Finally, the welding core diameter obtained from the presented analytical relationships by the finite element simulation results (validated with the experimental results [7]) was compared and the results were well matched. Moreover, the three-dimensional model has been presented as a thermal-electric coupling to simulate shunting phenomenon in the RSW joint [8]. In the current study, various experiments were performed in which the heat affected zone was considered as the study criterion to validate the proposed model.

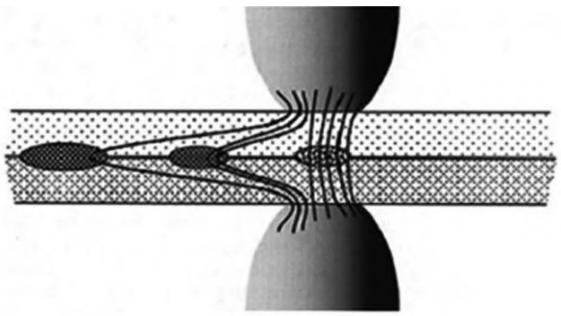

Figure 1. A schematic of the shunting phenomenon at a connection with more than one spot and diameter reduction of the welding core [4]

Wang et al. [9] have conducted a laboratory study about the effect of the shunting phenomenon on the resistance spot welding joint in the first part of their research. In the present research, several effective factors were investigated, including sheet material, sheet surface conditions, welding program, and welding process parameters. Among all of them, the electrode force is the most effective parameter that can reduce the shunting effects when the distance between spot welds is limited. Three different materials, including medium carbon steel, DP590 steel, and DP780 steel, were used in the current research. Furthermore, different thicknesses (1, 1.2, 1.25, 1.5, and 2 mm) were considered to include the effect of sheet thickness on the shunting phenomenon. Test specimens were prepared by connecting two sheets with five resistance spot welds. Then, nugget diameter was measured from the cut section for each of the studied cases. Finally, statistical analysis showed that the gap between spot welds is the most important factor in the shunting phenomenon. Therefore, if this gap is large enough, shunting phenomenon will not occur. The results showed that high contact resistance created by very strong surface conditions or electrode force increases the shunting intensity. Moreover, there is a close relationship between sheet material (chemical composition), sheet thickness, and resistance spot welding strength with shunting phenomenon. In the second part of their research, they analyzed the electrical resistance during the welding process and identified the shunting path [10]. The minimum value of welding parameters and the gap between spot welds were extracted as can create a suitable nugget diameter based on the welding time, sheet thickness, and other influential parameters. Moreover, sensitivity analysis was performed for each of these parameters, and gap diagrams between spot welds were extracted in terms of these parameters.

In recent years, the characteristics of the shunting phenomenon have been investigated in the RSW joints made of aluminum alloys with non-uniform thicknesses [11,12]. To this end, ANSYS software was used to simulate the finite element of gap effects between spot welds. The results showed that gap increase between spot welds is not an effective method to prevent shunting phenomenon. The main reason for this case is the low strength of the bulk in the aluminum alloy. Therefore, increasing the electric current was proposed to compensate the effect of shunting phenomenon. Also, the current density parameter in the component was measured to study the electric current escape in the

connection. In addition, shunting phenomenon has been investigated in RSW joint using both simulation and laboratory methods [13]. In this study, the welding joint was considered for two sheets with the same thickness which was connected by two consecutive spot welds. Furthermore, the distance between spot welds was considered as a variable in the range of 2-8 times the diameter of the electrode head. The nugget diameter was measured at both spot welds and the percentage of size reduction was considered as a criterion for the occurrence of the shunting phenomenon. The results showed that if the distance between spot welds is at least 6 times the diameter of the electrode head, the shunting effects can be neglected. As reported, the nugget diameter is more sensitive to the shunting phenomenon than the welding core height.

Yu et al. [14] have proposed an adaptive RSW process intended to decrease the shunting effect, especially in the connection of high-strength steel sheets with applications in the automotive industry [15]. They used an exponential model to predict weld pitch in terms of dynamic resistance. Also, they considered the weld pitch as a function of nugget diameter and heat input. Then, they established a combined model of logic algorithm and regression method that has the ability to evaluate the input heat compensation with the aim of shunting reduction. Eventually, in practice, they tried to reduce the shunting effects by adjusting the welding time and keeping the costant ampere current.

In the present research, the connection of three sheets with different materials and the same thicknesses was simulated as an electrical-thermal-mechanical coupling problem in finite element software. Afterwards, to validate the presented finite element model, nugget diameter extracted from the simulation results was compared to the test results. Then, various techniques, including electric current density, contact electrical conductivity, and electrode displacement diagram were used to estimate the shunting phenomenon in the spot welds. Eventually, the obtained results from different methods were compared to each other which have a very good agreement. The following can be mentioned among the innovations of the present study in comparison with previous studies:

- Simulation of three-sheet RSW joint and its validation using experimental data by comparison technic;
- Investigation of shunting effects in three-sheet RSW joint;
- Considering different materials for sheets in the RSW joint;
- A comprehensive study of shunting phenomenon using various methods, including measurement of new welding core diameter, electric current density, contact electrical conductivity, and diagram of electrode head displacement.

2. LABORATORY STUDY

In the current research, two types of DC03A and DC04A steel sheets with the same thickness of 0.8 mm were used. Thus, both middle and bottom sheets are made of DC03A and the top sheet is made of DC04A. The chemical composition of these two steels based on the results of Quantometric test are reported in Table 1. Also, sheet samples were prepared and metallographic test was performed after mounting and polishing the surface to determine the initial phase and grain size of the raw material. The microstructure of the sheets is shown in Figure 2 which was obtained from the metallographic test after etching by 3% nital solution.

Microstructure observations showed that the initial phase of both sheets is completely ferrite. In addition, the grain size for both materials is equal to 7 based on the NFA04-102 standard.

Next, standard electrode (F0-16-20-8) was used to fabricate test samples of three-sheet spot-welded joint. The electrode is made of copper alloy with 1.1% alumina. The geometric dimensions of the sheets and the location of the spot weld at the three-sheet joint are demonstrated in Figure 3. Also, the welding process parameters are presented in Table 2. Furthermore, an electric current was applied alternately with a frequency of 50 Hz [16, 17].

The laboratory sample was cut transversely from the middle of the spot weld after its preparation and metallographic observations including measurement of the nugget diameter and the Heat Affected Zone (HAZ) were performed (Figure 4).

From this figure, the two diameters created between the top and middle sheets and the bottom and middle sheets are 5.63 and 5.47 mm, respectively. Moreover, the length of the HAZ in the upper part (L = 7.04 mm) is different from the lower part (L = 6.48 mm) of the three-sheet RSW joint.

TABLE 1. Chemical composition of DC03A and DC04A steels based on the Quantometric test results

Steel grades	DC03A	DC04A
Fe	Base	Base
Al	0.0284	0.03
C	0.0377	0.034
Mn	0.2036	0.24
P	0.013	0.009
S	0.0047	0.011
Si	0.0036	0
Cr	0	0.03
Cu	0	0.01
Ni	0	0.02

(a)

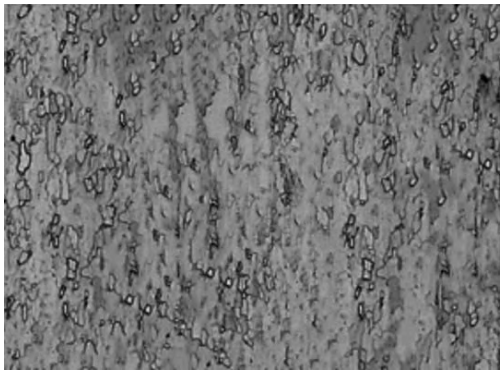

(b)

Figure 2. Metallographic images of raw materials with 100x magnification: a) DC03A steel and b) DC04A steel

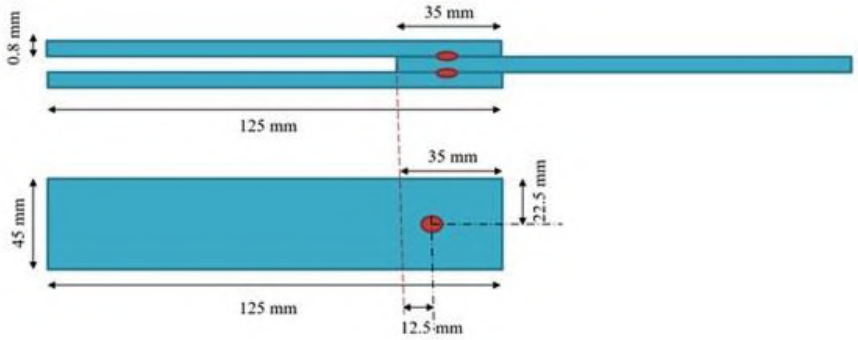

Figure 3. Geometric dimensions of three-sheet spot-welded joint [16]

TABLE 2. Resistance spot welding process parameters [16, 17]

Parameter	Unit	Value
Force	N	365
Welding current	KA	11.5
Squeeze time	Cycle	25
Up slope	Cycle	3
Welding time	Cycle	12
Hold time	Cycle	9

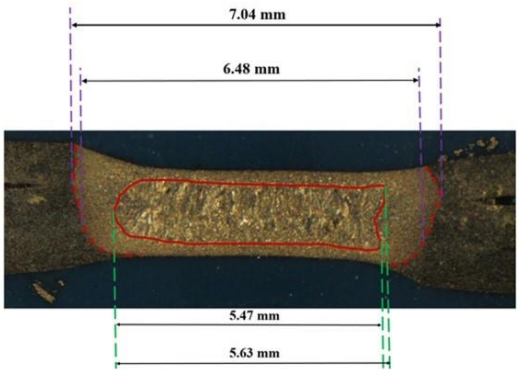

Figure 4. Measurement of nugget diameter and HAZ, experimentally [17]

3. FINITE ELEMENT SIMULATION

To extract the mechanical, electrical, and thermal properties of the raw materials, JMatPro software version 7 was used. To this end, percentage of chemical composition (Quantometric test results), the initial phase of the sheets, and its grain size (metallographic test results and microstructural studies) were used as input in the software. Afterwards, three-dimensional simulation of the RSW process as an electrical-thermal-mechanical coupling analysis was performed using Simufact Welding software (Edition 6). In other words, for the first time, a hybrid finite element-experiment method was used to simulate this type of welding process. Figure 5 represents the algorithm used to simulate the RSW process with higher accuracy than other models presented in the past. Also, the geometry and conditions of the spot welding process were applied following the experimental procedure.

Mesh sensitivity analysis was performed to obtain the optimal finite element model (independence of the response from the number of elements) and to reduce computational costs. Thus, the element size of 1 mm and two times refinement around the spot weld position were considered. Eventually, the final FE model consisting of

33750 elements along with the position of the electrodes on both sides of the sample is demonstrated in Figure 6. In addition, more details on finite element simulation of RSW process in the three-sheet joint can be found in a previous paper published by the authors [17].

Nugget diameter between the top and middle sheets (5.903 mm) and between the bottom and middle sheets (5.896 mm) was obtained as shown in Figure 7. Also, the results of finite element simulation were 4.8% and 7.9% different from the experimental data, respectively.

The sequential spot welding process was simulated to investigate the shunting effects after validating the finite element model. One of the most important innovation of the presented FEM in comparison with previous studies is to consider the deformation of the sheets during the creation of previous spot welds and

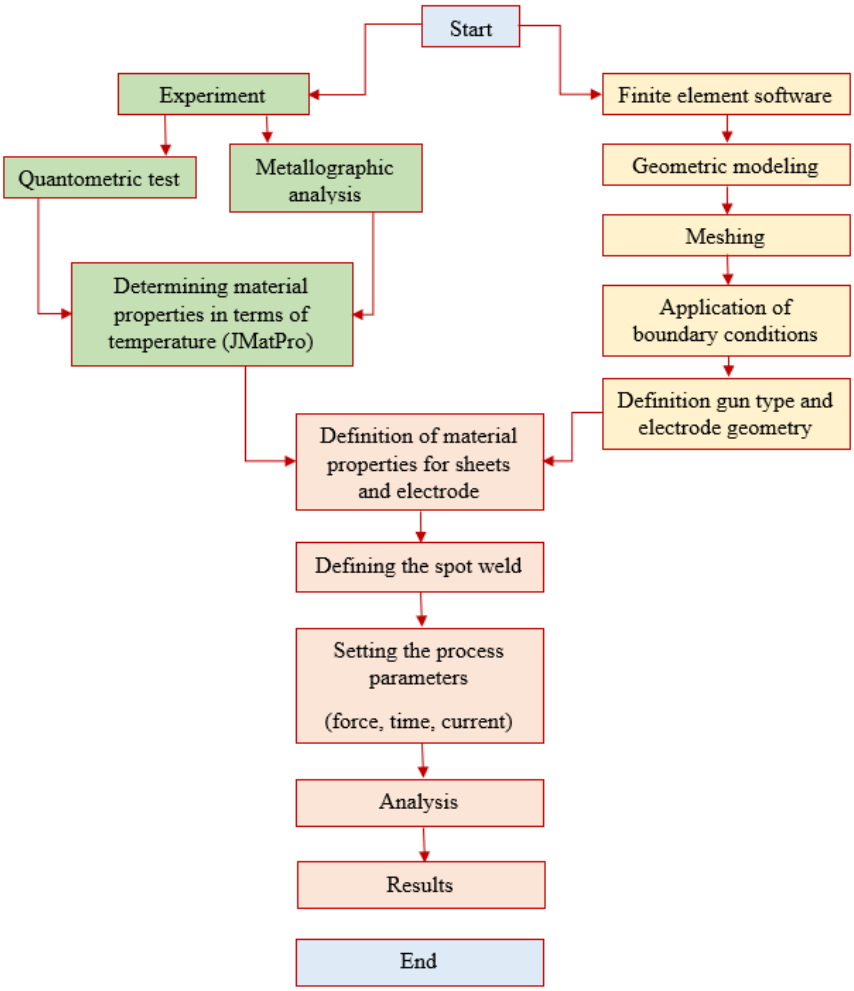

Figure 5. A hybrid finite element-experiment algorithm used to simulate RSW process with higher accuracy than available models

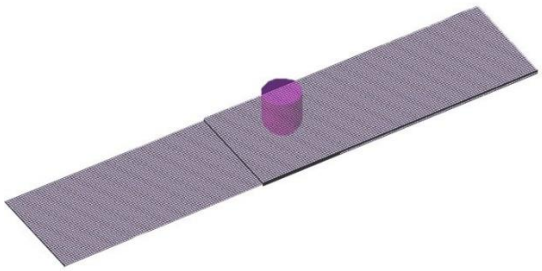

Figure 6. The 3D-FE model of RSW with 33750 elements

studying its effect on shunting phenomenon, for the first time. Also, the interval between two consecutive spot welds was considered 45 mm. This distance reduces the effect of electric current escape from previous spot welds as much as possible. Hence, the shunting effect becomes more noticeable for the deformation of the sheets. The welding sequence in a three-sheet connection with three spot welds is demonstrated in Figure 8. In addition, the conditions of welding process were considered completely in agreement with the previous case.

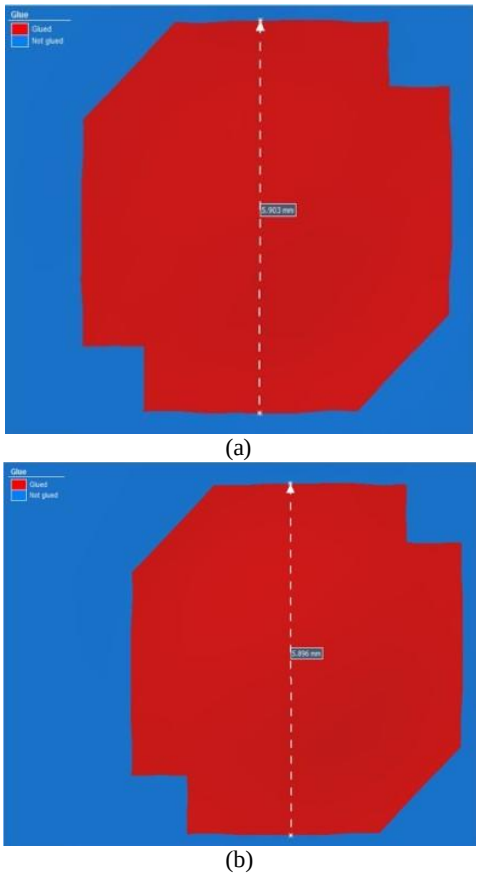

Figure 7. Geometry and size of welding core: a) between the top and middle sheets and b) between middle and bottom sheets

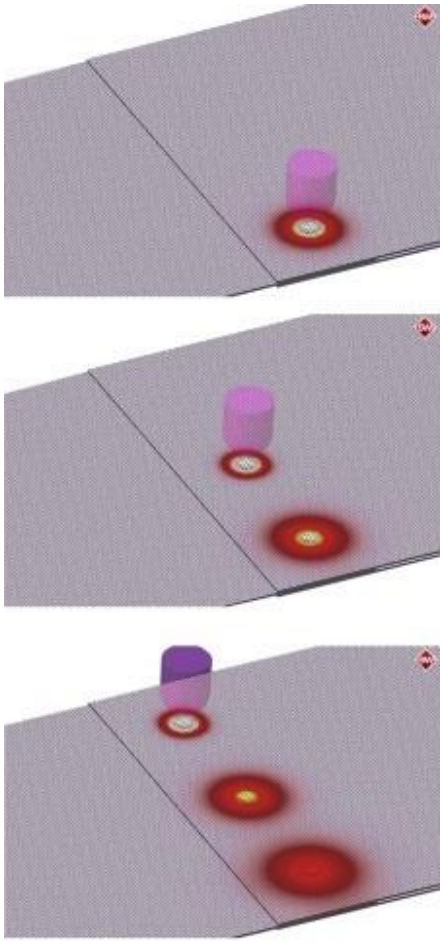

Figure 8. The sequence of welding in a three-sheet connection with three spot welds

4. RESULTS AND DISCUSSION

In the present research, various techniques, including measuring nugget diameter, electrical current density, contact electrical conductivity, and electrode displacement diagram, were used to study the shunting effects in the process of successive spot welding. Therefore, the results obtained using each method are reviewed as follows:

4. 1. Measuring the Nugget Diameter of New Spot Weld One of the most elementary methods to identify shunting phenomenon in the process of successive spot welding is to measure and compare the nugget diameter of new spot welds with the original one. Therefore, the nugget diameter between the top and middle sheets and the nugget diameter between the middle and bottom sheets in all three consecutive spot welds were extracted as given in Table 3.

From Table 3, the nugget diameter of the second spot weld has decreased compared to the first spot weld. Therefore, it is inferred that the second spot weld was impressed by the shunting phenomenon. However, the nugget diameter of the third spot weld has increased in comparison with the previous spot weld. Moreover, the nugget diameter of the third spot weld was obtained around the target diameter in the first spot weld. As a results, the third spot weld is not in the path of the electric current escape. Later, the main reason for this occurrence is analyzed in more detail using other techniques.

TABLE 3. Nugget diameter between different sheets in the process of successive spot welds

Number of consecutive spot welds	Nugget diameter	
	Between top and middle sheet (mm)	Between bottom and middle sheet (mm)
1	5.84	5.73
2	5.74	5.70
3	5.83	5.78

4. 2. Studying the Electric Current Density The electric current density equals the ratio of electric current

to the area of the passed surface through it. This parameter was extracted by software capabilities at the same times of the welding process in three different modes including one, two, and three spot welds via distance from the center of spot welds in four positive and negative paths of X and Y axes (Figure 9). The blue and red lines indicate the positive and negative directions of the coordinate axes, respectively.

Also, the center of the coordinate axis for each spot weld is located in its center. The positive direction of the X axis is to the right and the end of the top and bottom sheets and the negative direction is to the left and the end of the middle sheet. Moreover, the positive direction of the Y axis is considered for each spot weld towards the next spot weld and its negative direction is considered towards the previous spot weld. Furthermore, zero-interval means reporting the electric current density in the center of the spot weld.

It is clear that for the first spot weld, the changes in the electric current density in different directions, in the X directions are almost identical to each other and follow a specific procedure. The density of electric current slightly increases from the center of spot weld to the electrode surface separation area from the sheet surface. Afterward, its value decreases at a significant rate to the range of 4 mm from the center of the spot weld. Finally, the rate of the electric current density decreased to the interval of 6 mm from the center of the spot weld. This behavior is also seen in different Y directions. Also, this behavior is repeated for different Y directions for the second spot weld. Nonetheless, the difference between the two directions gradually increases in different X

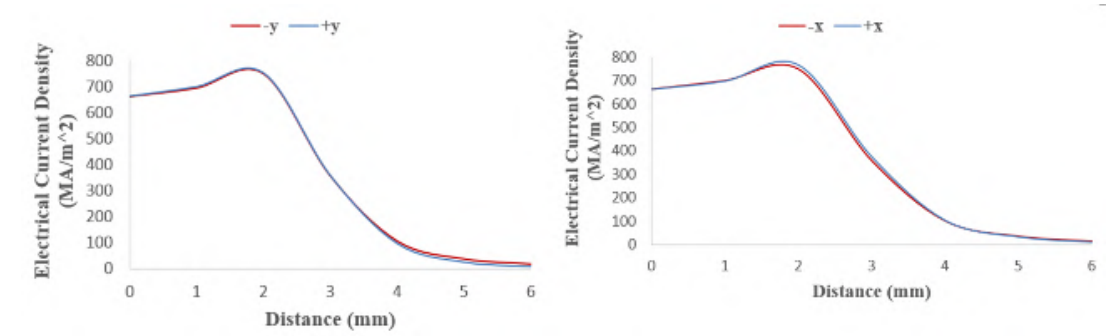

(a) The first resistance spot weld

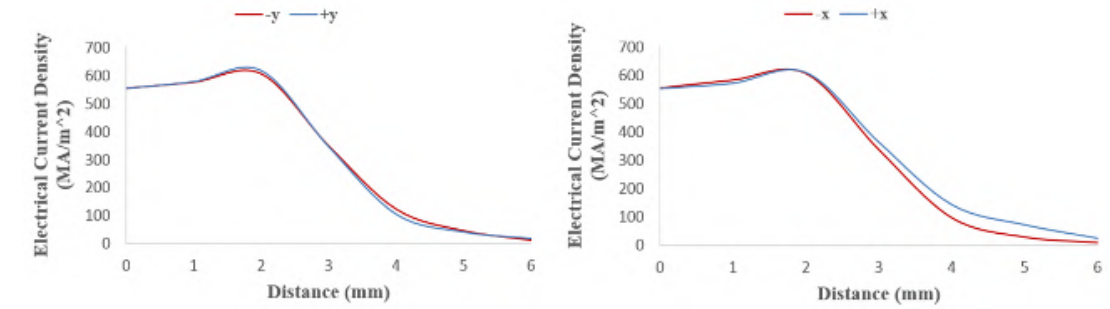

(b) The second resistance spot weld

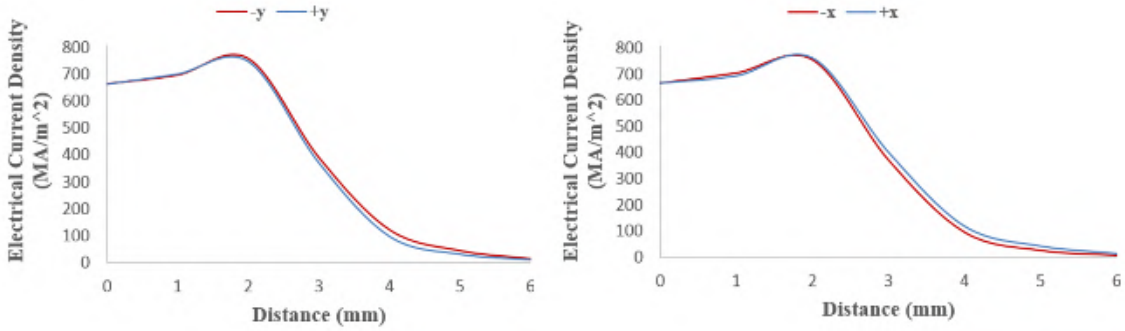

(c) The third resistance spot weld

Figure 9. Variations of the electric current density in terms of distance from the center of the spot weld in the sequential spot welding process, including a) The first resistance spot weld, b) The second resistance spot weld, and c) The third resistance spot weld

directions in the second spot weld from a 2 mm interval onwards. This difference shows that the electric current in the second spot weld is more inclined to pass in the positive X direction. Furthermore, the maximum level of electric current density in the second spot weld is much lower than its level in the first spot weld which shows the effect of the shunting phenomenon in the RSW process of the second spot. Nonetheless, it is observed in the third part of Figure 9 that the maximum level of electric current density has increased and reached its value in the RSW process of the first spot. The obtained results using this method are in complete agreement with the reported results about measurement of nugget diameter. Next, another effective parameter such as contact electrical conductivity was studied to find the reason for the re-increase of the electric current density in the third spot weld.

4. 3. Studying the Contact Electrical Conductivity Since three sheets are in contact with each other in the range of 135 × 35 mm from the beginning of the welding process, there is always contact electrical conductivity in this range of sheets. The exerted force by the electrodes on the surface of the sheets during compression makes a range at the contact surface of the sheets which has a higher electrical conductivity than other non-pressurized contact surfaces. On the other hand, one of the effective parameters in increasing the contact electrical conductivity is the presence of microscopic roughness on the surface. Electric current passes difficulty through these roughness and small spaces between them. This roughness is compressed and fitted together better when force is applied to a part of a sheet. In addition, some of the small spaces between them are completely or partially filled which makes it easier for electricity to pass through this contact area. Increasing the contact electrical conductivity in one area means the electrical resistance reduction in that area than the other areas. Moreover, electric current tends to pass through an area with less electrical resistance. This makes a significant electric current pass from the upper sheet to the lower sheet through the pressure range which finally makes a spot weld at that location. Therefore, there was a shunting phenomenon in the first spot weld because of the contact of three sheets from the beginning of the welding process. The contact electrical conductivity in the place of the first spot weld after posing force and before applying an electric current is illustrated in Figure 10.

From this figure, a range with high contact electrical conductivity is made in the mentioned place to make the first spot weld caused applying force by the electrode. In addition, there are spot welds on the contact surface. Although their contact electrical conductivity does not reach the pressure range, their size is big to the extent that causes a significant amount of electrical current to escape

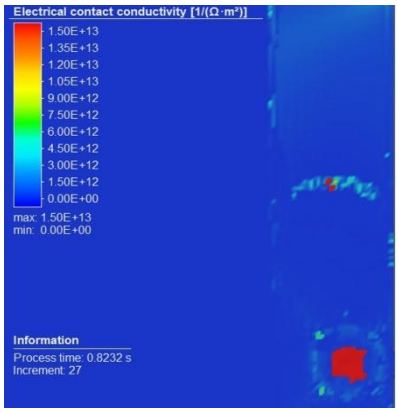

Figure 10. Contact electrical conductivity in the first spot weld

from those spot welds. One of these is nearly in the range of contact and the relative place of the second spot weld. In other words, by applying pressure by an electrode in the first spot welding place and sheets deformation, it is possible that the sheets will be pressured more than usual in a spot weld and higher contact electrical conductivity is made in those spot welds which are the main reason of increasing the contact electrical conductivity in the relative place of the second spot weld. Moreover, it was observed that contact electrical conductivity has increased in two both transverse ends of the sheets (the parts where the top edge of the sheet is in contact with the middle sheet and the edge of the middle sheet is in contact with the bottom sheet). Contact electrical conductivity actually increases regardless of the force applied in areas where the sharp edge of one sheet is in contact with another sheet. Therefore, the geometry and placement of the sheets relative to each other are effective on the shunting phenomenon.

From Figure 11, the amount of contact electrical conductivity at the transverse edge of the contact range decreases by increasing the number of previous spot welds. This makes the electric current in the Y direction more inclined to propagate than the X direction. In other words, the electric current becomes more concentrated in the Y direction. Consequently, shunting effects in the X direction will be less than in the Y direction for the third spot weld. One of the most important reasons for this event is the deformation parameter of the sheets and the weakening of the contact in the initial contact range.

4. 4. Investigating the Electrode Head Displacement During Spot Welding Process One of the newest methods that were provided in recent years is using an electrode displacement diagram during the welding process to study the shunting phenomenon [3]. In this regard, shunting can be investigated using the comparison technique for three statistical characteristics,

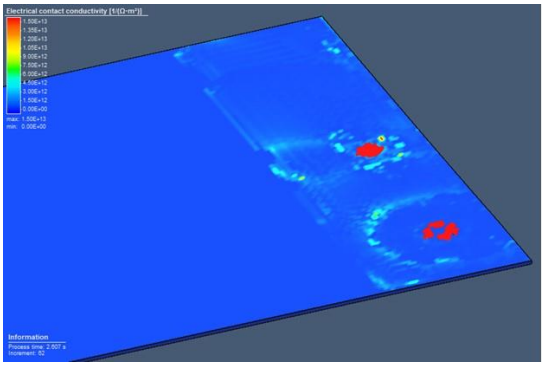

Figure 11. The effect of the current location on the contact electrical conductivity

including graph diagram, diagram slope to the maximum spot, and standard data scatter. The electrode head displacement diagram for three consecutive spot welds is illustrated in Figure 12.

In this figure, the blue dotted line displays the electrode head displacement during the RSW process at the first spot weld. Two vertical black lines show the beginning and end of the welding period. The time interval is related to the maintenance time after the second vertical line. The black horizontal line is drawn from the beginning of the welding interval. Furthermore, its surface difference with the end of the displacement figure of each spot welding shows the degree of penetration of the electrode at the end of the RSW process and before the start of the maintenance time. In this research, the figure of the first spot weld was used as a basis to detect the electric current escape. When the maximum spot welding diagrams of subsequent graphsis lower than the maximum spot welding diagram of the first spot weld, the shunting rate increases. This issue is true for the slope of reaching the maximum value and the standard scatter value of the chart data. Figure 12 clearly shows that the slope of reaching the maximum value is

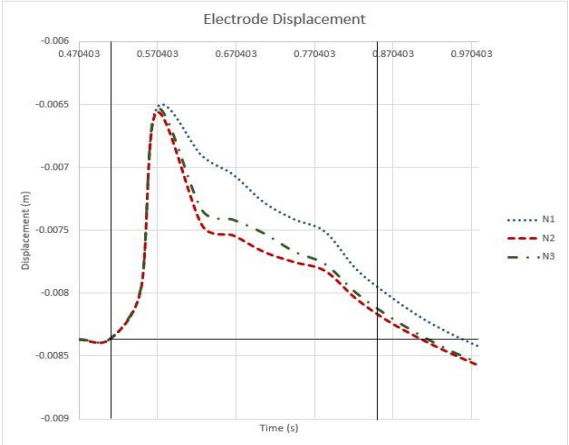

Figure 12. Electrode head displacement vs. time for three consecutive spot welds

the same for all three spot welds. However, the difference between the maximum value of the second and third spot welds is obvious with the first spot weld. This difference between the first and second spot welds is higher than the difference between the first and third spot welds. This matter shows that the effect of shunting phenomenon in the second spot weld is higher than the third spot weld which was analyzed in the previous part. It is clear by comparing the maximum first and second spot welds that there was a significant amount of electric current escape, and affect nugget diameter between the upper and middle sheets are tangible despite the great gap between their two centers. On the other hand, the tiny maximum difference between the first and third spot welds shows the intangibility of the electric current escape which has a slight effect on the nugget diameter between the upper and middle sheets which can be neglected.

5. CONCLUSION

In the present research, the shunting phenomenon in the successive RSW processes of three-sheets connection was studied. Various techniques were used to reach this goal, including nugget diameter measurement, investigating the electric current density, contact electrical conductivity, and displacement of electrode head during welding process. Findings of this research include:

- Providing a three-dimensional finite element model of RSW process as an electrical-thermal-mechanical coupling: the obtained results from simulation for nugget diameter between the top and middle sheets and between the middle and bottom sheets had a very good agreement with the experiment results.
- Considering the sheets deformation while previous spot welds and investigating its effect on the shunting phenomenon using finite element simulation.
- Investigating shunting phenomenon using various techniques: the obtained results are aligned with each other completely which shows the high precision of research.
- The most achievements of the present research show that the shunting phenomenon is neglected from the previous spot welds in a three-sheet connection based on a 45 mm interval. This matter is despite the published reports by considering the minimum 20 mm interval between the spot welds or the interval 6 times more than the electrode cross-section to reduce the effect of shunting phenomenon in two-sheet connection.
- The results reveal that the reduction of shunting effects for three consecutive spot welds is impressed by the deformation of the sheets which is less than or approximately equal to the electric current escape that occurs from previous spot welds. If the interval between

spot welds is less than the considered value in this research, the electric current escape will be higher than the previous spot welds. Therefore, the assumption of neglecting the deformation of the sheets in the simulation of RSW process will not significantly influence the results for more than one spot weld and short intervals. However, it is essential to consider the deformation of the sheets while investigating the electric current escape in more than one spot welding model with equal and higher than 45 mm intervals.

6. ACKNOWLEDGEMENTS

We sincerely appreciate Mr. Gholamreza Khanmohammadi, Seyed Mohammad Navidi, and Ramin Eslami who assisted us in this work.

7. REFERENCES

1. Habibizadeh. A, and Golabi. S, "Prediction of fatigue life of spot-welding connections subjected to unidirectional dynamic shear load", ***Modares Mechanical Engineering***, Vol. 14, No. 15, (2015), 361-368, in Persian.
2. Farrahi. GH, Ahmadi. A, and Reza Kashyzadeh. K, "Simulation of vehicle body spot weld failures due to fatigue by considering road roughness and vehicle velocity", ***Simulation Modelling Practice and Theory***, Vol. 105, (2020), 102168, DOI: 10.1016/j.simpat.2020.102168.
3. Ahmadi. A, Farrahi. GH, Reza Kashyzadeh. K, Azadi. S, and Jahani. K, "A comparative study on the fatigue life of the vehicle body spot welds using different numerical techniques: Inertia relief and Modal dynamic analyses", ***Frattura ed Integrita Stratturale***, Vol. 14, No. 52, (2020), 67-81, DOI: 10.3221/IGF-ESIS.52.06.
4. Jafari Vardanjani. M, Senkara. J, and Arayee. A, "A Review of Shunting Effect in Resistance Spot Welding", ***Przeglad Spawalnictwa***, Vol. 88, No. 1, (2016), 46-50, DOI: 10.26628/wtr.v88i1.562.
5. Xing. B, Xiao. Y, and Qin. QH, "Characteristics of shunting effect in resistance spot welding in mild steel based on electrode displacement", ***Measurement***, Vol. 115, (2018), 233-242, DOI: 10.1016/j.measurement.2017.10.049.
6. Jafari Vardanjani. M, Araee. A, Senkara. J, Jakubowski. J, and Godek. J, "Theoretical analysis of shunting effect in resistance spot welding (RSW) of AA2219", ***Journal of the Chinese Institute of Engineers***, Vol. 39, No. 8, (2016), 907-918, DOI: 10.1080/02533839.2016.1215940.
7. Jafari Vardanjani. M, Araee. A, Senkara. J, Jakubowski. J, and Godek. J, "Experimental and numerical analysis of shunting effect in resistance spot welding of Al2219 sheets", ***Bulletin of the Polish Academy of Sciences***, Vol. 64, No. 2, (2016), 425-434, DOI: 10.1515/bpasts-2016-0048.
8. Chang. HS, and Cho. HS, "A study on the shunt effect in resistance spot welding", ***Welding Journal***, Vol. 69, No. 8, (1990), 308-316.
9. Wang. BB, Lou. M, Shen. Q, Li. YB, and Zhang. H, "Shunting Effect in Resistance Spot Welding Steels — Part 1: Experimental Study", ***Welding Journal***, Vol. 92, (2013), 182-189.
10. Wang. BB, Lou. M, Shen. Q, Li. YB, and Zhang. H, "Shunting Effect in Resistance Spot Welding Steels — Part 2: Theoretical Analysis", ***Welding Journal***, Vol. 92, (2013), 231-238.
11. Bi. J, Song. JL, Wei. Q, Zhang. Y, Li. Y, and Luo. Z, "Characteristics of shunting in resistance spot welding for dissimilar unequal-thickness aluminum alloys under large thickness ratio", ***Materials and Design***, Vol. 101, (2016), 226-235, DOI: 10.1016/j.matdes.2016.04.023.
12. Li. Y, Bi. J, Zhang. Y, Luo. Z, and Liu. W, "Shunting characteristics in triangular arranged resistance spot welding of dissimilar unequal-thickness aluminum alloys", ***International Journal of Advanced Manufacturing Technology***, Vol. 91, (2017), 2447-2454, DOI: 10.1007/s00170-016-9926-0.
13. Seyyedian Choobi. M, Nielsen. CV, and Bay. NO, "Finite Element and Experimental Study of Shunting in Resistance Spot Welding", Proceedings of the 11th International Seminar Numerical Analysis of Weldability, Seggau, Austria, (2015).
14. Yu. J, Faridh. M, and Park. YW, "Adaptive resistance spot welding method that reduces the shunting effect", ***Journal of Manufacturing Processes***, Vol. 35, (2018), 604-613, DOI: 10.1016/j.jmapro.2018.09.002.
15. Yu. J, "Adaptive resistance spot welding process that reduces the shunting effect for automotive high-strength steels", ***Metals***, Vol. 8, No. 10, (2018), 775, DOI: 10.3390/met8100775.
16. Amiri. N, Farrahi. GH, Kashyzadeh. KR, and Chizari. M, "Aplications of ultrasonic testing and machine learning methods to predict the static & fatigue behavior of spot-welded joints", ***Journal of Manufacturing Processes***, Vol. 52, (2020), 26-34, DOI: 10.1016/j.jmapro.2020.01.047.
17. Farrahi. GH, Kashyzadeh. KR, Minaei. M, Sharifpour. A, and Riazi. S, "Analysis of resistance spot welding process parameters effect on the weld quality of three-steel sheets used in automotive industry: Experimental and finite element simulation", ***International Journal of Engineering, Transactions A: Basics***, Vol. 33, No. 1, (2020), 148-157, DOI: 10.5829/ije.2020.33.01a.17.

Persian Abstract

چکیده

هدف اصلی پژوهش حاضر بررسی پدیده فرار جریان الکتریکی در یک اتصال نقطه جوش مقاومتی سه ورقی با استفاده از شبیه‌سازی المان محدود است. برای دستیابی به این هدف، اتصال جوش نقطه ای مقاومتی سه ورق به عنوان یک مسئله کوپل الکتریکی-حرارتی- مکانیکی شبیه‌سازی شد. برای اعتبارسنجی شبیه‌سازی ارایه شده، نتایج اجزای محدود با نتایج تجربی، اعم از اندازه و شکل هندسی جوش در اتصال جوش نقطه ای مقاومتی مقایسه شد. پس از آن، فرآیند جوشکاری چند نقطه‌ای در اتصال فولادهای سه ورقی کم کربن با ضخامت‌های یکسان با در نظر گرفتن فاصله متوالی ۴۵ میلی‌متر مورد تجزیه و تحلیل قرار گرفت. تکنیک‌های مختلفی از جمله اندازه‌گیری قطر نطقه جوش جدید، چگالی جریان الکتریکی، هدایت تماس الکتریکی و جابجایی الکترود، برای مطالعه اثرات فرار جریان الکتریکی در فرآیند جوش نقطه‌ای متوالی مورد استفاده قرار گرفت. نتایج به دست آمده از روش‌های مختلف تا حد زیادی با یکدیگر مطابقت دارد. همچنین نتایج اجزای محدود نشان داد که فرض نادیده گرفتن اثر تغییر شکل ورق برای فواصل کم بین نقطه جوش‌های متوالی قابل قبول است. با این حال، لازم است تغییر شکل ورق برای فواصل متوالی بیش از ۴۵ میلی‌متر در نظر گرفته شود.

International Journal of Engineering

Journal Homepage: www.ije.ir

Conglomerate Energy Efficient Elgamal Encryption Based Data Aggregation Cryptosystems in Wireless Sensor Network

T. G. Babu*[a], V. Jayalakshmi

[a] *Department of Computer Applications, Vels Institute of Science, Technology and Advanced Studies, Pallavaram, Chennai, India*

P A P E R I N F O

Paper history:
Received 23 June 2021
Received in revised form 04 November 2021
Accepted 02 December 2021

Keywords:
Wireless Sensor Network
Data Aggregation
Elgamal Crytosystems
Encryption
Wireless Security

A B S T R A C T

Wireless sensor networks (WSN) are growing rapidly since the past decade mainly due to its efficiency and Ad-Hoc feature. The data aggregation has been extensively employed in WSN that also impact on the data transferring between the sensor nodes. The security issues, data integrity and confidentiality become vital during the deployment of sensor network in a hostile environment. The entire network comprises of sensors, base stations, gateways and nodes which are connected for the purpose of digital transmission. Many existing works have been evolved to address the security issues in WSN but all focused only on basic security features but lack to obtain reliable and effective results in terms of parameters like energy consumption, packet delivery ratio, and computational cost. This paper focussed on the primary research area of data aggregation and the mode of transmission in an energy efficient way without congestion. To obtain the objective, an integration of Conglomerate ElGamal energy efficient protocol has been employed and the performance of the proposed system are evaluated. Since the resource constraint nodes of the wireless sensor network requires less energy to cope up with limited battery power, the main purpose of the work is to build an efficient security mechanism that enhances the performance of the network with less energy, minimum delay, and maximum throughput. The performance parameters like packet delivery ratio, throughput, estimation of alive nodes and dead nodes for different rounds has been performed in the study. Furthermore, the effectiveness of the proposed system has been compared with state of art methods in terms of residual energy and depicted that deliberates the superior performance of the presented framework.

doi: *10.5829/ije.2022.35.02b.18*

1. INTRODUCTION

WSN comprise huge number of sensor nodes and are widely distributed in the sensor environment for evaluating and receiving data. The sensor nodes are controlled by Base Station (BS) and are used to monitor the environment and transmit the sensed data requested by the recipient node through BS [1]. WSN has been utilized in various application such as defence domain, medical field, weather forecasting and several other industrial and commercial applications [2]. The WSN sensors are generally compact and utilize limited battery constraint. The sensor aggregates the data and transmits to the server location which is stated as the base station. At the base station the data received are analysed to create a decision for several prescribed application. These nodes function as a repeated for transmitting the data to other sensors and sink. Further WSN power source must be utilized in an appropriate way since it could not be recharged or exchanged. These WSN frameworks are affected by several parameters such as fault tolerance, energy efficiency, scalability etc. The WSN sensors exhaust the energy mainly in two kinds of ways which are environmental parameter sensing and data transmission to base station through the sensor nodes. The inadequate power source are regarded as the key issue in wireless sensor network and hence the network failure and node failure arises [3]. Further the optimal energy usage in WSN is needed for obtaining high lifetime and more performance. So grouping of sensors into the corresponding clusters has been employed for decreasing the network energy consumption and thereby to increase the network reliability. Every Cluster possesses Cluster Head and an

*Corresponding Author Email: babuit.17@gmail.com (T. G. Babu)

Please cite this article as: T. G. Babu, V. Jayalakshmi, Conglomerate Energy Efficient Elgamal Encryption Based Data Aggregation Cryptosystems in Wireless Sensor Network, ***International Journal of Engineering, Transactions B: Applications***, Vol. 35, No. 2, (2021) 417-424

effective framework like our proposed system is required to reduce the consumption of energy. ElGamal encryption is the public key cryptographic algorithm used for secure exchanging of information between two parties which is based on D-H key exchange. However, ElGamal algorithm uses one way hash function and it is very difficult to break the encryption and the attacker cannot inverse the hash function to get the original message. Merkle–Hellman algorithm is one of the earliest public key algorithm based on sub-set sum problem which is now considered insecure after the evolution of many public key algorithm like RSA. The proposed system utilized ElGamal based encryption that enable effective data aggregation [4, 5]. ElGamal cryptosystem modifies Diffee Hellman protocol and employs Digital Signature Algorithm for signing digital documents. It comprises major process like effective key generation, encryption and decryption system. Its non-deterministic encryption the same plaintext multiple times will result in different cipher texts, since a random k is chosen each time [6, 7]. The cryptosystem needs one is Public key which is used for Encryption process and the other one is Private key which is used for Decryption process [8]. The algorithm in turn uses "Energy" as a parameter to find out the better routing to reach the destination. Normal nodes only communicated with its neighbour and every node will take data fusion in order. The distance of the connect nodes with each other have been shortened remarkably. Nodes take turns to be the cluster head, so it takes no energy. In this research work, the combination of ElGamal based encryption followed by data aggregation and Knapsack based Energy efficient AODV promotes the overall effectiveness of the crytptosystem. The main contribution of the proposed work are

- To frame an effective Conglomerate ElGamal based encryption associated with multiple key generations that allows reliable data aggregation and more security.
- To increase the performance of the network through secure transmission of keys with energy efficient strategy.

The organisation of the paper is as follows. Initial section provides the introduction and need for the study, Section 2 provides the survey of existing literature in accordance with the proposed work. Section 3 describes the methodology and section 4 offers the performance analysis of the proposed system. Section 5 concludes the work in detail:

2. REVIEW OF LITERATURE

This section provides the survey of prevailing works in accordance to the proposed system. Ara et al. [9] suggested a secured privacy preservation data aggregation system in accordance with bilinear pairing for improving data privacy and data aggregation efficiency. The suggested system has been proved to be secured under Diffe Hellman assumption. Further it utilized Elgamal cryptosystem for secured encryption. The suggested system showed effective data aggregation with reliable computational cost. Wang et al. [10]suggested a clustering algorithm for the selection of cluster heads with an enhanced ABC algorithm. The study introduced cluster head density, energy, location and other such similar factors into the suggested framework. This enhanced ABC has been utilized for the optimization of fuzzy c means to determine the effective clustering method. The study also employed an Ant colony based energy efficient routing protocol to improve network throughput. The study introduced a polling controlling mechanism to intra-cluster communication process. Agarkar et al. [11] presented a security mechanism based on lattice cryptography for data aggregation for WSN. It employed learning with errors over the rings for encryption of data. The security analysis employed that the suggested system offered integrity, confidentiality and authenticity during the process of communication. The efficiency of this lightweight system depicted that it is more better than ElGamal cryptosystem. Hamza and Al-Alak [12] used Kaiser Constant Modulus Algorithm (KCMA) technique for the generation of twelve experiments of Elgamal, Rivest Shamir Adleman (RSA) and Electrical Computer and Communication (ECC) algorithms. These chain of experiments merged with the hash function XOR and Secure Hash Algorithm 2 (SHA2). The study utilized Diehard test in the experiments for the evaluation of randomness of the generated secret key thereby displaying the security of the system. The study determined that SHA2 has been found to be better than XOR. Further the work assesse the efficiency time for the throughput network. Wang et al. [13] deliberated an reliable and efficient WSN clustering algorithm on the basis of quantum artificial bee colony (ABC) algorithm that aimed at unbalanced load in WSN clustering without the consideration of residual node energy, node position and node intensity. This algorithm could be able to adapt better to the network topology and also decreased the node energy consumption and extend the network lifetime. The experimental outcomes of the represented that the algorithm increased the stability of the overall system. The work aimed to further improve the algorithm for the data acquisition and network clustering of mobile WSN. Leelavathi et al. [14] investigated encryption of image and text data that has been embedding as elliptic curve point. The finite field arithmetic has been used effectively in the suggested cryptosystem. The pre computations for the image input conversion and text data has been performed with the use of MATLAB. Here the message size differs with various stream size and also

the mapping of input data has been presented with high security that indicates less vulnerability in attacks. The study also performed statistical analysis on the encrypted and plain images for assessing the strength of the suggested method.

Asma and Lehsaini [15] suggested an energy effective routing algorithm for balancing the energy during forwarding the information from source to the corresponding link. The system offered better effectiveness when compared to the prevailing routing algorithms in accordance to energy efficacy. The study also extended the network lifetime of WSN. The simulation results of the study depicted that knapsack based energy efficient system will be greatly utilised for addressing data aggregation problems. In future the study attempted to deal with the security issues for misbehaviouring nodes. Xing et al. [16] investigated a private data aggregation system on the basis of homomorphic encryption and digital signatures. This paper possess the capability of verifying the information from various nodes that have identifiability. Further confidentiality interference factor technique was introduced for defending the interior attack. Next the study adopted a homomorphic encryption property based on confidentiality sum algorithm without trust party. This avoided efficiency and safety problem that results from trusted third party. Finally the study provided the security proof and effectiveness analysis for the suggested scheme.

Prabu [17] investigated knapsack algorithm for avoiding brute drive attack through growing confusions. The modules are combined for performing knapsack encryption and decryption, matrix mapping and de mapping. The study utilized Verilog language for simulation and coding on Spartan 6 and Xilinx ISE. Entire cryptosystem has been executed with the frequency of 503 MHz. When compared with the previous work, the utilization area is found to be very less thereby satisfying the resource parameters of WSN. Al-Naamee and Ali [18] suggested a Cluster based data aggregation method in WSN that utilized Elliptical Curve Cryptography based on Elgamal homomorphic cryptosystem for the provision of integrity and confidentiality. This deliberated work offered security against several possible malicious behaviour and possible attacks with extended network lifetime. Maheshwari et al. [19] investigated the data aggregation efficiency for developing cluster-based routing algorithm for achieving the low energy consumption for data aggregation and security problems in WSN. The study analysed routing, clustering and protection protocol that is effective against the existing method. WSNs are also vulnerable to several threats and attacks. Among these, congestion is a serious form of attack that disrupts and collapses a WSN very deeply. This, in turn, causes tremendous increase in the rate of packet drops and also results in very high. In order to overcome the limitations of the existing works the presented proposed work attempted a better approach.

3. THE PROPOSED METHODOLOGY

The proposed methodology has been explained in this section with an explorative flow diagram in Figure 1.

The transmitting data are processed with prime number primitive root creation. The proposed key generation algorithm utilize one large prime number 'q', which is greater than size of the message 'n'. The set of primitive roots of prime number 'q' is determined. This is followed by the generation of public key and private key. This study employed ElGamal based conglomerate encryption and decryption. The encryption phase has been processed for cluster head selection. The developed cluster member was used for the determination of cluster weight and data acquisition. By performing aggregation logic the members were subjected to data aggregation phase. The transferred aggregated data has been subjected to performance analysis for the evaluation of the proposed method.

3. 1. Data Aggregation Based Conglomerate Elgamal Encryption ElGamal encryption is a public key cryptographic system and utilize asymmetric key encryption for the communication purpose in between the two parties and for encrypting the message [20, 21]. This was introduced by TaherElGamal in 1985 and is a probabilistic algorithm developed on the basis of Diffie- Hellman key exchange method. This exists a comprehensive encryption-decryption system which depend on discrete logarithm issues. A probabilistic encryption could be defined as the encryption system which develops various ciphertexts when the similar plaintext is encrypted various times and the discrete logarithm issue is determining the discrete logarithm to the group base. The data aggregation based ElGamal encryption system is defined below. Here the algorithmic steps for encryption, data aggregation and

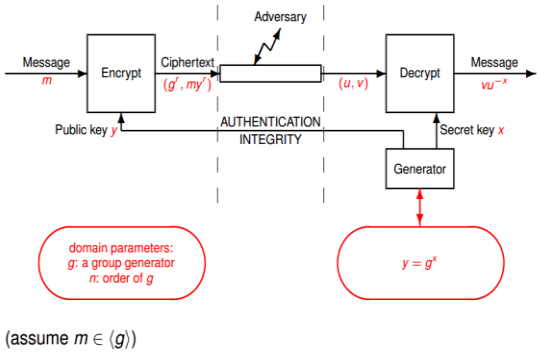

Figure 1. Overview of the ElGamal Scheme

decryption of the aggregated data has been deliberated below.

Algorithm I: Data aggregation based Elgamal Encryption
Input: sensors data S_N^D
Output: Aggregated Data D_{aggr}, encrypted data S_i^C and decrypted data S_i^{Decry}
Procedure:

1. **Key generation:**
   - Choose large prime number p
   - Choose a primitive value g in modulo p
   - Randomly choose m, such that $2 \leq m \leq p-2$
   - Now computes the secret integer, $c = mod(g^m, p)$
   - The combined public keys are $\{g, c, p\}$
   - The private keys are {m, p}
2. The sensed data is encrypted with public keys, the following process are performed during encryption process,

$$s = g^n \; mod \; p$$

$S_i^c = c \; mod \; p$ //S_i^C is the cryptography text

3. Perform data aggregation process for all sensed data,

$$D_{aggr} = S_i^{C_1} + S_i^{C_2} + \cdots + S_i^{C_t}$$

4. Apply decryption process for aggregated data,

$$s^m = c^n mod \; p$$
$$S_i^{Decry} = D_{aggr} . \overline{c^n} mod \; p$$

5. The usage of energy for transmitting their sensed S_N^D packet over distance d_i is,

$$E_{Tx}(m, d_i) = \begin{cases} mE_{elec} + m\delta_f d_i^2 d_i \leq \rho \\ mE_{elec} + m\delta_m d_i^4 d_i > \rho \end{cases}$$

Where,
δ_f – the free space
δ_m – multipath fading channel model
E_{elec} – electronic energy which is based on some factors includes the modulation and digital coding
ρ – threshold distance

6. Find the generation of CH selection based on the multi objective fitness function of knapsack problem with two parameters such as residual energy and sensing range φ

$$fit_{val} = c_1 \left[\frac{E_{res}^m - E_{res}^i}{E_{res}^m} \right] + c_2 \left[\frac{\varphi^m - \varphi^i}{\varphi^m} \right]$$

Where, E_{res}^m – maximum residual energy
E_{res}^i – residual energy for sensors
φ^m – maximum sensing range and φ^i sensing range of each sensor

The sensor nodes are deployed and all the nodes and base stations are in stationary mode. The presented paper utilized a simplified model for the consumption of communication energy. On depending on the distance in between the receiver and transmitter, the free space or the multipath fading channel method were employed. The energy required for transmitting the packet over distance has been estimated in the algorithm in step 7. The electronic energy relies on few factors comprising the modulation and digital coding whereas the amplifier energy relies on the transmitting distance. In order to receive such kind of packets the radio consuming energy has been determined in step 8. After random deployment, random number of nodes were chosen on the basis of probability for the selected node S_R. Based on the equation provided in step 8 the random nodes are chosen. Followed by that neighbouring nodes on the basis of minimum Euclidean distance was selected with the step 10 which provides the distance between random nodes and member nodes.

4. PERFORMANCE ANALYSIS

The experimental setup and performance of the proposed method are discussed in this section. The performance of the cluster based routing is analyzed using various metrics alive nodes, dead nodes, average energy consumption, total packet sent, and throughput. Existing LEACH protocol has been utilized for comparision. Table 1 shows the simulation parameters. The performance measures are explained as follows:

Alive nodes based on energy: Alive nodes define the number of nodes that are alive in the network. The network performance is improved, when the network has a high number of alive nodes.

Average energy consumption: It defines the average amount of energy consumed by each node during each iteration.

Total packets transmitted to the BS: The total packets transmitted to BS are directly proportional to the alive nodes and residual energy of the nodes. The total packets received by BS are high when alive nodes are high.

Throughput: The throughput is defined as the amount of bits transmitted to BS over WSN. Throughput is measured as bits per second. Packet drop ratio: The packet drop ratio is defined as the volume of packet loss occurred during the transmission from source node to the BS.

Figure 2 shows the coverage area and Figure 3 shows the initial node deployment. In Figure 4, the total energy consumption in Joules for the proposed system has been evaluated for different rounds. It has been observed that the energy consumption increases with an increase in rounds and time. The energy consumption for 300 milliseconds has been found to be 0.025 J which is less than the existing systems. Hence the proposed system proves be efficient in terms of energy consumption. The overall network of the proposed system at various nodes was evaluated in Figure 5. The network lifetime seems to be decreases for the processing rounds from 50 milliseconds to 300 milliseconds. It was observed that the network lifetime varies between 11000 milliseconds to 2500 milliseconds.

TABLE 1. Simulation Parameters

Simulation Parameters	Values
Simulation Area	200 * 200
Density of Nodes	1000 to 1500
Transmission range	20-30 ms
Radio Propagation Model	Two Ray Model
Environment	Urban
Node Initial Energy	150 J
Transmission Power (tx)	1.5 J per packet
Receiving Power (rx)	0.48 J per packet
Simulation Duration	50 Minutes
No of trails	65
Packet Size	30 Bytes

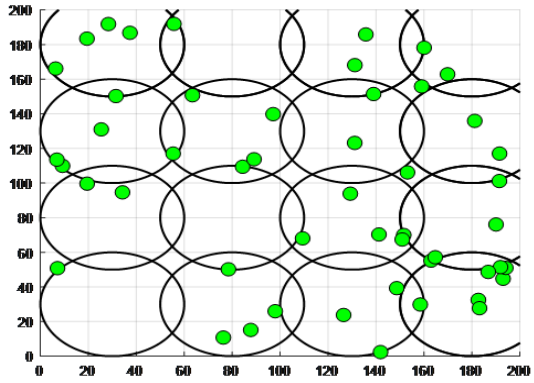

Figure 2. Coverage area

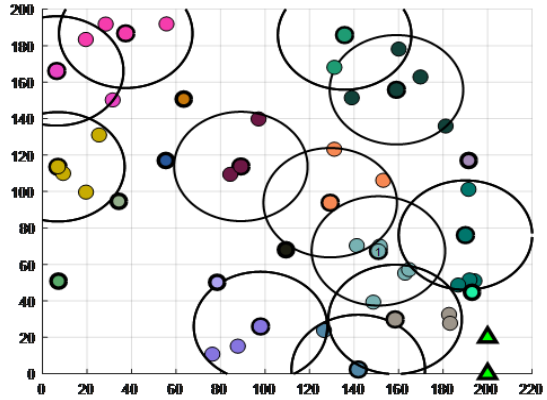

Figure 3. Node deployment

The average energy analysis for the proposed system has been assessed for the proposed system in Figure 6. It was observed that the average energy of each node of the

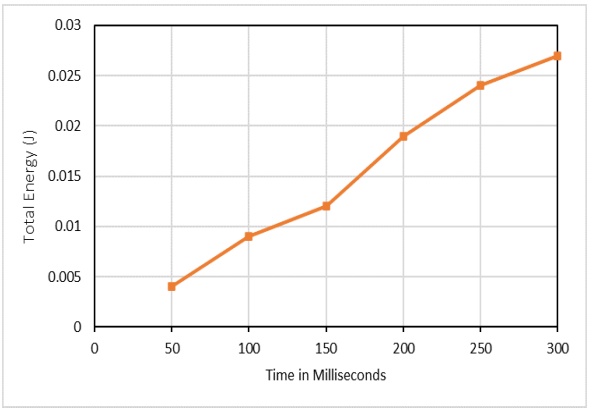

Figure 4. Total Energy consumption at different rounds

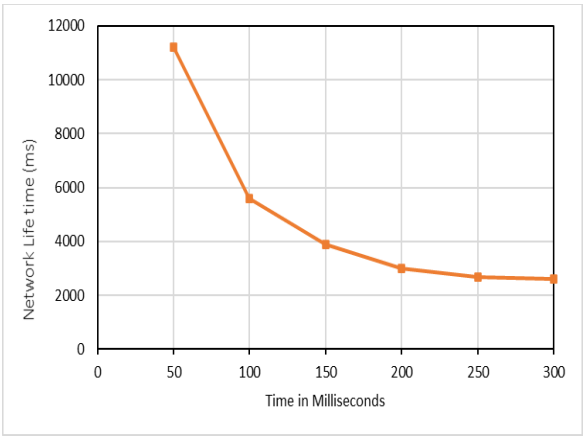

Figure 5. Overall Network Lifetime at different rounds

proposed system has been observed to be more that the existing system. Due to the prevalence of more energy the proposed system performs better in terms of performance parameters. Dead node is a generated node that is not to be expanded or explored any further. All children of a dead node have already been expanded. Figure 7 deliberates the dead node analysis for the proposed and existing system. It was observed that the existing approach has earlier dead nodes when compared to the proposed system.

Table 2 deliberates the security analysis through assessing several characteristics depicted in that table. Resiliency, efficiency, digital ledger, decentralization, smart contract and anonymity characteristics were assessed in accordance to problems such as third party access, eavesdropping, availability, single point failure, trust, immutability, botnet attacks and data privacy. These assessment proves the effective functioning of the proposed system.

Figure 8 offers a comparative assessment of the proposed method with the state of art method in terms of residual energy. This assessment proved the effectiveness of the proposed system.

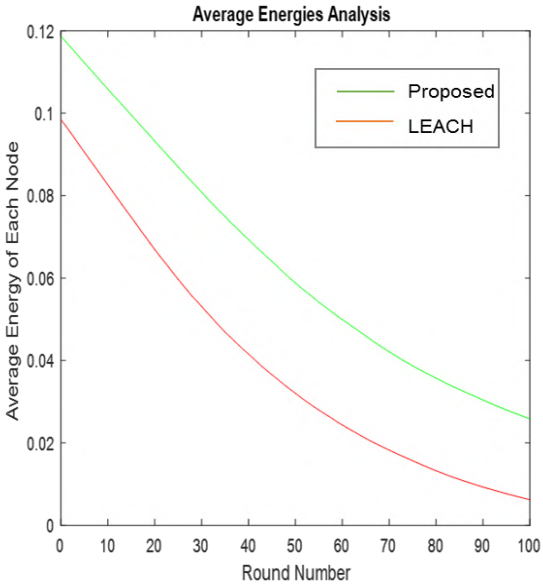

Figure 6. Average Energy Analysis

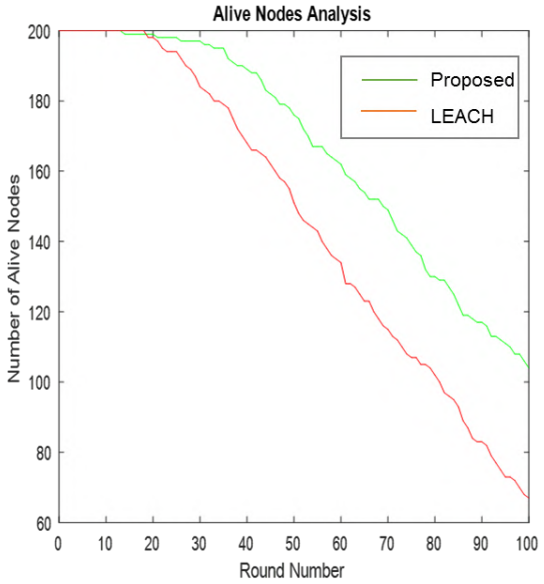

Figure 7. Alive node analysis

TABLE 2. Security analysis through proposed approach

Characteristics / Issues	Resiliency	Efficiency	Digital Ledger	Decentralization	Transparent & Verifiable	Smart Contract	Anonymity
Third Party	Yes	No	Yes	No	Yes	Yes	No
Eavesdropping	No	No	No	Yes	No	No	Yes
Access Control	Yes	Yes	NO	No	Yes	No	Yes
Availability	Yes	Yes	Yes	Yes	Yes	Yes	No
Integrity of Data	No	Yes	Yes	No	No	No	Yes
Single Point failure	No	Yes	Yes	Yes	No	Yes	No
Trust	Yes	Yes	No	No	Yes	No	Yes
Botnet Attacks	No	No	No	Yes	No	Yes	Yes
Immutability	No	Yes	Yes	Yes	No	No	No
Data Privacy	Yes	Yes	No	No	Yes	Yes	Yes

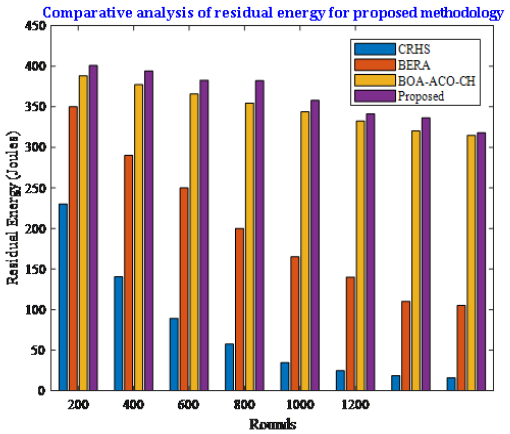

Figure 8. Comparative analysis of the residual energy of the proposed methodology

5. CONCLUSION

Data aggregation plays a vital role in WSN and also possess greater impact on the data transferring between the sensor nodes. ElGamal cryptosystem modifies Diffee Hellman protocol and employs Digital Signature Algorithm for signing digital documents. Hence the paper focussed on the integration of Conglomerate ElGamal Encryption and indicating the way of energy efficient protocol has been used and the performance of the proposed system are evaluated. The performance parameters such as packet delivery ratio, throughput, estimation of alive nodes and dead nodes for different rounds has been performed in the study. The efficacy of proposed framework has been compared with state of art methods in terms of residual energy and depicted that

deliberates the superior performance of the presented framework.

6. REFERENCES

1. Khan, T., Singh, K.J.J.o.D.M.S. and Cryptography, "Resource management based secure trust model for wsn", ***Journal of Discrete Mathematical Sciences and Cryptography*** Vol. 22, No. 8, (2019), 1453-1462, doi: 10.1080/09720529.2019.1695897
2. Alkalbani, A.S. and Mantoro, T., "Security comparison between dynamic & static wsn for 5g networks", in 2017 Second International Conference on Informatics and Computing (ICIC), IEEE. (2017), 1-4.
3. Mosavvar, I. and Ghaffari, A.J.W.P.C., "Data aggregation in wireless sensor networks using firefly algorithm", ***Wireless Personal Communications*** Vol. 104, No. 1, (2019), 307-324, doi: 10.1007/s11277-018-6021-x
4. Hayouni, H., Hamdi, M.J.I.A. and Computing, S., "A data aggregation security enhancing scheme in wsns using homomorphic encryption", ***Intelligent Automation & Soft Computing,*** (2017), 1-9, doi: 10.1080/10798587.2017.1327157
5. Randhawa, S. and Jain, S.J.W.P.C., "Data aggregation in wireless sensor networks: Previous research, current status and future directions", ***Wireless Personal Communications*** Vol. 97, No. 3, (2017), 3355-3425, doi: 10.1007/s11277-017-4674-5
6. Suriya Praba, T., Meena, V., Sethukarasi, T., Prachetha, K., Aravind, B., Bharathkumar, K.J.J.o.I. and Systems, F., "Energy measure cluster based concealed aggregation for confidentiality and integrity in wsn", ***Journal of Intelligent & Fuzzy Systems*** Vol. 38, No. 5, (2020), 6475-6482, doi: 10.3233/JIFS-179728
7. Vidhya, S., Sasilatha, T.J.J.o.C. and Nanoscience, T., "Performance analysis of ad-hoc on demand distance vector and energy power consumption aodv in wireless sensor networks", ***Journal of Computational and Theoretical Nanoscience*** Vol. 14, No. 3, (2017), 1265-1270, doi: 10.1166/jctn.2017.6442
8. Sowmyadevi, D. and Karthikeyan, K., "Merkle-hellman knapsack-side channel monitoring based secure scheme for detecting provenance forgery and selfish nodes in wireless sensor networks", in 2017 Second International Conference on Electrical, Computer and Communication Technologies (ICECCT), IEEE. (2017), 1-8.
9. Ara, A., Al-Rodhaan, M., Tian, Y. and Al-Dhelaan, A.J.I.A., "A secure privacy-preserving data aggregation scheme based on bilinear elgamal cryptosystem for remote health monitoring systems", Vol. 5, (2017), 12601-12617, doi: 10.1109/ACCESS.2017.2716439
10. Wang, Z., Ding, H., Li, B., Bao, L. and Yang, Z.J.I.A., "An energy efficient routing protocol based on improved artificial bee colony algorithm for wireless sensor networks", Vol. 8, (2020), 133577-133596, doi: 10.1109/ACCESS.2020.3010313
11. Agarkar, A.A., Karyakarte, M. and Agrawal, H., "Post quantum security solution for data aggregation in wireless sensor networks", in 2020 IEEE Wireless Communications and Networking Conference (WCNC), IEEE. (2020), 1-8.
12. Hamza, A.H. and Al-Alak, S.M.K., "Evaluation key generator of multiple asymmetric methods in wireless sensor network (wsns)", in Journal of Physics: Conference Series, IOP Publishing. Vol. 1804, No. 1, (2021), 012096.
13. Wang, H., Chen, Y. and Dong, S.J.I.W.S.S., "Research on efficient-efficient routing protocol for wsns based on improved artificial bee colony algorithm", Vol. 7, No. 1, (2017), 15-20, doi: 10.1049/iet-wss.2016.0006
14. Leelavathi, G., Shaila, K., Venugopal, K.J.I.J.o.V.I. and Systems, C., "Reconfigurable hardware architecture of public key crypto processor for vanet and wireless sensor nodes", ***International Journal of Vehicle Information and Communication Systems*** Vol. 5, No. 1, (2020), 11-25, doi: 10.1504/IJVICS.2020.107179
15. Chikh, A., Lehsaini, M.J.C., Practice, C. and Experience, "Combination of greedy and compass approaches for efficient multipath geographic routing in wireless multimedia sensor networks", ***Online First***, (2021), e6703, doi: 10.1002/cpe.6703
16. Li, X., Chen, D., Li, C. and Wang, L.J.S., "Secure data aggregation with fully homomorphic encryption in large-scale wireless sensor networks", Vol. 15, No. 7, (2015), 15952-15973, doi: 10.3390%2Fs150715952
17. Prabu, J., "An energy efficient secure data aggregation in wireless sensor networks", (2021), doi: 10.21203/rs.3.rs-364741/v1
18. Al-naamee, M.K., Ali, S.M.J.B.o.E.E. and Informatics, "Improved el gamal public key cryptosystem using 3d chaotic maps", ***Bulletin of Electrical Engineering and Informatics*** Vol. 10, No. 1, (2021), 404-411, doi: 10.11591/eei.v10i1.2124
19. Maheshwari, P., Sharma, A.K. and Verma, K.J.A.H.N., "Energy efficient cluster based routing protocol for wsn using butterfly optimization algorithm and ant colony optimization", **Ad Hoc Networks** Vol. 110, (2021), 102317, doi: 10.1016/j.adhoc.2020.102317
20. Talebi, Z. and Timarchi, S.J.I.J.o.E., "Improved distributed particle filter architecture with novel resampling algorithm for signal tracking", ", ***International Journal of Engineering, Transactions C: Aspects,*** Vol. 33, No. 12, (2020), 2482-2488, doi: 10.5829/ije.2020.33.12c.07
21. Bypour, H., Farhadi, M. and Mortazavi, R.J.I.J.o.E., "An efficient secret sharing-based storage system for cloud-based internet of things", , ***International Journal of Engineering, Transactions B: Applications*** Vol. 32, No. 8, (2019), 1117-1125, doi: 10.5829/ije.2019.32.08b.07

Persian Abstract

چکیده

شبکه‌های حسگر بی‌سیم از دهه گذشته عمدتاً به دلیل کارایی و ویژگی Ad-Hoc به سرعت در حال رشد هستند .تجمیع داده ها به طور گسترده در WSN استفاده شده است که همچنین بر انتقال داده بین گره های حسگر تأثیر می گذارد .مسائل امنیتی، یکپارچگی داده ها و محرمانه بودن در طول استقرار شبکه حسگر در یک محیط خصمانه حیاتی می شود .کل شبکه شامل حسگرها، ایستگاه های پایه، دروازه ها و گره هایی است که به منظور انتقال دیجیتال به هم متصل می شوند .بسیاری از کارهای موجود برای رسیدگی به مسائل امنیتی در WSN تکامل یافته‌اند، اما همه آنها فقط بر ویژگی‌های امنیتی اساسی متمرکز شده‌اند، اما از نظر پارامترهایی مانند مصرف انرژی، نسبت تحویل بسته‌ها و هزینه محاسباتی به نتایج قابل اعتماد و مؤثری دست نمی‌یابند .این مقاله بر حوزه تحقیقاتی اولیه تجمیع داده ها و نحوه انتقال به روشی کارآمد انرژی بدون ازدحام متمرکز شده است .برای دستیابی به هدف، ادغام پروتکل کارآمد انرژی کنگلومرا ElGamal به کار گرفته شده است و عملکرد سیستم پیشنهادی مورد ارزیابی قرار می گیرد. از آنجایی که گره های محدودیت منابع شبکه حسگر بی سیم به انرژی کمتری برای مقابله با توان باتری محدود نیاز دارند، هدف اصلی کار ایجاد یک مکانیسم امنیتی کارآمد است که عملکرد شبکه را با انرژی کمتر، حداقل تاخیر و حداکثر افزایش می دهد .توان عملیاتی پارامترهای عملکرد مانند نسبت تحویل بسته، توان عملیاتی، تخمین گره‌های زنده و گره‌های مرده برای دورهای مختلف در این مطالعه انجام شده است .علاوه بر این، اثربخشی سیستم پیشنهادی با روش‌های پیشرفته از نظر انرژی باقیمانده مقایسه شده و به تصویر کشیده شده است که عملکرد برتر چارچوب ارائه شده را مد نظر دارد.

International Journal of Engineering

Journal Homepage: www.ije.ir

Enhancing Performance of an Air Conditioner by Preheating and Precooling of Liquid Desiccant and Non-processed Air

B. Ebrahimpour[a], A. Moazemi Goudarzi*[b], A. Kaviani[c]

[a] *Faculty of Technology, University of Portsmouth, Portsmouth, United Kingdom*
[b] *Department of Mechanical Engineering, Babol Noshirvani University of Technology, Babol, Iran*
[c] *Faculty of New Sciences and Technologies, University of Tehran, Tehran, Iran*

P A P E R I N F O

Paper history:
Received 10 May 2021
Received in revised form 27 November 2021
Accepted 04 December 2021

Keywords:
Moisture Content
Liquid Desiccant Air Conditioner
Lithium Chloride
Counter-flow Enthalpy Exchanger
Opimization
Particle Swarm Optimization

A B S T R A C T

Corrosive fluids such as lithium chloride are often used in liquid desiccant air conditioners. Corrosion in enthalpy exchanger is one of the design problems. Some solutions are studied in this research, and based on them; an experimental setup is investigated. In this design, a counter-flow enthalpy exchanger is used to exchange moisture between the air and the liquid desiccant. First, the inlet air is preheated or precooled by an aluminium heat exchanger. Then, the liquid desiccant is preheated or precooled by thin-walled plastic tubes. By contacting this processed air and liquid desiccant, heat, and mass exchanging occurs. The variation of the air moisture content is investigated in laboratory conditions, and the rate of regeneration and dehumidification is studied. The results indicate that in general, the ambient air moisture content decreased around 20% during the dehumidification process and it enhanced around 14.28% during the regeneration process. Furthermore, the moisture content variation in the dehumidification process improved at least 9.92%, but the regeneration process decreased at least 10.76% compared to the previous study. In addition, utilizing the particle swarm optimization algorithm is desirable to identify the system's transient behavior and obtain the fitting parameters of a curve that is closely similar to the experimental data of the rate of dehumidification and regeneration and the average errors of the fitted curve were 10.43 and 1.52%, respectively.

doi: *10.5829/ije.2022.35.02b.19*

1. INTRODUCTION

Although air conditioners were considered luxury products in the past, these days, they have become a necessity of human life [1]. Rising living standards, advances in technologies, and population growth have caused about 15% of the world's energy to be used by air conditioners [2]. The air conditioners in use are almost the vapor compression type, which has low efficiencies and use of CFC, HCFC, and HFC refrigerants. These refrigerants are used to cool water in evaporators, and over time, due to their leakage into the atmosphere, they react with ozone in the stratosphere. They also need fossil fuels and a large amount of electricity. Therefore, due to the energy crisis and the destruction of nature, researchers have turned to other methods, including desiccant cooling systems (DCS). The optimal desiccant should have a high moisture absorbing capacity and, at the same time, a lower regeneration temperature[3]. Desiccant cooling systems include solid or liquid desiccant. Solid desiccants are inexpensive, non-flammable, non-corrosive, and environmentally friendly and regenerate faster than liquid desiccants. However, they consume more energy. Unlike liquid desiccants, dehumidification and regeneration in solid desiccants are usually done simultaneously [4].

Liquid Desiccant systems (LDSs) usually consist of components such as dehumidifier, liquid desiccant,

*Corresponding Author Institutional Email: goudarzi@nit.ac.ir (A. Moazemi Goudarzi)

Please cite this article as: B. Ebrahimpour, A. Moazemi Goudarzi, A. Kaviani, Enhancing Performance of an Air Conditioner by Preheating and Precooling of Liquid Desiccant and Non-Processed Air, ***International Journal of Engineering, Transactions B: Applications***, Vol. 35, No. 2, (2021) 425-432

regenerator, and packing material. Liquid desiccants such as lithium chloride, lithium bromide[5], and other salts are corrosive. Any transfer of liquid desiccant with the airflow (carryover) can seriously damage the habitant's health. Corrosion and carryover, which are the main problems of these systems, can be solved using plastic materials and microporous membranes as semi-permeable membranes, respectively.

Important properties of liquid desiccants include conductivity, dynamic viscosity, specific heat capacity, density, and surface vapor pressure. The materials with low vapor pressure are LiCl, LiBr, and $CaCl_2$, in which LiCl has the minimum vapor pressure.

Nowadays, the general policies of countries are to reduce energy consumption and use of renewable resources. Renewable energies such as solar energy [6] and wind energy [7] can generate the energy demanded in LDAC systems. Alizadeh and Saman [8] studied a solar collector's thermal performance as a regenerator and used a computer model for $CaCl_2$. They found that the theoretical model and experimental results had a good agreement [9]. Qiu et al. [10] used a system with a biomass boiler that supplied 554 Watts for regeneration. In this study, HCOOK was used which reduced the relative humidity by up to 13% for humid air. Turgut and Çoban [11] also conducted an experimental and numerical study and evaluated LiBr and LiCl dehumidification rates. The results indicated that LiCl had a higher dehumidification rate. In a theoretical and experimental research, Mohamed et al. [12] observed that the dehumidification was increased up to 1.33 times by increasing the packing length from 0.5 m to 1 m. Peng et al. [13] compared the efficiency of a system containing LiCl or $CaCl_2$. LiCl has about 60% more efficiency and 16% lower exergy efficiency compared to $CaCl_2$.

In the previous studies, various factors on a liquid desiccant air conditioner (LDAC) system were investigated. The fluid inlet temperature is an important parameter in a dehumidification process. Using a mathematical model for an LDAD system, Lu et al. [14] observed that as the inlet solution temperature increases, the ratio of outlet moisture and outlet air temperature increases. In a previous research, Moazemi et al. [15] were investigated an LDAC system with LiCl to reduce the effect of carryover.

This study proposes an innovative configuration of an LDAC system with LiCl in which preheating or precooling of the air and the liquid desiccant is done simultaneously. The effect of this new configuration on the variation of temperature, relative humidity, moisture content during the dehumidification and regeneration processes was studied and additionally, with the help of particle swarm optimization (PSO) algorithm, the system's transient behavior is determined.

2. SYSTEM DESCRIPTION

The corrosive of LiCl is one of the main limitations for the design of an LDAC system with LiCl desiccant. For instance, in an LDAC system with LiCl desiccant, a plate heat exchanger and pumps were made of stainless steel. After a few years, corrosion was visible in the system, which is shown in Figure 2. As a multi-criteria target, it is necessary to consider different strategies that find the best solution for this specific problem [16]. There are two different strategies that are adopted to deal with corrosion of the liquid desiccant. According to Figure 1, in the first strategy, to avoid corrosion, the liquid desiccant is not preheated or precooled, and only the inlet air passing through the enthalpy exchanger is preheated or precooled. In the second strategy, utilizing a polymer enthalpy exchanger, the liquid desiccant is also preheated or precooled, as well as the inlet air.

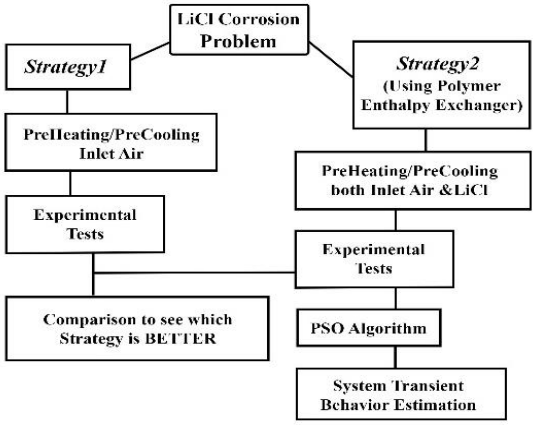

Figure 1. The flowchart of different strategies for LiCl corrosion problem in this research

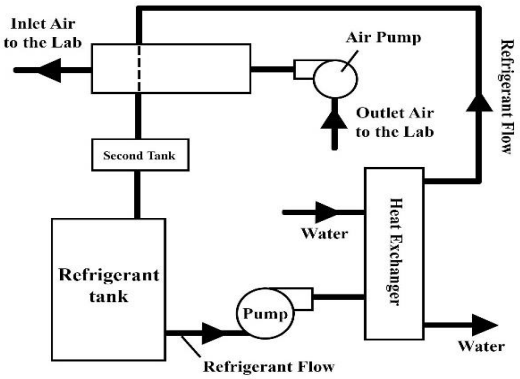

Figure 2. The schematic of liquid desiccant air conditioner with LiCl installed in Babol Noshirvani University of Technology

The first strategy was investigated in the previous study. Accordingly, the second strategy was chosen in this study and an LDAC system with LiCl was investigated, which is shown in Figure 3. A polymer counter-flow enthalpy exchanger was used for exchanging moisture content between the air and the liquid desiccant. Depending on the conditions, whether it is the dehumidification process or regeneration process, the inlet air passing through the enthalpy exchanger is precooled or preheated by an aluminium heat exchanger in which water flows in it. Utilizing thin-walled plastic tubes in the liquid desiccant bed, LiCl can be preheated or precooled simultaneously with the inlet air. Figure 3 depicts that the components of the experimental setup. The counter-flow enthalpy exchanger was made of 5 vertical-multi-channel polypropylene blocks for increasing the contact of desiccant and air. Each block had a dimension of 50×50×10 cm^3 at intervals of 1 cm from each other, and their channels had a size of 4×4 mm^2 at a thickness of 0.5 mm.

According to Figure 4, the inlet air at point 1 exchanges heat with the aluminium heat exchanger, which there is a flow of water in its coil, then exits at point 2. The processed air enters the enthalpy exchanger tower from downwards and moves upwards. It passes through the enthalpy tower channels and exchanges heat and mass with the liquid desiccant sprayed from above. Then, the air reaches point 3, and passing through the eliminator and trapping the solution particles along with the air, moves and reaches point 4. In addition, to prevent the carryover of the exhaust air, the enthalpy exchanger's channels were wicked, and the pumps were controlled to be on for 10 seconds and then off for 50 seconds. Now the air exits from the system through port 5 using the air pump. In the water flow path, first, the water is received by the pump from point 6 or the water tank outlet and is transferred to the inlet of the aluminium heat exchanger or point 7. The water flow passes through the aluminium heat exchanger and transfers heat to the inlet air. Then, it leaves the aluminium heat exchanger through port 8 and reaches the liquid desiccant bed. After passing through the thin-walled plastic tubes in the bed of liquid desiccant, it also exchanges heat with the liquid desiccant and exits from port 9 and then returns to the water tank. In the water tank, water was heated by three electrical heaters in the regeneration process. But, in the dehumidification process, the heaters were turned off, and the water was cooled by adding 10 kg of ice at 0 °C.

The liquid desiccant flow path is also shown in Figure 5. First, the liquid desiccant exits from the liquid desiccant bed by two centrifugal pumps made of polymeric materials and is transferred from point 10 to point 11. After passing through a suitable filter and the pipes and reaching the spray pipes at point 12, the solution is sprayed downwards. The liquid desiccant moves down through the channels by gravity and then, by contacting the processed air, which is moved from downwards to upwards, the heat and mass transfer occurs. Now, the solution reaches point 13 and returns to the liquid desiccant bed. It is worth mentioning that during the dehumidification process, cold water flowed in the direction of the aluminium heat exchanger and thin-walled plastic tubes for precooling. Also, during the regeneration process, hot water flowed in the path of the aluminium heat exchanger and thin-walled plastic tubes for preheating. In the design of the experimental setup, there was one enthalpy exchanger. As a result, the dehumidification and regeneration processes were performed in two separate durations. The experiments were designed as follows:

1. Dehumidification process (precooled air and liquid desiccant simultaneously).
2. Regeneration process (preheated air and liquid desiccant simultaneously).

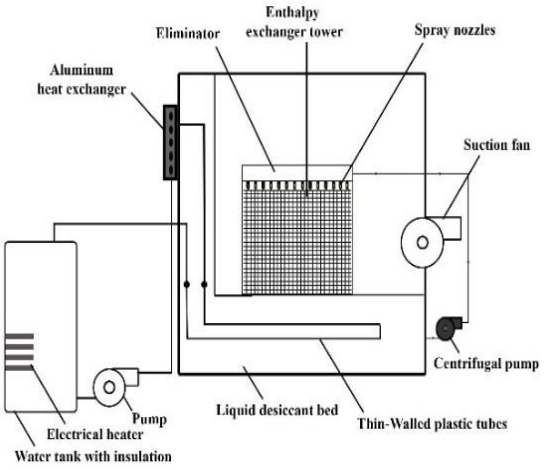

Figure 3. A schematic of the Liquid Desiccant Air Conditioner System consisting Absorbent Tower, Suction Fan, and Water tank

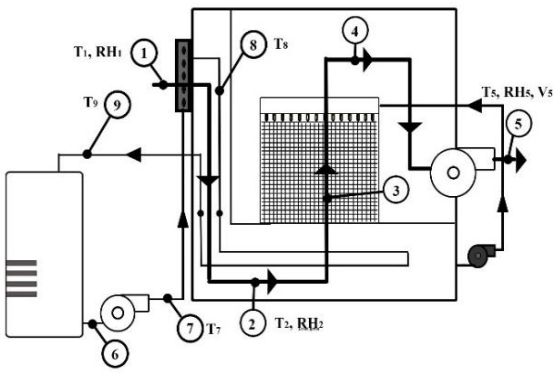

Figure 4. The direction of airflow, water flow and position of measuring instruments on the LDAC system

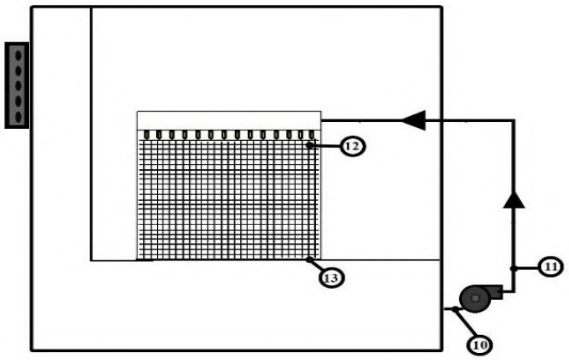

Figure 5. The direction of LiCl flow on the LDAC system

3. MEASUREMENT INSTRUMENTS

In this experiment, there were thermometer, thermocouples with data logger, air humidity meter, airflow velocity meter, and conductivity meter to measure the variation of temperature, relative humidity, airflow velocity and solution concentration, respectively. The position of measurement devices is shown in Figure 4. In addition, the solution concentration was measured before and after each process. The inaccuracy analysis of these measurement instruments is listed in Table 1, in which the expanded uncertainties have a confidence level of 95%.

4. EXPERIMENTAL RESULTS AND DISCUSSION

4. 1. Dehumidification Process In the dehumidification process, air and liquid desiccant were precooled simultaneously. During the process, $\dot{V}_5$ was 12.1 m/s. According to Figure 6, it is observed that T_7 was about 11.8 °C during the process. Due to the heat transfer from the inlet air to the cooling water inside the aluminium heat exchanger, the water temperature increases, and T_8 reaches the average of 17.6 °C. Then, the water passed through the liquid desiccant bed, and the water temperature increased, and the mean of T_9 reached about 17.9 °C. The dehumidification process was an exothermic reaction; T_5 was higher than T_2 and reached an average temperature of 27°C, which was approximately 14.64% on average higher than T_2. T_1 was almost 30.2°C during the process, but T_2 and T_5 were decreased by about 29% and 21.1% during the dehumidification process.

The RH_1 decreased slightly from 58.9% to 56.5% during the process. Then, as the air passes through the cold heat exchanger, the air relative humidity increased, which RH_2 was an average of about 66.7%. Then, by passing air through the enthalpy exchanger and exchanging the moisture content with the solution, its relative humidity was reduced, which RH_5 was an average of 56%.

TABLE 1. The specification of measurement devices

Type	Accuracy	Expanded Uncertainty
1-Digital air thermometer model IDR-RH101.	± 0.1 ºC	2.003ºC
2-K type thermocouple with Lutron data logger	± 0.1 ºC	2.003ºC
3-Digital air humidity meter model IDR-RH101.	± 0.1 %	2 %
4-Digital airflow velocity meter Omega HHF11A.	± 0.1 m/s	2.003 m/s
5-Conductivity meter for measuring the liquid desiccant concentration Orion Research Model 101.	± 0.1 ms/cm [msimense/cm].	1.006 ms/cm

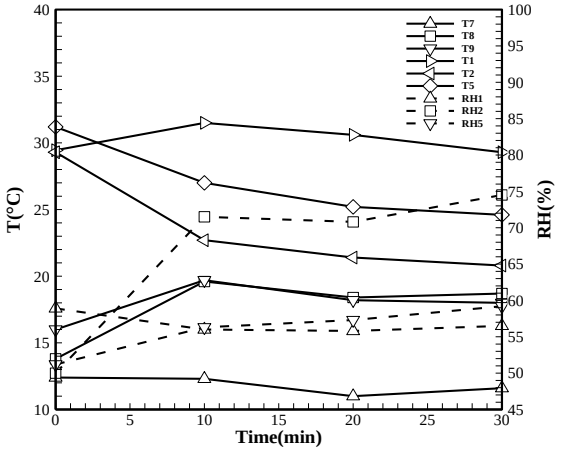

Figure 6. Temperature and relative humidity versus time in the dehumidification process

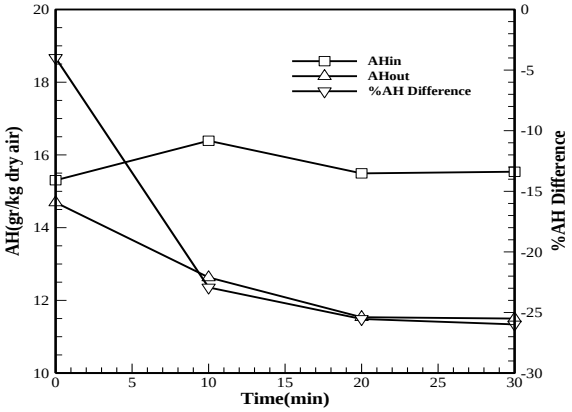

Figure 7. Absolute humidity versus time in the dehumidification process

Based on the psychometric chart, the air absolute humidity (or moisture content) was obtained. Figure 7 displays the moisture content of the inlet air and the exhaust air and the percentage of their difference. AH_5 was less than AH_1, and their difference was decreased from -3.9% to -25.9% during the dehumidification process. Therefore, the moisture content was reduced during the process, and the solution absorbed the moisture content of the inlet air. It is observed that the absolute humidity of the exhaust air has a higher rate at the beginning, and by the time and passing through the transition mode, it tends towards a certain amount equal to 11 g/kg of dry air. This is the same for the percentage difference between the absolute humidity of the inlet and exhaust air, and its value tends to be about -26% after about 30 minutes.

4. 2. Regeneration Process In the regeneration process, air and liquid desiccant were preheated simultaneously. $\dot{V}_5$ was on about 10.73 m/s during the process. Figure 8 depicts that T_7 was from 41.7 °C to 50.9 °C during the process. Due to the heat transfer from the hot water inside the aluminium heat exchanger to the inlet air, the temperature decreased, and T_8 reached the average of 44.1 °C. Then, by heat transferring of water with liquid desiccant after passing through thin-walled plastic tubes, the water temperature decreased, and the mean of T_9 reached about 41.6 °C. After heat exchanging with the inlet air and then with the solution, the hot water temperature dropped by about 9.42%. The inlet air passed through the aluminium heat exchanger, and the air temperature risen by about 5 °C on average. Since the regeneration process was endothermic, the T_5 was 1.4 °C lower than T_2 on average. In addition, T_1 was almost about 32.4 °C, but T_2 and T_5 increased by approximately 16.27 and 12.97% during the regeneration process.

RH_1 was almost about 55.8% during the process. Then, as the air passes through the warm heat exchanger, relative humidity decreased, which RH_2 was an average of 43.3%. Then, after exchanging the moisture content in the enthalpy exchanger, air relative humidity was increased, which RH_5 was a mean of 49.6%.

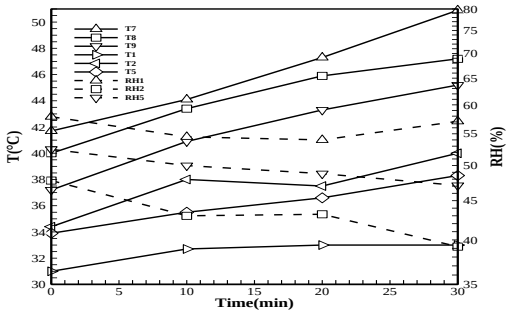

Figure 8. Temperature and relative humidity versus time in the regeneration process

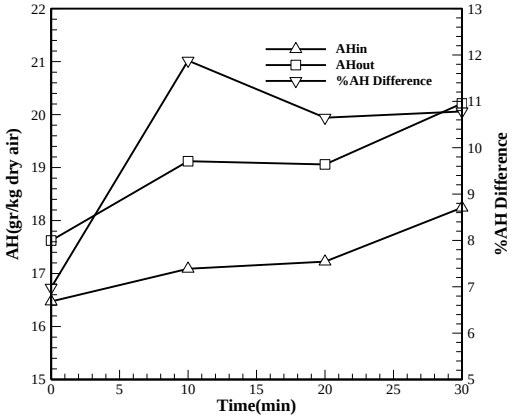

Figure 9. Absolute humidity versus time in the regeneration process

Figure 9 depicts the moisture content of the inlet air, and the exhaust air and the percentage of their difference. AH_1 was less than AH_5 and the percentage difference was increased from 6.9 to 10.7% during the regeneration process. Therefore, the moisture content was enhanced during the process, and the solution was regenerated. It is indicated that by the time and passing through the transition mode, the percentage difference between the absolute humidity of the inlet and exhaust air tends to be about 11%.

4. 3. System Transient.Behavior The PSO algorithm was used to fit a simulation curve to the dehumidification and regeneration rates and identify the transient behavior of the system [17, 18]. Research on various issues has been done utilizing this optimization algorithm [19, 20]. The fundamental of this algorithm is information sharing which is particle experiences. In the PSO algorithm, there are plenty of hypothetical particles that are distributed in the search domain, and they follow personal experiences and global experiences. There are two essential equations in the PSO algorithm as follows [21]:

$$x_{t+1}^{\ i} = x_t^{\ i} + v_{t+1}^{\ i} \quad (1)$$

$$v_{t+1}^{\ i} = w^{\ i} \times v_t^{\ i} + c_1 \times r_1 \times \left(p_t^{\ i} - x_t^{\ i}\right) + c_2 \times r_2 \times \left(p_t^{\ g} - x_t^{\ i}\right) \quad (2)$$

x, v, w, c_1, c_2, r_1, r_2, and p^g are position, velocity, weight coefficient, the first coefficient, second coefficient, the first random number, the second random number and the best global position, respectively. In Equation (2), the next direction of the i_{th} particle is determined according to the past direction, the best personal record and the best global record. In addition, the target was to reduce the difference between experimental data and fitted curve data in the cost function of this algorithm. An exponential

power series was used as an equation with fitting parameters as follows:

According to Equation (3), there are eight fitting parameters (a_1-a_8). The value of each fitting parameters is listed in Table 2. The air dehumidification rate and solution regeneration rate are shown in Figures 9. The rate of both processes was related to the time (t), and the results indicate that curve fitting had a good agreement with the experimental data and 10. For 1000 iterations and 300 populations, the average error of the fitted curve was 10.43 and 1.52% for regeneration rate and dehumidification rate, respectively.

According to Figure 10, the dehumidification rate curve had a downward trend. It tended to a particular value over time, which indicates that the device reached a steady state after approximately 10 minutes. The average dehumidification rate was equal to -14.76 kg/h. Also, Figure 11 shows that the regeneration rate curve had an upward trend, and it tended to a certain value over time, which indicates that the device reached near to steady-state after approximately 10 minutes. The average regeneration rate was equal to 7.18 kg/h.

$$\dot{m}_{water}(t) = a_1 \times \exp(a_2 \times t) + a_3 \times \exp(a_4 \times t) + a_5 \times \exp(a_6 \times t) + a_7 \times \exp(a_8 \times t) \quad (3)$$

TABLE 2. Variable coefficient of the fitted equation

Coeff	a_1	a_2	a_3	a_4	a_5	a_6	a_7	a_8
Deh. rate	22.821	19.163	41.628	0.282	-47. 752	0.734	-19. 578	0
Reg. rate	-12. 281	0.381	-1. 273	0.573	8.210	0.001	7.5452	0.578

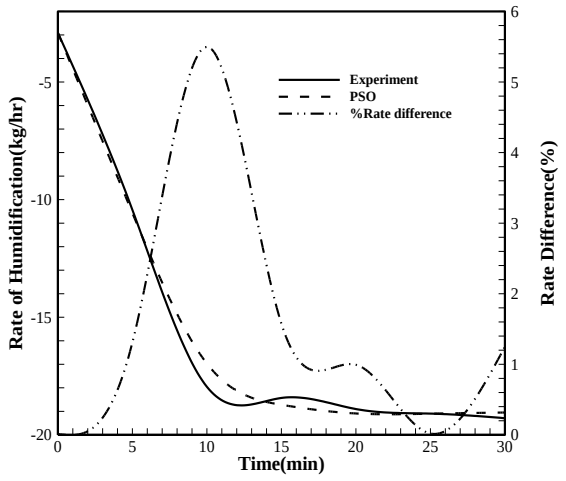

Figure 10. Curve fitting of the water flow rate of dehumidification with PSO

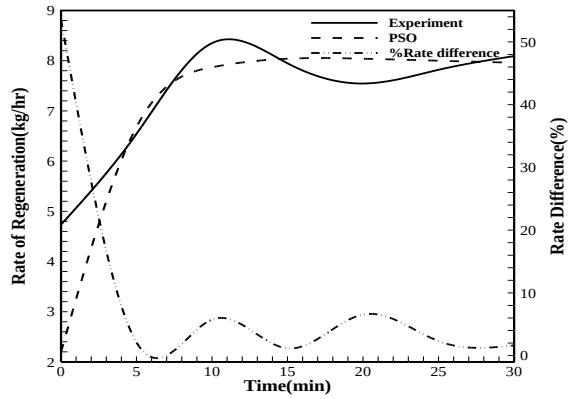

Figure 11. Curve fitting of the water flow rate of regeneration with PSO

5. COMPARISON WITH PREVIOUS STUDY

In the research conducted by Qiu et al.[10], relative humidity reduction during dehumidification process reached approximately 10% after 30 minutes. In this study, this amout is around 5% and one of the reason for it is high ambient relative humidity level in the experiment of Qiu et al.[10]. According to figures 7 and 9, the exhaust air moisture content reduced during the dehumidification process on average of 18.21%. But, about 9.78% on average was added to the exhaust air moisture content in the regeneration process. In the previous system[15], where the enthalpy exchanger and the eliminator were both wicked, the regeneration and dehumidification processes variation were on average of 34.07 and 8.29%, respectively. Also, in the case study where the enthalpy exchanger and the eliminator were both wicked, as well as the centrifugal pumps switcher was at the optimal frequency, the regeneration and dehumidification processes variation were on average of 20.54 and 7.25%, respectively.

6. CONCLUSION

In this study, a novel configuration of an LDAC with LiCl liquid desiccant was experimentally investigated. According to this configuration, inlet air and liquid desiccant was precooled during the dehumidification process and inlet air and liquid desiccant was preheated during the regeneration process, simultaneously. Additionally, PSO algorithm was utilizied to estimate transient behavior of the system in the dehumidification and regeneration processes. The following results are concluded:

- In the exothermic reaction between processed-air and LiCl during the dehumidification process, exhaust air temperature was approximately 14.64% on average higher than processed-air temperature and it was decreased by about 21.1% during this process. In addition, the ambient air moisture content was reduced around 20% during the process, and the solution absorbed the moisture content of the inlet air.
- In the endothermic reaction between processed-air and LiCl during the regeneration process, exhaust air temperature was approximately 1.4 °C on average lower than processed-air temperature and it was increased by about 12.97% during this process. Furthermore, the ambient air moisture content was enhanced around 14.28% during the process, and the solution was regenerated.
- The exhaust air moisture content variation in dehumidification and regeneration processes was -18.21 and 9.78%, respectively.
- It was observed that the dehumidification and regeneration rates were equal to -14.76 kg/h and 7.18 kg/h on average, respectively.
- The PSO algorithm was used to fit a curve on the dehumidification and regeneration rate curves, which had a good agreement with experimental data and the average error of the fitted curve was 10.43 and 1.52% for regeneration rate and dehumidification rate, respectively.
- It is observed that this moisture content in the dehumidification process was improved by at least 9.92% than the previous study. However, the previous system performed at least about 10.76% better than this system in the regeneration process, which had three electrical heaters to warm the inlet air.

In future study, solar collectors and photovoltaic panels can improve the efficiency of the experimental setup and minimize the dependence on the grid power.

7. REFERENCES

1. Lowenstein, A.J.H. and Research, R., "Review of liquid desiccant technology for hvac applications", ***HVAC&R Research*** Vol. 14, No. 6, (2008), 819-839, doi: 10.1080/10789669.2008.10391042
2. Sahlot, M. and Riffat, S.B.J.I.J.o.L.-C.T., "Desiccant cooling systems: A review", ***International Journal of Low-Carbon Technologies*** Vol. 11, No. 4, (2016), 489-505, doi: 10.1093/ijlct/ctv032
3. Rafique, M.M., Gandhidasan, P., Bahaidarah, H.M.J.R. and Reviews, S.E., "Liquid desiccant materials and dehumidifiers–a review", ***Renewable and Sustainable Energy Reviews,*** Vol. 56, No., (2016), 179-195, doi: 10.1016/j.rser.2015.11.061
4. Baniyounes, A.M., Ghadi, Y.Y., Rasul, M., Khan, M.M.K.J.R. and Reviews, S.E., "An overview of solar assisted air conditioning in queensland's subtropical regions, australia", ***Renewable and Sustainable Energy Reviews*** Vol. 26, (2013), 781-804, doi: 10.1016/j.rser.2013.05.053
5. Verma, A., Kaushik, S., Tyagi, S.J.H. and Journal, I., "Thermodynamic analysis of a combined single effect vapour absorption system and tc-co2 compression refrigeration system", ***HighTech Innovation Journal,*** Vol. 2, No. 2, (2021), 87-98, doi: 10.28991/HIJ-2021-02-02-02
6. Assari, M.R., Mirzavand, R., Tabrizi, H.B. and Gholi Beik, A.J., "Effect of steps height and glass cover angle on heat transfer performance for solar distillation: Numerical study", ***International Journal of Engineering, Transactions A,: Basics***, Vol. 35, No. 1, (2022), doi: 10.5829/ije.2022.35.01a.23
7. Ha, K.J.H. and Journal, I., "Innovative blade trailing edge flap design concept using flexible torsion bar and worm drive", ***HighTech Innovation Journal,*** Vol. 1, No. 3, (2020), 101-106, doi: 10.28991/HIJ-2020-01-03-01
8. Alizadeh, S. and Saman, W.J.S.E., "Modeling and performance of a forced flow solar collector/regenerator using liquid desiccant", ***Sol. Energy*** Vol. 72, No. 2, (2002), 143-154, doi: 10.1016/S0038-092X(01)00087-1
9. Alizadeh, S. and Saman, W.Y.J.S.e., "An experimental study of a forced flow solar collector/regenerator using liquid desiccant", ***Solar Energy*** Vol. 73, No. 5, (2002), 345-362, doi: 10.1016/S0038-092X(02)00116-0
10. Qiu, G., Liu, H. and Riffat, S.B.J.I.J.o.L.-C.T., "Experimental investigation of a liquid desiccant cooling system driven by flue gas waste heat of a biomass boiler", ***International Journal of Low-Carbon Technologies,*** Vol. 8, No. 3, (2013), 165-172, doi: 10.1093/ijlct/cts003
11. Turgut, O.E., Çoban, M.T.J.H. and Transfer, M., "Experimental and numerical investigation on the performance of an internally cooled dehumidifier", ***Heat Mass Transfer*** Vol. 52, No. 12, (2016), 2707-2722, doi: 10.1007/s00231-016-1782-9
12. Mohamed, A., Ahmed, M., Hassan, A. and Hassan, M.S.J.C.S.i.T.E., "Performance evaluation of gauze packing for liquid desiccant dehumidification system", ***Case Studies in Thermal Engineering*** Vol. 8, (2016), 260-276, doi: 10.1016/j.csite.2016.08.005
13. Peng, D.-g., Li, S.-y., Luo, D.-t., Fu, Y.-t., Cheng, X.-s. and Liu, Y.J.J.o.Z.U.-S.A., "Efficiency comparison and performance analysis of internally-cooled liquid desiccant dehumidifiers using licl and $CaCl_2$ aqueous solutions", ***Journal of Zhejiang University-Science A*** Vol. 21, No. 1, (2020), 44-63, doi: 10.1631/jzus.A1900241
14. Lu, J., Wang, M., Li, Y. and Yang, L.J.P.E., "Numerical study on dehumidification performance of a cross-flow liquid desiccant air dehumidifier", ***Procedia Engineering*** Vol. 205, (2017), 3630-3637, doi: 10.1016/j.proeng.2017.10.221
15. Moazemi Goudarzi, A., Alizadeh, S., Ramezanzadeh, H.J.J.o.R.E. and Environment, "Experimental investigation of a new enthalpy exchanger with low absorbent carryover designed for liquid desiccant dehumidification system", ***Journal of Renewable Energy and Environment*** Vol. 4, No. 4, (2017), 22-30, doi: 10.30501/JREE.2017.88329
16. Hassan, F.A.J.J.o.H., Earth, and Future, "Multi-criteria approach and wind farm site selection analysis for improving power efficiency", ***Journal of Human, Earth, Future*** Vol. 1, No. 2, (2020), 60-70, doi: 10. 28991/HEF-2020-01-02-02
17. Sadeghi, S.M.M., Hoseini, S., Fathi, A. and Daniali, H.M.J.I.J.o.E., "Experimental hysteresis identification and micro-position control of a shape-memory-alloy rod actuator", ***International Journal of Engineering, Transactions A,: Basics*** Vol. 32, No. 1, (2019), 71-77, doi: 10.5829/ije.2019.32.01a.09
18. Bagheri, A., Sadafi, M. and Safikhani, H.J.I.J.o.E., "Multi-objective optimization of solar thermal energy storage using hybrid of particle swarm optimization and multiple crossover and

mutation operator", ***International Journal of Engineering, Transactions B Applications*** Vol. 24, No. 4, (2011), 367-376, doi: 10.5829/idosi.ije.2011.24.04b.07

19. Aslipour, Z. and Yazdizadeh, A.J.I.J.o.E., "Identification of wind turbine using fractional order dynamic neural network and optimization algorithm", ***International Journal of Engineering, Transactions B Applications*** Vol. 33, No. 2, (2020), 277-284, doi: 10.5829/ije.2020.33.02b.12
20. Nahvi, H. and Mohagheghian, I.A., "Particle swarm optimization algorithm for mixed variable nonlinear problems", ***International Journal of Engineering, Transactions A,: Basics***, Vol. 24, (2011), 65-78, doi:
21. Jam, S., Shahbahrami, A. and Sojoudi Ziyabari, S.J.I.J.o.E., "Parallel implementation of particle swarm optimization variants using graphics processing unit platform", ***International Journal of Engineering, Transactions A,: Basics*** Vol. 30, No. 1, (2017), 48-56, doi: 10.5829/idosi.ije.2017.30.01a.07

Persian Abstract

چکیده

مایعات خورنده مانند لیتیوم کلرید در تهویه مطبوع با خشک کن مایع استفاده می شود. خوردگی در مبدل آنتالپی یکی از مشکلات طراحی است. برخی از راه حل ها در این تحقیق مورد مطالعه قرار گرفته و بر اساس آنها ، یک سیستم آزمایشگاهی بطور تجربی بررسی شده است. در این طرح ، از مبدل آنتالپی جریان مخالف برای تبادل رطوبت بین هوا و خشک کن مایع استفاده می شود. ابتدا هوای ورودی توسط مبدل حرارتی آلومینیومی از قبل گرم یا از قبل سرد می شود. سپس، خشک کن مایع توسط لوله های پلاستیکی دیواره نازک از قبل گرم یا سرد می شود. با تماس این مایع خشک کن و هوا ، تبادل گرما و جرم اتفاق می افتد. تغییرات محتوای رطوبت هوا در شرایط آزمایشگاهی بررسی شده و میزان احیا و رطوبت زدایی مورد مطالعه قرار می گیرد. نتایج حاکی از آن است که به طور کلی میزان رطوبت هوای محیط در طی فرآیند رطوبت زدایی، حدود ۲۰ درصد کاهش و در طول فرآیند احیا، حدود ۱٤/۲۸ درصد افزایش یافت. علاوه بر این، تغییرات محتوای رطوبت در فرآیند رطوبت‌زدایی حداقل ۹/۹۲ درصد بهبود یافت، اما فرآیند احیا حداقل ۱۰/۷٦ درصد نسبت به مطالعه قبلی کاهش یافت. همچنین، استفاده از الگوریتم بهینه سازی ازدحام ذرات برای شناسایی رفتار گذرا سیستم و به دست آوردن پارامترهای برازش منحنی، شباهت زیادی با داده های تجربی میزان رطوبت زدایی و احیا دارد و میانگین خطای برازش منحنی به ترتیب ۱۰/٤۳ درصد و ۱/۵۲ درصد برای دو فرآیند شده است.

IJE TRANSACTIONS B: Applications Vol. 35, No. 02, (February 2022) 433-450

International Journal of Engineering

Journal Homepage: www.ije.ir

An Efficient Task Scheduling Based on Seagull Optimization Algorithm for Heterogeneous Cloud Computing Platforms

R. Ghafari, N. Mansouri*

Department of Computer Science, Shahid Bahonar University of Kerman, Kerman, Iran

P A P E R I N F O

Paper history:
Received 18 August 2021
Received in revised form 19 November 2021
Accepted 29 November 2021

Keywords:
Cloud Computing
Task Scheduling
Meta-heuristic
Seagull Optimization

A B S T R A C T

Cloud computing provides computing resources like software and hardware as a service by the network for several users. Task scheduling is one of the main problems to attain cost-effective execution. The main purpose of task scheduling is to allocate tasks to resources so that it can optimize one or more criteria. Since the problem of task scheduling is one of the Nondeterministic Polynomial-time (NP)-hard problems, meta-heuristic algorithms have been widely employed for solving task scheduling problems. One of the new bio-inspired meta-algorithms is Seagull Optimization Algorithm (SOA). In this paper, we proposed an energy-aware and cost-efficient SOA-based Task Scheduling (SOATS) algorithm. The aims of proposed algorithm to make a trade-off between five objectives (i.e., energy consumption, makespan, cost, waiting time, and load balancing) using a fewer number of iterations. The experiment results by comparing with several meta-heuristic algorithms (i.e., Genetic Algorithm (GA), Particle Swarm Optimization (PSO), Ant Colony Optimization (ACO), and Whale Optimization Algorithm (WOA)) prove that the proposed technique performs better in solving task scheduling problem. Moreover, we compared the proposed algorithm with well-known scheduling methods: Cost-based Job Scheduling (CJS), Moth Search Algorithm based Differential Evolution (MSDE), and Fuzzy-GA (FUGE). In the heavily loaded environment, the SOATS algorithm improved energy consumption and cost saving by 10 and 25%, respectively.

***doi**: 10.5829/ije.2022.35.02b.20*

1. INTRODUCTION

In the era of technology, cloud computing is developing as a technology that dynamically provides the infrastructure to end users [1]. One of the most extensive areas of research in cloud computing is task scheduling. The main challenge in task scheduling is finding the optimal resource for input tasks. In single task scheduling, solely one parameter is taken into account, while in multi-objective task scheduling, two or more criteria are taken into account as one objective [2]. Researchers have used various kinds of task scheduling strategies. However, meta-heuristic scheduling has better results than traditional heuristic scheduling. Most existing task scheduling algorithms are more concerned with achieving better task execution time. In the cloud environment, not only we should consider the completion time, but also pay attention to the other Quality of Service (QoS) factors (e.g., costs and energy consumption). Among the existing meta-heuristic algorithms, Seagull Optimization Algorithm (SOA) [3] is one of the meta-heuristic algorithms used to solve optimization problems. In this paper, we present a task scheduling algorithm based on SOA, which takes into account several important parameters, namely energy consumption, cost, waiting time, load balancing, and makespan at the same time.

1. 1. Cloud Computing Cloud computing is known as a popular paradigm of business computing. Cloud computing can suggest to users the different computing services such as applications, servers, storage, and networks using the Virtual Machine (VM) over the internet [4]. Cloud computing can speed up the prediction process by utilization of high-speed computing. In the case of the COVID-19 epidemic, a prediction scheme

*Corresponding Author Insitiutional Email: n.mansouri@uk.ac.ir
(N. Mansouri)

Please cite this article as: R. Ghafari and N. Mansouri, An Efficient Task Scheduling Based on Seagull Optimization Algorithm for Heterogeneous Cloud Computing Platforms, ***International Journal of Engineering, Transactions B: Applications***, Vol. 35, No. 2, (2021) 433-450

based on the machine learning model could be used in remote cloud nodes for real-time prediction permitting governments and citizens to reply proactively [5].

As shown in Figure 1, cloud computing has five basic characteristics: on-demand self-service, resource pooling, rapid elasticity, broad network access, and measured services. The cloud has three service models: Software as a Service (SaaS) is cloud-based construction software that can be purchased for use on a pay-as-you-go basis; therefore, decreasing the cost of ownership, Infrastructure as a Service (IaaS) which presents infrastructure services such as storage systems, and computing resources, and Platform as a Service (PaaS) which can be procured to integrate databases from various project data generated by the various professionals on-site and those in the back office. Cloud services can be deployed as a private service, a public service, a community service, or a hybrid service depending on the access method as well as the classification of eligible users to access the service.

Cloud service providers sell resources to users as virtual resources. Users use these resources and execute tasks. Task scheduling is one of the most important applications used by end-users and cloud service providers [7]. One of the most challenging problems in task scheduling is finding the optimal resource for input tasks [8].

1. 2. Task Scheduling The problem of task planning is to schedule a set of specific tasks in a specific set of resources in the form of VMs that have limitations for optimizing some objective functions [9]. Figure 2 shows a model of task scheduling in the cloud environment. The Datacenter Broker (DB) is responsible for identifying and collecting all information about available resources (VMs) and any residual resource that may be available in the future, which collects this information with the aid of the Cloud Information Services (CIS). The interface between the host operating system and the VMs is a hypervisor. Tasks are sent to the task queue to be scheduled for VMs according to the scheduling algorithm defined in the DB.

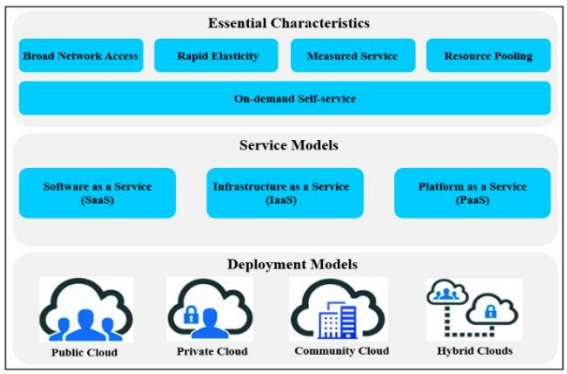

Figure 1. Cloud computing definition [6]

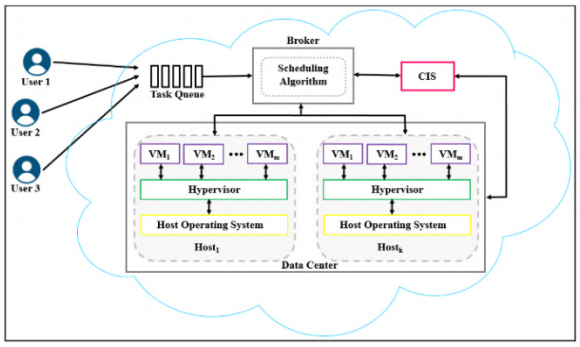

Figure 2. Task scheduling model in the cloud [10]

Task scheduling is an NP-hard optimization problem because the number of tasks increases and the length of the task varies rapidly [11]. In cloud computing, task scheduling efficiency is measured by different system performance criteria. In general, these cloud-based optimization metrics can be categorized into the goals of cloud users and the goals of cloud service providers. On the one hand, some metrics such as makespan and waiting time are user metrics. On the other hand, metrics such as the cost of the provider and energy consumption are the metrics of the provider [12, 13]. The popularity of cloud computing is growing day by day, so with an increasing demand for high-performance computing resources, energy consumption in the cloud data center is greatly increased [14]. Energy consumed by computing resources and connected cooling facilities is the main component of energy costs and high carbon emissions. According to research conducted by Uchechukwu and Shen [15], it is estimated that energy consumption by data centers around the world is about 1.4% of electricity consumption worldwide and is growing at a rate of 12% annually. The energy consumption of processing units is approximately 42%, cooling facilities about 15.4%, and storage facilities nearly 14.3% [16]. As a result, one of the main concerns in cloud computing is how to decrease energy consumption and related costs while keeping execution performance. Minimizing energy consumption improves overall efficiency and also increases system reliability and availability [17]. In other words, minimizing energy consumption while ensuring the user's QoS preferences is critical to achieving maximu m profit for service providers and ensuring the user's service level agreement (SLA). Moreover, minimizing energy consumption decreases energy costs as well as aiding to protect our natural environment because it decreases carbon emissions [18]. In addition to energy consumption, the cost of a cloud provider can be reduced by assigning the task to a suitable VM that executes the task at minimal cost and without violating QoS restrictions [19], which have not been addressed in most papers. Thus, efficient resource management is the key to balancing performance and cloud costs while keeping

service availability. We need a suitable task scheduling algorithm to find a trade-off between user goals (such as reducing makespan) and service provider goals (such as reducing energy consumption and cost). To solve such a problem, a large number of researchers focused their research work on heuristic, meta-heuristic, and hybrid scheduling algorithms [20, 21]. Currently, swarm intelligence algorithms are widely used to solve these types of problems.

1. 3. Meta-heuristic Algorithm The task scheduling problem in cloud computing is known as an NP-hard problem because of the large space of solutions. Therefore, we need a long time to discover an optimal solution [22]. It is possible to reach a near-optimal solution in a short time for such problems by using meta-heuristic strategies [23]. One of the advantages of meta-heuristic algorithms is that they are problem-independent and have a good approach to solve problems in different domains [24]. There are a variety of meta-heuristic algorithms. As shown in Figure 3, the bio-inspired meta-heuristic algorithms can generally be divided into three main categories [25]: evolution-based methods (are inspired by the laws of natural evolution), swarm-based methods (imitate the social behavior of groups of animals), and bacterial foraging methods (inherit the characteristics of bacterial foraging patterns).

Swarm intelligence is one of the attractive branches of population-based meta-heuristic algorithms. Concepts of swarm intelligence were first introduced in 1993 [26]. Swarm intelligence strategies mimic the social behaviors of organisms living in colonies, flocks, or herds [27]. Among the most popular swarm intelligence strategies are Particle Swarm Optimization (PSO) [28] and Ant Colony Optimization (ACO) [29]. One of the meta-heuristic algorithms that have been introduced in recent years is the SOA [3] to solve expensive computational problems. The principal inspiration of the SOA is the migration and attacking behavior of seagulls in nature.

The SOA starts by generating a random initial population. Search agents update their positions according to the best search agent during different iterations. Seagulls explore various promising areas of the search space. At the beginning of the optimization process, the search agents vary quickly. The experimental results are obtained by comparing SOA with other popular meta-heuristic algorithms (e.g., Spotted Hyena Optimizer (SHO), Grey Wolf Optimizer (GWO), Particle Swarm Optimization (PSO), Moth-Flame Optimization (MFO), Multi-Verse Optimizer (MVO), Sine Cosine Algorithm (SCA), Gravitational Search Algorithm (GSA), Genetic Algorithm (GA), and Differential Evolution (DE)) showed that SOA represents three various convergence behaviors while optimizing test functions [3]. In the early stages of iterations, SOA converges more quickly to the promising areas due to its adaptive mechanism. Also, SOA performs better in terms of average running time compared to other meta-algorithms. This is because SOA does not require crossover and mutation operators. As a result, SOA's computational efficiency is much better than other methods.

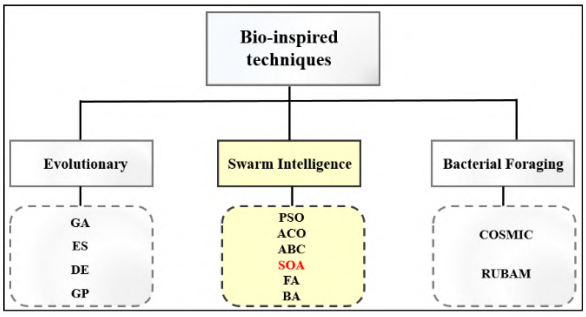

Figure 3. Taxonomy of bio-inspired techniques [25]

The main contributions are shown as follows:

1) The multi-objective optimized task scheduling algorithm is proposed considering multiple factors (i.e., energy consumption, makespan, cost, waiting time, and load balancing).
2) The Dynamic Voltage Frequency Scale (DVFS) model is included in the optimization method to reduce energy consumption.
3) The SOA is considered a global optimizer because it has good exploration and exploitation capability.
4) To show the applicability of the proposed algorithm in different scenarios, extensive experiments have been performed.

The rest of the paper is arranged as follows: Section 2 discusses the related papers which deal with existing strategies for scheduling in the cloud. Section 3 describes the SOA. Section 4 introduces the proposed algorithm. Section 5 deals with performance evaluation and experimental results. Section 6 contains the conclusion and future works.

2. RELATED WORKS

Task scheduling techniques that can effectively assign tasks to resources are still one of the challenges in the cloud environment. This is because requirements such as storage, response time, bandwidth, and resource cost may be different for each task, which greatly complicates the optimization problem, and also the heterogeneity and dynamics of the cloud environment make the issue more complex. Various techniques have been proposed to make good use of cloud resources.

Sreenu and Sreelatha [30] introduced a task scheduling algorithm for assigning tasks to suitable VMs in the cloud based on a multi-objective model and a Whale Optimization Algorithm (WOA) [31] and named

it W-Scheduler. To calculate the fitness value, the authors first obtained the fitness value by calculating the cost function of CPU and memory, and then makespan, as well as the budget cost function, are added to calculate the fitness value. They used the WOA to optimally assign tasks to VMs. The WOA for finding the optimal solution supposes that the current solution is the best and tries to find the best optimal solution based on the best search agent. Experimental results showed that W-Scheduler can optimize task scheduling and perform better in terms of makespan and average cost compared to PBACO [32], SLPSO-SA [33], and SPSO-SA [33]. Nevertheless, energy consumption is not considered.

Sreenivasulu and Paramasivam [34] presented a hybrid algorithm to efficiently assign tasks to VMs. The proposed algorithm first uses a hierarchical process to prioritize tasks. Then, it applies the Bandwidth-aware divisible task (BAT) model [35] and BAR model [36] to consider task properties and VM attributes for task scheduling. The authors used the minimum overload and minimum lease policy to apply pre-emption in the data center and decrease the overload of the VMs. The experimental results showed that the proposed algorithm has better performance in terms of resource utilization, bandwidth utilization, and memory utilization compared to other algorithms. The main weakness of the presented algorithm is that it does not take into account key QoS parameters such as cost and energy consumption.

Mansouri and Javidi [37] suggested a new job scheduling based on the cost and called it CJS. The proposed algorithm, in addition to simultaneously using the data-intensive and computation-intensive of the job, also takes into account the similar factors of the available distributed environment. To assign jobs, CJS considers processing power, data, and network features. The proposed algorithm calculates three important costs, namely network cost, computation cost, and data transfer cost. The results of simulations using CloudSim [38] showed that CJS performs better in terms of makespan and resource utilization compared to FUGE [39], Berger [40], MQS [41], and HPSO [42] algorithms. However, the CJS algorithm does not consider energy consumption.

Kumar and Kalra [43] suggested a hybrid task scheduling algorithm that combines Genetic Algorithm (GA) [44] and Artificial Bee Colony (ABC) [45] algorithms. GA is a bio-inspired algorithm and consists of two distinct operations (i.e., crossover and mutation). The goal of the proposed algorithm is to decrease makespan and energy consumption. The authors used the DVFS [46] power model to compute the total energy consumed by resources. The experimental results demonstrated that the proposed hybrid algorithm performs better in terms of makespan and total energy consumption compared to the modified GA [47]. But, conflicting objectives such as time and cost have not been discussed.

Jacob and Pradeep [48] offered a multi-objective task scheduling algorithm based on a combination of Cuckoo Search (CS) [49] and PSO [28] algorithms and called it CPSO. The authors considered cost, makespan, and deadline violation rate as a multi-objective function, and based on the multi-objective function, they reached the near-optimal task scheduling. To evaluate CPSO's performance, the authors used the CloudSim [38] simulator. Experimental results showed that the CPSO algorithm has better performance in terms of cost, makespan, and deadline violation rate than PBACO, ACO, MIN-MIN, and FCFS. However, CPSO also has weaknesses. One of CPSO's principal weaknesses is that there is a high probability that resources will be overloaded.

Wu [50] proposed a novel task scheduling algorithm based on improved PSO. The author improved the PSO algorithm by adding iterative selection inhibition operators and used the improved PSO to assign tasks to VMs. The advantages of the improved PSO algorithm include high convergence speed that helps to reduce task scheduling time costs, keep away from falling into local optimum through effective search and proper distribution of computational resources, improved optimization capability, and consideration of usability and scalability in resource allocation. Simulation results demonstrated that the improved PSO has a better performance compared to PSO in terms of average execution time. However, the authors did not consider the cost and energy consumption during the scheduling process.

Elaziz et al. [51] suggested a task scheduling algorithm in the cloud environment based on a combination of Moth Search Algorithm (MSA) [52] and Differential Evolution (DE) [53] named it MSDE. The purpose of the MSDE algorithm is to assign tasks to VMs in a way that minimizes makespan. The authors considered the DE algorithm as a local search strategy to improve MSA exploitation capability. Experimental results demonstrated that the MSDE algorithm performs better in terms of makespan for both synthetical and real trace data than Shortest Job First (SJF), Round Robin (RR), PSO, WOA, and MSA. But, MSDE focuses only on makespan and does not consider other QoS parameters such as energy consumption or cost.

Shojafar et al. [39] introduced a hybrid job scheduling based on fuzzy theory and a GA and name it FUGE. FUGE's goal is to create the optimal load balance by considering run time and cost. The authors applied fuzzy theory to improve the standard GA to devise a fuzzy-based steady-state GA to improve standard GA performance in terms of makespan. The proposed algorithm for assigning jobs to resources takes into account VM processing speed, VM memory, VM bandwidth, and job length. The experimental results showed that the FUGE performs better in terms of execution time, execution cost, and average degree of

imbalance compared to other algorithms. Nevertheless, the proposed algorithm does not include energy consumption.

Table 1 compares the discussed scheduling algorithms. As shown in Table 1, although most algorithms take into account makespan, cost, or energy, they did not simultaneously consider energy, cost, and makespan despite their important impact in the cloud environment. Considering all these objectives at the same time is a complex issue. To solve complex optimization problems in a reasonable time, using meta-heuristic techniques to find a near-optimal solution can be effective. Meta-heuristic algorithms are non-deterministic strategies that have been proposed to significantly solve the problem of task scheduling in a polynomial time. In this paper, we present an SOA-based task scheduling algorithm that simultaneously considers five objectives: waiting time, cost, energy consumption, makespan, and load balancing.

3. SEAGULL OPTIMIZATION ALGORITHM(SOA)

The Seagull Optimization Algorithm (SOA) [3] is a new meta-heuristic optimization algorithm inspired by the natural behavior of seagulls. Several types of seagulls vary in size and length. Seagulls are omnivorous and feed insects, fish, earthworms, reptiles, and amphibians. The Seagulls, that scientific name is Laridae, are smart birds. They use breadcrumbs to absorb fish and also absorb earthworms by making the rain-like sound with their feet. Seagulls generally live in colonies. They frequently migrate from one place to another place to find plenty of food. Seagulls attack prey when they reach a new place.

TABLE 1. Comparison of task scheduling algorithms

	Year	Makespan	Monetary cost	Resource utilization	Reliability	Energy consumption	Load balancing	Technique	Disadvantage
Sreenu and Sreelatha [30]	2017	✓	✓	×	×	×	×	Using multi-objective model and WOA	- Does not include objectives such as energy consumption and guarantee QoS.
Sreenivasulu and Paramasivam [34]	2020	×	×	✓	×	×	✓	Using BAT and Bar models	- The energy efficiency of the algorithm is very low, - Does not discuss a trade-off solution between conflict QoS parameters such as time and cost.
Mansouri and Javidi [37]	2019	✓	×	×	×	×	✓	Using data, processing power, and network characteristics to assign jobs to resources	- Does not take into account significant criteria such as energy consumption. - Resources may be overloaded or underutilization.
Kumar and Kalra [43]	2019	✓	×	×	×	✓	×	Using GA and ABC along with DVFS	- Does not consider the deadline and priority constraint as well as SLA violations, - Cost, reliability, and other QoS parameters do not consider.
Jacob and Pradeep [48]	2019	✓	✓	×	×	×	×	Using CS and PSO	- Cannot distribute the load uniformly, - Does not optimize QoS parameters such as energy consumption.
Wu [50]	2018	✓	×	×	×	×	×	Using Improved PSO	- The load balance on resources is not monitored during runtime, - The proposed algorithm is a single objective and does consider other QoS parameters such as cost, energy consumption, etc.
Elaziz et al. [51]	2019	✓	×	×	×	×	×	Using a combination of MSA and DE	- Does not take into account the usage of memory, the peak of the demand, and overloads, - High-time complexity.
Shojafar et al. [39]	2014	✓	✓	×	×	×	✓	Using GA and fuzzy theory	- Does not take into account VM energy consumption, - High monitoring overhead.

The most significant thing about seagulls is their migratory and attacking behavior. Therefore, SOA focuses on these two natural behaviors and provides a mathematical model. Figure 4 shows a conceptual model of these behaviors.

Initially, seagulls perform migratory behavior (indicating the exploration ability of SOA). When migrating, members of a group of seagulls should avoid colliding with each other. To obtain this, an additional variable A is used to compute the position of the new search agent.

$$\overrightarrow{C_s} = A \times \overrightarrow{P_s}(x) \tag{1}$$

where $\overrightarrow{C_s}$ indicates the position of the search agent which does not collide with other search agents, $\overrightarrow{P_s}$ indicates the current position of the search agent, x shows the current iteration, and A represents the movement behavior of the search agent.

$$A = f_c - \left(x \times \left(f_c / Max_{iteration}\right)\right) \tag{2}$$

where f_c is presented to manage the frequency of employing variable A which is linearly decreased from the initial value of f_c to 0. After avoiding collisions among neighbors, search agents move toward the best search agent.

$$\overrightarrow{M_s} = B \times (\overrightarrow{P_{bs}}(x) - \overrightarrow{P_s}(x)) \tag{3}$$

where $\overrightarrow{M_s}$ indicates the position of the search agent $\overrightarrow{P_s}$ towards the best search agent $\overrightarrow{P_{bs}}$ (i.e., the most suitable seagull). The coefficient B is a random value that can be used to make a trade-off between exploitation and exploration. B is computed as follows:

$$B = 2 \times A^2 \times rd \tag{4}$$

where rd indicates a random number in the range [0, 1]. Since search agents move toward the most appropriate search agent, they may stay close to each other.

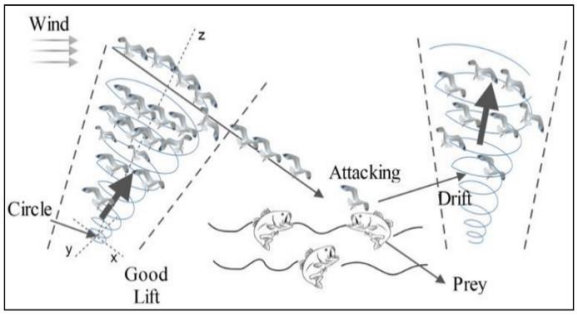

Figure 4. Migration and attacking behaviors of seagulls [3]

Therefore, search agents can update their position according to the best search agent based on the following equation:

$$\overrightarrow{D_s} = |\overrightarrow{C_s} + \overrightarrow{M_s}| \tag{5}$$

where $\overrightarrow{D_s}$ indicates the distance between the search agent and the best search agent.

Secondly, seagulls attack prey in a spiral movement after reaching a new place (indicating the exploitation ability of SOA). This behavior in x, y, and z planes is defined below:

$$x = r \times \cos(k) \tag{6}$$

$$y = r \times \sin(k) \tag{7}$$

$$z = r \times k \tag{8}$$

$$r = u \times e^{kv} \tag{9}$$

where r indicates the radius of each urn of the spiral, k represents a random number in the range $[0 \le k \le 2\pi]$. u and v are constants, and e is the base of the natural logarithm. The updated position of the search agent is computed as follows:

$$\overrightarrow{P_s}(x) = (\overrightarrow{D_s} \times x \times y \times z) + \overrightarrow{P_{bs}}(x) \tag{10}$$

Figure 5 represents the pseudocode of SOA.

4. SOA-BASED TASK SCHEDULING ALGORITHM

This section consists of three subsections. In subsection 4.1, the basic concepts related to the problem of task scheduling are explained. In subsection 4.2, the objective function and mathematical model are described. In subsection 4.3, the proposed algorithm is introduced.

4. 1. Task Scheduling Model Assigning all tasks among available VMs and discovering the optimal solution in the cloud environment is not simple work. For this reason, we need an effective task scheduling algorithm to balance the VM load and assign all user's tasks to the appropriate resources.

Suppose a cloud datacenter contains n tasks such as: $T = \{T_1, T_2, ..., T_n\}$, where T_i represents the *i-th* task in the task queue, m VMs such as: $V = \{V_1, V_2, ..., V_m\}$, where V_j represents the *j-th* VM in the cloud environment, but the condition for execution of such tasks is: $n > m$.

4. 2. Objective Functions The primary goal of the SOATS is to optimally schedule all the input tasks to the available VMs to minimize cost, makespan, load, energy

Algorithm : Seagull Optimization Algorithm

Input: Seagull population $\vec{P}_s$
Output: Optimal search agent $\vec{P}_{bs}$
procedure SOA
Initialize the parameters A, B, and $Max_{iteration}$
  Set f_c
  Set u
  Set v
  while $(x < Max_{iteration})$ **do**
    $\vec{P}_{bs} \leftarrow$ **ComputeFitness**$(\vec{P}_s)$ /* Calculate the fitness values of each search agent using **ComputeFitness** function*/
  /* Migration behavior */
    $rd \leftarrow Rand(0, 1)$ /* To generate the random number in range [0, 1] */
    $k \leftarrow Rand(0, 2\pi)$ /* To generate the random number in range $[0, 2\pi]$ */
  /* Attacking behavior */
    $r \leftarrow u \times e^{kv}$ /* To generate the spiral behavior during migration */
    Calculate the distance $\vec{D}_s$ using Eq. (5)
    $P \leftarrow x' \times y' \times z'$ /* Compute x, y, z planes using Eqs. (6) - (9) */
    $\vec{P}_s(x) \leftarrow (\vec{D}_s \times P) + \vec{P}_{bs}$
    $x \leftarrow x + 1$
  end while
return $\vec{P}_{bs}$
end procedure

procedure ComputeFitness$(\vec{P}_s)$
  for i ← 1 to n **do** /* Here, n represents the dimension of a given problem */
    $FIT_s[i] \leftarrow FitnessFunction(P_s(\vec{i}, :))$ /* Calculate the fitness of each individual */
  end for
  $FIT_{s_{best}} \leftarrow$ **BEST**$(FIT_s[])$ /* Calculate the best fitness value using **BEST** function */
return $FIT_{s_{best}}$
end procedure

procedure BEST$(FIT_s[])$
  $Best \leftarrow FIT_s[0]$
  for i ← 1 to n **do**
    if$(FIT_s[i] < Best)$ **then**
      $Best \leftarrow FIT_s[i]$
    end if
  end for
return $Best$ /* Return the best fitness value */
end procedure

Figure 5. The pseudocode of SOA [3]

consumption, and waiting time to keep both the user satisfied and the provider profit. The objective function is computed as follows. The final output of the scheduling algorithm is an $n \times m$ assignment matrix that specifies by which VM each task should be executed. We define the assignment matrix as follows:

$$X = \begin{pmatrix} x_{11} & \cdots & x_{1m} \\ \vdots & \ddots & \vdots \\ x_{n1} & \cdots & x_{nm} \end{pmatrix} \quad (11)$$

where x_{ij} is a decision variable and calculated by Equation (12):

$$x_{ij} = \begin{cases} 1 & if\ T_i\ is\ assigned\ to\ V_j \\ 0 & if\ T_i\ is\ not\ assigned\ to\ V_j \end{cases} \quad (12)$$

With the condition:

$$\sum_{j=0}^{m} x_{ij} = 1 \quad for\ 1 \le i \le n \quad (13)$$

Cost: Task scheduling in a cloud system (as a business service) in addition to being an efficient scheduler, must also decrease costs. Scheduling that decreases costs without violating QoS leads to both user and service provider satisfaction. To estimate the assignment cost, each use of resources such as processing element, memory, etc. must be computed. The following equation is used to calculate the cost of task completion [54]:

$$C_{V_j} = \sum_{j=1}^{m} sum(VM_j) \times (V_{cpu_j} + V_{ram_j} + V_{bw_j}) \quad (14)$$

where *sum(VM$_j$)* indicates the total number of tasks assigned to V_j. Equation (14) shows the processing cost in a V_j, which is closely related to CPU (V_{cpu_j}), memory (V_{ram_j}), and bandwidth performance (V_{bw_j}) of VMs.

Makespan: Makespan shows the completion time of the last task. One of the most popular scheduling criteria that researchers use to measure the performance of scheduling algorithms is makespan. This is because researchers believe that the performance of the scheduling algorithm is highly makespan-dependent. In addition, minimizing the makespan makes the user application execute faster; thus, reducing the makespan increases user satisfaction. Makespan can be described mathematically by Equation (15) [55]:

$$MS = Max\{VET_j\} \quad for\ 1 \le j \le m \tag{15}$$

where VET_j represents the *j-th* VM execution time and it is computed based on the decision variable x_{ij} by Equation (16):

$$VET_j = \sum_{i=1}^{n} x_{ij} \times ET_{ij} \quad for\ 1 \le j \le m \tag{16}$$

where ET_{ij} is the approximation calculation time for executing T_i on V_j and computed based on Equation (17):

$$ET_{ij} = \frac{TL_i}{PS_j} \tag{17}$$

where TL_i indicates the *i-th* task length in Million Instructions (MI) and PS_j indicates the *j-th* VM execution speed in Million Instructions Per Second (MIPS).

Load balancing: VMs are mostly processing elements in cloud environments. In scheduling, there is a situation where more than one task is assigned to each VM. Load balance distributes loads evenly between different cloud resources. The scheduler must be able to distribute the workload among available resources in a way that prevents resources from being overloaded or underloaded. Load balancing increases resource utilization and thus improves overall scheduling performance. The equation for calculating the degree of resource load balance in a VM is as follows [54]:

$$\varphi = \frac{\sqrt{\sum_{j=1}^{m} (VET_j - \overline{VET_j})^2}}{\frac{m}{n}} \tag{18}$$

where VET_j represents the total execution time of the V_j; $\overline{VET_j}$ represents the mean execution time of the V_j.

Energy consumption: One of the most important issues for individuals, organizations, and governments is energy consumption. There is a global concern about minimizing carbon emissions because it affects our environment in a way that endangers a healthy life and human health. CPU utilization and resource utilization directly affect the energy consumed by a task. Energy consumption will be high when CPUs are not properly utilized. This is because idle power is not effectively used. Sometimes energy consumption increases due to high requests for resources, and this may reduce efficiency. Proper scheduling algorithms are very significant to find the optimal assignment of tasks so that energy consumption is reduced. The total energy consumption of a DVFS-enable resource (DVFS lets resources operate at various voltage and frequency sets) contains static energy because of leakage current and dynamic energy because of switching activities. As shown in Equation (23), in this paper we consider only dynamic energy consumption [56]:

$$E = E_{sta} + E_{dyn} \tag{19}$$

where E_{sta} represents static energy and E_{dyn} represents dynamic energy consumption.

$$E_{dyn} = \alpha \times v_{j,s}^2 \times f_s \tag{20}$$

where α is a constant value, $v_{j,s}^2$ is V_j voltage, and f_s is the corresponding frequency of $v_{j,s}$.

$$E_{active} = \sum_{j=1}^{m} E_{dyn} \times ET_{ij} \tag{21}$$

where ET_{ij} is the execution time of the T_i executed on V_j.

$$E_{idle} = \sum_{j=1}^{m} \alpha \times v_0^2 \times f_0 \times t_{idle,j} \tag{22}$$

where α indicates a constant value, v_0 and f_0 is the resource minimum voltage and resource minimum frequency, respectively, and $t_{idle,j}$ represents the idle time of the V_j.

$$E_{total} = E_{active} + E_{idle} \tag{23}$$

Waiting time: It is the difference between the start time of execution and the submission time of the task. Reducing waiting time increases user satisfaction because the user has to wait less time. User waiting time can be defined mathematically as follows [54]:

$$WT_i = \underset{j=1}{\overset{m}{Max}} \sum_{i=1}^{sum(VM_j)} ET_{ij} \tag{24}$$

where ET_{ij} refers to the execution time T_i on V_j.

The main goal is to minimize the values of the above five functions, which is a multi-objective optimization problem; because each of the functions has various purposes that can conflict with each other. With a powerful CPU, we can increase the processing speed of a task, but the cost also increases. Also, for the situation that a VM with a large memory will be able to load a lot

of tasks, but the makespan could be long if the computing power of the CPU is low. Because the task scheduling function is not determined by a single objective function, the presented algorithm creates a task scheduling satisfaction function based on a priori preferences. Therefore, we turn the multi-objective problem of task scheduling into a single-objective problem. Assume that the cost range of task completion is $[C_{min}, C_{max}]$, the range of makespan is $[MS_{min}, MS_{max}]$, the satisfaction range of VM load balancing degree is $[\varphi_{\min}, \varphi_{\max}]$, the suitable range of energy consumption is $[E_{min}, E_{max}]$, and the range of the user's shortest waiting time is $[WT_{min}, WT_{max}]$. By introducing the minimum amount of ε [57], the five objectives are computed as follows:

$$O(C_{v_j}) = \begin{cases} 1 & C_{v_j} \le C_{\min} \\ \dfrac{C_{\max} - C_{v_j}}{C_{\max} - C_{\min}} & C_{v_j} \in (C_{\min}, C_{\max}) \\ \dfrac{\varepsilon}{C_{v_j}} & C_{v_j} \ge C_{\max} \end{cases} \quad (25)$$

$$O(MS) = \begin{cases} 1 & MS \le MS_{\min} \\ \dfrac{MS_{\max} - MS}{MS_{\max} - MS_{\min}} & MS \in (MS_{\min}, MS_{\max}) \\ \dfrac{\varepsilon}{MS} & MS \ge MS_{\max} \end{cases} \quad (26)$$

$$O(\varphi) = \begin{cases} 1 & \varphi \le \varphi_{\min} \\ \dfrac{\varphi_{\max} - \varphi}{\varphi_{\max} - \varphi_{\min}} & \varphi \in (\varphi_{\min}, \varphi_{\max}) \\ \dfrac{\varepsilon}{\varphi} & \varphi \ge \varphi_{\max} \end{cases} \quad (27)$$

$$O(E) = \begin{cases} 1 & E_{total} \le E_{\min} \\ \dfrac{E_{\max} - E_{total}}{E_{\max} - E_{\min}} & E_{total} \in (E_{\min}, E_{\max}) \\ \dfrac{\varepsilon}{E_{total}} & E_{total} \ge E_{\max} \end{cases} \quad (28)$$

$$O(WT_i) = \begin{cases} 1 & WT_i \le WT_{\min} \\ \dfrac{WT_{\max} - WT_i}{WT_{\max} - WT_{\min}} & WT_i \in (WT_{\min}, WT_{\max}) \\ \dfrac{\varepsilon}{WT_i} & WT_i \ge WT_{\max} \end{cases} \quad (29)$$

We used the geometric average method to convert five objectives into one objective. Therefore, the final optimization function which will be minimized through the proposed algorithm is as follows:

$$F_{opt} = Min\left\{\sqrt[5]{O(C_{v_j}) \times O(MS) \times O(\varphi) \times O(E) \times O(WT_i)}\right\} \quad (30)$$

4. 3. The SOATS Algorithm Based on all the above, Figure 6 represents the pseudocode of task scheduling based on SOA technique.

In addition, the flowchart of SOATS algorithm for task scheduling is shown in Figure 7. The principal steps of the SOATS algorithm can be described as follows:

Step 1) At first, initialization is performed, which usually contains mapping among cloud tasks and seagulls and initialization of seagulls positions. Also, some execution factors such as the number of search agents, the maximum number of iterations, and search space dimensions are initialized.

Step 2) The process of finding the optimal solution starts based on SOA. In this step, based on position information, the amount of cost, makespan, load, energy consumption, and waiting time are calculated according to Equations (14), (15), (18), (23), and (24), respectively. Then, according to Equation (30), the objective function value of each seagull is calculated. The position of the seagull with the smallest fitness value (i.e., fittest seagull)

Algorithm: Pseudocode for mapping of tasks onto VMs using SOA algorithm

Input: Tasks set, VMs set.
Output: Allocating tasks to VMs.
Begin
1 Initialize tasks set as: $T = \{T_1, T_2, \ldots, T_n\}$.
2 Initialize VMs set as: $V = \{V_1, V_2, \ldots, V_m\}$.
3 Initialize number of seagulls (i.e., population size), and maximum iteration.
4 Initialize SOA parameters (e.g., f_c, u, v).
5 Initialize C_{min}, C_{max}, MS_{min}, MS_{max}, E_{min}, E_{max}, WT_{min}, WT_{max}, ϕ_{min}, ϕ_{max}, and ε that represent limits of cost, makespan, energy consumption, waiting time, load balancing, and minimum value respectively.
6 Initialize seagulls' position randomly.
7 t = 1
8 **While** (t ≤ maximum iteration)
9 **For** (i =1 to number of seagulls)
10 Calculate fitness value for each seagull;
11 Find best seagull so far and set its position as P_{bs};
12 **End for**
13 Update variable A according to Equation (2);
14 **For** (i =1 to number of seagulls)
15 Perform migration according to Equation (5);
16 Perform attacking according to Equation (10);
17 **End for**
18 t++;
19 **End while**
20 Set the allocation matrix for the best seagull.

Figure 6. The pseudocode of SOATS

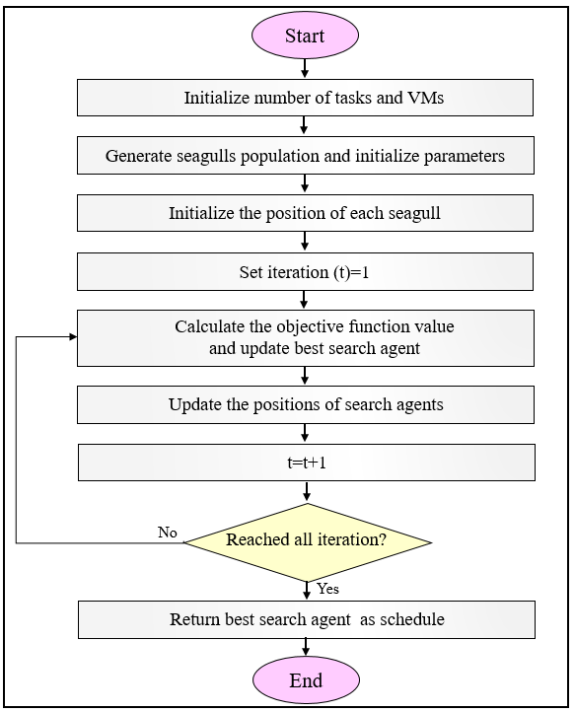

Figure 7. Flowchart of SOATS

will be recorded (which indicates the optimal solution so far).

Step 3) In this step, the positions of seagulls will be updated according to Equation (10).

Step 4) When the positions of all the seagulls are updated, an iteration is performed. If the maximum number of iterations is done, the search process is terminated and the position of the best search agent is transferred to the x_{ij} decision variables and finally returned as the best scheduling solution, otherwise, it goes to step 2 for the new search.

5. PERFORMANCE ANALYSIS

In this section, to evaluate the performance of the SOATS algorithm, we use MATLAB software that is installed on a PC with Intel(R) Core(TM) i5-7200U CPU with 2.50 GHz, and RAM of 8 GB running on 64-bit Windows 10 Pro operating system platform. The SOA-based task scheduling algorithm is compared with other well-known meta-heuristic algorithms, namely GA, PSO, ACO, and WOA for validation. In addition, we compare the performance of the SOATS algorithm in a heavily loaded environment with three scheduling algorithms, namely CJS, FUGE, and MSDE.

Table 2 shows the specific parameter settings for the comparative meta-heuristic algorithms [3, 58, 59].

Also, for each different scenario, the table of simulation parameters is presented. Most of the simulation parameters have been selected to conform to existing studies for the real representation of a typical cloud environment [60]. In addition, the parameters related to the SOA algorithm are also set [3]. According to each different scenario that is proposed, one of the parameters in each scenario is variable and the results are analyzed based on this parameter.

TABLE 2. Parameters settings of caparisoned meta-heuristic algorithms

Algorithms	Parameters	Values
GA	Crossover	0.9
	Mutation	0.05
PSO	C1	1.8
	C2	2
	Inertia factor	0.75
ACO	ρ	0.7
	P	0.3
WOA	a	[2, 0]

5. 1. Number of Tasks In this experiment, the number of tasks is changed among 100 and 500 tasks with a step of 100. The parameters of the cloud system and the SOA are described in Table 3.

In many works, makespan is used as one of the most popular performance criteria. Reducing the makespan value demonstrates the ability of scheduling to effectively choose resources for the appropriate allocation of tasks. Figure ۸ shows a graphical comparison of the makespan between SOATS and the task scheduling based on GA, PSO, ACO, and WOA using various numbers of tasks. Makespan is drawn on the vertical axis and the number of tasks on the horizontal

TABLE 3. Parameters setting (different number of tasks)

Parameters	Values
Number of tasks	100-500
Tasks size (MI)	100-2000
Number of VMs	40
VMs execution speed (MIPS)	500-4500
Storage cost	$0.1 per GB
Processing cost	$1 per 10^6 MI
Data transfer cost	$0.05 per GB
Maximum iteration	100
Population size	50
F_c	1
Constant u and v	1

axis. According to the results, it is clear that SOATS has a better makespan compared to other algorithms by increasing the number of tasks. The makespan minimization by SOA is 5-10% less than that of PSO for 100 through 500 number of tasks, respectively. This is because the SOA has good exploration and exploitation ability because variable *B* in the SOA is responsible for the smooth transfer between exploration and exploitation.

As shown in Figure 9, the proposed SOA-based task scheduling algorithm has obvious benefits in obtaining load balancing compared to other meta-heuristic algorithms. Load balancing must be done in such a way that all VMs must be balanced to achieve optimal use of their capabilities and improve system performance. The SOATS obtains the best balance between VMs in all numbers of tasks. Conversely, ACO-based task scheduling has the worst workload for all cases.

A comparison of the costs of using the VM for the SOATS and other meta-heuristic algorithms is shown in Figure 10. The cost increases as the number of tasks increases. Proper estimation of VM cost in a cloud computing environment is very important because as the cost decreases, the service provider's profit increases. The cost minimization by SOA is 12-3% less than that of WOA for 100 through 500 instances of tasks, respectively. Also, the cost minimization by SOA is 10-2% less than that of ACO for 100 through 500 tasks, respectively. The main reason is that ACO does not search the search space well and falls into the trap of local optimum.

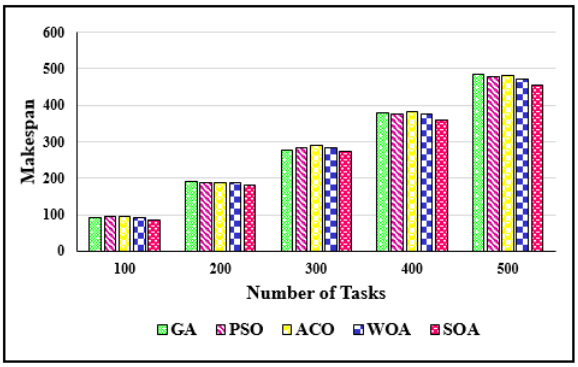

Figure 8. Makespan time with different numbers of tasks

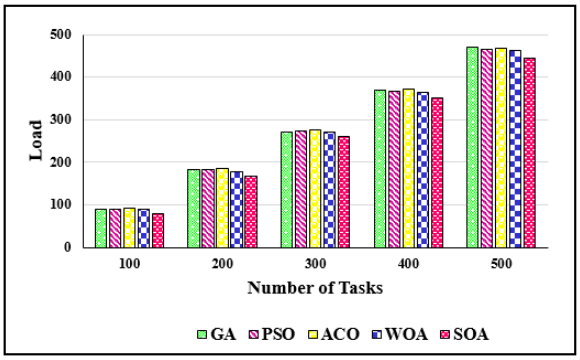

Figure 9. Degree of load balancing with different numbers of tasks

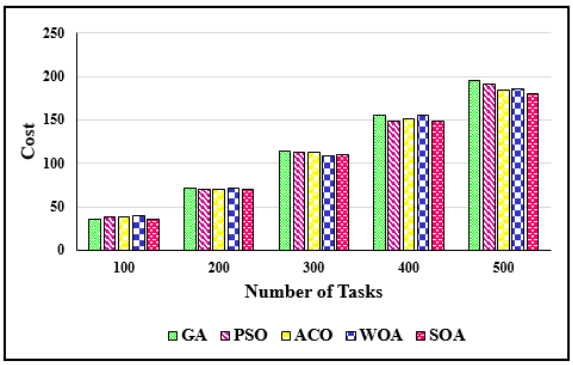

Figure 10. Cost with the different number of tasks

Energy consumption is also one of the main metrics in maximizing the overall performance of the cloud system. There is a direct linear relationship between energy consumption and VMs utilization because the optimal VMs utilization reduces the energy consumption of a server. The X-axis represents the number of tasks and the Y-axis indicates the energy consumption. In Figure 11, SOATS is more efficient and has a lower energy consumption in comparison to other algorithms. The energy consumption in the proposed algorithm is 31% better than that of GA, 22% that of PSO, 28% that of ACO, and 20% that of WOA in the case of 500 tasks assigned.

Waiting time is the total time a task spends in the task queue waiting for a VM to execute. Figure 12 shows the experimental results for the waiting time. As shown in Figure 12, SOATS waiting time is better than other algorithms for all cases. The GA provides the worst waiting time when the number of tasks is 500. The

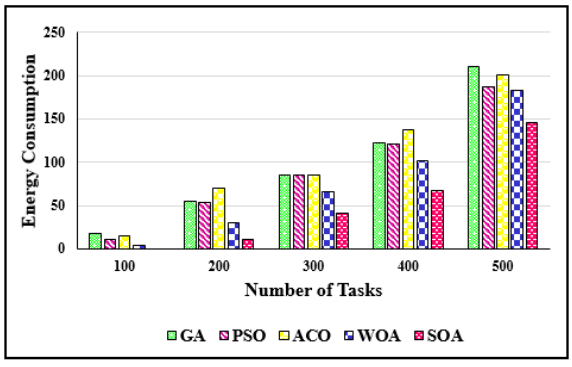

Figure 11. Energy consumption with the different number of tasks

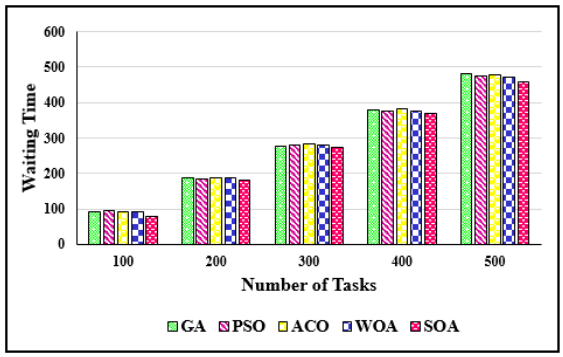

Figure 12. Waiting time with the different number of tasks

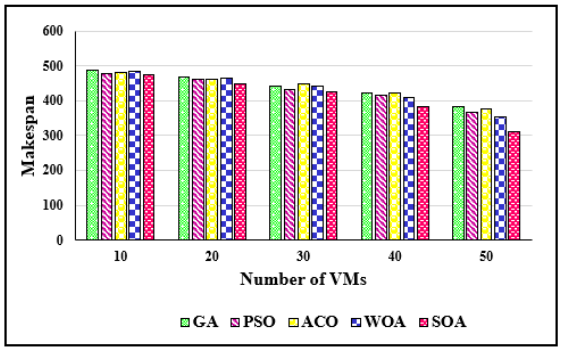

Figure 13. Makespan time with different numbers of VMs

waiting time in the proposed approach is 15-3%, 13-4%, and 13-2% less than PSO, ACO, and WOA for 100 through 500 tasks, respectively. Since f_c decreases from the initial value of f_c to 0, this allows the SOA to search well at the beginning and converges to the optimal solution by increasing the number of iterations.

5. 2. Number of VMs This experiment is performed with a variable number of VMs (between 10 and 50) while the number of tasks is considered fixed (500 tasks). Table 4 represents the parameters of the cloud system and the SOA.

Comparison of performance in terms of makespan, load, cost, energy consumption, and waiting time is shown in Figures 13-17 for different numbers of VMs with bar charts between different algorithms. It is clear that as the number of VMs increases, scheduling algorithms can process tasks in a shorter time, so parameters such as makespan and waiting time decrease with the increasing number of VMs (Figures 13 and 17, respectively). However, an increase in VMs number is increasing energy consumption. In Figure 16, as

TABLE 4. Parameters setting (different number of VMs)

Parameters	Values
Number of tasks	500
Tasks size (MI)	100-2000
Number of VMs	10-50
VMs execution speed (MIPS)	500-4500
Storage cost	$0.1 per GB
Processing cost	$1 per 10^6 MI
Data transfer cost	$0.05 per GB
Maximum iteration	1-100
Population size	60
F_c	1
Constant u and v	1

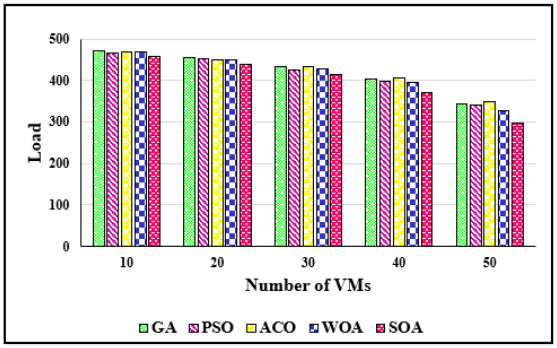

Figure 14. Degree of load balancing with different numbers of VMs

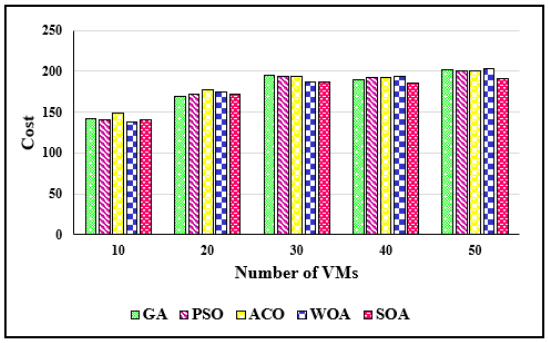

Figure 15. Cost with the different number of VMs

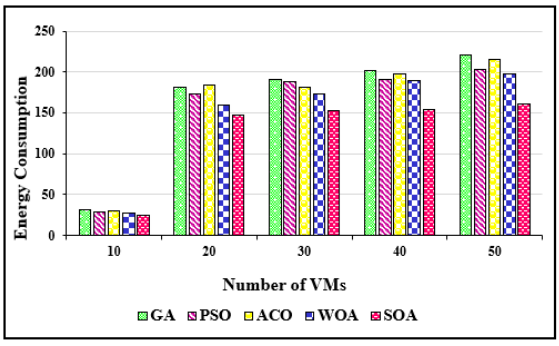

Figure 16. Energy consumption with the different number of VMs

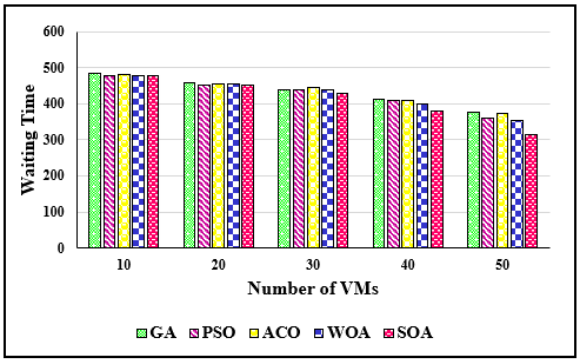

Figure 17. Waiting time with the different number of VMs

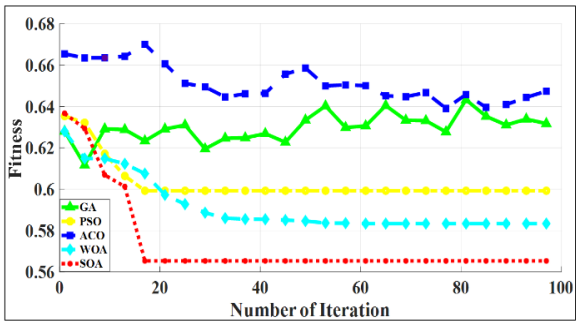

Figure 18. Convergence plot based on the number of iterations

expected, the energy consumption increases as the number of VMs increases. SOATS algorithm has the lowest energy consumption for different numbers of VMs and also GA in most cases has the maximum energy consumption due to poor exploitation capability. The difference between scheduling algorithms is evident in difficult situations such as when the number of VMs is low. As shown in Figures 13-17, the SOATS algorithm in most cases performs better than other algorithms for a different number of VMs with a certain number of tasks. This is because the SOA algorithm makes a balance between exploration and exploitation.

5. 3. Number of Iterations In the second scenario, we examine the performance of the SOATS compared to other algorithms by increasing the number of iterations. Table 5 presents the simulation parameters used in this scenario.

Figure 18 shows the convergence speed comparison of five meta-heuristic algorithms to solve the scheduling problem. Figure 18 shows that the fitness of the PSO, WOA, and SOA algorithms decreases with an increase in number of iterations, which indicates the efficiency of these algorithms in scheduling in the cloud environment. As shown in Figure 18, WOA and PSO perform better than GA and ACO algorithms. This is because PSO and WOA have better search capability and exploitation capability than GA and ACO. However, it can be observed that SOA has the best performance and, an increase in the number of iterations, SOA can achieve its optimal solution faster than PSO and WOA. SOA has better performance than the other four algorithms in terms of convergence speed and accuracy. This is because there is a trade-off between the local optimal value and the global optimal value in the search process. In other words, SOA has good exploration and exploitation capabilities. Initially, it searches the search space well and does not fall into the local optimal and then converges to the global optimal solution. Therefore, SOA has a good ability to solve complex optimization problems.

The convergence analysis of meta-heuristic algorithms is used for a better understanding of exploration and exploitation capabilities. Figure 19 shows the average convergence time of SOA and other metaheuristic algorithms. It can be seen that SOA takes less convergence time than other methods. The SOA

TABLE 5. Parameters setting (different number of iterations)

Parameters	Values
Number of tasks	400
Tasks size (MI)	100-2000
Number of VMs	20
VMs execution speed (MIPS)	500-4500
Storage cost	$0.1 per GB
Processing cost	$1 per 10^6 MI
Data transfer cost	$0.05 per GB
Maximum iteration	1-100
Population size	40
F_c	1
Constant u and v	1

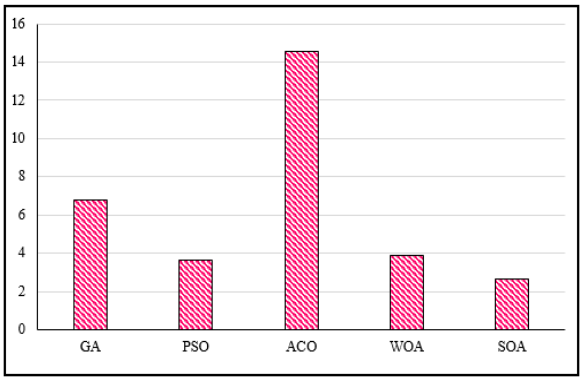

Figure 19. Average convergence time of meta-heuristic algorithms

converges after about 2.62 seconds, PSO 3.64 seconds, WOA about 3.91 seconds, GA 6.76 seconds, and ACO 14.54 seconds.

5. 4. Number of Search Agents In this subsection, we compare the performance of SOATS with other algorithms according to different population sizes. The cloud parameters and SOA parameters are presented in Table 6.

The number of seagulls in the SOA algorithm is known as the population size. Increasing the size of the population creates more parts of the search space that must be covered in each iteration. By increasing the population size, the number of iterations required to achieve the optimal solution can be reduced. However, increasing the population size increases the computational complexity in each iteration; therefore, it is time-consuming. In this experiment, we examine the performance of all five meta-heuristic algorithms in terms of task scheduling by considering the number of 100 iterations and different population sizes. We started the simulation with 40 search agents and increased it to 80 agents. The results in Figure 20, show that the ACO in most cases has the worst fitness and SOA has the best fitness value in all population sizes compared to other algorithms.

5. 5. F_c Parameter In this scenario, we run the SOA with different f_c values and compare the results. Table 7 proposed the simulation parameters used in this scenario.

f_c is one of the most important parameters in the SOA algorithm, which is introduced to control the frequency of variable A and reduces linearly from the initial value of f_c to 0. We implemented the SOA algorithm for various values of the f_c parameter by keeping the number of iterations and the number of search agents constant.

TABLE 6. Parameters setting (different number of agents)

Parameters	Values
Number of tasks	400
Tasks size (MI)	100-2000
Number of VMs	10
VMs execution speed (MIPS)	500-4500
Storage cost	$0.1 per GB
Processing cost	$1 per 10^6 MI
Data transfer cost	$0.05 per GB
Maximum iteration	100
Population size	40-80
F_c	1
Constant u and v	1

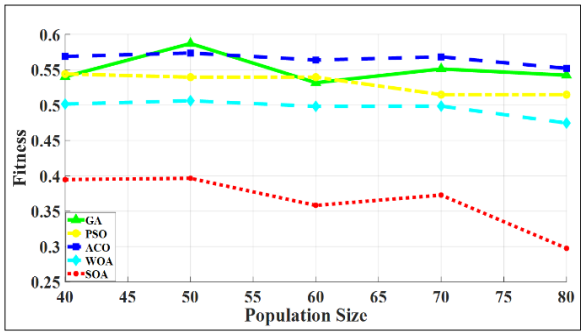

Figure 20. Convergence plot based on population size

TABLE 7. Parameters setting (different values of f_c)

Parameters	Values
Number of tasks	400
Tasks size (MI)	100-2000
Number of VMs	20
VMs execution speed (MIPS)	500-4500
Storage cost	$0.1 per GB
Processing cost	$1 per 10^6 MI
Data transfer cost	$0.05 per GB
Maximum iteration	100
Population size	40
F_c	1-5
Constant u and v	1

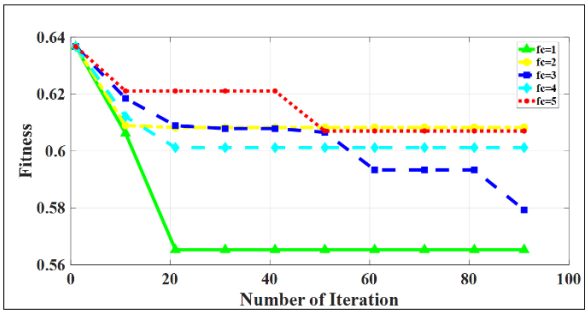

Figure 21. Effect of parameter f_c in our task scheduling algorithm

The f_c values used in experiments are 1, 2, 3, 4, and 5. As shown in Figure 21, the scheduling algorithm presented in this paper obtains the best optimal solution when the value of f_c is set to 1.

5. 6. Other Scheduling Algorithms In the last scenario, we compare SOATS performance with other scheduling algorithms, namely CJS [37], FUGE [39], and MSDE [51]. Table 8 shows the parameters settings. The

results obtained by comparing SOATS with other scheduling algorithms in terms of makespan, cost, degree of load, energy consumption, and waiting time are shown in Table 9.

Reducing makespan and waiting time is one of the most important requests of users because it makes their tasks execute faster. It is clear from Table 9 that SOATS has a shorter makespan and waiting time than other scheduling algorithms. Because the SOATS algorithm tries to distribute the tasks optimally between resources by considering the makespan and waiting time in the objective function and evaluating the value of the objective function in each iteration, which helps to reduce the execution time.

As Table 9 shows, the costs in SOA are 7, 10, and 12% lower than CJS, FUGE, and MSDE, respectively. MSDE has the worst performance in terms of cost compared to the rest, because MSDE only focused on reducing makespan and did not consider the cost. Also, the proposed algorithm performs better in terms of load balance as well as reducing energy consumption. SOA decreases energy consumption up to 27% in comparison with CJS, up to 24% in comparison with FUGE, and up to 23% in comparison with MSDE. Since SOATS uses the DVFS model and so consumes less energy because the resources operate with the minimum voltage and frequency required.

TABLE 8. Parameters setting (different scheduling algorithms)

Parameters	Values
Number of tasks	500
Tasks size (MI)	100-2000
Number of VMs	40
VMs execution speed (MIPS)	500-4500
Storage cost	$0.1 per GB
Processing cost	$1 per 10^6 MI
Data transfer cost	$0.05 per GB
Maximum iteration	100
Population size	50
F_c	1
Constant u and v	1

TABLE 9. The comparison between the different scheduling algorithms

Objectives/ Methods	Makespan	Cost	Degree of load	Energy	Waiting time
CJS	460	193	457	200	462
FUGE	463	201	453	191	460
MSDE	459	205	459	190	463
SOATS	455	180	445	146	457

6. CONCLUSION AND FUTURE WORKS

The problem of scheduling in cloud computing is an NP-hard problem due to the many parameters that exist (such as task priority, the dependency among tasks, and communication costs). One of the solutions to solve these problems is to use meta-heuristic algorithms. Although in the cloud system, finding a suitable task scheduling algorithm is very important for users and providers, most papers fail to offer an effective trade-off between makespan, energy consumption, and cost. In this paper, we present a new SOA-based task scheduling algorithm that simultaneously considers makespan, energy consumption, cost, load, and waiting time and named it SOATS. The experimental results show that the proposed tasks scheduling algorithm can improve the performance of the cloud computing system in terms of system load, makespan, cost, energy consumption, and waiting time compared to other well-known meta-heuristic algorithms such as GA, PSO, ACO, and WOA. In addition, SOATS has a better convergence speed and can find the optimal solution with more accuracy and speed compared to other meta-heuristic algorithms. This is because SOA has a good ability to explore and exploit. In the heavily loaded cloud environment. The proposed algorithm reduces energy consumption, cost saving and degree of load balancing by 10 and 25 and 3%, respectively. As part of our future work, we intend to combine the proposed algorithm with other meta-heuristic algorithms. In addition, we will consider other computational criteria such as security and availability. We also want to improve the proposed algorithm using fuzzy theory.

7. REFERENCES

1. Mohammad Hasani Zade. B, Mansouri. N, and Javidi. M. M, "Multi-objective scheduling technique based on hybrid hitchcock bird algorithm and fuzzy signature in cloud computing", ***Engineering Applications of Artificial Intelligence***, Vol. 104, (2021), DOI: 10.1016/j.engappai.2021.104372.
2. Kumar. M, Sharma. S. C, Goel. A, and Singh. S. P, "A comprehensive survey for scheduling techniques in cloud computing", ***Journal of Network and Computer Applications***, Vol. 143, (2019), 1-33, DOI: 10.1016/j.jnca.2019.06.006.
3. Dhiman. G, and Kumar. V, "Seagull optimization algorithm: Theory and its applications for large-scale industrial engineering problems", ***Knowledge-Based Systems***, Vol. 165, (2019), 169-196, DOI: 10.1016/j.knosys.2018.11.024.
4. Mansouri. N, Mohammad Hasani Zade. B, Javidi. M. M, "SAEA: A security-aware and energy-aware task scheduling strategy by Parallel Squirrel Search Algorithm in cloud environment", ***Expert Systems with Applications***, Vol. 176, (2021), DOI: 10.1016/j.eswa.2021.114915.

5. Pradhan. A, Bisoy. S. K, and Das. A, "A survey on PSO based meta-heuristic scheduling mechanism in cloud computing environment", ***Journal of King Saud University - Computer and Information Sciences***, (2021), DOI: 10.1016/j.jksuci.2021.01.003.
6. Shafiq. D. A, Jhanjhi. N. Z, and Abdullah. A, "Load balancing techniques in cloud computing environment: A review", ***Journal of King Saud University - Computer and Information Sciences***, (2021), DOI: 10.1016/j.jksuci.2021.02.007.
7. Velliangiri. S, Karthikeyan. P, Arul Xavier. V. M, and Baswaraj. D, "Hybrid electro search with genetic algorithm for task scheduling in cloud computing", ***Ain Shams Engineering Journal***, Vol. 12, No. 1, (2021), 631-639, DOI: 10.1016/j.asej.2020.07.003.
8. Wilczyński. A, and Kołodziej. J, "Modelling and simulation of security-aware task scheduling in cloud computing based on Blockchain technology", ***Simulation Modelling Practice and Theory***, Vol. 99, (2020), DOI: 10.1016/j.simpat.2019.102038.
9. NoorianTalouki. R, Hosseini Shirvani. M, and Motameni. H, "A heuristic-based task scheduling algorithm for scientific workflows in heterogeneous cloud computing platforms", ***Journal of King Saud University - Computer and Information Sciences***, (2021), DOI: 10.1016/j.jksuci.2021.05.011.
10. Alsaidy. S. A, Abbood. A. D, and Sahib. M. A, "Heuristic initialization of PSO task scheduling algorithm in cloud computing", ***Journal of King Saud University - Computer and Information Sciences***, (2020), DOI: 10.1016/j.jksuci.2020.11.002.
11. Pradhan. A, and Bisoy. S. K, "A novel load balancing technique for cloud computing platform based on PSO", ***Journal of King Saud University-Computer and Information Sciences***, (2020), DOI: 10.1016/j.jksuci.2020.10.016.
12. Kaur. R, Laxmi. V, and Balkrishan, "Performance evaluation of task scheduling algorithms in virtual cloud environment to minimize makespan", ***International Journal of Information Technology***, (2021), DOI: 10.1007/s41870-021-00753-4.
13. Sreenivasulu. G, and Paramasivam. I, "Hybrid optimization algorithm for task scheduling and virtual machine allocation in cloud computing", ***Evolutionary Intelligence***, Vol. 14, No. 2, (2021), 1015-1022, DOI: 10.1007/s12065-020-00517-2.
14. Zandvakili. A, Mansouri. N, and Javidi. M. M, "Energy-aware task scheduling in cloud compting based on discrete pathfinder algorithm", ***International Journal of Engineering, Transactions C: Aspects***, Vol. 34, No. 9, (2021), 2124-2136, doi: 10.5829/ije.2021.34.09c.10.
15. Uchechukwu. A, Li. K, and Shen. Y, "Energy consumption in cloud computing data centers", ***International Journal of Cloud Computing and Services Science***, Vol. 3, No. 3, (2014), 31-48, doi: 10.11591/closer.v3i3.6346.
16. Barroso. L. A, Clidaras. J, and Hölzle. U, "The datacenter as a computer: An introduction to the design of warehouse-scale machines", ***Synthesis Lectures on Computer Architecture***, Vol. 8, No. 3, (2013), 1-154, DOI: 10.2200/S00193ED1V01Y200905CAC006.
17. Sharma. M, and Garg. R, "HIGA: Harmony-inspired genetic algorithm for rack-aware energy-efficient task scheduling in cloud data centers", ***Engineering Science and Technology, an International Journal***, Vol. 23, No. 1, (2020), 211-224, DOI: 10.1016/j.jestch.2019.03.009.
18. Hussain. M, Wei. L.-F, Lakhan. A, Wali. S, Ali. S, and Hussain. A, "Energy and performance-efficient task scheduling in heterogeneous virtualized cloud computing", ***Sustainable Computing: Informatics and Systems***, Vol. 30, (2021), DOI: 10.1016/j.suscom.2021.100517.
19. Dong. M, Fan. L, and Jing. C, "ECOS: An efficient task-clustering based cost-effective aware scheduling algorithm for scientific workflows execution on heterogeneous cloud systems", ***Journal of Systems and Software***, Vol. 158, (2019), DOI: 10.1016/j.jss.2019.110405.
20. Singh. H, Tyagi. S, Kumar. P, Gill. S. S, and Buyya. R, "Metaheuristics for scheduling of heterogeneous tasks in cloud computing environments: Analysis, performance evaluation, and future directions", ***Simulation Modelling Practice and Theory***, Vol. 111, (2021), DOI: 10.1016/j.simpat.2021.102353.
21. Meshkati. J, and Safi-Esfahani. F, "Energy-aware resource utilization based on particle swarm optimization and artificial bee colony algorithms in cloud computing", ***The Journal of Supercomputing***, Vol. 75, No. 5, (2019), 2455-2496, DOI: 10.1007/s11227-018-2626-9.
22. Sanaj. M. S, and Joe Prathap. P. M, "An efficient approach to the map-reduce framework and genetic algorithm based whale optimization algorithm for task scheduling in cloud computing environment", ***Materials Today: Proceedings***, Vol. 37, (2021), 3199-3208, DOI: 10.1016/j.matpr.2020.09.064.
23. Alboaneen. D, Tianfield. H, Zhang. Y, and Pranggono. B, "A metaheuristic method for joint task scheduling and virtual machine placement in cloud data centers", ***Future Generation Computer Systems***, Vol. 115, (2021), 201-212, DOI: 10.1016/j.future.2020.08.036.
24. Houssein. E. H, Gad. A. G, Wazery. Y. M, and Suganthan. P. N, "Task Scheduling in Cloud Computing based on Meta-heuristics: Review, Taxonomy, Open Challenges, and Future Trends", ***Swarm and Evolutionary Computation***, Vol. 62, (2021), DOI: 10.1016/j.swevo.2021.100841.
25. Rai. D, and Tyagi. K, "Bio-inspired optimization techniques: a critical comparative study", ***ACM SIGSOFT Software Engineering Notes***, Vol. 38, No. 4, (2013), 1-7, DOI: 10.1145/2492248.2492271.
26. Beni. G, and Wang. J, "Swarm intelligence in cellular robotic systems", ***Robots and Biological Systems: Towards a New Bionics?***, Springer, (1993), 703-712, DOI: 10.1007/978-3-642-58069-7_38.
27. Shaheen. A. M, Spea. S. R, Farrag. S. M, and Abido. M. A, "A review of meta-heuristic algorithms for reactive power planning problem", ***Ain Shams Engineering Journal***, Vol. 9, No. 2, (2018), 215-231, DOI: 10.1016/j.asej.2015.12.003.
28. Kennedy. J, and Eberhart. R, "Particle swarm optimization", IEEE Proceedings of ICNN'95-International Conference on Neural Networks, Perth, WA, Australia, (1995), DOI: 10.1109/ICNN.1995.488968.
29. Dorigo. M, Maniezzo. V, and Colorni. A, "Ant system: optimization by a colony of cooperating agents", ***IEEE Transactions on Systems, Man, and Cybernetics, Part B (Cybernetics)***, (1996), 1996, DOI: 10.1109/3477.484436.
30. Sreenu. K, and Sreelatha. M, "W-Scheduler: whale optimization for task scheduling in cloud computing", ***Cluster Computing***, Vol. 22, (2019), 1087-1098, DOI: 10.1007/s10586-017-1055-5.
31. Mirjalili. S, and Lewis. A, "The whale optimization algorithm", ***Advances in Engineering Software***, Vol. 95, (2016), 51-67, DOI: 10.1016/j.advengsoft.2016.01.008.
32. Zuo. L, Shu. L, Dong. S, Zhu. C, and Hara. T, "A multi-objective optimization scheduling method based on the ant colony algorithm in cloud computing", ***IEEE Access***, Vol. 3, (2015), 2687-2699, DOI: 10.1109/ACCESS.2015.2508940.
33. Zuo. X, Zhang. G, and Tan. W, "Self-adaptive learning PSO-based deadline constrained task scheduling for hybrid IaaS cloud", ***IEEE Transactions on Automation Science and Engineering***, Vol. 11, No. 2, (2013), 564-573, DOI: 10.1109/TASE.2013.2272758.
34. Sreenivasulu. G, and Paramasivam. I, "Hybrid optimization algorithm for task scheduling and virtual machine allocation in

cloud computing", ***Evolutionary Intelligence***, Vol. 14, (2021), DOI: 10.1007/s12065-020-00517-2.

35. Lin. W, Liang. C, Wang. J. Z, and Buyya. R, "Bandwidth-aware divisible task scheduling for cloud computing", ***Software: Practice and Experience***, Vol. 44, No. 2, (2014), 163-174, DOI: 10.1002/spe.2163.
36. Del Acebo. E, and de-la Rosa. J. L, "Introducing bar systems: a class of swarm intelligence optimization algorithms", In AISB 2008 Convention Communication, Interaction and Social Intelligence, Vol. 1, (2008), 1-18.
37. Mansouri. N, and Javidi. M. M, "Cost-based job scheduling strategy in cloud computing environments", ***Distributed and Parallel Databases***, Vol. 38, No. 2, (2020), 365-400, DOI: 10.1007/s10619-019-07273-y.
38. Calheiros. R. N, Ranjan. R, Beloglazov. A, De Rose. C. A. F, and Buyya. R, "CloudSim: a toolkit for modeling and simulation of cloud computing environments and evaluation of resource provisioning algorithms", ***Software: Practice and Experience***, Vol. 41, No. 1, (2011), 23-50, DOI: 10.1002/spe.995.
39. Shojafar. M, Javanmardi. S, Abolfazli. S, and Cordeschi. N, "FUGE: A joint meta-heuristic approach to cloud job scheduling algorithm using fuzzy theory and a genetic method", ***Cluster Computing***, Vol. 18, No. 2, (2015), 829-844, DOI: 10.1007/s10586-014-0420-x.
40. Xu. B, Zhao. C, Hu. E, and Hu. B, "Job scheduling algorithm based on Berger model in cloud environment", ***Advances in Engineering Software***, Vol. 42, (2011), No. 7, 419-425, DOI: 10.1016/j.advengsoft.2011.03.007.
41. Karthick. A. V, Ramaraj. E, and Subramanian. R. G, "An efficient multi queue job scheduling for cloud computing", 2014 World Congress on Computing and Communication Technologies, Trichirappalli, India, (2014), DOI: 10.1109/WCCCT.2014.8.
42. Babu. G, and Krishnasamy. K, "Task scheduling algorithm based on Hybrid Particle Swarm Optimization in cloud computing environment", ***Journal of Theoretical and Applied Information Technology***, Vol. 55, (2013), 33-38.
43. Kumar. S, and Kalra. M. *A*, " Hybrid Approach for Energy-Efficient Task Scheduling in Cloud ", Proceedings of 2nd International Conference on Communication, Computing and Networking, Singapore, (2018), DOI: 10.1007/978-981-13-1217-5_99.
44. Holland. J. H, "Adaptation in Natural and Artificial Systems: An Introductory Analysis with Applications to Biology, Control, and Artificial Intelligence", MIT press, (1992).
45. Karaboga. D, " An idea based on honey bee swarm for numerical optimization " Technical report-tr06, Erciyes university, Engineering faculty, Computer engineering department, (2005).
46. Cotes-Ruiz. I. T, Prado. R. P, García-Galán. S, Muñoz-Expósito. J. E, and Ruiz-Reyes. N, "Dynamic voltage frequency scaling simulator for real workflows energy-aware management in green cloud computing", ***PloS One***, Vol. 12, No. 1, (2017), DOI: 10.1371/journal.pone.0169803.
47. Singh. S, and Kalra. M, "Scheduling of independent tasks in cloud computing using modified genetic algorithm", 2014 International Conference on Computational Intelligence and Communication Networks, Bhopal, India, (2014), DOI: 10.1109/CICN.2014.128.
48. Prem Jacob. T, and Pradeep. K, "A Multi-objective Optimal Task Scheduling in Cloud Environment Using Cuckoo Particle Swarm Optimization", ***Wireless Personal Communications***, Vol. 109, No. 1, (2019), 315-331, DOI: 10.1007/s11277-019-06566-w.
49. Yang. X.-S, and Deb. S, "Cuckoo search via Lévy flights", World Congress on Nature & Biologically Inspired Computing (NaBIC), Coimbatore, India, (2009), doi: 10.1109/NABIC.2009.5393690.
50. Wu. D, "Cloud computing task scheduling policy based on improved particle swarm optimization", Proceedings - 2018 International Conference on Virtual Reality and Intelligent Systems, ICVRIS 2018, Hunan, China, (2018), DOI: 10.1109/ICVRIS.2018.00032.
51. Elaziz. M. A, Xiong. S, Jayasena. K. P. N, and Li. L, "Task scheduling in cloud computing based on hybrid moth search algorithm and differential evolution", ***Knowledge-Based Systems***, Vol. 169, (2019), 39-52, DOI: 10.1016/j.knosys.2019.01.023.
52. Wang. G.-G, "Moth search algorithm: a bio-inspired metaheuristic algorithm for global optimization problems", ***Memetic Computing***, Vol. 10, (2018), No. 2, 151-164, DOI: 10.1007/s12293-016-0212-3.
53. Storn. R, and Price. K, "Differential evolution-a simple and efficient heuristic for global optimization over continuous spaces", ***Journal of Global Optimization***, Vol. 11, No. 4, (1997), 341-359, DOI: 10.1023/A:1008202821328.
54. Guo. X, "Multi-objective task scheduling optimization in cloud computing based on fuzzy self-defense algorithm", ***Alexandria Engineering Journal***, Vol. 60, No. 6, (2021), 5603-5609, DOI: 10.1016/j.aej.2021.04.051.
55. Sharma. M, and Garg. R, "An artificial neural network based approach for energy efficient task scheduling in cloud data centers", ***Sustainable Computing: Informatics and Systems***, Vol. 26, (2020), DOI: 10.1016/j.suscom.2020.100373.
56. Paknejad. P, Khorsand. R, and Ramezanpour. M, "Chaotic improved PICEA-g-based multi-objective optimization for workflow scheduling in cloud environment", ***Future Generation Computer Systems***, Vol. 117, (2021), 12-28, DOI: 10.1016/j.future.2020.11.002.
57. Wei. X, "Task scheduling optimization strategy using improved ant colony optimization algorithm in cloud computing", ***Journal of Ambient Intelligence and Humanized Computing***, (2020), DOI: 10.1007/s12652-020-02614-7.
58. Chen. X, Cheng. L, Liu. C, Liu. Q, Liu. J, Mao. Y, and Murphy. J, "A WOA-based optimization approach for task scheduling in cloud computing systems", ***IEEE Systems Journal***, Vol. 14, No. 3, (2020), 3117-3128, DOI: 10.1109/JSYST.2019.2960088.
59. Tubishat. M, Abushariah. M. A. M, Idris. N, and Aljarah. I, "Improved whale optimization algorithm for feature selection in Arabic sentiment analysis", ***Applied Intelligence***, Vol. 49, No. 5, (2019), 1688-1707, DOI: 10.1007/s10489-018-1334-8.
60. Tos. U, Mokadem. R, Hameurlain. A, Ayav. T, and Bora. S, "A performance and profit oriented data replication strategy for cloud systems", 2016 Intl IEEE Conferences on Ubiquitous Intelligence & Computing, Advanced and Trusted Computing, Scalable Computing and Communications, Cloud and Big Data Computing, Internet of People, and Smart World Congress (UIC/ATC/ScalCom/CBDCom/IoP/SmartWorld), Toulouse, France, (2016), DOI: 10.1109/UIC-ATC-ScalCom-CBDCom-IoP-SmartWorld.2016.0125.

Persian Abstract

چکیده

رایانش ابری منابع محاسباتی مانند سخت‌افزار و نرم‌افزار را به عنوان خدمات از طریق شبکه برای کاربران فراهم می‌کند. زمانبندی کارها یکی از مسائل اصلی برای دستیابی به اجرای مقرون به صرفه است. هدف اصلی زمانبندی کارها اختصاص کارها به منابع است تا بتواند یک یا چند معیار را بهینه کند. از آنجا که مسئله زمانبندی کارها یکی از مسائل زمان چندجمله‌ای غیرقطعی سخت (*NP-hard*) است، الگوریتم‌های فراابتکاری به طور گسترده‌ای برای حل مسئله زمانبندی کار به کارگرفته شده‌اند. یکی از الگوریتم‌های فراابتکاری جدید الهام گرفته از زیست الگوریتم بهینه سازی مرغ دریایی (*SOA*)است. در این مقاله، ما یک الگوریتم آگاه از انرژی و مقرون به صرفه زمانبندی کار مبتنی‌بر *SOA* (*SOATS*) ارائه می‌کنیم. الگوریتم پیشنهادی قصد دارد با استفاده از تعداد تکرارهای کمتر، بین پنج هدف (یعنی مصرف انرژی، زمان اتمام کار، هزینه، زمان انتظار، و تعادل بار) تعادل ایجاد کند. نتایج آزمایش‌ها با مقایسه با چندین الگوریتم فراابتکاری (یعنی، الگوریتم ژنتیک (*GA*)، بهینه‌سازی ازدحام ذرات (*PSO*)، بهینه‌سازی کلونی مورچه‌ها (*ACO*) و الگوریتم بهینه‌سازی نهنگ‌ها (*WOA*)) نشان می‌دهد که روش پیشنهادی عملکرد بهتری در حل مسئله‌ی زمانبندی کارها دارد. علاوه بر این، ما الگوریتم پیشنهادی را با روش‌های زمانبندی کار مقایسه می‌کنیم: زمانبندی کار مبتنی بر هزینه (*CJS*)، الگوریتم جستجوی پروانه مبتنی بر تکامل تفاضلی (*MSDE*) و *Fuzzy-GA* (*FUGE*). در محیط با بار زیاد، الگوریتم *SOATS* مصرف انرژی را ۱۰٪ و هزینه را ۲۵٪ بهبود می‌بخشد.

IJE TRANSACTIONS B: Applications Vol. 35, No. 02, (February 2022) 451-457

International Journal of Engineering

Journal Homepage: www.ije.ir

Analysis Randon Causes Repeatability Errors Inducted by Friction at Joints in Industrial Robots

A. Rezala*[a,b], M. Arbaoui[a]

[a] *Department of Transport and Hydrocarbons Equipment, Hydrocarbons and Chemistry Faculty, University of M'hamed Bougara -Boumerdes (UMBB), Boumerdes, Algeria*
[b] *Department of Mechanical and Production Engineering, Mechanical and Process Engineering Faculty, University of Science and Technology Houari Boumediene (USTHB), BP 32 El Alia 16111 Bab Ezzouar Alger, Algeria*

PAPER INFO

Paper history:
Received 30 September 2021
Received in revised form 26 November 2021
Accepted 08 December 2021

Keywords:
Repeatability
Friction
Asperity
Industrial Robot

ABSTRACT

The present study was carried out to investigate and analyze the positionning repeatability introduced by friction variations based on stochastic ellipsoids. A mixed friction model has been developed with improved properties compared to existing standard models. The contact is presented as a multitude of micro contacts whose nature can be of two types: lubricated and solid. This model is experimentally tested on a reciprocating tribometer under extreme friction conditions, with sliding speed varying from 0.1 to 3 m/s and load modified from 40N to 150N to discuss the effect of speed, the effect of nominal contact pressure and the effect of sliding distance on friction parameters. The results showed how this model can be represented as a sum of functions of the relevant states, which are linear and nonlinear in the friction parameters. Thus, these results were used to evaluate the covariance matrix in order to locate the different ranges of errors which have an impact on the repeatability of position.

doi: *10.5829/ije.2022.35.02b.21*

1. INTRODUCTION

Lately, robotic systems have been progressively carried out many engineering applications [1-3] to replace humans in simple, repetitive and dangerous tasks. In order to optimize trajectory planning, we can use the criteria of energies [4, 5] position as well as speed and acceleration. The criterion of energy consumption as in the transport and handling of industrial objects depends on the robots used as mobile robot or manipulator. The work in this case takes into account the aerodynamics of the robot (dynamic model) [5]. This part consists of optimizing the pneumatic energy. The phenomenon of abrupt change of orientation using continuous movement in position and tangent (first and second-degree continuity) is detrimental for the assembly. The trajectory planning discussed by Wan et al. [6] has determined by an initial starting point Pi as well as its arrival at the final point Pf, avoiding to collision phenomenon. This would require recording the position and orientation of a set of points. Then approximate by a curve (using Bezier, B-Splines and NURBS). Other authors translate the phenomenon by a description of an object gripper of different shapes as well as the functioning of the gripper jaws [7]. Another method of describing objects of complex shapes using a set of 3D points has been developed in order to position and orient these complex points [8].

The absolute precision of an industrial robot is affected by systematic errors, in which the causes are generally known and can be easily compensated by corrective actions during calibration. However, repeatability is usually affected by errors of a random nature, caused by the adjustments of the servo-controls and especially by non-geometric phenomena such as hysteresis, play and friction existing at the joints [9] difficult to model and not permanently compensating for precisely because of their random nature. For this reason,

*Corresponding Author Institutional Email: a.rezala@univ-boumerdes.dz (A. Rezala)

Please cite this article as: A. Rezala, M. Arbaoui, Analysis Randon Causes Repeatability Errors Inducted by Friction at Joints in Industrial Robots, ***International Journal of Engineering, Transactions B: Applications***, Vol. 35, No. 2, (2021) 451-457

repeatability is considered to be one of the most important specifications to consider when selecting a robot. The repeatability error quantifies the level of spatial dispersion of the programmed pose of a robot. This is a very important metrological characteristic of an industrial robot. There are many recommendations for modeling and calculating the repeatability of industrial robots. Among the most commonly used methods, we will retain the stochastic ellipsoid method [10] the Taguchi method (signal/ noise ratio), and the method of the ISO 9283 standard [11].

One of the major difficulties in the robotics is friction, therefore, the analysis of friction in the robot joint is an important topic in tribology and industrial robotics. The main issue with mechanical systems in industrial robots is the friction caused by complicated and multiple sets of microscopic interactions between surfaces that are contact and slide. These interactions are the result of the physic-chemical properties of the materials, the geometrical and topographical characteristics of the surfaces and the overall conditions under which the surfaces are made to slide against each others [12]. Therefore, friction is not simply a property of materials parameters; it is unique characteristics of the tribological system in which it is measured. In the design of an industrial robot, friction management is a permanent challenge [13]. Friction has been widely studied by many scientists, due to its importance in several areas of mechanical engineering. Uncompensated friction occurring at the joints level causes of non negligible positioning errors on the accuracy of the robot's terminal organ. Thus, the presence of friction at joints constitutes one of the main causes of performance loss in manipulator since the friction is a source of the deviations in poses causing of defect repeatability. But, the friction modeling is not an easy task then it is too difficult to expect its correction. Hence, the interest in seeking precise modeling of friction behavior requires a model of friction forces, which based on the real behavior of joints.

The main objective of present study is to study and analyze the repeatability of position induced by friction variations, using a probabilistic approach based on stochastic ellipsoids. This approach makes it possible to better characterize the repeatability of the robot at each point of its workspace and thus better plan its tasks. Therfore, a numerical model analysis of the mixed friction behavior of the components of the robot joints was used. This model is based on an analysis of the contact geometry and it is confronted with an experimental study by equivalent geometric model, in a lubricated medium, on an alternative tribometer in extreme conditions of friction, with a sliding speed varying from 0.1 to 3 m/s and a modified load from 40N to 150N to discuss the effect of speed, the effect of nominal contact pressure and the effect of sliding distance on friction parameters.

2. COMPARISON BETWEEN NUMERICAL AND REAL APPLICATION

In our work, we used a structure working in the 3D coordinate systemin translation including a gripper. It is of great interest for transfer operations. This structure is widely used in conditioning applications since in these applications the three translations are sufficient. A rotational movement along the z-axis is often added to the terminal organ.

The robot is designed by three joints with one degree of freedom each. Therefore, the positioning error is divided into three to ensure the positioning accuracy at the output of the terminal organe. In other words, the positioning repeatability is determined at the end of the segment. The proposed joint is a sliding link with one degree of freedom. It is real when it is driven by an engine, reducer, screw/nut and the movable part called the segment, which moves relative to the fixed part generally linked to the built called the slide (or guide). An schematic diagram of kinematic for a slide link attached to the terminal organe is shown in Figure 1.

The proposed kinematic link can be schematized by two bodies junction for complementary functions. The first body consists of transmission mechanism; engine-slide. A rigidity of spring k can idealize this part. The second body corresponds to the segment-slide part. An alternative translation tribometer can symbolize the latter. Therefore, the sources of errors request the repeatability dispersion, that can be devided into two parts. The first one brings together all mechanical and geometric errors (alignment, vibration, force and adjustment), while the second one contains the friction and wear errors (friction coefficient, mechanical games and energy loss). Therefore, the proposed kinematic link can be revealed by Figure 1, where it is detailed in the tribological part Segment-slide of the link, which proposed by a contact Pin-plate from the alternative tribometer to idealize the movement and simplify the positioning of the effector (output element). In addition, it is assumed that the mechanical contribution (elasticity of the spring) to the positioning repeatability is constant. While, the positioning repeatability only depends on the variation force or the coefficient friction and wear that appears

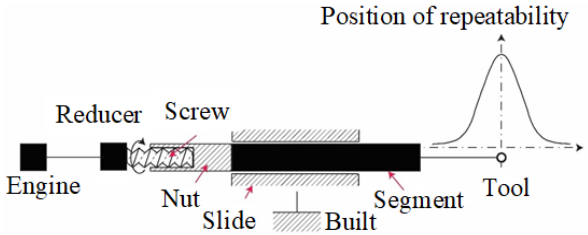

Figure 1. Kinematic diagram of a slide link attached to the terminal organe

between segment and slide, consequently the quantification of the tribological error on the positioning repeatability. The validation of experimental data an alternative tribometer is used as shown in Figure 2.

3. EXPERIMENTAL PROCEDURE

Alternative tribometer was produced and designed in Laboratory of Mechanical Structures and Materials Engineering (LISMMA), in Paris, was utilized to perform tribo test as seen in Figure 3 to study the work in progress at medium nominal contact pressure (up to12 Mpa), high sliding speed (up to 10 m/s) and normal load (up to 500 N).

The test pieces used on the tribometer are a plate representing a steel slide 42CD4 and a pin representing a segment made of 100C6 steel are shown in Figure 4.

Sliding tests were carried out at room temperature, with sliding speed in the span of 0.1-3 m/s and the load were changed from 40 N to 150 N. To ensure that the two rubbing surfaces make excellent, consistent contact, rubbing of segment specimens was carried out with a

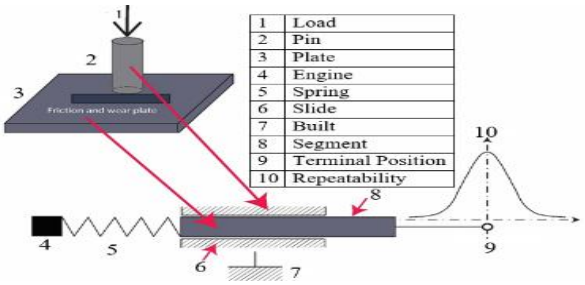

Figure 2. Experimental validation on an alternative tribometer

Figure 3. Alternative tribometer used

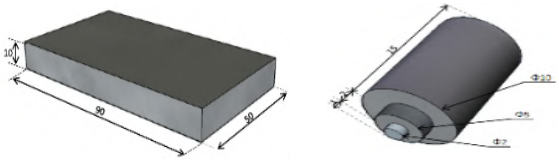

(a) (b)

Figure 4. Test simples : (a) Plate, (b) Pin

silicon abrasive paper before the tests. i. e. contacting surfaces. The frictional force was measured using a strain gauge present at the level arm that holds the specimen. The coefficient of friction value was calculated using the ratio of frictional force to normal load. After calculation, we were able to determine the speed error, which amounts to plus or minus 1%, as well as the load error, which is 0.05 mv.

4. CONSTITUTION OF A MIXED FRICTION MODEL

4. 1. Qualitative Analysis The diagram below shows that micro geometry plays a key role in lubrication, it constitutes the first stage of the modeling developed in the digital tool. We will adopt a circular approximation for the shape of asperities. Then, it is necessary to define the fraction of force α passing through the contacts working in thin film, the remainder 1-α corresponding to forces passing through the contacts working in thick film. We put f_s the coefficient of friction on the thin film contacts and f_l the coefficient of friction of the thick film contacts. We naturally have $f_s > f_l$. The total friction f is defined by the expersion below:

$$f = \alpha f_s + (1-\alpha) f_l \tag{1}$$

This justifies the name of mixed friction. The digital tool used makes it possible for a given situation to calculate α and therefore to deduce f from it by giving ourselves f_s and f_l.

4. 2. Modeling of Micogeometry The micro geometry is approximated by a succession of roughness of vertices spaces of AR whose vertices follow a normal law with mean R/2 and standard deviation:.

$$p_1(z) = \frac{1}{SAlt\sqrt{2\Pi}} \exp\left[-\frac{1}{2}\left(\frac{z-Alt}{SAlt}\right)^2\right] \tag{2}$$

where

$$SAlt = 0.35\sqrt{W^2 + SW^2}$$
$$Alt = \frac{1}{2}R \tag{3}$$

where $P_1(z)$ is statistical distribution of peak altitude; z is summit altitude of asperity; and Alt and SAlt are mean and root mean square of the peak altitude.

The radii of the asperities follow a lognormal distribution whose characteristics also depend on roughness parameters. The lognormal distribution is given by the following formula instead of a classical normal distribution:

$$p_2(R^*) = \frac{1}{aR^*\sqrt{2\prod}} \exp\left[\frac{1}{2a^2}\left(\log R^* - b\right)^2\right] \tag{4}$$

where R* is a dimensional expression of radius R; R is the radius of asperity; a and b are constants for radius distribution. This lognormal distribution is available only for the positive values and requires a dimension less parameter R*.

$$R^* = \frac{R}{SRAD} \tag{5}$$

4. 3. Modeling of the Contact Between Segment-slide of the Robot For a given position d counted from the mean line, it will be considered that the asperities whose vertices have an altitude z greater than d working in thin film with a friction f_s while those having an altitude z less than d working in thick film (coefficient of friction f_l).

The value d physically corresponds to the average thickness of the lubricant. Knowing the expressions of the behavior of each of these families of asperities (force on an asperity according to the crushing), it is possible to numerically determine the total coefficient of friction of the contact and the total loading which it undergoes. The model takes into account the deformations: elastic, elastoplastic, plastic, elastohydrodynamic and hydrodynamic of the asperities in contact. For roughness [14] working in thick film lubrication regime, mechanisms such as hydrodynamics with piezo-viscous effect and elastohydrodynamic were analyzed. Figure 5 depicts the description of the modelling of the contact between segment-slide of the robot.

The total friction f is defined by Equation (6):

$$\begin{aligned} W &= \sum W_E + \sum W_{EP} + \sum W_P + \sum W_{PVR} + \sum W_{EHD} \\ F &= \sum F_E + \sum F_{EP} + \sum F_P + \sum F_{PVR} + \sum F_{EHD} \\ \Rightarrow f &= F/W \end{aligned} \tag{6}$$

In this case, the proposed mixed friction model is represented by a sum of functions of the relevant states, which are linear and nonlinear in the friction parameters.

5. RESULTS AND DISCUSSION

5. 1. Result Obtained by the Model The results of friction coefficient calculation as a function of the Sommerfeld number, defined by the defined equation S = ηV/ p where η represents the viscosity, U is the sliding speed and p is the apparent pressure are shown in Figure 6.

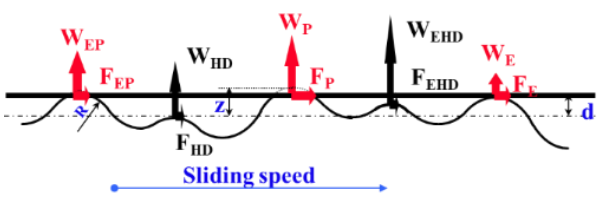

Figure 5. Description of the modelling

The results of calculation of the coefficient of friction followed the typical shape of the curve of Stibeck [15] where one notes a dispersion of the values of the coefficient of friction which is due to two types of lubricated and solid contact. The lubricated contact where there is a continuous film, with well separated bearing surfaces, the lubrication is in HD or EHD regime and the friction is viscous equal to approximately 0.004. The asperities are not in contact and therefore, the load is supported by the fluid. In addition, a solid contact where there is a discontinuous film and where tangential actions can occur due to the proximity of the bearing surfaces of the same nature as those which determine the solid friction. The lubrication is in mixed regime and the friction is coupled: viscous and solid equal to approximately 0.1, the asperities are in direct contact and therefore, the load is partly supported by the latter.

5. 2. Experimental Validation on an Alternative Tribometer This model is tested by the experiments carried out on the reciprocating tribometer. For each of these tests, we used the friction coefficient values.

By superimposing the curves obtained from the model illustrated in Figure 6 and the experimental data we obtained for the friction coefficients are illustarted in Figure 7, which combined the two experimental and theoretical predicted results by modelling.

5. 3. Discussion: Model-experiment Comparison A slight difference is observed between the experimental results and the model, for the value of the coefficient of friction on the contrary to the existing standard models This can be explained by imperfections in the model, and/or by those when performing the experiments.

The first approximation is erroneous because the distribution of contacts is considered not equal between all the types of micro switches: that is to say that there are not as many segment-slide contacts and this, at the level of the real contact area. The actual contact shown schematically in Figure 5 shows that this hypothesis is not

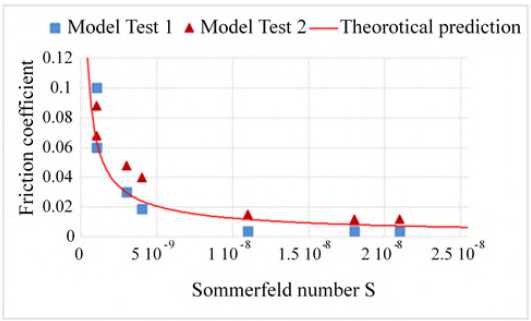

Figure 6. Friction coefficients determined by the model with respect to Sommerfeld number

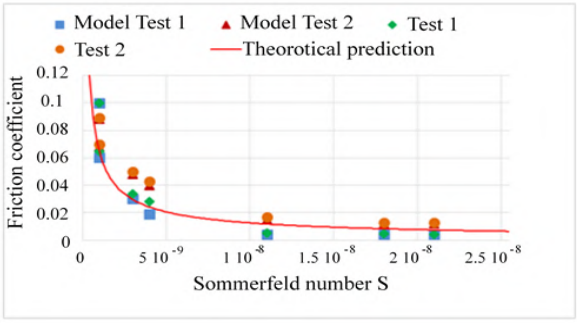

Figure 7. Comparaison of experimental and calculated friction coefficients as a function of S

valid because the radii of the asperities follow a lognormal distribution whose characteristics also depend on roughness parameters such as the average height of the roughness pattern R, the standard deviation of the pattem heights SR, the average width of the roughness pattem AR , the standard deviation of the SAR pattern widths, the mean height of the W ripple pattern, and the standard deviation of the SW ripple pattern heights. Thus, the surfaces are described by a statistical distribution function of peak altitude and asperities radius where the density function of the probability is illustrated in Figure 8, which is defined by the following equation:

$$p(z,R) = p_1(z) \cdot p_2(R) \quad (7)$$

To illustrate this analysis in a suitable manor, Figure 9 presents by level curves, shown as a Gaussian distribution of the heights of asperities as a function of their radii of curvature.

The second assumption of the model is the isotropy of the tribological properties. Although the steel is statically isotropic, that is to say on a macroscopic scale, the steel exhibits a strong anisotropy at least in terms of mechanical properties.

5. 4. Wear Figure 10 illustrates the evolution of the wear coefficient K as a function of Sommerfeld

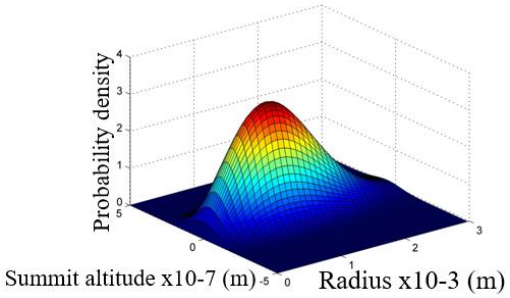

Figure 8. Density probability function of asperities as a function of radius and summit altitude

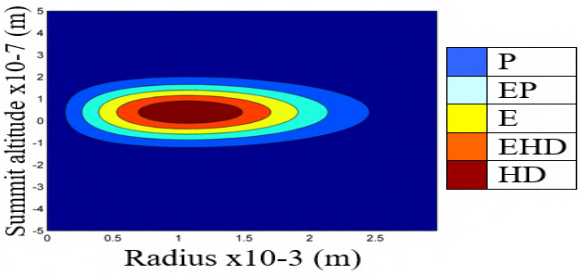

Figure 9. Gaussian distribution of the five types of asperities

number [16]. This is a complementary model to the wear Achard's law, which holds coccount of the dispersion induced by fluctuations in the characteristics of the microgeometries, from one contact area to another [17]. While, the Archard's law constitutes the major difficulty of a contact in a mixed lubrication situation. One of the assumptions of this Archard law is that the contact took place in a dry environment. In our study, the lubrication is mixed, therefore, Archard's law can be generalized on condition of taking into account the contact pressure supported by the non-lubricated asperities (in thick film). The wear process and its properties are studied on the basis of the mixed friction observed in the joint of an industrial robot, where it can be concluded that the dispersion observed in the results obtained is generated by variable lubrication conditions, the friction coefficient of which varies between 0.004 and 0.1.

The wear of peak altitude of the asperities due to the adaptation of the surfaces in the robot articulation can thus be used as an indicator of the state of the articulation and they cause considerable damage and constitute an excellent indicator of damage to the mechanical surfaces. Therefore, wear and tear processes can take several years to be significant, but can change rapidly once they start to appear. To conclude, the obtained results showed us that there is a proportionality between friction and wear in the joints of industrial robots.

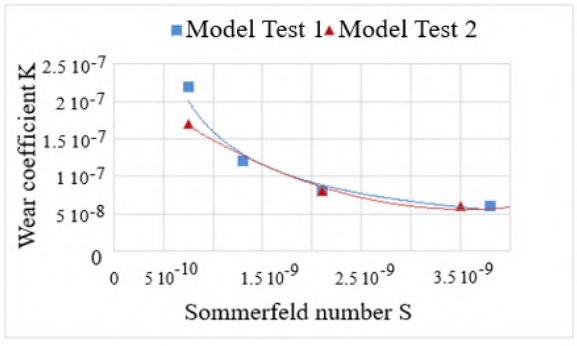

Figure 10. Evolution of wear coefficient K as a function of the Sommerfeld number

6. ANALYSIS RANDON OF THE POSE REPEATABILITY INDUCTED BY FRICTION

We made a simulation in a basic parallelepiped work volume (400 x 400 mm) in order to show the influence of friction on the field calculation of the organ's positioning repeatability of the robot terminal. Figures 11, 12 and 13 show the horizontal sections. It can be seen that the errors in the plane presented in Figure 11, show that the point cloud is located in an ellipsoidal zone where the limitation adopted on the joints has shown its effectiveness. This is due to the friction which is minimal, because we are in a situation of thick film lubrication. In this case, the friction results from a partition of the contact, the positioning of the terminal member of which is almost precise.

Indeed, beyond the limited working space, there is a significant increase in the positioning error of the terminal member of the robot illustrated in Figures 12 and 13. These figures also show that the friction is due in a significant way to the gap existing between the segment and the slide. In particular, for the high values of friction which resulted in from a partition of the contact in the thin film. By analyzing these graphs, we observed that by iteration, our robot performs a maximum error at the center of the plane perpendicular to the displacement. This error is mainly caused by the friction.

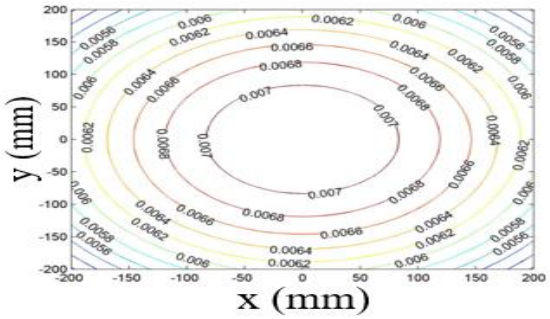

Figure 11. Repeatability field in µm at the plane z = - 400 (mm)

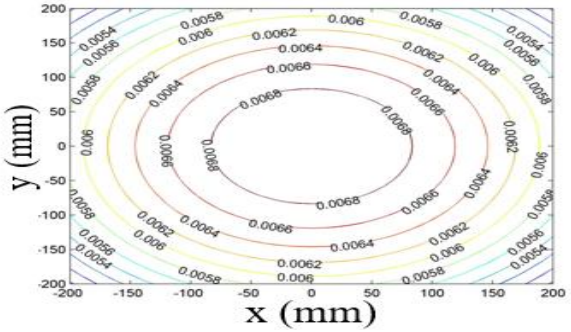

Figure 12. Repeatability field in µm at the plane z = - 500 (mm)

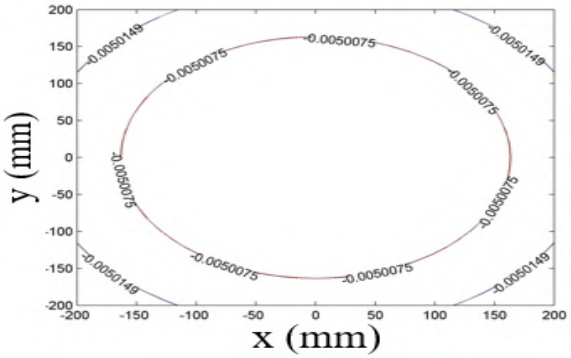

Figure 13. Repeatability field in µm at the plane z = - 600 (mm)

7. CONCLUSION

This research study presents the results and statistical analyses of a study devoted to the estimation of positioning repeatability induced by friction variations. The theory of stochastic ellipsoids has been used to describe the spatial distribution of workspace errors around the mean position where the results are graphically visualized. This model allowed us to choose the best location in the workspace to perform the task. The findings of this research and evaluation are listed below:

- The absolute value of the error made on the computation of repeatability is lower than 2.10^{-3}. This value of the calculated repeatability is considered acceptable.
- The repetitive positioning of the robot's terminal organ follows a normal distribution around the commanded position.
- The level of dispersion decreases as a function of time (asymptotic behavior) to reach its lowest value, then stabilizes at an almost constant value;
- In the plane z = -400 mm, the point cloud is located in an ellipsoidal zone where the friction is equal to 0.004,
- For high values of friction, there is an increase in the positioning errors of the terminal organ.
- The results obtained by the model of mixed friction in qualitative and quantitative adequacy with the experiment.
- The mixed friction model takes into account the roughness parameters, the nature of the materials, the lubricant, the forces and the speeds.

8. REFERENCES

1. Tang, G., Webb, P., Thrower, J.J.R. and Manufacturing, C.-I., "The development and evaluation of robot light skin: A novel robot signalling system to improve communication in industrial human–robot collaboration", ***Robotics and Computer-Integrated***

Manufacturing, Vol. 56, (2019), 85-94, doi: 10.1016/j.rcim.2018.08.005

2. Khorashadizadeh, S. and Fateh, M.M.J.R., "Uncertainty estimation in robust tracking control of robot manipulators using the fourier series expansion", Vol. 35, No. 2, (2017), 310-336, doi: 10.1017/S026357471500051X
3. Sangdani, M. and Tavakolpour-Saleh, A.J.I.J.o.E., "Parameters identification of an experimental vision-based target tracker robot using genetic algorithm", ***International Journal of Engineering, Transactions C: Aspects,*** Vol. 31, No. 3, (2018), 480-486, doi: 10.5829/ije.2018.31.03c.11
4. Savkiv, V., Mykhailyshyn, R., Duchon, F. and Mikhalishin, M.J.J.o.E.E., "Energy efficiency analysis of the manipulation process by the industrial objects with the use of bernoulli gripping devices", ***Journal of Electrical Engineering,*** Vol. 68, No. 6, (2017), 496, doi: 10.1515/jee-2017-0087
5. Mykhailyshyn, R., Savkiv, V., Mikhalishin, M. and Duchon, F., "Experimental research of the manipulatiom process by the objects using bernoulli gripping devices", in 2017 IEEE International Young Scientists Forum on Applied Physics and Engineering (YSF), IEEE. (2017), 8-11.
6. Wan, W., Igawa, H., Harada, K., Onda, H., Nagata, K. and Yamanobe, N.J.A.R., "A regrasp planning component for object reorientation", Vol. 43, No. 5, (2019), 1101-1115, doi: 10.1007/s10514-018-9781-y
7. Savkiv, V., Mykhailyshyn, R., Maruschak, P., Kyrylovych, V., Duchon, F. and Chovanec, Ľ.J.T., "Gripping devices of industrial robots for manipulating offset dish antenna billets and controlling their shape", Vol. 36, No. 1, (2021), 63-74, doi: 10.3846/transport.2021.14622
8. Wermelinger, M., Johns, R., Gramazio, F., Kohler, M., Hutter, M.J.I.R. and Letters, A., "Grasping and object reorientation for autonomous construction of stone structures", ***IEEE Robotics and Automation Letters***, Vol. 6, No. 3, (2021), 5105-5112, doi: 10.1109/LRA.2021.3070300
9. Deblaise, D., "Contribution à la modélisation et à l'étalonnage élasto-géométriques des manipulateurs à structure parallèle", INSA de Rennes, (2006),
10. Assoumou Nzue, R., Brethe, J.-F., Vasselin, E. And Lefebvre, D., "Comparaison de la répétabilité des robots manipulateurs sériels et parallèles à l'aide des ellipsoïdes stochastiques", in Congrès français de mécanique, AFM, Maison de la Mécanique, 39/41 rue Louis Blanc, 92400 Courbevoie, France, (2011).
11. Kumičáková, D., Tlach, V. and Císar, M., "Testing the performance characteristics of manipulating industrial robots", ***International Organization for Standardization*** (2016).
12. Al-Bender, F. and Swevers, J.J.I.C.S.M., "Characterization of friction force dynamics", ***IEEE Control Systems Magazine*** Vol. 28, No. 6, (2008), 64-81, doi: 10.1109/MCS.2008.929279
13. Bona, B. and Indri, M., "Friction compensation in robotics: An overview", in Proceedings of the 44th IEEE Conference on Decision and Control, IEEE. (2005), 4360-4367.
14. Venkata Vishnu. A and Sudhakar Babub. S, "Mathematical modeling and multi response optimization for improving machinability of alloy steel using rsm, grey relational analysis and jaya algorithm", ***International Journal of Engineering, Transactions C: Aspects***, Vol. 34, No. 09, (2021), 1257-1266, doi: 10.5829/ije.2021.34.09C.13
15. Belarifi, F., Blouet, J., Inglebert, G., Benamar, A.J.M. and Industry, "Confrontation d'un modèle théorique en lubrification mixte avec une étude expérimentale du comportement au frottement d'une denture d'engrenage droit", Vol. 7, No. 5-6, (2006), 527-536, doi: 10.1051/meca:2007010
16. Zailani. Z-A, R.N.S.N. and Shuaiba. N-A, "Effect of cutting environment and swept angle selection in milling operation", ***International Journal of Engineering, Transactions B: Applications***, Vol. 34, No. 11, (2021), 2578-2584, doi: 10.5829/ije.2021.34.12c.02
17. Robbe-Valloire, F., Progri, R., Paffoni, B. and Gras, R., "Prediction of wear rate dispersion in mixed lubrication", in World Tribology Congress. Vol. 42010, (2005), 453-454.

Persian Abstract

چکیده

مطالعه حاضر به منظور بررسی و تحلیل تکرارپذیری موقعیت‌یابی معرفی‌شده توسط تغییرات اصطکاک بر اساس بیضی‌های تصادفی انجام شد. یک مدل اصطکاک مختلط با خواص بهبود یافته در مقایسه با مدل های استاندارد موجود توسعه یافته است. کنتاکت به صورت انبوهی از میکرو کنتاکت ها ارائه می شود که ماهیت آنها می تواند دو نوع باشد: روغن کاری شده و جامد. این مدل به صورت تجربی بر روی یک تریبومتر رفت و برگشتی تحت شرایط اصطکاک شدید، با سرعت لغزش از ۰٫۱ تا ۳ متر بر ثانیه و بار تغییر یافته از ۴۰ نیوتن تا ۱۵۰ نیوتن برای بحث در مورد تأثیر سرعت، تأثیر فشار اسمی تماس و اثر لغزش آزمایش می‌شود. فاصله بر روی پارامترهای اصطکاک نتایج نشان داد که چگونه می توان این مدل را به صورت مجموع توابع حالت های مربوطه که در پارامترهای اصطکاک خطی و غیرخطی هستند، نشان داد. بنابراین، این نتایج برای ارزیابی ماتریس کوواریانس به منظور تعیین محدوده‌های مختلف خطاهایی که بر تکرارپذیری موقعیت تأثیر دارند، استفاده شد.

IJE TRANSACTIONS B: Applications Vol. 35, No. 02, (February 2022) 458-470

International Journal of Engineering

Journal Homepage: www.ije.ir

A Bi-objective Cold Supply Chain for Perishable Products Considering Quality Aspects: A Case Study in Iran Dairy Sector

M. Aghaei Afshar[a], S. M. H. Hosseini*[b], R. Sahraeian[a]

[a] *Department of Industrial Engineering, Shahed University, Tehran, Iran*
[b] *Department of Industrial Engineering and management, Shahrood University of Technology, Shahrood, Iran*

P A P E R I N F O

Paper history:
Received 29 September 2021
Received in revised form 01 December 2021
Accepted 04 December 2021

Keywords:
Cold Supply Chain
Bi-objective
Parametric Method
Quality Aspects
Dairy Product

A B S T R A C T

Improper handling in the food cold supply chain may compromise food safety and reduce quality, which can lead to economic losses and undesirable effects on food accessibility. Therefore, designing an efficient and reliable cold supply chain is extremely important for the company, suppliers, customers, and society. The majority of the traditional studies in the supply chain do not consider the cost of quality (prevention, appraisement, and failure) in supply chain network design. In this study, all dimensions of the cost of quality in a cold supply chain design such as the cost of quality related to suppliers and the cost of distribution service quality are investigated to close the problem to real-world conditions. Moreover, the quality of suppliers, manufacturers, and distributors is simultaneously considered throughout a supply chain with a new approach. To this end, the problem is formulated as a mathematical model for multi-item and multi-period cases considering two objective functions. The first objective function minimizes the total expected costs and the second objective function maximizes the total quality of the supply chain. The proposed bi-objective model has been transformed into a single-objective model by the solution of the parametric method (normalized weighted summation) and solved for a medium-sized instance considering data of a real-world case study. Computational results and analyzes indicate the efficiency of the proposed model as well as the exact solution method available for small and medium scales. The real case study which involves Kaleh Dairy Company is conducted to illustrate the potential of the proposed model and proper sensitivity analyses.

***doi**: 10.5829/ije.2022.35.02b.22*

1. INTRODUCTION

The supply chain includes all the steps (chain members) that are directly or indirectly involved in meeting a customer's request. In a typical supply chain, raw materials are sent from suppliers to factories, and then the products produced in the factories are sent to intermediate warehouses and distributors' warehouses, as well as to retailers and finally to the customer. They reach the end of the consumer. So a product goes through the supply chain to reach consumers.

Proper supply chain network design can provide ideal results and increase its revenues. Supply chain management has a vital impact on two outcomes. Firstly, it pays attention to any solution that reduces costs and plays a key role in meeting customer needs. In fact, in some supply chain analyses, it is necessary to focus on suppliers and customers because they have a huge impact on the formation of the chain. Second, supply chain management means increasing efficiency and reducing costs throughout the system. By applying the approaches in supply chain management, the cost of the whole system which includes transportation costs, inventory, material handling, etc. is reduced; Therefore, the purpose of designing a supply chain is to increase efficiency and reduce costs in the whole system but the emphasis is not only on reducing transportation costs, inventories, etc. but also on supply chain management using a device approach. It tries to improve the efficiency of the whole chain and also increase the level of customer service. In fact, customer satisfaction should be

*Corresponding Author Email: sh.hosseini@shahroodut.ac.ir (S. M. H. Hosseini)

Please cite this article as: M. Aghaei Afshar, S. M. H. Hosseini, R. Sahraeian, A Bi-objective Cold Supply Chain for Perishable Products Considering Quality Aspects: A Case Study in Iran Dairy Sector, ***International Journal of Engineering, Transactions B: Applications***, Vol. 35, No. 2, (2021) 458-470

considered in the supply chain which can include customer satisfaction with the quality of products and services provided.

The purpose of this study is to create a comprehensive and integrated model for supply chain planning that simultaneously increases the efficiency of the chain and on the other hand to meets the needs of customers effectively. For this purpose, two objectives have been considered for the above supply chain. The first objective function is to minimize the costs of the entire supply chain and the second one is to maximize the quality of the entire supply chain. The first objective focuses on supply chain efficiency while the second one is related to customer satisfaction.

For the supply chain costs, in addition to the tangible costs considered in most studies, intangible costs such as producer quality costs are considered as a very important cost factor that is by no means negligible.

In this study, quality costs are considered in three groups of costs of prevention, appraisement, and failure. In addition to the cost of quality of the manufacturer, the cost of quality of raw materials imposed by suppliers on the supply chain and the cost of quality of service are included in the total cost of the supply chain.

As mentioned above, in addition to minimizing the total cost of the entire supply chain, this article focuses on customer satisfaction which is a prominent advantage in today's competitive world. Customer satisfaction is achieved by providing both of products and quality services. Therefore, the function of the second objective proposed in this study is to maximize quality in the whole supply chain. In this regard, the quality of suppliers, manufacturers, and distributors are considered. Supplier quality includes the quality of raw materials provided by the supplier and the time of delivery of raw materials from suppliers to the manufacturer. Producer quality is expressed as a percentage of conforming units produced. Finally, the quality of service of distribution centers and the time of delivery of goods from the distributor to customers are also considered as quality factors for the distributor. To express the manufacturer's satisfaction with suppliers as well as customers with distributors which is obtained through the quality provided by them, the Huff model [1] is used after customizing for the problem at hand. So far, the Huff model is used only in the field of location.

In general, this paper deals with the design of a four-echelon supply chain consisting of suppliers, manufacturers, distributors, and customers and provides a comprehensive model for the supply chain that minimizes total costs and as well as maximizes quality simultaneously. In the proposed model, supplier selection and multi-period planning are considered which adds to the comprehensiveness of the above model due to the four-echelon supply chain and its complexity.

So far, there have been very few studies that have included quality aspects in supply chain design, and the existing research has considered all aspects of quality cost (prevention, evaluation, failure). In addition, the cost of suppliers quality and the cost of service quality of distribution centers are considered as a function of the cost objective, which is the first time these two cost elements have been used in this way in chains.

According to the abovementioned explanations, the contribution of the article can be introduced as follows:

- Introducing the four-echelon cold supply chain for perishable products considering quality aspects
- Formulating the problem at hand, as a bi-objective mathematical model
- Proposed a solution approach based on reaching the destination technique
- Investigating performance of the proposed model and solution approach in tackling the problem using data of a real case study
- Risk assessment of economic variables such as inflation and demand is sensitively analysed.

The outline of the paper is as follows. Section 2 is devoted to the survey of works related to this article. The problem at hand is described completely in section 3 and formulated as a bi-objective mathematical model. In section 4, a solution approach is developed to solve the proposed problem with real-sized scales. The considered case study is illustrated in section 5. Section 6 provides the result of solving the problem and some sensitivity analysis. Finally, a summary of the work and a conclusion with some suggestions for future research are given in section 7.

2. RELATED STUDIES

Supply chain design was first introduced in 1974 by Geffrin and Graves. They created a multi-product logistics network design model to optimize the flow of goods produced to distribution centers. Since then, extensive research has been conducted in the field of supply chain design [2]. Most supply chain design issues that minimize total cost do not take into account the cost of quality, which can be used as an indicator of quality and used in these articles, and so far only a handful of articles. They considered the cost of quality in their supply chain.

A review of the research literature shows that in the past, most supply chain articles had single-objective models. Some of the objectives which researchers have considered as a function of the supply chain goal are: minimizing the total cost of commissioning, minimizing the longest distance between facilities, maximizing customer service, minimizing the average time/distance traveled, minimizing the number of established facilities, and maximizing the customer responsiveness. In the following, a summary of research in the field of supply chain considering the quality issues is presented.

Franca et al. [3] considered the cost of quality as a function of the second objective. Their model includes

maximizing profits and minimizing the defective produced items as two objective functions. However, the discussion of the cost of quality has not been explicitly examined in their study [3]. Many studies have paid attention to the issue of quality and aimed to maintain the quality supply chain due to its complexity. Some of them have been looking for factors that can maintain and enhance quality in the supply chain. Supply chain coordination [4, 5,6], application of technology [7, 8], risk management [9], [10], and ensuring reliability [11, 12] are elements that have been paid attention in previous studies.

Two important aspects of quality are product quality and service quality. It is vital in the nowadays competitive marketing environment to produce products and services that exceed customer expectations and requirements. The emphasis on increasing the quality of products and services by companies has increased in response to the highly competitive environment. In other words, product and service quality are known as the main principles for the success and survival of today's competitive market. In each part of the supply chain, the quality of products and services must be considered, that is, each of the suppliers, manufacturers, and distributors must pay attention to issues that increase the quality of products and services and ultimately customer satisfaction [13].

Efficiency mechanisms for customer service have been reviewed in a variety of articles [14, 15]. In fact, retailers in a supply chain focus on activities and operations that differentiate them from their competitors. Therefore, they invest in service quality as a tool to improve the efficiency of the entire supply chain.

Hsieh et al. [16] dealt with the problem of supply chain network design consisting of one manufacturer and one supplier, and the inspection and production processes of this chain have quality problems and shortcomings. Both manufacturers and suppliers have invested in quality improvement activities in their production processes to reduce the production of defective items. In addition to investing in quality programs, the supplier inspects once before delivering his product to the manufacturer, and the manufacturer inspects twice, once when receiving products from the supplier and once when delivering the final product to customers. They investigated the quality and inspection strategies of the manufacturer and supplier based on the game theory technique and examined their profitability under different conditions [16].

One of the new topics that have been considered recently in the supply chain is the cold chain. A review of the most recent and relevant researches on the cold chain which applied quantities techniques is presented below.

Mendes and Matheus offered an analysis and optimization model of periodic inspection intervals in cold standby systems using Monte Carlo simulation. They developed a Monte Carlo simulation model to examine and optimize the time interval among periodic inspections in cold standby systems as the required availability and the deepest cost possible [17]. Mejjaouli and Babiceanu designed a cold supply chain system optimization model for real-time rerouting transportation solutions. They provided insights into the logistics decision models related to the cold supply chain of fresh products [18]. Zhang et al. [19] designed a decision-making framework of a regional cold chain logistics systemin view of low-carbon low-cost. They proposed a decision-making model of a cold chain logistics system based on the method of two-stage programming.. Qin et al. presented a Vehicle Routing Optimization Problem for Cold Chain Logistics Considering Customer Satisfaction and Carbon Emissions. Their study proposes a comprehensive cold chain vehicle routing problem optimization model with the objective function of minimizing the cost of a unit satisfied customer. For customer satisfaction, this paper uses the punctuality of delivery as the evaluation standard. For carbon emissions, this paper introduces the carbon trading mechanism to calculate carbon emissions costs.

Zhang et al. [20] presented a low-carbon cold chain logistics using a ribonucleic acid-ant colony optimization algorithm. Their study aims to introduce the low-carbon economy into cold chain logistics. There are various costs needed to be considered in cold chain logistics, and a cold chain logistics route optimization model included the carbon emission cost was developed [21].

Goodarzian et al. [22] designed a Multi-objective Sustainable Medicine Supply Chain Network Design using a Novel Hybrid Multi-objective Metaheuristic Algorithm. In their study, they developed sustainable objectives in the supply chain optimization framework with different constraints. The trade-off between economic, environmental, and social effects objectives has been identified by ensuring the optimal allocation of different products among various levels. In this regard, a new sustainability multi-objective mixed-integer linear programming mathematical model in the medicine supply chain network is developed.

Theeb et al. [23] presented an optimization model for vehicle routing with inventory allocation problems in cold supply chain logistics. The joint optimization model in their study consists of inventory allocation problem, vehicle routing problem, and cold supply chain (CSC) that is formulated and denoted as IVRPCSC model, to minimize the total cost including the transportation and inventory costs. As the proposed model is NP-hard, a multi-phases solution approach is designed to solve the model in a reasonable computational effort. Qi, Chengming, and Lishuan Hu [24] presented a new optimization model for vehicle routing problems for emergency cold chain logistics based on minimum loss. In this study, the proposed optimization model adjusts the pheromone updating strategy adaptively which can balance the convergence rate and diversification of solutions. Shafiee et al. [25] presented a robust multi-

objective optimization model for inventory and production management considering both environmental and social aspects with a real case of the dairy industry. Their research is about designing a three-echelon sustainable dairy supply chain under uncertainty. In addition, a multi-objective model is proposed to minimize the total costs and environmental impacts, and maximize the social impacts of a multi-period and multi-product chain composed of suppliers, producers, and retailers, which is applied to a dairy company. The delivery time and the first-in, first-out (FIFO) policy of the products are of particular importance in the proposed model. Theophilus et al. [26] presented a truck scheduling optimization at a cold-chain cross-docking terminal with product perishability considerations. Their study introduces a novel mixed-integer mathematical formulation for the truck scheduling optimization at a cold-chain CDT for the first time. Their considered objective function minimizes the total cost incurred during the truck service. Considering the complexity of the proposed model, a customized Evolutionary Algorithm (EA) is developed to solve the problem at hand with practical dimensions. The computational performance of the developed algorithm is assessed throughout the numerical experiments based on a detailed comparative analysis against the other metaheuristics. A set of additional sensitivity analyses are performed in order to provide some significant managerial implications, which would be of potential interest to the supply chain stakeholders that are involved in the distribution of perishable products in cold supply chains.

Wang et al. [27] developed a model to achieve a win-win scenario between cost and customer satisfaction for cold chain logistics. They focused on the customers' time requirements and establishes the penalty costs incurred when service time requirements are not met. In addition, in this paper combines different aspects, such as considering the refrigeration energy consumption and the damage costs.

TABLE 1. Comparison contributions on the problem of cold supply chain network design.

Reference	Main features				Objective functions					Case study	Solution approach
	Multi-period	Multi-product	Perishable products	Uncertainty	Cost	Time	Quality	Environmental impact	Social impact		
Ahmadi-Javid, and Hoseinpour [13]	✓		✓		✓						MINLP, Lagrangian relaxation
Saif and Elhedhli [28]		✓			✓			✓			MINLP, Simulation, Lagrangian decomposition
Hariga et al. [29]		✓	✓		✓			✓			MIP, Heuristic
Mejjaouli and Babiceanu [18]		✓	✓	✓	✓		✓			✓	RFID-WSN
Zhang et al. [19]	✓	✓			✓			✓	✓	✓	Bilevel programming (BLPM)-CSPO
Babagolzadeh et al. [30]		✓	✓	✓	✓			✓		✓	stochastic programming, Iterated Local Search (ILS)
Qi, and Hu [24]	✓		✓	✓	✓		✓				Heuristic based on Baidu map (API)
Shafiee et al. [25]	✓		✓	✓	✓	✓			✓	✓	Robust optimization, augmented ε-constraint
Theophilus et al. [26]	✓	✓			✓						MIP, Evolutionary Algorithm
Li and Zhou (2021) [31]		✓			✓	✓		✓			MIP, NSGA-II
Fasihi et al. [32]	✓		✓		✓	✓				✓	ε-constraint, Lp-metric
This study	✓	✓	✓	✓	✓	✓	✓			✓	MINLP-Parametric method (weighted)

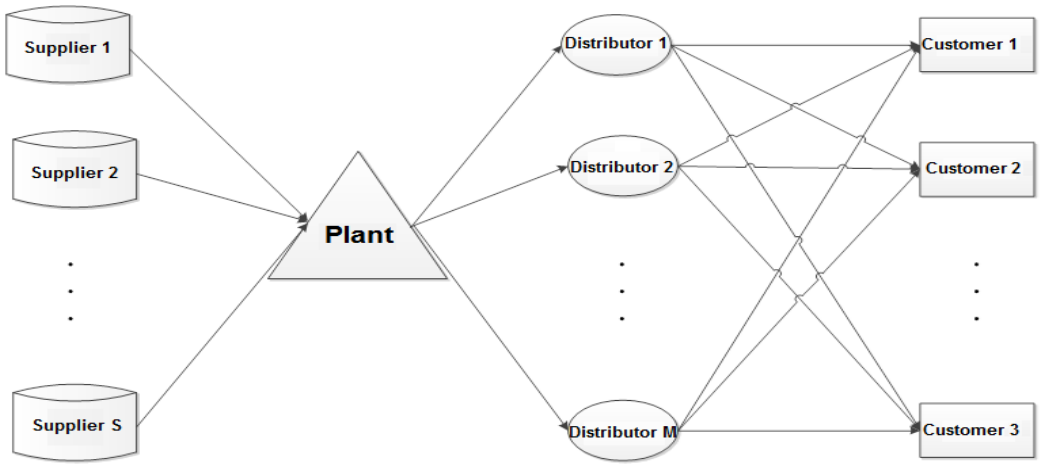

Figure 1. Proposed supply chain structure

Zhao et al. [33] presented a metaheuristics for solving the vehicle routing problem with the time windows and energy consumption in cold chain logistics. The objective of this study is to minimize the total cost including the fixed cost and the energy consumptions. An improved artificial fish swarm (IAFS) algorithm is proposed, where a special encoding approach is designed to consider the problem feature with a different types ofvehicles. Zhao et al. [33] presented a cold chain logistics path optimization via an improved multi-objective ant colony algorithm. In order to improve the performance and change the current situation of the cost minimization model widely used in the cold chain logistics distribution process, a multi-objective optimization model based on cost, carbon emissions, and customer satisfaction are proposed. Ji et al. [34] presented a robust optimization approach to two-echelon agricultural cold chain logistics considering carbon emission and stochastic demand. In this paper, a linear programming (LP) model is established, which takes the costs of vehicle transportation, time window, and carbon emission into consideration. The findings of this paper generate some implications for the low-carbon transformation of cold chain logistics enterprises [35].

Li and Zhou [31] designed Multi-objective cold chain logistic distribution center location based on carbon emission. This study presents the impact of carbon emission, customer satisfaction, construction cost, and operation cost on the location of cold chain logistics distribution center. A multi-objective location model for the cold chain logistics distribution centers considering carbon emission is established.

Fasihi et al. [32] developed a Bi-objective mathematical model to design a fish closed-loop supply chain. They tackled this problem to maximize responsiveness to customer demand and minimize the total cost of the fish closed-loop supply chain (CLSC) by proposing a novel mathematical model. To solve this model, the epsilon-constraint method and Lp-metric were employed. Then, the solution methods were compared with each other based on the performance metrics and a statistical hypothesis. The superior method is ultimately determined using the TOPSIS method.

Table 1 represents a summary of previous contributions of the existing literature related to this study's considered problem and novelty. As it is depicted in the table, the issue of quality in a cold supply chain network design such as the cost of quality related to suppliers and the cost of distribution service quality never have been faced by literature so far. Moreover, the quality of suppliers, manufacturers, and distributors is simultaneously considered in this study throughout a supply chain with a new approach.

3. PROBLEM DESCRIPTION

This study investigates the problem of four-echelon cold supply chain network design considering the quality aspects. Figure 1 represents a schematic view of the considered problem in this study. The problem at hand is a four-echelon cold supply chain including some suppliers, the main factory, some distributors, and several points as customers.

After problem definition, a bi-objective model is developed in this section for the problem at hand to optimize both the total cost as well as the quality of the performance. The first objective function is to minimize the total expected cost consisting of the following elements:

- The cost of purchasing raw materials and parts from suppliers
- The cost of processing raw materials (production cost) in the factory
- The cost of transporting raw material, parts, and final products from different suppliers to the factory, from the factory to distribution centers, and from distribution centers to customers
- The inventory costs

- The cost of quality (prevention, appraisement, and failure)
- The cost of documentation and return the low-quality raw materials and parts
- The cost of follow up complaints from suppliers related to the low-quality raw materials and parts

The second objective function is to maximize the quality of the performance and related satisfaction. Supply chain quality and satisfaction includes the following items:

- The factory satisfaction with the quality of suppliers (quality of raw materials and parts and how it is delivered by suppliers to the factory)
- The customer satisfaction with the performance of the distribution centers (services quality and on-time delivery)
- The quality of the final products

As is evident in the existing literature, the higher the number of supply chain echelons, the less multi-cycle planning is used due to the complexity of the chain. But in this study, a multi-period planning horizon is used for the proposed four-echelon cold supply chain, which increases the complexity and comprehensiveness of the proposed model.

Given the gap in the supply chain literature, first a comprehensive model is developed that covers all considered features of the problem. After that, a solution approach is developed to solve the problem with practical dimensions in a reasonable time.

To formulate the problem at hand, first, the indices, parameters, and decision variables are defined as follows:

Indices	
$s = 1, 2, \dots, S$	Index for suppliers (potential suppliers)
$c = 1, 2, \dots, C$	Index for customers
$r = 1, 2, \dots, R$	Index for raw materials
$u = 1, 2, \dots, U$	Index for service quality options
$t = 1, 2, \dots, T$	Index for time periods
$p = 1, 2, \dots, P$	Index for suppliers to supply raw materials
$j = 1, 2, \dots, J$	Index for distribution centers

Parameters

CP_{rst}	The cost of purchasing raw material r from supplier s in period t
CM_t	Raw material processing cost (production cost) in period t
CA_{ju}	The cost of service quality in distribution centre j related to option u
Q_u	The quality level related to service option u
D_{ct}	Demand of customer demand c in the period t
CAP	The maximum of production capacity per time period
$CAPS_s$	The maximum capacity of supplier s in each time period
$CAPDC_j$	The maximum capacity of distribution centre j in each time period
Vol_r	The amount of volume occupied by the raw material r
U_r	The amount of raw material r used in the production of the product
W_r	The important of material r in production
y_{rs}^{s}	Defective rate of material r provided by supplier s
α_s	The cost of transporting raw material from the supplier s to the factory
β_j	The cost of transporting product from the factory to the distribution center j
γ_{jc}	The cost of transporting product from the distribution center j to customer c
h_j	The cost of holding one product in the distribution center j during a unit time
C_1	The minimum cost of prevention and appraisal that occur in the least quality level
C_2	The minimum cost of failure that occurs in the maximum quality level
e^{μ_1}	The rate of increasing the cost of prevention and appraisal
e^{μ_2}	The rate of increasing the cost of failure
U^{PD}	Maximum product transfer rate from the factory to each distributed center
L^{PD}	Minimum product transfer rate from the factory to each distributed center
U^{DC}	Maximum product transfer rate from each distributed center to each customer
L^{DC}	Minimum product transfer rate from each distributed center to each customer
d_s^2	Distance between supplier s to the factory
dP_j^2	Distance between the factory to distributed center j
dD_{jc}^2	Distance between distributed center j to customer c
θ	The cost of documentation with any defective material
δ	The cost of complaint for any defective material
Ω	The cost of inspection of any material unit
λ	The inflation rate
φ_1	The modification factor of suppliers' quality function to unify it with other quality functions
φ_2	The modification factor of factory quality function to unify it with other quality functions
φ_3	The modification factor of distribution centre's quality function to unify it with other quality functions
M	A very large number

Decision variables

b_{rst}	The amount of raw material r shipped from supplier s to the factory in period t
x_t^P	The amount of product produced in the factory in period t
x_{jt}^{PD}	The amount of product shipped from the factory to the distribution center j in period t
x_{jct}^{DC}	The amount of product shipped from the distribution center j to the customer c in period t
y^P	Percentage of defective products in the factory
I_{jt}	The amount of inventory in the distribution center j during period t
V_{ju}	Binary variable takes value 1 If option u is selected for the service quality of distribution center j; 0 otherwise
S_{jt}^{PD}	Binary variable takes value 1 If the factory transports the product to the distribution center j in period t; 0 otherwise
SN_{jt}^{PD}	1 If the product is not shipped from the factory to the distribution center j in period t; 0 otherwise
S_{jct}^{DC}	Binary variable takes value 1 If the product is shipped from the distribution center j to customer c in period t; 0 otherwise
SN_{jct}^{DC}	1 If the product is not shipped from distribution center j to customer c in period t; 0 otherwise

Finally, the mathematical model of the problem at hand is developed as follows:

$$\begin{aligned} Z_1 = Min\ & \sum_{r=1}^{R}\sum_{s=1}^{S}\sum_{t=1}^{T} CP_{rst}.(1+\lambda)^{t-1}.b_{rst} + \\ & \sum_{r=1}^{R}\sum_{s=1}^{S}\sum_{t=1}^{T} \alpha_s.d_s^2.(1+\lambda)^{t-1}.b_{rst} + \\ & \sum_{t=1}^{T} CM_t.(1+\lambda)^{t-1}.x_t^p + \sum_{j=1}^{J}\sum_{t=1}^{T} \beta_j.dP_j^2.(1+\lambda)^{t-1}.x_{jt}^{PD} + \sum_{j=1}^{J}\sum_{t=1}^{T} h_j.(1+\lambda)^{t-1}.I_{jt} + \\ & \sum_{j=1}^{J}\sum_{c=1}^{C}\sum_{t=1}^{T} \gamma_{jc}.dD_{jc}^2.(1+\lambda)^{t-1}.x_{jct}^{DC} + \\ & \sum_{t=1}^{T}\left(c_1.e^{\mu_1\left(\frac{1-y^p}{y^p}\right)} + c_2.e^{\mu_2\left(\frac{1-y^p}{y^p}\right)}\right).(1+\lambda)^{t-1}.x_t^p + \\ & \sum_{r=1}^{R}\sum_{s=1}^{S}\sum_{t=1}^{T}(\theta+\alpha_s.d_s^2).(1+\lambda)^{t-1}.y_{rs}^s.b_{rst} + \\ & \sum_{r=1}^{R}\sum_{s=1}^{S}\sum_{t=1}^{T}\delta.(1+\lambda)^{t-1}.y_{rs}^s.b_{rst} + \\ & \sum_{r=1}^{R}\sum_{s=1}^{S}\sum_{t=1}^{T}\Omega.(1+\lambda)^{t-1}.b_{rst} + \\ & \sum_{j=1}^{J}\sum_{u=1}^{U} CA_{ju}.V_{ju} \end{aligned} \quad (1)$$

$$\begin{aligned} Z_2 = Max\Bigg(& \varphi_1 \sum_{s=1}^{S}\sum_{t=1}^{T}\left(\frac{1}{1+d_s^2}\right).\left(\prod_{r=1}^{R}(1-y_{rs}^s)^{w_r}\right).\left(\frac{\sum_r^R b_{rst}}{\sum_s^S\sum_r^R b_{rst}}\right) + \\ & \left(\varphi_2 \sum_{j=1}^{j}\sum_{c=1}^{C}\sum_{t=1}^{T}\sum_{u=1}^{U}\left(\frac{Q_u.V_{ju}}{1+dD_{jc}^2}\right).\left(\frac{x_{jct}^{DC}}{D_{ct}}\right)\right) + \\ & \left(\varphi_3(1-y^P)\right)\Bigg) \end{aligned} \quad (2)$$

$$\sum_{j=1}^{J} x_{jct}^{DC} = D_{ct} \qquad \forall\ C\ and\ t \qquad (3)$$

$$I_{jt} = I_{jt-1} + x_{jt}^{PD} - \sum_{c=1}^{C} x_{jct}^{DC} \qquad \forall\ j\ and\ t \qquad (4)$$

$$x_t^P \le CAP \qquad \forall\ t \qquad (5)$$

$$I_{jt} \le CAPDC_j \qquad \forall\ j\ and\ t \qquad (6)$$

$$\sum_{r=1}^{R} Vol_r.b_{rst} \le CAPS_{ss}.zz_s \qquad \forall\ s\ and\ t \qquad (7)$$

$$U_r.x_t^p = \sum_{s=1}^{S} b_{rst}.(1-y_{rs}^s) \qquad \forall\ r\ and\ t \qquad (8)$$

$$\sum_{j=1}^{J} x_{jt}^{PD} = (1-y^p).x_t^p \qquad \forall\ t \qquad (9)$$

$$x_{jt}^{PD} \le U^{PD}.S_{jt}^{PD} \qquad \forall\ j\ and\ t \qquad (10)$$

$$x_{jt}^{PD} \ge L^{PD} - M.SN_{jt}^{PD} \qquad \forall\ j\ and\ t \qquad (11)$$

$$S_{jt}^{PD} + SN_{jt}^{PD} = 1 \qquad \forall\ j\ and\ t \qquad (12)$$

$$x_{jct}^{DC} \le U^{DC}.S_{jct}^{DC} \qquad \forall\ j,c\ and\ t \qquad (13)$$

$$x_{jct}^{DC} \ge L^{DC} - M.SN_{jct}^{DC} \qquad \forall\ j,c\ and\ t \qquad (14)$$

$$S_{jct}^{DC} + SN_{jct}^{DC} = 1 \qquad \forall\ j,c\ and\ t \qquad (15)$$

$$\sum_{s=1}^{S} zz_{s=\rho} \qquad (16)$$

$$\sum_{u=1}^{U} V_{ju} = 1 \qquad \forall\ j \qquad (17)$$

$$b_{rst}, x_t^P, x_{jt}^{PD}, x_{jct}^{DC}, y^P, I_{jt} \ge 0 \qquad \forall\ r,s,j,c\ and\ t \qquad (18)$$

$$zz_s, S_{jt}^{PD}, SN_{jt}^{PD}, S_{jct}^{DC}, SN_{jct}^{DC} \in \{0,1\} \qquad \forall\ r,s,j,c\ and\ t \qquad (19)$$

3. 1. Objective Functions The first objective function calculated as Equation (1) includes the following elements respectively. Term 1 demonstrates the total cost of purchasing raw materials from suppliers. Term 2 is related to the cost of transporting raw materials from suppliers to the factory. Term 3 highlights the cost of producing the product in all periods, taking into account the inflation rate. Term 4 states the cost of transporting products produced from the factory to distribution centers. Term 5 shows the total cost of maintaining the remaining products at the end of each period, taking into account the time value of money. Term 6 considers the distance between the distribution center j from the customer c. The amount of product shipped from the distribution center j to customer c in period t. Terms 7 and 8 show costs of failure assessment (cost of quality products produced in all periods), or processing. Term 9 shows the cost of documenting and referring defective raw materials. Term 10 demonstrates the cost of reviewing complaints from suppliers. Finally, term 11 shows the cost of the raw material inspection.

The second objective function calculated as Equation (2) includes the following elements respectively. Term 1 shows the plant satisfaction with supplier s if it supplies all the required raw materials in p certain period. Term 2 demonstrates customer satisfaction from distribution centers in all periods. Finally, term 3 indicates the quality of manufactured products.

3. 2. Constraints Constraints include the following in respectively: Equation (3) ensures that the demand of customer c in period t is satisfied completely. Equation (4) states that in each period, the amount of inventory at the end of the period of each distribution center is equal to the sum of the inventory value at the end of the previous period and the amount received by those centers from the factory in this period mins the number of goods in this period from the distribution center for different customers. Equations (5) to (7) are required due to capacity limitations of the production process. Moreover, these Equations guarantee that in each period, the amount of inventory at the end of the period of each distribution center should not exceed the maximum capacity of that distribution center. This is also true for suppliers. In addition, each supplier has a limited

capacity due to the volume occupied by raw materials. Equation (8) ensures that the number of raw materials used in the production of a particular product is equal to the percentage of conforming raw materials supplied from that raw material by all suppliers. Equation (9) shows that the total number of products that arrive from the factory to the distribution centers is equal to the conforming units produced by the factory. Equations (10) to (12) indicate that the transfer of products from the factory to the distribution centers. Equations (13) to (15) guarantee that from each distribution center to a specific customer if the goods are to be delivered, at least more than a certain amount. The reason for these constraints is to avoid delivering very small quantities of goods, despite being optimal, which in these circumstances does not seem logical to transport due to the delivery of very small quantities of goods. For this purpose, a set of the above-mentioned restrictions is formed. Also, the goods can be delivered to a customer from each distribution center up to a certain size. Equation (16) emphasizes that the number of suppliers is specified and is equal to ρ. Equation (17) enforces that only one service quality option should be selected for each distribution center. Finally, Equations (18) and (19) specify the domains of the decision variables.

4. SOLUTION APPROACH

The technique of reaching the destination that is used in this study to solve the considered problem is one of the multi-objective decision-making techniques in which the preferential information of the decision maker is obtained before solving the model. This method requires the decision maker to provide the destination vector as well as the weight vector depending on the level of access to those destinations. In this method, the optimal solution which is the same as the partial optimal solution of the original model directly depends on the destination vector and the weight vector given by the decision maker.

One of the advantages of this technique, compared to other multi-objective decision-making techniques, is that, unlike interactive methods, fewer variables are required and solved in one step, which is a very computationally wide method. Althought this method was introduced in classic form to solve k maximization or minimization objective functions simultaneously, it has been developed for solving models consisting of both maximization and minimization objective functions simultaneously [36].

Since the proposed model consists of one maximization objective function and one minimization objective function, this technique is used as bellow to solve the problem:

$$\text{Min } Z = (\propto . Z_1 - (1 - \alpha) . Z_2)$$

Wherein,

$$0 \leq \propto \leq 1$$

In addition, augmented $\varepsilon-$constraint method (AUGMECON) is also used to provide the exact Pareto front solutions as different alternatives for decision makers.

5. CASE STUDY

In this section, a real case study with medium dimensions is presented and solved with the proposed mathematical model. We have investigated the Kaleh Dairy Products Company as an appropriate instance for the proposed problem. This example is solved using two approaches of reaching the destination (the so-called as parametric and weighted) and augmented $\varepsilon-$constraint method (AUGMECON) and run in GAMS. The Baron solver was used to find the exact Pareto front. All calculations and result in analyses were carried out on a PC running at Intel Core i5-4210U 2.4GHz CPU and 4GB RAM.

Kaleh Dairy Products Company is one of the subsidiaries of Soliko Group which was established in 1991. Over the years, the company has expanded greatly in various aspects of production capacity, quality, variety of products, global distribution network, and exports. Figure 2 represents a schematic view of this company's supply chain from receiving milk to sending the final products. The company currently has three business units of cheese, pasteurized products, and ultra high temeprature (UHT) that with its innovation, offers the highest quality and most diverse products in the high production volume. All factory production lines are flexibly designed so that the raw materials of different inputs enter the production line and various products leave. So that more than 20 products are sometimes produced through only one production line. Kaleh currently provides more than 160 different kinds of dairy products, which will be doubled in the near future in development plans.

We have considered 19 key suppliers, the planet, 2 main distributors, and 4 large chain stores as important customers. Summary information of these suppliers, distributors, and customers are shown in Tables 2 and 3.

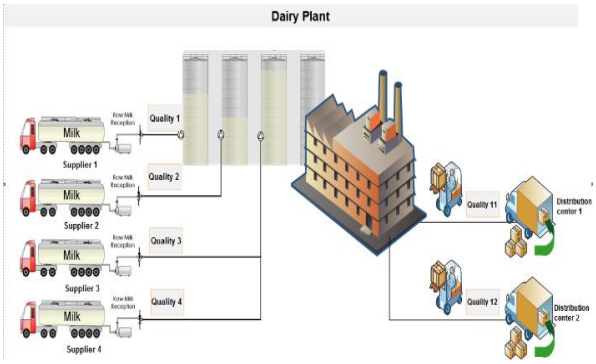

Figure 2. Receiving milk and sending the product in Dairy Products Company

TABLE 2. Data of suppliers

Supplier code	Distance (km)	Supply amount (Ton/Year)
S-1	744	5957
S-2	564	7762.8
S-3	644	8955.3
S-4	432	4304.2
S-5	159	1339
S-6	95	308.4
S-7	81	4936.9
S-8	256	15088.1
S-9	186	7942.8
S-10	186	4570.4
S-11	186	16541.6
S-12	186	2156.2
S-13	186	11032.5
S-14	1094	6395.4
S-15	336	3011.9
S-16	336	9912.2
S-17	336	7898.1
S-18	370	3282.2
S-19	370	4218.1

TABLE 3. Data of distributed centers

Distributers code	Distance from the plant	Related customers	Distance from the customer
D-1	212	C-1	42.1
		C-2	21.4
D-2	640	C-3	7.7
		C-4	4.3

Other characteristics of the case study are as follows: Factory production capacity is 9000 units, the values of β and γ are 0.03 and 0.04 monetary units respectively (each monetary unit is considered equal to 10^7 Iranian Rial). The annual inflation rate is equal to 10%. The upper bound and the lower bound of shipment from distributers centers to customers are considered 4000 and 100 respectively. Moreover, the upper bound and the lower bound of shipment from the factory to distributer centers are assumed as 3800 and 30 respectively. Distribution centers capacity is also 10000.

Production cost per unit s 0.04 monetary unit. In addition, the values of θ, δ, and Ω are 0.002, 0.001, and 0.003 monetary unit respectively. Correction coefficients of quality control functions are considered as 300, 50, and 1000 for suppliers, factories, and distribution centers respectively. Cost of transporting materials from supplier i to factory is demonstrated as α_i per unit distance. Furthermore, four different kinds of vehicles are available for transportation with different cost and capacities. The remain of data used in this case study has been obtained from the company site[1].

6. FINDINGS

6. 1. Result of Problem Solving This section presents the result analysis of solving these problems using the proposed mathematical model. The problem has been solved on a PC with COMPILATION TIME = 0.016 SECONDS 4 MB 24.1.3 r41464 WIN-VS8. Table 4 demonstrates the result of solving the problem with different values of α.

In this table, the first column shows the case number created using different values of α. The second and third columns demonstrate weights of two objective functions according to the different values of α. The fourth and the fifth columns show the optimal solutions for the first and the second objective function respectively obtained by solving the mathematical model. Finally, the last column shows the optimal rate of defective products.

Figure 3 represents the Pareto front of final solutions for the problem. Due to this figure, the model has provided

TABLE 4. Solution results with different values of alpha

Case	α	$1-\alpha$	Z_1	Z_2	y^p
1	1	0	60,236,010	-	0.041
2	0.99	0.01	57,030,945	3,450,560	0.021
3	0.9	0.1	62,665,456	16,273,504	0.045
4	0.9	0.1	63,665,456	44,522,304	0.031
5	0.9	0.1	64,665,456	66,297,904	0.021
6	0.8	0.2	66,556,987	28,957,348	0.035
7	0.6	0.4	67,564,958	10,762,312	0.042
8	0.5	0.5	68,546,235	8,156,475	0.042
9	0.4	0.6	71,002,564	7,075,526	0.042
10	0.3	0.7	72,356,214	5,062,549	0.043
11	0.2	0.8	74,256,325	3,467,381	0.042
12	0.1	0.9	75,659,125	1,680,228	0.043
13	0.1	0.96	76,256,124	1,604,948	0.043
14	0.05	0.95	126,820,064	800,256	0.029

[1] https://gb.kompass.com/c/amol-kaleh-dairy-products-mfg-p-j-s/ir036405/
https://en.wikipedia.org/wiki/Kalleh_Dairy

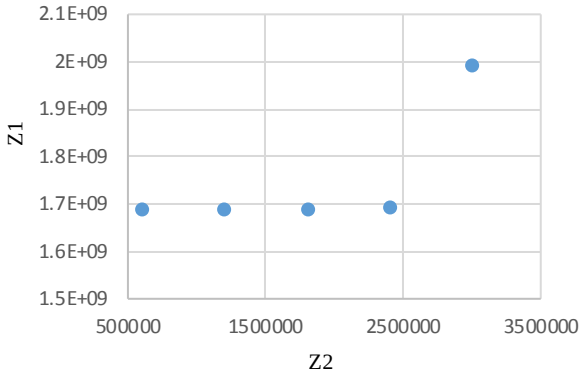

Figure 3. The Pareto optimal set for the numerical instance

five different solutions as options for choosing by decision makers. The trend of the first four points indicates that, although the second objective is improving, the total expected cost as the first objective function does not get worse significantly.

6. 2. Sensitivity Analysis In order to choose the proper strategy for the retailer, here we need to determine the impact of key parameters on the result. Therefore, in this section, the effect of four bellow key parameters on decision variables and objective functions are investigated:

The cost of purchasing raw material (cp);
The holding cost (h);
Number of Customer (C);
Elasticity of demand (α).

The results of model sensitivity analysis have been shown graphically as Figures 4 to 8 for uniform supply time mode. It is noteworthy that the weight of the first and second objective functions is considered equal to 0.6 and 0.4 respectively for sensitivity analysis. As can be seen, with increasing cost parameters (cp, h, C), the selling price will increase, the accumulated size will decrease, and as a result, the profit (Z^*) will increase due to the increase in selling price. As the elasticity of demand (α) increases, the accumulated size decreases because the more sensitive the commodity is to the selling price. The decline in demand will be more pronounced in the face of high prices. Changes in the resale point are also directly related to the service level.

In addition, changes in shortage costs will have the greatest impact on profit and service level, and the model is more sensitive to changes in shortage costs and purchase costs.

In addition, changes in shortage costs will have the greatest impact on profit and service level, and in determining the selling price, the model is more sensitive to changes in shortage costs and purchase costs. Given that the price is affected by the costs of purchase, maintenance, and shortage, in the present example the above parameters are considered equal.

The results show that the average accumulated size is also the level of customer service in a situation where supply time is exponentially distributed; It is higher, but in contrast to the amount of annual profit from the model with a uniform preparation time, is higher. In other words, if the retailer is looking to make more profit; A model with a uniform preparation time is proposed.

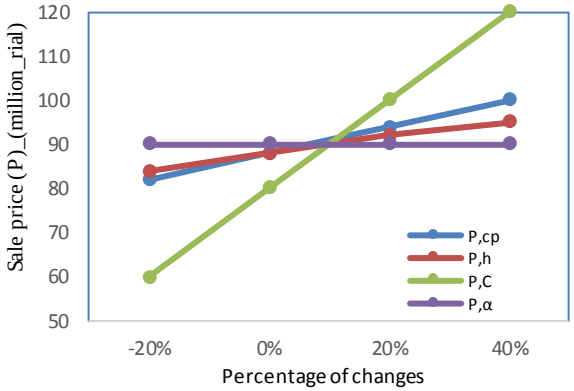

Figure 4. The sale price responding to changes in cp, h, C, and α

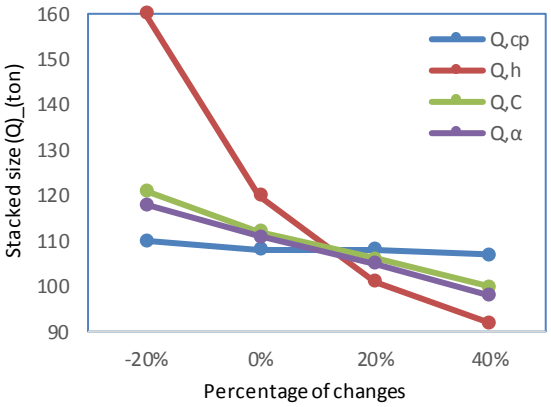

Figure 1. The Stacked size responding to changes in cp, h, C, and α

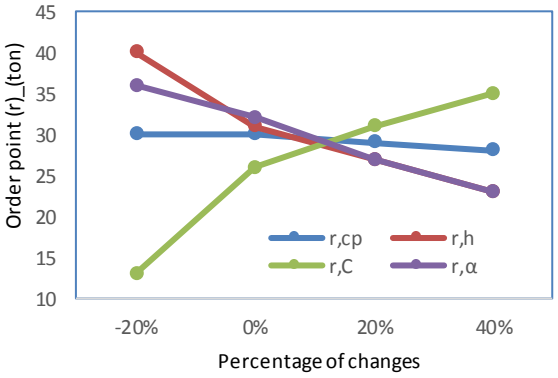

Figure 6. The order point responding to changes in cp, h, C, and α

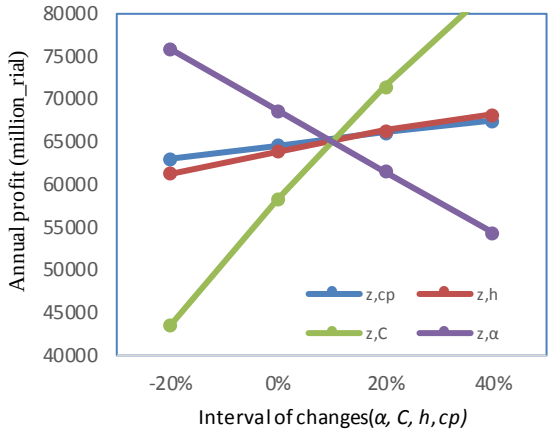

Figure 7. The annual profit responding to changes in cp, h, C, and α

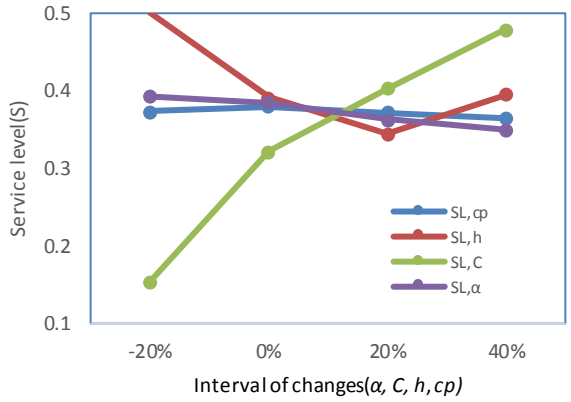

Figure 8. The service level responding to changes in cp, h, C, and α

6. 3. Managerial Insight The purpose of this study was to properly manage food cold supply chain for prevent of reducing food quality which the improper manage can lead to economic losses and undesirable effects on food accessibility. In addition, the proposed model can assist the food cold supply chain managers in making strategic decisions. According to conducted research in the field of food cold supply chain in Iran, it can be understood that despite many costs paid in this area and several facilities opened Iran has not reached its proper place in this field yet. In fact, if Iran can optimize costs and efforts in this area and have a proper food cold supply chain network, it is hoped that in recent years, it can improve its situation and be able to even provide a model for developing countries. In the following, some of the recommendations for food cold supply chain managers are presented to improve this chain in Iran:

- In order to be present in the international and even domestic arenas, quality control and cost management must be among the main goals of economic enterprises, because today the field of production is not only national and regional. Cost and standard costing policies alone cannot be responsible for product production and international integration and new methods such as activity-based costing and quality costing will be the solution to the problems of institutions in this field.
- For organizations that have a market development strategy, such as diversifying and increasing product production, supply chain management and using a quality costing approach is a vital requirement, because there is complete coordination between all the required activities that the operation helps to increase profitability.
- In order to produce in a timely manner and of course with appropriate quality, the product or service produced must be distributed in the right place and in a timely manner. Achieving this goal in order to create and expect customer satisfaction with the minimum cost and quality control costs at an acceptable level at the system level is a vital need.

7. CONCLUSION

The supply chain is the complete process of providing goods and services to the end consumer, and its management includes coordination between all activities required for an operation to increase profitability. In supply chain management, the goal is to optimize all the decisions that occur during this chain, and cost reduction is the driving force of supply chain management. Because the benefits of quality costs include lowering the cost of the product, creating greater competitiveness with competitors, investing and taking remedial steps to achieve more standard conditions, and the possibility of improving production, companies stay in the global competitive arena and produce products. Competing with cheaper and higher quality products of others, they need to use quality costing method and the present article has analyzed this field so that companies can have efficient management in the supply chain by using this costing method.

This study aimed to present an integrated and comprehensive model which greatly pays attention to important key factors of the efficiency and effectiveness in a cold supply chain. In the research, besides noticing comprehensively both supply chain quality and cost, an appropriate and comprehensive design is considered for four echelon supply chain consists of several suppliers, one manufacturing plant, different distribution centers and customers and the proposed model are used in a real world and can be customized a little in order to be applicable for other supply chain. In the supply chain costs include both tangible costs and intangible costs. Supplier Quality manufacture quality and distribution center quality are also considered. The proposed bi-objective model in changed by parametric optimization into the one objective function and solved by an exact solver for a numerical example (a

medium-sized problem) in the real condition. The computational results and the existed analysis represent the efficiency of the proposed model and the exact solution for small-sized scales.

8. REFERENCES

1. Huff, D.L., "Defining and estimating a trading area", ***Journal of Marketing***, Vol. 28, No. 3, (1964), 34-38, doi.org/10.1177/002224296402800307.
2. Geoffrion, A.M. and Graves, G.W., "Multicommodity distribution system design by benders decomposition", ***Management Science***, Vol. 20, No. 5, (1974), 822-844, doi.org/10.1287/mnsc.20.5.822.
3. Franca, R.B., Jones, E.C., Richards, C.N. and Carlson, J.P., "Multi-objective stochastic supply chain modeling to evaluate tradeoffs between profit and quality", ***International Journal of Production Economics***, Vol. 127, No. 2, (2010), 292-299, doi.org/10.1016/j.ijpe.2009.09.005.
4. Chao, G.H., Iravani, S.M. and Savaskan, R.C., "Quality improvement incentives and product recall cost sharing contracts", ***Management Science***, Vol. 55, No. 7, (2009), 1122-1138, doi.org/10.1287/mnsc.1090.1008.
5. Zhu, K., Zhang, R.Q. and Tsung, F., "Pushing quality improvement along supply chains", ***Management Science***, Vol. 53, No. 3, (2007), 421-436, doi.org/10.1287/mnsc.1060.0634.
6. Mohammadian, M., Babaei, M., Amin Jarrahi, M. and Anjomrouz, E., "Scheduling nurse shifts using goal programming based on nurse preferences: A case study in an emergency department", ***International Journal of Engineering, Transactions A: Basics***, Vol. 32, No. 7, (2019), 954-963, doi.org/10.5829/IJE.2019.32.07A.08.
7. Schiefer, G., "Computer support for tracking, tracing and quality assurance schemes in commodities", ***Journal für Verbraucherschutz und Lebensmittelsicherheit***, Vol. 1, No. 2, (2006), 92-96, doi.org/10.1007/s00003-006-0016-3.
8. Moradian, E., "Integrating web services and intelligent agents in supply chain for securing sensitive messages", in International Conference on Knowledge-Based and Intelligent Information and Engineering Systems, Springer. (2008), 771-778, doi.org/10.1007/978-3-540-85567-5_96.
9. Canbolat, Y.B., Gupta, G., Matera, S. and Chelst, K., "Analysing risk in sourcing design and manufacture of components and sub-systems to emerging markets", ***International Journal of Production Research***, Vol. 46, No. 18, (2008), 5145-5164, doi.org/10.1080/00207540701266807.
10. Wu, D.D. and Olson, D.L., "Enterprise risk management: Small business scorecard analysis", ***Production Planning and Control***, Vol. 20, No. 4, (2009), 362-369, doi.org/10.1080/09537280902843706.
11. Lin, C.-Y., "Determinants of the adoption of technological innovations by logistics service providers in china", ***International Journal of Technology Management & Sustainable Development***, Vol. 7, No. 1, (2008), 19-38, doi.org/10.1386/ijtm.7.1.19_1.
12. Kameli, A., Javadian, N. and Daghbandan, A., "Multi-period and multi-objective stock selection optimization model based on fuzzy interval approach", ***International Journal of Engineering, Transactions C: Aspects***, Vol. 32, No. 9, (2019), 1306-1311, doi.org/10.5829/IJE.2019.32.09C.11.
13. Ahmadi-Javid, A. and Hoseinpour, P., "A location-inventory-pricing model in a supply chain distribution network with price-sensitive demands and inventory-capacity constraints", ***Transportation Research Part E: Logistics and Transportation Review***, Vol. 82, (2015), 238-255
14. Hsu, C.C., Kannan, V.R., Tan, K.C. and Leong, G.K., "Information sharing, buyer-supplier relationships, and firm performance: A multi-region analysis", ***International Journal of Physical Distribution & Logistics Management***, (2008), doi.org/10.1108/09600030810875391.
15. Ren, Z.J. and Zhou, Y.-P., "Call center outsourcing: Coordinating staffing level and service quality", ***Management Science***, Vol. 54, No. 2, (2008), 369-383, doi.org/10.1287/mnsc.1070.0820.
16. Hsieh, C.-C. and Lu, Y.-T., "Manufacturer's return policy in a two-stage supply chain with two risk-averse retailers and random demand", ***European Journal of Operational Research***, Vol. 207, No. 1, (2010), 514-523, doi.org/10.1016/j.ejor.2010.04.026.
17. Mendes, A.A. and Lorenzoni, M.W., "Analysis and optimization of periodic inspection intervals in cold standby systems using monte carlo simulation", ***Journal of Manufacturing Systems***, Vol. 49, (2018), 121-130, doi.org/10.1016/j.jmsy.2018.09.006.
18. Mejjaouli, S. and Babiceanu, R.F., "Cold supply chain logistics: System optimization for real-time rerouting transportation solutions", ***Computers in Industry***, Vol. 95, (2018), 68-80, doi.org/10.1016/j.compind.2017.12.006.
19. Zhang, S., Chen, N., Song, X. and Yang, J., "Optimizing decision-making of regional cold chain logistics system in view of low-carbon economy", ***Transportation Research Part A: Policy and Practice***, Vol. 130, (2019), 844-857, doi.org/10.1016/j.tra.2019.10.004.
20. Qin, G., Tao, F. and Li, L., "A vehicle routing optimization problem for cold chain logistics considering customer satisfaction and carbon emissions", ***International Journal of Environmental Research and Public Health***, Vol. 16, No. 4, (2019), 576, doi.org/10.3390/ijerph16040576.
21. Zhang, L.-Y., Tseng, M.-L., Wang, C.-H., Xiao, C. and Fei, T., "Low-carbon cold chain logistics using ribonucleic acid-ant colony optimization algorithm", ***Journal of Cleaner Production***, Vol. 233, (2019), 169-180, doi.org/10.1016/j.jclepro.2019.05.306.
22. Goodarzian, F., Hosseini-Nasab, H. and Fakhrzad, M., "A multi-objective sustainable medicine supply chain network design using a novel hybrid multi-objective metaheuristic algorithm", ***International Journal of Engineering, Transactions A: Basics***, Vol. 33, No. 10, (2020), 1986-1995, doi.org/10.5829/IJE.2020.33.10A.17.
23. Al Theeb, N., Smadi, H.J., Al-Hawari, T.H. and Aljarrah, M.H., "Optimization of vehicle routing with inventory allocation problems in cold supply chain logistics", ***Computers & Industrial Engineering***, Vol. 142, (2020), 106341, doi.org/10.1016/j.cie.2020.106341.
24. Qi, C. and Hu, L., "Optimization of vehicle routing problem for emergency cold chain logistics based on minimum loss", ***Physical Communication***, Vol. 40, (2020), 101085, doi.org/10.1016/j.cie.2020.106341.
25. Shafiee, F., Kazemi, A., Chaghooshi, A.J., Sazvar, Z. and Mahdiraji, H.A., "A robust multi-objective optimization model for inventory and production management with environmental and social consideration: A real case of dairy industry", ***Journal of Cleaner Production***, Vol. 294, (2021), 126230, doi.org/10.1016/j.jclepro.2021.126230.
26. Theophilus, O., Dulebenets, M.A., Pasha, J., Lau, Y.-y., Fathollahi-Fard, A.M. and Mazaheri, A., "Truck scheduling optimization at a cold-chain cross-docking terminal with product perishability considerations", ***Computers & Industrial Engineering***, (2021), 107240, doi.org/10.1016/j.cie.2021.107240.
27. Wang, M., Wang, Y., Liu, W., Ma, Y., Xiang, L., Yang, Y. and Li, X., "How to achieve a win–win scenario between cost and customer satisfaction for cold chain logistics?", ***Physica A: Statistical Mechanics and its Applications***, Vol. 566, (2021), 125637, doi.org/10.1016/j.physa.2020.125637.
28. Saif, A. and Elhedhli, S., "Cold supply chain design with environmental considerations: A simulation-optimization

approach", ***European Journal of Operational Research***, Vol. 251, No. 1, (2016), 274-287, doi.org/10.1016/j.ejor.2015.10.056.

29. Hariga, M., As' ad, R. and Shamayleh, A., "Integrated economic and environmental models for a multi stage cold supply chain under carbon tax regulation", ***Journal of Cleaner Production***, Vol. 166, (2017), 1357-1371, doi.org/10.1016/j.jclepro.2017.08.105.
30. Babagolzadeh, M., Shrestha, A., Abbasi, B., Zhang, Y., Woodhead, A. and Zhang, A., "Sustainable cold supply chain management under demand uncertainty and carbon tax regulation", ***Transportation Research Part D: Transport and Environment***, Vol. 80, (2020), 102245, doi.org/10.1016/j.trd.2020.102245.
31. Li, X. and Zhou, K., "Multi-objective cold chain logistic distribution center location based on carbon emission", ***Environmental Science and Pollution Research***, (2021), 1-9, doi.org/10.1007/s11356-021-12992-w.
32. Fasihi, M., Tavakkoli-Moghaddam, R., Najafi, S.E. and Hajiaghaei-Keshteli, M., "Developing a bi-objective mathematical model to design the fish closed-loop supply chain", ***International Journal of Engineering, Transactions B: Applications***, Vol. 34, No. 5, (2021), 1257-1268. doi: 10.5829/ije.2021.34.05b.19
33. Zhao, B., Gui, H., Li, H. and Xue, J., "Cold chain logistics path optimization via improved multi-objective ant colony algorithm", ***IEEE Access***, Vol. 8, (2020), 142977-142995, doi.org/10.1109/ACCESS.2020.3013951.
34. Ji, Y., Du, J., Wu, X., Wu, Z., Qu, D. and Yang, D., "Robust optimization approach to two-echelon agricultural cold chain logistics considering carbon emission and stochastic demand", ***Environment, Development and Sustainability***, (2021), 1-24, doi.org/10.1007/s10668-021-01236-z.
35. Bai, X. and Liu, Y., "Robust optimization of supply chain network design in fuzzy decision system", ***Journal of Intelligent Manufacturing***, Vol. 27, No. 6, (2016), 1131-1149, doi.org/10.1007/s10845-014-0939-y.

Persian Abstract

چکیده

مدیریت نادرست زنجیره تامین سرد مواد غذایی ممکن است ایمنی غذایی را به خطر انداخته و کیفیت را کاهش دهد که می‌تواند منجر به ضررهای اقتصادی و اثرات نامطلوب بر دسترسی به غذا شود. بنابراین طراحی یک زنجیره تامین سرد کارآمد و مورد اعتماد برای شرکت، تامین کنندگان، مشتریان و جامعه بسیار مهم است. اکثر مطالعات سنتی در زنجیره تامین هزینه کیفیت (پیشگیری، ارزیابی و شکست) را در طراحی شبکه زنجیره تامین در نظر نمی‌گیرند. در این مطالعه، تمام ابعاد هزینه کیفیت در طراحی زنجیره تامین سرد مانند هزینه کیفیت تامین کنندگان و هزینه کیفیت خدمات توزیع مورد بررسی قرار گرفته است تا مشکل به شرایط دنیای واقعی نزدیک گردد. علاوه بر این، کیفیت تامین کنندگان، تولید کنندگان و توزیع کنندگان به طور همزمان در سراسر زنجیره تامین با رویکردی جدید در نظر گرفته می‌شود. برای این منظور، مسئله به عنوان یک مدل ریاضی برای موارد چند محصولی و چند دوره‌ای با در نظر گرفتن دو تابع هدف فرمول‌بندی شده است. تابع هدف اول کل هزینه‌های مورد انتظار را به حداقل می‌رساند و تابع هدف دوم کیفیت کل زنجیره تامین را به حداکثر می‌رساند. مدل دو هدفه پیشنهادی با حل روش پارامتری (جمع وزنی نرمال شده) به یک مدل تک هدفه تبدیل شده و برای یک نمونه متوسط با در نظر گرفتن داده‌های یک مطالعه موردی در دنیای واقعی حل شده است. نتایج محاسباتی و تحلیل‌ها نشان‌دهنده کارایی مدل پیشنهادی و همچنین روش حل دقیق موجود برای مقیاس‌های کوچک و متوسط است. مطالعه موردی واقعی که شرکت لبنیات کاله را شامل می‌شود، برای نشان دادن پتانسیل مدل پیشنهادی و تحلیل‌های حساسیت مناسب انجام شده است.

International Journal of Engineering

Journal Homepage: www.ije.ir

Hybrid Massive MIMO Channel Model Based on Edge Detection of Interacting Objects and Cluster Concept

M. M. Tamaddondar*, N. Noori

Department of Communication Technologies ICT Research Center Institute, Tehran, Iran

PAPER INFO

Paper history:
Received 14 August 2020
Received in revised form 03 November 2021
Accepted 29 November 2021

Keywords:
Channel Model
Clustering
Edge Detection
Massive MIMO
Doppler Effect

ABSTRACT

This paper presents a novel channel model based on the edge detection of the interacting objects (IOs) for massive multiple-input and multiple-output (MIMO) systems considering different propagation phenomena such as reflection, refraction, diffraction, and scattering occur at the edges of the IOs. This channel model also uses cluster concepts to model multipath components (MPCs). The time-variant condition of the channel as well as the Doppler effect is considered in this channel model. Also, the non-stationary property of the channel across the array axis can be observed in the simulations. Due to a large number of antenna elements utilized in the massive MIMO systems, the spherical wavefront is assumed instead of the plane wavefront which is used in the conventional MIMO channel model. The central limit theory is also utilized to model the MPCs of each cluster. Furthermore, specific channel characteristics such as channel impulse response (CIR), angle of arrival (AoA) as well as time of arrival (ToA) are extracted in the simulations of the channel.

doi: *10.5829/ije.2022.35.02b.23*

1. INTRODUCTION

In the fifth generation (5G) of wireless communication systems, significant improvement in energy and spectrum efficiency, as well as reliability, is considered in compare to the previuos generation [1]. Millimeter wave technology is an innovation that allows benefiting from large bandwidths and very high data rates. However, this technology imposes the constraints of high attenuation and blockage to the system design. To achieve projected theoretically specifications, massive MIMO is regarded as a cornerstone and the most promising technology for meeting 5G wireless communication systems [2]. A large number of antenna elements in massive MIMO systems yield to increase the channel capacity, spatial resolution, energy, and spectral efficiency as well as linkage reliability [3, 4]. Massive MIMO systems also provide superior channel orthogonality and more channel stability than conventional MIMO systems [5]. Another essential objective behind the use of massive MIMO in 5G is to scan the overall pattern of the antenna for interference reduction and long distance communication [2]. Three dimensional (3D) channel modeling has an important role in accurate designing and a better understanding of the wireless communication systems [4, 6]. Also, massive MIMO benefits severely depend on accurate channel estimation. The parametric channel model is a way to regularize the channel estimation, which exploits the fact that a signal arrives at the receiver via a limited number of MPCs [7, 8]. The channel model should consider several emerging features of massive MIMO such as spherical wavefront and appearance and disappearance of MPCs on both time and array axis. As the dimension of the antenna array becomes large, different kinds of non-stationary properties appear across the array and different array elements may observe different receiving paths [9, 10]. Likewise, the channel components such as Rx and IOs may have relative motion, the Doppler effect should be considered in the calculations. Furthermore, a comprehensive model should consider channel characteristics in the 3D space. Due to the complexity of many propagation environments, the simplicity and applicability of the

*Corresponding Author Institutional Email: tamaddondar@itrc.ac.ir
(M. M. Tamaddondar)

Please cite this article as: M. M. Tamaddondar, N. Noori, Hybrid Massive MIMO Channel Model Based on Edge Detection of Interacting Objects and Cluster Concept, ***International Journal of Engineering, Transactions B: Applications***, Vol. 35, No. 2, (2021) 471-480

channel model are very important. In recent years, the development of a comprehensive model that can take into account various aspects of the massive MIMO channel has attracted much interest from the researchers.

1. 1. Related Massive MIMO Channel Model Many efforts have been prepared for MIMO channel modeling. Some examples of these models include European Cooperation in Science and Technology [11]. Wireless World Initiative New Radio (WINNER) + [12]. WINNER II [13]. 3D Spatial Channel Model (SCM) [14].and IMT-A models. However, such models cannot be extended to the massive MIMO systems, because most of these models consider plane wave condition in their calculations. Also, the birth-death property of the clusters cannot be observed on the array axis of MIMO system, while this phenomenon may exist in the many massive MIMO systems. Recently, several channel models have been presented for massive MIMO systems, each of which incorporates some of the features of the corresponding channel.

Several channel models for massive MIMO technology are 3D twin cluster model [15]. 3D 5G channel model [16]. 3D ellipsoid model [17]. and 2D KBSM-BD-AA [18]. have been compared and evaluated by Bai et al. [19] The visibility region method with the birth-death process is utilized to model the non-stationary property of clusters in the massive MIMO channel [20]. This model assumes spherical wavefront to capture the characteristics of AoA shifts and Doppler frequency variations because of the near-field effects. We have also presented a channel model based on the cluster concept discussed by Tamaddondar and Noori [21].

Some other channel models are presented based on the channel measurements. Measurement results at 2.6 GHz by Gao et al. [22]show that some antennas in massive MIMO systems contribute more than the others, while in i.i.d. Rayleigh channels, all antennas have equal contributions. Hence, the CIR of the channel may vary significantly over the antenna array in massive MIMO systems. Some other measurement-based channel model with their overall output results are listed in Table 1.

1. 2. Our Contributions To the best of the authors' knowledge, a comprehensive and standardized channel model for massive MIMO systems is still missing in the literatures. This paper aims to cover the specifications of the massive MIMO channels and derives a hybrid channel model. This hybrid model includes two deterministic and stochastic modes. The deterministic mode uses numerical techniques for solving Maxwell's equations by taking into account the geometry of the environment. Due to the complexity of the channel, those parts of the channel that cannot be model in the deterministic mode are considered in the stochastic mode. The edge detection technique is utilized to find scattering of MPCs. The major contributions and novelties of this paper can be summarized as follows:

1) A novel 3D hybrid channel model for massive MIMO systems is presented in this paper based on the edge detection of the IOs and cluster concepts. The central limit theorem (CLT) is utilized to simulate arrived signal to the receiver.

2) The near-field effect caused by the massive number of the antennas is considered in the proposed channel model.

3) The Doppler effect is considered in this channel model due to the relative motion of different channel components such as transmitter, receiver and IOs.

4) Appearance and disappearance of the clusters due to the huge number of antenna in the massive MIMO systems are evaluated to observe the non-stationary property of the channel on the array axis

TABLE 1. Some measurement based channel model specification for massive MIMO systems

Freq. [GHz]	Ant. Top.	Type	Scenario	Result	Ref.
13–17	40×40	Planar	Outdoor	K-factor, DS, AoA, AoD, Spatial-non-stationary	[23]
5.95–6.05	256	Rectangular	Subway	Angle distribution, angle spread, inter and intera cluster parameter	[24]
3.33	64	Linear	Outdoor	Delay and spatial non-stationary, PDP, DS, angel spread	[25]
11	4×64	Rectangular	Indoor	Power, delay, AoD, spatial-non-stationary	[26]
2,4,6	64	Linear	Indoor	Pathloss, RMS delay, coherent bandwidth, spatial non-stationary	[27]
3.5	256	Planer	Indoor/Outdoor	Capacity, eigenvalue, evolotion of cluster	[28]
11,16, 28,38	51×51,76×76, 91×91,121×121	Planer	Indoor	Spatial non-stationary, PDP, PAP, RMS DS	[29]

The rest of the paper is organized as follows. Section II gives a general description of the proposed 3D hybrid channel model for massive MIMO systems. Theoretical mathematic relations are given in section III. Some simulation results are depicted in section IV. Conclusions are finally drawn in section V.

2. PROCESS OF CHANNEL MODELING

Different aspects of the channel can be extracted in the channel modeling. Here, we try to propose a novel channel model for a standard massive MIMO system with M antenna element at the base station (BS) which serves N mobile station (MS). The propagation channel usually produces MPCs that arrive with different time delays to the users. By finding these MPCs, the CIR of the channel can be calculated. However, theoretical methods may face a huge amount of computations due to the complexity of the channel. To overcome this challenge, a novel hybrid method including both deterministic and stochastic modes is utilized to model the channel. In the deterministic mode, the line of sight (LoS) and reflection components are calculated. The equivalent planes are defined and used instead of smooth surfaces of the environment such as walls, ramps, and the ground. Then, the image theory is applied to these planes to find if any reflection path exists. The LoS or reflection paths may cross other surfaces. In such cases, the transmission coefficients are also considered in the calculations. Figure 1 shows the propagation mechanism in the deterministic mode.

The mechanism of buildings simulation is shown in Figure 2. For buildings modeling, 3D coordinates of the building's front plane quadrangle are defined clockwise. Then, by extruding the front surface along the vector of extrusion, three other surfaces of the building are completed. Finally, the ceiling and floor of the building

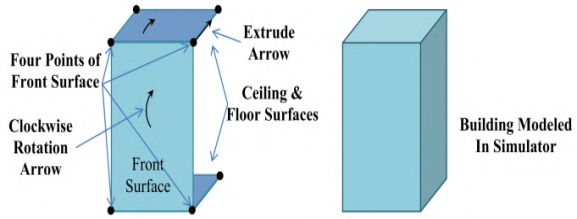

Figure 2. Procedure of building modeling in the simulator.

are defined. If the ground effect is considered, then definition of the floor is neglected.

Some parts of the channel that are too complex to be modeled in the deterministic mode are considered in the stochastic mode. Different kinds of propagation phenomena such as reflection, diffraction, and scattering occur at the edge of the IOs. These IOs are modeled with their equivalent structural geometry in the simulator as shown in Figure 3. Here, edge detection technique is utilized to distinguish the border of the IOs. Then, new MPCs are assigned to the edge of the IOs. We assume that the rays arriving at the MS follow the clustering behavior. Thus, the environment around the MS is divided into range cells (RCs). The edges of the IOs with the corresponding RCs are considered as active RCs. The MPCs may reach the MS from these active RCs. The mechanism of MPCs generation in the stochastic mode with the edge detection algorithm is shown in Figure 4. The number of MPCs in such RCs is modeled with Poisson random distribution.

The MPCs may cross the other RCs which are filled with other part of IOs. The pathloss of these IOs are considered in the calculations. Different components of the channel such as BS, MS, and IOs may have relative velocity. This causes frequency shifts due to the Doppler effect. This effect is considered in both deterministic and stochastic modes.

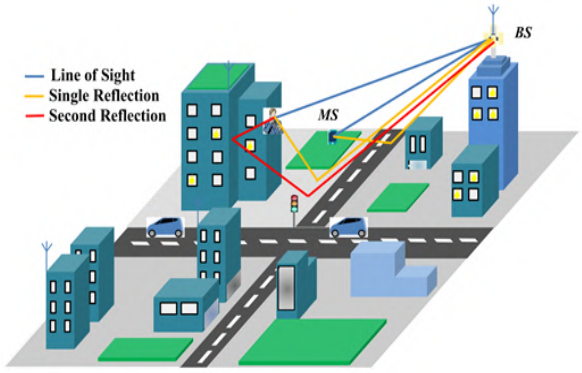

Figure 1. Model of the channel in the deterministic mode with equivalent planes

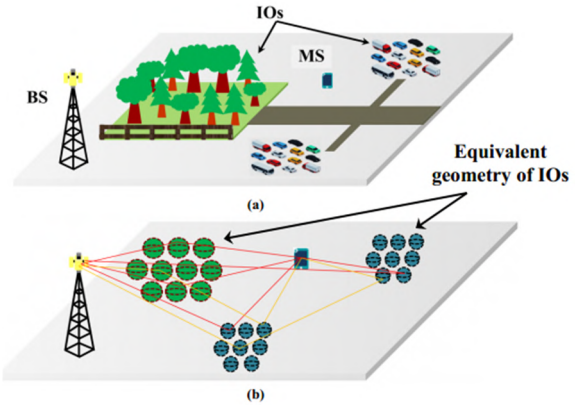

Figure 3. Illustration of a) Propagation Environment in the stochastic mode, b) Equivalent model in the simulator

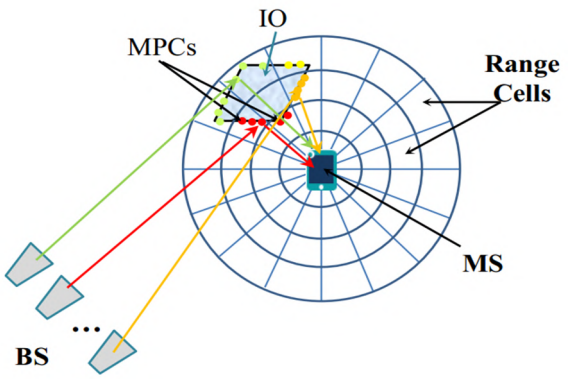

Figure 4. Mechanism of MPCs generation with edge detection algorithm

Finally, both derived deterministic and stochastic CIRs are integrated. Then the channel characteristics such as total CIR, delay spread, AoA, and ToA are extracted.

The flowchart in Figure 5 shows the presented channel modeling algorithm. As can be seen in Figure 5, several blocks are considered for channel modeling. In general, the initial parameters such as operating frequency, antenna radiation pattern, location of the BS and MS antennas, and the number of the antenna array elements with their configurations, as well as velocity vector should be defined at the first step. In the deterministic part, the equivalent surfaces are defined and in the stochastic part, the edges of the objects are drawn and the propagation environment is clustered.

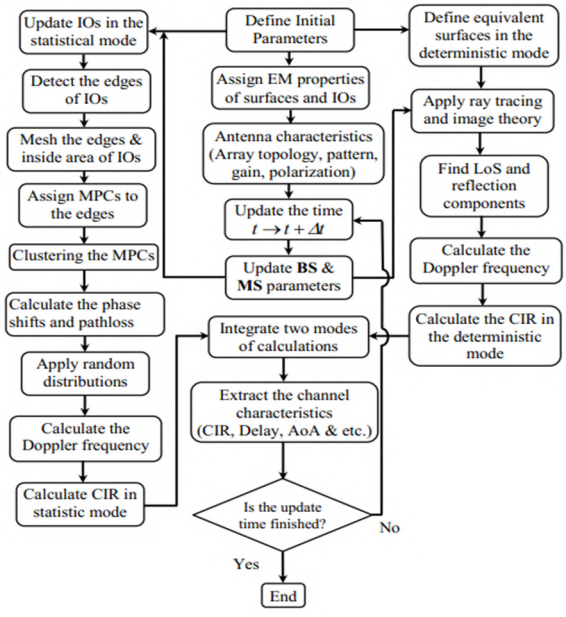

Figure 5. The flowchart of the channel modeling for massive MIMO systems

At any time instance, all time-variant variables are updated. All MPCs are found by applying ray tracing in the deterministic mode and the idea of detecting the edges of IOs in the stochastic mode. Then both deterministic and stochastic calculations are integrated. If the update time is finished, the required results will be extracted from the simulations.

Generally, deterministic channel models require geometrical information of the propagation environment, while, stochastic channel models are based on the channel statistics. In this paper, a hybrid channel model is proposed which includes two deterministic and stochastic modes. Such a channel model can be applied to a wide range of practical propagation channels. If the process of channel modeling is completely implemented in both deterministic and stochastic modes, the computational algorithm is shown in Figure 5 will extract different characteristics of a real channel. However, the deterministic mode needs geometrical information of the channel like other deterministic models.

3. MATHEMATICAL DESCRIPTION OF THE CHANNEL MODEL

The mathematical description of the channel is required for theoretical channel modeling. When an impulse is sent from a BS antenna element to the propagation environment, different MPCs may be produced and received at the MS. These MPCs pass through different propagation paths with different delay times. Regarding Figure 6, the time-variant CIR between the *m*th antenna at the BS and the *n*th user is dependent on time and delay axes.

Since the channel modeling mechanism is divided into two separate modes, the CIR can be expressed in terms of two separate channel response of deterministic and stochastic modes as follows:

$$h_{m,n}(t,\tau) = h^{d}_{m,n}(t,\tau) + h^{s}_{m,n}(t,\tau) \quad (1)$$

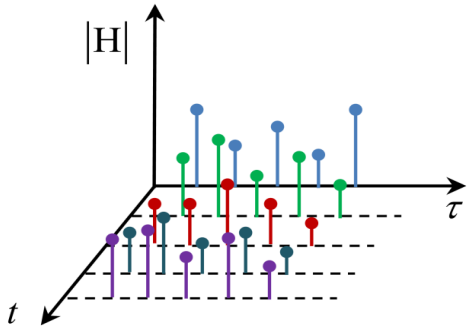

Figure 6. Time-variant channel impulse response diagram

where $h^d_{m,n}$ and $h^s_{m,n}$ are the multipath CIRs of the deterministic and stochastic modes, respectively. Here, the LoS and reflection components are calculated in the deterministic mode. Reflections up to second-order are considered in calculations. Thus the impulse response in the deterministic mode, $h^d_{m,n}$ can be rewritten as a combination of LoS and other reflection components:

$$h^d_{m,n}(t,\tau) = \sum_{i=1}^{T}\sum_{l=1}^{N_i} \alpha^d_{i,l} \exp(-j\beta r^d_{i,l}) \times \delta(\tau-\tau_l)\delta(t-t_i) \quad (2)$$

where $i = \{1,2,...,T\}$ is the total number of time instances, $\tau = \{\tau_{i,1}, \tau_{i,2}, ..., \tau_{i,N_i}\}$ is the delay series of the ith time instance. The number of MPCs in ith time instance is N_i. The propagation constant is β and the length of the lth MPC in ith time instance in the deterministic mode is denoted by $r^d_{i,l}$. The operator $\delta(\cdot)$ is the delta Dirac function. The amplitude of the MPCs in the deterministic mode is equal to:

$$\alpha^d_{i,l} = \frac{\lambda \Gamma^d_{i,l}}{4\pi r^d_{i,l}} \quad (3)$$

where $\Gamma^d_{i,l}$ is the attenuation factor related to the LoS or the first or second order reflection components and is defined by:

$$\Gamma^d_{i,l} = \begin{cases} 1 & \rightarrow \text{Line of sight} \\ \Gamma^{(1)}_{i,l} & \rightarrow \text{Reflection of the first order} \\ \Gamma^{(1)}_{i,l} \cdot \Gamma^{(2)}_{i,l} & \rightarrow \text{Reflection of the second order} \end{cases}$$

The attenuation factors of ith time instance and lth MPC for the first and second order reflections are denoted by $\Gamma^{(1)}_{i,l}$ and $\Gamma^{(2)}_{i,l}$, respectively.

As mentioned before, due to the complexity of many objects, they cannot be modeled in the deterministic mode. The stochastic mode is utilized here to overcome this problem. Here, we use this fact that different propagation phenomena such as reflection, diffraction and scattering typically occur at the boundaries of the medium discontinuities. Thus, an edge detection algorithm is proposed to diagnose the boundaries of the IOs. Accordingly, the boundaries and inner areas of the IOs are meshed separately for detecting boundaries and inner area of the IOs. The MPCs are attributed to the outer boundaries of the IOs. Simultaneously, as the propagation of MPCs has clustering behavior, the clustering technique is applied in the MS side to categorize the MPCs. Some characteristics of these MPCs are extracted by using random distributions. With such explanations, the CIR in the stochastic mode can be defined in the following form:

$$h^s_{m,n}(t,\tau) = \sum_{i=1}^{T}\sum_{c=1}^{C}\sum_{l=1}^{L^s_c} \alpha^s_{l,c,i} \exp(-j\phi_{l,c,i}) \times \delta(\tau-\tau_l)\delta(t-t_i) \quad (4)$$

where $c = \{1,2,...,C\}$ is the number of clusters, $\alpha^s_{l,c,i}$ and $\phi_{l,c,i}$ are the amplitude and phase shift of lth MPCs in the stochastic mode at the ith time instance in the cth cluster, respectively. The amplitude can be given by:

$$\alpha^s_{l,c.i} = \frac{\lambda D^s_{l,c,i}}{4\pi r^s_{l,c.i}} \quad (5)$$

The diffraction or scattering coefficient in the stochastic mode is denoted by $D^s_{l,c,i}$ and $r^s_{l,c,i}$ is the path length of the lth MPC at the ith time instance in the cth cluster. The phase shift of each MPC is obtained from a uniform distribution between $[0, 2\pi)$. Also, Poisson distribution is used to compute the number of MPCs of the cth cluster, L^s_c. Regarding the density of the propagation environment (sparse, medium or dense environments), and based on the various simulations such as what has been presented in [21], the proper average number of MPCs has been obtained between zero and five. In other words, as the diffraction parts of an IO are increased, the average number of MPCs used in Poisson distribution is also increased and vice versa.

The MPCs that arrive to the MS in each delay bin are summed with each other. It means that:

$$h_{m,n}(t,\tau_k) = \sum_{p=1}^{P_k} h_{m,n}(t,\tau_p)$$
$$\tau_k - \frac{\Delta\tau}{2} < \tau_p < \tau_k + \frac{\Delta\tau}{2} \quad (6)$$
$$\tau_k = k\Delta\tau, \qquad k = 0,1,2,...,K$$

where K is total number of successive delay bins and $p = \{1,2,...,P_k\}$ is the number of MPCs in the kth delay bin. The width of each delay bin is $\Delta\tau$. Both slow and fast fading are obtained during the channel simulations since the amplitude and phase of all received MPCs are calculated.

The average power delay profile (APDP) is generally used to calculate delay spread and remove impacts of the noise in time-invariant channel. It can be obtained from the PDP samples of the ith time instance which is defined as follows:

$$APDP_{m,n}(\tau_K) = \frac{1}{N_{cyc}} \sum_{i=1}^{N_{cyc}} PDP_{m,n}(\tau, t_i) \quad (7)$$

$$PDP_{m,n}(\tau,t_i)=\left|h_{m,n}(\tau,t_i)\right|^2 \tag{8}$$

where N_{cyc} is the number of PDP samples between the mth antenna of the BS and the nth user and t_i is the ith time instance. It should be emphasized that Equation (7) is considered for such a channel that is stationary on time axis. For time-variant channels, the samples should be taken in the duration of coherence time. Then, the root mean square (RMS) delay spread can be calculated using APDP as follows:

$$\tau_{rms}=\sqrt{\frac{\sum_q APDP(\tau_q)\tau_q^2}{\sum_q APDP(\tau_q)}-\left(\frac{\sum_q APDP(\tau_q)\tau_q}{\sum_q APDP(\tau_q)}\right)^2} \tag{9}$$

The AoA is another useful parameter which shows the angle of MPCs arrived to the MS. This parameter is used in the clustering of MPCs. The AoAs in elevation and azimuth planes are shown by θ_{AoA} and φ_{AoA}, respectively and defined as:

$$\theta_{AoA}=\cos^{-1}\left(\frac{\mathbf{a_z}\cdot\mathbf{IR}}{|\mathbf{IR}|}\right) \tag{10}$$

$$\varphi_{AoA}=\cos^{-1}\left(\frac{\mathbf{a_x}\cdot\mathbf{IR}}{|\mathbf{IR}|}\right) \tag{11}$$

where, the vector point from the IO to the MS is $\mathbf{IR}$ and $\mathbf{a_x}$ and $\mathbf{a_z}$ are the unit vectors on the x and z axes, respectively. Both AoA and time delay are used to separate arrival rays of different clusters. In fact, rays with similar AoAs and delays make one cluster. The MPCs are categorized by considering their time delay and AoAs using the K-mean algorithm. The paths of some MPCs go through clusters which are filled with IOs. Thus, the phase shifts and the pathloss due to these clusters are also added to total calculations.

3. 1. Antenna The channel response depends on the antenna characteristics such as radiation pattern and gain. Since in massive MIMO systems, the radiation pattern can be affected by adjacent antenna elements, the radiation pattern of the antenna element in the array are imported into the calculations. As the near-field effect may influence on the response of the channel, the radiation pattern of the antenna is calculated in the required distance from the antenna element. Therefore, the CIR in both deterministic and stochastic modes can be rewritten as follows:

$$\begin{aligned}h^d_{m,n}(t,\tau)=&\sum_{i=1}^{T}\sum_{l=1}^{N_i}\alpha^d_{l,i}\exp(-j\beta r^d_{l,i})\times\\ &F^{Tx}_m(R^{Tx}_{l,i},\theta^{Tx}_{l,i},\varphi^{Tx}_{l,i})\cdot F^{Rx}_n(R^{Rx}_{l,i},\theta^{Rx}_{l,i},\varphi^{Rx}_{l,i})\times\\ &\delta(\tau-\tau_l)\cdot\delta(t-t_i)\end{aligned} \tag{12}$$

$$\begin{aligned}h^s_{m,n}(t,\tau)=&\sum_{i=1}^{T}\sum_{c=1}^{C}\sum_{l=1}^{L^s_c}\alpha^s_{l,c,i}\exp(-j\phi^s_{l,c,i})\times\\ &F^{Tx}_m(R^{Tx}_{l,c,i},\theta^{Tx}_{l,c,i},\varphi^{Tx}_{l,c,i})\cdot F^{Rx}_n(R^{Rx}_{l,c,i},\theta^{Rx}_{l,c,i},\varphi^{Rx}_{l,c,i})\times\\ &\delta(\tau-\tau_{l,c})\cdot\delta(t-t_i)\end{aligned} \tag{13}$$

where F^{Tx}_m and F^{Rx}_n are the radiation pattern of the mth antenna element at the BS and the nth MS, respectively. The observation distances from BS and MS in spherical coordinates are $(R^{Tx}_{l,c,i},\theta^{Tx}_{l,c,i},\varphi^{Tx}_{l,c,i})$ and $(R^{Tx}_{l,c,i},\theta^{Tx}_{l,c,i},\varphi^{Tx}_{l,c,i})$, respectively.

3. 1. Doppler Effect Since the channel components typically have relative velocity, there is a Doppler effect in the channel. Accordingly, the Doppler frequency is calculated and considered in the CIR. Regarding Figure 7, the Doppler frequency can be expressed as follows:

$$f_D=f_{obs1}\left(1+\frac{v_{IO}\cos\theta_{IO,Rx}}{c_0}\right)\left(1+\frac{v_{Rx}\cos\theta_{Rx,IO}}{c_0}\right) \tag{14}$$

$$f_{obs1}=f_c\left(1+\frac{v_{Tx}\cos\theta_{Tx,IO}}{c_0}\right)\left(1+\frac{v_{IO}\cos\theta_{IO,Tx}}{c_0}\right) \tag{15}$$

where f_c is the carrier frequency and c_0 is the velocity of the transmitted signal. The v_{Tx}, v_{IO} and v_{Rx} are the velocity vectors of the Tx, IO and Rx, respectively. The angles $\theta_{Tx,IO}$, $\theta_{IO,Tx}$, $\theta_{IO,Rx}$ and $\theta_{Rx,IO}$ are shown in Figure 7.

The locations of the BS and MS with their corresponding velocity vectors as well as the location and velocity vector of IOs are imported into the simulator. The simulator computes the required angles

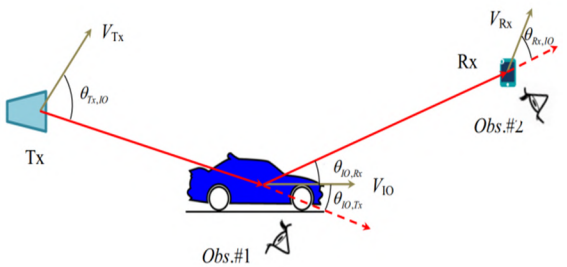

Figure 7. Illustration of parameters for Doppler effect calculations

for the Doppler frequency calculation based on the departure and arrival angles of each observation point. This information is used to implement in Equations (14) and (15) to model and calculate Doppler effect of each path.

4. SIMULATION AND RESULTS

In this section, simulations are carried out to extract channel characteristics. An outdoor propagation environment is defined to implement the proposed channel model. This channel includes several buildings, ground effect, car parking and garages. These obstacles are defined in our simulations based on the procedure of deterministic and stochastic modes presented in previous sections. Accordingly, the buildings and ground are modeled with their equivalent surfaces. However, the other parts of the channel including garages and car parking are modeled by stochastic mode as IOs with their edge boundaries (as depicted in Figure 3). The geometrical schematic of this channel is shown in Figure 8. The buildings and the ground as well as three IOs are depicted in this figure. The ray tracing algorithm is utilized to find all paths between the BS and MS which is shown in Figure 8. The LoS, as well as the first and second order reflection components is calculated in the deterministic mode. The edge detection algorithm is used to distinguish the MPCs in the stochastic mode.

At first, the received power at the MS is obtained versus the distances between transmitter and receiver where BS and MS antennas have omni-directional radiation pattern. The obtained results of the proposed channel model are compared with those obtained by classic ray tracing method. This comparison is shown in Figure 9. In the ray tracing model, only the LoS and reflections are considered in the calculations, while in the proposed model, in addition to the deterministic mode components, the cluster behavior of the channel is also included in the calculations. Thus, the proposed model considers more details of the channel in comparison with the ray tracing model.

Then, the simulations are done for a massive MIMO system including a 256-element antenna at the BS. The number of 256 elements represents a massive MIMO system, in which we want to show the non-stationary property of the channel along the array. The antenna element is placed in a linear configuration with half of the wavelength distance between successive elements. The frequency of simulation is set to 28 GHz since this frequency is a candidate for realizing millimeter-wave massive MIMO systems. All parameters of the considered system are listed in Table 2.

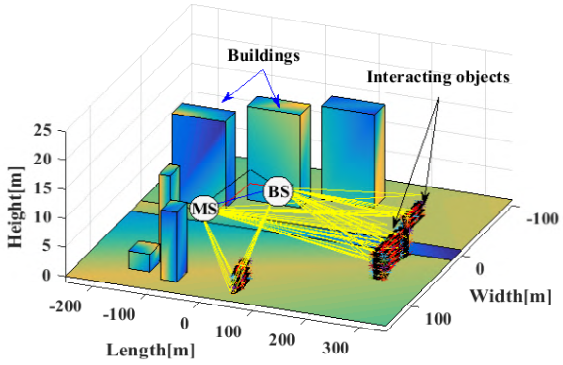

Figure 8. The propagation environment in the simulator

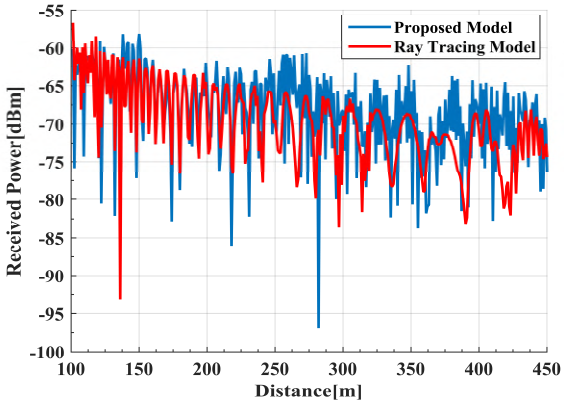

Figure 9. Received power versus the distance between the first antenna at BS and MS

TABLE 2. Preliminary Definitions in the simulations

Carrier Frequency : 28 GHz
BS Antenna: 256–Open-Ended Element, Linear Array, Vertical Polarization, Directive Pattern
MS Antenna: Single Dipole, Vertical Polarization, Omnidirectional Pattern
Transmit Power : 1W
BS Center Position: [120, 120, 18]
MS Position : [13, -130, 1.5]
MS Velocity Vector : $[\frac{17\sqrt{2}}{2}, \frac{17\sqrt{2}}{2}, 0]$
Building Characteristics : $\varepsilon_r = 4.1\ \mu_r = 1\ \sigma = 0.001$
IO Characteristics : $\varepsilon_r = 1\ \mu_r = 1\ \sigma = 1.45e6$

*The coordinates of the points are in meter.

The PDP with respect to the delay of the MPCs are depicted in Figure 10. This PDP can be considered as the CIR of the first antenna element at the BS and the MS. Different kinds of MPCs are separated in the simulation as shown in Figure 10. These MPCs include LoS, reflections of the first-order from one wall, reflection of the second-order from two walls, and single bounce components due to diffraction or scattering from IOs. Hence, these different MPCs are originated from different paths and propagation phenomena. The LoS component has the highest strength among all MPCs, while the MPCs from IOs have lower strengths in overall look of Figure 10. The threshold level is considered to be -160 dBm in the simulations. The AoAs in both elevation and azimuth planes are derived in the simulations. Thus, the PAP between the first BS antenna element and the MS with respect to the AoAs is shown in Figure 11. The cluster behavior of the MPCs can be viewed in both Figures 10 and 11. Since the distance between the array elements at the BS is low at 28 GHz, the sub-arrays in the massive MIMO system almost experience a stationary channel. However, the non-stationary property between these sub-arrays is significant.

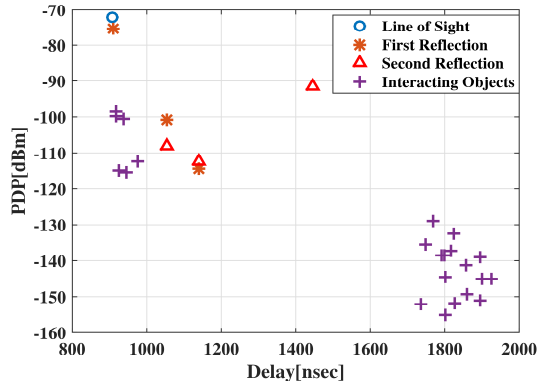

Figure 10. Power delay profile between the first Antenna at BS and MS with respect to the delay of MPCs

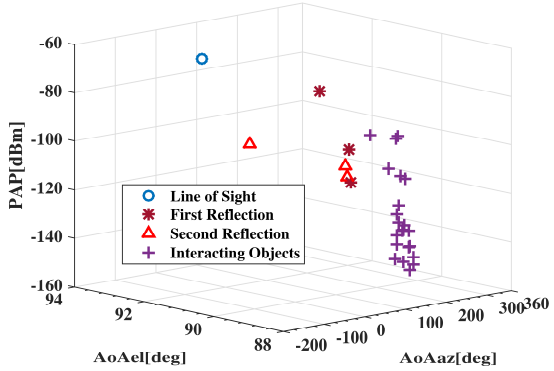

Figure 11. Power angle profile with respect to the angle of arrival

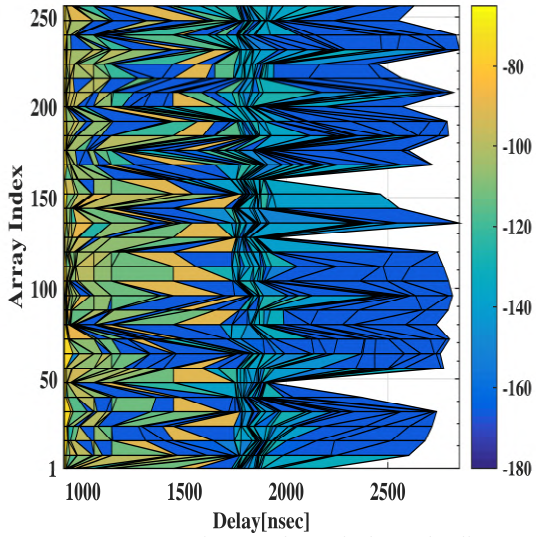

Figure 12. Non-Stationary channel along the linear array antenna with 256 elements

Figure 12 shows the non-stationary property of the channel along the array axis for 256-element antenna at the BS. The main reason of this phenomenon is that due to the huge number of the antenna elements and large size of the array against operating frequency wavelength, different channels are experienced along the massive MIMO array by distinct elements.

Here, the Doppler effect is considered in the simulations. As mentioned in Table 2, the MS has a relative velocity which causes a Doppler shift. The Doppler shift of the frequency for each MPC is shown in Figure 13. This shows that the Doppler shift of the frequency is about 3 kHz in this scenario.

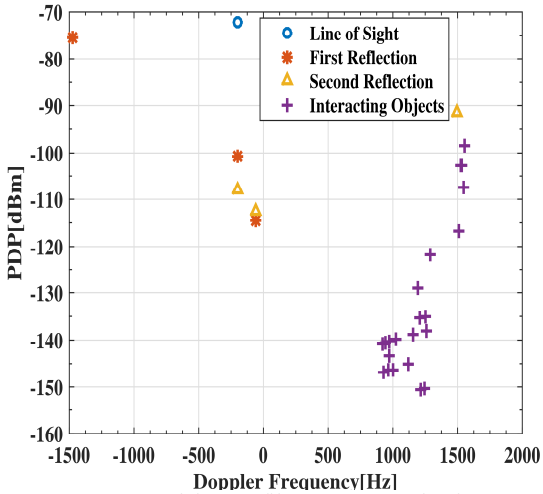

Figure 13. Power delay profile versus Doppler frequency

5. SUMMARY AND CONCLUSION

In this paper, we have proposed a novel channel model for massive MIMO systems. This hybrid channel model includes deterministic and stochastic modes. The smooth surfaces are defined in the deterministic mode. Then the ray tracing algorithm is utilized to find the LoS component along with the first and second order reflections. Other parts of the channel are defined in the stochastic mode. In this mode, the edge detection algorithm is used to find the boundaries of the IOs. This is because of the fact that different propagation phenomenon such as reflection, diffraction and scattering often occurred at the boundaries of the objects. Thus the MPCs are assigned to the outer edges of the IOs. The relative motion of the channel components cause Doppler shifts in the frequency. This Doppler effect is considered in this channel model to have a better overview of the received signals at the MS. Finally, the MPCs from both deterministic and stochastic modes are integrated to extract the desired characteristics of the channel such as CIR, delay spread, AoAs and Doppler shifts. The non-stationary property of the massive MIMO channel is observed in the simulation. This channel model can be considered as a time-variant channel model due to the capability of updating all channel specifications such as antenna positions and velocity vectors of the BS and MS in each snapshot.

6. REFERENCES

1. Jiang, H., Tang, D., Zhou, J., Xi, X., Feng, J., Dang, J. and Wu, L.J.I.A., "Approximation algorithm based channel estimation for massive mimo antenna array systems", ***IEEE Access*** Vol. 7, (2019), 149364-149372, doi: 10.1109/ACCESS.2019.2947533
2. El Misilmani, H. and El-Hajj, A., "Massive mimo design for 5g networks: An overview on alternative antenna configurations and channel model challenges", in 2017 International Conference on High Performance Computing & Simulation (HPCS), IEEE. (2017), 288-294.
3. Larsson, E.G., Edfors, O., Tufvesson, F. and Marzetta, T.L.J.I.c.m., "Massive mimo for next generation wireless systems", ***IEEE Communications Magazine*** Vol. 52, No. 2, (2014), 186-195, doi: 10.1109/MCOM.2014.6736761
4. Lu, L., Li, G.Y., Swindlehurst, A.L., Ashikhmin, A. and Zhang, R.J.I.j.o.s.t.i.s.p., "An overview of massive mimo: Benefits and challenges", ***IEEE Journal of Selected Topics in Signal Processing*** Vol. 8, No. 5, (2014), 742-758, doi: 10.1109/JSTSP.2014.2317671
5. Gao, X., Edfors, O., Rusek, F. and Tufvesson, F.J.I.T.o.W.C., "Massive mimo performance evaluation based on measured propagation data", ***IEEE Transactions on Wireless Communications*** Vol. 14, No. 7, (2015), 3899-3911, doi: 10.1109/TWC.2015.2414413
6. Nielsen, J.O., Fan, W., Eggers, P.C. and Pedersen, G.F.J.I.C.M., "A channel sounder for massive mimo and mmwave channels", ***IEEE Communications Magazine*** Vol. 56, No. 12, (2018), 67-73, doi: 10.1109/MCOM.2018.1800199
7. Sayeed, A.M.J.I.T.o.S.p., "Deconstructing multiantenna fading channels", IEEE Transactions on Signal processing Vol. 50, No. 10, (2002), 2563-2579, doi: 10.1109/TSP.2002.803324
8. Bazzi, S., Stefanatos, S., Le Magoarou, L., Hajri, S.E., Assaad, M., Paquelet, S., Wunder, G. and Xu, W.J.I.A., "Exploiting the massive mimo channel structural properties for minimization of channel estimation error and training overhead", ***IEEE Access*** Vol. 7, (2019), 32434-32452, doi: 10.1109/ACCESS.2019.2903654
9. Ali, A., De Carvalho, E. and Heath, R.W.J.I.W.C.L., "Linear receivers in non-stationary massive mimo channels with visibility regions", IEEE Wireless Communications Letters Vol. 8, No. 3, (2019), 885-888, doi: 10.1109/LWC.2019.2898572
10. Martínez, À.O., De Carvalho, E. and Nielsen, J.Ø., "Towards very large aperture massive mimo: A measurement based study", in 2014 IEEE Globecom Workshops (GC Wkshps), IEEE., (2014), 281-286.
11. Liu, L., Oestges, C., Poutanen, J., Haneda, K., Vainikainen, P., Quitin, F., Tufvesson, F. and De Doncker, P.J.I.W.C., "The cost 2100 mimo channel model", ***IEEE Wireless Communications*** Vol. 19, No. 6, (2012), 92-99, doi: 10.1109/MWC.2012.6393523
12. Meinila, J., Kyosti, P. and Hentila, L., "Winner+ final channel models", Wireless World Initiative New Radio WINNER, (2010), doi:
13. Döttling, M., Mohr, W. and Osseiran, A., "Radio technologies and concepts for imt-advanced, John Wiley & Sons, John Wiley \& Sons (2009).
14. Tennakoon, P. and Wavegedara, C.B., "A 3d geometry-based spatial correlation model for mimo channels", in 2019 Moratuwa Engineering Research Conference (MERCon), IEEE. (2019), 222-227.
15. Wu, S., Wang, C.-X., Alwakeel, M.M. and He, Y.J.I.j.o.s.a.i.c., "A non-stationary 3-d wideband twin-cluster model for 5g massive mimo channels", ***IEEE Journal on Selected Areas in Communications,*** Vol. 32, No. 6, (2014), 1207-1218, doi: 10.1109/JSAC.2014.2328131
16. Wu, S., Wang, C.-X., Alwakeel, M.M. and You, X.J.I.T.o.C., "A general 3-d non-stationary 5g wireless channel model", ***IEEE Transactions on Communications,*** Vol. 66, No. 7, (2017), 3065-3078, doi: 10.1109/TCOMM.2017.2779128
17. Bai, L., Wang, C.-X., Wu, S., Wang, H. and Yang, Y., "A 3-d wideband multi-confocal ellipsoid model for wireless mimo communication channels", in 2016 IEEE International Conference on Communications (ICC), IEEE. (2016), 1-6.
18. Wu, S., Wang, C.-X., Aggoune, E.-H.M. and Alwakeel, M.M., "A novel kronecker-based stochastic model for massive mimo channels", in 2015 IEEE/CIC International Conference on Communications in China (ICCC), IEEE., (2015), 1-6.
19. Bai, L., Wang, C.-X., Wu, S., Lopez, C.F., Gao, X., Zhang, W. and Liu, Y., "Performance comparison of six massive mimo channel models", in 2017 IEEE/CIC International Conference on Communications in China (ICCC), IEEE. (2017), 1-5.
20. Chen, J.-q., Zhang, Z., Tang, T., Huang, Y.-z.J.F.o.I.T. and Engineering, E., "Anon-stationary channelmodel for 5gmassive mimosystems", ***Frontiers of Information Technology \& Electronic Engineering*** Vol. 18, No. 12, (2018), 2101-2110, doi: 10.1631/FITEE.1700028
21. Tamaddondar, M.M. and Noori, N., "3d massive mimo channel modeling with cluster based ray tracing method", in 2019 27th Iranian Conference on Electrical Engineering (ICEE), IEEE. (2019), 1249-1253.
22. Gao, X., Edfors, O., Tufvesson, F. and Larsson, E.G.J.I.T.o.C., "Massive mimo in real propagation environments: Do all antennas contribute equally?", ***IEEE Transactions on Communications*** Vol. 63, No. 11, (2015), 3917-3928, doi: 10.1109/TCOMM.2015.2462350

23. Chen, J., Yin, X. and Wang, S., "Measurement-based massive mimo channel modeling in 13–17 ghz for indoor hall scenarios", in 2016 IEEE International Conference on Communications (ICC), IEEE. (2016), 1-5.

24. Li, J., Ai, B., He, R., Yang, M., Wang, Q., Zhang, B. and Zhong, Z.J.I.A., "Cluster-based 3-d channel modeling for massive mimo in subway station environment", ***IEEE Access,*** Vol. 6, (2017), 6257-6272, doi: 10.1109/ACCESS.2017.2779119

25. Fei, D., He, R., Ai, B., Zhang, B., Guan, K. and Zhong, Z., "Massive mimo channel measurements and analysis at 3.33 ghz", in 2015 10th international conference on Communications and Networking in China (ChinaCom), IEEE. (2015), 194-198.

26. Li, J., Ai, B., He, R., Yang, M., Zhong, Z., Hao, Y. and Shi, G., "The 3d spatial non-stationarity and spherical wavefront in massive mimo channel measurement", in 2018 10th International Conference on Wireless Communications and Signal Processing (WCSP), IEEE. (2018), 1-6.

27. Li, J., Ai, B., He, R., Guan, K., Wang, Q., Fei, D., Zhong, Z., Zhao, Z., Miao, D. and Guan, H., "Measurement-based characterizations of indoor massive mimo channels at 2 GHZ, 4 ghz, and 6 ghz frequency bands", in 2016 IEEE 83rd Vehicular Technology Conference (VTC Spring), IEEE. (2016), 1-5.

28. Zhang, J., Wang, C., Wu, Z. And Zhang, W.J.Z.C., "A survey of massive mimo channel measurements and models", ***ZTE Communications*** Vol. 15, No. 1, (2017), doi: 10.1155/2014/848071

29. Huang, J., Feng, R., Sun, J., Wang, C.-X., Zhang, W. and Yang, Y., "Multi-frequency millimeter wave massive mimo channel measurements and analysis", in 2017 IEEE International Conference on Communications (ICC), IEEE., (2017), 1-6.

Persian Abstract

چکیده

این مقاله، مدل کانال جدیدی را برمبنای آشکارسازی لبه‌های اشیاء متعامل برای سیستم‌های چندورودی چندخروجی انبوه بی‌سیم ارائه می‌کند. ایده مدل کانال براین اساس است که پدیده‌های انتشار امواج الکترومغناطیسی نظیر بازتابش‌ها، پراش، پراکندگی و انکسار غالباً در لبه اشیاء متعامل تولید می‌شوند. این مدل کانال همچنین از مفهوم خوشه‌بندی برای مدل کردن مؤلفه‌های چندمسیری استفاده می‌کند. شرایط متغیر بازمان بودن کانال و وجود اثر داپلر در مدل‌سازی کانال در نظر گرفته می‌شود. پدیده غیر ایستایی کانال در امتداد محور آرایه آنتن ایستگاه پایه در شبیه‌سازی قابل مشاهده می‌باشد. به‌دلیل تعداد زیاد عناصر آرایه آنتن در ایستگاه پایه در سیستم‌های چندورودی چندخروجی انبوه، شرایط جبهه موج کروی به جای جبهه موج تخت در فواصل نزدیک در نظر گرفته می‌شود. به منظور مدل کردن مؤلفه‌های چندمسیری در هر خوشه از قضیه تئوری حد مرکزی استفاده شده و پس از مدل‌سازی کانال انتشار، مشخصه‌های آن نظیر پاسخ ضربه کانال، زوایای ورود و زمان ورود از شبیه‌سازی‌ها استخراج می‌شود.

IJE TRANSACTIONS B: Applications Vol. 35, No. 02, (February 2022) 481-492

International Journal of Engineering

Journal Homepage: www.ije.ir

Experimental Study on Surface Integrity of Ti6Al4V by Broaching

P. Khanjanzadeh[a], H. Amirabadi*[b], J. Sadri[c,d]

[a] *Department of Mechanical Engineering, University of Birjand, Birjand, Iran*
[b] *Faculty of Engineering, University of Neyshabur, Neyshabur, Iran*
[c] *Department of Computer Science & Software Engineering, Concordia University, Montreal, Canada*
[d] *Camp in Labs Foundation, 1 Westmount Square, Bureau 1001, Westmount, Quebec, Canada*

PAPER INFO

Paper history:
Received 30 September 2021
Received in revised form 14 November 2021
Accepted 02 December 2021

Keywords:
Broaching Tool
Cutting Tool Design
Residual Stress
Titanium Alloy

ABSTRACT

The performance of many parts in the airplane, aircraft engine and biomedical implants is highly related to their fatigue life, which is clearly depend on the condition of their surface integrity. The geometry parameters of broaching tools have an important influence on the surface integrity after broaching Ti6Al4V alloy. Therefore, this research studies the surface integrity of Ti6Al4V by broaching. The surface integrity is studied at different geometric parameters such as rake angles (α, and α_0), clearance angles (β, and β_0), and radius of the cutting edge (r_0) in two last teeth of the broaching tool that perform chipping. The broached surface integrity is assessed in cases of surface roughness, microstructural, residual stresses, and micro hardness. These results show that the sample broached by tool number 1 ($\alpha = 18.4, \beta = 3.1, \alpha_0 = 45, \beta_0 = 9, r_0 = 0.02$) had higher surface integrity because it was the smoothest surface and the thinnest deformed layer among the other samples. Since the main criterions in selection of the optimal tool are to create the smoothest surface and the least deformed layer depth in the broached sample, tool number 1($\alpha = 18.4, \beta = 3.1, \alpha_0 = 45, \beta_0 = 9, r_0 = 0.02$) is suggested as the optimal tool.

doi: *10.5829/ije.2022.35.02b.24*

1. INTRODUCTION

Broaching is a machining process widely used to produce some aspects because of the surface integrity state and high dimensional quality. Therefore, the surface integrity feature gained in broaching is very important in increasing the life of fatigue [1]. The Ti6Al4V alloy is extensively used in aircraft engine and medical implants which high fatigue life and corrosion resistance are needed [2, 3]. Considering the working conditions of the turbine blade such as the presence of high centrifugal forces, and high temperatures during operation, the design of the broaching tool that creates the minimum residual stress on it is required [4].

Surface integrity is inherent or enhanced condition of a surface produced in machining or other surface generation operation [5]. Surface integrity states the performance and the quality of a machined part and contains of the metallurgical conditions (microstructure, phase transformation, etc.), mechanical properties (micro hardness, residual stresses, etc.), and surface roughness [6]. In most cases, to prevent early failure and fatigue of the parts, the smoothest surface finish is desirable [7]. After any thermos-mechanical manufacturing operation such as machining processes, different features of surface integrity are affected [8].

Here, a history of research performed in the area of surface integrity of alloys by machining, has been presented. He and Zhang [9] investigated the influences of cutting factors on the surface integrity of broached TC9 alloy. Schulze et al. [10] used FE simulation to estimate created residual stress on the broached surface of SAE 5120 alloy. Kong et al. [11] studied the influences of cutting factors on saw-toothed chip formation of nickel-base alloy GH4169, using FE simulation. Jafarian et al. [12, 13] developed a robust method to predict and improve surface residual stress in the turning operation of Inconel718. Ortize-de-Zarate et al. [14] presented an experimental and FE method analysis of surface integrity of broached Ti6Al4V. They studied the effect of cutting

*Corresponding Author Institutional Email: hamirabadi@neyshabur.ac.ir (H. Amirabadi)

Please cite this article as: P. Khanjanzadeh, H. Amirabadi, J. Sadri, Experimental Study on Surface Integrity of Ti6Al4V by Broaching, ***International Journal of Engineering, Transactions B: Applications***, Vol. 35, No. 2, (2021) 481-492

speed on cutting forces, chip morphology and surface integrity of broached Ti6Al4V. Kaway and Zhang [15] investigated surface integrity of Ti6Al4V in ball end milling process. Childs et al. [16] proposed a model that employs a failure criterion as a function of stress and temperature for Ti6AlV4. Bertolini et al. [17] evaluated the EBM Ti6Al4V machinability in terms of the relationship between the surface integrity with corrosion resistance and fatigue life. Khanjanzadeh et al. [18] proposed the optimal geometry for a broaching tool by using FE simulation which generates the lowest residual stress in the broached surface of the Ti6Al4V alloy. The mentioned studies showed that so far, relatively little study into surface integrity of Ti6Al4V by broaching has been done.

The main contribution of this manuscript is that for the first time, the experimental study is performed about the effect of broaching tool geometry on the surface integrity of Ti6Al4V. In our previous paper [18], based on finite element simulation and optimization using a genetic algorithm, it was shown that the optimal geometric parameters of the last two teeth of the broaching tool that perform chipping, depend on the percentage of effect of each of the temperature and effective strain factors.

2. MATERIALS AND METHODS

Figure 1 indicates the block diagram of the research method. In this research, based on the results of the Pareto diagram obtained in our previous paper [18], five tools with different optimal geometric characteristics were fabricated. Then the surface integrity of the broached samples was experimentally compared. Finally, the geometric parameters of the optimal broaching tool were introduced.

2. 1. Materials The test material is the grade 5 of Ti6Al4V. The wrought material was supplied in form of plates of 75mm × 25mm × 9mm and annealed at 955℃ for one hour. Table 1 summarized the chemical composition of the material. The mechanical properties of the material are listed in Table 2. The final specimens were produced using the wire cut machine. Then the samples were mounted on a fixture. The test workpieces are indicated in Figure 2.

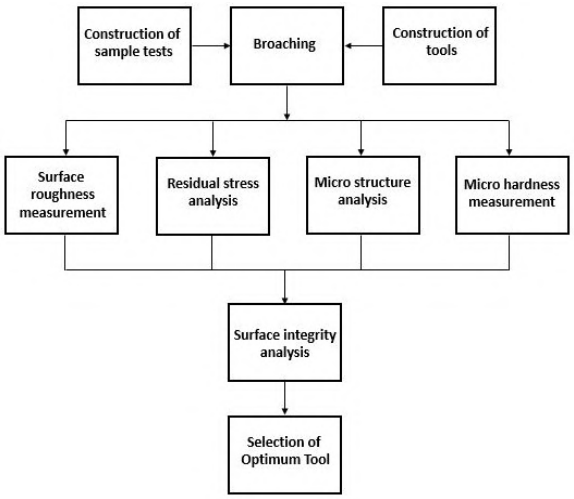

Figure 1. Block diagram of the research method

2. 2. Broaching Tests In our previous work [18], based on finite element simulation and optimization using a genetic algorithm, it was shown that the optimal geometric parameters of the last two teeth of the broaching tool that perform chipping, depend on the percentage of effect of the temperature and effective strain factors. In this study, based on the results of the Pareto diagram obtained in our previous research, five tools with different optimal geometric characteristics were constructed. Table 3 and Figure 3 show the geometric specifications of broaching tools based on our previous research work [18].

The broaching tools were made of a WC blade by a Robofil Charmilles wire cut machine. Thus, in total five tools were made. The cutting tools were mounted on a tool holder. The cutting speed of broaching operations was 3 m/min. Experimental tests were performed on an OKK PCV-55 3Axis CNC machine, 48"×22". Figure 4 shows the broaching setup. Three repetitions were done for each cutting condition. So in total, fifteen tests were carried out.

TABLE 1. Chemical composition of Ti6Al4V

Element	Ti	Al	V	Fe	Nb	Cr	Sn	Si	Mo	W	Mn	Cu	Zr
Mass%	Base	5.65	4.52	0.18	0.012	0.011	<0.03	0.006	<0.01	<0.02	<005	<0.005	<0.002

TABLE 2. Mechanical properties of annealed Ti6Al4V [19]

Yield stress (MPa)	Ultimate stress (MPa)	Young's Module (GPa)	Micro hardness (HV)	Poisson's ratio
880	950	113.8	350	0.342

a b

Figure 2. Test workpiece a) workpiece drawing, b) The workpieces mounted on the fixture

TABLE 3. Geometric dimensions of tools (α: Rake angle of the first tooth, β: Clearance angle of the first tooth, α_0: Rake angle of the second tooth, β_0: Clearance angle of the second tooth, r_1: The radius of curvature of the gullet behind of the first tooth, r_2: The radius of curvature of the gullet behind of the second tooth)

Tool's No.	α	β	α_0	β_0	r_0 (mm)	r_1 (mm)	r_2 (mm)
1	18.4^0	3.1^0	45^0	9^0	0.02	3.62	4.87
2	18.4^0	3.1^0	45^0	9^0	0.01	3.62	4.87
3	18.4^0	3.1^0	35^0	9^0	0.01	3.62	4.35
4	18.4^0	3.1^0	35.4^0	8.2^0	0.01	3.62	4.35
5	18.4^0	3.1^0	35^0	8.4^0	0.01	3.62	4.34

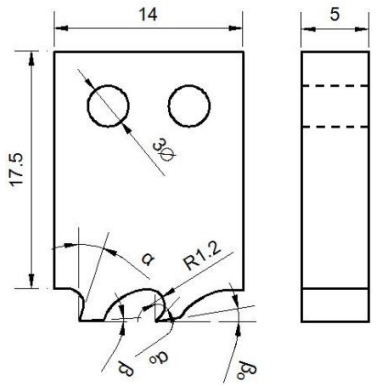

Figure 3. Broaching tool's drawing. (α: Rake angle of the first tooth, β: Clearance angle of the first tooth, α_0: Rake angle of the second tooth, β_0: Clearance angle of the second tooth, R: radius of the internal curvature of the gullet

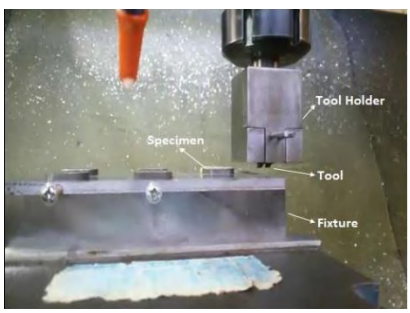

Figure 4. Broaching setup

2. 3. 1. Surface Roughness Analyze The surface roughness is measured at the center of each broached slot along the cutting direction using the contact method. Surface roughness measurements were done with a portable profilometer INNOVATEST® Model TR200 equipment. Table 4 indicates the conditions of surface roughness tests.

2. 3. 2. Residual Stresses Analyze The residual stresses were measured at the center of each broached slot using the X-Ray Diffraction (XRD) method via the $\sin 2\psi$ technique. Measurements of residual stress were performed with a HAOYUAN Model DX-2700BH. Tilting was done along the cutting direction. Poisson's ratio was assumed to be 0.342 and Young modulus 113.8 Gpa [19].

2. 3. 3. Microstructural Images Analyze Grinding of the Ti6Al4V samples were done using up to 2000 SiC

TABLE 4. Surface roughness measurement parameters

Cutoff	0.8 mm
Tracing length	4 mm
Radius of the probe tip	0.05 μm
Tracing speed	0.5 mm/s
Resolution	0.005 μm

grit paper. Then the samples polished by 3µm Al_2O_3 colloidal dispersion in distilled water. Finally, the polished samples were rinsed in distilled water and dried by a heater. To observe the microstructure of the samples, it is necessary to do chemical etching of the samples. Therefore, the specimens were reacted with an etchant (85% H_2O, 10%HF and 5%HNO_3) for 5 seconds. Then etched samples were washed in distilled water and then dried by a heater. The microstructure images were prepared by a UNION optical microscope and an scanning electron microscope Model JEOL840.

2. 3. 4. Micro Hardness Analyze Measurements of micro hardness were carried out using the Micromet 1 Buhler tester. The micro hardness test conditions are given in Table 5. Measurements were done on the middle line of the polished section surface of each. Indentations were made along a line consisted by six points, beginning the depth of 50 µm from the broached surface. The distance between two successive points kept enough to avoid measurement errors.

3. RESULTS AND DISCUSSION

3. 1. Surface Roughness The results of surface roughness measurements of the broached specimens are summarized in Table 6. As shown in Figures 5-7, the results of measuring the surface roughness of the broached specimens indicate that with an increase in r_0 (radius of the cutting edge of the second tooth) from 0.01 mm to 0.02 mm, the R_a and R_z of the broached surface decrease from 0.232 µm and 0.330 µm to 0.162 µm and 0.316 µm, respectively. An increase in the radius of the cutting edge reduces the penetration of the tool into the workpiece. As a result, the surface roughness is decreased. Also, with an increase in α_0 (second tooth rake angle) from 35 degrees to 45 degrees, the R_a and R_z of

TABLE 5. The micro hardness test conditions

Indenter	Force	Loading time
Diamond pyramid	100 grf	15 s

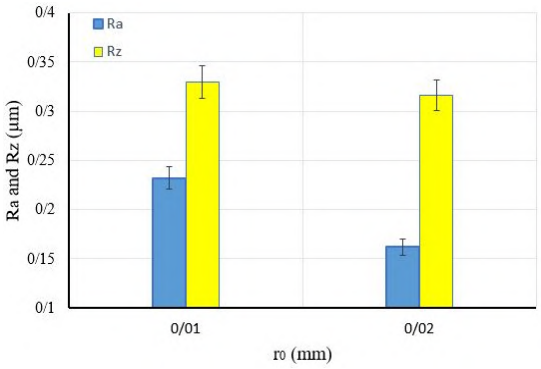

Figure 5. Effect of radius of cutting edge (r_0) on R_a and R_z

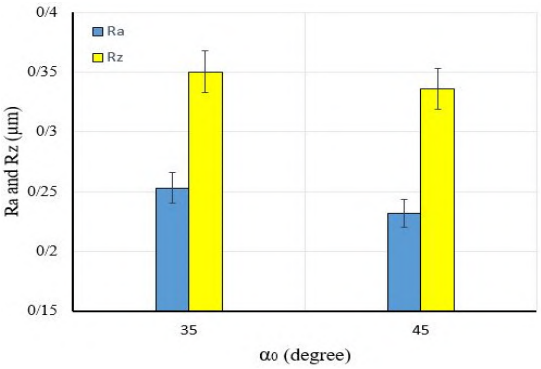

Figure 6. Effect of rake angle of the second tooth (α_0) on R_a and R_z

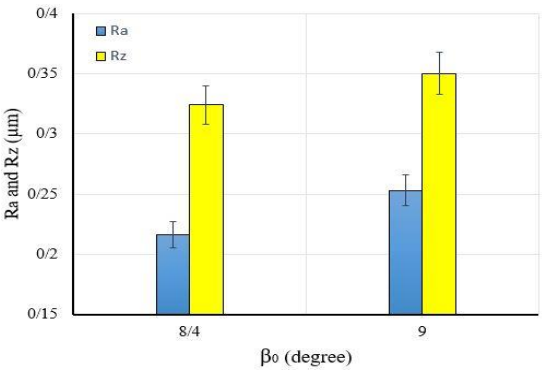

Figure 7. Effect of clearance angle of the second tooth (β_0) on R_a and R_z

TABLE 6. Surface roughness of specimens

Tool's No.	α	β	α_0	β_0	r_0 (mm)	Ra (µm)	Rz (µm)
1	18.4^0	3.1^0	45^0	9^0	0.02	0.162	0.316
2	18.4^0	3.1^0	45^0	9^0	0.01	0.232	0.330
3	18.4^0	3.1^0	35^0	9^0	0.01	0.253	0.350
4	18.4^0	3.1^0	35.4^0	8.2^0	0.01	0.342	0.387
5	18.4^0	3.1^0	35^0	8.4^0	0.01	0.216	0.324

the broached surface decrease from 0.253 µm and 350 µm to 0.232 µm and 0.336 µm, respectively. The cause of these changes can be found according Merchant circle (Figure 8) and Equations (1) and (2) in mechanic of orthogonal cutting [20].

$$F_c = \frac{tb\tau\cos(\beta-\alpha_0)}{\sin\emptyset\cos(\emptyset+\beta-\alpha_0)} \quad (1)$$

$$F_t = \frac{tb\tau\sin(\beta-\alpha_0)}{\sin\emptyset\cos(\emptyset+\beta-\alpha_0)} \quad (2)$$

where F_c is the cutting force, t is the thickness of chip before cutting, b is the cutting width, τ is the yield shear stress, β is the friction angle, α_0 is the rake angle, ϕ is the shear angle, and F_t is the thrust force [20]. Increasing α_0 reduces the thrust force and as a result, the surface roughness is decreased.

Moreover, with an increase in β_0 (clearance angle of the second tooth) from 8.4 degrees to 9 degrees, the R_a and R_z of the broached surface increase from 0.216 µm and 0.324 µm to 0.253 µm and 0.350 µm, respectively. Increasing β_0 reduces the contact of the tool with the workpiece surface. As a result, the surface roughness has increased.

3. 2. Residual Stresses The results of residual stress measurements of the broached specimens are shown in Table 7. In all cases, the residual stresses are compressive.

As shown in Figures 9-11, the results of measuring the residual stress of the broached specimens indicate that

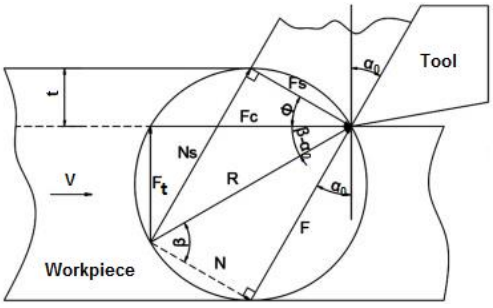

Figure 8. Merchant circle. F_c is the cutting force, t is the thickness of chip before cutting, β is the friction angle, α_0 is the rake angle, ϕ is the shear angle, and F_t is the thrust force [20].

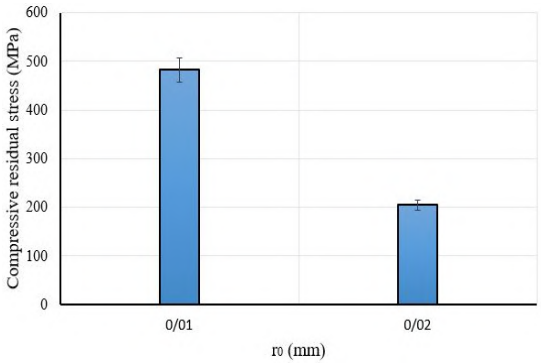

Figure 9. Effect of radius of the cutting edge (r_0) on residual stress

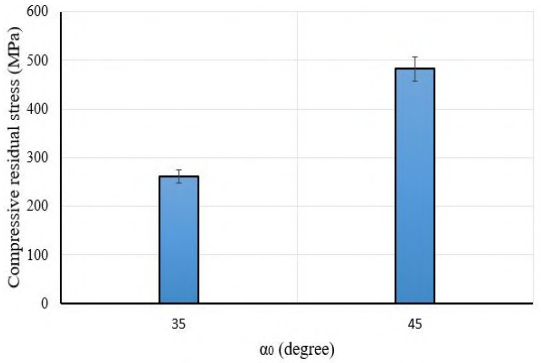

Figure 10. Effect of rake angle of the second tooth (α_0) on residual stress

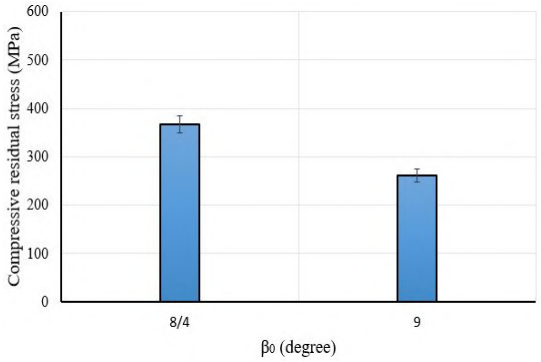

Figure 11. Effect of clearance angle of the second tooth (β_0) on residual stress

TABLE 7. Compressive residual stresses of specimens

Tool's No.	α	β	α_0	β_0	r_0 (mm)	Residual stress (MPa)
1	18.4^0	3.1^0	45^0	9^0	0.02	205
2	18.4^0	3.1^0	45^0	9^0	0.01	482
3	18.4^0	3.1^0	35^0	9^0	0.01	261
4	18.4^0	3.1^0	35.4^0	8.2^0	0.01	202
5	18.4^0	3.1^0	35^0	8.4^0	0.01	367

increasing r_0 (radius of the cutting edge of the second tooth) from 0.01 mm to 0.02 mm, causes a considerable decrease in the compressive residual stress created in the workpiece from 482 MPa to 205 MPa. Increasing the radius of the cutting edge reduces the penetration of the tool into the workpiece. As a result, reduces the residual stress created in broached surface.

Also, with increasing α_0 (rake angle of the second tooth) from 35 degrees to 45 degrees, the compressive residual stress created in the workpiece increases from 261 MPa to 482 MPa. Increasing α_0 increases the cutting force. As a result, the residual stress created in broached surface is increased. Moreover, with increasing β_0 (clearance angle of the second tooth) from 8.4 degrees to 9 degrees, the compressive residual stress created in the workpiece decreased from 367 MPa to 261 MPa. Increasing β_0 reduces the contact of the tool with the workpiece surface. As a result, the residual stress created in broached surface decreased.

3. 3. Microstructural Analysis Titanium alloys are classified according to the phases in their structure. Ti6Al4V alloy is the most important and widely used α+β titanium alloy. Aluminum and vanadium alloy elements are stabilizer of the alpha and beta phases, respectively. Figure 12 shows the phase diagram of Ti6Al4V [19]. Figure 13 depicts the microstructure of annealed material which contains a mixed α + β coaxial phase structure. The structure consists of α-shaped plates (light) and inter granular beta (dark). Figures 14-18 show the microstructure of the surface perpendicular to the broached surface of the test specimens.

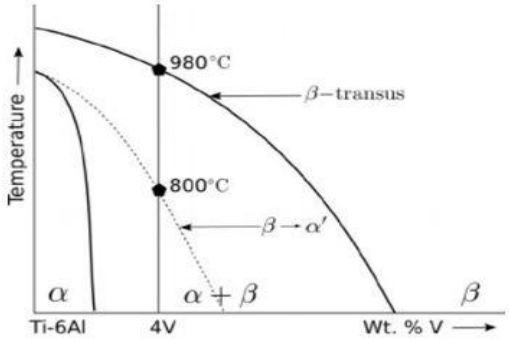

Figure 12. Phase diagram of Ti6Al4V [19]

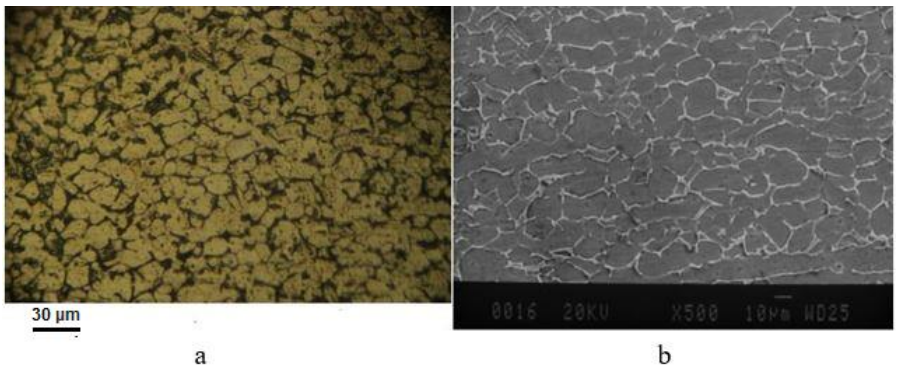

Figure 13. Microstructure of annealed Ti6Al4V (Etching solution: HF10%, HNO_3 5%, H_2O 85%). a) Imaging by optic microscope. The structure consists of α-shaped plates (light) and inter granular beta (dark). b) Imaging by scanning electron microscope (SEM). The structure consists of α-shaped plates (dark) and inter granular beta (light)

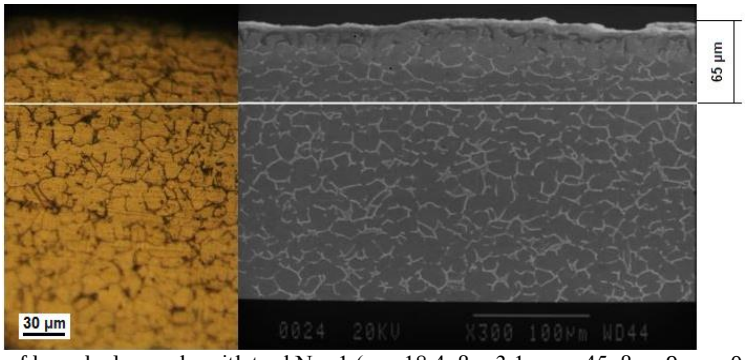

Figure 14. Microstructure of broached sample with tool No. 1 (α = 18.4, β = 3.1, α_0 = 45, β_0 = 9, r_0 = 0.02). The structure consists of α-shaped plates (light) and inter granular beta (dark). (Etching solution: HF10%, HNO_3 5%, H_2O 85%)

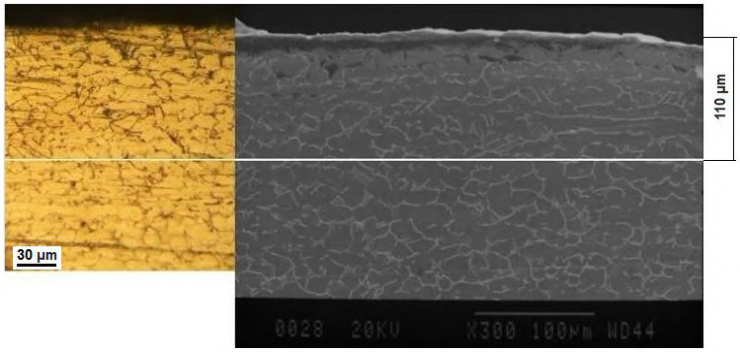

Figure 15. Microstructure of broached sample with tool No. 2 ($\alpha = 18.4$, $\beta = 3.1$, $\alpha_0 = 45$, $\beta_0 = 9$, $r_0 = 0.01$). The structure consists of α-shaped plates (light) and inter granular beta (dark). (Etching solution: HF10%, HNO_3 5%, H_2O 85%)

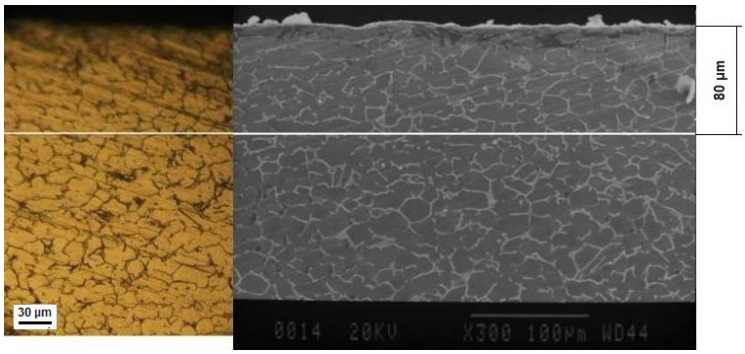

Figure 16. Microstructure of broached sample with tool No. 3 ($\alpha = 18.4$, $\beta = 3.1$, $\alpha_0 = 35$, $\beta_0 = 9$, $r_0 = 0.01$). The structure consists of α-shaped plates (light) and inter granular beta (dark). (Etching solution: HF10%, HNO_3 5%, H_2O 85%)

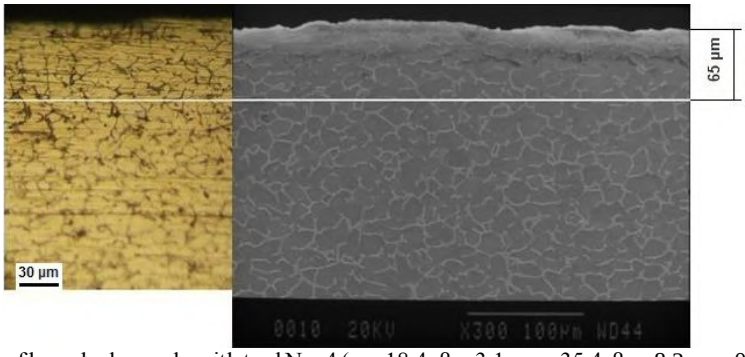

Figure 17. Microstructure of broached sample with tool No. 4 ($\alpha = 18.4$, $\beta = 3.1$, $\alpha_0 = 35.4$, $\beta_0 = 8.2$, $r_0 = 0.01$). The structure consists of α-shaped plates (light) and inter granular beta (dark). (Etching solution: HF10%, HNO_3 5%, H_2O 85%)

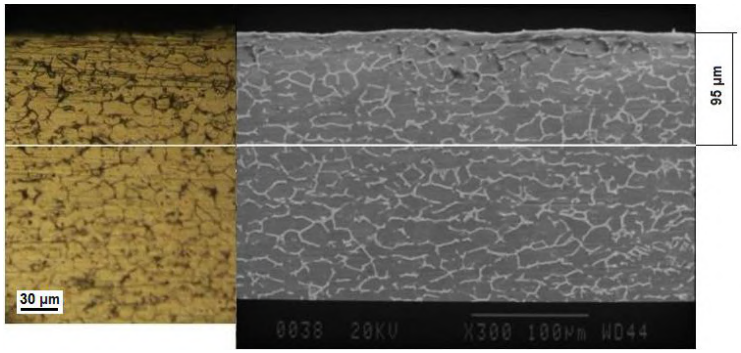

Figure 18. Microstructure of broached sample with tool No. 5 ($\alpha = 18.4$, $\beta = 3.1$, $\alpha_0 = 35$, $\beta_0 = 8.4$, $r_0 = 0.01$). The structure consists of α-shaped plates (light) and inter granular beta (dark). (Etching solution: HF10%, HNO_3 5%, H_2O 85%)

TABLE 8. The depth of deformed layer of broached specimens

Tool's No.	α	β	α_0	β_0	r_0 (mm)	Depth of deformed layer (μm)
1	18.4^0	3.1^0	45^0	9^0	0.02	65
2	18.4^0	3.1^0	45^0	9^0	0.01	110
3	18.4^0	3.1^0	35^0	9^0	0.01	80
4	18.4^0	3.1^0	35.4^0	8.2^0	0.01	65
5	18.4^0	3.1^0	35^0	8.4^0	0.01	95

As shown in Figures 14-18, in the thin layer below the broached surface, the grains are deformed perpendicular to the cutting direction. Comparing the microstructure of the broached specimens with the annealed specimen, despite the plastic deformation, no phase transformation can be detected; because of the cutting temperature is less than 800°C [18]. Table 8 summarized the results of the depth of deformed layer of broached specimens.

According to the Figures 19-21, the results of microstructural images of the broached specimens show that increasing r_0 (radius of the cutting edge of the second tooth) from 0.01 mm to 0.02 mm, causes a considerable decrease in the depth of the deformed layer in the broached specimen from 110 μm to 65 μm. Increasing the radius of the cutting edge reduces the penetration of the tool into the workpiece. As a result, the depth of the deformed layer reduced.

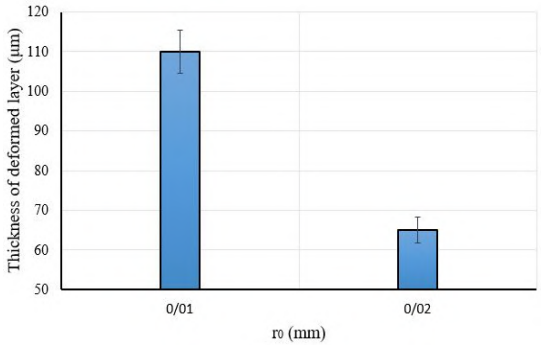

Figure 19. Effect of radius of the cutting edge (r_0) on the depth of the deformed layer

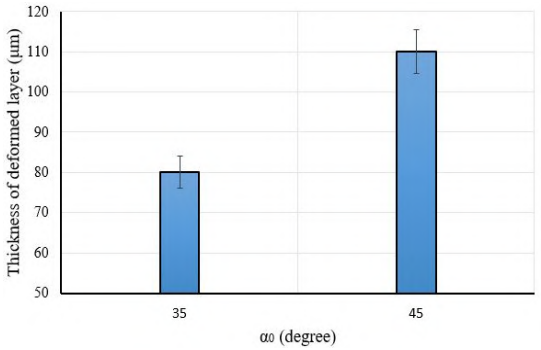

Figure 20. Effect of rake angle of the second tooth (α_0) on the depth of the deformed layer

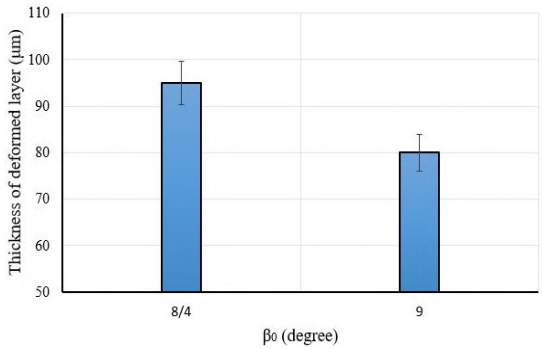

Figure 21. Effect of clearance angle of the second tooth (β_0) on the depth of the deformed layer

Also, with increasing α_0 (rake angle of the second tooth) from 35 degrees to 45 degrees, the depth of the deformed layer in the broached sample increases from 80 μm to 110 μm. Increasing α_0 increases the cutting force. As a result, the depth of the deformed layer is increased. Moreover, by increasing β_0 (clearance angle of the second tooth) from 8.4 degrees to 9 degrees, the depth of the deformed layer in the broached sample decreases from 95 μm to 80 μm. Increasing β_0 reduces the contact of the tool with the workpiece surface. As a result, the depth of deformed in workpiece decreased.

3. 4. Micro Hardness Profiles Figure 22 shows the effect of the geometric parameters of the tool on the micro hardness profiles of the broached specimens. These results show that the micro hardness of the samples increases at the broached surface and gradually decreases with an increase in the distance from the surface. Table 9 shows the maximum micro hardness of broached specimens.

According to Figures 23-25, the micro hardness measurement results of the broached workpieces show that increasing r_0 (radius of the cutting edge of the second tooth) from 0.01 mm to 0.02 mm, decreases the maximum micro hardness created in the workpiece from 401 Vickers to 380 Vickers. Increasing the radius of the cutting edge reduces the penetration of the tool into the

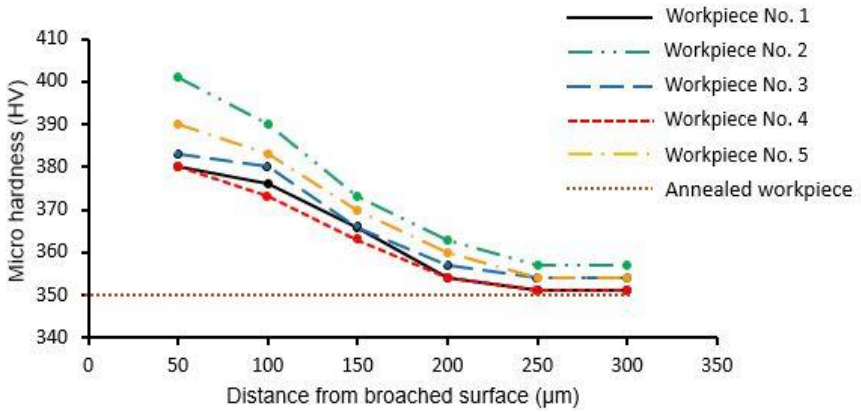

Figure 22. The micro hardness profiles of the broached samples

TABLE 9. The maximum micro hardness of workpieces

Tool's No.	α	β	α_0	β_0	r_0(mm)	Maximum micro hardness (HV)
1	18.4^0	3.1^0	45^0	9^0	0.02	380
2	18.4^0	3.1^0	45^0	9^0	0.01	401
3	18.4^0	3.1^0	35^0	9^0	0.01	383
4	18.4^0	3.1^0	35.4^0	8.2^0	0.01	380
5	18.4^0	3.1^0	35^0	8.4^0	0.01	390

workpiece. As a result, reduces the strain hardening in the broached workpiece. Also, by increasing α_0 (angle of the second tooth chip) from 35 degrees to 45 degrees, the maximum micro hardness created in the workpiece has increased from 383 Vickers to 401 Vickers. Increasing α_0 increases the cutting force. As a result, strain hardening in the broached workpiece increased.

Moreover, by increasing β_0 (clearance angle of the second tooth) from 8.4 degrees to 9 degrees, the maximum micro hardness created in the workpiece decreased from 390 Vickers to 383 Vickers. Increasing β_0 reduces the contact of the tool with the workpiece surface. As a result, the strain hardening in the broached workpiece decreased.

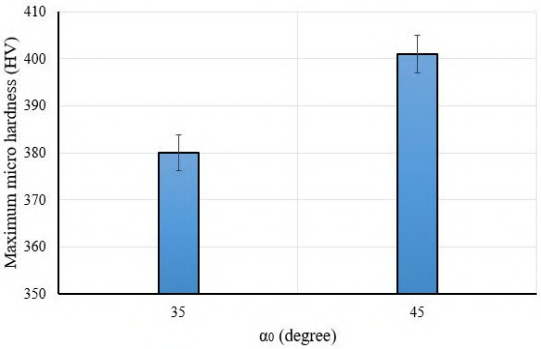

Figure 24. Effect of the rake angle (α_0) on the maximum micro hardness of broached specimens

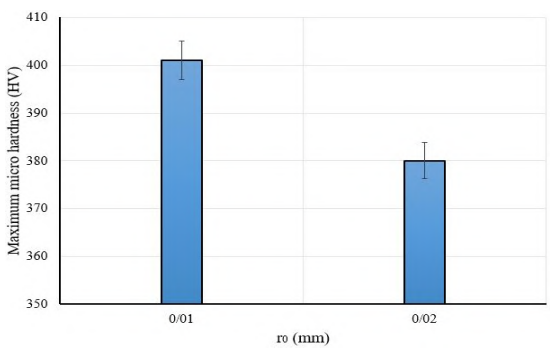

Figure 23. Effect of radius of the cutting edge (r_0) on the maximum micro hardness of broached specimens

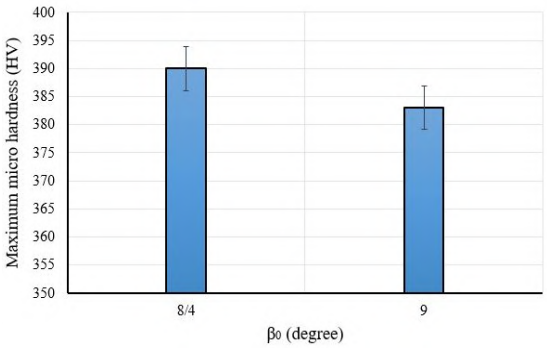

Figure 25. Effect of the clearance angle (β_0) on the maximum micro hardness of broached specimens

The results of the surface integrity investigation of broached samples are shown in Table 10. These results show that the sample broached by tool number 1(α = 18.4, β = 3.1, α_0 = 45, β_0 = 9, r_0 = 0.02) has higher surface integrity because it has the smoothest surface and the thinest deformed layer, is less thick than the other samples. Since the main criterions in selecting the optimal tool are to create the smoothest surface and the least deformed layer depth in the broached sample, tool number 1(α = 18.4, β = 3.1, α_0 = 45, β_0 = 9, r_0 = 0.02) is suggested as the optimal tool.

TABLE 10. Results of the surface integrity investigation of broached samples

Tool's No.	Ra (µm)	Rz (µm)	Residual stress (MPa)	Depth of deformed layer (µm)	Maximum micro hardness (HV)
1	0.162	0.316	205	65	380
2	0.232	0.330	482	110	401
3	0.253	0.350	261	80	383
4	0.342	0.387	202	65	380
5	0.216	0.324	367	95	390

4. CONCLUSION

This study investigates the surface integrity of Ti6Al4V by broaching. The different surface integrity aspects including: surface roughness, residual stress, microstructural, and micro hardness, are investigated.

- The results of measuring the surface roughness of the broached specimens indicate that an increase in r_0 (radius of the cutting edge of the second tooth) from 0.01 mm to 0.02 mm, decrease the R_a and R_z of the broached surface from 0.232 µm and 0.330 µm to 0.162 µm and 0.316 µm, respectively. Increasing the radius of the cutting edge reduces the penetration of the tool into the workpiece. As a result, reduces the residual stress created in broached surface. Also, with increasing α_0 (rake angle of the second tooth) from 35 degrees to 45 degrees, the R_a and R_z of the broached surface decrease from 0.253 µm and 0.350 µm to 0.232 µm and 0.336 µm, respectively. Increasing α_0 reduces the thrust force and as a result, the surface roughness is decreased. Moreover, with increasing β_0 (clearance angle of the second tooth) from 8.4 degrees to 9 degrees, the R_a and R_z of the broached surface increase from 0.216 µm and 0.324 µm to 0.253 µm and 0.350 µm, respectively. Increasing β_0 reduces the contact of the tool with the workpiece surface. As a result, the surface roughness increased.
- The results of measuring the residual stress of the broached specimens indicate that increasing r_0 (radius of the cutting edge of the second tooth) from 0.01 mm to 0.02 mm, causes a considerable decrease in the compressive residual stress created in the work piece from 482 MPa to 205 MPa. Increasing the radius of the cutting edge reduces the penetration of the tool into the work piece. As a result, reduces the residual stress created in broached surface. Also, with increasing α_0 (rake angle of the second tooth) from 35 degrees to 45 degrees, the compressive residual stress created in the work piece increases from 261 MPa to 482 MPa. Increasing α_0 increases the cutting force. As a result, the residual stress created in broached surface is increased. Moreover, with increasing β_0 (clearance angle of the second tooth) from 8.4 degrees to 9 degrees, compressive residual stress created in the work piece decreases from 367 MPa to 261 MPa. Increasing β_0 reduces the contact of the tool with the work piece surface. As a result, the residual stress created in broached surface decreased.
- The results of microstructural images of the broached specimens show that increasing r_0 (radius of the cutting edge of the second tooth) from 0.01 mm to 0.02 mm, causes a considerable decrease in the depth of the deformed layer in the broached specimen from 110 µm to 65 µm. Increasing the radius of the cutting edge reduces the penetration of the tool into the work piece. As a result, reduces the depth of the deformed layer. Also, with increasing α_0 (rake angle of the second tooth) from 35 degrees to 45 degrees, the depth of the deformed layer in the broached sample increases from 80 µm to 110 µm. Increasing α_0 increases the cutting force. As a result, the depth of the deformed layer is increased. Moreover, by increasing β_0 (clearance angle of the second tooth) from 8.4 degrees to 9 degrees, the depth of the deformed layer in the broached sample decreases from 95 µm to 80 µm. Increasing β_0 reduces the contact of the tool with the workpiece surface. As a result, the depth of deformed in workpiece decreased.
- The micro hardness measurements results of the broached workpieces show that increasing r_0 (radius of the cutting edge of the second tooth) from 0.01 mm to 0.02 mm, decreases the maximum micro hardness created in the workpiece from 401 Vickers to 380 Vickers. Also, with increasing α_0 (rake angle of the second tooth) from 35 degrees to 45 degrees, the maximum micro hardness created in the workpiece has increased from 383 Vickers to 401 Vickers. Increasing α_0

increases the cutting force. As a result, strain hardening in the broached workpiece is increased. Moreover, by increasing β_0 (clearance angle of the second tooth) from 8.4 degrees to 9 degrees, the maximum micro hardness created in the workpiece decreases from 390 Vickers to 383 Vickers. Increasing β_0 reduces the contact of the tool with the workpiece surface. As a result, the strain hardening in the broached work piece decreased.

- These results show that the sample broached by tool number 1(α = 18.4, β = 3.1, α_0 = 45, β_0 = 9, r_0 = 0.02) has higher surface integrity because it has the smoothest surface and the thinnest deformed layer among the other samples. Since the main criterions in selecting the optimal tool are to create the smoothest surface and the least deformed layer depth in the broached sample, tool number 1(α = 18.4, β = 3.1, α_0 = 45, β_0 = 9, r_0 = 0.02) is suggested as the optimal tool.

5. REFERENCES

1. DeGarmo, E., Black, J., and Kohser, R. DeGarmo's materials and processes in manufacturing. John Wiley & Sons.
2. Bordin, A., Sartori, S., Bruschi, S., and Ghiotti, A. "Experimental investigation on the feasibility of dry and cryogenic machining as sustainable strategies when turning Ti6Al4V produced by Additive Manufacturing." ***Journal of Cleaner Production***, Vol. 142, (2017), 4142–4151. https://doi.org/10.1016/j.jclepro.2016.09.209
3. Bruschi, S., Bertolini, R., Bordin, A., Medea, F., and Ghiotti, A. "Influence of the machining parameters and cooling strategies on the wear behavior of wrought and additive manufactured Ti6Al4V for biomedical applications." ***Tribology International***, Vol. 102, (2016), 133–142. https://doi.org/10.1016/j.triboint.2016.05.036
4. Davim, J. P. Machining: fundamentals and recent advances. London: Springer Science & Business Media, 2008. https://doi.org/10.1007/978-1-84800-213-5
5. Davim, J. Surface integrity in machining. Springer Science & Business Media, 2010. Retrieved from https://link.springer.com/content/pdf/10.1007/978-1-84882-874-2.pdf
6. Ulutan, D., and Ozel, T. "Machining induced surface integrity in titanium and nickel alloys: A review." ***International Journal of Machine Tools and Manufacture***, Vol. 51, No. 3, (2011), 250–280. https://doi.org/10.1016/j.ijmachtools.2010.11.003
7. Novovic, D., Dewes, R. C., Aspinwall, D. K., Voice, W., and Bowen, P. "The effect of machined topography and integrity on fatigue life." ***International Journal of Machine Tools and Manufacture***, Vol. 44, No. 2–3, (2004), 125–134. https://doi.org/10.1016/j.ijmachtools.2003.10.018
8. Liao, Z., la Monaca, A., Murray, J., Speidel, A., Ushmaev, D., Clare, A., Axinte, D., and M'Saoubi, R. "Surface integrity in metal machining - Part I: Fundamentals of surface characteristics and formation mechanisms." ***International Journal of Machine Tools and Manufacture***, Vol. 162, (2021), 103687. https://doi.org/10.1016/j.ijmachtools.2020.103687
9. He, G., and Zhang, Y. Z. "Experimental Investigations of the Surface Integrity of Broached Titanium Alloy." ***CIRP Annals***, Vol. 34, No. 1, (1985), 491–494. https://doi.org/10.1016/S0007-8506(07)61818-6
10. Schulze, V., Osterried, J., and Strauß, T. "FE analysis on the influence of sequential cuts on component conditions for different machining strategies." ***Procedia Engineering***, Vol. 19, (2011), 318–323. https://doi.org/10.1016/j.proeng.2011.11.119
11. Kong, X., Li, B., Jin, Z., and Geng, W. "Broaching Performance of Superalloy GH4169 Based on FEM." ***Journal of Materials Science & Technology***, Vol. 27, No. 12, (2011), 1178–1184. https://doi.org/10.1016/S1005-0302(12)60015-2
12. Jafarian, F., Amirabadi, H., and Fattahi, M. "Improving surface integrity in finish machining of Inconel 718 alloy using intelligent systems." ***The International Journal of Advanced Manufacturing Technology***, Vol. 71, No. 5–8, (2014), 817–827. https://doi.org/10.1007/s00170-013-5528-2
13. Jafarian, F., Amirabadi, H., and Sadri, J. "Experimental measurement and optimization of tensile residual stress in turning process of Inconel718 superalloy." ***Measurement***, Vol. 63, , (2015), 1–10. https://doi.org/10.1016/j.measurement.2014.11.021
14. Ortiz-de-Zarate, G., Madariaga, A., Garay, A., Azpitarte, L., Sacristan, I., Cuesta, M., and Arrazola, P. J. "Experimental and FEM analysis of surface integrity when broaching Ti64." ***Procedia CIRP***, Vol. 71, (2018), 466–471. https://doi.org/10.1016/j.procir.2018.05.033
15. Kaway, P. K., and Zhang, X. "Experimental Study on Surface Integrity of Titanium Alloy Ti6Al4V by Ball End Milling" ***Journal of the Institute of Engineering***, Vol. 14, No. 1, (2018), 115–121. https://doi.org/10.3126/jie.v14i1.20074
16. Childs, T. H. C., Arrazola, P.-J., Aristimuno, P., Garay, A., and Sacristan, I. "Ti6Al4V metal cutting chip formation experiments and modelling over a wide range of cutting speeds." ***Journal of Materials Processing Technology***, Vol. 255, (2018), 898–913. https://doi.org/10.1016/j.jmatprotec.2018.01.026
17. Bertolini, R., Lizzul, L., Bruschi, S., and Ghiotti, A. "On the surface integrity of Electron Beam Melted Ti6Al4V after machining." ***Procedia CIRP***, Vol. 82, (2019), 326–331. https://doi.org/10.1016/j.procir.2019.04.166
18. Khanjanzadeh, P., Amirabadi, H., and Sadri, J. "Design of Broaching Tool Using Finite Element Method for Achieving the Lowest Residual Tensile Stress in Machining of Ti6Al4V Alloy." ***International Journal of Engineering, Transaction A: Basics***, Vol. 33, No. 4, (2020), 557–567. https://doi.org/10.5829/ije.2020.33.04a.17
19. Lampman, S. "Wrought Titanium and Titanium Alloys." In Properties and Selection: Nonferrous Alloys and Special-Purpose Materials (pp. 592–633). ASM International. https://doi.org/10.31399/asm.hb.v02.a0001081
20. Groover, M. Fundamentals of modern manufacturing: materials, processes, and systems. John Wiley & Song.

Persian Abstract

چکیده

کارآیی بسیاری از قطعات هواپیما، موتور فضاپیما و ایمپلنت های پزشکی به شدت با عمر خستگی آنها مرتبط بوده و بالطبع به وضعیت یکپارچگی سطح آنها، بستگی دارد. پارامترهای هندسی ابزار خانکشی تاثیر زیادی بر یکپارچگی سطح آلیاژ Ti6Al4V خانکشی‌شده دارند. این تحقیق، یکپارچگی سطح آلیاژ Ti6Al4V خانکشی‌شده را مورد مطالعه قرار داده است. تاثیر پارامترهای هندسی ابزار شامل زاویه براده (α و α_0) ، زاویه آزاد (β و β_0) و شعاع نوک ابزار (r_0) در دو دندانه انتهایی ابزار خانکشی که براده برداری را انجام می‌دهند، بر روی یکپارچگی سطح آلیاژ Ti6Al4V خانکشی‌شده به طور تجربی، مورد بررسی واقع شده است. یکپارچگی سطح خانکشی‌شده در موارد صافی سطح، تنش باقیمانده، ریزساختار و میکروسختی، بررسی و ارزیابی شده است. مجموعه نتایج بدست‌آمده نشان می‌دهد که نمونه خانکشی‌شده توسط ابزار شمار ۱ ($\alpha = 18.4°, \beta = 3.1°, \alpha_0 = 45°, \beta_0 = 9°, r_0 = 0.02mm$)، به دلیل دارا بودن صافترین سطح و کمترین لایه تغییر فرم یافته در بین نمونه‌های آزمایشی، از مناسب‌ترین یکپارچگی سطح برخوردار است. از آنجا که معیارهای اصلی در انتخاب ابزار بهینه، ایجاد صافترین سطح و کمترین ضخامت لایه تغییر فرم یافته در نمونه خانکشی‌شده می‌باشد، ابزار شماره ۱ ($\alpha = 18.4°, \beta = 3.1°, \alpha_0 = 45°, \beta_0 = 9°, r_0 = 0.02mm$) به عنوان ابزار بهینه پیشنهاد شده است.

AIMS AND SCOPE

The objective of the International Journal of Engineering is to provide a forum for communication of information among the world's scientific and technological community and Iranian scientists and engineers. This journal intends to be of interest and utility to researchers and practitioners in the academic, industrial and governmental sectors. All original research contributions of significant value focused on basics, applications and aspects areas of engineering discipline are welcome.

This journal is published in three quarterly transactions: Transactions A (Basics) deal with the engineering fundamentals, Transactions B (Applications) are concerned with the application of the engineering knowledge in the daily life of the human being and Transactions C (Aspects) - starting from January 2012 - emphasize on the main engineering aspects whose elaboration can yield knowledge and expertise that can equally serve all branches of engineering discipline.

This journal will publish authoritative papers on theoretical and experimental researches and advanced applications embodying the results of extensive field, plant, laboratory or theoretical investigation or new interpretations of existing problems. It may also feature - when appropriate - research notes, technical notes, state-of-the-art survey type papers, short communications, letters to the editor, meeting schedules and conference announcements. The language of publication is English. Each paper should contain an abstract both in English and in Persian. However, for the authors who are not familiar with Persian, the publisher will prepare the latter. The abstracts should not exceed 250 words.

All manuscripts will be peer-reviewed by qualified reviewers. The material should be presented clearly and concisely:

- *Full papers* must be based on completed original works of significant novelty. The papers are not strictly limited in length. However, lengthy contributions may be delayed due to limited space. It is advised to keep papers limited to 7500 words.
- *Research* notes are considered as short items that include theoretical or experimental results of immediate current interest.
- *Technical notes* are also considered as short items of enough technical acceptability with more rapid publication appeal. The length of a research or technical note is recommended not to exceed 2500 words or 4 journal pages (including figures and tables).

Review papers are only considered from highly qualified well-known authors generally assigned by the editorial board or editor in chief. Short communications and letters to the editor should contain a text of about 1000 words and whatever figures and tables that may be required to support the text. They include discussion of full papers and short items and should contribute to the original article by providing confirmation or additional interpretation. Discussion of papers will be referred to author(s) for reply and will concurrently be published with reply of author(s).

INSTRUCTIONS FOR AUTHORS

Submission of a manuscript represents that it has neither been published nor submitted for publication elsewhere and is result of research carried out by author(s). Presentation in a conference and appearance in a symposium proceeding is not considered prior publication.

Authors are required to include a list describing all the symbols and abbreviations in the paper. Use of the international system of measurement units is mandatory.

- On-line submission of manuscripts results in faster publication process and is recommended. Instructions are given in the IJE web sites: www.ije.ir-www.ijeir.info
- Hardcopy submissions must include MS Word and jpg files.
- Manuscripts should be typewritten on one side of A4 paper, double-spaced, with adequate margins.
- References should be numbered in brackets and appear in sequence through the text. List of references should be given at the end of the paper.
- Figure captions are to be indicated under the illustrations. They should sufficiently explain the figures.
- Illustrations should appear in their appropriate places in the text.
- Tables and diagrams should be submitted in a form suitable for reproduction.
- Photographs should be of high quality saved as jpg files.
- Tables, Illustrations, Figures and Diagrams will be normally printed in single column width (8cm). Exceptionally large ones may be printed across two columns (17cm).

PAGE CHARGES AND REPRINTS

The papers are strictly limited in length, maximum 6 journal pages (including figures and tables). For the additional to 6 journal pages, there will be page charges. It is advised to keep papers limited to 3500 words.

Page Charges for Papers More Than 6 Pages (Including Abstract)	
For International Author ***	**$55 / per page**
For Local Author	**100,000 Toman / per page**

AUTHOR CHECKLIST

- Author(s), bio-data including affiliation(s) and mail and e-mail addresses).
- Manuscript including abstracts, key words, illustrations, tables, figures with figure captions and list of references.
- MS Word files of the paper.

International **J**ournal of **E**ngineering, P.O. Box 13145-1659, Tehran, I.R. Iran
Materials and Energy Research Center, 5 Ahuramazda St., Alvand Ave., Argentina Sq., Tehran, Islamic Republic of Iran
www.merc.ac.ir - www.emerc.ac.ir

THOMSON REUTERS

WEB OF SCIENCE

Scopus®

CAS®
A DIVISION OF THE
AMERICAN CHEMICAL SOCIETY

Google
Scholar